High temperature fatigue crack growth modeling in Nickel-based superalloys using a local approach to fracture

Olivier Voreux

université PARIS-SACLAY

High temperature fatigue crack growth modeling in Nickel-based superalloys using a local approach to fracture

Modélisation de la propagation de fissure en fatigue à haute température dans les superalliages base Nickel par une approche locale de la rupture

Thèse de doctorat de l'Université Paris-Saclay

École doctorale n°579, sciences mécaniques et énergétiques, matériaux et géosciences (SMEMaG)
Spécialité de doctorat: Mécanique des matériaux
Graduate School : Sciences de l'ingénierie et des systèmes
Référent: ENS Paris-Saclay

Thèse préparée dans l'unité de recherche Matériaux et Structures (Université Paris-Saclay, ONERA), sous la direction de Serge KRUCH, Directeur de Recherche, le co-encadrement de Sylvia FELD-PAYET, Ingénieure de Recherche et de Pascale KANOUTE, Ingénieure de Recherche, et la co-supervision de Noémie RAKOTOMALALA, Ingénieure de Recherche (Safran Tech).

Thèse soutenue à l'ONERA Châtillon, le 31 mai 2022, par

Olivier VOREUX

Composition du jury

Véronique LAZARUS Professeure, ENSTA Paris	Présidente du jury
Pierre-Olivier BOUCHARD Professeur, CEMEF Sophia Antipolis, Mines ParisTech	Rapporteur
Bruno MICHEL HDR, Directeur de Recherche, CEA Cadarache, DEN/DEC	Rapporteur
Jacques BESSON Directeur de Recherche CNRS, Centre des Matériaux, Mines ParisTech	Examinateur
Sylvia FELD-PAYET Ingénieure de Recherche, ONERA, MAS	Examinatrice
Pascale KANOUTE Ingénieure de Recherche, ONERA, MAS	Examinatrice
Arjen ROOS HDR, Ingénieur de Recherche, Safran Tech	Examinateur
Serge KRUCH HDR, Directeur de Recherche, ONERA, MAS	Directeur de thèse

THESE DE DOCTORAT
NNT : 2022UPAST059

This research project has been carried out at the ONERA - The French Aerospace Lab in the "Materials and Structures" department with the financial support of Safran Group.

The Ph.D. project has been prepared at the École Normale Supérieure Paris-Saclay, part member of the Graduate School "Engineering and Systems Sciences".

Olivier VOREUX

"*High temperature fatigue crack growth modeling in Nickel-based superalloys using a local approach to fracture*".

This thesis was prepared with LaTeX and compiled with *pdfLaTeX*.

Printed in June 2022 by the ONERA - The French Aerospace Lab, Châtillon, France.

À ma famille.

Always keep your ego in check and not be afraid to listen.
Listening is a great art form.

Clint EASTWOOD

Remerciements

L'expérience d'une thèse touche à sa fin lorsqu'on en est à rédiger ces mots. Bien que déjà suffisamment conséquent, je ne pouvais achever ce document sans remercier les parties prenantes de ce projet, car je ne l'ai pas mené seul, bien au contraire.

Je commencerai donc ces quelques lignes par des remerciements relativement "formels".
Les travaux de recherche associés à cette thèse ont été réalisés à l'ONERA - l'Office National d'Etudes et Recherches Aérospatiales de Châtillon. Je tiens en tout premier lieu à remercier la Direction Scientifique Générale de l'ONERA, ainsi que le Département Matériaux et Structures, pour leur confiance et leur soutien dans la réalisation de ce projet de thèse.
Le financement étant mixte, mes sincères remerciements reviennent également au groupe Safran pour la confiance également témoignée à mon égard.
La matière première associée au volet expérimental de cette thèse, à savoir des bruts de forge d'AD730™, a été fournie par l'industriel Aubert & Duval. Par ces mots, je les remercie pour cet approvisionnement matière qui est venu enrichir le périmètre de ma thèse par le biais de l'étude d'un nouveau matériau probablement en vol d'ici quelques années.

J'en viens maintenant à mes ressentis post-thèse et aux remerciements plus "personnels".
De manière générale, l'expérience d'une thèse de doctorat en sciences "marque" la vie de celui qui s'y engage. Certes sanctionnée par un diplôme, cette expérience marque la transition parfaite entre la vie étudiante et le parcours professionnel d'un jeune chercheur. Il n'en demeure pas moins que la transition ne se fait pas en douceur car le chemin peut s'avérer long, tortueux et plein d'embûches. Il faut donc faire preuve d'abnégation, d'enthousiasme et de persévérance pour venir à bout d'un tel projet. Cela reste néanmoins une expérience très enrichissante car elle permet d'éprouver son opiniâtreté, son autonomie et de développer des compétences personnelles indéniables. Plus largement, et bien que comportant un large spectre relevant du "solitaire", la thèse permet de s'ouvrir aux autres, ingénieurs, chercheurs et techniciens d'horizons différents.
Je pense que bon nombre de thésards se retrouveront dans ces mots : on pense souvent, au point de départ, que trois ans c'est long... mais finalement cela passe très vite ! A condition d'être bien occupé, autonome et de parcourir le sujet de thèse dans son intégralité (même s'il faut en laisser pour les études à venir...).

Je tiens vivement à remercier mes deux rapporteurs : Pierre-Olivier BOUCHARD et Bruno MICHEL. Vous choisir comme rapporteurs pour ce travail m'a (nous a) semblé cohérent avec la thématique et les intérêts scientifiques mutuels. Pierre-Olivier, nous avons eu l'occasion de nous croiser lors d'évènements scientifiques : le GT PMMER à l'Ecole des Mines (en tout début de thèse) en 2017, lors du colloque MécaMat à Aussois sur *l'endommagement et la rupture* en 2019, ainsi qu'au congrès CFRAC à Braunschweig en 2019. Bruno, nous avons également longuement discuté autour de mon poster lors du colloque MécaMat à Aussois en 2020 sur les *contraintes*

résiduelles. Vos deux noms n'étaient donc pas que de simples "références" mais plutôt des "pièces du puzzle" qui constitue mon doctorat. Avant toute chose, merci à vous pour votre présence à ma soutenance. Après deux années compliquées sur le plan sanitaire sur fond de pandémie liée à la Covid-19, il est bien plus gratifiant de présenter et soutenir ses travaux de thèse devant un auditoire plutôt que face à son ordinateur doté d'une caméra... La symbolique de la soutenance a ainsi retrouvé sa place, pour le plaisir de tous. Merci également pour votre investissement, votre patience pour parcourir le (long) manuscrit (soulignons le !) et pour la qualité de vos rapports. Ceux-ci, très détaillés, m'ont permis de prendre de la hauteur sur mon travail et ont mis en évidence (et conforté) les limites de cette étude, déjà pressenties en interne. Il est toujours bénéfique d'avoir des avis extérieurs et objectifs sur son travail de thèse, et vos rapports m'ont permis de m'émanciper petit à petit de ce travail. Je vous remercie également pour la pertinence de vos questions lors de la soutenance. Votre expertise respective est largement ressortie au travers de nos discussions, et je pense que les points abordés aideront à la mise en place d'axes de poursuite de mon travail.

Ma gratitude revient également à mes trois examinateurs pour leur participation à ce jury : Véronique LAZARUS, Jacques BESSON et Arjen ROOS.
Véronique d'abord, qui m'a fait l'honneur de présider mon jury de thèse. Merci pour cette tâche pas toujours évidente et qui a été rondement bien menée : les débats ont été nombreux et chacun a pu s'exprimer sur des points particuliers de la thèse, ce qui a montré la richesse des profils de ce jury. Jacques, merci à toi pour tes nombreux conseils avisés durant nos fameuses réunions "Erode" avec Sylvia, Amar, Éric, Thomas... Ces points d'avancement réguliers nous ont permis à Amar et moi de converger vers des solutions communes pour mener à bien nos travaux respectifs. Merci pour ta sympathie, ton écoute et ta disponibilité à tout instant. Bien que sous-entendue depuis quelques temps, ta participation à mon jury m'a beaucoup touché. Merci à toi d'avoir suivi cette soutenance malgré la distance géographique ce 31 mai dernier.
Enfin, Arjen, mes remerciements sont doubles. J'ai d'abord eu l'occasion de te côtoyer à l'UTT lorsque j'étais étudiant (au même titre que Pascale, j'y reviendrai...). Merci pour ces enseignements que j'ai pu recevoir de toi. Je garde un souvenir de quelqu'un de pédagogue, attentif, et disponible. Ensuite, bien que je t'ai fait faux bond pour la thèse à l'UTT avec Benoît PANICAUD et Emmanuelle ROUHAUD, j'ai eu l'occasion de te retrouver au sein de Safran Tech où tu as été mon référent en tant que chef de l'équipe *Computational Solid Mechanics*. Cette thèse n'aurait pu se faire sans le soutien financier du groupe SAFRAN, merci encore. A chacune de mes venues à Magny-les-Hameaux, tu m'as toujours réservé le meilleur accueil possible et ton enthousiasme tout au long de cette thèse a toujours été porteur. Merci encore à ton (ancienne) équipe pour les échanges que nous avons pu avoir et merci à toi pour la pertinence de tes remarques sur mon travail.

Ces mots font la transition parfaite vers des remerciements à destination du corps enseignant de l'UTT. Merci à Khémaïs SAANOUNI d'avoir accepté de participer à mon jury de thèse en première année. Merci pour les remarques constructives et avisées sur mes travaux préliminaires. L'expertise certaine que vous avez pu acquérir au travers de vos travaux sur la mécanique de l'endommagement a permis de mettre en avant des points de réflexion sur mes propres travaux.
Enfin, plus globalement au LASMIS et au GAMMA3 de l'UTT, je remercie chaleureusement mes principaux enseignants : Emmanuelle ROUHAUD, Carl LABERGERE, Benoît PANICAUD, Pascal LAFON, Delphine RETRAINT, Manuel FRANCOIS, Houssem BADREDDINE, Houman BOROUCHAKI, Laurence MOREAU, Léa LE JONCOUR, Guillaume MONTAY, Xiao-Lu GONG,

Zhidan SUN... Merci à eux pour les enseignements qu'ils m'ont donnés en mécanique et matériaux. Ces enseignements ont façonné le socle scientifique sur lequel j'ai pu construire mes travaux de thèse. Je garde un excellent souvenir de mes années d'étude avec vous tous et de l'interaction que nous avons pu avoir en cours.

Comme souligné en préambule de ce document, cette thèse a été suivie par l'école doctorale SMEMaG, rattachée à l'ENS Paris-Saclay. Je remercie chaleureusement Olivier HUBERT son directeur pour son accompagnement, sa confiance et les interactions que nous avons pu avoir au sein du Conseil de l'Ecole Doctorale dans lequel j'ai siégé 1 année en tant que représentant des doctorants. Je remercie également Elodie HUDIK et Nathalie CORNAY pour leur support administratif tout au long de ce parcours.

La réussite de ce projet revient enfin et surtout à l'accompagnement de mon équipe de thèse : Serge KRUCH, Sylvia FELD-PAYET, Pascale KANOUTE et Noémie RAKOTOMALALA.

Serge, discret mais pour autant très présent. Je ne sais comment te remercier pour ce que tu m'as transmis, et surtout pour ta gentillesse du quotidien. Tu as été un directeur de thèse prévenant et attentif, ce que j'ai apprécié tout au long de ces années. Tu m'as laissé une part d'autonomie tout en gardant un œil avisé sur mes choix. Je te remercie pour les retours que tu as pu me faire sur mon travail et surtout pour la persévérance dont tu as su faire preuve face aux longs chapitres de ma thèse que je t'ai soumis pour corrections. Merci pour ta confiance dans ce projet et pour les conseils que tu as pu m'apporter. Ton recul certain sur les travaux de l'équipe (et plus largement du département) est d'une grande valeur pour les études en cours et celles à venir.

Sylvia, un grand merci pour ton aide, surtout sur la dernière année en lien avec les développements numériques. Tu as su m'aiguiller dans les difficultés, tu as proposé une solution alternative lorsque la chaîne de calcul ne fonctionnait pas, tu es restée vigilante et à l'écoute, je t'en suis infiniment reconnaissant. J'ai eu du mal à synthétiser mes idées et mes résultats alors que tu as maintes fois tenté de m'inculquer la bonne méthode. J'espère avoir atteint cet objectif désormais. Merci pour ta gentillesse et ton optimisme. Tu as su me remotiver lorsque j'étais dubitatif (voire carrément démotivé). Tes qualités humaines et professionnelles font de toi une future directrice de thèse en devenir... ! Enfin, merci pour ton initiation récente au yoga. Je ne doute pas d'en tirer des bénéfices sur le plan personnel.

Pascale, notre parcours est le plus ancien parmi ceux cités dans ces lignes. Initialement sur les bancs de l'UTT il y a quelques années maintenant, tu as su me donner le goût pour la recherche et pour ce domaine qui est le nôtre aujourd'hui. Merci pour ta confiance durant cette thèse et pour la poursuite de mes activités dans l'équipe. Tu as su être à la fois ferme et pédagogue. Tu as su me recadrer quand je m'éparpillais un peu trop et tu as su remonter les points de questionnement sur mon travail, je t'en remercie. Merci pour les nombreuses discussions que nous avons pu avoir et pour la bonne humeur, la sympathie et la confiance que tu témoignes aux membres de ton équipe. C'est un réel plaisir de travailler avec toi, et même si initialement ta participation à ma thèse ne devait être que ponctuelle, tu t'es montrée curieuse et force de proposition dans ce projet, et tu t'y es investie avec enthousiasme, ce qui s'est avéré très bénéfique. Merci pour ta patience également dans le travail de relecture de ce manuscrit.

Noémie, j'ai regretté ton absence le jour de ma soutenance, mais tu m'avais explicité la raison. Bien que nos points d'échanges aient été ponctuels, je tiens par ces quelques mots à te remercier pour ton accueil toujours chaleureux à Safran Tech. Merci pour ton suivi malgré mon absence sur site, ainsi que pour tes conseils avisés. Hasard ou coïncidence, je me penche actuellement sur ta thèse dans le cadre de mes nouveaux travaux de recherche...

Il ne serait pas rigoureux de m'en tenir à ces premières lignes sans intégrer les autres acteurs de mon projet de thèse au sein de l'ONERA. Ceux qui auront eu le courage de lire ce manuscrit (ou qui auront tout simplement suivi ma présentation orale) savent qu'un important volet expérimental y est présent. Celui-ci n'existe que par l'expertise et l'aide de mes collègues expérimentateurs. Côté "comportement", Camille LIARD et Alexis VOLANT se reconnaîtront dans mes essais. Côté "fissuration", je me tourne vers Vincent BONNAND et Didier PACOU. Et oui Didier, même si j'ai fait durer la rédaction de ce manuscrit, je ne t'aurai toujours pas amené jusqu'à la retraite. Je laisse Maxime s'en charger... ? Maël n'en a pas les épaules non plus vus les délais avant sa soutenance ! Quoi qu'il en soit, ta présence dans l'équipe et au labo est d'une grande richesse.
Un grand merci à vous quatre pour votre aide, votre gentillesse et pour les moments de travail tout aussi agréables les uns les autres. Camille, j'ai été très content de travailler avec toi dans le cadre de mes essais mais également de la procédure de dépouillement sous Python. La team "Biche-volley" a perdu un maillon fort de son équipe. Au passage, on doit toujours aller à Amsterdam avec Maël, il va falloir qu'on se penche sur le projet... Alexis, (plus tout) jeune embauché, tu as eu la (mal)chance "de te cogner" ma dernière série d'essais, ceux les plus compliqués. Je te remercie pour ton efficacité et suis ravi de poursuivre mes travaux de recherche avec toi dans l'équipe. Pour finir, je remercie également Théo GUERIN et Didier LOCQ pour leur aide sur les observations MEB faites sur mes éprouvettes en AD730™.

A tous mes collègues du bâtiment E4 : un grand merci. J'ai eu l'occasion de vous côtoyer pendant ces quelques années et cela a été un réel plaisir d'interagir et d'évoluer avec vous. A tous les jeunes doctorants et stagiaires des équipes M3S & MS2 : Maël, Maxime, Manon, Grégoire, Dorian, Antoine, Amina : bon courage pour vos travaux et soyez en fiers. Je suis ravi de la dynamique et de l'entente qu'il y a entre vous tous, cela contribue à la cohésion et à la bonne humeur générale de l'équipe !
J'ai quand même quelques petits clins d'œil à faire en particulier... Lors du séminaire de cohésion du DMAS en juin 2018 à Lille : merci Louise pour ces quelques pas de danse le soir au bar dansant, Serge pour la partie de bowling en équipe, Johann, Florent & Vincent C. pour les coups à boire... Merci pour les bons moments passés à Aussois, lors des plénières mais aussi au bar ou sur les pistes. Maxime et Maël ont pu voir le "chasse-neige" passer de près, ils s'en souviendront sûrement !

Enfin, une dédicace à la team volley de l'ONERA : Patrick, Alain, Denis, Cédric, Sébastien, Frédéric, Antoine(s), Laura, Rocco, Clément et bien évidemment celui qui m'y a amené, notre super passeur Jean-Didier. Merci à toi J-D pour ta sympathie, ta pédagogie, ta disponibilité permanente et la qualité de tes passes, que je sois attaquant 2 ou 4, et même lorsque je joue central ! C'est un plaisir de jouer à tes côtés. Merci à toute l'équipe pour ces années de volley avec vous. Ces entraînements et matchs m'ont permis de me défouler quelques soirs en parallèle de la thèse. J'ai apprécié votre bonne humeur, le (quasi) sérieux de nos entraînements, les échanges de balles sur le terrain, et les bières après les matchs !

Enfin, un dernier lot, et pas des moindres : ma famille et mes amis. Merci d'abord à mes parents de m'avoir donné les conditions matérielles pour mener à bout ces études et poursuivre mon parcours. Merci à eux pour tout ce qu'ils m'ont transmis, pour leur confiance, leur soutien et leur bienveillance depuis presque 30 ans.
Merci à tous mes frères et sœurs – Cécile, Benoît, Emmanuel, Estelle et Jean-Baptiste – pour leur soutien indéfectible. Merci pour la bienveillance que vous m'avez témoignée depuis tant d'années. Votre présence à mes côtés compte énormément pour moi. Merci plus largement à mes beaux-frères et belles-sœurs, ainsi que mes (10) petits neveux et nièces ! Vous avez aussi contribué à apporter des moments festifs et conviviaux tout au long de ces années, et vous voir évoluer reste pour moi une source de bonheur.
Merci à Pierre & Claudine pour leur accueil à Antony durant les premières années de ma thèse, et pour leur amitié de tous les jours. Merci pour vos conseils et votre soutien lors de ce parcours et dans les moments plus délicats.
A Limoges, merci également à Pierre & Catherine pour votre accueil toujours chaleureux et bienveillant. J'ai apprécié apprendre à vous connaître davantage durant ces années de thèse, notamment durant le 1er confinement de mars 2020. Merci Pierre pour les sorties running, trails et vélo qui m'ont permis de m'aérer l'esprit les quelques fois où l'occasion s'est présentée. Plus généralement, merci à vous deux pour votre soutien et votre gentillesse à bien des égards, j'y suis sensible.
Enfin, mes amis, les (faux) parisiens d'abord : Romain, Anthony, Bertrand, Valentin... Vous trouverez toute ma gratitude dans ces quelques mots. Merci pour votre patience et votre tolérance pour les nombreuses fois ou j'ai décliné ma présence à vos côtés. Les moments partagés ont malgré tout apporté de l'énergie et de l'enthousiasme dans mon quotidien. Bertrand, colocataire depuis plusieurs années, merci pour les rires et le quotidien partagé. Je n'oublie évidemment pas mes amis de Limoges : Guillaume, Alexandre, Tom, Robin, Hugo, Jessica... merci pour les (trop) rares moments passés ensemble, mais qui m'ont toujours remémoré notre amitié et notre complicité des "années lycée". On aura d'autres occasions de rire tous ensemble, je n'en doute pas...

Et pour finir, mes très sincères remerciements et toute ma gratitude vont à Sophie, fidèle compagne depuis tant d'années. Malgré la distance, mon absence chronique et les difficultés, tu as su rester à mes côtés et parcourir ce chemin avec moi. Oreille attentive, ta bienveillance et ta résilience ont formé la clef de voûte de mon équilibre personnel, je t'en suis reconnaissant. Une nouvelle page de notre vie s'ouvre à nous désormais, il ne reste qu'à l'écrire (personnellement, j'ai eu ma dose d'écriture pour quelques temps, je te laisse la priorité !). Sophie, une fois encore, merci. J'espère t'apporter autant que tu m'apportes.

Olivier

Abstract

This study is related to fatigue crack growth problems in aerospace structures. The present work aims at simulating the high temperature fatigue crack propagation within a Nickel-based superalloy using a local approach to fracture. The proposed developments follow from three major axes.

First, on an experimental scope, a new Nickel-based superalloy, namely AD730™ is studied. To this end, both cyclic characterization and crack propagation tests are performed at three target temperatures of 20, 550 and 700°C. Axisymmetric laboratory specimens are subjected to complex loading schemes (monotonic, fatigue and dwell-fatigue) in order to emphasize the non-linear response of the material. For the cyclic crack growth tests, SEN-T specimens are subjected to fatigue and creep-fatigue conditions. The sensitivity of AD730™ to extrinsic parameters (temperature, load ratio, dwell-periods, over-loads) is studied and creep-fatigue interaction effects are evidenced. Mesoscopic observations on fracture surface allow to highlight crack growth peculiarities (tunneling effect, flat-to-slant transition). Fractographic analyses also enable to evidence the main crack growth mechanisms. As a complement, flat specimens are also subjected to very low-cycle fatigue in order to study the ductile crack growth.

Then, in the modeling framework, cyclic constitutive equations related to the elastic-viscoplastic behavior of AD730™ are proposed. Such a material model is implemented within the Z-set software in a user-defined subroutine. The differential system associated with the evolution equations is solved using a fully implicit backward-Euler scheme. A consistent calibration process is carried out with respect to the physical mechanisms associated with both strain- and time-hardening processes. The predictive capabilities of the constitutive model are finally demonstrated under complex loading schemes. Considering the local approach to fracture, a strong coupling between damage and the elastic-viscoplastic constitutive equations at the material point level is performed. Damaging mechanisms associated with fatigue, creep or ductile processes are included in the model using distinct scalar damage variables. The adopted strong coupling formalism leads to a stress-softening response when performing finite elements calculations, resulting in the well-known mesh-dependency effect. To retrieve the well-posedness of the mechanical problem, a regularization method consisting in a non-local implicit gradient enhancement is proposed. The non-local damage model is re-implemented in Z-set and the multi-fields problem is solved using a monolithic scheme. Structural calculations under both monotonic and cyclic loading schemes demonstrate the ability of the non-local extension to achieve mesh-converged results.

Finally, on the numerical scope, an error-based mesh adaption strategy is considered in order to refine the mesh in the fracture process zone. Once the mesh is optimal and the width of the localization band is controlled, structural calculations can be performed up to crack onset. In order to accurately define the position of the crack front and the geometry of the singularity, a crack path tracking algorithm is used. The algorithm follows the ridge of the damage-related scalar field and, by marching steps, finds the position of the next crack front. The whole numerical scheme – including a damage-to-crack transition through mesh intersection and remeshing, field transfers and equilibrium recovery – is finally benchmarked on fatigue crack propagation tests. The capabilities of the method are assessed and the limitations of the modeling work are finally discussed.

Résumé

Cette étude est en lien avec les problématiques de propagation de fissure en fatigue dans des structures aéronautiques. Ce travail vise à simuler la propagation de fissure de fatigue à haute température dans un superalliage base Nickel à l'aide d'une approche locale de la rupture. Les développements proposés reposent sur trois axes principaux.

Sur le plan experimental d'abord, un nouveau superalliage base Nickel, l'AD730™ est étudié. Pour ce faire, des essais de caractérisation et de propagation de fissure sont réalisés aux trois températures cibles 20, 550 et 700°C. Des éprouvettes de laboratoire sont soumises à des chargements complexes (monotone, fatigue et fatigue avec temps de maintien) de sorte à mettre en évidence la réponse non-linéaire du matériau. Pour les essais de fissuration, des éprouvettes SEN-T sont soumises à des chargements de fatigue et fatigue-fluage. La sensibilité de l'AD730™ aux paramètres extrinsèques (température, rapport de charge, temps de maintien, surcharges) est étudiée et les intéractions fatigue-fluage mises en évidences. Des observations mésoscopiques sur les surfaces de rupture mettent en évidence les anomalies de propagation (effet tunnel, déversement). Des analyses fractographiques permettent également d'identifier les principaux mécanismes en lien avec la propagation de fissure. En complément, des éprouvettes plates sont testées en fatigue à très faible nombre de cycles afin d'étudier la propagation ductile de la fissure.

Ensuite, sur le plan de la modélisation, des équations représentatives du comportement élasto-viscoplastique de l'AD730™ sont proposées. Ce modèle matériau est implémenté dans la suite Z-set à l'aide d'une loi utilisateur. Le système différentiel associé aux lois d'évolution est résolu à l'aide d'un schéma de résolution implicite de type "Backward-Euler". Puis, un processus de calibration est effectué, conformément aux phénomènes physiques observés en lien avec les écrouissages et les effets du temps. Les capacités prédictives du modèle de comportement sont finalement démontrées sous des chargement complexes. En lien avec l'approche locale de la rupture, un couplage fort entre l'endommagement et le comportement à l'échelle du point matériel est effectué. Pour cela, les endommagement associés aux mécanismes de fatigue, fluage et de ductilité sont intégrés dans le modèle à l'aide de variables d'endommagement scalaires dédiées. Le couplage fort entre l'endommagement et les propriétés mécaniques amène à une réponse adoucissante en contrainte lors du calcul via les éléments finis, conduisant ainsi au problème de la dépendance des résultats au maillage. Afin de retrouver le caractère bien posé du problème mécanique, une méthode de régularisation associant une extension non-locale de type gradient implicite est proposée. Le modèle non-local est réimplémenté dans Z-set et le problème multi-champs est résolu avec un schéma monolithique. Des calculs structuraux sous chargements monotones et cycliques démontrent la capacité de l'approche non-locale à retrouver la non dépendance des résultats à la finesse du maillage.

Finalement, sur le plan numérique, une méthode d'adaptation de maillage basée sur un estimateur d'erreur est considérée afin de raffiner le maillage au niveau de la *process zone* en front de fissure. Lorsque le maillage est optimal et que la largeur de la bande de localisation est contrôlée, des calculs sur structures peuvent être réalisés jusqu'à amorçage de la fissure. Afin de définir précisémment la position du front de fissure et sa géométrie, un algorithme de suivi du trajet de fissure est employé. Cet algorithme suit une ligne de crête associée à un champs scalaire relié à

l'endommagement et, de manière incrémentale, estime la position du front de fissure au cours du chargement. La chaîne de calcul globale – incluant une transition endommagement-rupture par intersection de maillage et remaillage global, le transfert des champs, et le retour à l'équilibre de la structure – est finalement mise en oeuvre et évaluée sur des cas de propagation de fissure en fatigue. Les capacités de la méthode sont évaluées et ses limites en terme de modélisation sont finalement discutées.

Contents

Notations

Superscripts and subscripts

$(.)^{tot}$	total part
$(.)^{e}$	elastic part
$(.)^{in}$	inelastic part ("in" stands either for plastic or viscoplastic)
$(.)^{T}$	transpose of $(.)$
$(.)_{int}$	internal
$(.)_{aux}$	auxiliary

Representation of quantities

a	scalar (0 order tensor)
$\underline{x}$, x_i	vector (1^{st}-order tensor)
$\underline{\underline{x}}$, x_{ij}, x_m	2^{nd}-order tensor in 3D space ($\forall i, j \in [1, 3]$)
$\underline{\underline{\underline{\underline{x}}}}$, x_{ijkl}, x_{mn}	4^{th}-order tensor in 3D space ($\forall i, j, k, l \in [1, 3]$)

Specific notations

$\overline{\mathcal{V}}$	non-local quantity (direct counterpart of $\mathcal{V}$)
$\underline{\underline{\tilde{T}}}$	Effective tensor (coupled to damage)
$\underline{\underline{x}}_{+/-}$	positive (resp. negative) part of tensor $\underline{\underline{x}}$ w.r.t. its principal values

Mathematical operators

$\dot{x}$	rate of change of quantity x w.r.t. time $(= \mathrm{d}x/\mathrm{d}t)$
$x_{i,j}$	spatial gradient of $\underline{x}$ $(= \nabla \underline{x})$
$\|x\|$	euclidean norm of quantity x, $\|x\| = \sqrt{x : x}$
$\mathrm{sgn}(x)$	sign function for quantity x, $\mathrm{sgn}(x) = \begin{cases} 1, & x > 0 \\ 0, & x = 0 \\ -1, & x < 0 \end{cases}$

$\mathcal{H}(x)$	Heaviside step function for quantity x, $\mathcal{H}(x) = \begin{cases} 1, & x \geq 0 \\ 0, & x < 0 \end{cases}$
$\langle\, x \,\rangle_{\pm}$	weighted step function or Macauley brackets, $\langle x \rangle_{\pm} = 0.5\left(x \pm \lvert x \rvert\right)$
$\underset{\sim}{1}$, δ_{ij}	2[nd]-order identity tensor, $\delta_{ij} = 0$ if $i = j$ or $\delta_{ij} = 0$ if $i \neq j$ $\quad \forall i, j \in [1,3]$
$\underset{\approx}{I}$, I_{ijkl}	4[th]-order identity tensor, $\underset{\approx}{I} = \delta_{ik}\delta_{jl} \quad \forall i, j, k, l \in [1,3]$
$\underset{\approx}{I}^{S}$, I^{S}_{ijkl}	4[th]-order sym. identity tensor, $\underset{\approx}{I}^{S} = \frac{1}{2}\left(\delta_{ik}\delta_{jl} + \delta_{il}\delta_{jk}\right) \quad \forall i, j, k, l \in [1,3]$
.	contracted product, $\underline{u} \,.\, \underline{v} = u_i v_i$
:	double contracted product, $\underset{\sim}{A} : \underset{\sim}{B} = A_{ij}B_{ij}$
$\times$	cross product, $\underline{u} \times \underline{v} = u_i v_j \, \epsilon_{ijk} e_k$
$\otimes$	1[st] tensorial product, $\underset{\sim}{A} \otimes \underset{\sim}{B} = A_{ij}B_{kl}$
$\underset{\sim}{x}^{D}$	deviatoric part of $\underset{\sim}{x}$, $\underset{\sim}{x}^{D} = \underset{\sim}{x} - \frac{1}{3}\,\mathrm{tr}(\underset{\sim}{x})\,\underset{\sim}{1}$
$\underset{\sim}{x}^{S}$	spherical (hydrostatic) part of $\underset{\sim}{x}$, $\underset{\sim}{x}^{S} = \frac{1}{3}\,\mathrm{tr}(\underset{\sim}{x})\,\underset{\sim}{1}$
$\lvert x \rvert$	absolute value of x
$\overline{x}$	mean value of x
Δx	incremental change over a time step of x (x_{n+1} - x_n), range of x (x_{max} - x_{min})
δx	variation of x, or virtual quantity of x
d, ∂	differential operators (total or partial)
$\nabla(.)$	gradient operator of (.)
$\nabla.(.)$	divergence operator of (.)
$\nabla^2(.)$, $\Delta(.)$	Laplace operator of (.)
$\underset{\approx}{P}_{i}$	projection tensor in the i-th direction, $\underset{\approx}{P}_{i} = \underline{n}_i \otimes \underline{n}_i \otimes \underline{n}_i \otimes \underline{n}_i$
$\underset{\approx}{P}^{+/-}_{\sigma}$, $P^{+/-}_{\sigma_{ijkl}}$	orthogonal projection tensor giving the positive (resp. negative) part of $\underset{\sim}{\sigma}$

Finite Element discretization

Ω^e	Finite sub-domain (element)
Ω	Domain in current configuration
$\partial\Omega^e$	Finite surface of a sub-domain (element)
$\partial\Omega$	Boundary of domain Ω in current configuration
$\underline{n}_t$	Outward unit normal to $\partial\Omega_t$
$\underline{f}_b$	body force per volume element

$\underline{u}^p$	prescribed boundary value for the displacement field
$\underline{t}^p$	prescribed boundary value for the traction field
$\underline{\underline{N}}^a$	Shape functions evaluated at node a
$\underline{\underline{B}}^a$	Derivatives for the shape functions evaluated at node a
n_a	Number of nodes per element
n_i	Number of integration points per element
n_e	Number of elements in the structure
$\underline{u}^{(*)}$	(Virtual) Displacement field
$\underline{q}_x$	Global vector for the nodal unknowns x of the system
$\underline{q}^a$	Nodal vector for the unknowns associated with node a
$\underline{f}^e_{int}$	Vector for the elementary internal force
$\underline{F}_{int}$	Vector for internal force
$\underline{f}^e_{ext}$	Vector for the elementary external force
$\underline{F}_{ext}$	Vector for external force
$\underline{R}$	Residual vector of the problem
$\underline{R}_x$	Global residue associated with x
$\underline{r}^e_x$	Elementary residue associated with x
$\underline{\underline{k}}^e$	Elementary tangential stiffness matrix
$\underline{\underline{K}}$	Tangential stiffness matrix of the structure
$\underline{\underline{\underline{C}}}$, $\underline{\underline{C}}$, C	Consistent material tangents (4^{th}-, 2^{nd}- and 0-order)
$\overset{(r)}{.}$	Non-linear global iteration index
ϵ^{glob}_{tol}	Global convergence criterion (target error)

Mesh adaptivity

$\mathcal{M}$ / $\mathcal{M}'$	Current/new mesh
h_e / h'_e	Current/new element size
r_e	Element size modification ratio
θ_x	Exact (point-wise) error on x
θ^e_x	Local error on x
$\left\| \theta \right\|_\Omega$	Norm of the exact global error
$\left\| \theta_h \right\|_\Omega$	Norm of the approximated global error
η_x / η^e_x	Global/local relative error on x
ϵ^h_x	Prescribed global error related to x over a given mesh
f^a	Scalar field f at a given node
$\widehat{f}^a$	Recovered approximation of the continuous field f at a given node
$f^\star$	Smoothed approximation of the continuous field f

Local integration process for material equations

θ	$\theta-$method parameter (general trapezoidal method)
Δt	Time step size, $\Delta t = t_{n+1} - t_n$
$\mathcal{R}_{\mathcal{V}}$	Material residual w.r.t. internal variable $\mathcal{V}$
$.^{(k)}$	Non-linear local iteration index
ϵ_{tol}^{loc}	Local convergence criterion (target error)

Invariants for 2nd order tensors

$I_1(\underset{\sim}{x})$	First invariant of $\underset{\sim}{x}$, $I_1(\underset{\sim}{x}) = \mathrm{tr}(\underset{\sim}{x})$
$I_2(\underset{\sim}{x})$	Second invariant of $\underset{\sim}{x}$, $I_2(\underset{\sim}{x}) = \mathrm{tr}(\mathrm{com}(\underset{\sim}{x}))$
$I_3(\underset{\sim}{x})$	Third invariant of $\underset{\sim}{x}$, $I_3(\underset{\sim}{x}) = \det(\underset{\sim}{x})$
$J_1(\underset{\sim}{x}^D)$	First invariant of $\underset{\sim}{x}^D$, $J_1(\underset{\sim}{x}^D) = \mathrm{tr}(\underset{\sim}{x}^D) = 0$
$J_2(\underset{\sim}{x}^D)$	Second invariant of $\underset{\sim}{x}^D$, $J_2(\underset{\sim}{x}^D) = \frac{1}{2}\,\underset{\sim}{x}^D : \underset{\sim}{x}^D$
$J_3(\underset{\sim}{x}^D)$	Third invariant of $\underset{\sim}{x}^D$, $J_3(\underset{\sim}{x}^D) = \det(\underset{\sim}{x}^D)$

Symbols / Mechanical or physical constants

t	Time	s
$\rho_{(t)}$	Current density	$kg.m^{-3}$
ρ_0	Initial density	$kg.m^{-3}$
T	Temperature	$^\circ C$
ψ	Helmholtz specific free energy	MPa
ψ^*	Gibbs specific free enthalpy	MPa
$\mathcal{D}_{int}$	Intrinsic dissipation	-
c	non-local material parameter	mm^2
ℓ_c	internal length scale parameter	mm
E	Elasticity (Young) modulus	MPa
G	Shear modulus	MPa
K	Bulk modulus	MPa
ν	Poisson coefficient	-
λ, μ	Lamé coefficients for elasticity / shear modulus	MPa
$\underset{\approx}{\Lambda} = \Lambda_{ijkl}$	Elastic stiffness tensor	MPa
$\underset{\approx}{S} = S_{ijkl}$	Elastic compliance tensor $(\underset{\approx}{S} = \underset{\approx}{\Lambda}^{-1})$	MPa^{-1}
$\mathbf{a}_j$	Generic set of internal (state) variables	-
$\mathbf{A}_j$	Generic set of thermodynamical forces	MPa

$\mathcal{V}_{int}$	Generic set of internal variables	-
$\underset{\sim}{\sigma}$	Cauchy stress tensor	MPa
$\underset{\sim}{Z}$	Apparent stress tensor	MPa
$\underset{\sim}{\varepsilon}$	Total strain tensor	mm/mm
$\underset{\sim}{\varepsilon}^{e}$	Elastic strain tensor	mm/mm
$\underset{\sim}{\varepsilon}^{in}$	Inelastic strain tensor	mm/mm
$\underset{\sim}{X}$	Kinematic hardening or back stress	MPa
$\underset{\sim}{\alpha}$	Internal variable associated with kinematic hardening	-
C	Kinematic hardening modulus	MPa
γ	Kinematic hardening rate of saturation	-
X_{∞}	Kinematic hardening saturated value	MPa
R_0	Initial yield stress	MPa
R	Isotropic hardening or internal stress	MPa
r	Internal variable associated with isotropic hardening	-
Q	Isotropic hardening modulus	MPa
b	Isotropic hardening rate of saturation	-
R_{∞}	Isotropic hardening saturated value	MPa
σ_{eq}	Equivalent stress	MPa
σ_h	Hydrostatic stress	MPa
T_X	Stress triaxiality ratio $\quad (T_X = \sigma_h/\sigma_{eq})$	MPa
D_f	Fatigue damage	-
Y_f	Fatigue damage associated force (energy release rate)	MPa
D_c	Creep damage	-
Y_c	Creep damage associated force (energy release rate)	MPa
D_v	Volumetric damage associated with porosity	-
D_{tot}	Total damage	-
$\overline{D}$	Non-local total damage	-
$\mathcal{F}_y$	Limit of the loading surface (yield criterion)	MPa
$\underset{\sim}{n}$	Normal to the loading surface (yield direction)	-
$\phi_v(.)$	Flow rule	-
$\dot{\lambda}$	(Visco-)Plastic multiplier	-
p	Accumulated plastic strain	mm/mm
h	Micro-cracks closure parameter	-
$\underset{\approx}{H}$	Effective tensor for equivalent stress	-
φ_c	Hydrostatic stress sensitivity coefficient in yield criterion	-

$\dot{\epsilon}_0$	Speed limit for the hyperbolic sine flow rule	$1/s$
K	Parameter for the hyperbolic sine flow rule	MPa
n, m	Exponents for the hyperbolic sine flow rule	-
Y_{f_0}	Threshold for the fatigue damage associated force	MPa
S_f	Fatigue damage resistance	MPa
m_f	Fatigue damage exponent	-
β_f	Non-linearity parameter for fatigue damage	-
η_D	Scaling parameter for the softening function $f^*(D)$	-
$\chi_c(\underset{\sim}{\sigma})$	Generalized equivalent stress (of Hayhurst-type) for creep	MPa
α_c, δ_c	Coefficients for linear combination of stress invariants in χ_c	-
S_c	Creep damage resistance	MPa
m_c	Creep damage exponent	-
β_c	Non-linearity parameter for creep damage	-
$\Omega^*_{vp/p}$	(Visco-)Plastic dissipation potential	MPa
Ω^*_r	Time-recovery effects-related dissipation potential	MPa
$\Omega^*_{D_f}$	Fatigue damage-related dissipation potential	MPa
$\Omega^*_{D_c}$	Creep damage-related dissipation potential	MPa

E^t, E^c	Tensile and compressive elasticity moduli	MPa
σ^t_{eff}, σ^c_{eff}	Tensile and compressive effective (friction) stresses	MPa
X^t, X^c	Tensile and compressive (internal) back-stresses	MPa
$\Delta\sigma$, $\frac{\Delta\sigma}{2}$	Stress range / amplitude	MPa
$\overline{\sigma}$, σ_m	Mean stress	MPa
ΔX, $\frac{\Delta X}{2}$	Back-stress range / amplitude	MPa
$\Delta\varepsilon^{tot}$, $\frac{\Delta\varepsilon^{tot}}{2}$	Total strain range / amplitude	mm/mm
$\Delta\varepsilon^{e}$, $\frac{\Delta\varepsilon^{e}}{2}$	Elastic strain range / amplitude	mm/mm
$\Delta\varepsilon^{in}$, $\frac{\Delta\varepsilon^{in}}{2}$	Inelastic strain range / amplitude	mm/mm
$R_{\sigma/\varepsilon}$	Loading ratio w.r.t. stress / strain	-
N	Number of cycles	-

Abbreviations

ASTM	American Society for Testing and Materials
BC	Boundary Condition
CDI	Clausius-Duhem Inequality
CDM	Continuum Damage Mechanics
CDT	Continuous-Discontinuous Transition
CG/FG	Coarse- / Fine-Grained
CM	Continuum Mechanics
CSSC	Cyclic Stress-Strain Curve
CTO	Consistent Tangent Operator
CTOD	Crack Tip Opening Displacement
C&W	Cast & Wrought
CZ(M)	Cohesive Zone (Model)
DA	Direct Aged
(DC)PD	(Direct Current) Potential Drop
DFCG(R)	Dwell-Fatigue Crack Growth (Rate)
DIC	Digital Image Correlation
DoF	Degree of Freedom
DSA	Dynamic Strain Aging
EBSD	Electron Back-Scattered Diffraction
EDM	Electrical-Discharge Machining
E-FEM	Embedded Finite Element Method
ENS	Ecole Normale Supérieure
ESR	Electro-Slag Remelting
E(V)P	Elastic-(Visco)Plastic
FCC	Face-Centered Cubic
FCG(R)	Fatigue Crack Growth (Rate)
FE(M)	Finite Element (Method)
FM	Fracture Mechanics
FPZ	Fracture Process Zone
GB	Grain Boundary
GSM	Generalized Standard Materials
HCF	High-Cycle Fatigue

HPT/LPT	High/Low Pressure Turbine
HT	High Temperature
I(B)VP	Initial (Boundary) Value Problem
I(G)P	Integration (Gauss) Point
KKT	Karush-Kuhn-Tucker
LCF	Low-Cycle Fatigue
MHR	Multiple Hardening-Relaxation
MLS	Moving Least-Squares
MPZ / CPZ	Monotonic / Cyclic Plastic Zone
MR	Marching Ridges
MS	Multiple Speed
NDT	Non-Destructive Testing
(N)LEFM	(Non-)Linear Elastic Fracture Mechanics
N-R	Newton-Raphson
OL / UL	Over-Load / Under-Load
ONERA	Office National d'Etudes et Recherches Aérospatiales
PDE	Partial Differential Equation
PICC	Plasticity-Induced Crack Closure
PLC	Portevin - Le Châtelier
PSB	Persistent Slip Bands
ROI	Region Of Interest
RT	Room Temperature
RVE	Representative Volume Element
SEM	Scanning Electron Microscopy
SEN-T	Single Edge Notched - Tension
SIF	Stress Intensity Factors
SPR	Superconvergent Patch Recovery
SRS	Strain Rate Sensitivity
SSY / LSY	Small- / Large-Scale Yielding
TEM	Transmission Electron Microscopy
TIP	Thermodynamics of Irreversible Processes
UC	Unilateral Conditions
VAR	Vacuum Arc Remelting
VIM	Vacuum Induction Melting
VLCF	Very Low-Cycle Fatigue
X-FEM	eXtended Finite Element Method
ZZ2	*Zienkiewicz & Zhu 2*

List of Figures

List of Tables

Introduction

Context

Turbojet engines include some critical parts such as turbine disks. These rotating components can be exposed to temperatures up to about 600°C and experience a continuous mechanical load (mostly at the maximum level) during the cruising period. In addition, during engine ignition and shutdown, there are mechanical load transients inducing a combination of cyclic and sustained loads to the critical components. The failure of these parts in service is inadmissible because it may result in a total inoperability of the engine, thus compromising the safety of the flight. The propagation of a crack within the constitutive material is one of the mechanisms that can lead to failure. Therefore, the design of critical components requires the determination of their fatigue crack propagation life by approaches such as damage tolerance analysis (*fail-safe* design).
Due to both environmental and economic concerns, demand for more efficient gas turbines materials drastically tends to increase, in contrast to the obvious necessity to rethink our transportation needs so as to limit the specific footprint of air traffic. For gas turbines applications (aircraft, aerospace and power-plant), Nickel-based superalloys have emerged as materials of choice. Such materials are necessary when significant resistance to loading under static, fatigue and creep conditions is required [Reed, 2006].

Problematic

In previous studies, specimens made of Nickel-based superalloys (Inconel 718, N18, Udimet 720Li, N19, ...) and subjected to high temperature fatigue or dwell-fatigue (550-700°C) have exhibited very disturbed crack fronts. In particular, a pronounced curvature of the crack front as well as shearing effects associated with flat-to-slant transition have been highlighted in DA Inconel 718 [Fessler, 2017]. These crack growth anomalies cannot be modeled by global energetic approaches associated with *Linear Elastic Fracture Mechanics* (LEFM), but only by taking into account the presence of non-linear phenomena (viscoplasticity and damage) in the vicinity of the crack-tip. The use of a local approach to fracture [Pineau, 2006] to simulate such crack front anomalies seems the only modeling approach capable of relating these complex issues.

Most of the time, once a macro-crack has initiated inside a structure, the subsequent crack growth is treated using the *Fracture Mechanics* concepts, disregarding the dissipative and non-linear mechanisms occurring close to the material discontinuity. The goal of the present study is to assess the capability of *Damage Mechanics* together with Finite Element calculations to deal with crack propagation situations, as opposed to classical approaches, see Fig. 1.

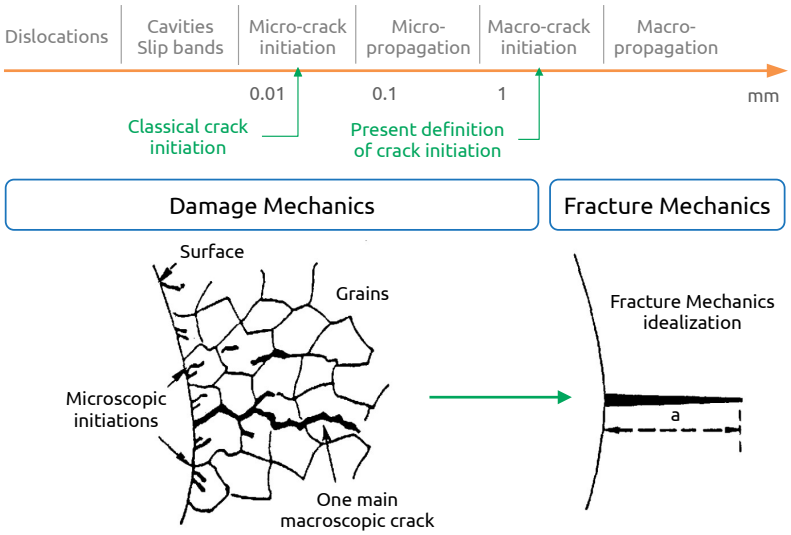

Figure 1: Schematic representation of fatigue crack growth length scales and associated modeling theories (adapted from [Chaboche, 1987]).

Purpose of the present Ph.D. project

The Ph.D. thesis has been carried out in the laboratory of the *ONERA - The French Aerospace Lab* located in Châtillon, France. This Ph.D. project has also been conducted with the help and financial support of the *Computational Solid Mechanics* team of *Safran Tech*, the research entity affiliated with *Safran Group*.
The present study is part of the "MEANDRES" (*Modélisation numErique des ANomalies de fissure Dans les supeRalliagES base nickel*) research project (2017-2020) conducted at the ONERA. This project deals with experimental observations and numerical modeling of crack growth anomalies in Nickel-based superalloys under complex loading conditions at elevated temperatures.
The framework of this Ph.D. thesis is focused on the use of a ***local approach to fracture*** in close relationship with results obtained through experimental tests conducted on laboratory specimens.

The major goal of the present research project is to propose a damage model in the context of a local approach to fracture that enables the simulation of crack propagation within a structure subjected to cyclic loading. To this end, the material under concern will be AD730™, a new Nickel-based superalloy. The strategy adopted to reach the target is to realize a strong coupling between damage and constitutive equations of the material in order to simulate the evolution of a crack during FE calculations. Since coupled damage models suffer from spurious mesh-dependency of the numerical results, a non-local extension of the model will be considered.
Then, even if the crack evolution may be estimated with the help of a suitable damage model, the numerical representation of the crack in the context of Finite Element (FE) simulations may be a tricky task. A last important point is the analysis of the transition from damage (continuous state) to finite crack (discontinuous state). This requires the insertion of a "discrete" crack in the region where some variables related to the degradation processes within the material have reached their critical value and where it is no longer possible to continue the calculation, as the elements are too degenerated [Feld-Payet, 2010]. This critical step can be made with several numerical approaches. In the present work, focus is made on mesh intersection and remeshing techniques associated with

mechanical fields transfer, which is a procedure that has been considered in previous studies, see *e.g.* [Feld-Payet, 2010], [El Khaoulani El Idrissi, 2010].

Outline of the dissertation

The organization of the present document and the main information addressed in the successive chapters are outlined below:

- In an usual way, **Chapter 1** is devoted to some fundamental aspects. First, general concerns about fatigue and cracks are recalled. Specific time-incremental cyclic crack growth models are also shortly introduced. Then, some basics on material modeling are given. In the following, the fatigue and creep-fatigue crack growth behavior of AD730™ and related crack growth anomalies are discussed. In a next section, the *Continuum Damage Mechanics* framework for fracture analysis is introduced. Regularization techniques used to solve the mesh-dependency effect are briefly introduced with a special focus on non-local approaches. Volumetric-locking issues are also shortly discussed. Finally, numerical methods for crack growth simulation in structural calculation are recalled;
- In the **Chapter 2**, the non-linear elastic-viscoplastic constitutive equations associated with the cyclic behavior of AD730™ under several temperatures are detailed and calibrated. To this end, the superalloy under concern is presented, both in terms of elaboration process and microstructure. Then, the experimental set-up is introduced as a preliminary to a significant part dedicated to the characterization of the cyclic behavior of the material under different testing conditions in terms of temperature, loading rates and loading ratios. Experimental results are then examined in a systematic approach in order to highlight the main non-linear phenomena and governing mechanisms. The whole constitutive equations for AD730™ Ni-based superalloy are finally established and consistently calibrated;
- The purpose of **Chapter 3** is to present the experimental procedures associated with the crack propagation analyses conducted on the studied material. Pure fatigue and dwell-fatigue crack growth tests are performed on Single-Edged Notched specimens and analyzed in a systematic manner. Three different length scales are considered: the macroscopic, mesoscopic and microscopic scales in order to analyze the crack growth data as well as the fracture surfaces and the microscopic features. Such a systematic examination process is aimed at identifying the crack driving mechanisms as well as the fracture modes. Apart from cyclic loading conditions, Very Low Cycle Fatigue tests are also considered on flat specimens in order to analyze the ductile crack growth process;
- A local approach to fracture is then presented in the **Chapter 4** in order to settle a strong coupling between damage and constitutive equations in order to simulate material's degradation preceding fatigue crack evolution. To that extent, the desired properties of the fatigue crack growth model are discussed as well with the modeling assumptions. The fatigue damage model is then derived using a consistent thermodynamics framework. An extension to other damaging effects follows, so as more physical mechanisms can be embedded in the model as well as complex loading conditions can be simulated. The numerical implementation of the proposed model into a Finite Element code is detailed, in particular at the

integration point level. A sensitivity analysis of the model is performed on a RVE. Finally, the mesh-dependency effect resulting from the strong coupling between damage and behavior is evidenced in a structural calculation;

- **Chapter 5** concentrates on the non-local extension of the proposed damage model thanks to an implicit gradient formulation related to some specific state variables of the damage-behavior problem. Firstly, a brief description of the localization phenomenon occurring in numerical softening problems is given. The next part deals with the choice made for the current local approach enhancement: choice for the regularization method, choice for the underlying problem's variable and choice for the characteristic length scale. Focus is made on the modifications of the damage model induced by such a non-local extension from both theoretical and numerical points of view. The implementation of a two-fields non-local finite element follows. Finally, some structural calculations under both monotonic and cyclic loading schemes are discussed so as to evidence the capabilities of the approach;
- Finally, in the **Chapter 6**, the numerical strategy suggested in the context of fatigue crack growth during FE calculations is presented. The need for a continuous-discontinuous transition in continuum cracking problems is discussed and the numerical strategy adopted in this research project is presented. An error-based mesh adaption procedure to refine the mesh in the FPZ is achieved while use is made of a dedicated crack path tracking algorithm to track the crack increments. Then, mesh intersection procedures with field transfer and equilibrium recovery step are used to insert a crack within the mesh and resume the calculation. Some numerical examples are given to illustrate the capabilities of the proposed damage model under cyclic loading conditions. A sensitivity analysis of the approach is finally performed.

The overall approach of the Ph.D. project is finally summarized in the Fig. 2.

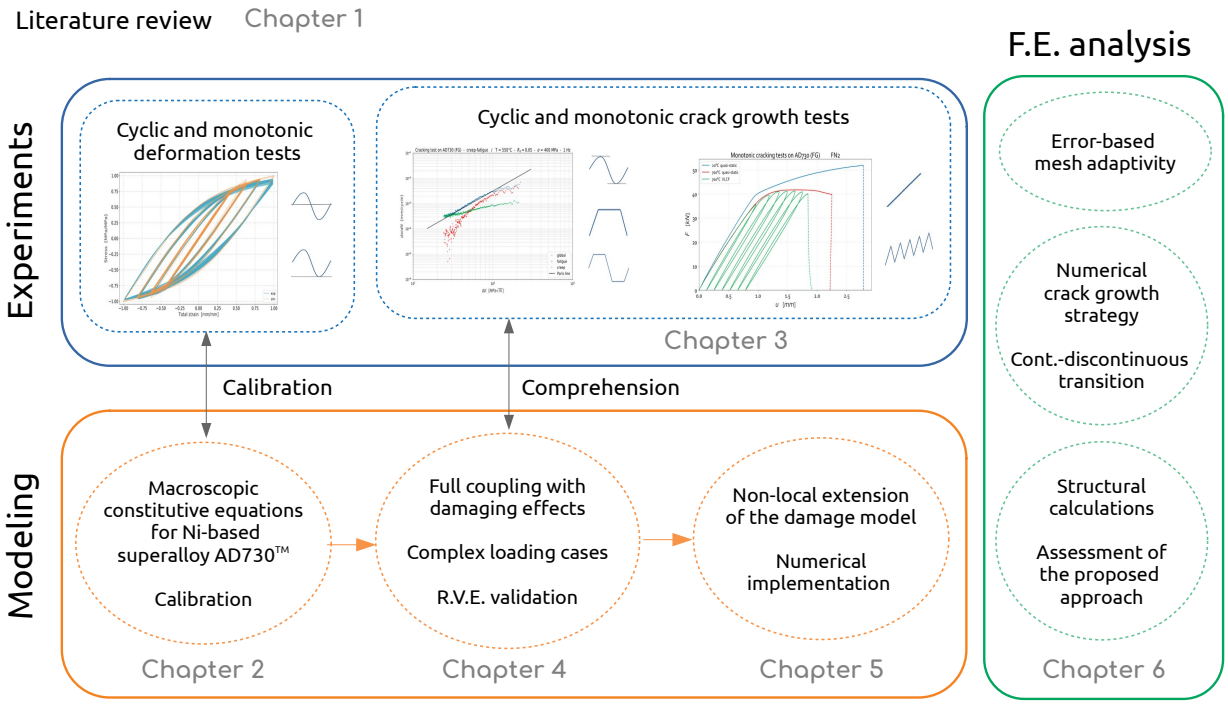

Figure 2: Flowchart of the Ph.D. project and structure of the dissertation.

Part I - State of the art

1 Literature review

This first chapter is devoted to some general aspects related to the present Ph.D. project. It starts with some concepts associated with fatigue crack propagation in metallic alloys, with the definition of fatigue long cracks. Next, some time-incremental fatigue crack growth models are briefly discussed. Then, fundamentals on material modeling are shortly introduced. The following section is devoted to the high temperature crack growth analysis in Nickel-based superalloys under complex loading schemes. A special focus is made on the crack growth anomalies observed for these alloys under complex loading schemes. Concepts related to the local approach to fracture, namely the coupled damage models and the theoretical concepts of the Continuum Damage Mechanics framework are introduced. Related numerical issues, namely the spurious mesh-dependency effect and the volumetric-locking issue, are discussed next with associated overcoming solutions. As a final step, the numerical methods associated with the crack growth modeling in finite element calculations are introduced. All these concepts, although different in nature, will be considered in the rest of this document as a support to the research activity.

Contents

1.1 Fatigue crack growth in metallic alloys

1.1.1 Introduction

Fatigue damage accumulation process is a multi-scale phenomenon which involves different spatial and temporal scales. For the spatial scale, fatigue involves small crack initiation at the nano- and micrometer scales to the structural failure at the meter (or even larger scales). For the temporal scale, fatigue accumulates from sub-second to tens of years.
Traditionally, fatigue analysis is performed in a reversal-based manner, in which the cyclic driving forces are used to correlate with fatigue damage (*e.g.* stress range in the S - N curve approach and the stress intensity factor (SIF) range in the da/dN - ΔK approach). This type of fatigue analysis is generally referred to as the *reversal-based approach* (or cycle-based). Unlike the static failure, fatigue failure is caused by cyclic stresses. As a consequence, it is natural considering cyclic quantities to describe the fatigue damage. Thus, the number of cycles becomes the temporal measure of fatigue. Earliest studies on reversal-based fatigue analysis can be traced back to [Wöhler, 1860] and [Basquin, 1910]. In 1960's, [Paris and Erdogan, 1963] proposed that fatigue can be analyzed by crack growth which is driven by the SIF range ΔK. The crack growth rate can then be expressed as:

$$\frac{da}{dN} = C\Delta K^m \tag{1.1}$$

where C and m are temperature-dependent material parameters.

The Paris' law in eq. (1.1) has become the most popular Fracture Mechanics-based method for fatigue lifetime estimation. However, Paris' law does not incorporate the stress ratio effect and is only applicable to growth rates in a certain range, *e.g.* 10^{-6} m/cycle to 10^{-8} m/cycle. Many modifications of Paris' law have been proposed in the literature, such as the modification for the near threshold crack growth [Forman et al., 1967], small/short cracks growth [Kitagawa and Takahashi, 1976], and crack closure [Elber, 1970].

This short introduction has given a brief overview of the FCG considerations for which pioneer studies traced back to the 1950's. For further details, the reader is referred to [Suresh, 1998] or [Bathias and Pineau, 2010]. No matter the considered crack growth model, different crack propagation regimes can experimentally be distinguished, depending whether the propagation is stable or unstable. Considering cracks, there are different length scales below which the growth rate may depend on the size of the crack. Fatigue cracks may thus be classified according to their size, *i.e.* short and long cracks. In the present work, the target application is the propagation of a long crack in fatigue situations. Consequently, the propagation of short cracks won't be addressed. The clear distinction between short and long cracks is given hereafter.

1.1.2 Fatigue crack propagation

Before introducing short and long cracks, it seems reasonable to recall the main crack growth stages upon cyclic loading. Since the present work is not intended to deal with the fatigue crack initiation stage, this one is disregarded but details can be found in [Suresh, 1998], [Bathias and Pineau, 2010]. The subsequent crack growth stage is finally analyzed.
When considering fatigue cracking, a crucial distinction is made between the microscopic initiation mechanisms that lead to the creation of a microcrack, and the propagation mechanisms that occur on a more macroscopic scale (the smallest detectable crack is generally of the order of the grain size, *i.e.* about 100 µm for a polycrystal). The fatigue cracking process can be decomposed into three main stages including crack initiation (*stage I*) followed by the crack propagation regime (*stage II*) and finally the sudden failure due to the presence of a macroscopic crack (*stage III*), Fig. 1.1a.

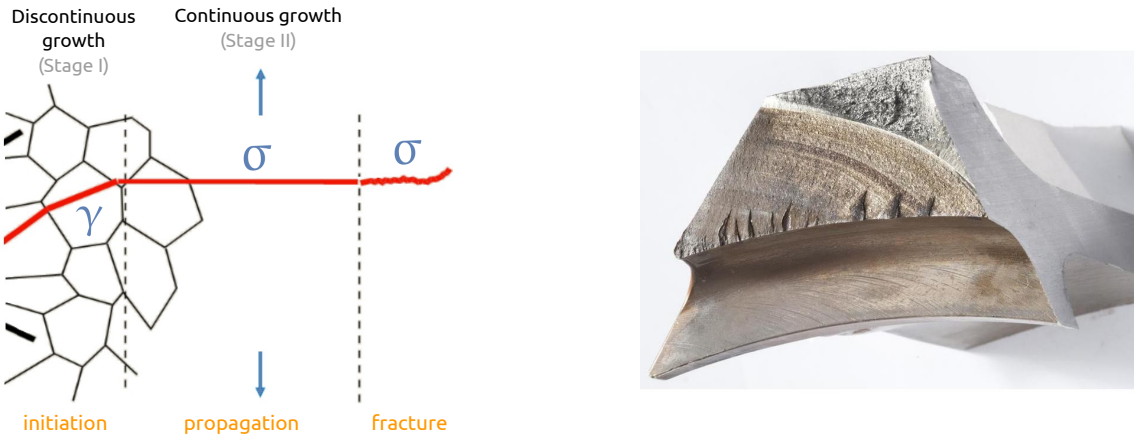

(a) Schematic view of the fatigue cracking process. (b) Example of a gas turbine blade failed under fatigue.

Figure 1.1: The three main stages on fatigue failure.

The Fig. 1.1b is an example of a component that failed under fatigue loading with the evidence of the three stages of the cracking process: crack started from a defect, probably close to the surface and then some fatigue striations appear during the progressive crack growth stage and finally the component failed in a sudden way due to increasing ductile mechanisms as long as the crack grew.

1.1.3 Long fatigue cracks

The clear separation between long and short cracks (as well as between the different short cracks) is sometimes an object of confusion. Although not detailed here, a common feature to short cracks is their abnormal propagation behavior as compared with the "classical" Paris-type behavior. This specific point constitutes a valuable distinction for the present work since we are mainly interested in the growth of a long crack under cyclic loading.
Short cracks can be identified as having a size comparable to the size of the plastic zone. Such an aspect induces that *Linear Elastic Fracture Mechanics* (LEFM) concepts are not applicable and alternative approaches such as *J*-integral [Rice, 1968] or *Continuum Damage Mechanics* (CDM) [Kachanov, 1986], [Lemaitre and Chaboche, 1990] are necessary to deal with such crack growth in fatigue loading. In the present work, long fatigue cracks are preferentially considered, as well as their propagation using LEFM or alternative approaches. In this sense, the novelty of the present Ph.D. project relies on the assessment of CDM-based approaches to deal with fatigue crack growth situations. The final prospect is to compare the lifetime predictive capabilities of a CDM-based approach to that of standard LEFM models.

According to [Suresh and Ritchie, 1984], a crack is considered to be a *long crack* when, besides the intrinsic crack-driving force at the crack-tip, the extrinsic influence factors are fully developed. One major extrinsic factor is related to the crack-closure effects in the wake of the crack-tip, thus altering the crack driving force. A long crack is hence related to the *stage II* of the (stable) crack growth process, as depicted in Fig. 1.1a. Some general properties about long cracks (in opposition to short cracks) must be given:

- long cracks are mainly tensile driven (fairly insensitive to the microstructure);
- they are mostly analyzed by Fracture Mechanics-based models since the plastic zone is sufficiently small so as to use the SIF range to estimate the crack growth rates.

A convenient background to discussing *Fatigue Crack Growth* (FCG) law is the well-known double-logarithmic FCG rate $\mathrm{d}a/\mathrm{d}N$ vs. ΔK curve, schematically shown in Fig. 1.2. Note that such a diagram, defined at a prescribed condition (environmental and stress ratio), is only valid for so-called *long cracks*, the plastic zone of which is embedded in a stress intensity factor dominated stress field. The typical curve is of a sigmoidal shape and is bounded at the extremes by the range of SIF at the threshold ΔK_{th} and the critical ΔK_c.

Such a curve shape is reasonably generic for long crack growth under constant amplitude loading in a normal (air) environment. There are three main regions of crack growth, according to the curve shape, the mechanisms of crack growth and various influences on the curve.

- **Region I:** Non-continuum crack growth mechanisms with large influences of microstructure, mean stress and environment. In such a region, there are also high crack closure levels but minor effects of the stress state. Cyclic plastic zone size is smaller or equal to the grain size;
- **Region II:** Crack-growth are commonly characterized by fatigue striations, and with small to large influences of microstructure, depending on the material, also large effects of certain combinations of environments, mean stress, cycle frequencies as well as the thickness of the considered specimen, thus having an influence on the stress state. The cyclic plastic zone size in this region

is greater or equal to the grain size;

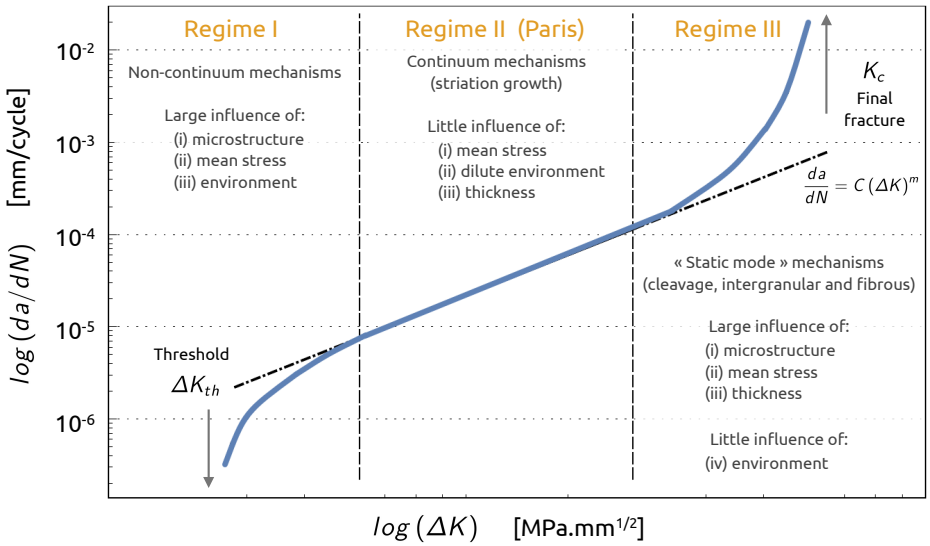

Figure 1.2: Schematic da/dN versus ΔK diagram for long crack growth under constant amplitude loading.

- **Region III:** large contributions of *static mode* mechanisms, generally microvoid coalescence and, in some materials, cleavage or intergranular fracture, with great influence of the microstructure, load ratio, thickness and finally a little influence of the environment (crack growth is too fast for the environment to have an significant impact on the cracking process). In this last region, the cyclic plastic zone size is far greater than the grain size.

In the following, since we are mainly interested in the growth of a crack in stable conditions, both the near threshold and the unstable regimes will be disregarded. Interested reader is referred to [Suresh, 1998], [Bathias and Pineau, 2010]. As a result, only the Region II (*i.e.* the Paris's regime) will be discussed in further details.

Paris' regime

The second part of the da/dN curve given in Fig. 1.2 is commonly referred to as the *Paris' regime*. Such a regime was studied by [Paris et al., 1961] and [Paris and Erdogan, 1963] in the early 1960's, who have demonstrated that Fracture Mechanics is a useful tool for characterizing Fatigue Crack Growth (FCG) and who suggested the well known *Paris law* for long fatigue crack growth. Such a law, initially developed for small constant-amplitude cyclic load, is a power function of the range of the SIF that applies almost generally to long fatigue cracks in metal and alloys:

$$\frac{\mathrm{d}a}{\mathrm{d}N} = C\,(\Delta K)^m = C\left(\Delta\sigma\sqrt{\pi\,a}\,Y\right)^m \tag{1.2}$$

where C and m are material parameters and $\Delta K = K_{max} - K_{min} = (\sigma_{max} - \sigma_{min})\sqrt{\pi\,a}\,Y$, and Y is a geometry function. Parameters C and m are determined in experiments and depend on the material and various influencing factors such as temperature, environment and loading ratio. Such a power law relationship in eq. (1.2) proposes a linear variation of $\log(\mathrm{d}a/\mathrm{d}N)$ vs. $\log(\Delta K)$,

which pertains to a portion of the total fatigue crack growth curve, Fig. 1.2.
In that regime, crack propagates leaving behind some striations on the fracture surface. During loading, the material ahead of the crack is stretched. When the crack grows, this stretched material is left in the wake of the crack, leaving behind a striation on the fracture surface.

Although extensively considered for FCG problems, the Paris-type approach is limited to crack cases where the size of the plastic zone is negligible as compared to the crack length, *i.e.* where small-scale yielding conditions (SSY) apply (LEFM), or when the crack length is large as compared to the characteristic microstructure length (*e.g.* grain size), *i.e.* when large-scale yielding (LSY) conditions apply (hence requiring *Non-Linear Fracture Mechanics* - NLFM). This restriction to long cracks and physically short cracks is fulfilled for most practical applications of Fracture Mechanics in fatigue-life assessment, since existing cracks smaller than approximately 500 µm cannot be detected by typical methods of non-destructive testing, *e.g.* ultrasonic, eddy current or dye-penetrant inspection.

It is worth mentioning that the Paris' law has been studied for different materials and testing conditions. Some researchers also developed other equations based on this law in order to take into account the dependence on the loading ratio $R = K_{min}/K_{max}$ as well as the stress history $\mathcal{H}$ or crack closure effects that play an important role in the crack growth rate evaluation, see references in sub-sect. 1.1.1.

$$\frac{\mathrm{d}a}{\mathrm{d}N} = f\left(\Delta K, R, \mathcal{H}\right) \tag{1.3}$$

where $\mathcal{H}$ indicates the history dependence, which results from prior plastic deformation.
All the equations of the type eq. (1.3) have been proved to be capable of correlating the fatigue crack growth rate under SSY conditions. Indeed, let us recall that the SIF K being initially defined for brittle materials and not applicable for plastic/ductile materials, the law proposed by [Erdogan and Sih, 1963] remains applicable as long as the plasticity remains low [Bathias and Pineau, 2010].

In the present Ph.D. project, and as previously said, long cracks are under concern. The aim of the research project relies on the assessment of a CDM-based model to predict the fatigue crack advance in a Nickel-based superalloy. To this end, experimental fatigue crack growth tests will be performed on laboratory specimens (see Chap. 3) and a damage model will be settled to simulate the fatigue crack growth process (see Chap. 4). To do so, the stable Paris' regime will be the central aspect of the comparison process. As a final step, the results from the present study should provide results validating (or not) the ability of Continuum Damage Mechanics to deal with fatigue crack growth (as opposed to classical crack initiation analyses).

1.1.4 Time-incremental fatigue crack growth models

Fatigue lifetime estimation up to crack initiation is a common approach in design offices since the major part of the service life of a component is related to the crack initiation phase. In the present work, the propagation of an existing crack is under concern so far we are mainly interested in fatigue crack growth models.

The brief introduction given in sub-sect. 1.1.1 has shown that there are various different modeling

approaches to simulate the fatigue crack growth (FCG). However, most of existing FCG prediction models perform the analysis in a cycle-based manner, in which the cyclic driving force quantities are used to correlate with fatigue damage. This means that the smallest time scale is one loading cycle. However, fatigue damage accumulation process is a multi-scale phenomenon, which involves very different spatial and temporal scales [Lu and Liu, 2012]. As a consequence, the cycle-based approach is not able to capture the detailed mechanism at the sub-cycle scale.
In addition, some inherent difficulties can be evidenced. First, reversal-based approach makes impossible to continue reducing the time scale for more fundamental investigation since the smallest time scale is one reversal. Then, reversal-based fatigue analysis requires cycle-counting techniques for realistic random loading [Downing and Socie, 1982], [Bathias and Pineau, 2010]. A realistic loading history needs to be transformed to cycle history for fatigue analysis. In engineering practice, loading history is usually complex or even far from being cycle. Consequently, the conversion from random load history to the cycle load sequence usually modifies the load history.

Small time scale or *time-incremental* models are based on the incremental crack evolution and growth at any instant during the loading cycle. Such models, although quite more complex, enable the possibility to consider complex (random) loading schemes different from standard constant amplitude loading regimes. This type of model is discussed in this section.

$$\frac{da}{dt} = f\left(\sigma\left(t\right), a\left(t\right), E, \sigma_y, ...\right) \tag{1.4}$$

where $f\left(\sigma(t), a(t), E, \sigma_y, ...\right)$ is a general form of the crack growth kinetics function depending on the stress level, the crack length, elastic modulus and yield strength of the material, etc.

A specific aspect of this Ph.D. comes from the use of a local approach to fracture as well with time-incremental properties of the fatigue damage model developed for FCG prediction (see Chap. 4). As a result, and for the sake of brevity, we will mainly discuss some existing FCG models, of incremental-type and differing nature, and disregard the others. Extensive reviews on FCG models relying on Fracture Mechanics concepts can be found in [Ellyin, 1997], [Bathias and Pineau, 2010]. Let us also note that the numerical simulation of FCG with the use of coupled approaches to fracture has not been extensively studied, hence representing a challenge to this Ph.D. research project.

A literature survey conducted in this work has evidenced four main time-incremental models dedicated to the prediction of fatigue crack growth. These models are briefly discussed hereafter with their capabilities and limitations.

- **A cohesive zone model (CZM)** has been proposed by [Bouvard, 2006], [Bouvard et al., 2009] to simulate both fatigue and dwell-fatigue crack growth. Relying on a local approach to fracture, that is, a coupling between the material behavior and damage mechanisms, an attempt has been proposed in this work to relate the fatigue crack growth to a traction-separation model governing cohesive zone elements. The model predictions have been proved to be in very good agreement with experimental data. Moreover, it is able to relate the retardation effect due to crack-tip plasticity. A fairly good prediction of frequency and time effects has also been observed in different crack growth regimes. A similar approach based on cohesive elements for FCG can be found in [Nijin and Banerjee, 2021].
  Unless interesting, the choice for CZM to simulate the fatigue crack growth has not been

retained in the present work since it supposes that the fracture process is exclusively restricted to surfacic features. Thus, the damage growth in the bulk material is not accounted for. Moreover, the ability for cohesive elements to reproduce the crack growth peculiarities observed in Ni-based superalloys (see sub-sect. 1.3.3 hereafter) seems limited.

- **A physically-justified model**, mainly known as the *condensed plasticity model*, has been proposed by [Pommier and Risbet, 2005], [Pommier and Hamam, 2007]. Mainly based on the physical mechanisms responsible for the crack advance, it is one of the most renown model aiming at introducing a new small time formulation for fatigue analysis. The underlying concept of the model comes from the fact that "pure" fatigue crack growth stems from crack-tip plasticity, namely plastic blunting. Consequently, a plasticity model adapted to the crack-tip region should be able to cope with the fatigue crack advance process.
  The model possesses two governing laws: *i)* a plastic blunting law that defines the evolution of the crack-tip blunting as a function of the applied external load (and internal history variables); and *ii)* a crack growth law that provides the instantaneous cracked area velocity per unit length of the crack front as a function of the evolution of the plastic blunting at the crack-tip. A comprehensive review on the model is given in [Pommier, 2015].
  Thanks to numerous dedicated studies, the condensed plasticity model has been proved to show a good agreement with experiments in both monotonic and variable amplitude crack growth tests. It has been improved with successive studies, hence including crack propagation in mode *I* under variable amplitude loading both at room and high temperatures as well as mixed mode conditions. Extension to oxidation effects has also been studied. Finally, crack retardation, load sequence and over-load effects are also in agreement with experimental results. Such a thermodynamics-based model, relying on the principle of virtual power, the energy balance equation and the inequality of Clausius-Duhem, belongs to the Fracture Mechanics-based models. Intensively studied during the last two decades, it offers promising features and remains one the most advance time-incremental fatigue crack growth model. Nevertheless, as mainly related to Fracture Mechanics concepts and only valid under small-scale yielding conditions, this model cannot assess complex crack situations in three-dimensional calculations.

- **A small-time scale model**, has been proposed by [Lu and Liu, 2010]. Relying on both the crack-tip opening displacement (CTOD) and angle (CTOA), the model predicts the instantaneous crack growth kinetics through geometric relationships and the temporal evolution of the stress along the loading path.
  Such a model can be used for fatigue analysis at various time and length scales. It has been proved to be very convenient for the fatigue analysis under random variable amplitude loading without cycle-counting with addressing the stress ratio effect. Moreover, predictions have been reported to agree very well with the experimental data. The model has also been extended to time-related effect [Lu et al., 2012], hence enabling for fatigue and creep-fatigue loading conditions to be studied. However, such a model cannot cope with the three-dimensional features associated with the crack growth peculiarities observed in Ni-based superalloys under complex loading schemes. Moreover, few studies have used this approach, hence leading to insufficient feedback.

- At last, a **CDM-based model** dedicated to fatigue crack propagation in aircraft alloys has been proposed by [Hamon, 2010], [Hamon et al., 2012]. The model has been settled following

a consistent thermodynamics framework. It consists in an extension of the Lemaitre damage model including two damage variables: one for static damage mechanisms (ductile fracture modes) at high ΔK values, and the other one for cyclic damaging processes (quasi-cleavage) from low to high ΔK. Using this damage model, a fairly accurate estimation of the FCG curves for two aircraft alloys has been reported.
In this approach, the numerical method to simulate the crack advance relies on an element-deletion technique. In order to reduce the mesh-dependency associated with the erosion process, an energy-based criterion has been considered [Mazars and Pijaudier-Cabot, 1996]. This way, the mesh size has been explicitly accounted for through the value of the critical energy required for an element to be removed. As a result, no regularization of the stress-softening model has been performed. Moreover, elastic-plastic conditions at low temperatures have been only considered. The case where viscoplasticity and time-related effects (creep, oxidation...) occur still have to be considered. Finally, a proper representation of the discontinuity in the structure would be of great interest in order to study crack growth orientation and possible bifurcations. Only 2D calculations have been performed. Hence, specific features related to the crack front anomalies observed in Ni-based superalloys cannot be captured.
Nevertheless, the CDM-based damage model of [Hamon, 2010] has provided interesting results while considering a local approach to fracture to simulate the propagation of a fatigue crack in metallic alloys. As a consequence, such a modeling framework can be considered valid for the target of this Ph.D. project.

Assessing the three-dimensional crack front peculiarities observed in Ni-based superalloys under complex loading schemes requires the use of a specific and predictive model. On this purpose, a local approach to fracture [Pineau, 2006] enabling to evaluate the crack-tip stress-strain fields and to use specific fracture criteria seems to be required.
In view of the above-described models and their limitations, choice for a local approach to fracture seems to be the best way when addressing crack growth problems involving complex material behavior and three-dimensional aspects. Moreover, such a modeling approach has already been considered for ductile tearing problems, hence providing some predictive fracture criteria based on local mechanical fields [Besson et al., 2003], [Xue and Wierzbicki, 2009], [Algarni et al., 2017].

1.2 Modeling framework

When using a local approach to fracture, the accurate description of the material behavior, particularly at the crack-tip, is of primary importance. To this end, constitutive equations must be derived before any coupling with damage mechanisms accordingly to a specific modeling framework. High temperature component failures are primarily induced by out-of-phase thermomechanical, creep-fatigue damage accumulation among many other factors [Ahmed, 2013]. Due to start-up and shut-down cycles, repeated thermomechanical stresses are induced that gradually degrade the life of the components. These material complexities in high temperature components are related to time-dependent processes such as creep, oxidation, dynamic strain aging (DSA), creep-fatigue, thermo-mechanical fatigue (TMF) and cyclic creep (or ratcheting). As a result, cyclic viscoplastic

advanced constitutive models for inelastic design-by-analysis are essential for the design of components experiencing thermally induced stresses as well as reverse loading conditions.

1.2.1 Different length-scales for the material modeling process

In order to describe the behavior of a material subjected to cyclic loading, several approaches may be considered, depending on the considered length scale, see Fig. 1.3. Their complexity strongly depends on the nature and number of phenomena that one seeks to describe simultaneously. The consideration of these phenomena is necessarily induced by the thermo-mechanical loads to which the structures are subjected.

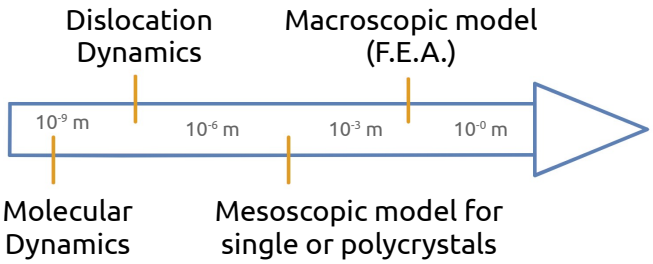

Figure 1.3: The different length scales for the modeling of a material behavior.

For a material modeling process, several approaches may be considered:

- **molecular dynamics:** which represents the behavior through the physical movements of its atoms and molecules (10^{-10} - 10^{-8} m). This type of modeling is limited to small time scales;
- **dislocations dynamics:** which relates the strain-hardening properties of the material to both the movements and pinning/annihilating processes of discrete dislocations (10^{-8} m) or dislocation patterns (10^{-7} m). Discrete dislocation models and/or phase-field type modeling can be considered. These approaches mainly concentrate on the effect of grain/precipitates size or their mutual interaction on the behavior. They require the knowledge of various energies (*i.e.* stacking fault energies) and dominant deformation mechanisms which can be accessed through numerous experiments;
- **crystallographic models:** for single or polycrystalline materials, which consider a high number of internal variables related to physical mechanisms such as crystal slip. Crystal plasticity models use the crystal orientation and active slip systems (10^{-6} - 10^{-3} m). At a fine scale, dislocation density based models are used, while at a coarse scale, the dislocation related effects are smeared into general flow and hardening formulations. Unlike phase-field models, the deformation mode is not characterized in crystal plasticity models. Note that microstructure features (grain/precipitate size, volume fraction) can be incorporated in the formulation. The calibration of these models requires LCF experiments under a series of "usual" loading conditions (monotonic, various loading rates, stress relaxation, ...);
- and the **macroscopic level:** in which the deformation behavior of the specimen (or structure) is described by an internal state variable type model (10^{-3} - 10^{-2} m). Such a model relies on classical plasticity theory and does not consider the grain orientation or active slip systems as the crystal plasticity does. The knowledge of the active deformation mode is not a necessity and this scale requires fewer material parameters compared to finer scale models.

Since the target application aims at simulating the crack advance under cyclic loading conditions in laboratory specimens, the first two length scales are not able to cope neither with long calculations nor large scale problems. The crystal plasticity approach could be considered for LCF calculations. However, a higher degree of complexity concerning the introduction of damage mechanisms would arise. Should the damage be incorporated at the scale of the grain, or at the boundaries between grains? In order to ease the numerical task, at least in this preliminary study considering a local approach to fracture for fatigue crack growth prediction, a macroscopic model, of phenomenological nature has been favored. This modeling approach has already proven to effectively cope with damage coupling [Lemaitre and Chaboche, 1990]. Moreover, computational costs are intended to be lower using a macroscopic model.

Macroscopic models are mostly based on the classical scheme of an elastic domain described by a Von Mises plasticity criterion (isotropic materials), a set of kinematic strain-hardening variables defining the rapid evolutions during each inelastic transient and additional isotropic variables representing the slower evolutions taking into account the phenomena of cyclic hardening or softening [Nouailhas, 1988], [Chaboche, 2008]. This approach relies on thermodynamic arguments used as a foundation on which phenomenological constitutive laws can be formulated. This theoretical framework is expressed by the existence of thermodynamic potentials as shown by [Halphen and Nguyen, 1974]. Based on this formalism, the complexity of the models depends on the studied phenomena. Therefore, the macroscopic approach is part of the *Continuum Mechanics* (CM) framework allowing the quantitative determination of the constitutive laws in a given area of validity using appropriate isothermal mechanical tests [Nouailhas et al., 1983].

In the present study, the macroscopic mechanical response of the material will be studied, see Chap. 2 later on. The considered Ni-based superalloy, namely AD730™ being subjected to cyclic and monotonic loading over a wide range of strain and temperature values will thus be described with the aid of a phenomenological material model associated with the so-called *unified viscoplasticity theory* [Chaboche, 1986].

According to [Lemaitre, 2001], the viscoplasticity model refers to the mechanical response of materials in plastic condition which exhibit time-dependent effect represented by a viscosity function. One of the most well-known model is the unified viscoplasticity model proposed by [Chaboche, 1977b]. Such a model is referred to as *unified* for two reasons [Chaboche, 1989]:

1. the plastic and creep strains are represented simultaneously by only one parameter (contrarily to non-unified theories, see *e.g.* [Cailletaud and Saï, 1995]) and these strains are referred to as *viscoplastic* strain. It is thus a coupled approach between plasticity and creep (as opposed to uncoupled approaches, see *e.g.* [Deshpande et al., 2010]);
2. the same hardening rules, as the time-independent plasticity rules, are employed.

Such unified models have been designed to model the multiple deformation mechanisms occurring during various loading cases such as monotonic tension, creep, fatigue and stress relaxation. In general, such phenomenologically-based models are capable of predicting the behavior of undamaged material for which the stress-strain prediction of the model is true up to a certain number of cycles (or the stabilized conditions) and normally covers the vast majority of the fatigue lifetime. In order to simulate the behavior of the material for the whole fatigue process, constitutive equations

can be combined to Continuum Damage Mechanics theory [Chaboche, 1988a], [Lemaitre et al., 2009]. Such an approach enables the modeling of the degradation of the strength of the material up to failure. This point will be discussed later on (see sect. 1.4 & Chap. 4).

1.2.2 A stress partition related to macroscopic strain-hardenings

In the material modeling process, attempts to relate the nature of stress to the material microstructure have been proposed in the last decades. In order to improve the understanding of cyclic hardening/softening mechanisms, the separation of the microstructure into soft and hard zones can be considered [Mughrabi, 1985], [Suresh, 1998]. As a result, the flow stress can also be partitioned into two components: the effective (σ_{eff}) and the internal stress (X). This partition is used to investigate the mechanisms responsible for the mechanical behavior of crystalline materials under cyclic loading. In the forthcoming sub-sect. 2.2.1, the Cottrell's partition method [Cottrell, 1953] will be considered for the analysis of hysteresis loops. This method enables the distinction between two components within the macroscopic stress: the effective and internal stresses.

From a modeling viewpoint (*cf.* Chap. 2), the effective and internal stresses are related respectively to the two strain-hardening variables, R and X. These are used to describe the evolution of the loading surface of a material during its deformation. The effective stress is associated with isotropic hardening R and results in an (isotropic) increase of the radius of the yield surface, while the internal stress is related to kinematic hardening X resulting in a displacement of the center of this surface. Due to the fact that kinematic internal stress can be influenced by the direction of flow stress, a tensorial variable $\underset{\sim}{X}$ will be used to account for the directional aspect.

Up to now, the context of this study (propagation of a long crack under fatigue and dwell-fatigue loading) and the modeling framework (phenomenological macroscopic model considering the unified viscoplasticity theory associated with a time-incremental formulation for complex loading simulation) have been discussed. The motivations for considering a local approach to fracture for the prediction of the FCG also come from experimental evidences obtained during FCG tests.

1.3 High temperature fatigue and dwell-fatigue crack growth in Nickel-based superalloys

1.3.1 General facts

The fatigue crack growth (FCG) resistance of the studied material needs to be addressed in order to highlight the governing mechanisms leading to failure. To do so, loading conditions close to those experienced in real applications must be examined in laboratory tests. Then, useful data gained from experimental results can be extrapolated to real application situations.

In the present study, the experimental work is focused on the fatigue and dwell-fatigue propagation of long cracks. The growth behavior of a long crack is the synergistic result of microstructure, temperature and environment, in combination with loading modes, although the influence of microstructure becomes less significant compared with short cracks [Bathias and Pineau, 2010]. The resulting fracture mode can be either transgranular or intergranular, even a mixture of both of them, depending on the specific in-service (or testing) conditions. Correspondingly, the fatigue behavior can be termed as *cycle-* or *time-dependent* on the basis of the degree of crack growth associated with time-related effects. Generally, low temperature, high frequency in combination with vacuum (or inert) environment tend to promote pure fatigue crack growth, whereas a high temperature, low frequency as well as aggressive environments tend to produce time-dependent crack growth patterns [Gabb et al., 2013]. It can be noted that crack growth may also be mixed with both time- and cycle-dependent contributions, as frequently reported in the literature [Pineau, 1981], [Branco and Byrne, 1995].

The scope of this section is to discuss the FCG behavior of the polycrystalline Nickel-based superalloy AD730™ at high temperatures (400-900°C). The main conclusions are deduced from da/dN - ΔK curves with the influence of both so-called *extrinsic* (temperature, load ratio, loading frequency, over-loads, ...) and *intrinsic* (microstructure, mechanical state at the crack-tip, ...) effects.

1.3.2 Fatigue, creep and creep-fatigue crack growth in AD730™

1.3.2.1 Fatigue and creep-fatigue crack growth in AD730™

The fatigue crack growth resistance of AD730™ has been reported to be better compared to similar class Ni-based superalloys [Aubert&Duval, 2017]. Compared to standard Inconel 718 or Udimet 720 alloys, AD730™ exhibits lower crack growth rates. This effect is to be attributed to the high mechanical properties of this alloy with increasing the temperature. At 700°C, mechanical properties of AD730™ have been proved to be maintained (while a drop in yield strength and Young modulus are observed for the two others), hence resulting in a better crack growth resistance.

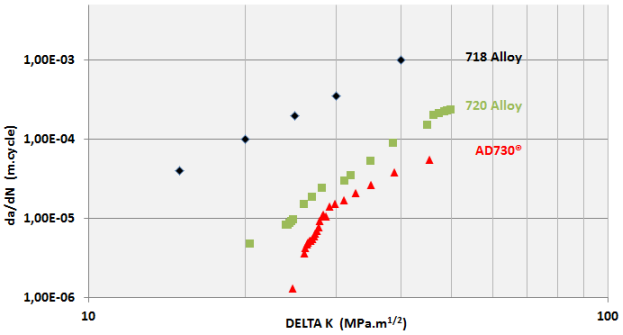

Figure 1.4: Fatigue crack growth resistance of various C&W Nickel-based superalloys at 650°C - R_σ = 0.1 - 10-300-10 s (after [Aubert&Duval, 2017]).

The fatigue and dwell-fatigue crack growth analysis of AD730™ at 750°C under $R_\sigma = 0.05$ has recently been achieved by [Mrozowski, 2020] on both coarse- (CG) and fine-grained (FG) microstructures. In his work, several loading conditions have been assessed, namely 10-0-10 s triangular and 10-300-10 s trapezoidal waveforms, see Fig. 1.5. Comparison of tests conducted under air and vacuum are also depicted in this figure. The effect of the initial pre-cracking conditions from low to high ΔK_i on the FCG resistance is also investigated.

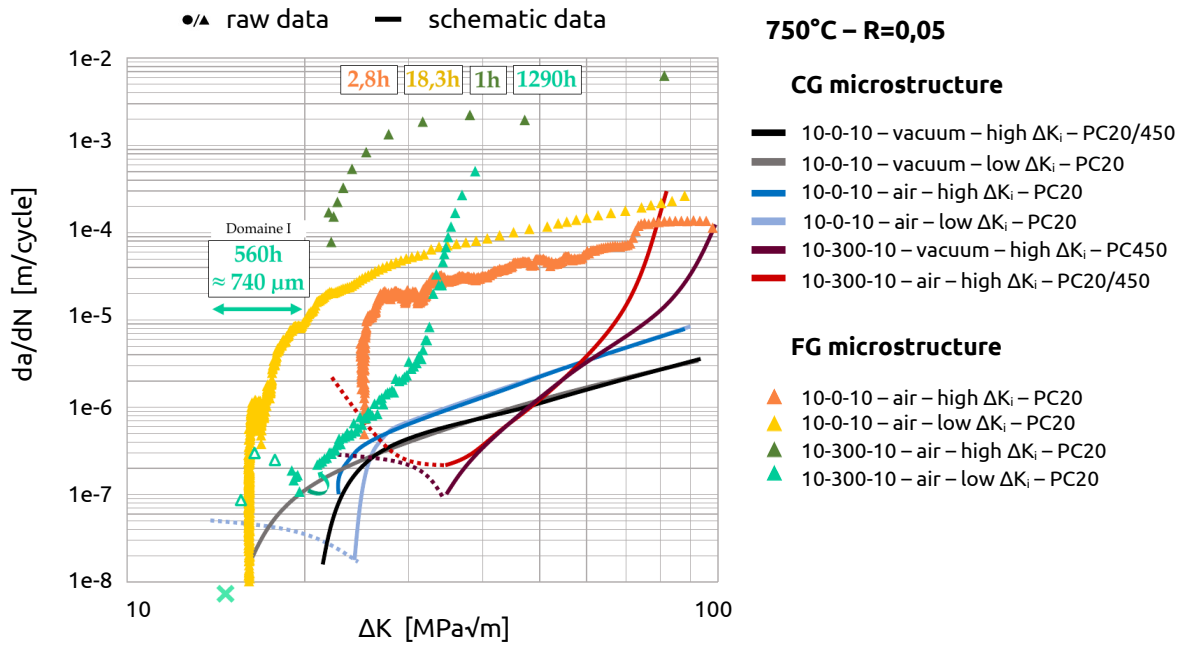

Figure 1.5: Comparison of the fatigue crack growth behavior of AD730™ at 750°C for coarse- and fine-grained microstructures (adapted from [Mrozowski, 2020]).

From this Fig. 1.5, some general conclusions can be drawn:

- a coarse-grained microstructure favors the fatigue crack growth resistance;
- air testing conditions lead to faster crack growth rates;
- the introduction of a dwell time results in an increase in fatigue and dwell-fatigue crack growth rates, particularly for the FG microstructure. For the CG microstructure, a crack deceleration is observed. In both cases, intergranular fracture patterns are observed;
- the deceleration effect evidenced for the FG microstructure in case low ΔK_i have been applied at the beginning of the test results in a decrease in FCGR for the 10-300-10 s signal compared to the 10-0-10 s one.

As for the balance from both cycle- and time-dependent contributions to the overall FCG rates, [Mrozowski, 2020] also conducted some investigations in order to estimate the crack growth driving mechanisms under dwell-fatigue regimes on the two microstructures. In the case of the coarse-grained (CG) AD730™ at 750°C, a larger contribution of the time-dependent (creep) part compared to that of the cycle-dependent (fatigue) part was reported, when subjecting CT specimens to 10-300-10 s with $R = 0.05$ under air. The trend was reported to be inverted when performing the tests under vacuum. For the fine-grained (FG) microstructure under the same testing conditions, Fig. 1.6, the tendency was reported to be the same, with an even greater contribution of the creep part over the global DFCG rate. Such a result can probably be related to the higher proportion of grain boundaries compared to the CG microstructure, favoring a greater extent of GB sliding and cavity growth and finally resulting in higher crack growth rates.
From the Fig. 1.6, it is confirmed that for elevated temperatures, the creep contribution may become predominant over the fatigue one. When compared to a pure fatigue loading scheme (zero dwell-time cycle), one can also notice in Fig. 1.6 the significant change in slope of the $da/dN - \Delta K$ curve, hence evidencing far greater growth rates when including a dwell-time of 300 s at 750°C. It

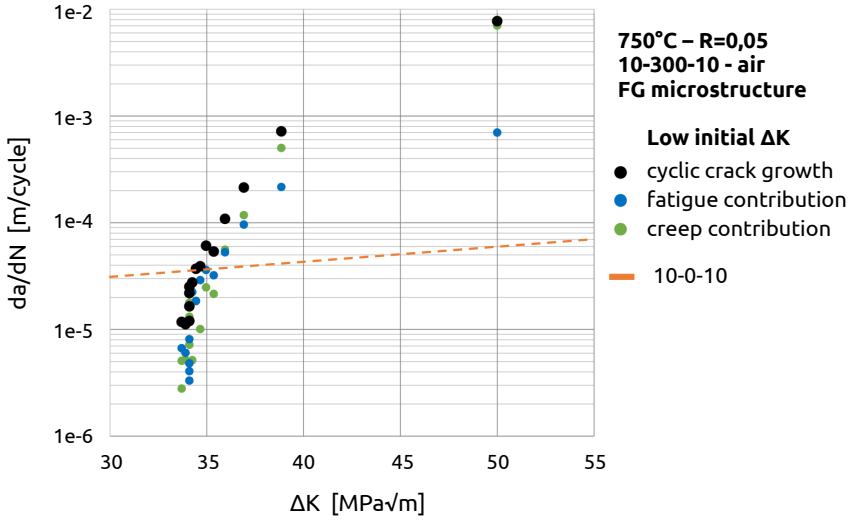

Figure 1.6: Cycle- and time-dependent contributions to DFCG rates in FG AD730™ at 750°C under a 10-300-10 s waveform with $\Delta K_i = 400\,\mathrm{MPa}\sqrt{\mathrm{m}}$ and $R = 0.05$ (adapted from [Mrozowski, 2020]).

can be noted that such a result has already been reported by [Carbou, 2000] for Astroloy and N18 Ni-based superalloys at 750°C under 10-300-10 s loading scheme.

1.3.2.2 Creep crack growth in AD730™

The creep properties of AD730™ with both coarse- and fine-grained microstructures have been investigated by [Thébaud, 2017] and [Vultos, 2019]. The complex interaction between creep and fatigue damages during dwell-fatigue loading conditions renders the grain-size influence even more tricky. It his study conducted on N18, [Flageolet, 2005] has shown that fatigue lives for dwell-fatigue loading are one order of magnitude lower than those for pure creep or pure fatigue loading. Such a strong coupling is directly related to the dwell-period duration at maximum force, as viscoplastic mechanisms such as creep or stress relaxation may intervene during this loading scheme.

Studies conducted on different Ni-based superalloys at a given temperature evidenced a proper holding duration Δt (for each material) during which a transition between creep- to fatigue-dominated behavior appears. This is the case for N18 in [Flageolet, 2005], Udimet 720Li in [Billot, 2010] and AD730™ in [Thébaud et al., 2016]. For AD730™ at 700°C, the dwell-fatigue curves associated with short hold times ($\Delta t = 10\,\mathrm{s}$) are close to the case of pure fatigue loading with very limited cyclic ratcheting [Thébaud et al., 2016], see Fig. 1.7a. For greater holding periods ($\Delta t = 300\,\mathrm{s}$), the apparent mechanical behavior is closer to that of pure creep with typical 3-stages process (primary, secondary and tertiary creep), see Fig. 1.7b. Moreover, a change in deformation mechanisms was reported to occur depending on the applied stress between 750 and 850 MPa. Such a result of dual deformation mechanisms at high temperature in AD730™ has also been recently observed by [Durand et al., 2020] in FG conditions at 760°C.

Up to now, few experimental results have been published on AD730™ due to its recent development. In the experimental work of the Chap. 3, pure fatigue and dwell-fatigue crack growth

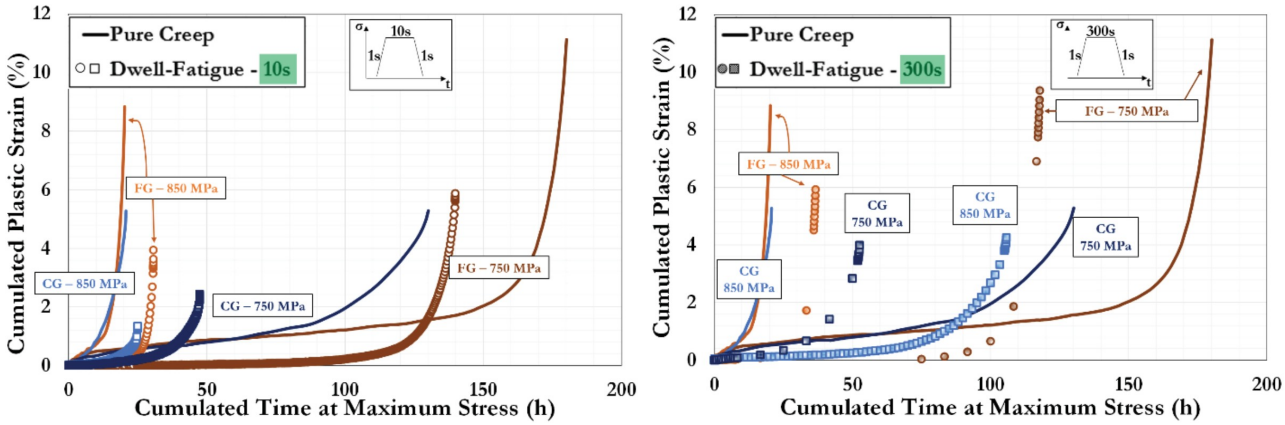

(a) Dwell periods of $\Delta t = 10\,\text{s}$. (b) Dwell periods of $\Delta t = 300\,\text{s}$.

Figure 1.7: Pure creep tests and dwell-fatigue counterparts in both FG and CG AD730™ in air at 700°C under 750 & 850 MPa and varying dwell periods from 10 to 300 s (from [Thébaud et al., 2016]).

tests will be conducted in order to evidence the main governing mechanisms. This will provide further insights concerning the FCG resistance in AD730™ under complex loading conditions. In addition, the possible occurrence of crack propagation anomalies will also be investigated. The latter, generally observed in Nickel-based superalloys, are discussed in the next sub-sect. 1.3.3.

1.3.3 Crack growth anomalies

When subjected to complex loading conditions during laboratory tests (fatigue and creep-fatigue), Nickel-based superalloys have been proved to be prone to disturbed crack propagation stage. Indeed, some of these superalloys, namely Inconel718, N18, René65, Udimet 720Li and AD730™, have exhibited complex fracture topologies, not conform with the standard modeling hypotheses relying on Fracture Mechanics considerations. Such peculiarities include:

- a crack front *tunneling effect* associated with a more or less significant curvature of the crack front along the specimen thickness once a dwell period is superimposed to a standard cyclic scheme;
- and the development of shear lips along the crack propagation plane as long as the crack is subjected to pure mode *I* cracking in the stable crack growth regime. The crack propagation problem is no more characterized by two-dimensional features but requires a three-dimensional modeling since the *flat-to-slant transition* occurs.

The occurrence of unstable shear fracture raises a major question regarding the applicability of fatigue data to construct databases of crack propagation life for materials used in fatigue limited applications such as gas turbines [Brooks and Rainforth, 2000]. These crack growth anomalies hence should be studied in more details so as to get a better understanding. In the following, each crack front anomaly will be discussed in more details and illustrated.

1.3.3.1 Flat-to-slant transition

Flat (mode *I*) crack propagation in fatigue is generally stress-dominated, that is, associated with low stresses in the vicinity of the crack-tip, while the slant (mode *II* and *III*) crack propagation is shear-dominated and corresponds to high stress levels at the tip [Chowdhury and Sehitoglu, 2016]. A schematic representation of the flat-to-slant transition is given in Fig. 1.8. On the one hand, the change from flat to slant crack propagation is a phenomenon generally observed in ductile tearing problems in thin specimens made of steel [Esnault, 2014] or aluminum alloy [Schijve, 1981], [Zuidema and Blaauw, 1988].

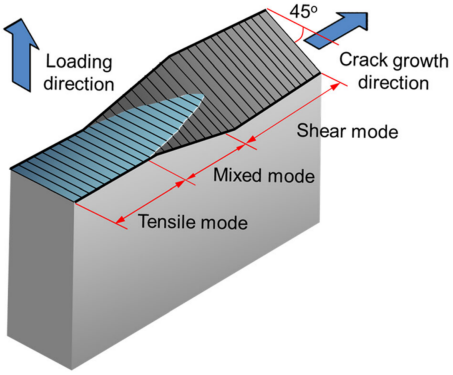

Figure 1.8: Schematic representation of the flat-to-slant transition (from [Chowdhury and Sehitoglu, 2016]).

On the other hand, studies dedicated to Ni-based superalloys are less numerous. One can still mention the work from [Brooks and Rainforth, 1999], [Loo-Morrey and Reed, 2000], [Schoettle et al., 2012], [Schoettle, 2013] conducted on Udimet 720Li. In these latter studies, fractographic observations evidenced a competition between opening (mode *I*) and shear (mode *II* + *III*) modes of crack growth. Besides, mixed cracking modes (*i.e.* inter- and transgranular) have been evidenced in the deflected area with no particular explanation from the microstructure (grain orientation or texture) for the deflected crack growth. Local and evolving crack-tip stress state is assumed to play a role in this process.

Recent tests conducted at ONERA have evidenced the flat-to-slant transition in N18 when subjected to pure fatigue loading conditions [Tourjansky, 2013]. This process is illustrated in Fig. 1.9.

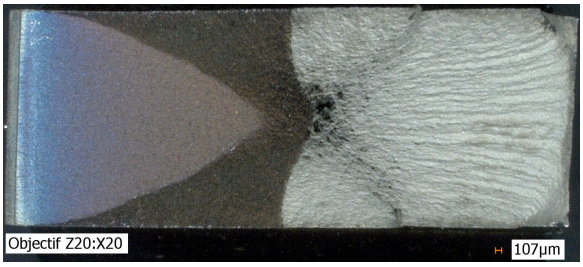

(a) Fracture surface with corresponding crack front and slanted area.

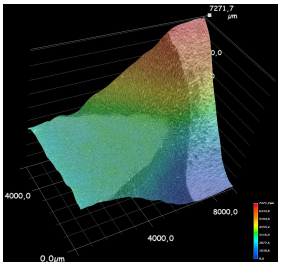

(b) Topography of the fracture surface.

Figure 1.9: Fractography of a 6 mm-thick SEN-T specimen made of N18 subjected to pure fatigue loading at 550°C.

The deflection of the crack growth in Ni-based superalloys under pure fatigue regime has been evidenced at low (20°C) to moderate temperatures (550°C) but is less pronounced at high temperatures ($T > 550$°C). Such a tendency for a suppression of the deflection at high temperature has also been confirmed in the work of [Schoettle et al., 2012]. For dwell-fatigue loading, the deflection seems to be even less pronounced, as can be seen in Fig. 1.10 in which the topology of the fracture surface is less pronounced compared to the pure fatigue case at 550°C, Fig. 1.9b.

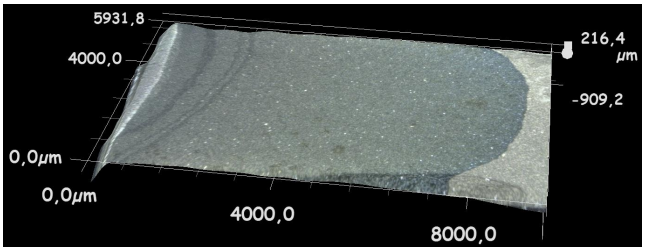

Figure 1.10: Fractography of a 6 mm-thick SEN-T specimen made of N18 subjected to dwell-fatigue loading at 550°C.

The flat-to-slant transition has been reported to preferentially occur in fine-grained (high-strength) microstructures of C&W Ni-based alloys compared to their coarse-grained (low-strength) counterparts [Brooks and Rainforth, 1999]. Moreover, this crack deflection has been related to the slip character within the material by [Loo-Morrey and Reed, 2000]. Slip processes are expected to be more heterogeneous at low temperatures, hence resulting in a planar slip. On the contrary, increasing the temperature seems to result in a more homogeneous slip with different characteristics. According to [Schoettle et al., 2012] who studied the tilt angles from slanted zones, if the deflection exceeds the crack-tip plastic zone, the crack is expected to become a mixed macroscopic mode (opening and shear mode) crack that can be described by conventional LEFM (with a local k_I and k_{II} controlling the crack growth). In addition, plastic instabilities at the crack-tip such as Dynamic Strain Aging (DSA) effects may offer a partial explanation for the onset of crack deflection [Brooks and Rainforth, 1999], [Schoettle, 2013]. It also seems accepted that a strong microstructural component is driving the shear fracture process and therefore determining the macroscopic crack shape. Stable flat fracture is also ensured as long as damage accumulation ahead of the crack-tip in the plastic zone is stable. In opposition, shear instability leading to crack deflection may result from situations where dislocation glide is severely impeded [Brooks and Rainforth, 2000].
In all cases, it seems that the mechanistic origins of the anomalous crack growth behavior are still to be fully determined.

On the numerical prospect, the simulation of the flat-to-slant transition under quasi-static monotonic conditions have been addressed in numerous papers [Lan et al., 2006], [Xue and Wierzbicki, 2008], [Huang and Xue, 2009], [Morgeneyer et al., 2010], [Besson et al., 2013], [Ohata et al., 2014], [Ren et al., 2016]. Nonetheless, for pure fatigue or creep-fatigue loading conditions, the simulation seems not to have been addressed yet. Such a point is intended to be a mid-term outlook to the present Ph.D. work. For the considered material, the basic idea is to assess in a following chapter (*cf.* Chap. 3) the propensity of AD730™ to crack deflection upon testing. To this end, fractographic observations and tilt angles will serve as a comprehensive understanding of the underlying mechanisms, at least in a qualitative way.

1.3.3.2 Tunneling effect

The crack tunneling effect, also referred to crack front curvature, often occurs in plane strain conditions (*i.e.* triaxial stress state) for high temperature testing [Antunes et al., 2001]. The extent of tunneling, that is the degree of retardation at the surface compared to the core material,

is strongly influenced by time-dependent crack propagation, that is, when high temperatures are reached or for long dwell cycles [Tong et al., 1997], [Branco et al., 1999].

Experimentally, this effect can be observed while analyzing the fractographic surfaces of the specimens. To this end, the crack front can be evidenced thanks to dedicated heat or mechanical marking procedures, hence leaving beachmarks or zones with a change in roughness, respectively. The N18 superalloy studied by [Tourjansky, 2013] has evidenced a slight tunneling effect at 550°C under pure fatigue loading conditions, see Fig. 1.11. One can notice on this figure a slight apparition of shear lips from the free edges and a well-defined "thumbnail-shaped" crack front.

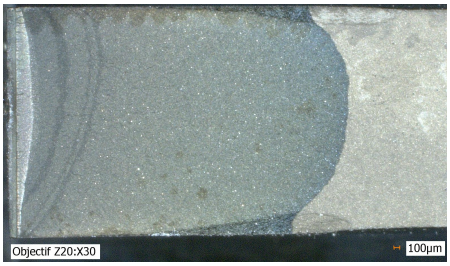

Figure 1.11: Fractography of a 6 mm-thick SEN-T specimen made of N18 subjected to dwell-fatigue loading at 550°C.

For Direct Aged (DA) Inconel718, the study of [Fessler, 2017] also revealed the occurrence of tunneling effect. Under pure fatigue conditions, this effect is not so pronounced, see Fig. 1.12, for which the crack front on a 4 mm-thick SEN-T specimen can be seen to be slightly non-linear, Fig. 1.12a, while that of a 3.5 mm-thick reduced KB specimen is almost of ellipsoidal-shape starting from the notch, Fig. 1.12b.

(a) SEN-T specimen - 0.05 Hz.

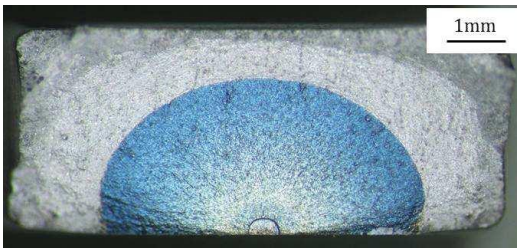

(b) KBr specimen - 20 Hz.

Figure 1.12: Fractography of specimens made of Inconel718 subjected to pure fatigue loading - triangular signal at 550°C (after [Fessler, 2017]).

Switching to creep-fatigue loading conditions results in a more significant tunneling effect, see Fig. 1.13. Still at 550°C under a trapezoidal scheme (10-1200-10 s), the crack front from a SEN-T specimen is no longer straight but exhibits a significant curvature. The crack front seems to have a higher velocity in the core material compared to the free edges, Fig. 1.13a. It seems there is a differential in the crack growth rate along the front. As for the KBr specimen, the front is no more of ellipsoidal-shape but almost circular. The crack advance seems to be faster in the mid-thickness of the specimen, Fig. 1.13b.

Tunneling effect has been reported to preferentially occur in the fine-grained microstructure of AD730™ compared to its coarse-grained counterpart [Mrozowski, 2020]. Nowadays, there is no consensus on the physical or mechanical explanations of this tunneling effect. It is probably the contribution of several phenomena that may explain such a trend. The convexity of the crack front can be explained by the non-uniform processes occurring at the crack-tip (plastic-

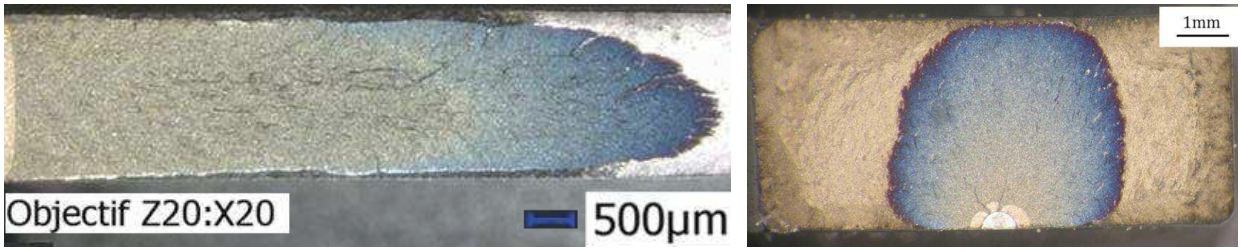

(a) SEN-T specimen - 10-1200-10 s. (b) KBr specimen - 10-1200-10 s.

Figure 1.13: Fractography of specimens made of Inconel718 subjected to creep-fatigue loading - trapezoidal signal at 550°C (after [Fessler, 2017]).

ity induced crack closure [Antunes et al., 2001], [Branco et al., 2008], [de Matos and Nowell, 2008], plastic instabilities, stress relaxation, DSA [Brooks and Rainforth, 1999], change in stress triaxiality ratio [Branco et al., 2012], Lode parameter [Xue and Wierzbicki, 2008], [Danas and Ponte Castañeda, 2012], oxidation, ...). This in turn results in a differential in crack growth rates.

Let us note that attempts to simulate the tunneling effect under cyclic loading conditions have been proposed by [González-Herrera and Zapatero, 2008], [Vor, 2009], [Fiordalisi, 2014], [Gardin et al., 2016a]. However, in these studies, the curvature of the crack front was assimilated and driven by plasticity-induced crack closure mechanisms.
However, creep-fatigue conditions have been little addressed. One can mention the work of [Jing et al., 2017] and [Tang et al., 2020], using a cycle-based multi-mechanism damage model. Such an approach has proved to yield promising results with a correct reproduction of the tunneling effect, see Fig. 1.14.

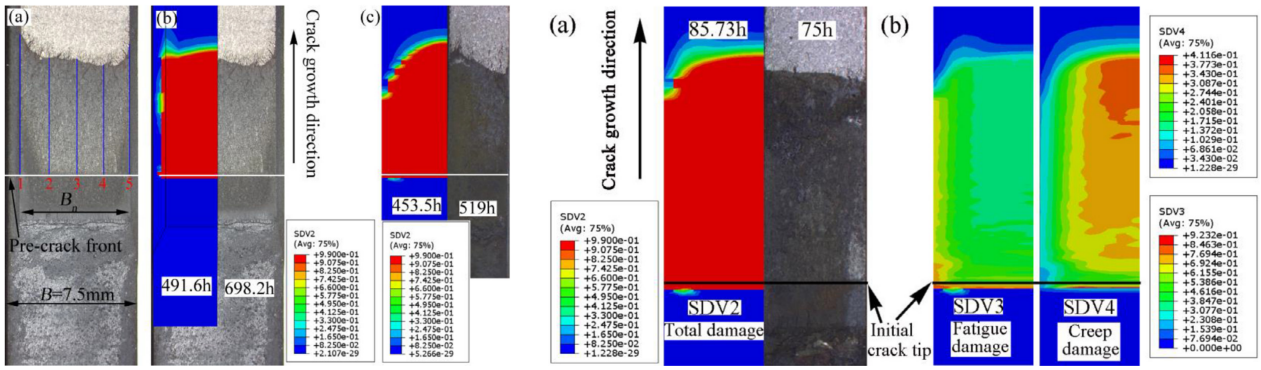

(a) Specimen with and without side groove under 180 s hold time. (b) Total, fatigue and creep damage contours under pure fatigue conditions.

Figure 1.14: Crack growth profiles with simulated damage contours vs. experimental fracture surfaces for creep-fatigue (left) and pure fatigue (right) loading conditions (from [Tang et al., 2020]).

As a way of summary, for the observed flat-to-slant transition as well as crack front tunneling, local mechanical phenomena seem to play a role in the deflected crack growth and differential crack growth rates. Even if no clear explanations can be formulated, some key points have been understood and encourage considering the local stress state at the crack-tip as driving mechanisms. In turn, all these aspects promote the intention to consider a local approach to fracture to address these crack growth anomalies in numerical structural simulations.

1.4 Fracture modeling in Finite Element Analysis

When dealing with fracture problems, several methods exist to calculate the response of a structure (cracked or not) whose material has a more or less ductile behavior. Two major approaches can be classified according to the literature, depending on the scale of the analysis:

- the **global approaches to fracture**, which consider a macroscopic crack. Such methods aim at relating some energetic parameters to the failure process of a structure without considering the non-linear phenomena occurring within the material and close to the crack-tip.
  As said before, the global approach to fracture is not able to reproduce the disturbed crack front shape and topologies associated with the fracture process of Ni-based superalloys under complex loading conditions. As a result, a second option should be favored;
- the **local approaches to fracture**, which are located at the scale of material points (or RVE). These methods focus on the physical mechanisms associated with fracture such as both plastic work and subsequent degradation processes through cavities nucleation, growth and coalescence [Pineau, 2006].

When dealing with difficult situations involving complex loading conditions, which is the case here with fatigue and dwell-fatigue schemes, choice for a local approach needs to be favored in order to accurately assess the non-linear phenomena and the stress redistribution occurring in the fracture process zone (FPZ).

1.4.1 The local approach to fracture: an overview

Physical mechanisms governing the damage process strongly interact with the material behavior. For metallic alloys, as long as the material plastically deforms, its mechanical properties first increase thanks to strain-hardening effect, and then decrease due to the detrimental effect of damage, see Fig. 1.15. Hence, a coupling between damage and material behavior should be taken into account to model the stress-softening effect associated with damage increase [Saanouni, 2012].

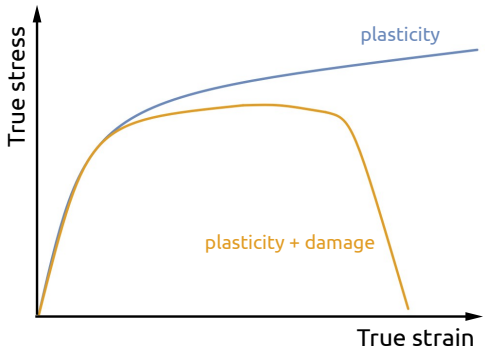

Figure 1.15: Difference between coupled and uncoupled models on the mechanical behavior of a ductile material.

In the absence of coupling effect between damage and plasticity, the schematic response of the Fig. 1.15 becomes unrealistic, evidencing the major role damage process plays on the overall material response. Apart from the standard monotonic loading as the one depicted in Fig. 1.15, the problematic is the same for cyclic loading conditions where the hysteresis viscoplastic loops should evolve as long as damage increases.

Nowadays, macroscopic fracture models relying on Finite Element Analyses (FEA) remain the most successful approach to apprehend the fracture problems at the scale of the structure. However, the local approach has been less developed in the area of fatigue crack propagation for several reasons. First of all, Fracture Mechanics offers, in many practical cases, a correct response to the needs of industrial applications (ΔK or cyclic J approaches) [Anderson, 2017]. In addition, some phenomena render the use of the local approach more delicate compared to the case of monotonous stresses [Qian et al., 1996]. Thus, the constitutive equations are often of higher complexity since they have to translate some particular phenomena related to, *e.g.* the reversed flow (introduction of kinematic strain-hardening). Similarly, the possibility of crack closure must also be taken into account in fatigue situations. Finally, the precise mechanisms of crack propagation are often less well understood in fatigue than in the monotonic case. Nevertheless, the optimization in the design of structures now requires the ability to predict crack propagation in complex cases such as generalized plasticity [Maurel et al., 2017], anisothermal stresses [Otin et al., 2007], time-dependent plasticity [Marchal, 2006], [Aslan, 2010], and complex geometries, etc. The developments from the last 30 years in material modeling and FEA allow researchers to benefit from a relevant use of local approaches to fracture in order to address such complex cases of fatigue crack propagation.

For the *local* approach, contrary to the *global* one, the crack is not the main object of the study, it is damage, *i.e.* the progressive degradation of the integrity of the material, potentially leading to failure. The main advantage of local approaches relies on the fact that their parameters only depend on the material and not on the geometry. Thus the transferability of results obtained on laboratory specimens to the calculation on real structures is easier [Besson et al., 2004]. Moreover, the tests do not require the respect of strict conditions on the state of stress or deformation.

1.4.1.1 General framework

When considering fracture problems through crack propagation at the material point level, two distinct approaches can be found in the literature:

1. The ***fracture criteria*** which are associated with a volumetric damage process. They rely on a critical state of plastic strain or stress and consider the Representative Volume Element (RVE) as broken once such a state is reached [Berdin, 2004], [Wierzbicki et al., 2005], [Besson, 2010], [Bai and Wierzbicki, 2015], [Seidenfuss and Linse, 2016]. Owing to the fact that damage is considered as an external parameter which does not alter the material behavior, such models belong to the class of *uncoupled models*.
   A general form for uncoupled fracture criteria is given by the damage indicator D in eq. (1.5):

$$D = \int \mathrm{d}D = \int_0^{\bar{\varepsilon}^p(t)} \mathcal{F}\left(\underset{\sim}{\sigma}, \underset{\sim}{\varepsilon}\right) \mathrm{d}\bar{\varepsilon}^p \geq 1 \tag{1.5}$$

   where the kernel function $\mathcal{F}\left(\underset{\sim}{\sigma}, \underset{\sim}{\varepsilon}\right)$ is a scalar function of both the stress and strain tensors, generally influenced by stress triaxiality, and $\mathrm{d}\bar{\varepsilon}^p$ is the incremental equivalent plastic strain in the current configuration. It is worth mentioning that fracture criteria act as damage indicator but have no direct effect on the element mechanical resistance. Hence, the strain softening effect is not represented, which may lead to a poor description of the strain localization process and the subsequent crack path associated with the loss of load-bearing

capability of the structure due to damage.

2. The ***damage models*** which also consider some degradation mechanisms within the bulk material. These models rely on the evolution of one (or several) damage variable(s) whose effects result in the stress softening of the mechanical behavior [Desmorat, 2004], [Pardoen and Besson, 2004] [Besson, 2010]. The coupling between damage and material response makes these models to belong to the class of *coupled models*.

No matter the chosen approach for the in-volume *coupled* damage models, the general scope is based on the modeling of cavities growth through *micromechanical* modeling (*e.g.* for ductile or creep fracture problems), or on the use of proper mathematical functions representing the macroscopic effects of damage through *phenomenological* or *macroscopic* modeling, thanks to the Continuum Damage Mechanics (CDM) framework [Besson, 2010]. In such a case, the damage variable is defined based on the influence of an internal degradation observed on the macroscopic properties such as stiffness modulus, yield stress and density of materials [de Souza Neto et al., 2011]. Advantages and drawbacks of these approaches can be found in, *e.g.* [Bonora et al., 2005].

1.4.1.2 Damage models (coupled approaches)

Conversely to the fracture criteria, *coupled* damage models consider the use of an internal variable whose evolution during loading has a direct impact on the material properties, Fig. 1.15.

The mostly used models are either the *Gurson* model [Gurson, 1975], [Gurson, 1977] or *Gurson-Tvergaard-Needleman* (GTN) [Chu and Needleman, 1980], [Tvergaard and Needleman, 1984] and the *Rousselier* model [Rousselier, 1986], [Rousselier, 1987], [Rousselier, 2001] which belong to the *porous solid plasticity* models. They are originally based on micro-cracks analyses (former) or on thermodynamics considerations (latter). Micro-mechanics based damage models have proven their potential in the ductile fracture prediction over the five past decades. To the best of the author's knowledge, there have been few attempts using the GTN model for fatigue crack growth predictions. Indeed, the mechanisms leading to fatigue damage generally differ from that of ductile failure. The former mainly comes from micro-crack initiation at the surface of the specimen due to dislocations accumulation in persistent slip bands while the latter is mainly governed by cavity nucleation, growth and coalescence in the bulk material at the boundaries of inclusions [Lemaitre, 1985b]. Consequently, for micro-based models, the reduction in the yield surface is to be related to void concentration within the bulk material resulting in a plastic-damage coupling.
Despite significant improvements for the GTN model over the last years, one aspect can be mentioned: there is no coupling between damage and elastic behavior. For ductile damage prediction or metal forming process, the large plastic strain undergone by the material makes such a restriction not dominant. However, for fatigue problems where plastic strain levels are lower and successive load reversals may alter the elastic properties, such a point may be detrimental.

Apart from micro-based models, another class of meso-based models has been introduced in the late 1970's and still remains of practical utilization in the industrial and research fields: the *Continuum Damage Mechanics* (CDM) models. This framework has been proved to deal with fatigue problems which seems in better adequacy with our problematic [Lemaitre and Desmorat, 2005].

1.4.2 Continuum Damage Mechanics framework

This category of damage models belongs to the class of the so-called *phenomenological constitutive damage models*, which do not rely on micro-mechanics, contrarily to the previously described models, but mostly on meso-mechanics considerations. Such models mainly rely on the Continuum Damage Mechanics (CDM) framework [Lemaitre and Chaboche, 1990], [Desmorat, 2004], [Besson, 2010]. They are considered as "phenomenological" because their developments are essentially based on macroscopic considerations and because the internal damage variable directly affects the macroscopic material properties such as the elastic stiffnesses.

1.4.2.1 A short historical review

CDM has emerged in the last four decades as a viable framework capable of describing microcracks initiation, growth and coalescence in metals. Initially introduced for creep failure problems [Kachanov, 1958], [Rabotnov, 1969], [Leckie and Hayhurst, 1974], [Lemaitre and Chaboche, 1974], the concepts have since been extended to other damaging processes [Skrzypek and Ganczarski, 1999] as well as other materials, *e.g.* [Arnold and Kruch, 1994], [Chaboche et al., 1998] (composites) and [Mazars, 1986], [Desmorat et al., 2007] (concretes). CDM concepts have been applied to model creep damage, ductile plastic damage, brittle damage and fatigue damage [Lemaitre and Desmorat, 2005]. More particularly, the fatigue damage has been investigated in the pioneer studies of [Lemaitre, 1971], [Lemaitre, 1974], [Chaboche, 1974], [Plumtree and Lemaitre, 1984], [Dufailly and Lemaitre, 1995]. Creep-fatigue interaction models also emerged from these studies, hence resulting in predictions closer to real loading cases [Lemaitre et al., 1974], [Lemaitre and Plumtree, 1979]. Since the development of "standard" fatigue damage models [Chaboche, 1978], several CDM-based HCF damage models have been proposed in the literature such as, *e.g.* the two-scale damage model of [Lemaitre et al., 1999] or that of [Brighenti and Carpinteri, 2013] based on endurance surface.

1.4.2.2 General concepts

The CDM theory represents an extension to Continuum Mechanics with the objective of describing the evolution of defects within a material from a macroscopic point of view. An homogenization process allows these material defects to be considered as sufficiently numerous and evenly distributed within a given Representative Volume Element (RVE). At a macroscopic scale, the damaged volume can hence be assimilated to a continuous medium.
When a component is subjected to external forces, internal degradation, described as the density of micro-cavities and micro-voids, is accumulated. The resistance of the component to the applied load decreases, which may be quantified by a damage variable D in CDM. Generally, the evolution of such a damage variable D is defined as a function of stress or strain components:

$$\dot{D} = \mathcal{F}\left(\underset{\sim}{\sigma}, \underset{\sim}{\varepsilon}\right) \tag{1.6}$$

The evolution of this damage variable primarily depends on the external conditions, depending on the loading modes (temperature, stress amplitude, mean stress, loading frequency...).

In order for the damage to be introduced in a material model, some modeling assumptions have to be specified.

Effective stress concept

Let us consider a RVE loaded by a force $\underline{F} = F\,\underline{n}$ with $\underline{n}$ its normal. The usual uniaxial stress is given by: $\sigma = F/S$. If all the defects are open in such a way that no micro-forces can act on the surfaces of micro-cavities represented by S_D, it is hence convenient to introduce the *effective stress* $\tilde{\sigma}$ related to the *net* surface that *effectively* bears the load, namely $S - S_D$:

$$\tilde{\sigma} = \frac{F}{S - S_D} = \frac{F}{S_{net}} \tag{1.7}$$

If only the undamaged surface (the net surface) is able to carry the load, the stress must increase. The introduction of the damage variable D yields the effective stress:

$$\tilde{\sigma} = \frac{S_{total}}{S_{net}}\,\sigma = \frac{\sigma}{1 - D} \qquad \text{with} \qquad D = \frac{S_D}{S} \in [0., 1] \tag{1.8}$$

Consequently, the effective stress describes the impact of damage on the macro-behavior of the material through a supposedly homogeneous micro-cracks density within the material. The effective stress concept is hence particularly convenient in a computational viewpoint [Simo and Ju, 1987].

Equivalence principles

A way to avoid any micromechanical analysis for each type of damage mechanism is to postulate a principle at the mesoscale. Thus, one should consider an equivalence principle between a virgin material and a damaged material [Lemaitre, 1996]. The effective stress concept has been extended by [Lemaitre, 1971], [Chaboche, 1977a] who proposed the *principle of strain equivalence*, Fig. 1.16.

This principle assumes that the deformation behavior of the material is only affected by damage through the effective stress. As a consequence, the strain ε of the undamaged material due to the effective stress $\tilde{\sigma}$ equals the strain ε of the damaged material due to macroscopic stress σ, see Fig. 1.16.
According to this statement, the effective stress is necessarily greater (or equal) to the stress. Moreover, only the stresses are affected by damage while the strains remains unaffected, eq. (1.9).

$$\underset{\sim}{\tilde{\varepsilon}}\,(\underset{\sim}{\tilde{\sigma}}, 0) = \underset{\sim}{\varepsilon}\,(\underset{\sim}{\sigma}, D) \tag{1.9}$$

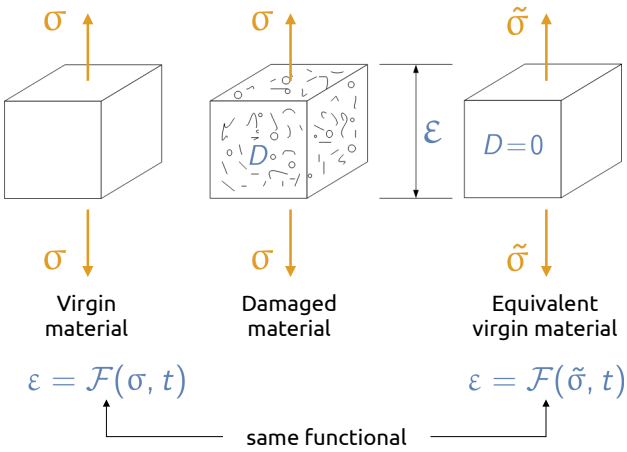

Figure 1.16: Principle of strain equivalence in CDM (adapted from [Haddag, 2007]).

$$\text{For elasticity:} \quad \tilde{\underset{\sim}{\sigma}} = \underset{\approx}{\Lambda} : \tilde{\underset{\sim}{\varepsilon}}^{e} \quad \leftrightarrow \quad \underset{\sim}{\sigma} = \tilde{\underset{\approx}{\Lambda}} : \underset{\sim}{\varepsilon}^{e} \tag{1.10}$$

with $\underset{\approx}{\Lambda}$ the 4^{th}-order tensor for the elastic moduli and $\tilde{\underset{\approx}{\Lambda}} = \underset{\approx}{\Lambda}(1-D)$ its damaged counterpart.

Conversely to the micro-based models detailed above in sub-sect. 1.4.1.2, the phenomenological damage models initially focus on the progressive loss of stiffness, see eq. (1.9), hence consisting in an elastic-damage coupling, although the plasticity criterion may also been related to damage growth thanks to the effective stress concept [Lemaitre, 1985a], [Lemaitre and Marquis, 1988]. Although numerous studies rely on the principle of strain equivalence, such an assumption is not entirely rigorous, as pointed out by [Lemaitre and Chaboche, 1990]. Indeed, this principle assumes that the different behaviors (elasticity & viscoplasticity) are affected by the surface density of defects, all corrected in the same way, which does not seem to be verified. Nevertheless, its simplicity allows for a coherent and efficient formalism to be established [Haddag, 2007].

Let us note that other equivalence principles exist in the literature, in particular: the *principle of stress equivalence* [Simo and Ju, 1987], the *principle of elastic energy equivalence* [Cordebois and Sidoroff, 1979]; the *principle of strain energy or complementary energy equivalence* [Sidoroff, 1981] and the *principle of total energy equivalence* [Chow and Lu, 1992], [Saanouni et al., 1994]. For the sake of concision, they are not described in this document.
Since the growth of micro-cracking of a material usually influences both the stress and the strain distributions, the energy-based equivalence hypothesis [Saanouni, 2012] is more realistic than the principle of strain equivalence for which the local stiffness drop results in a local stress decrease exclusively. The principle of total energy equivalence hence allows for a fully symmetrical formulation of the problem with respect to both the strain- and stress-like variables [Paris, 2008]. Nevertheless, the strain equivalence principle works reasonably well for isotropic damaged materials. It will be considered in the forthcoming Chap. 4.

For the sake of brevity, all the underlying concepts are not recalled here. Interested reader may find additional information about CDM concepts and relative applications in the following references: [Lemaitre and Desmorat, 2005], [Lemaitre et al., 2009], [Saanouni, 2012].

Choice for the present work

Phenomenological damage models have benefited from numerous improvements in last decades. Thanks to the coupling assumptions between damage and material behavior, a stress redistribution directly follows the change in damage state, the latter being a state variable of the problem. The main benefits of such a *coupled model* rely on the direct assessment of the stress and strain fields in the surrounding of the *fracture process zone* (FPZ), hence allowing the crack initiation and subsequent crack growth to be modeled, the latter aspect being the topic of this Ph.D. project.

The literature review on the topic of fatigue crack initiation and propagation reveals a higher proportion of studies taking into account a phenomenological damage model rather than micromechanics-based ones. This comes from the greater ability such macroscopic models possess to represent cyclic loading related aspects such as the Bauschinger effect due to the change in plastic flow during reverse loading conditions as compared to the Gurson or Rousselier model [Besson, 2010].

Indeed, [Skallerud and Zhang, 1997] & [Besson and Guillemer-Neel, 2003] have shown in their studies the limits of the GTN model when dealing with cyclic loading schemes. Owing to the loading schemes to be simulated (*i.e.* cyclic), this fact represents a key element for the damage model to be suggested for FCG analysis. In addition, the well-known Lemaitre damage model has already been considered in fatigue damage problems [Chaboche, 1981], [Lemaitre, 1985a], especially for superalloys [Kaminski, 2007], [Otin, 2007], [Barbier, 2009], hence making it a supporting point for developments to come.

Once the modeling framework has been adopted thanks to practical considerations and a literature survey, one major aspect has to be discussed. It has been proved that coupled damage models suffer from spurious mesh-dependency associated with the loss of unicity of the solution in case of stress-softening material response [Forest and Lorentz, 2004]. This issue, highly detrimental for the predictive capabilities of the damage model, should be corrected in order to retrieve realistic physical predictions. To this end, regularization techniques can be considered.

1.5 Regularization strategies in Finite Element Analysis

1.5.1 General overview

In order to overcome the difficulties associated with the mesh-dependent nature of the local approach in strain-softening conditions, several regularization methods have been proposed in the last decades, particularly for monotonic ductile fracture problems.
However, the scope of the present study focuses on the cyclic crack growth under LCF conditions, which intrinsically means to perform several loading cycles, contrarily to single monotonic loading schemes encountered during ductile cracking problems. Moreover, crack growth prediction in time-dependent loading conditions (creep) is also a much less developed research axis due to complex material models embedded as well with damage localization at the stress singularity close to the crack-tip [Murakami, 2012]. To the author's knowledge, few applications of regularization strategies in the context of cyclic/creep cracking problems can be found in the literature. As a consequence, although major references will be related to ductile fracture problems, applications of regularization methods to creep and fatigue crack growth will be preferentially focused in this work.

Regularization methods can rely on different approaches:

- **the control of the dissipated energy**: which ensures that the energy necessary for a crack to grow is controlled by the model and that the process remains equivalent regardless the mesh size. The most common approaches are:
  - the *Crack Band* method (see [Hillerborg et al., 1976], [Bažant and Oh, 1983] for theoretical developments, and [Hamon et al., 2012] for an application to fatigue crack growth);
  - the *Phase-Field* approach (see [Francfort and Marigo, 1998], [Bourdin et al., 2000] for theo-

retical developments, and [Alessi et al., 2018a], [Azinpour, 2020], [Eldahshan et al., 2021] for applications to ductile fracture, or [Alessi et al., 2018b], [Schreiber et al., 2020], [Hasan and Baxevanis, 2021], [Seleš et al., 2021], [Ulloa et al., 2021] for cyclic crack growth in brittle and ductile materials, and [De Lorenzis and Gerasimov, 2020] for an up-to-date review);

  - and the *Gradient Enhanced Energy* approach (see [Lorentz and Cano, 2005], [Lorentz and Godard, 2011] for theoretical developments, and [Zhang, 2016], [Chen, 2019] for applications);

- **the control of the spread of the strain-softening variables** (referred to as *spatial localization limiters*): which ensures that the strain-softening variables (damage/plasticity) do not localize within a given band of FE. Thus, an internal length controls the non-local interaction of the IP with each others so that to "spread" these strain-softening variables. This can be achieved thanks to a spatial regularization operator or the introduction of gradient terms within the constitutive relations, hence overcoming the limitations of the *local state method*. Among them, one can cite:

  - the *Non-local* approaches (integral as well with both explicit and implicit gradient-type), described hereafter in sub-sect. 1.5.2;
  - the *Second-gradients* methods (see [Truesdell and Toupin, 1960], [Aero and Kuvshinskii, 1961], [Mindlin, 1965]);
  - the *Thick Level Set* approach (see [Moës et al., 2011], [Moës et al., 2014]);
  - the *Eikonal* method (see [Rastiello et al., 2018], [Thierry et al., 2019]);
  - and the *peridynamics* approach, which has recently emerged as an interesting approach as mathematically unifying the mechanics of continuous media and cracks through a spatial operation (see [Silling, 2000], [Littlewood, 2011] for theoretical developments, and [Silling and Askari, 2014], [Zhang et al., 2016], [Liu et al., 2021] for applications to fatigue);

- **the control of the rate of change of the strain-softening variables**: which ensures that the behavior depends on the loading rate, hence allowing for the damage to be delayed and localization to be prevented. This approach is mainly dedicated to dynamic fracture problems. The *bounded rate* or the *delayed* damage models belong to this class of regularization tools (see [Ladevèze, 1992], [Allix and Deü, 1997], [Allix et al., 2019]);

- **the enhancement of the kinematic relations**: which are mainly referred to as *micropolar* (Cosserat) or *micromorphic* continuum models. Although different from the modeling aspects and the theoretical developments, such non-local models are particular cases of the straightforward *Generalized Continuum Theories* (see [Cosserat and Cosserat, 1909], [Eringen and Suhubi, 1964], [Forest, 2009] for theoretical aspects, and [Diamantopoulou et al., 2017], [Aldakheel, 2017], [Davaze, 2019] for ductile fracture, or [Aslan et al., 2011], [Langenfeld et al., 2021] for fatigue loading conditions).

All these techniques will not be detailed as they are not considered in the present work due to the lack of preliminary work. Moreover, their applicability in design offices is not straightforward and further work needs to be achieved so as to ensure their potentialities in solving with robustness the mesh-dependency effect in FE calculations. Nevertheless, interested readers may find a current state of the art on regularization methods in, *e.g.* [Bažant and Jirásek, 2002], [Jirásek

and Rolshoven, 2003b], [Forest and Lorentz, 2004], [Besson, 2010], [César de Sá et al., 2015]. As a consequence, in the forthcoming sections, focus will only be made on spatial localization limiters which are the most generally applicable techniques. Such a choice comes from the acknowledged robustness of these methods to cope with mesh-dependency, together with the relative ease in the numerical implementation prospect [Jirásek and Bažant, 2001]. Moreover, this choice is to be related to the quasi-static loading cases encountered in the present study, together with tools integrated in the Z-set FE solver for which feedback was available.

1.5.2 Spatial localization limiters

Two types of models are usually distinguished: *(i)* integral-type models and *(ii)* gradient-type models. These two approaches are described in the following paragraphs.

1.5.2.1 Convolution / integral-type method

The non-local theory, as opposed to point wise approach, introduces short-range microstructural interaction by assuming that the variable response at a material point is dependent on the state of its neighborhood, in addition to the state point itself. In order to operate a spatial averaging procedure around a material point, a non-local integral equation, eq. (1.11), was first proposed by [Kröner, 1967] and [Eringen and Edelen, 1972] for elastic material models. Later on, [Pijaudier-Cabot and Bažant, 1987] extended this concept into CDM-based models. The regularization operator is hence defined as the convolution product between a weighting function ψ and the local quantity $\mathcal{V}$ in a material point $\underline{x}$:

$$\overline{\mathcal{V}}(\underline{x}) = \int_{\Omega} \psi\left(\underline{x}, \underline{\xi}, \ell_c\right) \mathcal{V}(\underline{\xi}) \, \mathrm{d}\underline{\xi} \qquad \text{with} \qquad \psi(\underline{x}, \underline{\xi}, \ell_c) = \frac{\psi_0\left(\underline{x}, \underline{\xi}, \ell_c\right)}{\int_{\Omega} \psi_0\left(\underline{x}, \underline{\xi}, \ell_c\right) \mathrm{d}\underline{\xi}} \tag{1.11}$$

where Ω is the spatial domain, $\underline{\xi}$ the position vector of the infinitesimally small volume $\mathrm{d}\Omega$, $\psi\left(\underline{x}, \underline{\xi}, \ell_c\right)$ a characteristic length related averaging function for the non-local treatment (*e.g.* of Gaussian-type). Note that the homogeneous weighting function must generally satisfy a normalizing condition, see the right-hand side of eq. (1.11), so as to ensure that the non-local operator does not alter uniform fields after averaging [Xenos, 2015]. Several weighting functions ψ can be found in the literature, see *e.g.* [Pijaudier-Cabot et al., 2004], [Jirásek, 2007]. Strictly speaking, the integral-type formulation given in eq. (1.11) truly abandons the principle of local action. For a discussion about *strong* or *weak* non-locality, the reader is referred to [Bažant and Jirásek, 2002].

The non-local approach is often used due to both its strong theoretical background and numerical robustness, and it can, in principle, be applied to every type of constitutive models. Some questions about the proper formulation of BC (*e.g.* free edges, notches, preexisting flaws) remain however still open [Peerlings et al., 2001], [Rastiello et al., 2018]. Moreover, the complex numerical implementation associated with the time-consuming process related to the averaging procedures in complex geometries make this method difficult to use in an industrial context [Peerlings et al., 1996a]. Further details on the method are given in [Bažant and Jirásek, 2002].

Focusing on **creep crack growth** analyses using an integral-type modeling approach, the literature review, although not so exhaustive, has revealed some interesting papers.
The pioneer applications of non-local analysis of creep fracture hence traced back to the end of the 1980's. One can cite the starting impulsion given by [Saanouni et al., 1989], [Kruch et al., 1991] for creep crack growth (CCG) prediction in superalloys. They showed that the use of a non-local law could greatly decrease the mesh-size effects. These studies were followed by that of [Hall and Hayhurst, 1991] for the analysis of the size effect between small and large CT specimens. Later on, [Murakami and Liu, 1995] put an effort on understanding the mesh-dependency effect in creep problems, with significant insights using of integral non-local averaging. Other researchers used a similar approach, *e.g.* [Duddu and Waisman, 2013] and [Mobasher, 2017] for the creep cracking of ice sheets. Still for engineering materials, the few studies of [Pandey et al., 2019a] for the mesh-dependency to be removed in creep cracking problems are, to the author's knowledge, the most recent ones. All of them rely on an integral-type formulation for the non-local interaction of neighboring points. Although [Sabnis et al., 2016] tried to use a micromorphic approach for the regularization of CCG problems, very little studies considering other non-local treatments can be found in the literature on the topic.

In the context of **fatigue**, a preliminary work was conducted by [Xia et al., 1993] using an integral-type non-local formulation for the analysis of damage distribution in the fracture process zone of an elastic material. Later on, [Qian et al., 1996] studied the fatigue crack growth (FCG) in an elastic-viscoplastic material using a non-local damage variable. Their results showed good agreements with experimental results as well with a good improvement gained from the non-local averaging. In the same way, but out of the scope of CDM-based models, [Fish and Oskay, 2005] proposed a modified non-local GTN model for fatigue and multiscale analysis based on a local model derived earlier in [Oskay and Fish, 2004]. Their model has also proven to be insensitive to the mesh size, both for VLCF & LCF conditions. Recently, [Pandey et al., 2019b], [Pandey et al., 2021] applied several methods to solve for the mesh-dependency effect, among which use was made of the integral-type formulation. They succeeded in modeling FCG under LCF conditions. Moreover, they were able to capture the so-called *constraint effect* associated with differing loading specimens/conditions. In the context of cyclic elastic-viscoplasticity, an attempt was recently made to extend the Chaboche model to non-local interactions by [Maniar et al., 2017], [Kuczynska et al., 2021]. Authors succeeded in obtaining quasi mesh-independent results using an integral-type non-local approach applied to the damage rate together under LCF conditions.

1.5.2.2 Gradient-type models

Using a certain averaging function and expanding eq. (1.11) into a truncated Taylor series, the non-local integral equation can be converted to a gradient-type model equation. Such a result was first derived by [Peerlings et al., 1996b]. Gradient-type models do not modify the kinematic nor the equilibrium equations, but only the constitutive relations. Depending on the specific formulation for the Taylor's expansion, explicit and implicit models are distinguished [Peerlings et al., 2001]. In the present work, since explicit gradient formulations are known to require higher implementation cost (occurrence of 2^{nd}-order partial derivatives and the dialogue between Gauss points which is required to evaluate the gradients), they have not been considered. Moreover, this regularization technique may suffer from a lack of vanishing stress level at failure, which may be an obstacle

in the context of the local approach to fracture [Comi and Perego, 1996], [Engelen et al., 2003]. Compared with non-local integral-type approaches, explicit gradient formulations also possess significant numerical disadvantages [Peerlings et al., 2001], [Jirásek and Rolshoven, 2009]. That is the reason why implicit formulations are often preferred. Moreover, difficulties associated with the non-local integral form, see sub-sect. 1.5.2.1, seem apparently to have been overcame using the implicit gradient approach.

Implicit gradient models

In implicit formulations, the non-local quantity $\overline{\mathcal{V}}$ is implicitly defined by a PDE which is solved in addition to the standard equilibrium PDE at the global level. Thus, the following diffusion equation of Helmholtz-type is considered:

$$\overline{\mathcal{V}}(\underline{x}) \; - \; c\,\nabla^2\,\overline{\mathcal{V}}(\underline{x}) \; = \; \mathcal{V}(\underline{x}) \qquad \text{in} \;\; \Omega \tag{1.12}$$

In eq. (1.12), the incorporation of the characteristic length of the material (through the term c) into the continuum framework of damage mechanics models allows for the microstructural influence on the macroscopic level to be modeled. Indeed, the Laplacian term in eq. (1.12) acts as a *diffusion* term responsible for a larger or lesser spreading of the localization zone regardless of the mesh size. Hence, the difference between the two fields acts as a source term making it possible to regard $\overline{\mathcal{V}}$ as a material average of $\mathcal{V}$ though the zone whose size depends on the length scale parameter c. It is to be noticed that such a relationship eq. (1.12) was postulated and does not result from thermodynamic considerations [Sornin, 2007]. Moreover, it is worth noting that if $c = 0$ the non-local model recovers its local form and there is no effect of the non-local extension on the damage model.

The form in eq. (1.12) can be shown to be equivalent to the integral-type formulation with special weight functions used for the averaging [Peerlings, 1999], [Engelen et al., 2003], hence ensuring a *strong* non-locality. In opposition to the explicit formulation [Peerlings et al., 2001], the implicit form in eq. (1.12) is truly non-local in the sense that variations of the local variable $\mathcal{V}$ in the neighboring of $\underline{x}$ always affect the non-local variable $\overline{\mathcal{V}}(\underline{x})$ due to the definition of the Green functions and thanks to the fact that eq. (1.12) is satisfied exactly during the computation [Wu et al., 2012].

For the averaging PDE given in eq. (1.12) to be solved and in order to uniquely define the non-local quantity, an additional BC of Neumann- or Dirichlet-type must be added to the eq. (1.12). Providing the fact that $\overline{\mathcal{V}}$ is generally unknown on the entire body, a Neumann-type BC is preferred. This aspect is not fully clarified and deserves much further investigations.

$$\frac{\partial \overline{\mathcal{V}}}{\partial \underline{n}} \; = \; \nabla\,\overline{\mathcal{V}}.\underline{n} \; = \; 0 \qquad \text{on} \;\; \partial\Omega \tag{1.13}$$

with $\underline{n}$ the external normal vector at every point in the edge $\partial\Omega$ and ∇ the gradient operator. The physical interpretation of the additional BC is still unresolved. The simple natural form given in eq. (1.13), although rather mathematically motivated, was suggested by [Lasry and Belytschko, 1988], [Peerlings, 1999] so as to ensure that the overall considered local quantity within the continuum is preserved in the non-local averaging [Peerlings et al., 1996b], [Peerlings et al., 1998]:

$$\int_{\Omega} \overline{\mathcal{V}} \, \mathrm{d}\Omega \;=\; \int_{\Omega} \mathcal{V} \, \mathrm{d}\Omega \tag{1.14}$$

where $\overline{\mathcal{V}} = \mathcal{V}$ holds for homogeneous deformations and for the limiting case of a vanishing length scale. Moreover, the Neumann BC defined in eq. (1.13) prohibits a damage flux through the boundary of the domain, resulting in an increased contribution of points to the non-local field when approaching the external boundary, which can be explained, in case of damage, by the increased sensitivity of the material towards formation of surface defects [Samal, 2007].
A critical discussion of possible BC can be found in [Peerlings et al., 2001].

Since the pioneer publication of [Peerlings et al., 1996b] on the implicit gradient-enhanced damage formulation for monotonic loading fracture, the concept has been applied in many other works. Restricting ourselves to the Lemaitre-type damage model, one can mention the studies from [Peerlings et al., 2001], [César de Sá et al., 2006], [Enakoutsa et al., 2007], [Khoei et al., 2013a], [Seupel et al., 2018].

As for applications dedicated to **fatigue applications**, the literature review can be seen to be more tenuous. A first attempt is the study of [Kowalsky et al., 2012] & [Heinrich et al., 2013] who studied the damage evolution within a structural steel subjected to a seismic excitation. In their work, only few loading cycles were considered during structural applications due to the fact that seismic stresses are infrequent and concern damped structures. However, the non-local formulation of implicit gradient-type seemed to yield satisfactory results [Velde, 2010]. In the same way, [Khoei et al., 2013a] studied the ductile crack growth within metallic alloys under cyclic loading conditions. In this work, only VLCF conditions were met with promising results for structural calculations. The implicit gradient-enhanced formulation incorporated so that for the mesh-dependency to be removed also seemed to be accurate enough. For thermomechanical fatigue applications, the recent work from [Yin et al., 2022] also provides an interesting achievement considering a time-dependent non-linear material model. Authors evidence the fact that the damage-softening-induced ill-posed equation has been overcome in fatigue situations. Moreover, issues of numerical instability and mesh sensitivity have been shown to be improved to a large extent, hence providing a significant outcome and enforcing the relevance of the choices associated with the work at hand (see the remainder of the chapter).

Finally, to the best of the author's knowledge, no papers have yet been published for **creep** problems using gradient-enhancement for damage modeling.

The literature review provided some interesting and up-to-date uses of non-local models, particular for cyclic loading situations (with and without sustained loads), thus helping for a choice in the present Ph.D. work (*cf.* Chap. 5 later on). Once the use of a regularization strategy has been considered as a complement to the local approach to fracture, another numerical problem may arise, namely the volumetric locking effect, briefly introduced in the next sect. 1.6.

1.6 Volumetric locking issues in numerical simulations

Apart from the solutions to the spurious mesh-dependency effect described in sect. 1.5, another numerical issue may arise during FE calculations. When considering fracture problems in isochoric conditions, due to the quasi-incompressibility constraint imposed at each integration points of the FE, the effective dimension of the displacement space is reduced [Chen, 2019]. Such a reduction may be too restrictive, hence leading to the lack of spatial convergence.

1.6.1 Context and solutions

It is now well-known that standard displacement-based FE formulations may lead to numerical issues associated with locking phenomena when dealing with isochoric transformations. For example, *volumetric locking* occurs when the inelastic flow is only governed by the deviatoric stress. This locking phenomenon may lead to over-estimated solutions (too stiff), under-estimated displacements, and numerical results exhibiting oscillations, particularly noticeable for the stress fields [Javani, 2011]. The mathematical explanations on the topic have been given in [Babuška, 1971], [Brezzi, 1974], [Bellet, 1999].

According to [Bargellini et al., 2009], [Feld-Payet et al., 2011] and [Michel-Ponnelle, 2011], there exist several possibilities to get rid of the volumetric locking effect, to name a few:

- the Reduced-order Integration (RI) in the FE (all the terms of the formulation are under-integrated) [Zienkiewicz et al., 1971], [Doll et al., 2000], and the Selective Reduced Integration (SRI) technique (some of the terms of the formulation are under-integrated) [Doherty et al., 1969], [Hughes, 1980], [Ramesh and Maniatty, 2005];
- and the mixed formulations (additional DoF are embedded in the formulation) [Washizu, 1955], [Boussetta, 2005], [Lorentz et al., 2008], [El Khaoulani and Bouchard, 2013], among which there is the well known *B-Bar* approach [Hughes, 1980], [Seabra, 2012], [Wolf, 2016].

Discussions on other (new) methods can be found in, *e.g.* [Feld-Payet, 2010] and [Chen, 2019].

Nowadays, there are plenty formulations of enriched FE suitable for a small strain framework which are available in the literature [Zienkiewicz et al., 2013]. According to the comparative review conducted by [Besson and Lorentz, 2006], triangular elements with a 3-fields formulation (displacement, pressure and dilatation) have proved to provide accurate results. Let us note that mixed formulations can easily be used in combination with non-local formulations when necessary [Lorentz et al., 2008], [Bargellini et al., 2009], [Javani et al., 2009], [Feld-Payet, 2010]. In this work, a 4-fields mixed non-local element developed in the Ph.D. project of [Feld-Payet, 2010] will be used to alleviate volumetric locking when simulations of ductile failure are provided to validate some specific points (see Chap. 5 and Chap. 6). This formulation involves 4 DoF: the standard displacement fields $\underline{u}$, the assumed volume change θ, the assumed pressure fields P (*i.e.* the volumetric part of the assumed strain/stress fields, respectively) and the non-local variable $\overline{\mathcal{V}}$, with a linear interpolation ($\mathrm{p1}^2$) for θ, P and $\overline{\mathcal{V}}$, and a quadratic interpolation ($\mathrm{p2}^1$) for the displacements $\underline{u}$, see Fig. 1.17a.

Let us note that, when simulating crack advance upon fatigue cycling, see Chap. 6, provided that no large deformation might be reached in fatigue loading situations, volumetric locking issues will not necessarily occur and a standard FE formulation should be sufficient. In such a case, a 2-fields enhanced non-local element developed in the Ph.D. project of [Germain, 2006] will be used. 2 DoF are included: the standard displacement fields $\underline{u}$ and the additional DoF, the non-local variable $\overline{\mathcal{V}}$. The FE discretization is done using quadratic interpolation functions for $\underline{u}$ (p2) and linear ones for $\overline{\mathcal{V}}$ (p1) [Peerlings et al., 1996b], [Simone et al., 2004], see Fig. 1.17b.
One can still mention that considering the 4-fields mixed formulation represents a balance between increased numerical cost (more DoF in each FE) and a better convergence of the solver (better regularity of the fields).

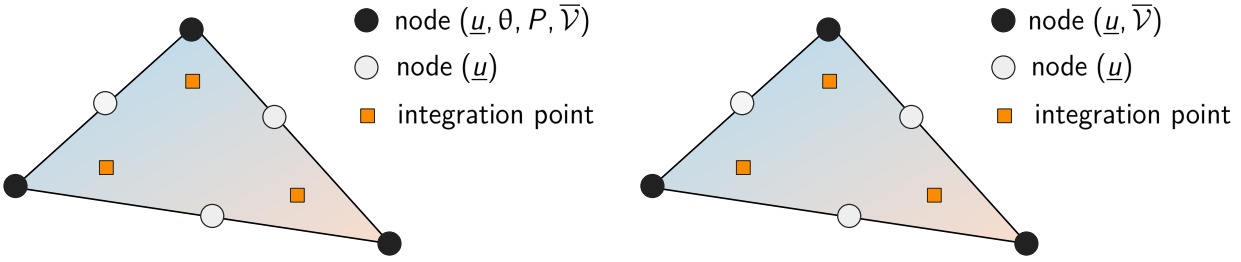

(a) 4-fields finite element (p2-p1-p1-p1). (b) 2-fields finite element (p2-p1).

Figure 1.17: Enhanced c2d6r triangular Finite Elements with reduced integration used for structural calculations in *Z-set*.

In future structural FE calculations, the use of either the 2-fields non-local or the 4-fields mixed non-local FE will be expressively indicated (*cf.* Chap. 5 & Chap. 6).

1.6.2 Illustration

Considering a specimen subjected to a shear loading with a damage model resulting in an apparent stress-softening response, one can analyze the pressure fields in order to assess the extent of volumetric locking. In Fig. 1.18, the hydrostatic pressure is reported for both the standard (p2p1) and the mixed (p2p1p1p1) non-local FE formulations. One can notice on Fig. 1.18a some oscillations of the pressure field close to the upper notch where damage initiates. The lack of regularity of the solution has been proved to slow down the resolution process as well as to decrease the accuracy of the solution. The use of a mixed 4-fields formulation, Fig. 1.18b, enables removing the spurious oscillations with a better continuity of the hydrostatic stress field.

At last, once numerical issues (mesh-dependency and volumetric locking) have been solved, the simulation of the crack growth process remains to be considered in FE numerical calculations. This topic is discussed in the next sect. 1.7.

[1] "p2" stands for a standard quadratic interpolation.

[2] "p1" stands for a linear interpolation using only the vertex nodes.

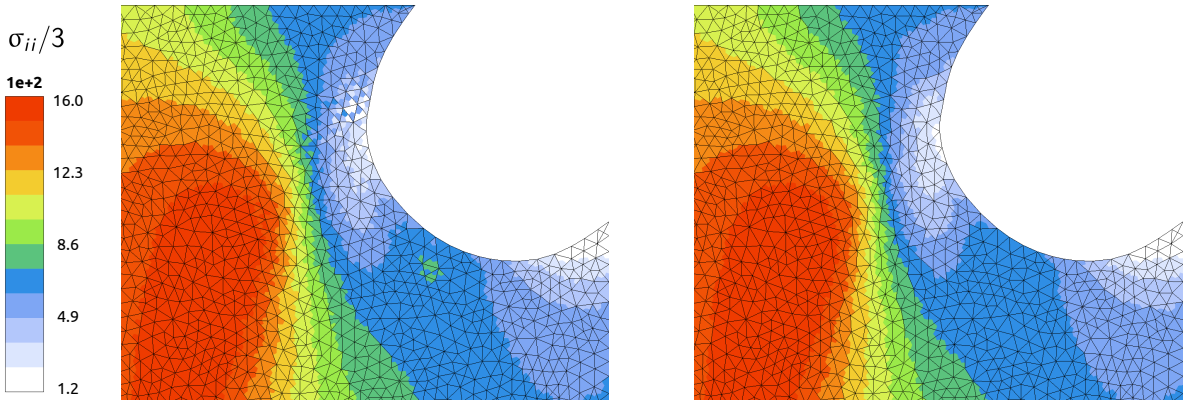

(a) $\sigma_{ii}/3$ - standard non-local formulation. (b) $\sigma_{ii}/3$ - mixed non-local formulation.

Figure 1.18: Comparison of the pressure field using both standard (p2p1) and mixed (p2p1p1p1) FE formulations on the double-notched specimen at $u = 0.1688\,\text{mm}$ with $h_e = 0.2\,\text{mm}$.

1.7 Numerical fracture modeling

1.7.1 On the requirement for a damage-to-fracture transition

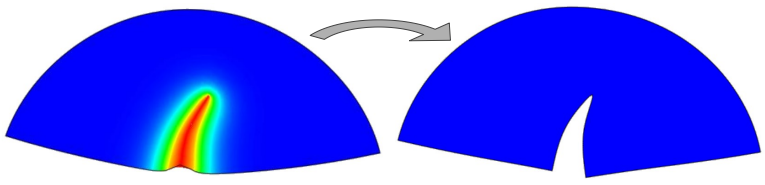

Figure 1.19: Continuous (diffusive) vs. discontinuous (discrete) crack modeling (after [Seleš et al., 2021]).

The Lemaitre model has been proved to be adequate to simulate the fracture process in metallic alloys through simulating elasticity, strain-hardening and stress-softening stages. Areas where crack onset is likely to occur can also be evaluated. Nevertheless, the final stage of macro-crack propagation cannot be captured by this model and a discontinuous representation of the crack is required [Feld-Payet, 2022]. A crack within a structure can be seen as a strong discontinuity of the continuum. The representation of such a discontinuity in the FE mesh requires a special numerical treatment which has given birth to different methods. Some of them rely on the standard FE-framework while others require the introduction of improved FE formulations. In a non-exhaustive manner, a brief review is given in what follows with the most popular methods.

The possibilities for the modeling of failure (in the context of the FEM) can roughly be categorized in three groups: discontinuous (discrete), continuous (diffuse) and combined approaches. Classically, discrete approaches are used in the field of Fracture Mechanics (FM), while continuous approaches are commonly associated with Continuum Damage Mechanics (CDM), Fig. 1.19.

- **continuous (diffuse) approaches**: they use a continuous displacement field when dealing with both the softening and fracture process, *i.e.* $\underline{u}^+ = \underline{u}^-$. In such a case, the failure process is modeled using damage mechanics / porous plasticity. Failure is hence introduced in the problem formulation thanks to a softening material behavior. The localization of deformation essentially models the fracture process. As discussed in the sect. 1.5, suitably regularized damage models are currently available in the literature so as to effectively rely on a continuous approach within FE calculations. A continuous approach is known to possess the distinct advantage (over a discrete one) to account for the effects of void phenomena and stress redistribution/triaxiality on the material behavior. However, the actual material separation associated with the extension of the crack must ultimately still be modeled by accomplishing geometrical separation between the two crack faces.
- **discontinuous (discrete) approaches**: they allow to incorporate displacement discontinuities as the crack is explicitly modeled, with a discontinuous jump of the displacement field across crack faces [Shakoor et al., 2019], *i.e.* $\underline{u}^+ \neq \underline{u}^-$. Such approaches idealize the material degradation by the propagation of a sharp discrete crack. The failure process is incorporated by embedding cracks in the geometrical contour discretized by the FE model. As a consequence, the mesh needs to be adapted so as to trace the progressing crack. One significant advantage (over continuous methods) is that crack kinetics can be assessed.

In fact, according to the critical discussion above, it appears that the combination of continuous and discrete approaches seems to be a promising way for crack growth modeling. For these reasons, new combined approaches have been suggested in recent years. In what follows, and for the sake of briefness, only some numerical methods relying on a FE-framework for the crack propagation to be modeled will be discussed [1]. Since continuous methods have already been introduced in sub-sect. 1.4.1 with possible non-local extension in sect. 1.5, they won't be discussed in further details. Focus is made in the following on the discontinuous methods.

1.7.2 Discontinuous (discrete) crack modeling in FEA

In the discontinuous approach to fracture, the crack is modeled in a discrete way, which is consistent with the displacement discontinuities observed across the crack faces. In a FE framework, the proper modeling of discrete cracks of any arbitrary geometry requires either the use of cohesive elements, element-deletion techniques, enhanced FE formulations or mesh adaption procedures.

[1] For the sake of completeness, one can mention the other approaches that exist in the literature, enabling the crack evolution without remeshing, namely: the meshless methods of *element-free Galerkin* (EFG) [Belytschko et al., 1994], [Belytschko et al., 1995], [Simkins and Li, 2006], [Li et al., 2011], [Wu et al., 2016], [Leclerc, 2020]; the *reproducing kernel* method [Liu et al., 1995], [Simonsen and Li, 2004] and the *cracking smooth particle* approach of [Gingold and Monaghan, 1977], [Rabczuk and Belytschko, 2007]. Note that the *boundary elements method* (BEM) [Aliabadi, 1997], [Yan and Nguyen-Dang, 1995], [Tuhkuri, 1997], [Aliabadi, 2002], [Sládek et al., 2003] or the well-known *Phase-Field* approach [Miehe et al., 2010b], [Miehe et al., 2010a] (for which the crack is supposed to propagate along the minimum energy path) can also be considered for fracture modeling. An exhaustive review on all these alternative methods can be found in [Rabczuk, 2013].

Cohesive Zone Model

In the present work, choice has been made to disregard Cohesive Zone Model (CZM) for several reasons. First, since the fracture process up to crack initiation is described in a continuous manner with the damage model (coupled approach), the material response is assumed to be altered with the increase of damage, hence resulting in an almost zero effort transmission along the crack lips. Consequently, the use of a CZM to dissipate the remaining energy is not required. Then, since cohesive elements are generally inserted at interfaces between bulk elements, the resulting crack path is generally mesh dependent. Moreover, CZM suffers from some limitations concerning the initial guess of the crack path which has to be known, *a priori*, unless adaptive remeshing techniques are used to dynamically insert cohesive elements all along the crack advance process [Shakoor et al., 2019]. According to [Hosseini et al., 2018], the fatigue crack growth process in ductile materials is in essence plasticity-driven and so decohesion-based models are known to be inconsistent with the fundamental mechanisms responsible for cyclic crack advance. Moreover, cohesive elements require their behavior to be related to the mechanical state of the surrounding volume so as to provide good results [Simatos, 2010]. In light of this, [Hosseini et al., 2018] argued that any physical justification for the use of CZM for FCG in ductile materials seems deficient. Nevertheless, applications can be found in, *e.g.* [Bouvard et al., 2009], [Sun et al., 2013], [Zhao et al., 2021].

Let us recall that the target of this work is to simulate the crack growth peculiarities observed in Ni-based alloys (see sub-sect. 1.3.3). These issues can only be assessed in 3D computations since the flat-to-slant transition is an out-of-plane problem (while cohesive elements are mainly related to interfacial fracture). As a reminder, this aspect has motivated considering a local approach to fracture rather than a global one (based on LEFM). Finally, even if adaptive insertion of cohesive elements could have been considered [Chiaruttini et al., 2012], an intrinsic choice related to this Ph.D. was to compare CDM-based approaches and LEFM ones.

Node-release / element-deletion

Apart from CZM and mesh adaption techniques, let us note that other (simpler) solutions for the modeling of FCG also exist and are recalled hereafter.

- **Node-release technique:** this is the simple method for the modeling of crack advance. The crack growth is modeled by releasing the crack-tip node constraints such that the crack advances by the crack-tip element size each time the node is released. A criterion based on a critical damage parameter (or a stress level) is used to evaluate the best instant for node release. However, as the crack growth increment per cycle is dictated by the FE size, this technique leads to mesh-dependent results. Consequently, proper FCG rates cannot be predicted in an accurate manner [Hosseini et al., 2018]. Moreover, this requires that the crack path is known in advance. Applications in fatigue can be found in, *e.g.* [Pommier and Bompard, 2000], [Solanki et al., 2004], [Hosseini et al., 2018], while those in creep or creep-fatigue crack growth prediction in [Zhao et al., 2012], [Xu et al., 2017].
- **Element-deletion method:** also known as *erosion*, can be considered once a continuous damage formulation is used so as to explicitly model the crack. It consists in eliminating the *broken* FE from the mesh according to some predefined criteria. Such a method, not requiring any representation of the crack's topology, may be used either with a local (see *e.g.* [Lian

et al., 2013], [Davaze et al., 2020]) or a regularized damage model (see *e.g.* [Seupel et al., 2018]). Although the erosion process is capable of modeling crack separation without requiring any specific type of element, the method possesses several limitations:

- the method is inherently mesh-dependent [Song et al., 2008]. The deletion of one element may create uncontrolled stress concentration zones;
- the geometric crack path cannot be properly captured since the crack is represented as a sequence of elements;
- mass loss is also incriminated to occur when using erosion techniques;
- with non-local damage models, the treatment of the non-local variable upon erosion can lead to numerical issues in relation with the newly defined BC [Hütter et al., 2013].

Applications in ductile fracture are numerous [Bouchard et al., 2011], [El Khaoulani and Bouchard, 2012], [Davaze, 2019], while there are few in fatigue [Peerlings et al., 2000].

Enriched FE formulations

Contrarily to the case with a mesh conforming to the crack as described above, one can mention the Enriched Finite Element Methods that can also be considered. This way, it may seem advantageous to allow for discontinuities in the FE model to be non conforming with the mesh. Based on the *partition of the unity concept* [Babuška and Melenk, 1997], the standard displacement-based formulation of the FEM can be enhanced with additional degrees of freedom:

- **eXtended-Finite Element Method (X-FEM):** the displacement-based approximation is enriched near the crack by incorporating both discontinuities fields and the near tip asymptotic fields, as first proposed by [Belytschko and Black, 1999], [Moës et al., 1999]. The (global) enrichment is made at the nodal level. Using X-FEM, the crack is not restricted to the FE boundaries, instead, it can freely run through the whole FE mesh, hence enabling for coarser mesh to be used in case of large scale computations. A review can be found in [Belytschko et al., 2009];
- **Embedded-Finite Element Method (E-FEM):** was initially proposed by [Simo et al., 1993], [Oliver, 1996]. Its formulation is based on elemental (local) enrichment accounting for a (potential) displacement jump (through element-wise constant functions). One major advantage of the E-FEM over the X-FEM is that the additional unknowns could be condensed on the element level so that discontinuities could be captured with very small changes in the existing FE code [Rabczuk, 2013]. Standard Newton algorithms are able to solve the global problem. However, as evidenced by [Wolf, 2016], the E-FEM, as opposed to the X-FEM, is not capable of reproducing a conforming displacement field.

In their works, [Jirásek and Belytschko, 2002] & [Oliver et al., 2006] have made the comparison between E-FEM and X-FEM which demonstrates that they are equivalent from a qualitative and quantitative point of view [Javani, 2011]. There is no superior method, but both have advantages and drawbacks compared to the other method.

Mesh adaption techniques

Finally, the more accurate way of modeling the crack-induced discontinuity in a FE mesh is probably to modify the part topology (due to crack growth) and to perform an automatic remeshing [Bouchard et al., 2000], [Vaz and Owen, 2001], [Bouchard et al., 2003], [Mediavilla et al., 2006c], [Saanouni, 2008], [Feld-Payet, 2010]. As pointed out by [Mediavilla Varas, 2005], remeshing techniques hence adapt the mesh topology to the geometry of the crack. Such a procedure, although requiring a significant numerical implementation effort, has been proven to be particularly suitable when highly distorted FE need to be removed from the computation.

Once the new mesh containing the extended crack has been generated, additional steps need to be performed so as for the calculation to be resumed. Namely, the transfer of history data from one mesh to another is to be performed and remains a tricky task due to the fact that the energy of the system must be conserved all along the successive crack insertions. In case of significant change in the energy of the system, the restoration of equilibrium also needs to be considered, but its success is not always ensured when highly non-linear phenomena occur in the FPZ [Feld-Payet, 2010]. In addition, the successive remeshing steps together with the need for a transport of mechanical variables may lead to the so-called *numerical diffusion* process [Andrade Pires et al., 2004], [Réthoré et al., 2004]. Nevertheless, let us note that the finer the mesh size in the FPZ, the lower the numerical diffusion upon data transfer.
In any case, remeshing procedures embed some interesting features:

- remeshing allows for a classical contact process between lips upon closure phenomena (fatigue);
- element quality during the crack growth process is also preserved [Bouchard, 2000], hence limiting highly distorted elements close to the crack-tip and favoring the numerical accuracy;
- remeshing procedures reduce the artificial mass loss due to element-deletion since the elements within the damage localization regions are automatically refined prior to deletion [El Khaoulani and Bouchard, 2012];
- mesh generation algorithms are currently mature enough to be coupled with FE solvers so that for complex industrial cases to be studied [Bouchard, 2005], [Chiaruttini et al., 2010] [Khoei et al., 2013b], [Feld-Payet et al., 2015], [Yang et al., 2018], [Eldahshan et al., 2021].

While some limitations can also be mentioned:

- accessing the output of time history variables at selected points is a more difficult task since the mesh is evolving upon simulating;
- the entire data management is computationally expensive since the problem is associated with many meshes. This is particularly true for highly non-linear material models as well with complex (cyclic) loading schemes.

Applications of remeshing techniques for crack growth modeling can be found in, *e.g.* [Saouma and Zatz, 1984], [Chiaruttini et al., 2013] for FCG using LEFM, and in [Mediavilla et al., 2006b], [Peerlings et al., 2008], [Feld-Payet, 2010], [El Khaoulani and Bouchard, 2012], [Javani et al., 2016] for cracking in ductile materials. Despite its computationally demanding cost and not easy implementation, such a method has nevertheless provided very promising results.

Résumé du chapitre en français

Ce chapitre a permis d'introduire les principaux concepts associés aux développements de cette thèse. Un état de l'art relatif à chaque thématique abordée, qu'elle soit sur le plan expérimental, sur le plan de la modélisation ou même numérique, a ainsi été dressé:

- **la propagation de fissure dans les matériaux métalliques:** cette section a donné quelques principes fondamentaux en matière de propagation de fissure en fatigue dans les alliages métalliques. L'intérêt a majoritairement été porté sur les fissures longues. Pour finir quelques modèles de propagation de fissure, basés sur une formulation incrémentale en temps, ont été décrits;
- **la propagation de fissure en fatigue et fatigue-fluage dans les superalliages base Nickel:** les principaux modes de rupture ont été rappelés, en relation étroite avec les effets exrinsèques et intrinsèques au processus de croissance de fissure. En complément, le comportement en fissuration de l'AD730™ étudié dans cette thèse a été brièvement décrit à l'aide de travaux récents. Enfin, les anomalies de fissure observées dans les superalliages base Nickel, portant notamment sur le déversement du plan de propagation et la courbure du front, ont été introduites et discutées;
- **formalisme des lois de comportement:** quelques principes fondamentaux sont rappelés, avec un accent spécial sur l'échelle macroscopique considérée pour la modélisation, la méthode de partition de la contrainte en lien avec la plasticité cyclique des matériaux écrouissables, et la théorie de la viscoplasticité unifée, telles que considérées dans ce travail;
- **les modèles d'endommagement couplés:** l'approche locale de la rupture dédiée à la prévision de la rupture des structures a été introduite, ainsi que son champs d'application. Un intérêt a été porté sur les modèles d'endommagement couplés, en lien notamment avec la mécanique de l'endommagement;
- **les stratégies de régularisation:** celles-ci sont introduites de sorte à donner quelques éléments de base et un état de l'art relatif aux méthodes aujourd'hui disponibles pour résoudre le problème associé à la dépendance en maillage lors de l'usage de modèles d'endommagement couplés conduisant à une réponse adoucissante. Les méthodes non-locales, notamment les limiteurs spatiaux de localisation (de type intégral et à gradient) sont décrits. Un accent est porté sur l'application de ces méthodes dans des contextes de fissuration sous chargement de fatigue ou fatigue-flage, réputés moins nombreux en comparaison aux problèmes de rupture ductile;
- **le problème de verrouillage volumique dans les matériaux quasi-incompressibles:** cet aspect est brièvement décrit et les solutions apportées sont écrites de sorte à présenter les éléments finis multi-champs considérés dans la suite de ce travail;
- **les méthodes de gestion de la rupture dans les calculs EF:** elles permettent l'insertion d'une discontinuité dans un maillage éléments finis pour simuler l'avancée d'une fissure. Les méthodes discontinues applicables dans un contexte EF sont détaillées, avec pour cuacune leurs avantages et leurs limites.

Ces apects, bien que différents par nature, vont servir de support aux développements à venir.

Part II - Research activity

2 Elastic-viscoplastic material model for AD730™ under cyclic and monotonic loading conditions

The accurate description of the behavior of a material is a preliminary step when studying the damaging and subsequent cracking processes (no matter the considered theory between global or local approaches). Thus, the first step of the present study is to establish an accurate material model at moderate to high temperatures for the specific Nickel-based superalloy AD730™.
In this chapter, the experimental set-up and material characterization process are described in a first section. The chemical composition of the studied material together with its heat treatments are discussed. The testing procedures are motivated and justified according to the need of the present study. In a second part, some general experimental evidences, prior to any data treatment, are discussed before introducing the main examination procedures associated with a comprehensive study of the governing mechanisms. Then, the third section is dedicated to the phenomenological formulation of the material model which is justified with experimental observations. The last section is devoted to the calibration process of such a phenomenological macroscopic material model with corresponding prediction capabilities.

Contents

Life prediction of critical components at elevated temperatures requires plasticity and viscoplasticity analyses. In order to achieve a high level of accuracy in the computing methods, it is necessary to develop fundamental constitutive equations to describe the macroscopic behavior of the material. Continuum Mechanics represents the foundation for a phenomenological description of the macroscopic behavior of a given material submitted to a mechanical load and subsequently undergoing deformation. For the last past decades, several advanced material models have been developed to allow more and more accurate modeling of materials behavior under cyclic loading conditions at high temperatures. For a comprehensive review, some are given in the following references [Lemaitre et al., 2009], [Besson et al., 2010], [Cailletaud et al., 2018]. One of these material models initiated numerous further works in both the research and industrial communities and dates back to the 1970's with the work of [Chaboche, 1977b]. In this paper, the author proposed some constitutive equations for nonlinear plasticity and viscoplasticity dedicated to the description of the mechanical behavior under cyclic repetitive loads of steel alloys at different temperatures. Later on, the equations were extended to the modeling of other metallic alloys, leading to the so-called *unified viscoplasticity theory* [Benaarbia et al., 2018].

Since the purpose of this Chap. 2 is to establish a unified material model for creep-fatigue loading conditions for AD730™, a relatively new Ni-based superalloy for HP turbine disks applications, a preliminary step is to detail the whole characterization process in the following sub-sect. 2.1.2 & sub-sect. 2.1.3, and then to justify the material model, according to experimental evidences, in the sect. 2.2. The formulation of the material model will then be given in sect. 2.3 whereas its proper calibration will be discussed in sect. 2.4.

2.1 Material characterization and experimental procedures

2.1.1 Motivations for the material modeling

The accurate knowledge of the material behavior related to engineering components allows for an increase in the operational temperature and subsequent better system efficiency. In addition,

less conservative designs can be achieved which in turn reduces the cost of components, since the material is used in an optimal way [Staroselsky et al., 2014].

The description of fatigue crack growth is, still to present days, a research field of great interest. Cyclic plastic zone (also referred to as *reverse plastic zone*) acts as a primary mechanical driving force for the fatigue crack propagation process under cyclic loading [Park et al., 1996]. The Fig. 2.1 gives a schematic illustration of the different zones ahead of a crack-tip. Both reverse and monotonic plastic zones are demonstrated in this figure, as well as the elastic zone.
In the cyclic plastic zone, measurable amount of plastic strain takes place in every loading cycle (*i.e.* a clear hysteresis loop can be formed). This may occur in the really vicinity of the crack-tip. Apart from this cyclic zone, there exists a monotonic plastic zone, located next to the cyclic plastic zone ahead of the crack-tip, where only measurable plastic strain during the initial monotonic loading takes place and where thereafter cyclic elastic strain is observed in the remaining cycles (elastic loading/unloading). A purely elastic response is obtained far ahead from the crack-tip, and this, from the very beginning of the loading cycles.

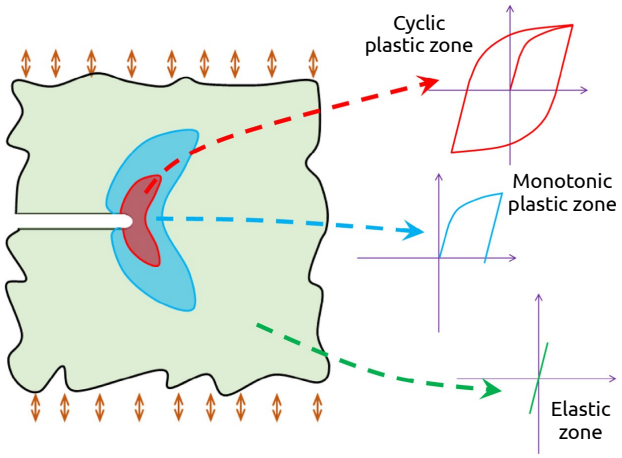

Figure 2.1: Schematic diagram illustrating the different zones at the fatigue crack-tip and corresponding stress-strain responses in those zones (adapted from [Paul, 2016]).

For the present study, it is of first importance to rely on a material model capable of an accurate description of the cyclic non-linear behavior of the material. The three zones detailed above have to be described by the model so as to ensure a reliable description of damaging effects responsible for fatigue crack growth in the context of a local approach to fracture (*cf.* Chap. 4 later on).

Realistic analyses of cracks under cyclic loading have been performed numerically thanks to a variety of elastic-plastic constitutive models [Mishra and Parida, 1985], [Rahman and Bahrami, 2010]. They have used an isotropic hardening rule, which represents a limit for such analysis due to the fact that some mechanisms associated with cyclic schemes such as Bauschinger effect, plastic shakedown, ratcheting and mean stress relaxation cannot be addressed by isotropic hardening rules [Jiang and Zhang, 2008], [Chaboche, 2008]. Therefore, the cyclic stress-strain response at the crack-tip during cyclic loading conditions must be addressed considering advanced cyclic material models including both isotropic and kinematic hardening rules, no matter the material (single- or polycrystal) or the constitutive model (macroscopic or crystallographic) [Marchal et al., 2006], [Bouvard et al., 2009], [Hamon et al., 2010]. As a result, a mixed isotropic-kinematic strain-

hardening formulation will be considered in this work to suitably model cyclic loading conditions.

2.1.2 Material, testing samples and experimental setup

In order to increase the aircraft engine's efficiency, the turbine inlet temperature needs to be constantly increased. As a result, manufacturers have turned to the so-called family of *new-generation* polycrystalline $\gamma - \gamma'$ Ni-based superalloys which are capable of withstanding such mechanical requirements associated with severe operating loading cases and environment.

2.1.2.1 AD730 Nickel-based superalloy

The Nickel-based superalloy AD730™ has been recently developed by Aubert & Duval and introduced especially for the first stages of the turbine disks with high properties up to 700°C [Devaux et al., 2011], [Aubert&Duval, 2017]. The main reason leading to the development of AD730™ was to provide a better combination between mechanical properties and cost compared to René88, N18, and so on. This alloy has mechanical properties close to those of Udimet 720Li and significantly higher than those of 718 Plus™, Waspaloy and "standard" Inconel 718. Moreover, its good workability enables it to be manufactured through the cast & wrought (C&W) route [Devaux et al., 2012]. However, due to its recent development, some of its fundamental properties are still unknown and need to be studied.

AD730™ owns its properties, like most of the $\gamma - \gamma'$ alloys, from the solid solution hardening and precipitation hardening of the γ'-phase, almost coherent with the γ-matrix (small misfit parameter). Contrarily to other Ni-based superalloys with a high content of Nb [Donachie and Donachie, 2002], AD730™ does not possess any precipitated γ''-phase. Other precipitated phases such as δ, η or TCP, are far from being preponderant in AD730™ and thus won't be further discussed in the following [Devaux et al., 2011].

Up to date, the mechanical properties of AD730™ are known for the most standard testing procedures (tensile and creep loading conditions for both fine- and coarse-grained microstructures, see [Thébaud, 2017], [Vultos, 2019], and more recently for fatigue and dwell-fatigue cracking regimes [Mrozowski, 2020]). These studies have provided significant insights into this material, unless some aspects still remain to be well understood prior to any usage of the alloy in real service conditions. Indeed, to the best of the author's knowledge, no constitutive equations for cyclic elastic-viscoplastic (EVP) loading conditions have been yet established and calibrated.

2.1.2.2 As-received material

Melting and forging processes

Like alloy Inconel 718, the new generation of polycrystalline Ni-based superalloys are produced and shaped by the conventional C&W method. Such a process starts with the casting of an ingot

under vacuum, according to the Vacuum Induction Melting (VIM) process. However, after this first casting, many defects such as porosities, macro-segregations and inclusions are present in the ingot. The latter therefore needs to be refined using remelting processes such as Electro-Slag Remelting (ESR) and Vacuum Arc Remelting (VAR) [Pollock and Tin, 2006].
Once all the melting and remelting processes are completed, the ingot undergoes a first series of forging, also known as *conversion* [Forbes Jones and Jackman, 1999]. The objective of the conversion is to break the solidification microstructure in order to obtain a much finer and homogeneous microstructure. At the end, the semi-finished product, namely the billet, is formed.

Chemical composition

The bulk material used during this study was supplied by Aubert & Duval in the form of 2160 mm-high pieces with a diameter of 204 mm coming from a billet. The material has been supplied in a rough metallurgical state (see Fig. A.1 page 267 in the appendix Chap. A). Its exact chemical composition is given in Tab. 2.1. Such a composition has been finely controlled to ensure a consequent precipitation of γ' phase in order to meet required mechanical properties, but also to maintain the shaping capability of the alloy.

C	Ni	Cr	Mo	W	Al	Co	Ti	Nb	Fe	B	Zr
0.01	Bal.	15.46	2.82	2.59	2.22	8.27	3.48	1.11	4.16	0.0094	0.034

Table 2.1: Chemical composition in wt% of as-received AD730™.

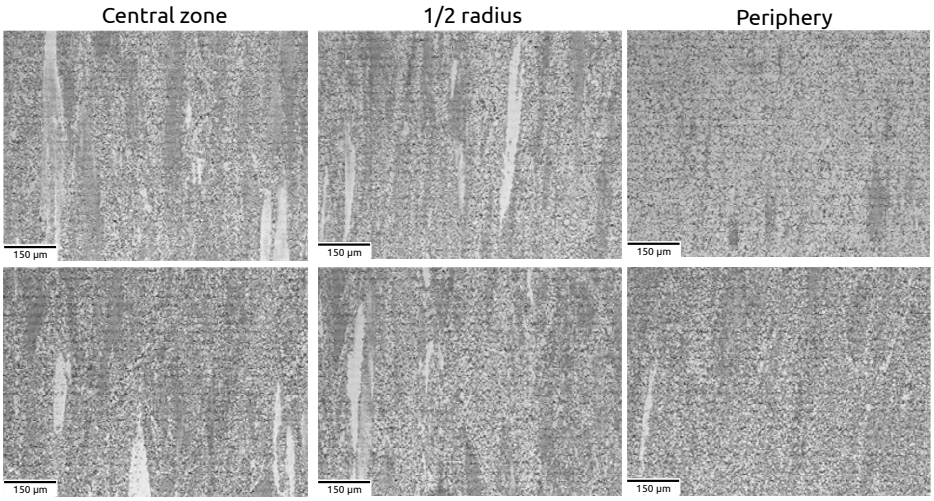

Figure 2.2: Metallurgical state of as-received AD730™ material (from [Bonnand et al., 2019]).

The microstructural state of the as-received material is given in Fig. 2.2. We can mention the obvious disparity in the initial state between the core material of the bar and its periphery. At the latter, only small grains are present, as opposed to the core where long grains elongated in the direction of the bar are easily observable. We can already point out that the heat treatments that will then be applied will not completely erase these initial differences.

2.1.2.3 Heat treatments and microstructural aspects

The present study focuses on the fine-grained (FG) microstructure of AD730™. Such a microstructure was designed in the R&D offices of Aubert & Duval [Devaux et al., 2014] and at P' Institute [Thébaud, 2017] in order to provide the best compromise between static and cyclic properties [Devaux et al., 2011]. The series of heat treatments is described in what follows.

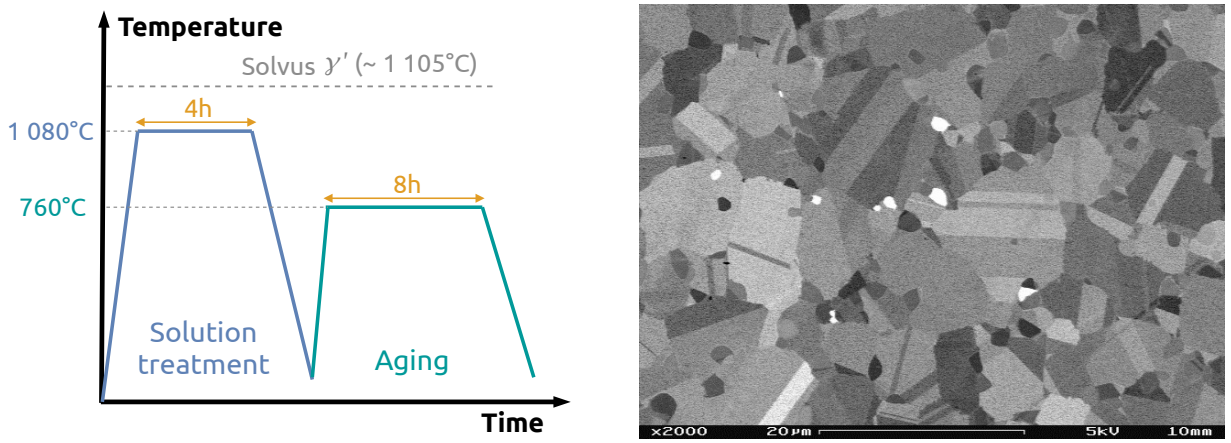

(a) Sequence of heat treatments. (b) Typical microstructure of FG aged AD730™.

Figure 2.3: Successive heat treatments for AD730™ with corresponding fine-grained microstructure.

The material has been subjected to a series of heat treatments starting from subsolvus solution heat treatment under vacuum at 1080°C for 4h, see Fig. 2.3a. A similar heat treatment was applied by [Thébaud, 2017], [Durand et al., 2020] and resulted in a fine-grained microstructure with average grain size of $\sim$8 - 10 µm (ASTM 10), Fig. 2.3b. Then, a cooling under argon (112°C.min^{-1}) up to room temperature (RT) has been achieved. The cooling rate after solutioning is known to control the size and distribution of secondary and tertiary γ' precipitates: the faster the cooling process, the finer the final microstructure [Devaux et al., 2012]. As a final step, aging heat treatment was conducted under vacuum at 760°C for 8h followed by a cooling under argon up to RT.

2.1.3 Material testing procedures

Testing samples

Cyclic and monotonic characterization samples consist of a batch of 16 cylindrical specimens with a diameter of 6 mm, with a length of the useful zone in the middle area equal to 12.328 mm. A representation of the axisymmetric testing specimens is given in Fig. 2.4 whereas the sampling plans from the bulk material are given in the appendices, see Fig. A.1a page 267. A detailed sketch of this specimen is given in the appendices, see Fig. B.1 page 269.

Material testing equipment

Experimental tests were conducted within the ONERA facilities. These tests were conducted on a uniaxial servo-hydraulic *MTS 810* testing machine. Its load cell capacity for static testing ranges from 25 to ± 100 kN and is particularly suited for fatigue and monotonic testing. Axial measurements were taken using a longitudinal 0.5-class *MTS* extensometer (632.51C.04) with a gauge length of 12 mm for relative displacement measurement. Its measuring range for strains is in [+20%, -10%]. This extensometer was thus used for direct strain monitoring with the help of a controlling software. The latter allows for the control of the test in displacement, deformation or force depending on the need for testing.

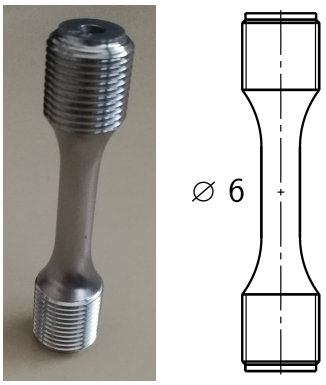

Figure 2.4: Axisymmetric testing specimen.

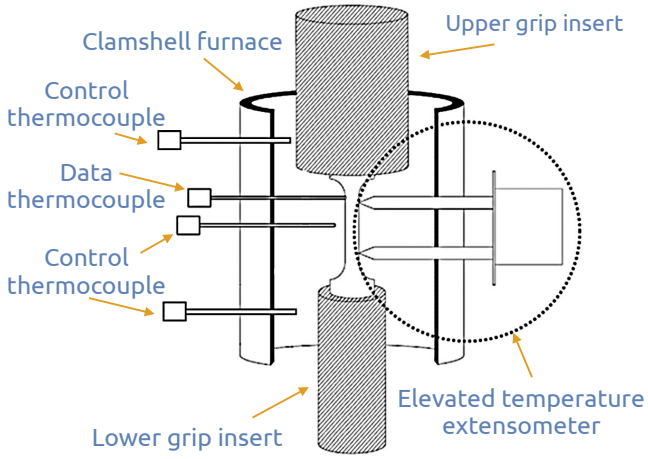

(a) Schematic view of the testing apparatus.

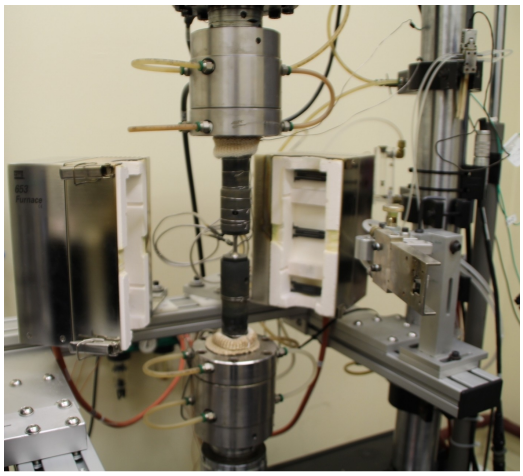

(b) Overall set-up with specimen, heating clamshell furnace, threaded grips and hydraulic wedge grips.

Figure 2.5: Experimental set-up for cyclic testing on a *MTS 810* testing machine at the ONERA facilities.

For high temperature (HT) testing, a *MTS 653* clamshell resistive furnace was used to control the temperature of the tested material. Three independent controlled temperature zones are used so that to ensure an homogeneous heating of the specimen. K-type thermocouples (chromel/alumel) were placed on the back face of the specimen. All the experimental tests were conducted on air, both for those at ambient (RT) and elevated temperatures. Before HT testing, the specimen was heated up to the target temperature (550, 650 or 700°C).

A schematic view of the testing apparatus is given in Fig. 2.5a and a real view of the experimental set-up Fig. 2.6. Highlight is given on the thermocouple as well as the extensometer in Fig. 2.6.

(a) Close-up view on data thermocouple (probe).

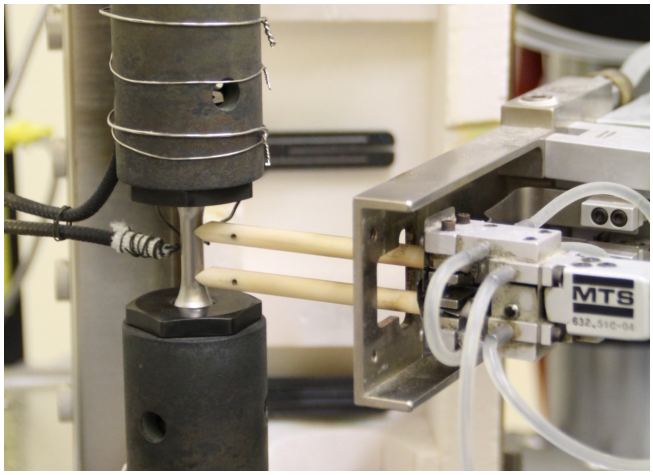

(b) Close-up view on axial extensometer.

Figure 2.6: Thermocouple and axial extensometer for high temperature cyclic test monitoring on a *MTS 810* testing machine at the ONERA facilities.

2.1.3.1 Monotonic and cyclic characterization tests

The sub-sect. 2.1.1 has shown that crack-tip stress fields analysis must rely on an advanced cyclic unified material model. Material modeling requires the proper definition of characterization tests. To this end, a precise testing matrix including 16 cylindrical specimens machined and heat treated has been dedicated to this task (see Fig. A.1 in the appendices).

Characterization tests are aimed to calibrate a proper constitutive model. For the studied material, two specific features should be included in the material model:

- the elastic-plastic behavior which only depends on the mechanical loading;
- and the viscous behavior, which depends on the rate at which the material is loaded as well as the operating temperature [Chaboche, 2008].

In the present study, thermal effects are disregarded.

As previously said, the macroscopic mechanical response of AD730™ under cyclic loading conditions has not been yet studied in details. The isothermal non-linear behavior of Inconel 718, known to have almost similar properties compared to AD730™, has been extensively studied in the past decades [Chaboche et al., 1991], [Gustafsson et al., 2011c], [Goulmy, 2017], [Prisacari, 2018]. This constitutes some guidelines for the definition of the testing process.

Nickel-based superalloys, including Inconel 718, are known to exhibit the following main deformation mechanisms under LCF loading conditions:

- **cyclic softening**: this aspect is mainly associated with the shearing process of hardening γ' and γ'' precipitates [Xiao et al., 2005]. The smaller the precipitates, the greater the shearing process by generated dislocations;

- **temperature effect**: classically, temperature increase will make the mechanical properties of the alloy to decrease. The latter are known to be stable up to $\sim 600°C$, and then decrease. The extent of cyclic softening is greater with temperature rise [Warren and Wei, 2006]. Plastic instabilities and inverse strain rate sensitivity have also been reported at specific temperature around 550°C;
- **partial mean stress relaxation or ratcheting**. the first aspect corresponds to a partial decrease of the mean stress for non-symmetric hysteresis loops under strain-controlled loading conditions. The second relates to the same effect under stress-controlled conditions, with successive accumulation of strain for increasing loading cycles. Such effects have been proved to have an effect on fatigue lifetime [Lukáš and Kunz, 1989], [Chaboche and Jung, 1997];
- **strain range memory effect**: for which there exists a relationship between cyclic hardening/softening and applied strain range. Such an aspect relates the material behavior to its prior loading history with a possible evanescent effect depending on the loading conditions [Nouailhas et al., 1985].

Most of the listed aspects were studied on a similar class material, that is Inconel 718, by [Gustafsson et al., 2011c], [Chaboche et al., 2012] (standard 718 alloy), [Goulmy, 2017] and [Prisacari, 2018] (Direct-Aged state). Their modeling approach through unified theories of viscoplasticity thus seems to be adapted for a similar Ni-based alloy as the one considered here, AD730™.

Finally, in connection with the literature review as well as the knowledge of typical response of the material (what remains an *a priori*), some relevant questions can thus be formulated so that to give an orientation to the characterization tests to be carried out:

- what are the main strain-hardening mechanisms within the material? (*i.e.* cyclic hardening/-softening, plastic strain range memory effect, Masing-type behavior [Masing, 1926], ...)
- is the material sensitive to strain rate and are there any time-activated effects?

To this end, monotonic, cyclic and dwell characterization tests have been designed and are described in what follows.

Uniaxial monotonic testing

In the present study, 16 specimens made of fine-grained AD730™ were available for material behavior characterization purpose. Choice has thus been made to use "only" 3 specimens for monotonic loading scenarios. Two types of tests were designed for high temperature analysis in isothermal conditions:

- **Type-1 monotonic test**: this single test is performed at 550°C under strain control in order to study both strain- and time-hardening effects. Strain rate is thus varying from one strain level to another in an alternating way between (high) strain rate of $\dot{\varepsilon} = 10^{-3}$ s^{-1} to (low) strain rate of 10^{-5} s^{-1}, Fig. 2.7a. For this reason, this test is referred to as *Multiple Speed* (MS) test. At the end of the loading ramp, if failure does not occur, stress relaxation at constant strain level (the last) is performed during 24h;

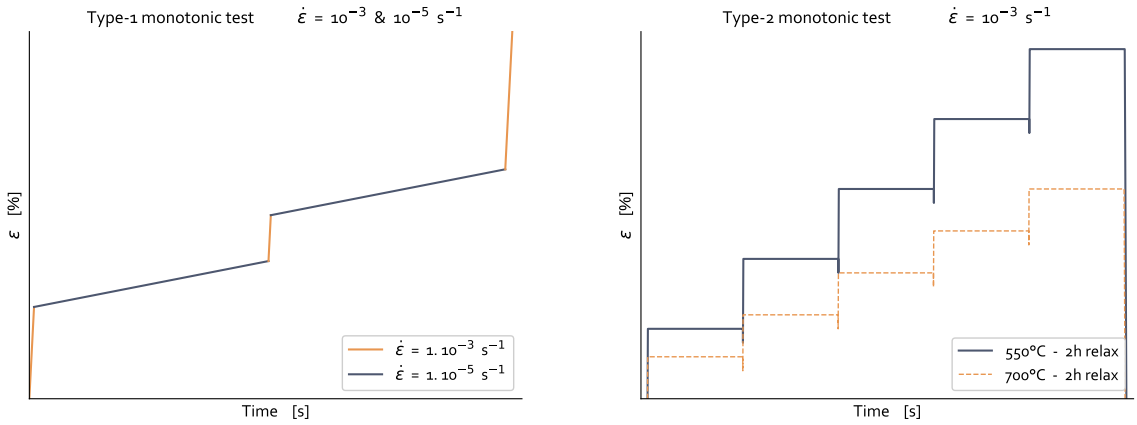

(a) Load signal of type-1 monotonic test. (b) Load signal of type-2 monotonic test.

Figure 2.7: Load signals for type-1 & 2 monotonic tests for material behavior characterization.

- **Type-2 monotonic test**: it is performed to study strain-hardening and time-variant effects (viscosity, static recovery...) at 550 and 700°C. Consequently, this test is referred to as *Multiple Hardening-Relaxation* (MHR) test. It is conducted under strain control for increasing tensile loading at constant strain rate of $\dot{\varepsilon} = 10^{-3}$ s^{-1}. An holding period of 2h is performed at specific strain levels, followed by a partial unloading of the sample. This unloading is performed up to a predefined strain level in order to guarantee that the material remains in an elastic domain without modifying the strain-hardening state, Fig. 2.7b.

Uniaxial cyclic testing

Such tests consist in subjecting a specimen to a periodic load (stress or strain depending on the test-control) so that the evolution of the cyclic response can be studied. One can hence study the stress-strain relation as well as the evolution of hardening characteristics from one cycle to another. Theoretically, these tests are conducted up to the so-called *stabilized state* (if existing) of the mechanical response under cyclic loading. Indeed, structural calculations dedicated to fatigue lifetime estimation mainly rely on the stabilized state of the mechanical behavior so as to apply fatigue criteria [Chaboche et al., 2012], [Kruch et al., 2015].

To this end, 4 types of characteristic tests have been designed following the guidelines from [Chaboche et al., 2013], [Goulmy, 2017], [Prisacari, 2018], [Benaarbia et al., 2018]. Due to the few number of specimens (16) and the necessity to investigate 3 target temperatures (20, 550, 700°C) as well as several loading schemes (negative and positive loading ratios), tests were performed in a multi-steps manner, thus using one specimen for several loading levels. Such a testing method is referred to as *incremental*, in opposition to the use of one specimen per load level (single-step) [Lemaitre and Chaboche, 1990].

- **Type-1 cyclic test**: this test is performed under strain control. The loading ratio is $R_\varepsilon = -1$ to get a symmetric loading between tensile and compressive phases. A sinusoidal wave is used with a constant strain rate of $\dot{\varepsilon} = 10^{-3}$ s^{-1}. Considering incremental tests, we have an incremental increase of the load ($\Delta\varepsilon_i/2$, with $i = 1, 2, ...$), see Fig. 2.8a.

The test is performed at 20, 550, 650 and 700°C. At the end of the test, depending if specimen failure occurs or not, a stress relaxation at constant strain level (the last investigated) is conducted so that for the viscous part of the stress to be observed.
Such a loading scheme is used to study the evolution of stress amplitude with increasing cycles and strain levels as well as the evolution of hysteresis loop shape.

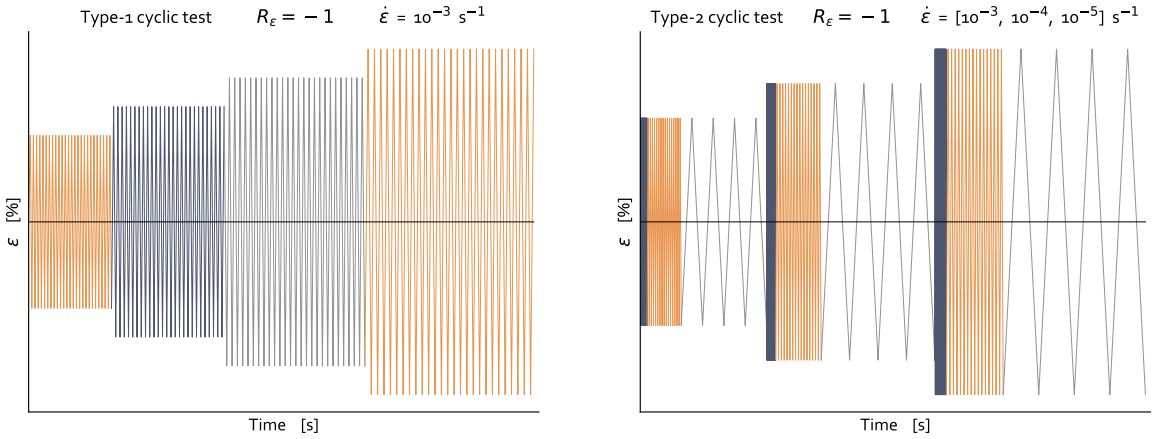

(a) Load signal of type-1 cyclic test. (b) Load signal of type-2 cyclic test.

Figure 2.8: Load signals for type-1 & 2 cyclic tests for material behavior characterization.

- **Type-2 cyclic test**: this test is also performed under strain control. The loading ratio is $R_\varepsilon = -1$. A sinusoidal wave is used with variable strain rates ranging in $\dot{\varepsilon}_j = [10^{-3},\ 10^{-4},\ 10^{-5}]$ s^{-1}. For the first (highest) loading rate at $\dot{\varepsilon}_1 = 10^{-3}$ s^{-1}, 64 cycles are performed, for the lower speed rate of $\dot{\varepsilon}_2 = 10^{-4}$ s^{-1}, 32 cycles are performed and finally for the last (lowest) strain rate of $\dot{\varepsilon}_3 = 10^{-4}$ s^{-1} only 8 cycles are realized. Considering incremental testing, several strain levels ($\Delta\varepsilon_i/2$, with $i = 1, 2, ...$) are considered, see Fig. 2.8b. The test is performed at 20, 550 and 700°C. Here again, at the end of the test, depending if specimen failure occurs or not, a stress relaxation at constant strain level is conducted.
Such a loading scheme is used to study the strain-rate sensitivity of the material highlighted by viscosity effects. Moreover, the evolution of stress amplitude and the change in shape of hysteresis loops with increasing cycles and strain levels is also analyzed. This test is close to type-1 test, with the slight difference that the number of investigated cycles for a given strain amplitude is not the same, thus allowing for a comprehensive analysis of cumulative plastic effect in opposition to that of plastic strain amplitude.

- **Type-3 cyclic test**: this test is very similar to type-1 cyclic test, with the major difference coming from the loading ratio that is fixed to $R_\varepsilon = 0$ so that to get a non-symmetric loading between tensile and compressive phases, see Fig. 2.9a. As the test is strain-controlled under dissymmetric loading, it is used to study the partial/total relaxation of the mean stress as well as the evolution of stress amplitude with increasing cycles and strain levels.

- **Type-4 cyclic test**: this last test is much more complicated than the three previous ones and is associated with cyclic relaxation process. This test is performed under strain control. The loading ratio is again $R_\varepsilon = -1$. This test assumes evolving holding periods and decreasing strain rates. For this reason, both triangular and trapezoidal waves are used with alternating

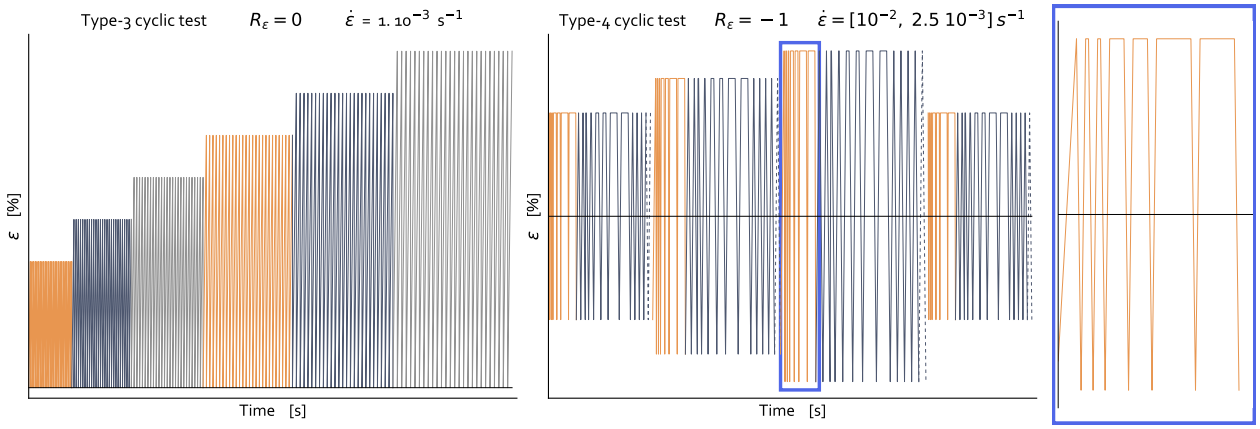

(a) Load signal of type-3 cyclic test. (b) Load signal of type-4 cyclic test (+ close-up view on phase 1).

Figure 2.9: Load signals for type-3 & 4 cyclic tests for material behavior characterization.

signals. The Holding Times (HT) are performed at the peak tensile stress and range in $HT_k = [60, 300, 720]$ s. The two considered strain rates are $\dot{\varepsilon}_j = [10^{-2},\ 2.5\ 10^{-3}]\ s^{-1}$, see Fig. 2.9b, and the test is performed at 550 and 700°C.
Such a test can be decomposed into several blocks (corresponding to a strain level $\Delta\varepsilon_i/2$, with $i = 1, 2, ...$) in which there are 5 successive steps (corresponding to evolving speeds or signal forms):

$\frac{\Delta\varepsilon_i}{2}$

Step 1: 1 cycle with triangular signal at $\dot{\varepsilon}_1 = 10^{-2}\ s^{-1}$
Step 2: 6 cycles with trapezoidal signal at $\dot{\varepsilon}_1 = 10^{-2}\ s^{-1}$
2 cycles with HT_1, 2 cycles with HT_2 and 2 cycles with HT_3
Step 3: 2 cycles with triangular signal (null HT) at $\dot{\varepsilon}_2 = 2.5\ 10^{-3}\ s^{-1}$
Step 4: 6 cycles with trapezoidal signal at $\dot{\varepsilon}_2 = 2.5\ 10^{-3}\ s^{-1}$
2 cycles with HT_1, 2 cycles with HT_2 and 2 cycles with HT_3
Step 5: 25 cycles with triangular signal (null HT) at $\dot{\varepsilon}_2 = 2.5\ 10^{-3}\ s^{-1}$

$\frac{\Delta\varepsilon_{i+1}}{2}$

Step 1: 1 cycle with triangular signal at $\dot{\varepsilon}_1 = 10^{-2}\ s^{-1}$
Step 2: ...

Such a loading scheme is used to study the evolution of stress amplitude with increasing cycles and strain levels. Last but not least, viscosity effects in combination with accumulated plasticity and strain-rate decrease (from $\dot{\varepsilon} = 10^{-2}\ s^{-1}$ to $\dot{\varepsilon} = 2.5\ 10^{-3}\ s^{-1}$) can also be analyzed thanks to such a testing scheme.

Synthesis of the characterization tests

As a matter of generic overview of the mechanical tests dedicated to the material's non-linear behavior estimation, the following Tab. 2.2 gathers the different testing conditions for the 16 spec-

imens. It is to be noted that the occurrence of an holding period at constant load, *i.e.* strain level in the present case, thus results in a stress relaxation analysis.

Test type	Specifications	Hold. period	Temp.	Spec. ID
Monotonic	**Type-1 test**: tensile loading under variable strain rate	✓	550°C	CAR8
Monotonic	**Type-2 test**: tensile loading under constant strain rate with holding times and unloadings	✓	550°C	CAR2
		✓	700°C	CAR10
Cyclic	**Type-1 test**: symmetric loading under constant strain rate and increasing strain level	✗	20°C	CAR1
		✗	550°C	CAR3 & 4
		✓	650°C	CAR6
		✗	700°C	CAR5
Cyclic	**Type-2 test**: symmetric loading under variable strain rate and increasing strain level	✓	20°C	CAR7
		✗	550°C	CAR9
		✓	700°C	CAR11
Cyclic	**Type-3 test**: non-symmetric loading under constant strain rate and increasing strain level	✗	20°C	CAR13
		✗	550°C	CAR15
		✗	700°C	CAR16
Cyclic	**Type-4 test**: symmetric loading under variable strain rate and increasing strain levels / holding times	✓	550°C	CAR12
		✓	700°C	CAR14

Table 2.2: Characterization tests performed during the present study on 16 cylindrical specimens made of fine-grained AD730™.

2.2 Systematic examination procedures for experimental data

There exists several formulations for material modeling. As a result, one restrictive aspect comes from the analyses conducted on the experimental data. Due to the expected dissipative and non-linear mechanisms occurring at the crack-tip, hysteresis stress-strain loops will serve as support for the analyses. Following the work of [Cottrell, 1953], [Feaugas, 1999], recently applied to similar materials [Goulmy, 2017], [Prisacari, 2018], a procedure dedicated to the study of the hysteresis loops has been considered. This allows for a guideline for the formalism establishment as well as material model calibration processes.

In the present study, two levels of analysis of the experimental results will then be conducted. The first one relies on a global analysis of the mechanical response according to the raw data of the tests, while the second relies on a stress partition scheme defined hereafter in sub-sect. 2.2.1. The purpose of this section is to expose some general macroscopic results together with specific features associated with the accurate analysis of hysteresis loops. The macroscopic elastic-plastic behavior

of the material for the considered loading schemes is first analyzed in sub-sect. 2.2.2. Strain-rate related effects are then discussed in sub-sect. 2.2.3 according to the tests conducted with variable loading rates (type-1 monotonic test, type-2 & 4 cyclic tests) as well with stress relaxation profiles. Finally, particular effects related to cyclic loading schemes are discussed in sub-sect. 2.2.4.

For most of the uniaxial tests whose results are discussed below, it seems justified to make the assumption of small perturbations. The longitudinal strain and stress in the specimen are respectively defined by the relations:

$$\varepsilon_n = \frac{\Delta L}{L_0} \qquad \sigma_n = \frac{F}{S_0} \tag{2.1}$$

where L_0 is the gauge length, ΔL its change in length measured by the testing extensometer, F is the uniaxial applied force measured by the load cell of the testing machine, and S_0 the initial cross-section in the useful zone. Such strain/stress are known to be *nominal* (or *engineering* stress/strain) and used to evaluate tensile properties of the material (yield limit, ultimate strength...). If **no particular mention** is made, the **nominal** (engineering) measures are used (as opposed to true measures), where cross-sectional variation is hence neglected.

2.2.1 Cottrell's partition method

One way to get information about the hardening mechanisms under cyclic loading is the fine analysis of the hysteresis loops, as suggested by [Cottrell, 1953]. For uniaxial fatigue loading, such a method is quite easy to represent [Feaugas, 1999]. In Fig. 2.10, a typical stress-strain hysteresis loop is plotted and relevant cyclic parameters are emphasized.

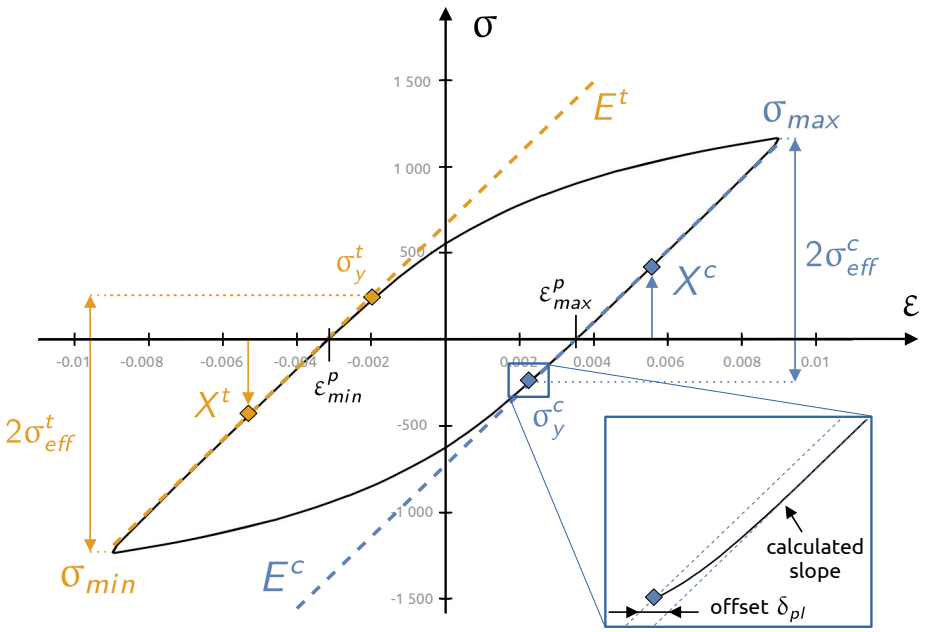

Figure 2.10: Cottrell's partition method for cyclic elastic-plastic material behavior (after [Feaugas, 1999]).

During the present work, a *Python* program has been implemented to extract the relevant data from each hysteresis loop of the whole loading scheme. Then, one gets:

- the elastic moduli in tensile – E^t – and compressive – E^c – going phases, thanks to a linear regression on the linear segment of the curve;
- both yield limits in tension – σ_y^t – and compression – σ_y^c. The yield limits correspond to the point situated at the end of the linearity of the hysteresis loop. For elastic-plastic materials at low or moderate temperature, in the absence of visco-elasticity, the elastic domain is well defined. However, such a statement is no longer guaranteed in the presence of viscous effects. Consequently, the value of the yield points highly depends on a given plastic strain offset δ_{pl}. Such an offset conditions the other quantities which depend on it;
- the size of the elastic domain during forward – σ_{eff}^t – and backward σ_{eff}^c – flows (for which a partition between thermal (over-stress) and athermal (isotropic hard.) parts may apply);
- the position of the center of the elastic domain during each single half-cycle – X^t and X^c.

The plastic strain offset δ_{pl}, as stated, has proven to have a relative importance on the extracted results. The smaller the offset, the better the yield definition. Subsequently, the lower the effective stress and thus the higher the internal back-stress. According to [Gaudin et al., 2001], this offset highly depends on the sensitivity of the extensometer, the sampling and data acquisition frequencies. A critical discussion about the choice of this plastic offset is given in [Wu and Yeh, 1991]. A wide range of values can be found in the literature, namely $5.10^{-6} \leq \delta_{pl} \leq 1.10^{-3}$ [Guillemer-Neel et al., 2000], [Risbet et al., 2001], even if no clear consensus exists about any best value. Generally, for metallic materials, a plastic strain offset of $\delta_{pl} = 2.5\ 10^{-5}$ ($2.5\ 10^{-3}$ %) is assumed so as to get rid of possible measurement noises (signal analysis, sampling frequency) and the uncertainty of the extensometer [Belattar et al., 2016], [Marnier et al., 2016], [Zhou et al., 2018]. Unless intentionally specified, such a value has been considered in the present work.

2.2.2 Elastic-plastic behavior

2.2.2.1 Elasticity

The elastic (reversible) behavior can easily be studied using the material response in a stress-strain diagram and evidencing a linear trend up to (visco)plastic yielding where the stress tends to deviate from the linear part of the curve. Thus, elastic properties of the material are summarized in Tab. 2.3 for different temperatures.

2.2.2.2 Plasticity / Strain-hardening

Under uniaxial monotonic loading, the strain-hardening of the material is clearly visible once the stress level is located above the yield limit of the material. From both the Fig. 2.11 and the Tab. 2.3, two aspects are noticeable. The lower the temperature, the higher the elastic modulus and the yield strength. Moreover, it seems that the yield stress at 700°C is close to that at 550°C.

However, at high temperatures (HT), some viscous effects should be present. No conclusion can be drawn up to now about the yield limit for each temperature. One can notice from Tab. 2.3 that there seems to be a slight sensitivity of the elastic properties to the loading rate (known as *visco-elasticity effect*) at HT. Indeed, the Young modulus seems to increase with increasing strain rate, especially at high temperatures.

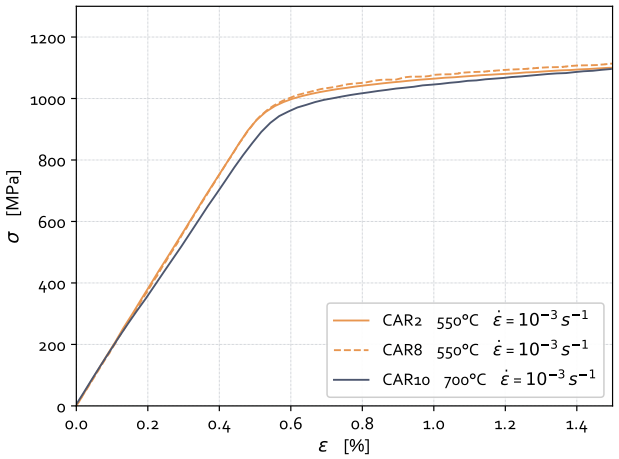

Figure 2.11: Monotonic tensile curves at 550 and 700°C.

At 550 and 700°C, this strain-hardening seems to be approximately the same, the curves having a very close plastic modulus, Fig. 2.11. The stability of the mechanical properties up to 700°C for AD730™ seems to be visible on such a plot owing to the fact that a strain-hardening of the material still exists even at 700°C.

Temp.	**Load. type**	**Spec.**	**Strain rate**	**Young modulus**	**0.02% yield limit**	**0.2% yield limit**
°C	-	-	s^{-1}	MPa	MPa	MPa
20	cyclic	CAR13	10^{-3}	212 495.	1095.	-
550	monotonic	CAR2	10^{-3}	188 671.	930.	1031.
	monotonic	CAR8	10^{-3}	186 890.	964.	1046.
	cyclic	CAR12	10^{-2}	190 769.	907.	-
	cyclic	CAR15	10^{-3}	185 474.	953.	-
700	monotonic	CAR10	10^{-3}	172 641.	921.	1012.
	cyclic	CAR14	10^{-2}	181 726.	860.	-
	cyclic	CAR16	10^{-3}	177 970.	911.	-

Table 2.3: Elastic properties from monotonic and cyclic (1^{st} 1/4 loop) tensile curves on FG AD730™.

In order to study the whole cyclic strain-hardening capabilities of the material over a wide range of strain amplitudes and temperatures, the last hysteresis loops for each representative type-1 cyclic test are given in Fig. 2.12, where the monotonic tensile curve is also reported.

On Fig. 2.12a, the material exhibits at 550°C a slight cyclic hardening (the monotonic curve is located on or below the peak stress level of each hysteresis loop). On the contrary, at 700°C, cyclic softening predominates, see Fig. 2.12b. Additional results for the testing temperatures of 20°C and 650°C are given in the appendices, see Fig. C.2a & Fig. C.2b.

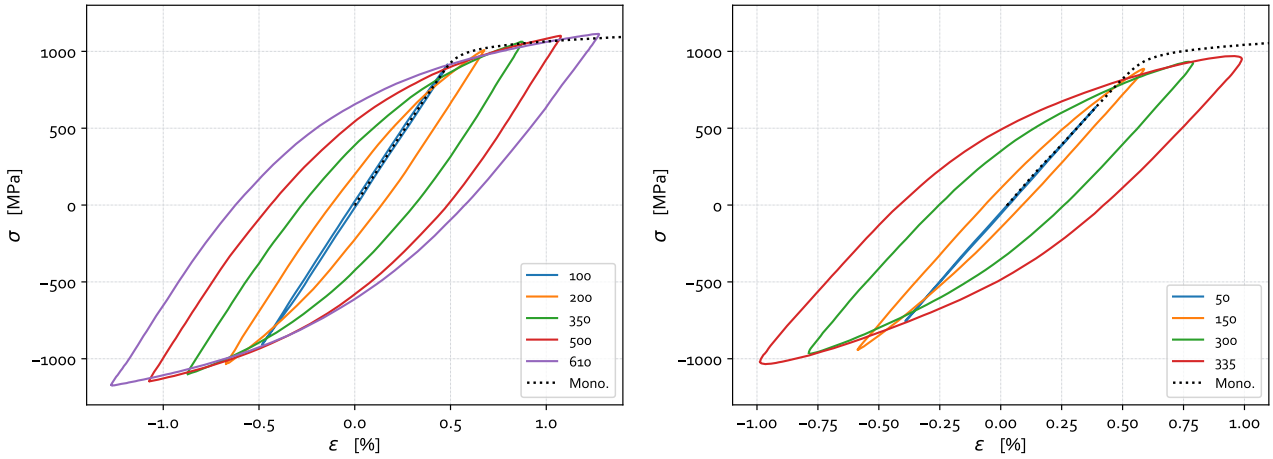

(a) 550°C / $R_\varepsilon = -1$ (spec. CAR4). (b) 700°C / $R_\varepsilon = -1$ (spec. CAR5).

Figure 2.12: Last hysteresis loops for each strain amplitude at 550 and 700°C at $\dot{\varepsilon} = 10^{-3}$ s^{-1}.

2.2.2.3 Bauschinger effect

As cyclic loading conditions are under concern for the present study, reverse flow may induce a *Bauschinger effect*, which can be significant for some metallic alloys. Bauschinger effect reflects the fact that the compressive yield strength of a specimen pre-stressed in tension is – in absolute value – lower than the initial one in tension (and *vice versa*) [Bauschinger, 1881].

From a macroscopic point of view, the Bauschinger effect is generally assimilated to the translation of the yield surface as a rigid body in the stress space. However, most of the time this effect has been proved to result from both the change in size of the initial elastic domain, due to isotropic hardening/softening, and from the movement of the elastic surface within the stress space, which is a direct manifestation of kinematic hardening. For metallic alloys, these phenomena are often coupled. As result, combined hardenings should be considered to precisely define the Bauschinger effect.

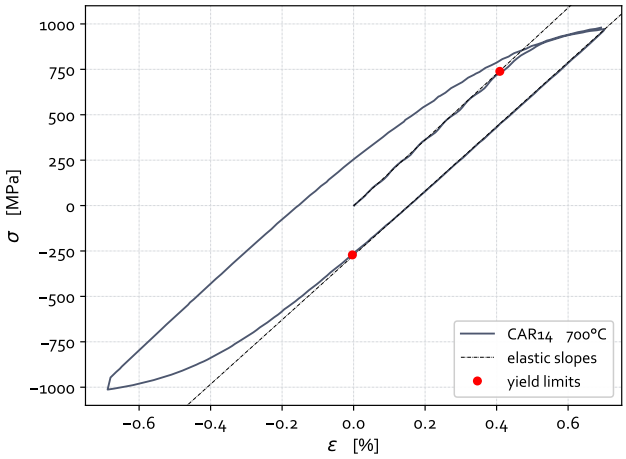

Figure 2.13: 1st hysteresis loop at 700°C at 10^{-2} s^{-1} (spec. CAR14).

The analysis of the Fig. 2.13 allows for evidencing the Bauschinger effect in AD730™ at 700°C (the same trend has also been reported at 20 and 550°C, see *e.g.* Fig. C.4a). Indeed, a lower compressive yield stress (in absolute value) is observed compared to that measured in tension (see the red points in Fig. 2.13 delimiting the linear elastic segments). Nonetheless, such an aspect is normally dependent on the strain amplitude. This will be investigated in a further sub-sect. 2.2.2.5.

2.2.2.4 Apparent cyclic hardening/softening

In order to evidence the cyclic hardening/softening properties of the material, a common approach consists in comparing both monotonic and cyclic stress-strain hardening curves [Lemaitre and Chaboche, 1990]. The *cyclic stress-strain curves* (CSSC), corresponding to the plot $\Delta\sigma/2 = f\left(\Delta\varepsilon^p/2\right)$ at stabilized state, as compared to the monotonic curve at 550 and 700°C are reported in Fig. 2.14 (those at 20°C are given in the appendices, see Fig. C.4b). From these plots, one can notice some differences between each temperature:

- at 550°C, the cyclic hardening curves are located above the monotonic ones thus emphasizing an hardening process of the material under cyclic loading conditions, Fig. 2.14a. As the temperature is sufficiently high ($T/T_m \simeq 0.38$), viscosity effects may also interact. The difference between the monotonic and cyclic curves is not that pronounced, the order of magnitude being around 50-80 MPa for large plastic strain amplitudes, see Fig. 2.14a;

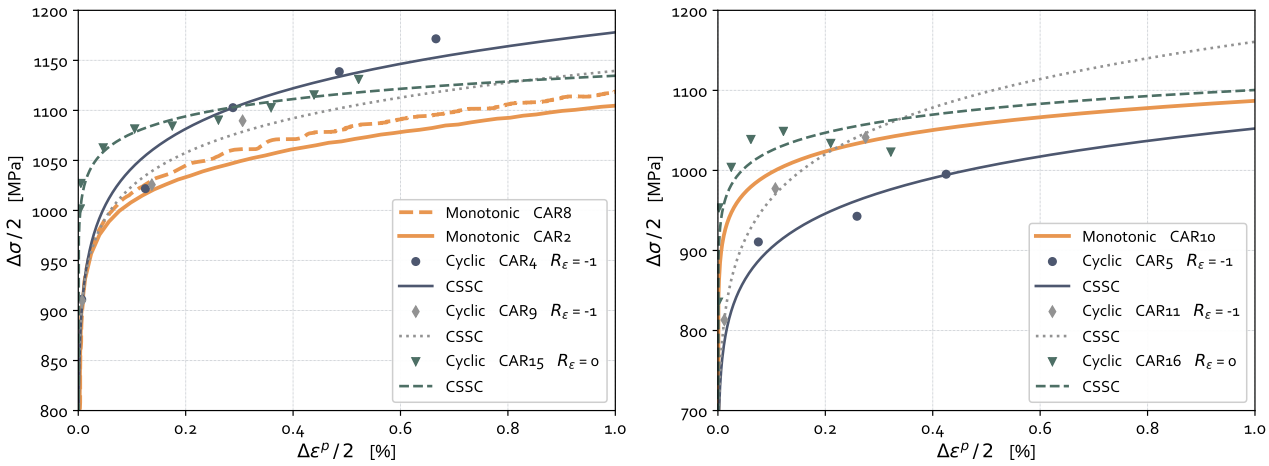

(a) Cyclic hardening curves at 550°C (zoom). (b) Cyclic hardening curves at 700°C (zoom).

Figure 2.14: Cyclic hardening curves of AD730™ at 550 and 700°C, $\dot{\varepsilon} = 10^{-3}$ s^{-1}.

- at 700°C where time-related effects may be more pronounced ($T/T_m \simeq 0.48$), strain-rate effects need to be carefully uncounted for. Only the tests conducted at the same strain rate of $\dot{\varepsilon} = 10^{-3}$ s^{-1} are plotted in order to compare curves obtained with approximately the same time-hardening (viscous) contribution. In the case of the cyclic curve obtained from the spec. CAR5, an alternate loading ($R_\varepsilon = -1$) seems to lead to a softening response of the material, Fig. 2.14b. On the contrary, the curves obtained thanks to the spec. CAR16 loaded under a repeated loading ($R_\varepsilon = 0$) and the one under alternate loading scheme ($R_\varepsilon = -1$), spec. CAR11, seem to emphasize a cyclic hardening of the material as compared to the monotonic curve. No clear conclusion can be drawn on the cyclic softening/hardening process of the material at this temperature owing to the fact that time-hardening effects interact with strain-hardening mechanisms.

Thus, one should keep in mind that for such high temperatures, thermal activity may interact with plasticity, hence involving viscosity effects. Once the yield stress is reached, viscoplasticity may appear with more or less viscous stress, also referred to as the *over-stress*. This aspect will be discussed in a forthcoming sub-sect. 2.2.3.

In order to study the overall cyclic response of the material along the whole tests, the stress envelopes, namely the stress amplitude $\Delta\sigma/2$ can be analyzed with increasing loading cycles N.

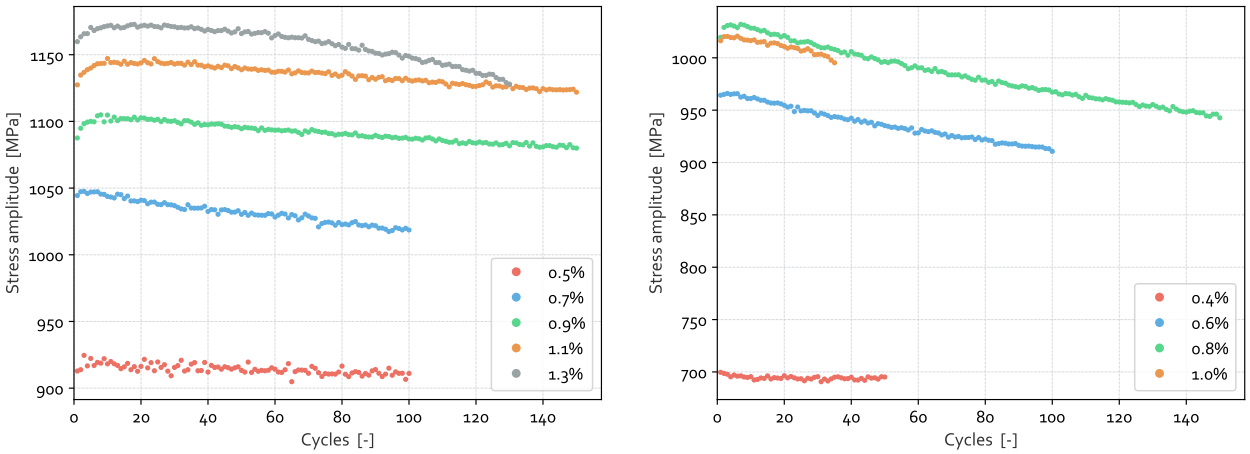

(a) Cyclic softening at 550°C at 10^{-3} s^{-1} (CAR4). (b) Cyclic softening at 700°C at 10^{-3} s^{-1} (CAR5).

Figure 2.15: Evolution of the stress amplitude at 550 and 700°C, $\dot{\varepsilon} = 10^{-3}$ s^{-1}, $R_\varepsilon = -1$ (CAR 4 & 5).

The plots of the $\Delta\sigma/2 = f(N)$ at 550 and 700°C are given in Fig. 2.15a and Fig. 2.15b, respectively (additional results at 20 and 650°C are reported in the appendices, see Fig. C.3). Because of the incremental testing procedure, a reset on N has been carried out at each starting cycle for every investigated strain level. Some points can be discussed:

- at 550 and 700°C, there is a systematic decrease of the stress amplitude for the highest strain levels. For the initial strain level of 0.5% (resp. 0.4%), the material does not seem to exhibit macro-plasticity since no hardening/softening mechanisms are noticeable. Moreover, the trend does not stabilize for the investigated strain levels even if a large number of cycles have been performed. The material does not have reached a stabilized state of macroplasticity. Finally, the stress drops for each strain level range within [-10 ; -40] MPa at 550°C and [-10 ; -80] MPa at 700°C, which represent a small part of the overall stress;
- for both testing temperatures of 550 and 700°C, one can observe a slight increase of the stress level at each change of imposed strain level, hence corresponding to a fast hardening phase. This one seems to occur during the first 5 to 10 loading cycles.

From the Fig. 2.15, one can conclude that the material exhibits a slight cyclic softening owing to the observation of the decrease of the stress amplitude with both increasing loading cycles and strain amplitudes. Even if a slight initial hardening is noticeable for the highest plastic strain amplitudes, the general trend is related to a softening response of the material under cyclic loading conditions, no matter the temperature ranging in [20, 550, 650, 700]°C.

While the cyclic hardening/softening response of AD730™ is not that clear and does not seem to be so pronounced (regarding both the cyclic stress-strain curves in Fig. 2.14 and the apparent response in Fig. 2.15), the previous Fig. 2.13 finally enables to rule on this point. After a first loading up to plastic deformation, upon unloading, the size of the elastic domain evolves. The latter, during the first $^1/_4$ loop, is equal to the yield limit, that is 832 MPa at 550°C (resp. 753 MPa at

700°C). This yield limit was estimated assuming a plastic strain offset $\delta_{pl} = 5.\,10^{-5}$. Then, once the specimen is unloaded, the radius of the yield surface corresponding to the elastic region is equal to 569 MPa (resp. 630 MPa). The material thus exhibits a cyclic softening since the elastic domain decreases. As a result, both the decrease of the elastic domain (through isotropic hardening) and the overall (slight) macroscopic hardening of the material indicate the presence of an additional hardening mechanism, that is the kinematic hardening related to the Bauschinger effect, as explained above in sub-sect. 2.2.2.3. The individual contribution of each of these strain-hardening mechanisms still remains to be estimated.

2.2.2.5 Effective and internal stresses evolution

The stress partition method (see sub-sect. 2.2.1) as applied to the experimental results allows for the accurate split between effective and internal stresses contributions to the strain-hardening mechanisms. As depicted in Fig. 2.10, the first contribution is related to the isotropic hardening of the material, while the second to the kinematic hardening. The results associated with this partition scheme at 550 and 700°C are reported in Fig. 2.16 (complementary results at 20 and 650°C are given in the appendices, see Fig. C.5a & Fig. C.5b). In these representations, red dots indicate the exit of the elastic domain whereas black crosses represent the 1-D position of the center of the yield surface in the stress space.

At 550°C, the plastic strain offset of $\delta_{pl} = 2.5\ 10^{-5}$ has been proved accurate enough to detect the exit of elastic domain at 20 and 550°C, Fig. 2.16a. At 700°C, this criterion has been "loosen" to $\delta_{pl} = 5.10^{-5}$ so as to avoid any excessive penalization of the method, hence leading to a better partition of the stress, as can be seen in Fig. 2.16b.

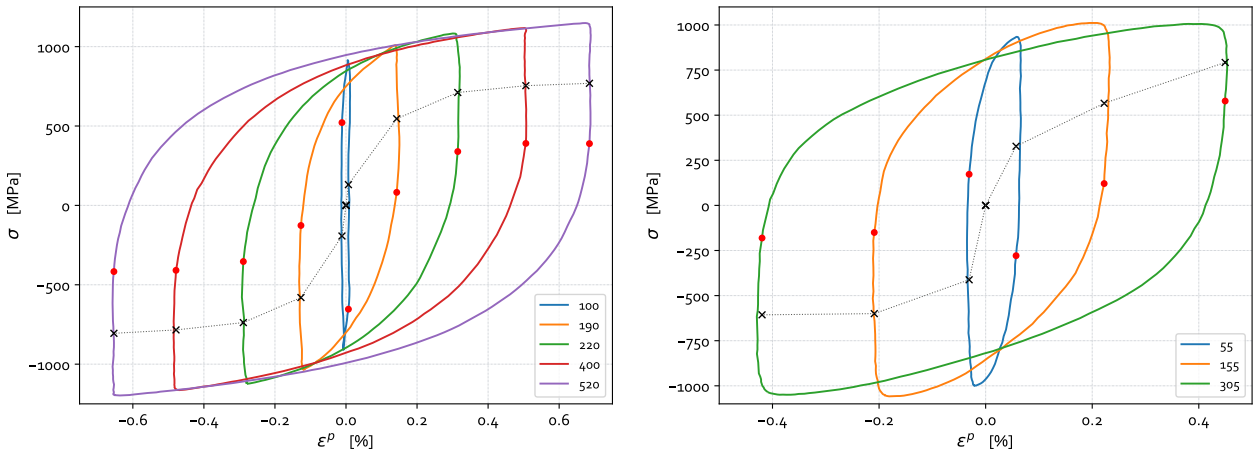

(a) Stabilized hysteresis loops at 550°C.

(b) Stabilized hysteresis loops at 700°C.

Figure 2.16: Stabilized hysteresis loops for type-1 cyclic tests at 550 & 700°C, R_ε = -1 with $\dot{\varepsilon} = 10^{-3}$ s^{-1} (spec. CAR 4 & 5). ● : yield limits; ✖ : yield surface's center.

- in both Fig. 2.16a and Fig. 2.16b, one can notice a significant change in size of the elastic domain, as indicated by the decrease of the elastic segment delimited by both red dots and peak stresses of each plastic loop. The global trend throughout the whole strain amplitudes

evidences a cyclic softening behavior with increasing strain level at 550 and 700°C. Moreover, the center of the yield surface, as indicated thanks to the black crosses, moves to a large extent in the stress space. The Bauschinger effect seems to be significant as the yield limits evolve with increasing strain amplitude;

- at 550°C, one can notice that once a sufficiently large plastic strain amplitude has been reached during the incremental test, namely $\sim \Delta\varepsilon_p/2 = 0.3\%$, a slight stabilization of the hardening mechanisms is apparent, see Fig. 2.16a. On the contrary, at 700°C, there is no clear stabilization of the hardening mechanisms, see Fig. 2.16b;
- one can notice a change in shape of the hysteresis loops (rounded tips) from Fig. 2.16a to Fig. 2.16b owing to the significant presence of viscosity effects at high temperature (the closed loops are not as well-defined as for lower temperatures). Consequently, the detection method relying on plastic strain offset and linear regression over the elastic segment is less accurate (hence suggesting the change for the plastic strain offset δ_{pl}). Finally, the small mismatch of the black cross and corresponding plastic strain evidences the occurrence of latent viscoplasticity upon the unloading/reloading phase at peak stresses.

In order to assess the extent of the cyclic softening and the evolution of the center of the yield surface, their evolution are reported in the following plots with respect to both accumulated plasticity p and plastic strain amplitudes $\Delta\varepsilon^p/2$. The effective stress will be reported with solid circles (primary y-axis), whereas the internal stress will be with blank squares (secondary y-axis). Both forward and backward flows are studied in order to analyze each component of the stress (in absolute value) as well as the presence of any *tension/compression* (T/C) asymmetry effect.

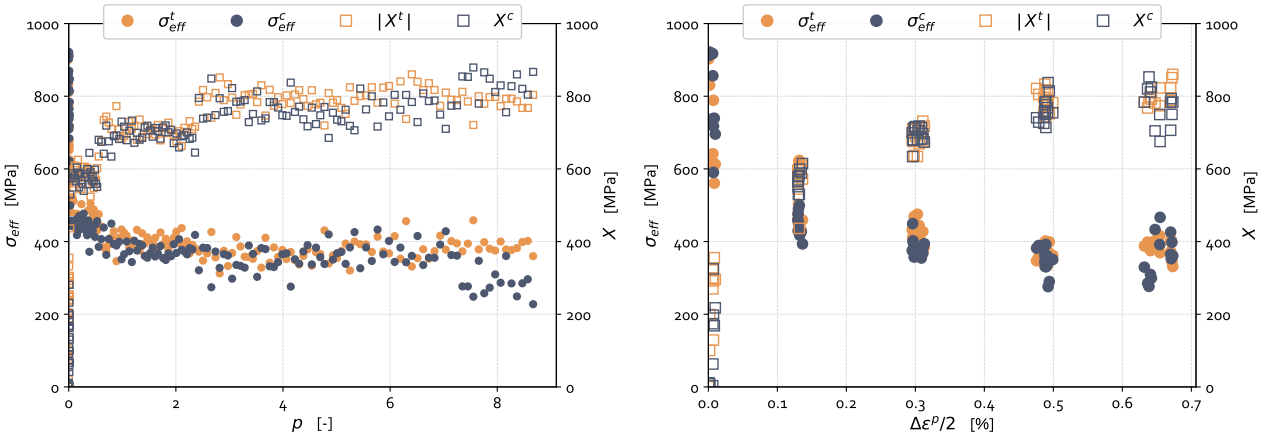

(a) Effect. and int. stresses evolution w.r.t. p.

(b) Effect. and int. stresses evolution w.r.t. $\Delta\varepsilon_p/2$.

Figure 2.17: Effective and internal stresses evolution with respect to plastic strain amplitude and accumulated plasticity for type-1 cyclic tests at 550°C, R_ε = -1, $\dot{\varepsilon} = 10^{-3}$ s^{-1} (spec. CAR4). ● : effective stress = radius of yield surface; □ : internal stress = yield surface's center.

In Fig. 2.17, the results at 550°C clearly evidence a significant reduction of the elastic domain as long as the load is increased, as already reported through the analysis of Fig. 2.16a. The global cyclic softening process is non-linear with respect to plastic strain amplitudes, Fig. 2.17b. Moreover, for each strain level, there is no significant evolution of the effective stress with cumulative plasticity, Fig. 2.17a. For the sake of brevity, similar analyses for results at 20 and 700°C are depicted in the appendices, see Fig. C.6 & Fig. C.7.

The Fig. 2.17b reports a highly non-linear evolution of the internal stress with plastic strain amplitude. The internal stress is almost constant for a given strain level, which makes possible to conclude on the absence of cumulative plasticity coupling effect for large plastic levels.
At 700°C (depicted in Fig. C.7 in the appendices page 275), the cyclic softening process is less pronounced. This can possibly be associated with the presence of viscosity effects. The clear partition between (athermal) effective stress and (thermal) over-stress is not that easy if only relying on this partition method. However, type-4 cyclic dwell tests with tensile holding periods may allow for the partition between strain- and time-hardening (over-stress) contributions to be performed (see sub-sect. 2.2.3 later on). Despite the noisy data and poorer partition capability of the approach, the global trends are similar to those at lower temperatures: both non-linear reduction and translation of the yield surface, no evolution with cumulative plasticity.

2.2.3 Time-related effects

In the present work, time-variant effects have been highlighted with both testing procedures including evolving loading rates and stress relaxation at constant load. Each test allows for a specific range of loading rates to be analyzed. As a result, relaxation tests during dwell periods (low viscoplastic strain rates) together with tests including a change in the loading rate (high viscoplastic strain rates) allow for a wide range of loading rates to be encompassed in the modeling.

2.2.3.1 Strain-rate effect

Multiple speeds monotonic tensile test

In the present study, monotonic tensile test with varying strain rate was only conducted at 550°C. The applied strain rates were $\dot{\varepsilon} = 10^{-3}$ and 10^{-5} s^{-1}.

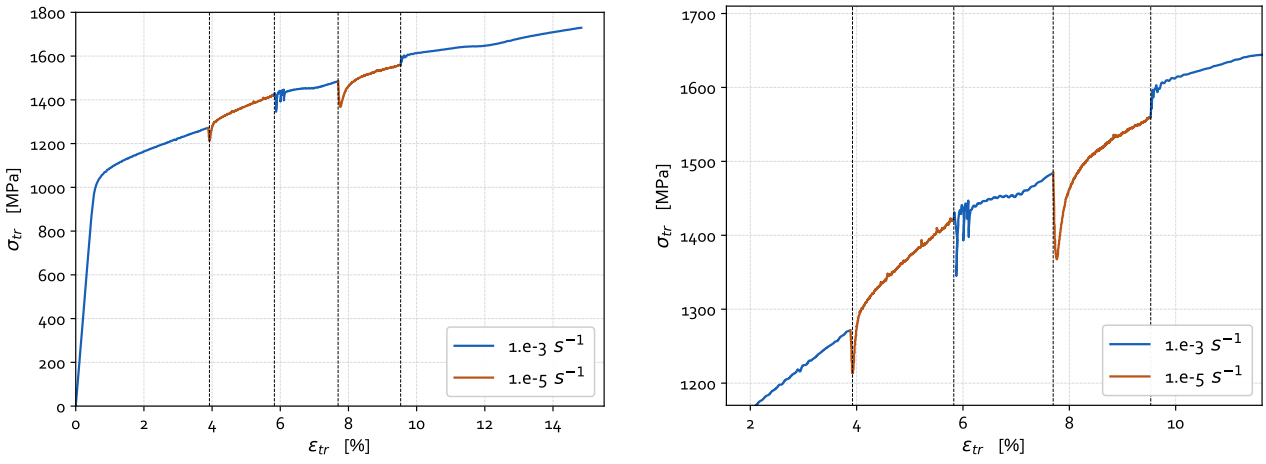

(a) Global tensile curve of the MS test.

(b) Close-up view on stress jumps for varying loading strain rates.

Figure 2.18: Strain-rate sensitivity analysis under monotonic tensile test at 550°C (spec. CAR8).

From the macroscopic results reported in Fig. 2.18, one can notice a negative (inverse) strain-rate sensitivity (SRS) of the stress with decreasing the loading strain rate. Indeed, positive (standard) SRS corresponds to an increase of the stress level for a faster loading strain rate, whereas negative (inverse) SRS results in a decrease of the stress for a higher strain rate [Chaboche et al., 2013]. For the present test, when the strain rate changes from 10^{-3} to 10^{-5} s^{-1}, in the strain range of [0 - 8]%, negative SRS is observed as the stress level is higher for the lower strain rate. However, the tendency is not the same for a greater strain level (above 8%). Moreover, some small striations are visible on the stress response, see Fig. 2.18b, which may be attributed to plastic instabilities within the material.

Up to now, no clear explanation can be formulated about such effects (stress serrations and inverse SRS) in AD730™ due to the lack of repeatability of the testing procedure. Nevertheless, negative SRS is known to be one of the manifestations of Dynamic Strain Aging (DSA) [Nouailhas, 1989], [Mannan, 1993] being often observed in several Ni-based superalloys [Venables and King, 1984]. Let us note that the SRS of a Ni-based superalloy is known to be highly dependent on the loading temperature [Fournier et al., 2001]. Results observed at 550°C do not necessarily apply at 700°C (not tested here). In the present work, for simplicity reasons and due to the minimal effects observed on experimental curves, only the positive SRS of the material to the loading rate and/or temperature will be considered during the modeling task.

Cyclic tests

From the analysis of the macroscopic results of the type-2 cyclic tests (cyclic tests with varying strain rates) at the two highest temperatures, some differences may be discussed:

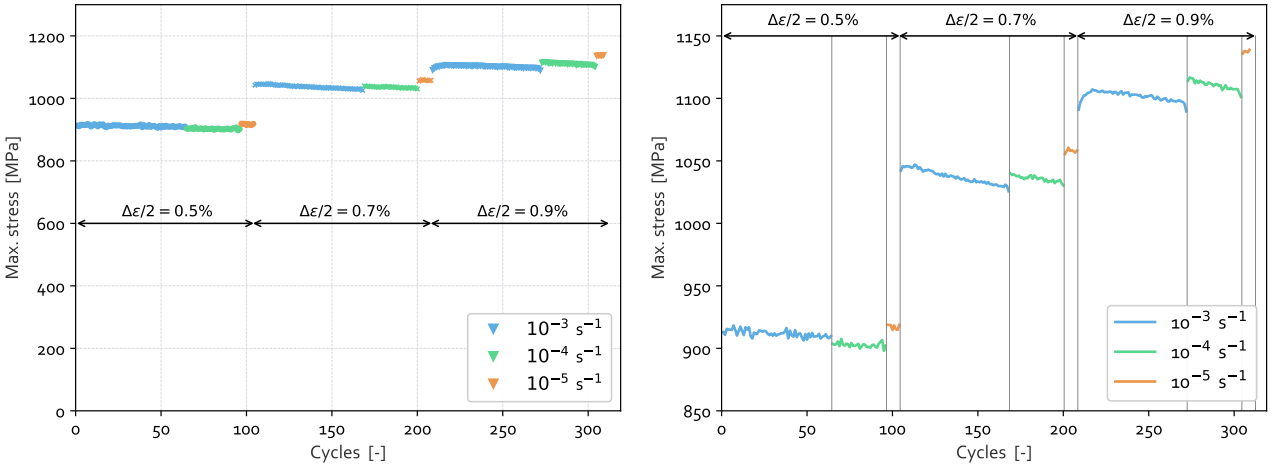

(a) Stress jumps for varying strain rates. (b) Close-up view on stress jumps for varying strain rates.

Figure 2.19: Strain-rate sensitivity analysis under cyclic loading at 550°C, $R_\varepsilon = -1$, strain levels 1-3 (spec. CAR9).

- There is no significant strain-rate sensitivity of the mechanical state at 20°C. In Fig. C.10 (in the appendices page 276), one can observe that decreasing the strain rate from 10^{-3} to 10^{-4} s^{-1}, the stress level is slightly lower. For the next speed variation, one can observe a

slight negative SRS, but with a so small stress jump so that to be disregarded;

- At 550°C, the SRS is more pronounced, as seen in Fig. 2.19. Moreover, a negative SRS of the mechanical response is also noticeable. One can observe that with decreasing the strain rate from 10^{-3} to 10^{-4} s^{-1}, the stress level is slightly higher. For the next speed variation, from 10^{-4} to 10^{-5} s^{-1}, the stress jump is more pronounced. Moreover, the higher the strain amplitude, the more pronounced the inverse SRS;
- Finally, the highest temperature of 700°C shows a different trend. A positive (standard) SRS of the material is observed, that is to say: the lower the strain rate, the lower the stress level. For this temperature, the jump in stresses starts to become non-negligible as the stress drop is close to 100 MPa in some cases. Moreover, the stress jump gets higher as the strain amplitudes increases, Fig. 2.20. It can be noticed that a similar positive SRS of the material at 700°C, though not studied in the present study under monotonic control, was also reported by [Thébaud et al., 2016] for monotonic tensile tests with variable strain rates ranging from 5. 10^{-3} to 10^{-3} s^{-1}.

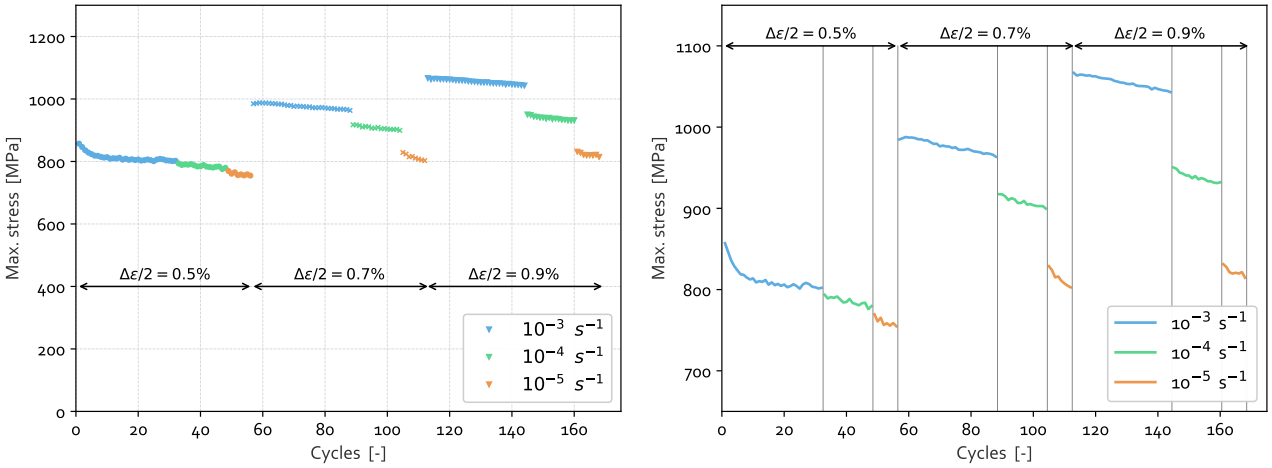

(a) Stress jumps for varying strain rates. (b) Close-up view on stress jumps for varying strain rates.

Figure 2.20: Strain-rate sensitivity analysis under cyclic loading at 700°C, $R_\varepsilon = -1$, strain levels 1-3 (spec. CAR11).

2.2.3.2 Stress relaxation

Relaxation after monotonic tests

Stress relaxation tests were performed during multiple hardening-relaxation (MHR) tensile tests at 550 and 700°C. Performed at constant strain level, the stress evolution with respect to time was acquired. The synthesis of the relaxation tests is given in Tab. 2.2. It is commonly admitted that the stress relaxation behavior can be affected by a number of factors, such as temperature, initial stress, initial strain and so on. In the present study, the effect of initial strain as well as temperature can be studied thanks to the MHR tests.

In the figure Fig. 2.21b, the first relaxation profiles for the first strain level of the MHR test at both 550 and 700°C are reported. One can see that the stress relaxation profiles obtained are

typical of Ni-based superalloy behavior at moderate to high temperatures [Rahimi et al., 2017]. Indeed, one can notice a quick drop of the stress level right from the beginning of the holding period ($\sim$ 20 min), corresponding to the first stage of relaxation, and then the stress decreases slowly during the second stage up to a (quasi-)stable value ($\sim$ 2 h), assumed to be equal to the asymptotic value for long times. A similar trend was also recently observed by [Durand et al., 2020] on FG AD730^{TM} at 760°C for stress relaxation at $\varepsilon = 0.28$ and 0.58%.

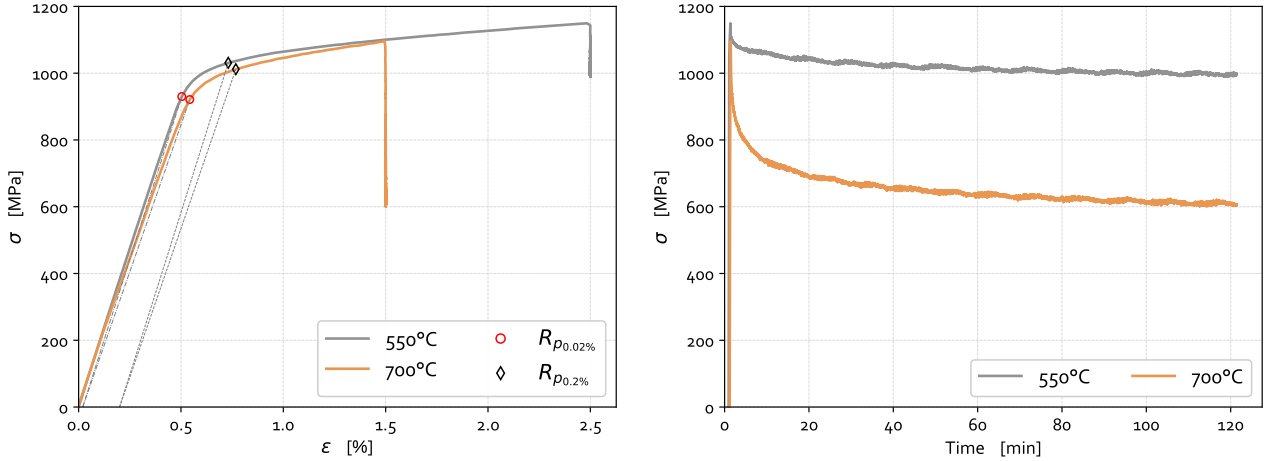

(a) Tensile curves with 2h holding time.

(b) Stress relaxation curves w.r.t. time.

Figure 2.21: Stress relaxation analysis during the 1st holding period of the MHR tests at $T = 550$°C (resp. 700°C), $\dot{\varepsilon} = 10^{-3}$ s^{-1}, $\varepsilon = 2.5\%$ (resp. 1.5%) (spec. CAR 2 & 10).

At 550°C, the over-stress (or viscous stress) represents $\sim$150 MPa of the total stress level if the strain level kept constant equals 2.5%. In addition, one can also notice in Fig. 2.21b the presence of stress serrations in the stress response w.r.t. time that can be attributed to data noise of the sampling system. At 700°C, the extent of over-stress represents approximately 500 MPa, so by far a larger contribution of viscous effects as compared to that at 550°C.

Relaxation during cyclic tests

Some relaxation tests have also been conducted after type-2 cyclic tests, or during type-4 cyclic tests, see Tab. 2.2 (the description of each monotonic/cyclic test is given in sub-sect. 2.1.3.1). As expected, at 20°C, AD730^{TM} does not exhibit significant time-variant effects (see Fig. C.10 and Fig. C.11 in the appendices page 276). This is in accordance with the lack of strain rate sensitivity (SRS) of the material at RT.

In Fig. 2.22, the hysteresis loops and stress relaxation profiles for the 1st dwell period of 720 s (HT_3) of type-4 cyclic test at 700°C are plotted. The 4 strain amplitudes are represented for $\dot{\varepsilon} = 1.\ 10^{-2}$ s^{-1} (the same results for the second loading rate of $\dot{\varepsilon} = 2.5\ 10^{-3}$ s^{-1} are given in the appendices, see Fig. C.15 page 277, while results at 550°C are also given in that appendices, see Fig. C.13 & Fig. C.14). For the sake of readability, the stress relaxation curves are all shifted to the same stress level at the beginning of the holding period (say, the larger one). Such a representation allows for the quantitative assessment of over-stress relaxation with respect to strain level.

The stress relaxation profiles at 700°C for cyclic-dwell loading conditions are comparable to that of MHR test (see Fig. 2.21) . Indeed, one can observe two distinct phases of the stress relaxation process: a fast drop in stress for the first 100 s, followed by a slower, almost linear, decrease up to a quasi-stabilized state. The vast majority of the over-stress is here again relaxed during the first period of the holding time. For increasing strain amplitudes ($0.7 \rightarrow 0.9 \rightarrow 1.1\%$), no clear stabilization of the stress after 720 s is noticeable, Fig. 2.22b.

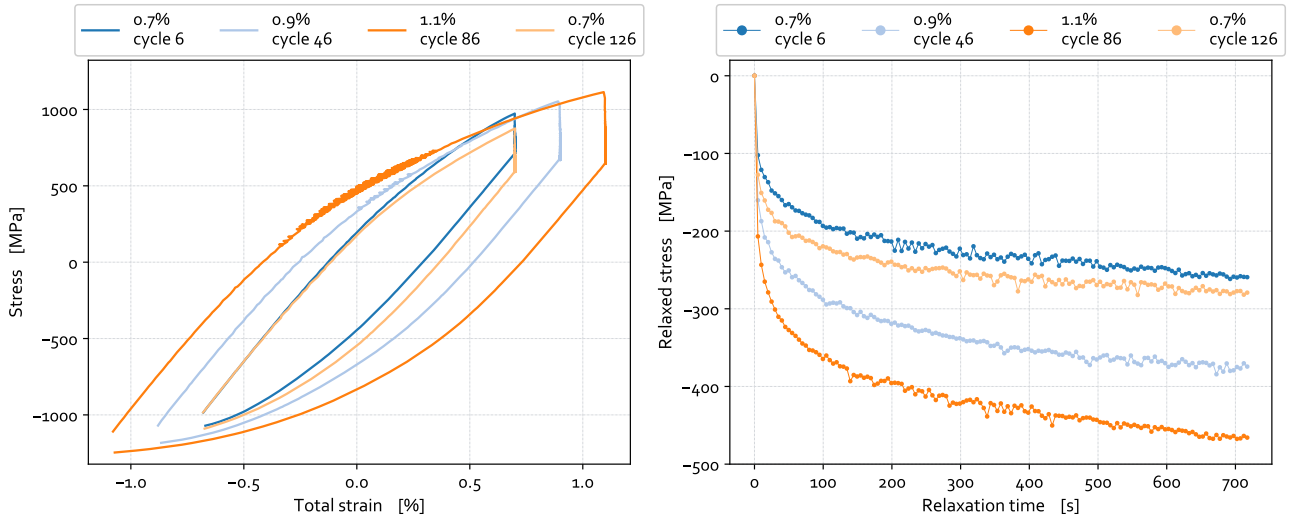

(a) Hysteresis loop with dwell-time at $\dot{\varepsilon}_1 = 10^{-2}$ s^{-1}. (b) Stress relax. during $HT_3 = 720$ s at $\dot{\varepsilon}_1 = 10^{-2}$ s^{-1}.

Figure 2.22: Hysteresis loops and corresponding stress relaxation profiles during the 1st holding period of the type-4 cyclic test at $T = 700$°C, $\dot{\varepsilon} = 1.\,10^{-2}$ s^{-1}, $HT_3 = 720$ s (spec. CAR14).

The lack of stabilization of the relaxed over-stress effect suggests the presence of two different deformation mechanisms. According to [Thébaud, 2017] & [Durand et al., 2020], when the stress level is close to the yield stress, the fast stress relaxation in FG AD730™ seems to be driven by dislocation mechanisms, whereas for lower stress levels, diffusion mechanisms seem to be predominant.

The comparison of the 2 hysteresis loops at $\Delta\varepsilon/2 = 0.7\%$ from the 1st and 4th levels can also be discussed (see Fig. 2.22a). The difference in peak stresses is approximately equal to 50-60 MPa. Between these strain levels 1 & 4, loading cycles with increasing strain amplitudes were performed, thus causing the accumulation of plasticity. Two observations can then be made:

- the peak stress for the level 4 is lower than that of the level 1 (for the same strain amplitude $\Delta\varepsilon/2 = 0.7\%$), confirming the cyclic softening of the material already stated;
- the stress drops during the relaxation phase being approximately the same for the 2 levels (1 & 4) suggest that there is no particular (or little) influence of the accumulated plasticity on the (relaxed) over-stress.

Let us note that similar results have been reported at 550°C, see Fig. C.13 in the appendices.

Evolution of the over-stress contribution

Since the fine-grained AD730™ reveals an elastic-viscoplastic behavior once the temperature exceeds 550°C, a split between time-dependent and time-independent parts of the stress needs to be performed. The cyclic strain-hardening mechanisms (isotropic and kinematic hardening) can be estimated thanks to the use of the Cottrell's partition method, as already studied in the previous sub-sect. 2.2.2.5. However, the over-stress contribution (*i.e.* the thermal- and time-dependent part of the effective stress) still needs to be quantified.
Isothermal relaxation test represents a simple and relatively accurate method to evaluate the extent of over-stress within the material, especially at high temperatures ($T/Tm \geq 0.5$) along a wide range of strain rates. Some assumptions still need to be done:

- one considers the stress partition between the time-hardening and the strain-hardening contributions of the stress, that is:
$$\sigma = \sigma_{ov} + \sigma_{int} \tag{2.2}$$
where σ_{ov} is the over-stress (time-dependent part) and σ_{int} the internal stress (time-independent part), the latter including the initial yield stress and the strain-hardenings;
- one considers a very slight evolution of the internal stress σ_{int} during the relaxation phase (*i.e.* no static-recovery effect for the strain-hardenings).

The acquisition of the stress evolution with respect to time during the test allows for the determination of the viscoplastic strain rate. The slope in each point of the $\sigma(t)$ curve finally gives the instantaneous value of the viscoplastic strain rate, see Fig. 2.23.

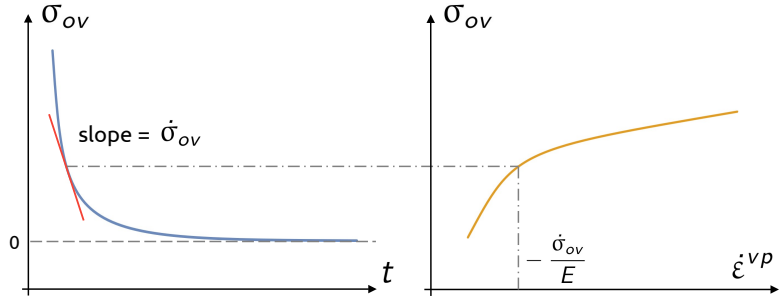

Figure 2.23: Schematic representation of the determination method of the over-stress related to viscoplastic strain rate.

Since sufficient plastic strain is expected to develop at the tip of a growing crack, choice has been made to focus on relaxation data of the first strain level of MHR tests, that is: $\varepsilon = 2.5\%$ at 550°C and 1.5% at 700°C, Fig. 2.24a. In addition, data for the highest strain level of type-4 cyclic-dwell tests ($\Delta\varepsilon/2 = 1.2$ and 1.1%) will also be discussed, Fig. 2.24b.

Even if no clear asymptotic line (steady-state stress) is noticeable, the over-stress that is relaxed has then be estimated for sufficiently long holding durations. Looking at Fig. 2.24, the extent of over-stress that is relaxed for the same hold duration is significantly higher at 700°C, compared to that at 550°C. In case of Fig. 2.24a, the contribution of the over-stress has been estimated to 144 MPa (resp. 491 MPa) for a strain rate of $\dot{\varepsilon}^{in} = 10^{-3}$ s^{-1}.

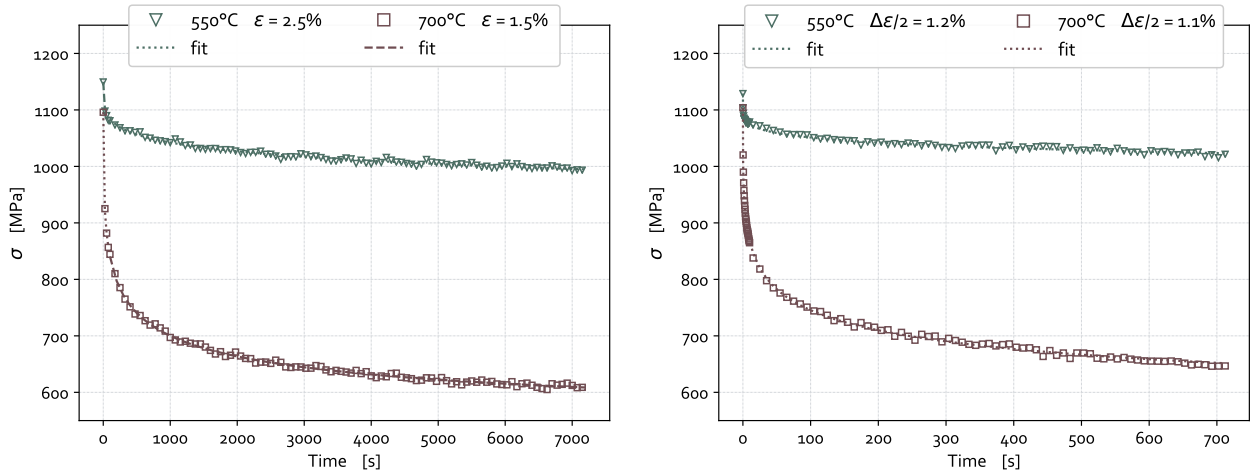

(a) 2h relaxation tests (MHR tests). (b) 720s relaxation tests (cyclic-dwell tests).

Figure 2.24: Stress relaxation curves for the 1st holding period of the MHR and cyclic-dwell tests at 550 and 700°C (spec. CAR 2 & 10).

Estimated viscoplastic strain rates from experimental data were extremely noisy. To overcome this aspect, a power-law fit of the viscoplastic strain of the form $y = Ax^B + C$ was considered to get smoother evolutions [Rouse et al., 2020]. Overall data were also re-sampled in order to get legible results. Using a backwards difference method, the evolution of the over-stress as a function of the viscoplastic strain rate can be plotted, see Fig. 2.25.

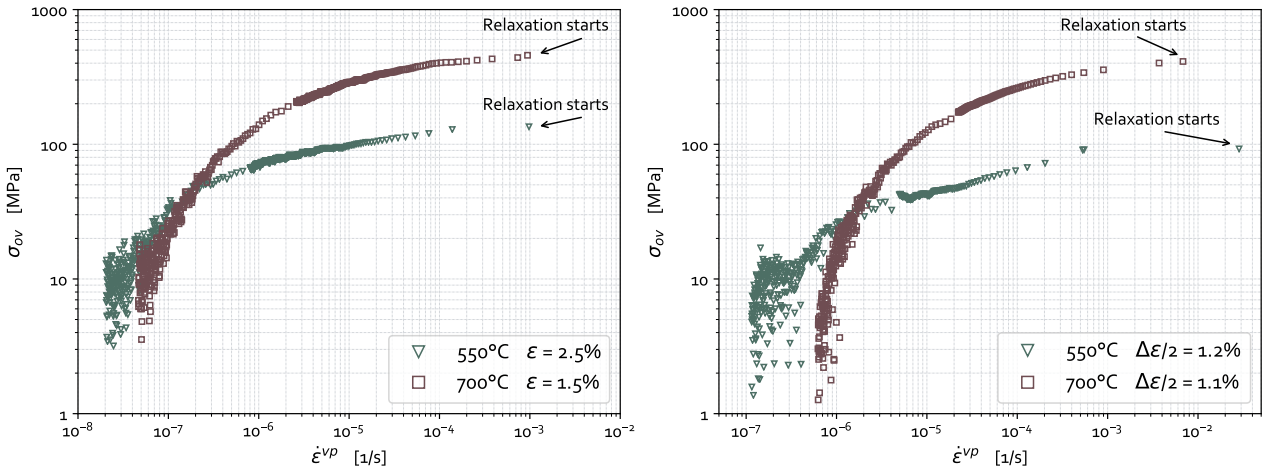

(a) Stress relax. after monotonic tensile tests. (b) Stress relax. during cyclic-dwell tests.

Figure 2.25: Over-stress evolution with decreasing viscoplastic strain rate during dwell-sequences of MHR and cyclic-dwell tests at 550 and 700°C (with (a) $\dot{\varepsilon} = 10^{-3}$ s^{-1} and (b) $\dot{\varepsilon} = 10^{-2}$ s^{-1}).

According to the Fig. 2.25, some aspects should be discussed:

- the stress relaxation curves exhibit a change in shape for plastic strain rates below $\dot{\varepsilon}^{vp} \sim 10^{-6}$ (550°C) and $\sim 10^{-5}$ s^{-1} (700°C). The curves admit a knee which evidences a change in viscosity regime (*i.e.* the occurrence of dual deformation mechanisms), as also confirmed by [Durand et al., 2020] for FG AD730™ at 760°C;

- the over-stress admits a quasi-saturated state as soon as the viscoplastic strain rate is greater than 10^{-4} s^{-1} at 550°C. This finding is in agreement with the absence of significant strain rate sensitivity of the material at 550°C for strain rates ranging in [10^{-3} - 10^{-5}] s^{-1};
- the over-stress decreases in a quasi-linear way (in a log-log scale) for strain rates in [10^{-2} - 10^{-5}] s^{-1}, Fig. 2.25. Below $\dot{\varepsilon}^{vp} = 10^{-6}$ s^{-1}, the over-stress significantly decreases for viscoplastic strain rate ranging from 10^{-8} to 10^{-6} s^{-1}. Such viscoplastic strain rates are close to that of classical creep/time-recovery domain [Nouailhas, 1989], [Chaboche, 2008]. The (assumed) change in viscosity process might thus be attributed to time-recovery effect of the strain-hardening mechanisms.

Finally, the main point to be kept in mind refers to the fact that the relation $\sigma_{ov} = f(\dot{\varepsilon}^{vp})$ is highly non-linear in a log-log scale, which will require a specific modeling feature. In addition, the absence of stabilization of the over-stress after long relaxation durations together with the two-periods relaxation process (see Fig. 2.25) might be representative of some time-recovery effects, especially at 700°C [Pétry, 2006]. The first period corresponds to a pure relaxation of the over-stress while during the second period, a recovery phenomenon seems to be superimposed, [Bucher, 2004]. Although discussed, static recovery effects won't be modeled in the remaining of this work.

2.2.4 Particular effects associated with cyclic loading conditions

It is somehow well admitted that metallic materials may be prone to plasticity-induced particular effects under cyclic loading conditions [Lemaitre and Chaboche, 1990]. The brief literature review concerning such effects discussed in sub-sect. 2.1.3.1 gives a starting point when studying cyclic plasticity mechanisms in Ni-based superalloys [Chaboche et al., 2012], [Goulmy, 2017], [Prisacari, 2018]. In the case of FG AD730™, strain range memory effects as well as other cyclic transient effects (isotropic-kinematic hardening coupling, mean stress relaxation...) need to be investigated to guide the further modeling process.

2.2.4.1 Masing-type behavior and strain range memory effect

The stabilized state of the mechanical response in terms of stress-strain amplitudes can be depicted by the cyclic stress-strain curve (CSSC), although this curve is unable to explain the shape of the hysteresis loops [Ellyin, 1997]. For this latter aspect, the Masing's hypothesis should be studied [Masing, 1923], [Masing, 1926]. When shifting the minima of stable cyclic loops for increasing strain amplitudes to a common origin, the Masing model allows for the loading branches to overlap each others [Ellyin and Kujawski, 1984]. Such a plot can be studied in the frame coordinates ($\varepsilon^p - \varepsilon^p_{min}$, $\sigma - \sigma_{min}$), see Fig. 2.26. Moreover, a material following the

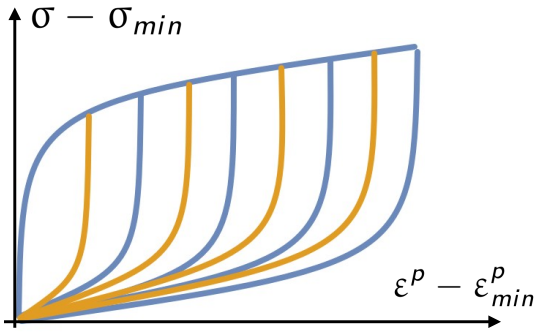

Figure 2.26: Masing-type elastic-plastic material response.

Masing model would have identical loading/unloading branches for the hysteresis loops and their elastic region remain unaltered with a change in strain amplitude [Paul et al., 2011].

The examination procedures conducted until now did not allow to check the Masing-behavior ability of AD730™ at investigated temperatures. Further analyses of the hysteresis loops are conducted in this subsection in order to address this point. The Fig. 2.27a shows the shifted saturated uniaxial stress-plastic strain loops for increasing strain amplitudes at 550°C. Relevant information can be obtained thanks to this representation:

- with progressive cycling and increasing strain range, the size of the elastic segment tends to reduce, hence confirming the cyclic softening effect;
- for the stable hysteresis loops, the shape of the loops is fairly the same, given an overall homothetic change of the loop for increasing loading levels. As it can be seen, the loading arms of all the loops fairly overlap each others and the global trend is close to the schematical representation of the Masing model, Fig. 2.26. For the 3 first strain levels, one can notice that the loading arms of the loops do not coincide, Fig. 2.27a. Thus, a *quasi Masing-behavior* can be reported in FG AD730™ at 550°C.

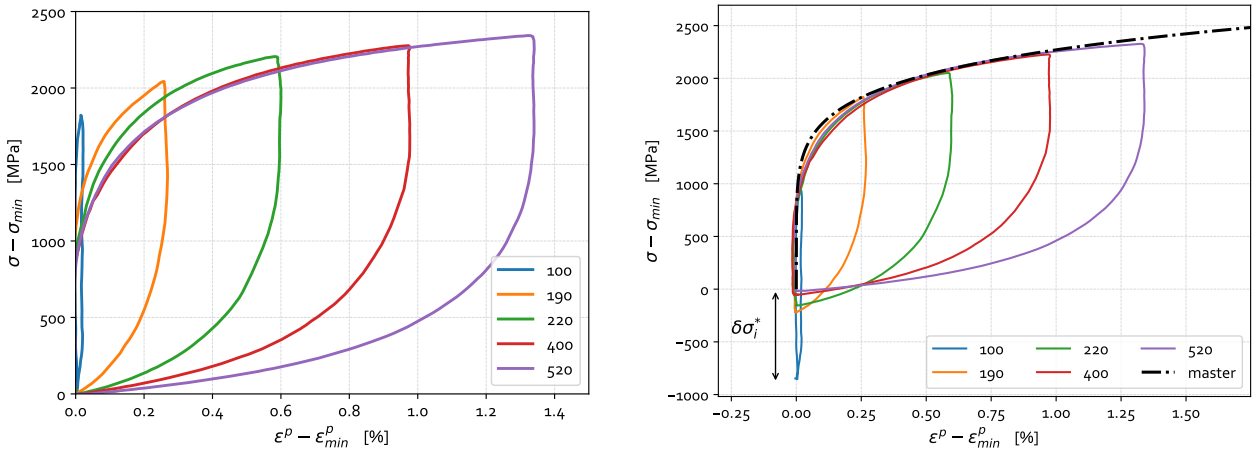

(a) Shifted quasi-saturated hysteresis loops.

(b) Shifted hysteresis loops with master curve.

Figure 2.27: Shifted hysteresis loops for Masing-type behavior analysis at 550°C, $R_\varepsilon = -1$, $\dot{\varepsilon} = 10^{-3}$ s^{-1} (spec. CAR4).

In order to investigate the deviation from the Masing-rule of the material, a common approach consists in shifting the saturated hysteresis loops along the elastic segment until the loading arms well overlap [Chaboche, 1986], [Arora et al., 2021]. Such a construction is shown in Fig. 2.27b at 550°C with corresponding master curve representing twice the cyclic stress-strain curve (CSSC) [Lemaitre and Chaboche, 1990]. The extension of linear segment $\delta\sigma^*_i$ for each strain amplitude i (taking the origin as reference) is therefore referred to as *the magnitude of non-Masing stress*. It represents the additional quantity required for the elastic domain of the material to reach the origin and hence perfectly validate the Masing-rule. In the present case, considering the compressive tip of the loop of the highest strain level (cycle 520) at the origin (0., 0.), a negative deviation along the elastic line confirms the softening response of the material.

The Masing model applies for the stabilized state. However, the lack of stabilization for the first

strain levels is in agreement with the stress deviation from the perfect Masing-rule. A greater number of cycles should have been conducted for the few first strain levels so as to reach a stabilized state and lead to a Masing-type response, Fig. 2.27b. The observed quasi-Masing behavior of AD730™ is finally assumed to be related to the non-stabilization of the cyclic response due to an insufficient number of loading cycles. Similar results have been reported at 20 and 700°C. For the sake of brevity, corresponding plots are given in the appendices, see Fig. C.8 & Fig. C.9. The forthcoming paragraph will allow to check for the adequacy of AD730™ with Masing model.

Bauschinger strain

The adequacy of the response of the material with Masing-rule can also be checked considering the so-called *Bauschinger strain*, β [Plumtree and Abdel-Raouf, 2001], [Li et al., 2019]. The latter corresponds to the plastic strain on stress reversal at 75% of the peak stress, see Fig. 2.28. Bauschinger strain β has been measured on all the quasi-saturated hysteresis loops for every testing temperature. Example at 550°C is reported in Fig. 2.29a while the evolution of β with respect to plastic strain range $\Delta\varepsilon^p$ is reported in Fig. 2.29b.

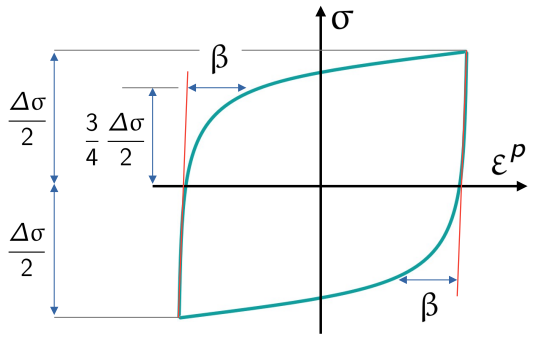

Figure 2.28: Bauschinger strain in cyclic hysteresis loop (adapted from [Li et al., 2019]).

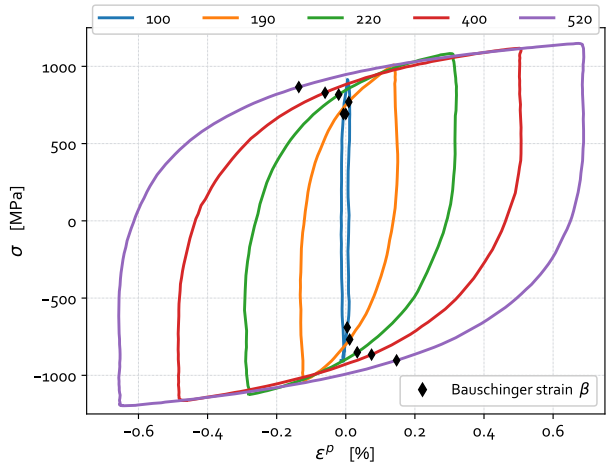

(a) Bauschinger strain on stable hysteresis loops at 550°C (spec. CAR4).

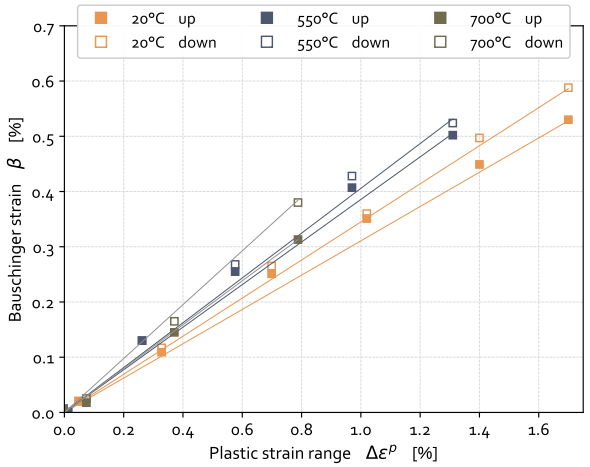

(b) Bauschinger strain evolution with plastic strain ranges.

Figure 2.29: Bauschinger strain evolution with increasing plastic strain range in FG AD730™.

The linear evolution of $\beta = f(\Delta\varepsilon^p)$ evidenced for the target temperatures of 20, 550 and 700°C, Fig. 2.29b, confirms the Masing behavior of AD730™ at considered temperatures [Plumtree and Abdel-Raouf, 2001], [Goyal et al., 2017]. In addition, the adequacy of the cyclic response with Masing model, for investigated strain amplitudes and temperatures, allows not to consider any plastic strain range memory effect [Lemaitre and Chaboche, 1990] in the modeling.

2.2.4.2 Isotropic-kinematic hardening coupling

The saturated state on hysteresis loops is not sufficient when considering cyclic loading schemes as transient effects may also be present. Despite the lack of stabilization of the mechanical state for some investigated strain levels (see sub-sect. 2.2.4.1), paying attention to the cyclic loops' evolution for a given strain amplitude may also be relevant.
In Fig. 2.30, the internal (back) stress evolution for the first and last cycles of each strain level of the type-1 cyclic incremental tests at 550 & 700°C are reported to analyze the change in shape.

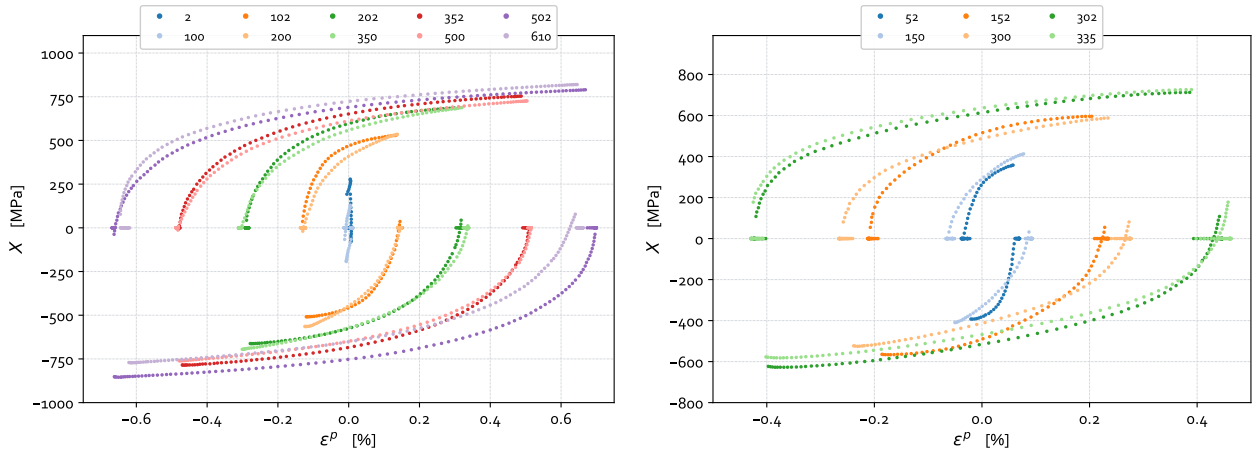

(a) Back-stress evolution at 550°C (spec. CAR4). (b) Back-stress evolution at 700°C (spec. CAR5).

Figure 2.30: Back-stress evolution between first and last cycles for incremental type-1 cyclic tests at 550 and 700°C, $R_\varepsilon = -1$, $\dot{\varepsilon} = 10^{-3}$ s^{-1}.

The Fig. 2.30a (resp. Fig. 2.30b) shows, for each strain amplitude, the internal back-stress evolution at 550°C (resp. 700°C), during the transient phase from the first cycle up to stabilization. One can notice an evolution of the plastic (or tangent) modulus of the internal back-stress, especially for the first strain levels (*i.e.* a change in the shape of the hysteresis loops). Such an effect of back-stress evolution at low strain levels evidences a coupling between the kinematic hardening and the cyclic hardening of the material through accumulated plasticity. This aspect should hence be included in the modeling, as suggested by [Marquis, 1979] for cyclic loading conditions.

2.3 Phenomenological formulation of the unified constitutive material model

2.3.1 On the choice of a material modeling framework

The experimental results obtained from previous sect. 2.2 have evidenced the presence of time- and strain-hardening mechanisms within the studied material under monotonic and cyclic loading

conditions. Furthermore, the strain-hardening mechanisms have been proved to be of dual-form with both isotropic and kinematic mechanisms, each of them exhibiting various kinetics. In view of the scope of the present Ph.D. project which aims at the modeling of the fatigue crack growth in structural calculations, the choice for a robust material modeling is of primary importance. For these reasons, the choice for a **unified viscoplasticity modeling** framework can be qualitatively justified [Chaboche, 1989].

The unified viscoplastic material model of [Chaboche, 1978], [Chaboche and Nouailhas, 1989] has proven to be efficient for the modeling of Ni-based superalloys [Maciejewski, 2013], [Barrett et al., 2014], [Goulmy, 2017], [Prisacari, 2018]. Moreover, it is designed so as to reproduce all the above-mentioned phenomena discussed in sect. 2.2. Such a material model represents a robust framework for the material modeling of AD730™ from moderate to high temperatures. In the following, the constitutive equations are established within the framework of the so-called *Generalized Standard Materials* (GSM) [Halphen and Nguyen, 1975] associated with the *Thermodynamics of Irreversible Processes* (TIP) [Germain, 1973], [Nguyen, 2000]. In this sect. 2.3, the main equations enabling the modeling of the mechanical behavior of the material are detailed.

2.3.2 Elasticity

For unified elastic-viscoplasticity, the linear rule, the so-called *Hooke's law* is considered for metallic materials in elastic domain. This reads, in the 1-dimensional form (uniaxial characterization tests):

$$\sigma = E\left(\varepsilon^{tot} - \varepsilon^{in}\right) = E\,\varepsilon^{el} \qquad \text{with} \qquad \varepsilon^{tot} = \varepsilon^{el} + \varepsilon^{in} \tag{2.3}$$

in which thermal effects have been disregarded due to isothermal conditions. With this linear equation, the stress σ and elastic strain ε^{el} are proportional to each others thanks to Young modulus E (in 1D).

2.3.3 Time-related effects

For most of the metallic materials under viscoplastic loading, the elastic domain is defined thanks to a loading surface defined by:

$$\mathcal{F}_y^{vp} = \mathcal{F}_y - \sigma_{ov} = |\sigma - X| - R - R_0 - \sigma_{ov} \leq 0 \tag{2.4}$$

where σ and X are the uniaxial stress and back-stress, respectively, R the isotropic stress, R_0 the initial yield stress and σ_{ov} the over-stress (related to viscosity).

As presented before for the studied material, see Fig. 2.25, the evolution of the over-stress is highly non-linear. Two major regimes can be distinguished, mainly depending on the testing conditions:

(i) a first one mainly focuses on high stress levels with significant viscoplastic strain rates: in such a case, the viscoplastic strain rate is an exponential or hyperbolic function of the stress;

(ii) a second regime tends to describe the creep properties at low stress levels: the viscoplastic strain rate is generally a power-law relation of the stress.

According to the Fig. 2.31 (together with the results given in Fig. 2.25 page 76), the over-stress evolution with decreasing viscoplastic strain rate is highly non-linear in a log-log diagram. Thus, a simple Norton-Perzyna power-law relation [Norton, 1929] is not sufficient to cover the large range of viscoplastic strain rates. Moreover, a quasi-saturation of rate effect ensues for high viscoplastic strain rates and should be embedded in the modeling.

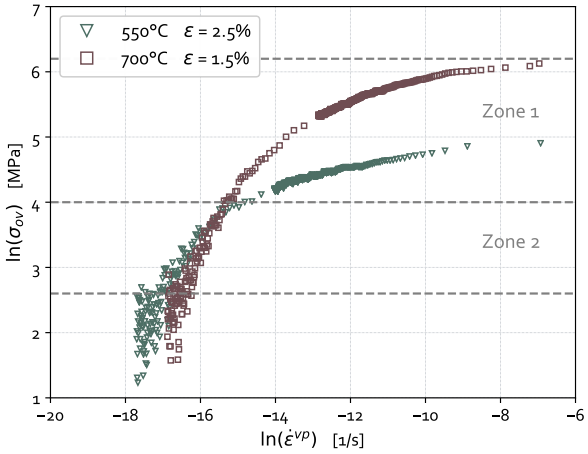

Figure 2.31: Sensitivity of the over-stress to the viscoplastic strain rate.

One variation of the Norton-Perzyna's power-law relationship is the hyperbolic sine function first proposed mathematically by [Sellars and McTegart, 1966]. The advantage of this flow rule over the classical Norton power-law has already been demonstrated in the literature. It was also successfully applied, *e.g.* by [Pétry, 2006], [Paris, 2008], [Szmytka et al., 2010] or [Bartošák et al., 2020].

$$\dot{\varepsilon}^{in} = \dot{\epsilon}_0 \left[\sinh \left\langle \frac{\sigma_{ov}}{K} \right\rangle^{n} \right]^{m} \operatorname{sgn}(\sigma - X) \tag{2.5}$$

where $\dot{\epsilon}_0$, K, m and n introduced in the hyperbolic sine law eq. (2.5) are the initial viscoplastic strain rate, the viscoplastic resistance coefficient (also referred to as the *drag stress*) and the viscoplastic exponents, respectively. In eq. (2.5), material constant $\dot{\epsilon}_0$ plays the role of a saturation parameter and is then intended to saturate the viscous stress at high strain rate regime.

The 1-D over-stress defined in the previous discussion should be generalized in 3-D thanks to a viscoplastic potential leading to equipotential visco-surfaces in the stress space, see Fig. 2.32. The viscoplastic part of the total strain rate is directly dependent on the chosen dissipation potential:

$$\dot{\underset{\sim}{\varepsilon}}^{in} = \frac{\partial \Omega^*(\underset{\sim}{\varepsilon}, \underset{\sim}{\sigma}, \underset{\sim}{X}, R, T)}{\partial \underset{\sim}{\sigma}} \tag{2.6}$$

with Ω^* the viscoplastic potential defining the equipotential visco-surfaces. Compared to the time-independent (plasticity) case, the stress may lay out of the yield surface.

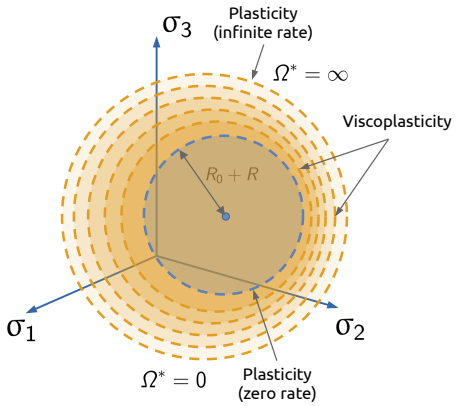

Figure 2.32: Equipotential visco-surfaces in principal stress space (adapted from [Lemaitre and Chaboche, 1990]).

Remark: Since low temperatures are also under concern in the present Ph.D. project, the eq. (2.5) is also appropriate for time-independent situations ($K \to 0$ or $m \to \infty$) [Chaboche, 2008].

2.3.4 Strain-hardening effects

Modeling aspects of isotropic hardening

In material modeling, isotropic hardening is related to the change in size of the elastic domain. It is therefore associated with the effective stress defined in sect. 2.2 (see Fig. 2.10 page 62) which is related to the short-range interaction between dislocations, *i.e.* the friction stress [Feaugas, 1999]. Moreover, the athermal part of the effective stress corresponds to the yield surface radius. The following relations finally read, see Fig. 2.10 page 62:

$$\begin{cases} \sigma^c_{eff} = \dfrac{\sigma_{max} - \sigma^c_y}{2} = R_0 + R^c \\ \sigma^t_{eff} = \dfrac{\sigma^t_y - \sigma_{min}}{2} = R_0 + R^t \end{cases} \tag{2.7}$$

where R_0 is the initial size of the elastic region and $R_0 + R$ is the instantaneous radius of the yield surface in the reverse direction, see Fig. 2.33. The relation eq. (2.7) evidences the change in size of the elastic domain with progressive cycles. For alternate loading conditions, in the absence of tension/compression asymmetry, R^c and R^t are assumed to be equal.

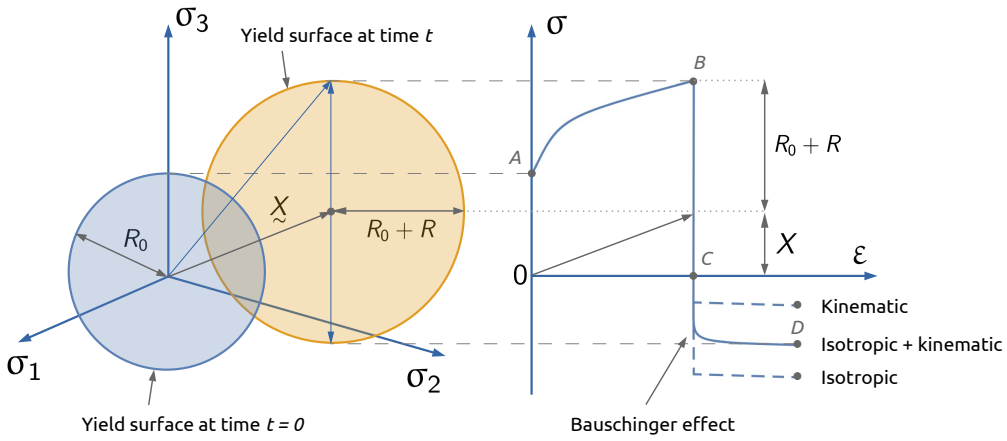

Figure 2.33: Schematic representation of the isotropic and kinematic strain-hardening mechanisms in principal stress space.

Along a material modeling process, the expansion/contraction of the radius of the yield surface is often related to accumulated plasticity, $R(p)$, as in eq. (2.4). Owing to the observations conducted in sub-sect. 2.2.2.5, the isotropic hardening R (through the effective stress σ_{eff}) may admit several regimes, *e.g.* a fast decrease for the first strain level, followed by a slower decrease of the elastic domain with increasing accumulated plasticity, see *e.g.* Fig. 2.17 page 69. Hence, the total isotropic hardening can be decomposed in a series of additive terms, each of them adapted for a dedicated regime depending on the linear or non-linear (and/or fast or slow) evolutions. The most commonly

used formalism is probably the exponential form proposed by [Voce, 1955]:

$$\dot{R} = \sum_i \dot{R}^i \qquad \text{with} \qquad \dot{R}^i = b^i \left(R^i_\infty - R^i\right) \dot{p} \tag{2.8}$$

where $R^i_\infty = Q^i$ and b^i control the saturation value and the pace toward saturation of the isotropic hardening, respectively, and $\dot{p}$ is the accumulated (visco-)plastic strain rate.
The integrated form of eq. (2.8) results in the following rule:

$$R^i = Q^i \left[1 - \exp(-b^i p)\right] \tag{2.9}$$

With such a formulation, eq. (2.9), the change in size of the elastic region only depends on the accumulated plastic strain in a non-linear way, as reported in sub-sect. 2.2.2.5. Moreover, such hardening is isotropic in nature (scalar term), as the expansion/contraction of the yield surface is supposed to be isotropic. Note that any strain range dependency of Q^i as well as time-recovery effects have been considered in conformity to experimental evidences reported in sub-sect. 2.2.4.1.

Modeling aspects of kinematic hardening

The internal stress estimated with the help of the Cottrell's partition method (see Fig. 2.10 page 62) hence helps for the estimation of the kinematic hardening, the latter representing the Bauschinger effect through the translation of the yield surface in stress space, see Fig. 2.33. From a microscopic point of view, the back-stress is associated with long-range interactions with mobile dislocations [Guillemer et al., 2011]. According to eq. (2.7) and Fig. 2.10, one has [Feaugas, 1999]:

$$\begin{cases} X^c = \sigma_{max} - \sigma^c_{eff} \\ X^t = \sigma_{min} + \sigma^t_{eff} \end{cases} \tag{2.10}$$

One can notice that for cyclic loading conditions with $R_\varepsilon = -1$, in case there is no particular tension/compression asymmetry, X^c and $|X^t|$ can be assumed to be equal.

As observed in sub-sect. 2.2.2.5, the kinematic hardening X (through the internal stress X) can admit several regimes, *e.g.* a fast increase for the first strain level, followed by a slower increase with increasing plastic strain amplitude, see *e.g.* Fig. 2.17 page 69. Thus, in an analogous way to isotropic hardening, the kinematic one can be decomposed in a series of additive terms, each of them suited for a defined plastic strain range [Frederick and Armstrong, 1966], [Chaboche and Rousselier, 1983]:

$$\dot{X} = \sum_k \dot{X}^k \qquad \text{with} \qquad \dot{X}^k = C^k \dot{\varepsilon}^{in} - \gamma^k X^k \left|\dot{\varepsilon}^{in}\right| \tag{2.11}$$

where C^k is the tangent modulus of the back-stress and γ^k controls the speed of saturation of the hardening. Here again, as for the isotropic hardening, eq. (2.8), time-recovery effects have been omitted for simplicity reasons. The integrated form of eq. (2.11) results in the following

exponential rule under tension/compression loading:

$$X^k = \pm \frac{C^k}{\gamma^k}\left[1 - \exp(\pm \gamma^k p)\right] \tag{2.12}$$

Generally, in order to get an accurate description of *(i)* the initial elastic-plastic transition, *(ii)* the transient region and *(iii)* the long range plasticity, 3 variables are considered to describe the kinematic hardening (*i.e.* $k = 1, 2, 3$), [Chaboche and Rousselier, 1983]. In particular cases, more variables are sometimes employed, *e.g.* for the study of ratcheting effects [Bari and Hassan, 2000].

2.3.5 Transient effects in cyclic viscoplasticity

It has been reported in sub-sect. 2.2.4.2 a change in plastic modulus with increasing loading cycles (through accumulated plasticity), particularly at low strain levels. The introduction of a cyclic hardening coupling effect within the kinematic hardening rule was first proposed by [Chaboche, 1977b] and successful applications were done later on by [Marquis, 1979], [Benallal and Marquis, 1987]. In the present study, such a modification is required for the modeling of the transient hardening, especially for the first few cycles, as evidenced in Fig. 2.30.
The concept relies on the introduction of an evolutionary function associated with the rate of convergence γ^k of the back-stress. This allows for the eq. (2.11) to be re-written:

$$\dot{X}^k = C^k \dot{\varepsilon}^{in} - \gamma^k \varphi^k(p) X^k \left|\dot{\varepsilon}^{in}\right| \tag{2.13}$$

$$\text{with} \qquad \varphi^k(p) = \varphi^k_\infty + \left(1 - \varphi^k_\infty\right) e^{-\omega^k p} \tag{2.14}$$

The function $\varphi^k(p)$ allows for the description of the changes in the plastic tangent modulus of the kinematic hardening as a function of cyclic hardening/softening [Marquis, 1979]. It enables a progressive value of the back-stress lower than the saturated one (*i.e.* C^k/γ^k). It can be noted that when $\varphi^k_\infty = 1$ in eq. (2.14), X^k reduces to the classical Armstrong-Frederick formulation eq. (2.11). Such a modeling procedure has proven to be efficient for the cyclic behavior modeling of various Ni-based superalloys [Maciejewski, 2013], [Goulmy, 2017].

2.3.6 Summary of the overall material model

The previous sub-sect. 2.3.2 to sub-sect. 2.3.5 have enabled a consistent formulation of the material model suited for the experimental evidences reported in sect. 2.2. The main constitutive equations of the present material model are finally summarized in Tab. 2.4 with corresponding material parameters. Then, in order to perform the calibration, the simulation of the database is achieved using the "gen-evp" routine, see [Armines et al., 2020a], from the Z-set implicit code [Foerch et al., 1997], [Besson and Foerch, 1997]. Let us note that the Z-set Finite Element software, co-developed by École des Mines de Paris and the ONERA, has been used throughout this Ph.D. project.

Mechanism	Constitutive equation	Parameters	Units
Elasticity	$\dot{\varepsilon}^{e} = \dfrac{\dot{\sigma}}{E}$	E, ν	MPa, -
Viscoplasticity	$\dot{\varepsilon}^{in} = \dot{\epsilon}_0 \left[\sinh \left\langle \dfrac{\sigma_{ov}}{K} \right\rangle^{n} \right]^{m} \operatorname{sgn}(\sigma - X)$	$\dot{\epsilon}_0$, K, m, n	s^{-1}, MPa, -, -
Accumulated plasticity	$\dot{p} = \left\lvert \dot{\varepsilon}^{in} \right\rvert$	-	-
Yield (visco-)surface	$\sigma_{ov} = \lvert \sigma - X \rvert - R - R_0$	R_0	MPa
Isotropic hardening	$\dot{R} = \sum_i \dot{R}^i \qquad i = 1,2$	-	-
	$\dot{R}^i = b^i \left(Q^i - R^i \right) \dot{p}$	Q^i, b^i	MPa, -
Kinematic hardening	$\dot{X} = \sum_k \dot{X}^k \qquad k = 1,2,3$	-	-
	$\dot{X}^k = C^k \dot{\varepsilon}^{in} - \gamma^k \varphi^k(p) X^k \left\lvert \dot{\varepsilon}^{in} \right\rvert$	C^k, γ^k	MPa, -
Marquis' effect	$\varphi^k(p) = \varphi^k_\infty + \left(1 - \varphi^k_\infty\right) e^{-\omega^k p}$	φ^k_∞, ω^k	-, -

Table 2.4: One-dimensional form of the constitutive equations of the cyclic non-linear material model for FG AD730™ from low to high temperatures.

The whole model includes a set of 23 independent material constants which need to be calibrated consistently so as to match experimental results. Such a calibration process is made possible through a systematic and methodological approach aimed at exploiting the whole capabilities of the model [Chaboche and Nouailhas, 1989]. Such a task is described in the next sect. 2.4.

2.4 Calibration of the unified material model

The previously governing mechanisms described in sect. 2.3 separate the necessary parameters into several class: *(i)* elastic, *(ii)* cyclic softening, *(iii)* non-linear back-stress and *(iv)* time-dependent material parameters. Despite the existence of complex multi-objective functions (*i.e.* genetic algorithms [Kuna and Wippler, 2010], [Mahmoudi et al., 2011]; stochastic methods [Harth and Lehn, 2007]; neural network approaches [Huber and Tsakmakis, 2001] or Bayesian methods [Adeli,

2019]), such approaches are susceptible to a lack of physical correspondence of the identified set of parameters, as the solution is far from being unique. Consequently, the approach adopted in the present work aimed at using an accurate examination of experimental data associated with a step-by-step methodology, in order to identify material parameters relying on mechanistic (physical) correspondence and representation of experimentally-observed phenomena.

2.4.1 General approach

Unified viscoplastic material models allows for the strict split between time-independent and time-dependent mechanisms [Chaboche and Nouailhas, 1989], [Nouailhas, 1989]. Such a property hence enables the possibility to first estimate the elastic-plastic material model parameters prior to the introduction of time-variant effects. As reported in Tab. 2.4, up to 23 material parameters have to be calibrated at each target temperature of the isothermal tests:

- E, ν, R_0 which are related to the material elastic properties at null or very small strains;
- $\dot{\epsilon}_0$, K, n, m which are related to the time-variant mechanisms within the material at low and high strain rates under viscoplastic deformation;
- Q^i, b^i ($i = 1,2$), C^k, γ^k, φ^k_∞, ω^k ($k = 1,2,3$) which allow for the description of the cyclic evolution of the material as a combination of cyclic hardening/softening during transient cycles up to stabilization.

The large number of material parameters renders the calibration process a difficult task. Although each parameter describes a specific property, the combination of all (or some) of them remains interdependent and possible redundancy may exist between specific material constants. The parameters are hence successively calibrated step-by-step using the experimental tests so as to avoid such redundancies.

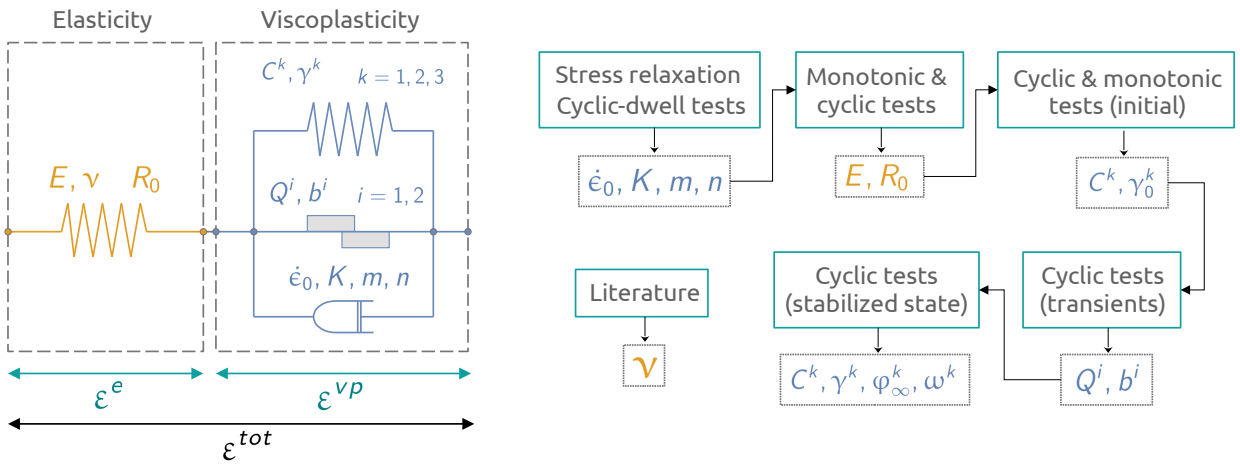

(a) 1-D rheological scheme of the constitutive EVP material model.

(b) Flowchart for the identification stages of the material model parameters.

Figure 2.34: Overview of the whole calibration process for the unified material model at low to high temperatures using monotonic and cyclic characterization tests.

A general rheological representation of the whole model together with a representation of the main steps associated with the calibration process are given in Fig. 2.34. In order to perform the calibration, assuming an ideal uniaxial stress state over a RVE, the *model simulation* tool implemented within the Z-set suite was used [Armines et al., 2020a]. Simulations were then run so that to compare numerical and experimental results. Numerical integration of the differential system was performed using an explicit 2^{nd}-order *Runge-Kutta* resolution scheme with automatic time stepping.

2.4.2 Elastic properties

Material parameters related to elastic properties of the material, E, ν and R_0 are first calibrated. These are estimated with the help of monotonic tensile tests (up to plastic onset) as well as cyclic tension-compression tests, see Fig. 2.34b. Poisson ratio ν of the material is not documented due to the few studies conducted up to now on AD730™. A value close to that related to Ni-based superalloys is hence taken, *i.e.* $\nu = 0.3$.

2.4.3 Strain-hardening properties

The calibration procedure is performed using data tests at constant strain rate in order to consider viscous effects almost constant [Chaboche, 2008]. The calibration of strain-hardening mechanisms is carried out on monotonic tensile and stabilized cyclic data. The limiting case of time-independent plasticity is considered. Consequently, time-related parameters are assumed null or assigned to a value enabling their contribution to vanish ($K \sim 1\,\text{MPa}$, $n = m = 1$, $\dot{\epsilon}_0 = 10^{-3}$ s^{-1} for the viscoplastic potential). Such a procedure remains valid for low temperatures for which viscosity effects can be neglected.

The absence of any strain range memory effect enables the isotropic and kinematic hardening rules to be identified separately [Chaboche, 1986]. Hence, isotropic softening parameters $(Q^i,\, b^i)$ with $i = 1, 2$ are calibrated thanks to the effective stress evolution with increasing cumulative plasticity p, according to the stress partition method presented in sub-sect. 2.2.1. Material constants $(Q^1,\, b^1)$ are associated with the fast softening for the few first cycles whereas $(Q^2,\, b^2)$ are associated with the transient and slower decrease of the elastic domain with accumulated plasticity.

Once both transient and stabilized data for isotropic softening are obtained using the results from the Cottrell's partition method, pure kinematic effects may be estimated, Fig. 2.34b. The use of 3 kinematic variables has been chosen so as for the shape of the hysteresis loops in LCF tests as well as monotonic tensile tests to be well caught. To this end:

- a large value of γ^1 with a small value of X^1_∞ gives the initial non-linearity at plastic onset, thus resulting in a large plastic tangent modulus C^1;
- then, parameters C^2 and γ^2 are dedicated to the description of the transient part of the curve (medium to large strains);
- the last back-stress is used for the behavior at greater inelastic deformations once X^1 and X^2

have reached their saturated state. To do so, a low value of γ^3 is assigned and the parameter C^3 is determined thanks to the plastic modulus for large strains levels. If necessary, the last back-stress X^3 may also have a pure linear evolution, setting $\gamma^3 = 0$;

- finally, it should be noted that the choice for material constants should ensure some guidelines, namely: $C^1 > C^2 > C^3$ and $\gamma^1 > \gamma^2 > \gamma^3$.

For the calibration of the transient effects, the initial plastic loading (from monotonic tensile test or first $^1/_4$ cycle, see Fig. 2.34b) is first used to estimate the initial back-stress components. Tangent modulus of the plastic curve is thus related to the initial state and corresponds to the parameters (C^i, γ_0^i) with:

$$\gamma_0^k = \gamma^k \varphi(0) = \gamma^k \tag{2.15}$$

Since the transient effect has been proved to be only noticeable at low strain levels, *cf.* sub-sect. 2.2.4.2, choice has been made here to apply the transient effect function eq. (2.14) only to the first two back-stress terms. This assumption allows for setting $\varphi_\infty^3 = 1$ and $\omega^3 = 0$. Moreover, to ease the calibration process, the same evolution eq. (2.16) is applied to both X^1 and X^2. The steady-state is then calibrated using the cyclic stress-strain curve, Fig. 2.34b. For large values of accumulated plasticity p, the Marquis' function eq. (2.14) reduces to:

$$\varphi^k(p) \underset{p \to +\infty}{\longrightarrow} \varphi_\infty^k \qquad k = 1, 2 \tag{2.16}$$

so that we have:

$$\dot{X}^k = C^k \dot{\varepsilon}^{in} - \gamma^k \varphi_\infty^k X^k \left| \dot{\varepsilon}^{in} \right| \qquad k = 1, 2 \tag{2.17}$$

Up to this point, the material constants related to the elastic-plastic behavior have been calibrated in close relationship with experimental observations as well as results obtained from the stress partition method. Both initial and steady-state behaviors have been accounted for in such a strain-rate independent formulation. Time-variant effects still need to be included so that to cover the whole viscoplastic capabilities of the unified formulation.

2.4.4 Time-related effects

As evidenced in sub-sect. 2.2.3, FG AD730™ exhibits a complex time hardening behavior which depends on the strain rate regime. Moreover, looking at the plot of $\sigma_{ov} - \dot{\varepsilon}^{vp}$ in a log-log diagram (Fig. 2.25), observation of an highly non-linear trend has been reported. The hyperbolic sine function detailed in eq. (2.5) was preferred covering a wider range of viscoplastic strain rates. Its calibration was carried out using the stress relaxation profiles, see Fig. 2.34b and following some guidelines from [Rouse et al., 2020]. Corresponding plots for the first holding period of the MHR tests are given in Fig. 2.35. One can observe the ability of the hyperbolic sine viscosity function to accurately predict the over-stress evolution over a large range of quasi-static strain rates while keeping a quasi-saturation at high strain rates, see Fig. 2.35.

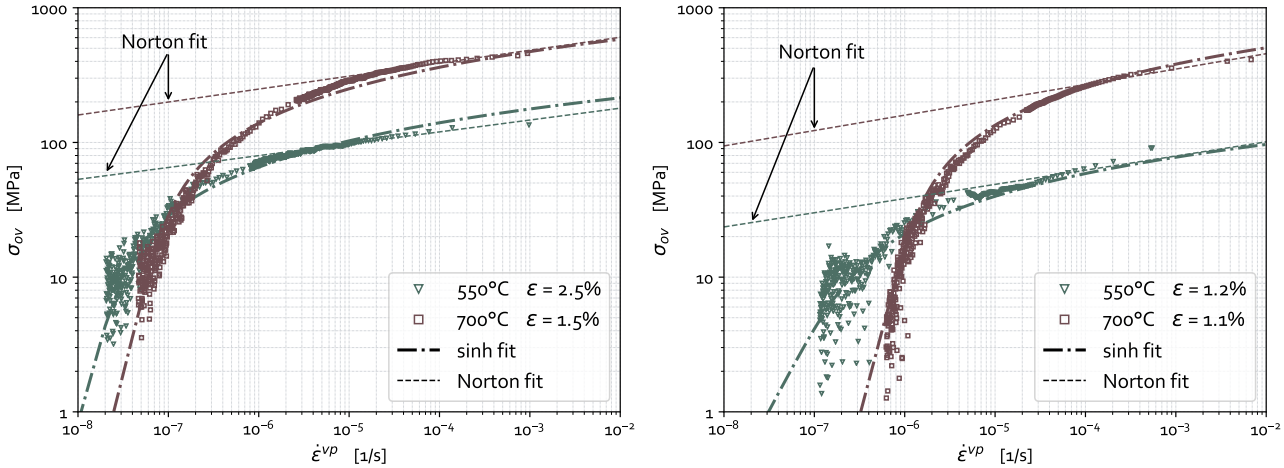

(a) Relax. after MHR tests at $\dot{\varepsilon} = 1.\,10^{-3}$ s^{-1}. (b) Relax. during cyclic-dwell tests at $\dot{\varepsilon} = 1.\,10^{-2}$ s^{-1}.

Figure 2.35: Over-stress evolution with decreasing viscoplastic strain rate during dwell-sequences of MHR and cyclic-dwell tests at 550 and 700°C.

2.4.5 Overall model calibration

Once the material constants have been calibrated, some comparison between experimental data and model predictions can be drawn. To this end, 4 typical loading schemes are studied, that are: the monotonic tensile loading, the stress relaxation tests as well as cyclic loading schemes under symmetric and non-symmetric load ratio, with and without tensile holding periods. These tests are representative of the vast majority of the present testing conditions.

2.4.5.1 Monotonic tensile behavior

First, the initial tensile loading is studied for the two temperatures of 550 and 700°C.

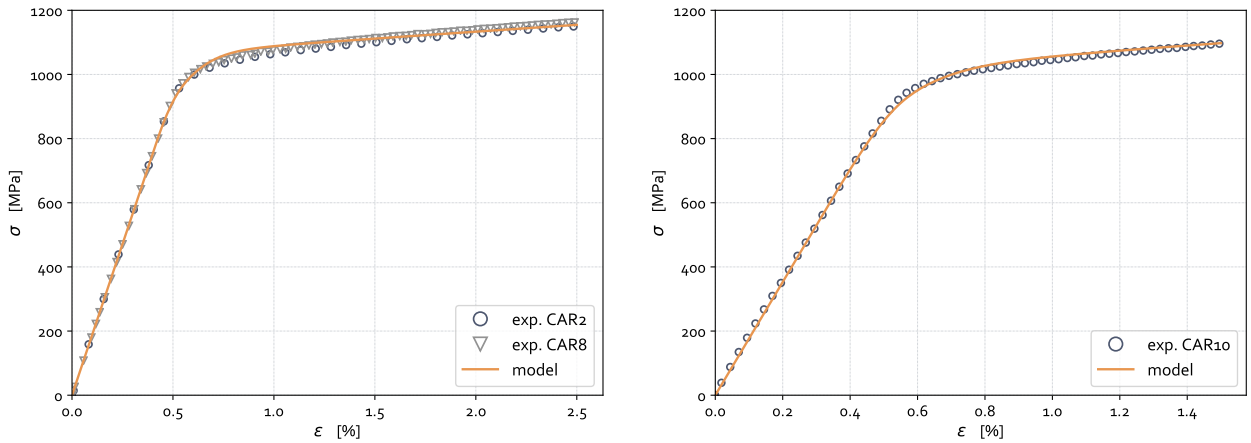

(a) Monotonic tensile loading at 550°C. (b) Monotonic tensile loading at 700°C.

Figure 2.36: Comparison of model prediction on monotonic tensile loading at 550 & 700°C.

It can be noticed that experimental responses are well reproduced by the model thanks to the introduction of transient evolution rules within the back-stress terms (see eq. (2.13)), see Fig. 2.36.

2.4.5.2 Stress relaxation behavior

The stress relaxation profiles are quite well estimated, see Fig. 2.37. Hyperbolic sine model has hence proven to be adapted and suits the curve for short to long durations. Such a modeling made it possible to neglect the time-recovery terms in order to retranscribe the entire relaxation phase.

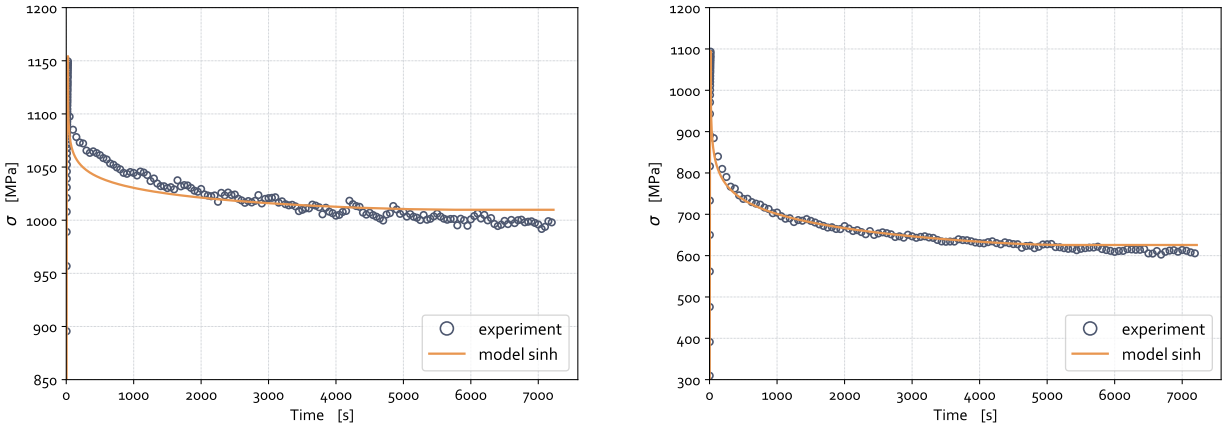

(a) Stress relaxation profile at 550°C. (b) Stress relaxation profile at 700°C.

Figure 2.37: Comparison of model prediction on stress relaxation profile at 550 & 700°C.

2.4.5.3 Cyclic behavior

The cyclic predictive capabilities of the present material model are analyzed. Stable hysteresis loops for the whole strain ranges and the three target temperatures are well simulated, see Fig. 2.38, Fig. 2.39a & Fig. 2.39b. The slight tension/compression asymmetry can be seen when comparing both experimental and simulated peak stresses. The low-to-high plastic strain levels are well accounted for with the present calibration of the model's parameters.

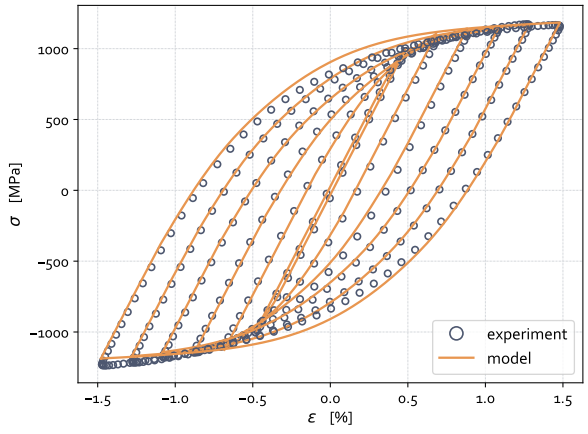

Figure 2.38: Stabilized cycles at 20°C.

For the cyclic-dwell tests, the overall strain levels and relaxation phases are also quite well reproduced, Fig. 2.40 & Fig. 2.41. A slight difference may be revealed for the peak stresses. Such a result seems to be attributed to some (slight) differences in the transient mechanisms between pure cyclic and cyclic-dwell tests. Indeed, it can be noted that material parameters for the simulated loops in Fig. 2.40 & Fig. 2.41 are those

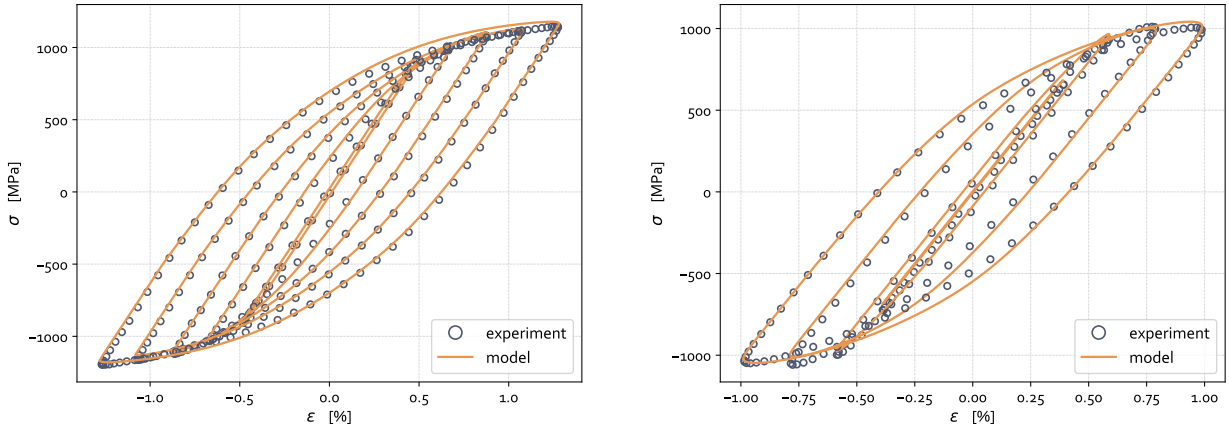

(a) Stabilized cycles at 550°C. (b) Stabilized cycles at 700°C.

Figure 2.39: Comparison of model prediction on cyclic stabilized cycles - $\dot{\varepsilon} = 1.10^{-3}$ s^{-1} - 550 & 700°C.

estimated from the stable and symmetric loops of the type-1 cyclic tests. Hence, accumulated plasticity has not reached the same level and cyclic softening is not saturated at the same time. Moreover, less cycles have been performed in type-4 cyclic-dwell tests for each investigated strain level, hence delaying the cyclic softening process.

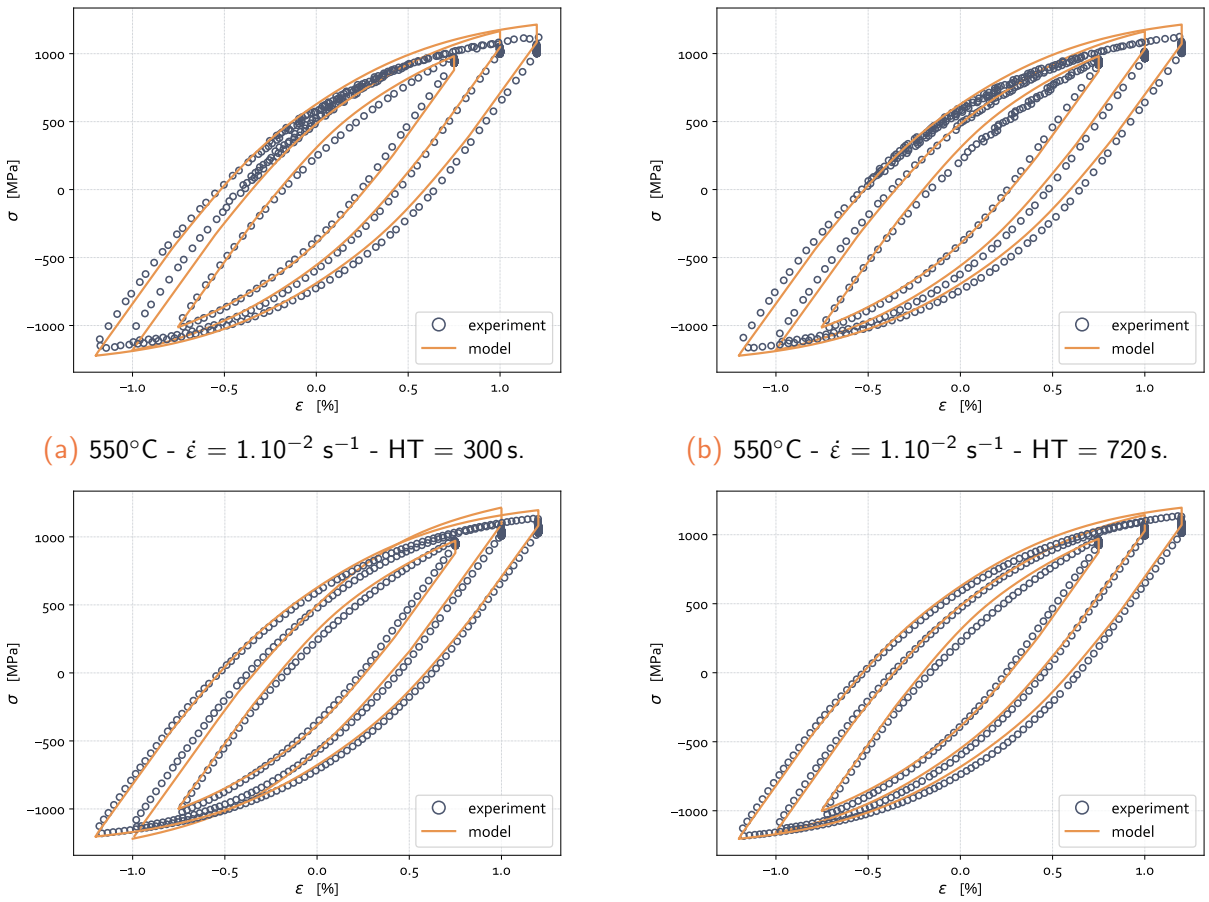

(a) 550°C - $\dot{\varepsilon} = 1.10^{-2}$ s^{-1} - HT = 300 s. (b) 550°C - $\dot{\varepsilon} = 1.10^{-2}$ s^{-1} - HT = 720 s.

(c) 550°C - $\dot{\varepsilon} = 2.5\ 10^{-3}$ s^{-1} - HT = 300 s. (d) 550°C - $\dot{\varepsilon} = 2.5\ 10^{-3}$ s^{-1} - HT = 720 s.

Figure 2.40: Comparison of model prediction on cyclic-dwell tests - $R = -1$ - 550°C.

However, global trends and stress-strain levels are well captured and give satisfactory predictions.

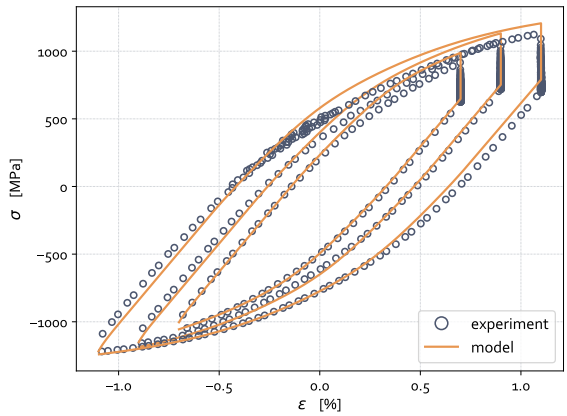

(a) 700°C - $\dot{\varepsilon} = 1.10^{-2}$ s^{-1} - HT = 300 s.

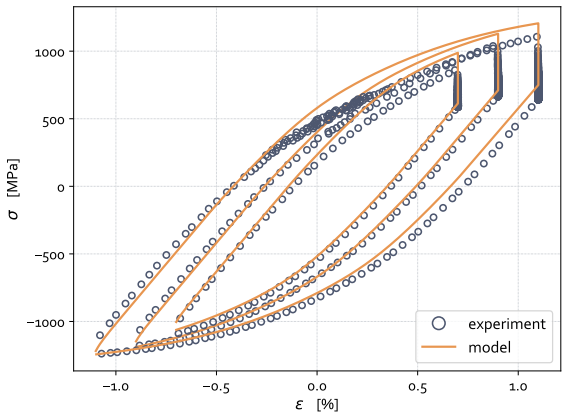

(b) 700°C - $\dot{\varepsilon} = 1.10^{-2}$ s^{-1} - HT = 720 s.

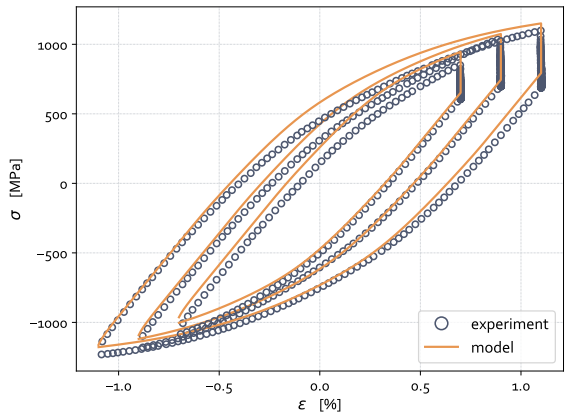

(c) 700°C - $\dot{\varepsilon} = 2.5\ 10^{-3}$ s^{-1} - HT = 300 s.

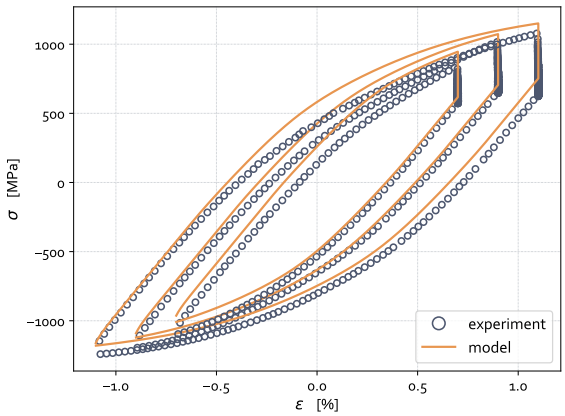

(d) 700°C - $\dot{\varepsilon} = 2.5\ 10^{-3}$ s^{-1} - HT = 720 s.

Figure 2.41: Comparison of model prediction on cyclic-dwell tests - $R = -1$ - 700°C.

Finally, for non-symmetric loading conditions with $R_\varepsilon = 0$ at stabilized state, the hysteresis loops are also well captured by the model, see Fig. 2.42.

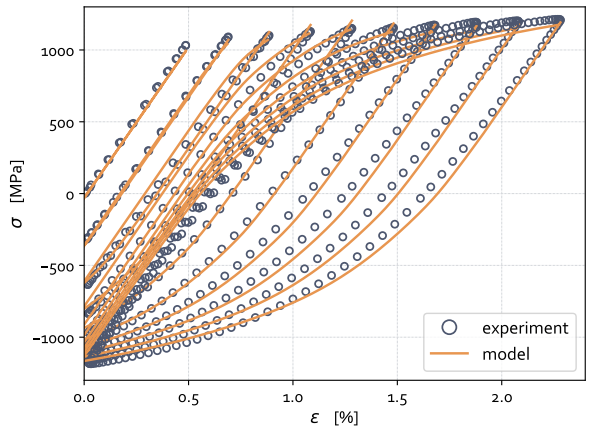

(a) Stabilized cycles at 20°C.

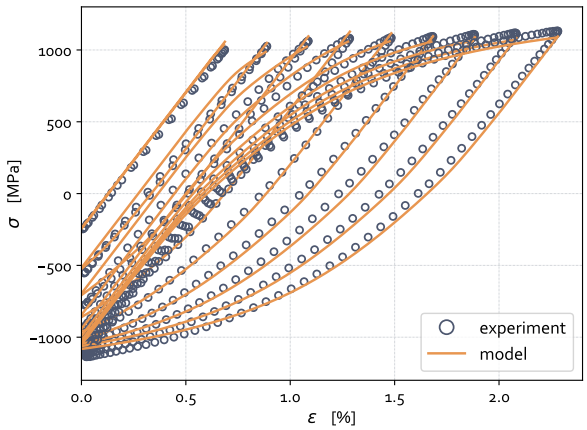

(b) Stabilized cycles at 550°C.

Figure 2.42: Comparison of model prediction on stabilized cycles - $\dot{\varepsilon} = 1.10^{-3}$ s^{-1} - $R = 0$ - 20 & 550°C.

2.5 Conclusion of the chapter

In the present chapter, the elastic-viscoplastic non-linear behavior of FG AD730™ has been studied. A proper material modeling with associated parameter calibration procedure have been discussed. The proposed material model seems to be adapted for several temperatures ranging from low to high temperatures up to 700°C, both for monotonic and cyclic loading conditions. Up to date, and to the best of the author's knowledge, no macroscopic material model for cyclic loading conditions was established for AD730™, hence making this point a significant contribution.

Thanks to the sect. 2.2 to sect. 2.4, the main conclusions concerning the cyclic behavior of AD730™ are summarized below. AD730™ has proven to exhibit cyclic softening together with strong kinematic hardening. The material is sensitive to the strain rate for the highest temperature of 700°C, while a slight negative SRS has been observed at 550°C. Over-stress relaxation has been evidenced for the two high temperatures. Static-recovery effects have been discussed but not modeled. No strain range dependence has been observed and the material behaves as a Masing material. No specific tension/compression asymmetry has been revealed. Finally, transient effects at low strain levels have been observed for the back-stress evolution with increasing plasticity.

Due to a restrictive number of testing specimens, the whole spectrum of loading schemes has not been covered. This is particularly true for stress-controlled tests highlighting ratcheting effect. Such aspect has not been studied and still needs to be for an accurate modeling of both strain- and stress-controlled loading conditions. Moreover, the introduction of thresholds in back-stress dynamic recovery term for mean stress relaxation control (or any modification of the kinematic hardening rule for that purpose) should also be considered, as discussed in [Chaboche et al., 2012]. Up to now, for the sake of simplicity and robustness of the current material model, no thresholds have been taken into account in back-stress evolution so as to limit the number of material model parameters. In addition, time-recovery effects should be studied in further details so that to well understand the contribution from static-recovery in the effective stress (R) as opposed to that of the back-stress (X).

For FE analyses, one rule prevails: the more complex the material model, the greater the CPU time consumption. Thus, limiting the number of embedded mechanisms (and consequently the number of material constants) is of primary importance. A "sufficiently adapted" material model capable of accurately transcribing the material response in FE calculations is therefore necessary. In the present Ph.D. project which aims to model the fatigue crack growth through a strong coupling between material behavior and damage mechanisms (through the so-called *local approach to fracture*), the proposed material model seems to be accurate enough. Moreover, numerical techniques associated with crack growth will increase the level of complexity, hence justifying the necessity to keep such a "standard" material model, at least for this preliminary study.

Résumé du chapitre en français

Dans ce chapitre, une brève étude bibliographique sur la modélisation du comportement cyclique et monotone des alliages métalliques a été introduite. Le lien entre les mécanismes de plasticité, la microstructure et la nature des contraintes au sein de la matière ont également été rappelés en vue d'un processus d'analyse de la réponse matériau.
S'en est suivie une étude détaillée du comportement du superalliage base Nickel AD730™, support de la présente étude. Le procédé d'élaboration du matériau ainsi que les traitements thermiques appliqués ont été décrits. Ensuite, la procédure de caractérisation du comportement cyclique et monotone à basse et hautes températures a été décrite. Les éprouvettes de caractérisation ainsi que les moyens d'essais ont été présentés, de même que les différents essais réalisés. Ces essais, de nature incrémentale, ont permis de mettre en évidence les phénomènes prédominants dans la réponse cyclique et monotone du matériau lorsqu'il est sollicité. Ainsi, les mécanismes d'écrouissages, de viscosité et les possibles effets particuliers liés aux trajets de chargement cycliques dans la réponse du matériau ont été mis en exergue grâce à des schémas de chargement bien définis.
Il a ensuite été montré que l'AD730™ présente un durcissement associé à des écrouissages mixtes, et ce à 20, 550, 650 et 700°C. Un fort adoucissement cyclique a été mis en évidence, par la méthode de partition de la contrainte énoncée par Cottrell, via la diminution significative de la taille du domaine d'élasticité. Il a ensuite été montré que cet adoucissement est largement compensé par un fort effet Bauschinger (évolution de la limite élastique du matériau entre les charges et décharges successives et déplacement du centre du domaine de réversibilité mécanique). Le matériau a ensuite été testé à plusieurs vitesses de chargement et lors d'essais de relaxation de contrainte à basse et hautes températures de sorte à étudier les effets liés au temps dans la réponse du matériau. A température ambiante (*i.e.* 20°C), le matériau présente un comportement globalelement élasto-plastique, tandis qu'à 550, 650 et 700°C, celui-ci tend à devenir élasto-viscoplastique en raison d'effets de viscosité plus ou moins prononcés à mesure que la température augmente. La contrainte visqueuse présente une évolution fortement non-linéaire à mesure que la vitesse de déformation viscoplastique évolue. De plus, le matériau présente une sensibilité inverse à la vitesse de sollicitation à 550°C, tandis qu'à 700°C, la viscosité suit une évolution standard. Le matériau présente un comportement de type Masing, assurant alors l'absence d'effet mémoire de la déformation plastique sur le niveau d'adoucissement cyclique du matériau. De plus, un effet transitoire est apparu pour les premiers niveaux de chargement, établissant alors un couplage entre la forme des boucles d'hystérésis et le niveau de plasticité cumulée.
Une étape de modélisation du comportement a ensuite été effectuée suivant les principes de la viscoplasticité unifiée (une seule variable pour les déformations plastiques et celles liées au fluage). Ainsi, un formalisme comportant un double écrouissage isotrope non-linéaire, couplé à un écrouissage cinématique non-linéaire à 3 composantes permet de représenter fidèlement la mixité des écrouissages présents dans le matériau et la forme des boucles d'hystérésis. Un potentiel viscoplastique de type sinus hyperbolique permet de traduire les effets du temps à hautes températures, de sorte à inclure une contribution visqueuse dans la contrainte totale. Le modèle a été calibré suivant les résultats d'essais à l'aide d'une méthodologie spécifique. La réponse du modèle vis-à-vis des résultats expérimentaux a ensuite été validée sur des cas de chargement représentatifs.

3 Experimental study of the cyclic and monotonic cracking behavior of AD730™ at elevated temperatures

In the present chapter, the crack growth process in AD730™ is studied under various loading conditions. The chapter first starts with details associated with fatigue and dwell-fatigue crack propagation tests at low to elevated temperatures performed on SEN-T specimens. Dedicated specimen geometries as well with testing benches and crack growth monitoring techniques are discussed. Further VLCF tests are also conducted on flat specimens and analyzed in the second section. For each loading mode (pure fatigue, dwell-fatigue and VLCF), macroscopic data are first compared. Additional observations at both mesoscopic and microscopic scales allow the main crack growth driving mechanisms to be evidenced. Crack propagation peculiarities and underlying mechanisms are finally discussed.

Contents

The non-linear cyclic elastic-viscoplastic behavior of AD730™ at target temperatures of 20, 550 and 700°C has been studied in the last Chap. 2. Then, associated constitutive equations have been proposed and calibrated consistently with experimental data.
Fatigue crack growth (FCG) as well as dwell-fatigue crack growth (DFCG) behavior of this Ni-superalloy still remains to be studied. To this end, the present chapter is devoted to some experimental work dedicated to the analysis of fatigue crack propagation under complex loading conditions from low to high temperatures, under fatigue and creep-fatigue conditions.

The literature review given in sect. 1.3 has reported that the FCG behavior of Ni-based superalloys is sensitive to both extrinsic, *e.g.* loading frequency, dwell-times, stress ratio, temperature and operating environment; and intrinsic factors, *e.g.* grain/precipitates size or aging [Chang and Liu, 2001]. The present chapter hence focuses on the extrinsic effects of temperature, stress ratio and holding periods on the FCG behavior of AD730™. As a complement, quasi-static VLCF tensile tests will also be studied with dedicated specimen geometries so that for the main failure mechanisms as well as the crack propagation regimes to be exhibited.

The first sect. 3.1 is devoted to the cyclic crack growth tests performed during the present Ph.D. project for the three target temperatures already considered in the Chap. 2, namely 20, 550 and 700°C. Several loading conditions are studied to emphasize the effect of both loading ratio and signal on the Crack Growth Rates (CGR). Moreover, for creep-fatigue problems, different dwell periods are studied to quantify the effect of the holding period on the global FCG rates. Macroscopic results will be supplemented with mesoscopic considerations as well with microstructural observations on fracture surfaces in order to suggest scenarios explaining the cracking process. Once LCF loading conditions are detailed, Very Low-Cycle Fatigue (VLCF) tests are also studied in sect. 3.2. These fatigue, dwell-fatigue and VLCF crack growth tests consist in a preliminary work for the understanding of driving-mechanisms responsible for crack propagation as well as *flat-to-slant* transition due to the mixity of the cracking modes. Hence, throughout the sect. 3.1 & sect. 3.2 dedicated to crack propagation, the damage mechanisms will be identified prior to the modeling process consisting in a coupling between damage and behavior in the context of **the local approach to fracture** (see Chap. 4 later on).

3.1 Crack growth analysis in AD730™ under cyclic loading conditions

Isothermal cyclic crack propagation tests have been carried out during the Ph.D. project in order to highlight the main cracking mechanisms in the fine-grained (FG) microstructure of AD730™ at several temperatures. The global cyclic crack growth curves da/dN *vs.* ΔK for the FG AD730™ are analyzed and discussed. When possible qualitative and quantitative comparisons with the coarse-grained (CG) counterpart will be discussed. Fractographic analyses will also be detailed so as to emphasize on the main crack growth mechanisms and the progressive changes in fracture modes. This way, the so-called *flat-to-slant transition*, described in sub-sect. 1.3.3, will thus be discussed.

3.1.1 Experimental samples and procedures

3.1.1.1 Testing material and selected geometries

As a reminder, the chemical composition of the as-received material prior to any heat treatments is given in Tab. 2.1 from sub-sect. 2.1.2.2, together with applied heat treatments detailed in sub-sect. 2.1.2.3. Single Edge Notched Tension (SEN-T) fatigue crack growth testing specimens have been considered in the present work, see Fig. 3.1. Two different geometries have been used:

- 4 mm-thick *short* specimens for high temperature testing under furnace, see Fig. 3.1a;
- 4 mm-thick *long* specimens for high temperature testing with inducting coils, see Fig. 3.1b.

The detailed sketches of these specimens are given in the appendices, see Chap. B page 270-271, together with the sampling plans, Fig. A.1, see Chap. A page 267.

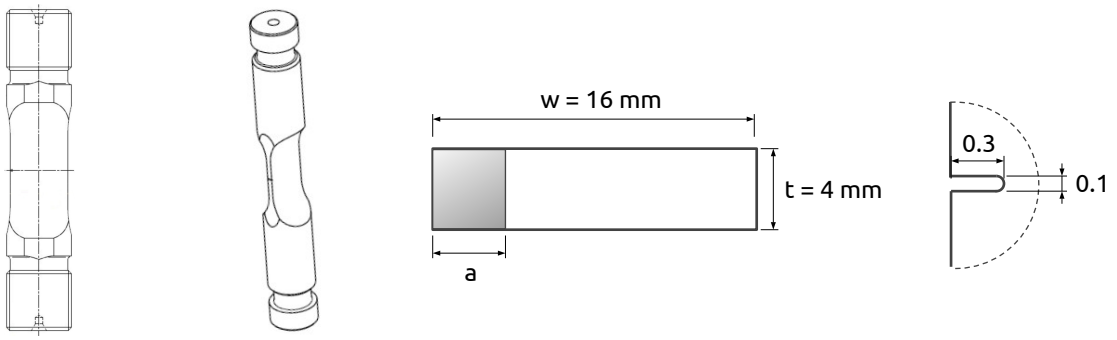

(a) Short SEN-T. (b) Long SEN-T. (c) Cross-sectional view. (d) Notch details.

Figure 3.1: SEN-T specimens for fatigue and dwell-fatigue crack growth testing.

Chosen SEN-T specimens have a rectangular cross-section of 16 mm width (w) and 4 mm thickness (t), see Fig. 3.1c. The useful length is of 15 mm. The SEN-T geometry is suited for both positive/negative load ratio R as well as the positioning of an extensometer close to the notch for crack opening displacement analysis. It also ensures a preferential crack initiation and subsequent propagation from the notch as long as this one ranges from 0.15 to 0.5 mm [Bouvard, 2006]. Thus, a 0.3 mm notch was machined in one edge of the specimens, at mid-height and along the whole thickness, hence allowing for a through-thickness propagation of the crack in a supposed straight manner, see Fig. 3.1d. Moreover, this geometry is particularly suitable for long crack propagation analysis (up to a few millimeters), hence covering a wide range of Stress Intensity Factors (SIF) ΔK. The post-mortem observations and the numerical reconstruction of the fracture surface are also facilitated thanks to this simple geometry.

3.1.1.2 Experimental facilities

Cyclic crack growth tests were performed within the ONERA facilities. To this end, two specific testing benches have been used, according to the considered loading scheme and corresponding heating device. In addition, the necessity to settle specific instrumentation such as cameras or

long-range microscope for Digital Image Correlation (DIC) allowing for the track of the crack growth is also considered.

- Tests carried out with an induction-heating system were performed on a uniaxial servo-hydraulic *Schenck* fatigue testing machine. Its load cell has a static capacity of 40 kN and the machine is equipped with force and displacement sensors. The use of an inductor was motivated by the need to have a visual accessibility to the surface of the specimen in order to use optical methods. This experimental set-up was dedicated to **pure fatigue** testing, Fig. 3.2.

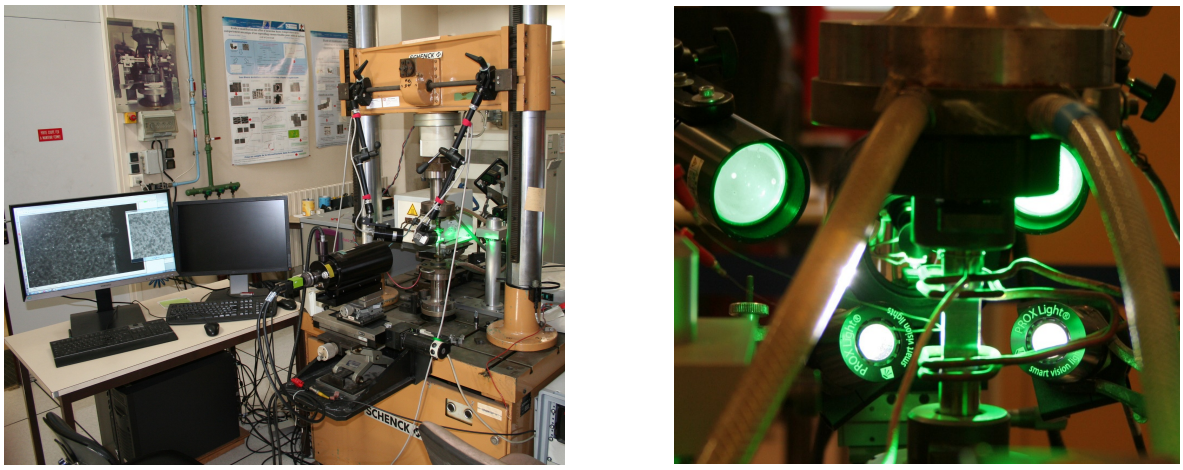

(a) Overall view of the 40 kN *Schenck* testing machine with dedicated tracking equipment.

(b) Close-up view on the experimental set-up with the testing specimen, the induction coils and green light projectors.

Figure 3.2: View of the pure fatigue testing bench with a *Schenck* uniaxial testing machine and additional instrumentation.

- Those carried out under a *MTS 653* clamshell resistive furnace (whose specimen ID involves an "F") were hence deprived of optical tools due to enclosed testing conditions. Tests were performed on a multiaxial servo-hydraulic *Schenck* fatigue testing machine with a load cell capacity of ± 63 kN. In the present case, only uniaxial tensile/compression tests were considered. Force and displacement sensors ensure the monitoring of the test driving parameter. Such an experimental set-up was developed for **creep-fatigue** testing, Fig. 3.3.

For the two considered testing machines and all the tests, the cylinder stroke was force-controlled. For each control mode, a *Proportional Integral Derivative* (PID) controller was associated with force sensor (no strain gauges were used during the experiments).
All along the crack growth procedure, data acquisition was ensured by a continuous or a cycle-dependent (at every peaks) recording. Finally, a security system, based on a setting relative to a threshold in force or displacement, was used to stop the machine operation at specimen failure.

Tests were conducted either at room temperature (RT) or at elevated temperatures of 550 and 700°C. For the two high temperatures, the regulation of the testing temperature was ensured by a specific control procedure, depending whether the heat source was provided by furnace or induction-heating system. Note that such testing benches were almost similar to those used in the

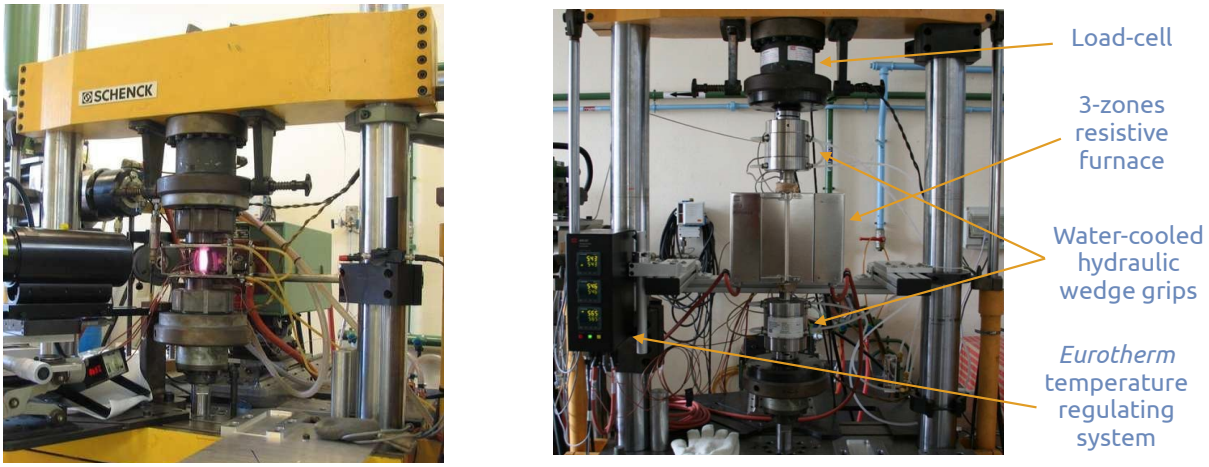

(a) Overall view of the 63 kN *Schenck* testing machine (from [Kaminski, 2007]).

(b) Close-up view on the 63 kN *Schenck* testing machine equipped with a 3-zones resistive furnace.

Figure 3.3: View of the dwell-fatigue testing bench with a *Schenck* tension/torsion testing machine and additional instrumentation.

preliminary work of [Fessler, 2017] dedicated to fatigue and creep-fatigue crack growth analysis in DA Inconel 718. Due to confidentiality aspects of the latter study, choice has been made to only recall in the present work the main key points of the testing procedures.

3.1.1.3 Overall sequences of a fatigue crack growth test

Fatigue crack growth tests were not designed to evaluate the lifetime up to crack initiation. Thus, in order to avoid the "initiation period" of the material up to the onset of a short crack, the SEN-T test-pieces were all pre-cracked prior to conducting crack propagation tests. Such tests and associated procedures are described in Fig. 3.4 following the guidelines given in [ASTM, 2015], while details for the crack growth step are given below.

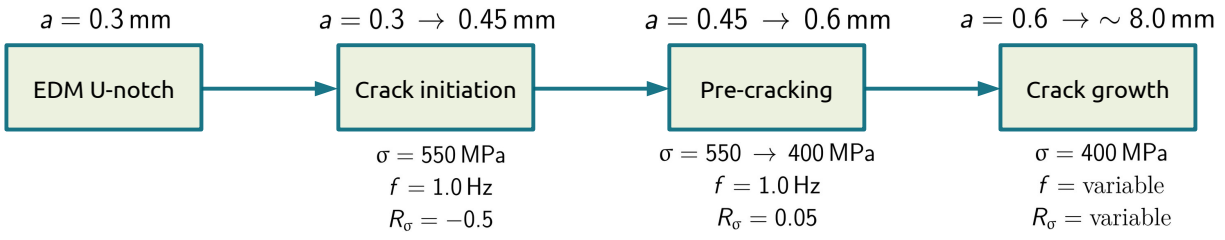

Figure 3.4: Overall sequences of a fatigue crack growth test on laboratory SEN-T specimen.

The 0.6 mm-long pre-crack has been estimated so as to ensure a crack propagation process out of the generated plastic zone (during crack initiation and pre-cracking), and far from the zone affected by the machined U-notch. This way, the effects of pre-crack load history or change in crack front shape on the subsequent crack growth rate data are normally eliminated [ASTM, 2015]. The crack is also expected to be sharp with an intrinsic front as straight as possible.

After these preliminary steps, the crack propagation test itself can be conducted. Choice has been made in this study to focus on constant-ΔF test control. Consequently, the increase in ΔK results from the crack growth and causes the progressive acceleration of the crack.
In the following, different loading wave-forms will be considered under **isothermal conditions**:

- pure fatigue crack growth tests under sinusoidal signal with a 1 Hz frequency, Fig. 3.5a;
- dwell-fatigue crack growth tests for creep-fatigue interaction studying under trapezoidal waveform with holding-times of 300 or 3 000 s, Fig. 3.5b.

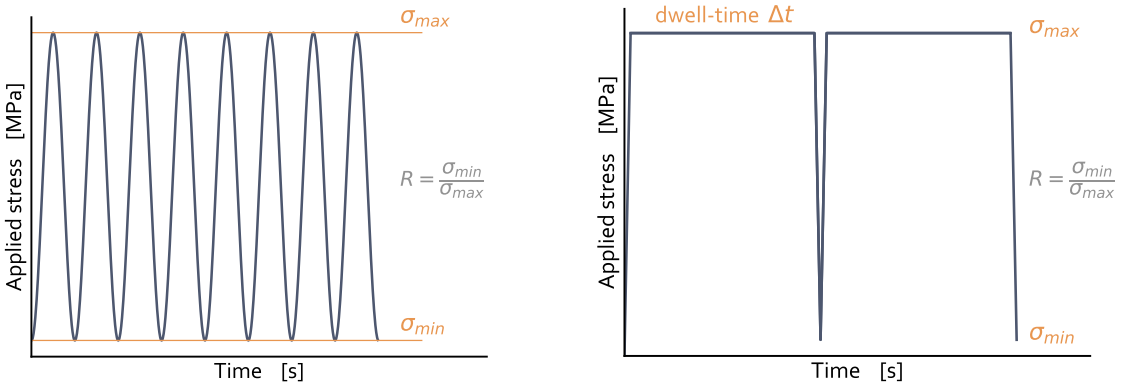

(a) Sinusoidal loading for fatigue testing.

(b) Trapezoidal loading for dwell-fatigue testing.

Figure 3.5: Schematic view of the loading signals for fatigue and dwell-fatigue crack growth testing.

In all the cases, the nominal applied stress is of 400 MPa during the peak tensile phase, with a load ratio of $R = 0.05$, $R = 0.5$ or $R = -1$. These loading parameters may evolve depending on each single test, see Tab. 3.1.

N°	Test type	Waveform	R_σ	σ_{max}	Δt	Dwell	T	Spec. ID
1	Fatigue	Sinus 1Hz	0.05	400 MPa	0 s		550°C	S4-2
2	Creep-fatigue	10-300-10 s	0.05	440 MPa	300 s	+	550°C	S4-F1
3	Fatigue	Sinus 1Hz	0.05	400 MPa	0 s		700°C	S4-F2
4	Creep-fatigue	10-300-10 s	0.05	400 MPa	300 s	+	700°C	S4-F3
5	Fatigue	Sinus 1Hz	0.05	400 MPa	0 s		20°C	S4-7
6	Creep-fatigue	10-3000-10 s	0.05	400 MPa	3000 s	+	700°C	S4-F4
7	Creep-fatigue	10-300-10 s	-1	400 MPa	300 s	−	700°C	S4-F6
8	Creep-fatigue	10-300-10 s	-1	400 MPa	300 s	+/−	700°C	S4-F7
9	Creep-fatigue	10-300-10 s	-1	400 MPa	300 s	+	700°C	S4-F8
10	Fatigue	Sinus 1Hz	0.5	400 MPa	0 s		20°C	S4-9

Table 3.1: Testing conditions for cyclic crack growth tests performed on 10 specimens made of fine-grained AD730™ for the present study. A "+" (respectively a "−") in the dwell type means a hold-time in tensile (respectively compressive) loading.

A synthesis of the considered loading schemes for fatigue and dwell-fatigue crack growth analysis for the present Ph.D. project is given in Tab. 3.1. Note that test numbering corresponds to the **chronological sequence** of tests.

According to the initial crack length of 0.6 mm (0.3 mm-notch obtained *via* EDM + 0.3 mm pre-crack) and owing to the fact that the stress amplitude is assumed to be equal to 190 MPa with $R = 0.05$ ($\sigma_{max} = 400$ MPa), then the initial ΔK equals 18.6 MPa.m$^{1/2}$. Such a value is close to *stage I* fatigue crack propagation. It is to be noticed that those points at low ΔK should be carefully handled due to the fact that they are obtained after the pre-cracking phase for which high plasticity is assumed to have developed at the crack-tip. Although the pre-cracking phase was carried out according to some guidelines given in [ASTM, 2015], a residual cyclic plastic zone resulting from previous higher-level steps may persist and disrupt the subsequent crack propagation process. The macroscopic results should help the understanding on this point.
Finally, the crack propagation phase has been carried out until the crack reaches a 8 mm-length. Such a choice allows, for the considered loading stress levels, the material to remain in an overall elastic state, thus ensuring small scale yielding (SSY) conditions.

3.1.1.4 Crack growth monitoring

Direct Current Potential Drop technique:

There are several Non-Destructive Testing (NDT) methods to evaluate crack length. An overall review of most of them can be found in [Si et al., 2020]. The *Direct Current Potential Drop* (DCPD) method is one of the most reliable and convenient techniques employed for measuring the crack extension during laboratory testing [Tarnowski et al., 2018a]. The DCPD technique has been widely used for the FCG analysis in several Ni-based superalloys due to the good conductivity of such materials, see *e.g.* [Lee et al., 2008] for Haynes 230 and Hastelloy X, [Doremus, 2014] and [Fessler, 2017] for DA Inconel 718, or [Gourdin, 2015] for René 65, hence supporting its usage in the present study. The general concept of the method is depicted in Fig. 3.6. Besides, the crack length for the considered SEN-T specimen has been estimated according to the eq. (3.1) first suggested by [Johnson, 1965]:

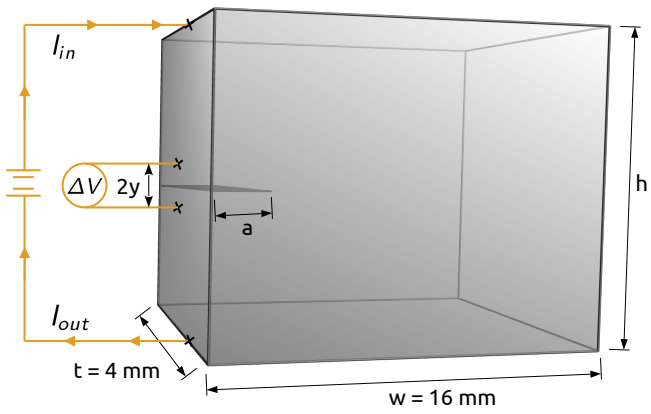

Figure 3.6: Schematic view of the DCPD crack growth monitoring technique on a SEN-T specimen.

$$a = \frac{2w}{\pi} \cos^{-1} \left[\frac{\cosh\left(\pi y / 2w\right)}{\cosh\left\{ \frac{V}{V_0} \cosh^{-1}\left(\frac{\cosh(\pi y/2w)}{\cos(\pi a_0/2w)} \right) \right\}} \right] \tag{3.1}$$

where a and a_0 are the instantaneous and initial crack lengths, respectively, and V and V_0 the corresponding actual and initial values of the PD voltage. Here, y is one half of the gauge span for V and w is the specimen width. One of the main advantages of the eq. (3.1) is its general form which means that it can be directly applied to any initial crack length [Tarnowski et al., 2018a].

It should be noted that prior to the use of the DCPD method, it is necessary to establish the relation between the potential drop ΔV and the crack length a by means of a calibration curve [ASTM, 2015], [Fessler, 2017]. Obviously, the relation should take into account the specimen geometry and the potential probes position, Fig. 3.7a.

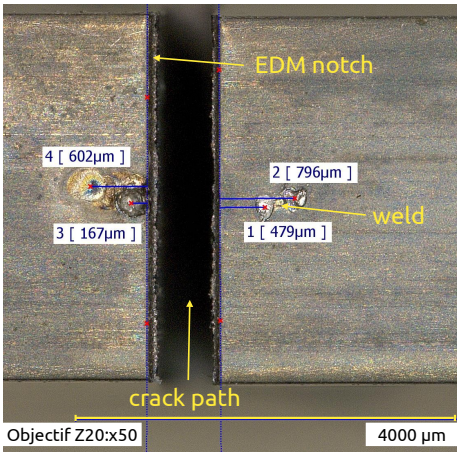

(a) Estimation of the distance between the two DCPD wire probes (spec. S4-F6).

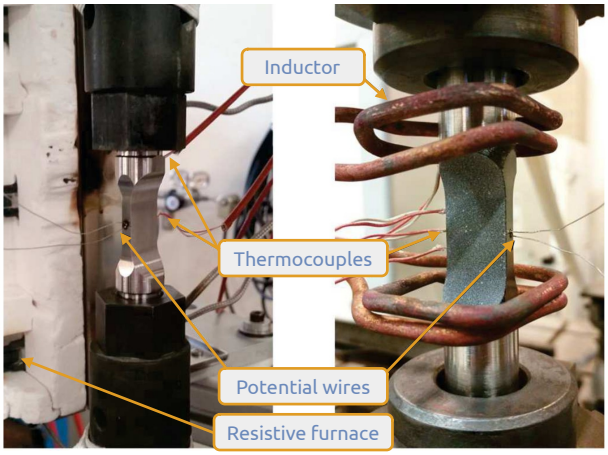

(b) Overall view of both DCPD and temperature monitoring probes (adapted from [Fessler, 2017]).

Figure 3.7: Direct Current Potential Drop setup with corresponding wires for crack growth monitoring.

Heat tints on fracture surface:

In addition to DCPD crack growth estimation, some heat tinting steps were applied so as to get another crack length estimation. The basic principle of such a marking technique relies on the periodical interruption of the mechanical test at a sufficiently high stress level (but not too high) to ensure the crack to be opened (say $\sim 5\%$ of the yield strength $R_{p_{0.2}}$) and to keep the load constant during a dwell of 1 h, see Fig. 3.8. Due to the high temperature conditions, an oxide scale is formed, thus evidencing the crack front. Generally for Ni-based superalloys, optical microscope analyses are sufficient to distinguish the heat tints thanks to a significant change in colors from one tint to another [Doremus, 2014], [Fessler, 2017]. This point is particularly useful: apart from the *a posteriori* crack length estimation, it also enables the possibility to evaluate the crack front morphology during *post-mortem* fracture surface analyses. This aspect will be discussed in the forthcoming sub-sect. 3.1.2.3.

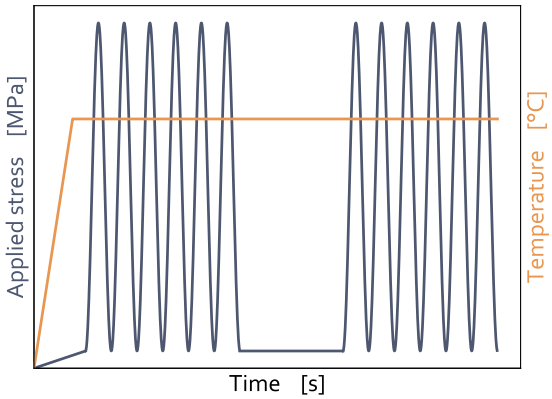

Figure 3.8: Temperature & load signals for heat tinting process upon testing.

Nominal Stress Intensity Factors evaluation:

The knowledge of the instantaneous crack length a thanks to the calibrated DCPD technique allows for the estimation of the Stress Intensity Factors (SIF) which are necessary to study the FCG capability of the material. For the SEN-T specimen and corresponding dimensions, see Fig. 3.1, the SIF range, denoted as ΔK, can be deduced from analytical solutions derived in previous works by [Gross et al., 1964] (thanks to a least square fitting), also referred to as the Murakami's formula [Murakami and Aoki, 1987]:

$$\Delta K = \frac{F_{max} - F_{min}}{t.w} \sqrt{\pi a}\, f(\alpha) = (1 - R)\, \sigma_\infty \sqrt{\pi a}\, f(\alpha) \qquad \text{with} \qquad \alpha = a/w \tag{3.2}$$

where a is the actual crack length, σ_∞ is the far-field applied stress, R the load ratio and w the width of the specimen. In eq. (3.2), $f(\alpha)$ is a geometrical function (or *compliance function*) which accounts for differing component geometries and shapes through the ratio between the crack length and the width. It should be noted that for SEN-T specimens, such a formula, eq. (3.2), remains valid as long as the crack is rectilinear and the material is under plane strain conditions. Hence, the applied force (or stress) should be uniform without any bending moment.

The geometrical function $f(\alpha)$ of empirical-type is given in the following relation:

$$f(\alpha) = 1.122 - 0.231\alpha + 10.550\alpha^2 - 21.710\alpha^3 + 30.382\alpha^4 \tag{3.3}$$

which is the one used in AFNOR A03-404 [AFNOR, 1991]. It remains valid as long as $\alpha = a/w < 0.6$, that is a crack length of $\sim$9 - 10 mm. The accuracy of the geometrical function eq. (3.3) is close to 0.5 - 1% which is considered satisfactory.

Some Finite Element (FE) calculations were performed in previous studies using the *Z-cracks* tools from the FE analysis suite Z-set [Chiaruttini et al., 2011], [Fessler et al., 2017]. It was proven that for pure *mode I* fatigue crack growth in 4 mm-width SEN-T specimens, corresponding SIF were estimated with a good accuracy by the Murakami's formula eq. (3.3) together with the Johnson equation eq. (3.1).

Crack growth rates estimation:

The evaluation of crack growth rate may be performed according to the secant method or the increment polynomial method [ASTM, 2015]. In the present study, we used the secant method which simply evolves calculating the slope of the straight line connecting two adjacent data points on the $a = f(N)$ curve. This finally yields:

$$\left(\frac{\mathrm{d}a}{\mathrm{d}N}\right)_i = \left(\frac{\Delta a}{\Delta N}\right)_i = \frac{a_{i+1} - a_i}{N_{i+1} - N_i} \tag{3.4}$$

where N_i is the number of cycles associated with the identical crack length a_i.
Due to the fact that the computed CGR $\mathrm{d}a/\mathrm{d}N$ is an average rate over the $(a_{i+1} - a_i)$ increment, the average crack length eq. (3.5) is normally used to calculate ΔK:

$$a_{mean} = \frac{a_{i+1} + a_i}{2} \tag{3.5}$$

To ensure accurate values, estimated crack lengths were checked and re-calibrated, post-test, using beachmarks (when available) formed on the fracture surface.

3.1.2 Fatigue and dwell-fatigue crack growth tests

Once the whole testing procedures have been detailed, this section aims at exposing the main results of the fatigue crack growth (FCG) and dwell-fatigue crack growth (DFCG) tests carried out during the Ph.D. project. We first discuss the macroscopic results in terms of crack lengths and cyclic crack growth rates for the 3 target temperatures of 20, 550 and 700°C. Some possible loading mode effects are also discussed. Then, a mesoscopic scale is introduced in order to discuss the fracture surface analysis obtained from optical microscopy prior to the microscopic observations of the fracture surfaces. This last point should enable evidencing the main crack driving forces and fracture mechanisms in the material under fatigue and dwell-fatigue conditions.

It is important to recall that all the tests have been performed in laboratory air conditions. Specimen surfaces as well as crack lips were hence exposed to high-temperature oxidation processes. For fatigue loading conditions, the load ratio is of $R = 0.05$ except for one test at 20°C also carried out with $R = 0.5$, see Tab. 3.1. Load ratios are in this case positive, hence limiting the crack closure effect. However, for the lowest load ratio, the fracture surface roughness may induce a slight crack closure effect. Due to this aspect, an electric contact may be created between the cracked surfaces, thus disturbing the potential acquisition upon testing.

Finally, due to the absence of experimental measurements of the crack opening and closure (*e.g.* through the CTOD and *via* a dedicated extensometer), only the change in the range of SIF $\Delta K = K_{max} - K_{min}$ will be considered, not the effective one $\Delta K_{eff} = K_{max} - K_{op}$. When necessary, a comparison with K_{max} may also be discussed.

3.1.2.1 Macroscopic results

Fatigue crack growth tests

In Fig. 3.9, the whole FCG results are reported. In this plot, only the propagation phase is reported. Corresponding cycles until crack initiation and for the pre-cracking step are reported in Tab. 3.2, together with the corresponding crack lengths.

In Fig. 3.9, the temperature effect is clearly visible. Indeed, the lower the temperature, the longer the fatigue lifetime (see Tab. 3.2). One can also notice higher FCG rates at 700°C for a given SIF range ΔK (compared to 20 and 550°C) but a slower slope to this curve, hence evidencing a slight decrease in fatigue crack growth rate (FCGR) with increasing ΔK.

Spec.	T [°C]	R_σ [-]	N_{ini} [cycles]	a_{ini} [mm]	N_{pre} [cycles]	a_{pre} [mm]	N_{cra} [cycles]	a_{tot} [mm]	N_{tot} [cycles]
S4-7	20	0.05	5 267	0.449	5 045	0.599	39 818	12.675	50 130
S4-9	20	0.5	14 782	0.449	4 410	0.599	163 795	9.830	182 987
S4-2	550	0.05	×	0.45	2 939	0.6	10 494	7.852	13 433
S4-F2	700	0.05	×	0.45	2 632	0.6	3 299	9.683	5 931

Table 3.2: Synthesis of the fatigue crack growth tests performed on 4 specimens made of fine-grained AD730™ for the present study. Cycle sinus 1 Hz with $\sigma = 400$ MPa.

The difference between FCGR at 550°C and those at 700°C mainly comes from a decrease in material mechanical properties with increasing temperature, especially around 700°C for AD730™ (*cf.* Chap. 2). Moreover, since the tests were performed in a laboratory environment, oxidation can occur around the crack-tip with an effect as pronounced as the temperature is high. Microscopic observations of the fracture surfaces presented in sub-sect. 3.1.2.4 will try to emphasize on this point. In Fig. 3.9, one can also notice the occurrence of a near-threshold regime at 20 and 550°C as a small deviation from the linear trend is visible for low ΔK values. Moreover, the slope of each crack growth curve seems to be close, especially at 20 and 550°C.

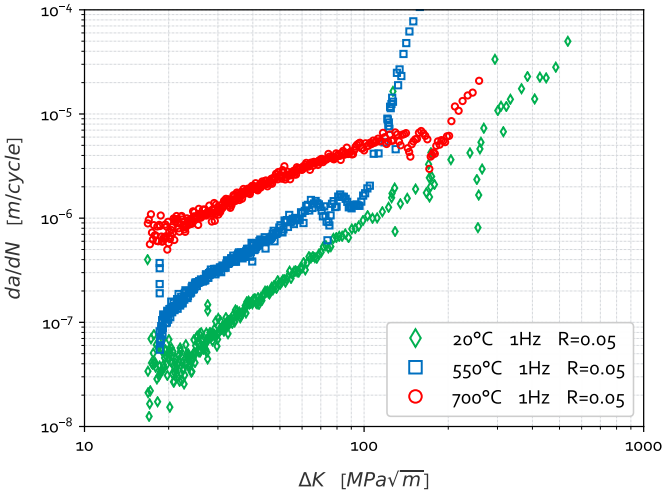

Figure 3.9: Fatigue crack growth results on SEN-T specimens at 20, 550 and 700°C under $\sigma = 400$ MPa, $f = 1$ Hz and varying load ratio R.

As a preliminary work, only few pure fatigue tests have been performed during this project. Some additional tests conducted with varying loading frequency should be of great interest so as to observe any frequency effect on the FCG rates within FG AD730™ under pure fatigue cycling. Such an aspect remains an outlook for incoming studies.

Dwell-fatigue crack growth tests

In this section, dwell-fatigue crack growth tests at elevated temperatures (550 & 700°C) are exposed. These tests have also been conducted under air, hence favoring the high-temperature oxidation process. The load ratio is variable, changing from positive $R = 0.05$ to pure symmetrical $R = -1$ conditions, depending on the considered test, see Tab. 3.1. Cyclic-dwell tests are characterized by a trapezoidal waveform, see Fig. 3.5b, with loading/unloading ramps of 10 s and an hold-time HT generally of 300 second except for one test for which it is amplified by a factor 10 (see spec. S4-F4 detailed in Tab. 3.1). The nominal loading cycle is then identified as 10-HT-10 s. All tests are conducted under force control with a maximum stress level of $\sigma = 400$ MPa.

Fig. 3.10 shows the results of all the dwell-fatigue crack growth tests conducted during the present study on 4 mm-width SEN-T specimens. To help the comparisons, similar tests conducted under pure fatigue loading conditions (sinus 1 Hz) are also reported. They correspond to the limiting case of null hold-time cycles and reflect the cycle-dependent aspect of the crack propagation phase.

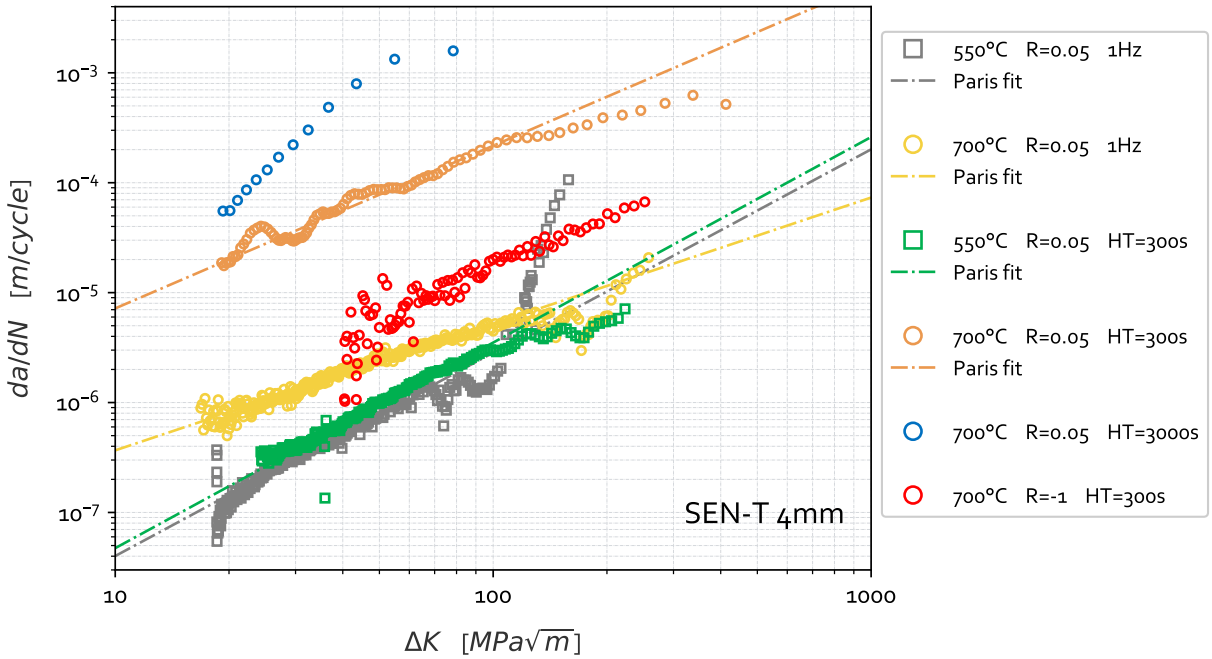

Figure 3.10: Overall view of the dwell-fatigue crack propagation tests on FG AD730™ under laboratory environmental conditions.

As it can be seen in Fig. 3.10, there is no great influence of the holding period on the FCG rates at 550°C. Moreover, the slope of the two corresponding curves in the Paris' regime is approximately identical. The slight increase in FCG rate is hence related to time-related mechanisms occurring during the dwell periods. When comparing the same FCG curves at 700°C, one can see that the introduction of a dwell period within the loading cycle has a great influence on the FCG rates. An increase, greater than one order of magnitude, is estimated between pure fatigue and dwell-fatigue loading conditions at 700°C. Here again, the slopes of the Paris' equation fits for both curves are assumed to be close to each others. The acceleration of the crack propagation may thus be attributed to time-assisted effects such as creep and oxidation.
It should be noted that such statements are made for the same load ratio of $R = 0.05$. Further experiments would be needed to confirm such tendencies with a reasonable repeatability.

When only looking at the dwell-fatigue crack growth tests, one can see the highly detrimental effect of temperature on FCG, Fig. 3.11. The dwell-fatigue lifetime of two specimens subjected to similar loading conditions, excepted the temperature change, are compared in Fig. 3.11a, whereas the effect of dwell-time duration at 700°C is reported in Fig. 3.11b. As expected, higher temperatures and/or longer dwell-times in tensile loading induce reduced fatigue lifetimes, see Tab. 3.3.

Moreover, one can notice in Fig. 3.11b a noticeable change in slope for the two $\mathrm{d}a/\mathrm{d}N$ curves in the Paris' regime. The greater the ΔK, the higher the difference in terms of crack growth rates.

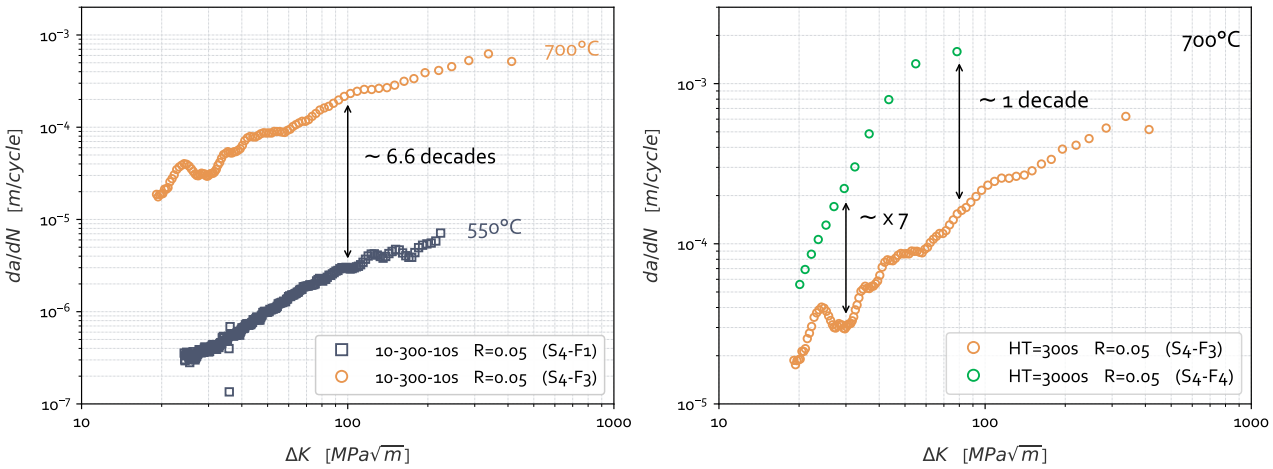

(a) Temperature effect on fatigue crack growth. (b) Dwell-time effect on fatigue crack growth.

Figure 3.11: Temperature and dwell-time effects on DFCG in SEN-T specimens at 550 & 700°C under $\sigma = 400\,\text{MPa}$, $R = 0.05$, trapezoidal waveforms with 10-HT-10 s (spec. S4-F1, S4-F3 & S4-F4).

According to the literature review detailed in sect. 1.3, time-related effects such as creep and oxidation are favored during longer dwell periods, which result in a decrease in fracture toughness of the material due to, *e.g.* cavity growth and grain boundary embrittlement. On the contrary, the slope of the curve between 550 and 700°C is almost similar, see Fig. 3.11a.

At last, the load ratio effect can be studied. In Fig. 3.12, the load ratio effect on the dwell-fatigue lifetime is studied. The curves plotted in Fig. 3.12 exhibit the decrease in DFCG rates with the change in load ratio from $R = 0.05$ to $R = -1$. A lower load ratio results in slower crack growth rates and subsequently in a greater lifetime. This may be attributed to more pronounced crack closure effects. The load ratio of $R = -1$ being negative, the material is subjected to compressive stresses which in turn make the crack to close.

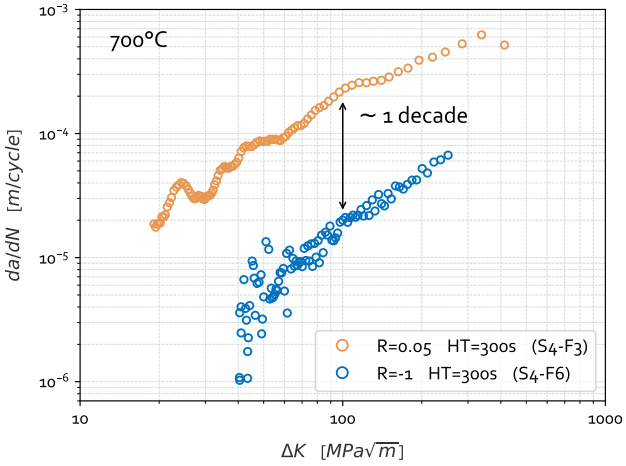

Figure 3.12: Load ratio effect on DFCG at 700°C under $\sigma = 400\,\text{MPa}$, trapezoidal waveforms with 10-300-10 s (spec. S4-F3 & S4-F6).

At elevated temperatures with loading cycles including dwell-periods, time-related effects have been proven to play a significant role in the increase in FCG rates in Ni-based superalloys [Fessler, 2017], [Mrozowski, 2020]. In the present case, time-assisted effects including grain boundaries oxidation along crack lips and around the crack-tip, together with creep processes through cavity growth, may be the major causes for the decrease in fracture toughness with the increase in load ratio. Consequently, the higher the loading ratio, the more open the crack during the dwell period and finally the greater the oxidation-assisted embrittlement of the grain boundary (GB) and the easier the creep processes. On the contrary,

a lower load ratio eases the closure of creep-induced cavities, hence lowering the FCG rates. In addition to these points, one can also note in Fig. 3.12 the increase in the crack growth threshold ΔK_{th} with the decrease of the load ratio from $R = 0.05$ to $R = -1$, everything else being equal. Such a result is consistent with the observations already reported in Ni-based superalloys [Soniak and Rémy, 1987], [Reed et al., 1993].
Finally, a synthesis of the quantitative results related to final crack lengths, corresponding number of cycles for crack initiation, pre-cracking as well as crack growth steps for dwell-fatigue crack growth tests are summarized in Tab. 3.3.

Spec.	T [°C]	R_σ [-]	HT [s]	N_{ini} [cycles]	a_{ini} [mm]	N_{pre} [cycles]	a_{pre} [mm]	N_{cra} [cycles]	a_{tot} [mm]	N_{tot} [cycles]
S4-F1	550	0.05	300	···	0.45	6 480	0.6	6 423	9.281	12 903
S4-F3	700	0.05	300	1 871	0.45	546	0.57	99	9.690	2 516
S4-F4	700	0.05	3 000	1 903	0.45	571	0.57	15	7.953	2 489
S4-F6	700	-1	300	1 330	0.45	348	0.57	429	6.619	2 107
S4-F7	700	-1	300	1 778	0.45	685	0.57	48	10.019	2 511
S4-F8	700	-1	300	1 732	0.45	462	0.57	82	9.690	2 276

Table 3.3: Synthesis of the dwell-fatigue crack growth tests performed on 6 specimens made of fine-grained AD730™ for the present study. Trapezoidal waveform with 10-HT-10 s under $\sigma = 400$ MPa.

3.1.2.2 On the partition between fatigue and creep contributions to DFCG

For dwell-fatigue loading conditions, a common approach consists in partitioning the fatigue and creep contributions of the crack extension. Indeed, as a first approximation, it is possible to assume that simultaneous action of cycle- and time-dependent effects can be represented by a direct summation [Leo Prakash et al., 2009]. Hence, the global crack propagation stage is split so that both the fatigue and creep contributions to be evidenced [Nikbin and Webster, 1984], [Carbou, 2000], [Fessler, 2017]. Generally, the fatigue contribution relates the crack extension during the loading/unloading phases (transients) of the representative cycle while the creep contribution is associated with the crack growth during dwell-periods. The sum of these two contributions gives the total FCG rate, see eq. (3.6):

$$\frac{da}{dN} = \left.\frac{da}{dN}\right|_{fatigue} + \left.\frac{da}{dN}\right|_{creep} = \left.\frac{da}{dN}\right|_{fatigue} + \int_{t}^{t+HT} \frac{da}{dt}\,dt \tag{3.6}$$

As a prospective issue, further detailed experimental investigations are required in order to explore the exact interaction between both cycle- and time-dependent mechanisms and hence identify suitable mathematical descriptions of the FCGR dependence on the relevant parameters [Lundström, 2014], [Storgärds, 2015]. Indeed, the partition given in eq. (3.6) enables the possibility to emphasize the possible interaction mechanisms (cross-effects) between both fatigue and creep processes. This latter point represents a major aspect to be included in a proper creep-fatigue crack growth modeling.

Such a method has already been used at the ONERA during the work of [Fessler, 2017]. More recently, [Mrozowski, 2020] applied a similar decomposition method when studying the dwell-fatigue crack growth in both coarse- and fine-grained AD730™ at 750°C. To be applied, the creep process first needs to be active during the dwell-period. Then, during the dwell-periods, since there might be only a slight potential drop (PD) which might induce a poor quality of the measurements, it is thus of primary importance to ensure the good insulation of the electrical set-up in order to rely on this decomposition scheme.

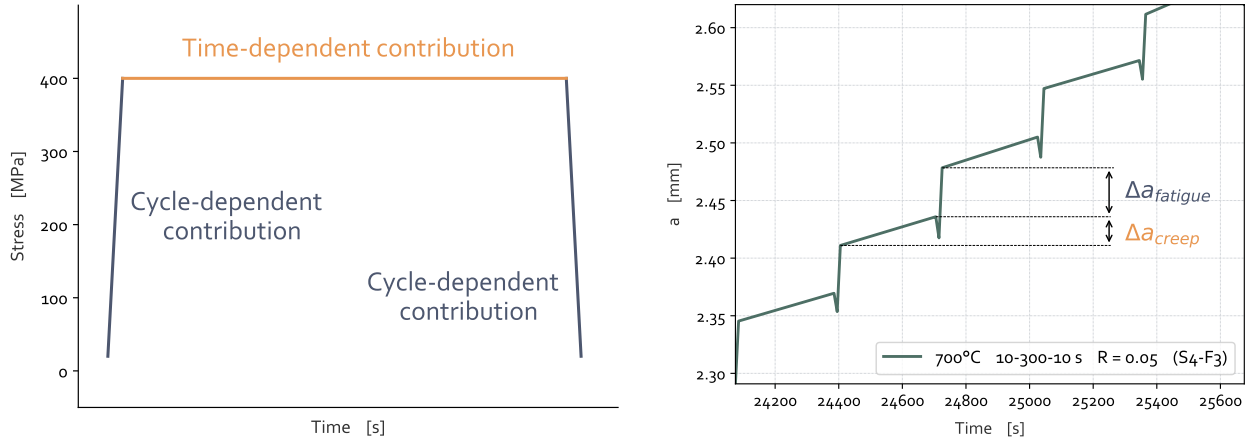

(a) Schematic representation of the cycle- and time-dependent contributions to crack extension.

(b) Partition between creep and fatigue contribution to the crack extension during 10-300-10 scyclic loading.

Figure 3.13: Partition between cycle- and time-dependent contributions to crack growth during dwell-fatigue crack propagation testing.

As a matter of example, the creep-fatigue crack growth partition during a 10-300-10 s loading cycle at 550°C is given in Fig. 3.13. The contribution to crack advance are reported in Fig. 3.13a. In Fig. 3.13b, one can remark a slight decrease of the crack length upon unloading/reloading. Such a decrease is directly associated with the unloading phase for which the PD is varying due to the contact of the crack lips. Moreover, it has been specified in sub-sect. 3.1.1.4 that the DCPD highly depends on the inter-probes distance. Choice has been made to acquire the PD only at the peaks of the loading signal to account for the elongation of the specimen upon loading and avoid any bias in the measurements (V_0 being also evaluated at a peak of the loading signal).

In Fig. 3.14a, the cycle- and time-dependent contributions of the crack growth are extracted and plotted at 550°C, with a loading signal of 10-300-10 s under $\sigma = 400$ MPa and $R = 0.05$. From the Fig. 3.14a, one can notice that the fatigue contribution is limited for low ΔK values, hence suggesting a far larger contribution from the time-dependent part of the loading cycle. As long as ΔK increases, the time-dependent contribution decreases and is counterbalanced by the cycle-dependent contribution. Such a trend of larger fatigue contribution on 10-300-10 s loading cycles at 550°C has already been observed in other studies conducted on DA Inconel 718 [Gustafsson et al., 2011b], [Fessler, 2017], but generally for the whole range of ΔK.

Similar plot at 700°C is reported in Fig. 3.14b. The trend is not the same and seems to be dependent on the dwell-time. For a dwell-period of HT = 300 s and from low to large values of ΔK, the fatigue contribution is greater than that of the dwell period. For high values of ΔK, the time-

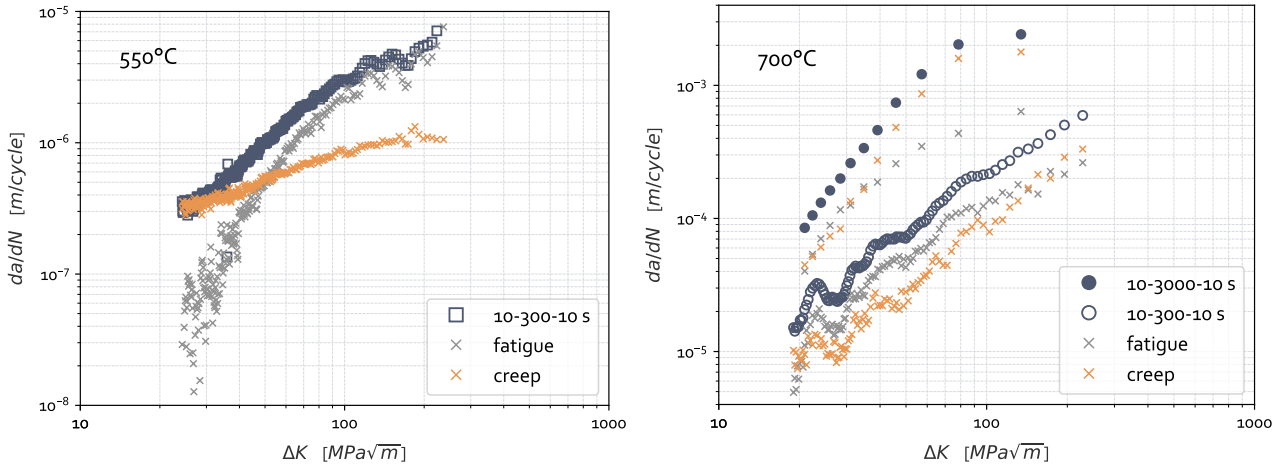

(a) Creep-fatigue partitioning at 550°C (10-300-10 s). (b) Creep-fatigue partitioning at 700°C (10-HT-10 s).

Figure 3.14: Cycle- and time-dependent contributions to DFCG rates in FG AD730™ at 550 and 700°C under a 10-HT-10 s waveform with $\sigma = 400$ MPa and $R = 0.05$ (spec. S4-F1, S4-F3 & S4-F4).

dependent contribution starts becoming predominant over the cycle-dependent one, Fig. 3.14b. This might be explained by a greater extent of oxidation over the crack-lips, since the crack is even more opened as it grows. A similar results has been reported by [Carbou, 2000] in N18 at 750°C for high values of ΔK. Nevertheless, for the vast majority of the test, a larger increment of the crack extension occurs upon unloading/reloading. Such a result is also clearly noticeable in Fig. 3.13b. On the contrary, for a longer dwell-time of HT = 3000 s, the time-dependent creep contribution is predominant, see Fig. 3.14b. Still for HT = 3000 s, as long as ΔK increases, the fatigue contribution decreases while the creep one grows, Fig. 3.14b.
For the FG microstructure of AD730™, it seems that there is a dwell duration threshold below which cycle-dependent contribution prevails, whereas for a sufficiently long duration (HT > 300 s) and high ΔK values, the time-dependent contribution becomes predominant, Fig. 3.14b. Complementary results on both coarse- and fine-grained AD730™ can be found in [Mrozowski, 2020].

It is finally interesting to compare the cycle-dependent (fatigue) contribution of the FCG rate during dwell-fatigue testing with that of the pure fatigue tests. This way, the (possible) creep-fatigue interaction can be highlighted. At 550°C, such a comparison is reported in Fig. 3.15a. At a given ΔK value in the linear Paris regime (since FCG is expected to be modeled in this Ph.D. project), say 80 MPa.$\sqrt{\text{m}}$, one can notice only a slight difference between each of the fatigue crack growth rates ($\sim$1.2e-6 *vs* 1.5e-6 m/cycle). Time-dependent effects (creep and oxidation processes) are hence not so pronounced and have only a slight impact on the FCG rate. Such a result is in agreement with the fact that the material behavior is not so affected by the temperature rise up to 550°C, as compared with its behavior at 20°C (*cf.* Chap. 2 on this point).
Moreover, **for the modeling prospect**, such an aspect allows for creep-fatigue interaction effects to be neglected at 550°C. In other words, the creep mechanisms are not supposed to have a significant effect on the fatigue ones, so any coupling terms can be neglected.

Increasing the temperature to 700°C has evidenced an increase in FCG rates, Fig. 3.10, probably in close relation with a change in the crack growth governing mechanisms. The comparison between pure fatigue contributions from dwell-fatigue loading schemes with that of a pure fatigue test is

given in Fig. 3.15b. Such a plot reveals a larger contribution of the cycle-dependent contribution to FCG rate if an hold period is applied. Indeed, at a given ΔK value (say 80 MPa.$\sqrt{m}$), the fatigue contribution changes from $\sim$3.7e-6 m/cycle in pure fatigue to 1.1e-4 m/cycle in dwell-fatigue loading. Thus, successive holding periods have had a significant effect on the loading/unloading contribution to crack advance. Moreover, temperature- and time-related effects were reported to be more noticeable on the material behavior at 700°C (*cf.* Chap. 2). It seems hence reasonable to argue that introducing holding-times over a sinusoidal loading scheme results in an increase in the cycle-dependent contribution to crack growth rate.

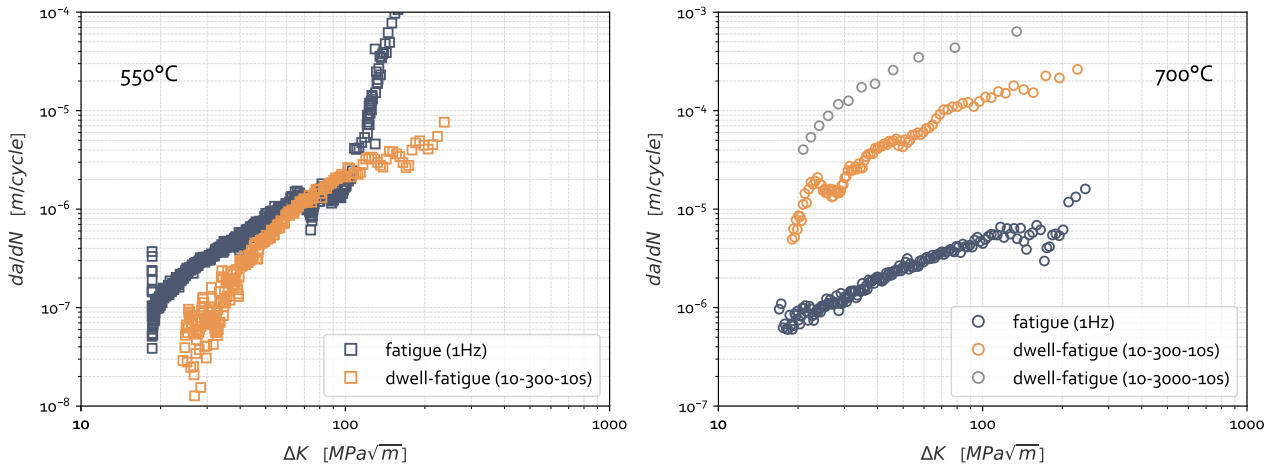

(a) Fatigue contributions to DFCG at 550°C. (b) Fatigue contributions to DFCG at 700°C.

Figure 3.15: Comparison of the cycle-dependent contributions to DFCG rates in FG AD730™ at 550 & 700°C under a 10-HT-10 s waveform with $\sigma = 400$ MPa and $R = 0.05$.

For tests performed at 700°C, it seems reasonable to consider the probable presence of a *damaged zone* ahead of the crack-tip associated with both creep and oxidation damaging mechanisms, as already reported in the work of [Gustafsson et al., 2011a], [Storgärds, 2015], [Fessler, 2017], [Mrozowski, 2020] on Ni-based superalloys. Such a damaged zone created upon dwell-holding results in the embrittlement of the grain boundary (GB) in the vicinity of the crack-tip, hence lowering the fracture toughness. Thus, there is a unilateral interaction process due to creep mechanisms over the fatigue contribution upon dwell-fatigue testing. As evidenced earlier in Fig. 3.14b, the higher the temperature and the longer the holding period, the larger the time-dependent contribution. In addition, the comparison between the 300 & 3000 s holding periods in Fig. 3.15b reveals an increase of the fatigue contribution from $\sim$1.1e-4 to 4.4e-4 m/cycle (for a given SIF value, say 80 MPa.$\sqrt{m}$). The damaged zone is more prone to develop for longer dwell-periods, resulting in a greater lowering of the fracture toughness during the transients of the trapezoidal loading spectrum. All these aspect argue for the introduction of **coupling terms in the modeling work**. Indeed, **creep-fatigue interaction** has been evidenced to be significant at 700°C. As a result, creep and fatigue damage mechanisms are expected to interact each others.

Now, considering the split of the global crack growth rate given in eq. (3.6), the time-dependent (creep) contribution during HT can be estimated with the following relation based on the work from [Gayda et al., 1988]:

$$\frac{da}{dt} = \frac{1}{HT} \cdot \left.\frac{da}{dN}\right|_{HT} \tag{3.7}$$

Using the eq. (3.7), the contribution related to time-assisted processes for DFCG tests with differing dwell-times can be compared each others. To this end, the Fig. 3.16 depicts the time-dependent parts of the DFCG tests in terms of $da/dt = f(K_{max})$ with HT = 300 and 3000 s, respectively.

In Fig. 3.16, one can see that the time-dependent contributions to global DFCG rates are nearly identical, no matter the dwell-time. An almost stable creep-dominated crack growth process seems to be evidenced thanks to this plot, which is characterized by a close slope between the two curves. Further tests with longer dwell-periods must be performed in order to conclude about any steady-state creep process with increasing the dwell-time [Dahal et al., 2012], [Fessler et al., 2017].
In addition, pure creep tests should be of great interest in order to study possible differences between both dwell-fatigue and pure creep tests, as done by [Gustafsson, 2012] & [Fessler, 2017] for Inconel 718 and by [Thébaud, 2017] for AD730™.

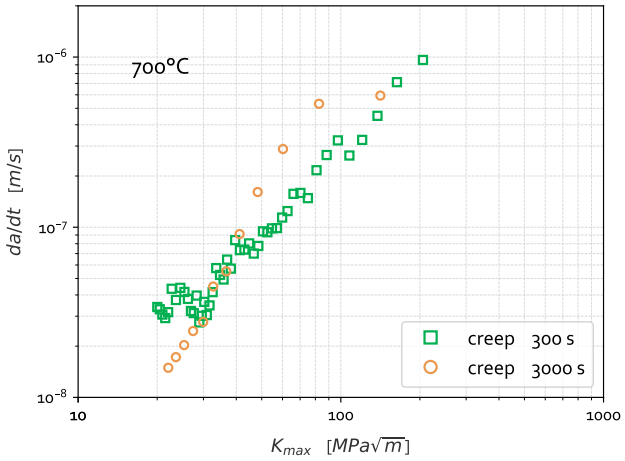

Figure 3.16: Time-dependent contribution to DFCG rate in FG AD730™ at 700°C under a 10-HT-10 s waveform with $\sigma = 400$ MPa and $R = 0.05$ (spec. S4-F3 & S4-F4).

Finally, this last sub-sect. 3.1.2.2 has served for modeling purposes since creep-fatigue interaction effects have been emphasized and discussed. Almost inactive at 550°C, this interaction has been seen to be more pronounced at 700°C for which standard modeling assumption will probably fail. Additional features will have to be included in the model to well account for this cross-effects.

3.1.2.3 Mesoscopic analysis

In the previous sub-sect. 3.1.2.1, the macroscopic data have been studied in order to evidence the crack growth behavior of the FG AD730™ under pure fatigue and dwell-fatigue loading conditions. However, owing to the fact that the Johnson formula, see eq. (3.1) in sub-sect. 3.1.1.4, remains valid as long as the crack front is straight along the through-thickness of the specimen, the macroscopic data studied in sub-sect. 3.1.2.1 may be slightly distorted due to such underlying hypotheses used for crack growth monitoring.
For high temperature testing, it has been proven in previous studies conducted on several Ni-based superalloys that a change in crack front shape may occur, see *e.g.* [Gourdin, 2015] in René 65, [Antunes et al., 2001], [Gustafsson, 2012], [Lundström, 2014] in Inconel 718, [Doremus, 2014] and [Fessler, 2017] in DA Inconel 718, as well as by [Mrozowski, 2020] in AD730™. In this latter work, the author reported a greater propensity of the fine-grained microstructure of AD730™ to tunneling effect compared to its coarse-grained counterpart. [Fessler, 2017] also evidenced a close relationship between the crack front morphology and corresponding crack growth rates. It thus seems interesting to analyze the crack front geometry as well with the fracture surface topography so as to emphasize on these points. To this end, fatigued specimens were then monotonically

loaded up to quasi-static failure at room temperature, so as to have a look at the fractured surfaces through a so-called *mesoscopic scale*.

Fractography and morphology of sectioned fracture surfaces

Fracture surfaces of one half of the FCG SEN-T testing specimens have been observed using a *Keyence VHX 2000* numerical optical microscope (see Keyence website for details), Fig. 3.17a. Specific studied features, namely the crack front and crack propagation plane are schematically demonstrated in Fig. 3.17b, where the monotonic fractured zone will not be studied in further details.

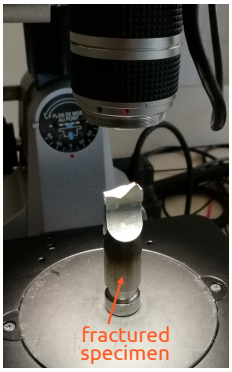

(a) Fracture surface observation using an optical microscope.

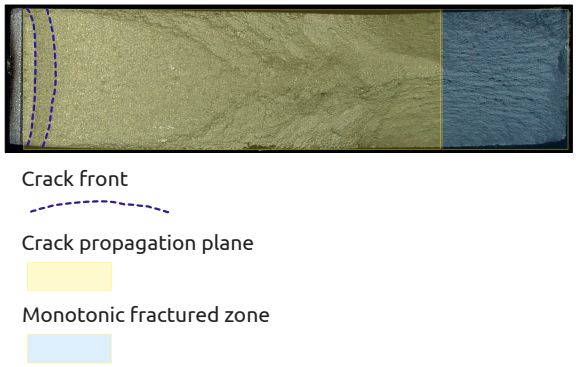

(b) Distinction between crack front and crack propagation plane on a SEN-T fracture surface.

Figure 3.17: Fracture surface observation using a *Keyence* numerical optical microscope.

In Fig. 3.18a, the fracture surface of the S4-7 specimen fractured under pure fatigue conditions at 20°C is reported. The plot gives the FCG rate as a function of the crack length. The fracture surface of the sample is also plotted on the graph in order to establish a parallel between the crack growth rates and the morphology of both the crack front and plane.

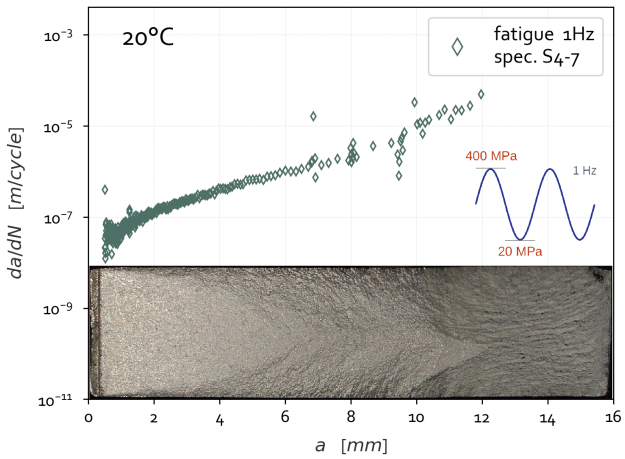

(a) Crack growth test data and corresponding fracture surface of the spec. S4-7 at 20°C - $R = 0.05$.

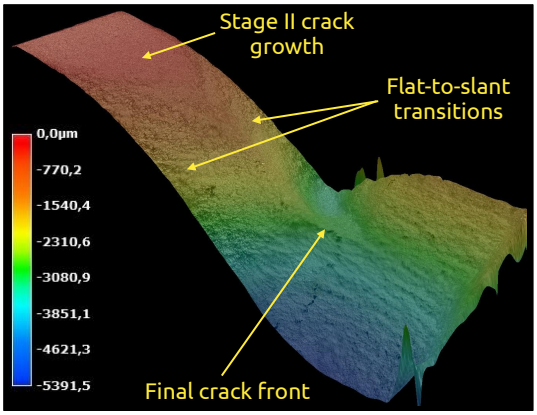

(b) 3D reconstruction of the fracture surface of the spec. S4-7 at 20°C - $R = 0.05$.

Figure 3.18: Crack growth rate under pure fatigue loading at 20°C - $R = 0.05$ with corresponding overview of the fracture surface and topological reconstruction (spec. S4-7).

The accuracy of the DCPD technique has been said to be ensured as long as the crack front is nearly straight in the through-thickness of the specimen. One can see, thanks to the accuracy of the estimated crack length through the DCPD method, Fig. 3.18a and optical observations (as well with heat tints at high temperature) that the crack front is nearly straight along the propagation process. Paying attention to the crack plane morphology in Fig. 3.18b, one can notice that the crack propagation plane admits symmetrical shear lips apart from the flat center zone. Such a process initiates from $a \simeq 3\,\text{mm}$ up to final crack length. The central flat zone is mainly related to the Paris regime of stable crack propagation.

Increasing the temperature to 550°C for self-similar testing conditions results in higher crack growth rates and shorter lifetime. At elevated temperatures, both desired beachmarks (heat tints) as well as colored oxide scale formation ease the visibility of the crack front, see Fig. 3.19. The crack front can be seen nearly straight (see heat tints) hence indicating a through-thickness quasi-homogeneous crack growth. The colored zones on the crack plane correspond to the fatigue crack growth region, whereas the brightest one is associated with the final quasi-static failure of the specimen upon monotonic tensile loading at room temperature, Fig. 3.19a. In this case, symmetrical shear lips appear once reaching a length of $a \sim 3\,\text{mm}$. As long as the crack plane remains almost flat, the propagation follows the stable Paris regime, Fig. 3.19a. Once the center flat zone vanishes, giving way to shear lips through a flat-to-slant transition, Fig. 3.19b, the crack propagation becomes unstable and FCG rates approach the unstable fracture regime evidenced by the knee in the $\mathrm{d}a/\mathrm{d}N - \Delta K$ curve.

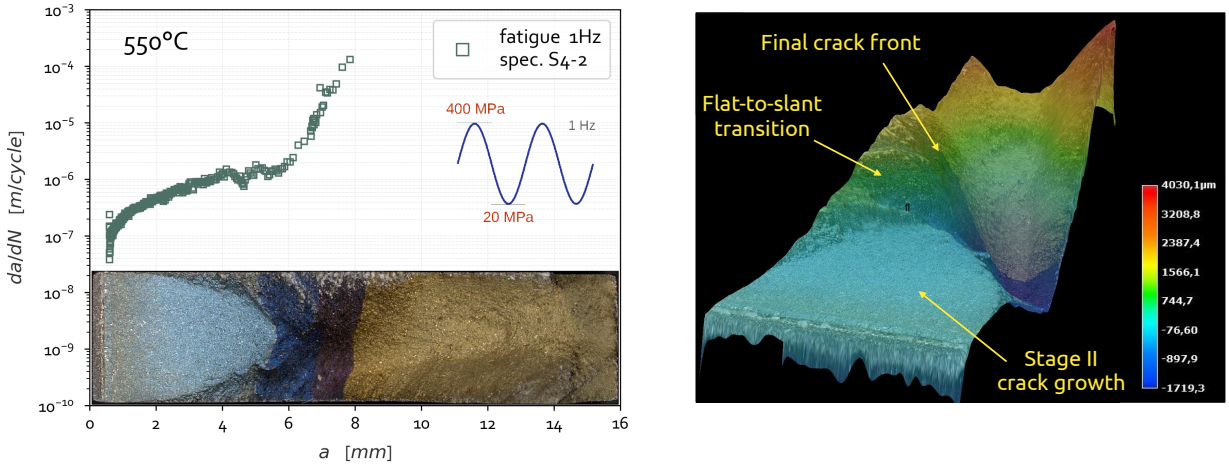

(a) Test data as opposed to fracture surface. (b) 3D reconstruction of the fracture surface.

Figure 3.19: Crack growth rate under pure fatigue loading at 550°C - $R = 0.05$ with corresponding overview of the fracture surface and topological reconstruction (spec. S4-2).

Almost similar results have been reported for the pure fatigue case at 700°C. For brevity reasons, corresponding plots are reported in the appendices, see Fig. E.2b page 281.

Dwell-fatigue:

Fracture surfaces have also been observed for dwell-fatigue crack growth tests using the *Keyence VHX* digital optical microscope. Here again, for the sake of brevity, all the results are not discussed but only the main tendencies. Additional results are reported in the appendices, see sect. E.2.

At 700°C with the application of a dwell-period, both the crack front and crack plane morphologies evolve. The crack front is hence no longer quasi-straight but exhibits a much pronounced curvature, Fig. 3.20. Such a result is in opposition to the case at 550°C (see Fig. E.8a in the appendices). The ellipsoidal shape of the crack front in Fig. 3.20 and Fig. E.8b is referred to as *crack tunneling effect*. It corresponds to a faster crack propagation in the bulk (mid-thickness) of the specimen compared to that at both free edges, hence leading to the formation of a "thumbnail shaped" crack front profile. Such a crack growth feature is often seen in stable tearing crack growth tests on specimens made of ductile materials and containing through-thickness cracks with initially straight crack front [Zuo et al., 2004]. The origin of such phenomenon is not yet fully understood, and possible explanations will be given in the sub-sect. 3.1.3 later on.
Paying attention to the Fig. 3.20 and Fig. E.8b for the same testing conditions but with an increasing dwell-time from 300 to 3000 s, a more pronounced curvature of the crack front for the longest holding period is revealed. As a consequence, the tunneling effect seems to be mainly related to thermal- and time-assisted effects.

Nevertheless, such a curvature of the crack front makes the Johnson assumption no longer valid. As a consequence, the final crack length seems to be misestimated, see the blind items in Fig. 3.20a. It has already been reported that final crack sizes estimated from the DCPD method during DFCG tests often do not agree with optical measurements from the post-test fracture surface [Fessler et al., 2017], [Tarnowski et al., 2018b]. In such cases, guidance in [ASTM, 2019] suggests a correction factor to be applied taking into account a linear interpolation, which results in better final crack length estimation [Tarnowski et al., 2018b]:

$$a = \left[\frac{(a_f - a_0)}{(a_{pf} - a_0)} \times (a_p - a_0)\right] + a_0 \tag{3.8}$$

where a, a_0 and a_f are the instantaneous, initial and final crack lengths, respectively, the latter being estimated thanks to optical measurements, and a_p and a_{pf} the actual and final crack length estimated using the DCPD method.

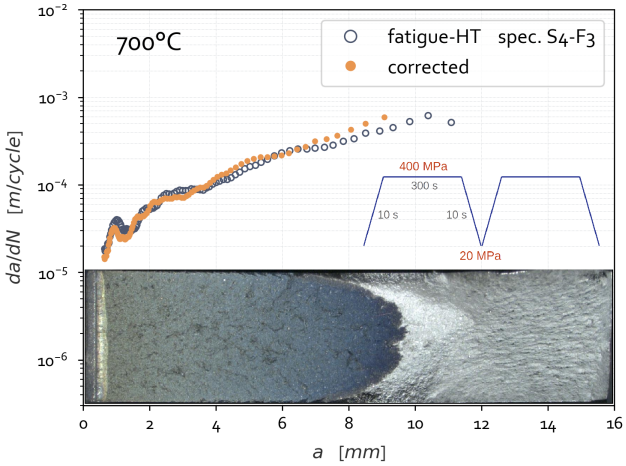

(a) Test data as opposed to fracture surface.

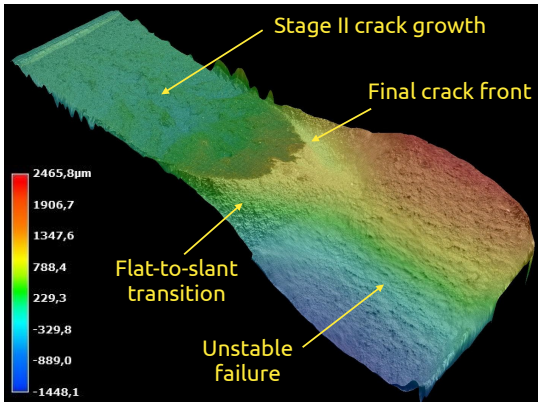

(b) 3D reconstruction of the fracture surface.

Figure 3.20: Crack growth rate under dwell-fatigue loading at 700°C - $R = 0.05$ - HT = 300 s with corresponding overview of the fracture surface and topological reconstruction (spec. S4-F3).

Applying such a corrective factor results in a better agreement between estimated and real crack lengths, see Fig. 3.20 (as well with Fig. E.8b in the appendices). Nevertheless, a slight difference still subsists in terms of final crack length. Indeed, it is specified in [ASTM, 2019] that such a correcting method remains valid as long as the difference between the crack extension estimated by the PD technique and that gained through optical measurements on fracture surface does not exceed 15%. In the case of the spec. S4-F3 (HT = 300 s), the difference was reported to be of 22.5%. Such a discrepancy hence results in poor corrective effect of the linear interpolation method suggested by eq. (3.8). However, final crack length is closer to real value, thus confirming the ability of this method to refine the raw results.

In parallel, another aspect is noticeable on the fracture surfaces. Apart from the whole crack front curvature, one can also notice its so-called *tortuosity*. Such a tortuosity is clearly visible when looking at a detailed view of the crack front, especially at mid-thickness, see *e.g.* Fig. 3.21. This aspect seems to be present at elevated temperatures as long as a dwell-time is imposed during the loading cycle. It should be noted that the fracture surfaces under pure fatigue loading, such as those shown in Fig. 3.19a & Fig. E.2b, do not reveal any tortuosity of the crack front, the latter being relatively uniform across the width of the sample. The occurrence of tortuous crack front seems to be associated with time-dependent mechanisms.

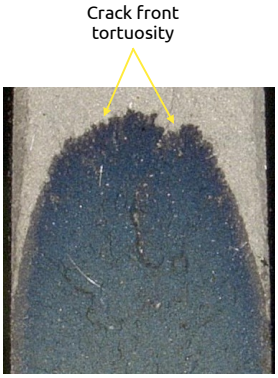

Figure 3.21: Details of the crack front tortuosity on the spec. S4-F4 at 700°C.

The introduction of a dwell-period under compression should be of great interest so as to better understand the driving mechanisms responsible for both tunneling and tortuosity effects. To this end, the Fig. 3.22 gives the FCG rates, the fracture surface as well as the topographic reconstruction of a specimen subjected to dwell-fatigue testing, but with a compressive dwell period at minimum stress level, the load ratio being equal to $R = -1$. In Fig. 3.22a, it is interesting to notice that the crack front is almost straight, with no significant tunneling effect. Moreover, the crack front seems to be relatively even with no evidence of tortuosity effects. Such facts hence suggest the inhibition of oxidation processes at the crack-tip due to crack closure during the compressive holding periods. Moreover, the dwell-period being in a compressive stress state, the crack should be closed throughout the sample thickness, thus limiting access to the crack-tip to aggressive elements causing oxidation. Finally, creep-induced cavity growth should also be limited in case of compressive holding period.

One can also notice in Fig. 3.22 the flat zone where stable (*stage II*) crack propagation occurs. This zone seems to have a less pronounced roughness compared to that of Fig. 3.20 under tensile dwell-times for the same holding period of 300 s. The negative load ratio in the case of spec. S4-F6, Fig. 3.22, may result in a greater surface matting for the crack lips, hence limiting their roughness. Finally, as the crack front is fairly straight, the crack length estimation through the DCPD method remains valid, according to the matching between macroscopic data and fractographic observations, Fig. 3.22a.

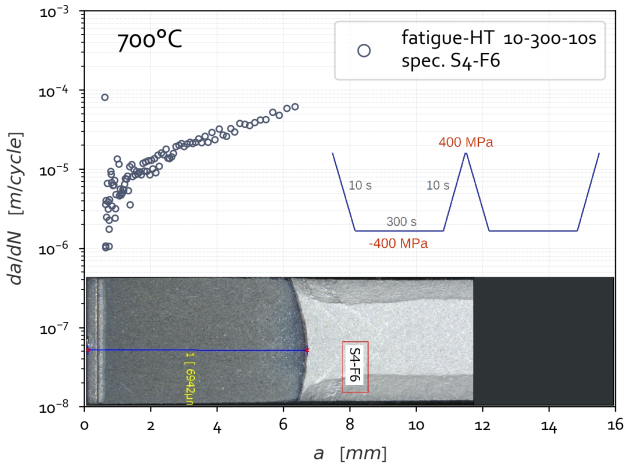

(a) Test data as opposed to fracture surface.

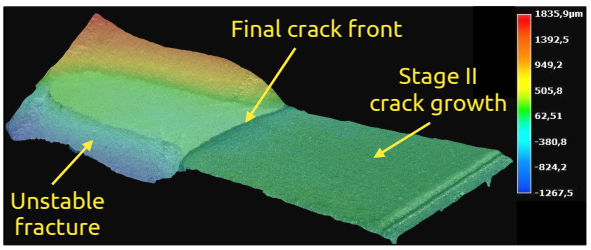

(b) 3D reconstruction of the fracture surface.

Figure 3.22: Crack growth rate under dwell-fatigue loading at 700°C - $R = -1$ - HT = 300 s with corresponding overview of the fracture surface and topological reconstruction (spec. S4-F6).

Topographic analysis of the crack path

The *Keyence VHX* numerical microscope is particularly useful because it enables for 3-dimensional (3D) reconstructions of fracture surface topographies, see *e.g.* Fig. 3.19b. Once the surface topography is built, both crack path and trajectories can be analyzed [Esnault, 2014], [Abecassis, 2017], [Trabelsi, 2019].

In Fig. 3.18b, the flat-to-slant transition has been observed at 20°C, thanks to the 3D-topographical reconstruction of the fractured surface. The value of the twist angle of the slant zone with respect to the load direction was estimated to 49°. One can also notice that shear lips are symmetrical with respect to the mid-plane of the crack front.
Increasing the testing temperature results in an asymmetrical flat-to-slant transition at 550°C, Fig. 3.19b (as well as 700°C, see Fig. E.3b in the appendices). For high temperature fatigue crack growth testing, similar crack profiles were revealed. Twist angles for the flat-to-slant transition were reported to equal 56° at 550°C (resp. 48° at 700°C).

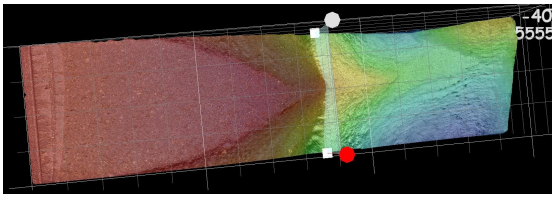

(a) Transverse cross-section.

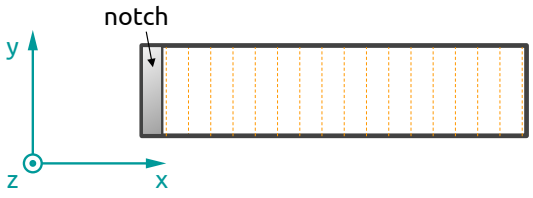

(b) Through-thickness topographical profiles.

Figure 3.23: Transverse cross-sections and topological profiles of a SEN-T specimen using the *Keyence* numerical microscope (spec. S4-F1).

Once the 3D-surface reconstruction is performed, one gets a cloud of points associated with the topographic data of one side of the fracture surface, consisting in (x, y, z) triplets where x denotes the distance from the notch root along the specimen width, y the position in depth and

z the height from the notch plane, Fig. 3.23b. Such data can be extracted to be used during a post-treatment. This way, longitudinal and transverse cross-sections have been extracted at different times of the propagation process in order to analyze in a more accurate way the crack growth direction, see Fig. 3.23.

With the help of the three-dimensional reconstruction of the topography obtained through digital optical microscopy, it becomes possible to evaluate as accurately as possible the so-called *twist* angle of the fracture surfaces [Esnault, 2014], [Abecassis, 2017], [Trabelsi, 2019]. The knowledge of this angle enables the possibility to quantify the so-called *flat-to-slant transition* during the fatigue crack growth process (see sub-sect. 1.3.3 for more details).

The twist angle θ corresponds to the angle between each side of the specimen with respect to the thickness at a given abscissa in the case of single (or double) shear lip(s), see Fig. 3.24. Such an angle characterizes the flat-to-slant transition. For each position of the crack-tip, the flat-to-slant transition can be estimated at a given abscissa plotting the twist angle θ along the specimen width [Esnault, 2014], [Abecassis et al., 2019]. The computation of the twist angle can be determined using the derivative of the transverse $z(y)$ height profile:

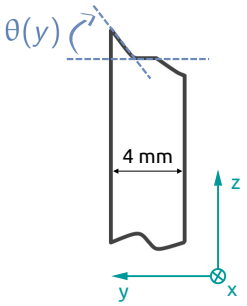

Figure 3.24: Twist angle θ.

$$\textbf{Twist angle}: \quad \theta(y) = \arctan\left(\frac{dz}{dy}\right) \tag{3.9}$$

From the Fig. 3.25a, one can easily see that the longitudinal crack profile along the crack growth direction x exhibits a flat-to-slant transition. The mid-thickness of the sample remains flat, at least up to a crack length of $a \leq 4\,\text{mm}$, see Fig. 3.25a, and the profile then starts becoming disturbed.

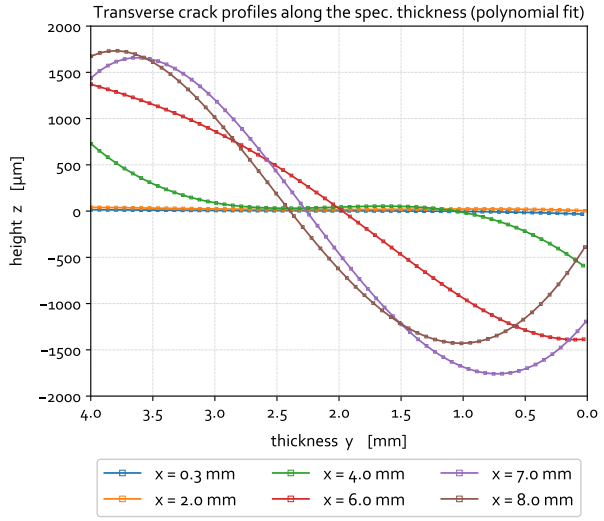

(a) Transverse profiles along the spec. thickness (fitted).

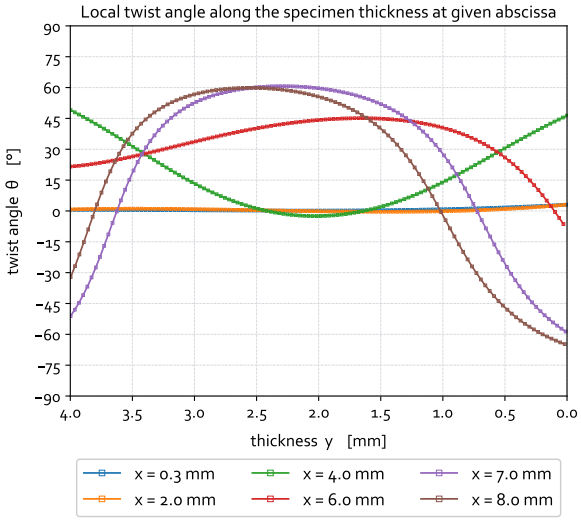

(b) Local twist angles along the spec. thickness.

Figure 3.25: Transverse crack profiles $z(y)$ and corresponding twist angles $\theta(y)$ at given through-thickness positions for SEN-T specimens under pure fatigue conditions at 550°C (spec. S4-2).

The transverse profiles in Fig. 3.25a along the specimen thickness allow for the estimation of the local twist angles, Fig. 3.25b. Note that these transverse profiles have been approximated thanks to a 4th degree polynomial fit (once plotted, if no particular mention is made, the raw data are used). One can see in Fig. 3.25a that the longer the crack length, the more disturbed the crack front profile. The asymmetrical flat-to-slant transition is clearly noticeable on these transverse profiles, the latter showing some "ridges" and "valleys" for the longest crack lengths. The change from double (4 mm) to single (6 $\rightarrow$ 8 mm) transverse profiles evidences the change from twin to single shear lips, Fig. 3.25a (which can be confirmed using the Fig. 3.19b). Then, local twist angles follow the crack front morphology with greater values along the slanted zones, Fig. 3.25b. The value of 45° is reached once the crack length equals 4 mm in the case of the S4-2 specimen. Such a result may also be retrieved in Fig. 3.19b. The peak value for the twist angle θ is not reached at the free surfaces but somewhat inside the specimen. It seems to be around 60° for the longest crack lengths.

For the sake of clearness, other temperatures are not detailed here. Associated results have been reported in the appendices, see Fig. E.4 (fatigue 20°C) page 282, and Fig. E.5 page 282 (fatigue 700°C). However, one can simply notice that increasing the testing temperature from 550 to 700°C in the case of pure fatigue loading leads approximately the same results. On the contrary, decreasing the temperature to 20°C leads to symmetrical flat-to-slant transition.

Dwell-fatigue:

For dwell-fatigue cracking, as evidenced in Fig. 3.20a (and Fig. E.8b in the appendices), increasing the holding period from 300 to 3000 s (spec. S4-F3 *vs* S4-F4) results in the same fractured surfaces with asymmetrical flat-to-slant transition at the very late phase of the cracking process. In opposition, the 3D topography of the test including a compressive holding period of 300 s (spec. S4-F6) at −400 MPa clearly confirms the flat crack growth for the whole cracking process. Tunneling effect as well as flat-to-slant deviation(s) are not observed in such a 3D view, Fig. 3.22b.

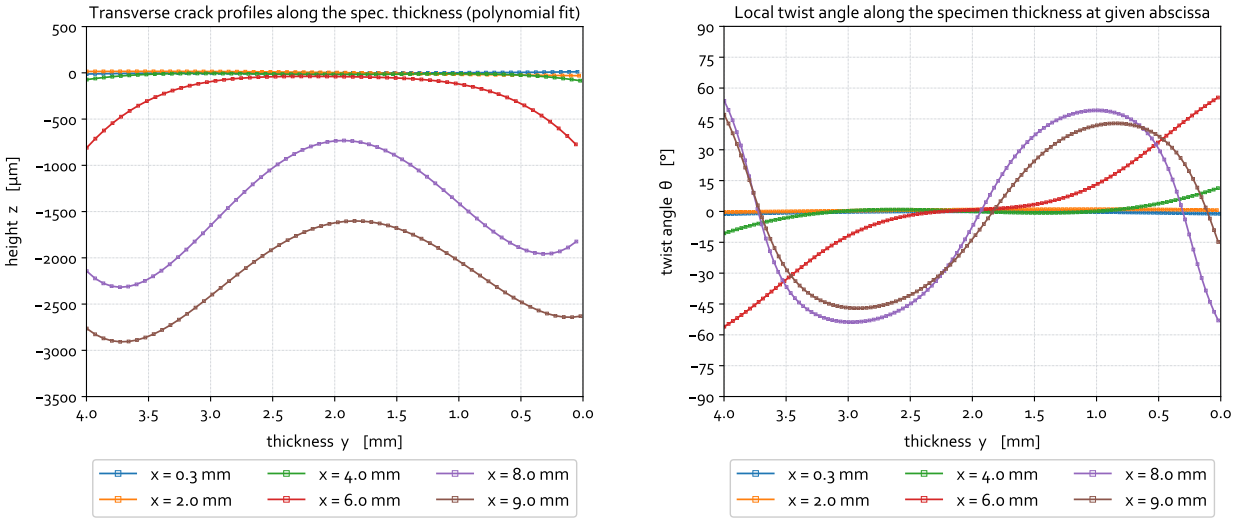

(a) Transverse profiles along the spec. thickness (fitted). (b) Local twist angles along the spec. thickness.

Figure 3.26: Transverse crack profiles $z(y)$ and corresponding twist angles $\theta(y)$ at given through-thickness positions for SEN-T specimens under dwell-fatigue conditions at 550°C (spec. S4-F1).

In Fig. 3.26a (resp. Fig. E.10a), the transverse height profiles $z(y)$ of the crack front for the 550°C (resp. 700°C) dwell-fatigue cases are reported. In both cases, the crack bifurcation results in symmetrical slanted areas. Indeed, the height profiles for each longitudinal position x evidence symmetric properties with respect to the mid-thickness of the specimen, that is $y = 0.2\,\text{mm}$. The flat zone ($x \in [0.3 - 4.0]\,\text{mm}$) is hence followed by symmetrical shear lips apart from the mid-thickness plane ($x > 4.0\,\text{mm}$), that is, from each free side of the sample, with the normal flat area getting smaller as long as the crack grows, Fig. 3.26a.

Finally, similarly to the pure fatigue cases, the local twist angles can be deduced from the polynomial fits of the transverse profiles of the crack, see Fig. 3.26b (and Fig. E.10b page 285 in the appendices). At 550°C under dwell-fatigue conditions, due to symmetry properties of the shear lips, opposite twist angles in the slanted areas are reported, see Fig. 3.26b. Similarly to the pure fatigue cases, the peak values of $\sim 50°$ for the twist angles are found somewhat within the specimen. Contrarily to the pure fatigue case, see Fig. 3.25b, symmetric flat-to-slant transition is observed in creep-fatigue loading conditions.

As done for the pure fatigue loading cases, additional plots are given in the appendices, see Fig. E.10 and Fig. E.11 (dwell-fatigue 700°C) page 285, so as for a comprehensive review on each specific specimen to be carried on.

Overall review:

From these mesoscopic analyses, one can finally conclude about the occurrence of flat-to-slant transition process under both pure fatigue and dwell-fatigue loading conditions at low to elevated temperatures in FG AD730™. Such results clearly evidence the presence of mixed loading modes, despite the pure *mode I* loading scheme. The crack first propagates following the opening mode (*mode I*). Then, a progressive contribution from out-of-plane shear (*mode III*) is finally noticeable once the crack path admits some roughness, hence suggesting a close interaction between the crack and the microstructure. Such a *mode III*-induced flat-to-slant transition is assumed to be correlated with high plastic strain levels together with damage mechanisms [Trabelsi, 2019]. Such observations are fairly well known for ductile tearing problems [Zuidema and Blaauw, 1988], [Besson, 2010], [Besson et al., 2013], [Maurel et al., 2020]. The close interaction between crack path and material microstructure is about to be discussed in the next sub-sect. 3.1.2.4 using micro-graphic observations of the fractured surfaces.

3.1.2.4 Microscopic observations

The purpose of this section is to identify the main cracking mechanisms expected to be observed in Ni-based superalloys subjected to high temperature cracking under cyclic loading schemes. To this end, *Scanning-Electron Microscope* (SEM) views of the fracture surfaces have been exploited.

Post-failure SEM observations (using the secondary electrons for topographical viewing) were carried out in order to determine the main failure modes governing the crack growth process as well as the temperature effect. To this end, some specific *Regions of Interest* (ROI) have been selected in order to put a focus on particular zones of the crack path, Fig. 3.27. Secondary electron images

were produced using an acceleration voltage of 5 kV at magnifications of 500, 1 000 and 2 000. The typical working distance was revealed to be of ∼15-20 mm.

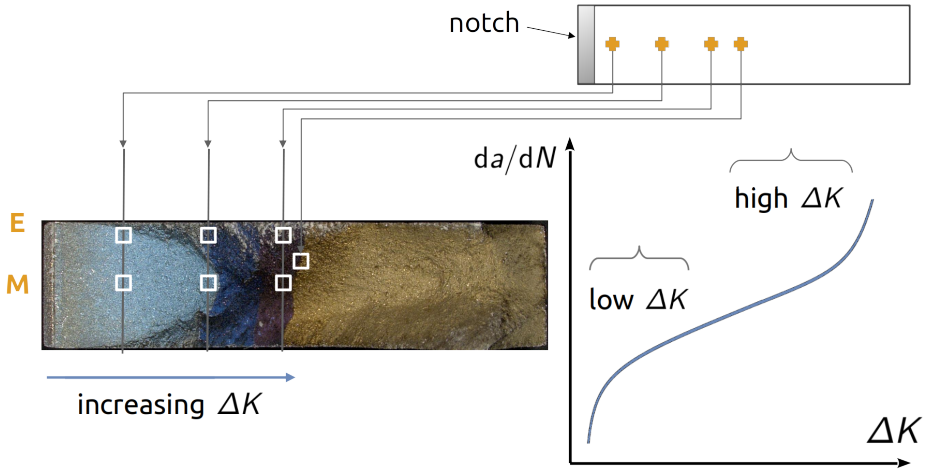

Figure 3.27: Schematic view of the SEM observations zones on fractured SEN-T specimens after fatigue crack growth testing. **E** and **M** is for *Edge* and *Middle*, respectively.

In order to compare analyses from one specimen to another, observations have been carried out at approximately identical ΔK values. This was done as much as possible, depending on the final crack length and visible ROI.

20°C:

In Fig. 3.29, the SEM micrographs of the S4-7 specimen tested at 20°C are reported. One can see two zones along the crack path for which fracture modes can be analyzed, namely at $\Delta K \simeq 50$ and 132 MPa$\sqrt{\text{m}}$. In Fig. 3.28 and Fig. 3.29b, secondary micro-cracking can be noticed as indicated with red arrows. Moreover, in Fig. 3.29a, some typical *stage II* fatigue striations associated with Paris crack growth regime are noticeable at a scale lower than average grain size, hence evidencing a transgranular mode of failure. A crude evaluation of the inter-striations spacing and resulting FCG rate has been conducted following the guidelines from [Pelloux, 1970]. To this end, 13 fatigue striations were estimated within a 5 µm width, see Fig. 3.29a, hence yielding in a FCG rate of about 3.85e-7 m/cycle. This is in relatively good agreement with the estimation provided by the DCPD technique associated with data extraction processes detailed in sub-sect. 3.1.1.4 which gives a FCG rate of about ∼3.e-7 m/cycle.

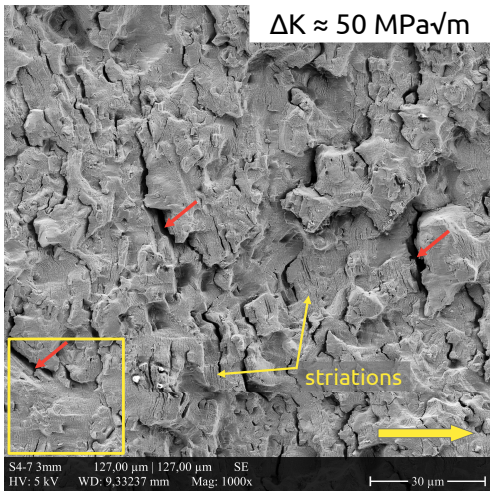

Figure 3.28: $a \simeq 3.0$mm / $\Delta K \simeq 50$ MPa$\sqrt{\text{m}}$.

In Fig. 3.29b, the fracture surface is different from that of the Fig. 3.28 for lower SIF values. The topography of the Fig. 3.28 evidences a predominantly transgranular mode of propagation whereas

a greater extent of intergranular fracture is noticeable in Fig. 3.29b. The apparition of a slight grain boundary decohesion may be the manifest of the transition from transgranular to mixed-mode of crack propagation. Finally, observations carried out in the last crack front have revealed a more faceted-like fracture surface with the apparition of dimples. The fracture mode is hence mainly ductile with mixed intergranular and transgranular features.

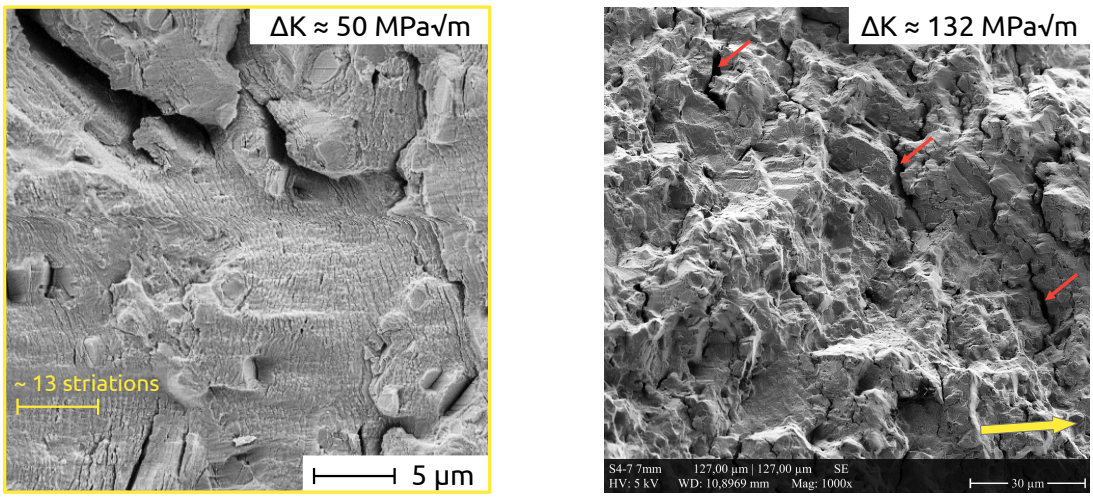

(a) Close-up view on Fig. 3.28. (b) $a \simeq 7.0$mm / $\Delta K \simeq 132\,\mathrm{MPa}\sqrt{\mathrm{m}}$.

Figure 3.29: SEM fracture surface analyses for the S4-7 specimen subjected to pure fatigue at 20°C (1 Hz, 400 MPa, $R = 0.05$). Identification of the main cracking mechanisms.

550°C:

The FCG curve as well as some SEM observations for the specimen fatigued at 550°C are given in Fig. 3.31. In Fig. 3.30 to Fig. 3.31b, predominant transgranular fracture mode is noticeable. The apparition of a thin oxide scale due to high temperature testing makes the fatigue striations less visible. One can also notice the initiation of multiple secondary cracks, almost perpendicular to the crack growth direction as indicated with red arrows. Such secondary cracks may be representative to some degree of GB decohesion, hence suggesting the competing effect of intergranular fracture mode. In Fig. 3.31a, almost similar fractographical conclusions can be drawn that are, the occurrence of mixed fracture modes with both intergranular and transgranular features. Some fatigue striations are also visible, though a bit masked by the oxide scale.

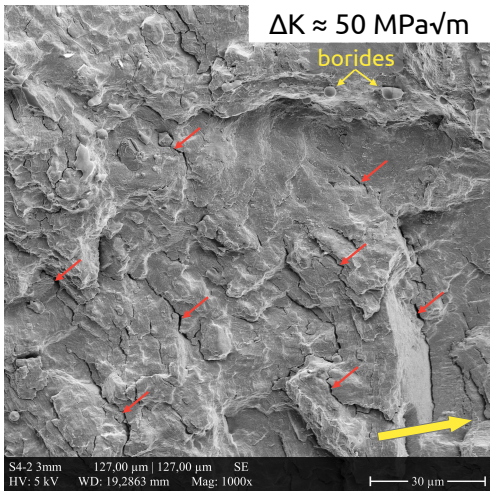

Figure 3.30: $a \simeq 3.0$mm / $\Delta K \simeq 50\,\mathrm{MPa}\sqrt{\mathrm{m}}$.

As long as the SIF range increases, the topography of the fracture surface tends to admit more intergranular features with the apparition of locally gathered small dimples typical of ductile-like mode of failure, see Fig. 3.31b. The slanted zone (not depicted here), ahead of the crack front, has evidenced some faceted-like fracture surface with secondary cracks.

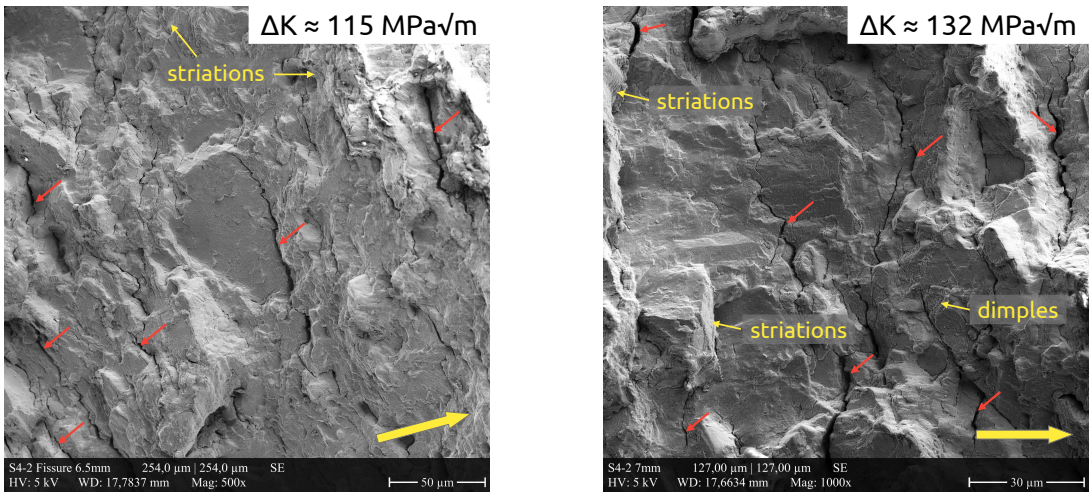

(a) $a \simeq 6.5$mm / $\Delta K \simeq 115\,\mathrm{MPa}\sqrt{\mathrm{m}}$. (b) $a \simeq 7.0$mm / $\Delta K \simeq 132\,\mathrm{MPa}\sqrt{\mathrm{m}}$.

Figure 3.31: SEM fracture surface analyses for the S4-2 specimen subjected to pure fatigue at 550°C (1 Hz, 400 MPa, $R = 0.05$). Identification of the main cracking mechanisms.

700°C:

Increasing the temperature up to 700°C results in a higher extent of oxidation, hence making the observation of fatigue striations a difficult task. Looking at SEM micrographs with a lower magnitude, Fig. 3.32, one can distinguish the three main initial stages of the crack growth process starting with the crack initiation from the EDM U-notch and followed by the pre-cracking phase prior to the crack growth step. One can notice the change in crack propagation mode from transgranular crack-initiation at high stress level to progressively mixed inter- and trans-granular crack propagation mode upon pre-cracking and subsequent crack propagation. At 700°C, the main results are: the presence of a vast majority of intergranular features, especially at the mid-thickness of the specimen, with dispersed transgranular zones. Ductile-like features such as small dimples are also noticeable at a finer scale, hence suggesting a more ductile-like fracture mode close to the edges. The occurrence of mixed crack modes is hence validated. Supporting results are given in the appendices, see Fig. E.6.

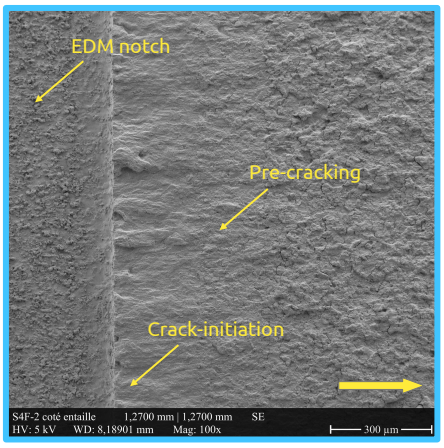

Figure 3.32: SEM fracture facies for the spec. S4-F2 under pure fatigue conditions at 700°C evidencing a characteristic *stage II* crack propagation regime.

In his work on FG AD730™, [Mrozowski, 2020] reported a dominating intergranular crack propagation mode at 750°C under both fatigue and dwell-fatigue conditions. For a lower temperature, [Govaere, 2020] also confirmed the occurrence of intergranular cracking mode at 700°C on the same microstructure. The large occurrence of secondary cracking under air confirms this trend.

Dwell-fatigue:

The same observations have been conducted for the creep-fatigue conditions. To this end, specific regions at given ΔK values have still been considered in order to ease the comparison between the two target temperatures of 550 and 700°C under the same loading conditions (10-300-10 s, $R = 0.05$, $\sigma = 400$ MPa) or for differing dwell-periods and/or load ratio (see the synthesis of the tests in Tab. 3.3). Note that for the S4-F1 specimen at 550°C, stress level was increased up to 440 MPa due to crack arrest after pre-cracking.

At 550°C, the fracture mode is of intergranular-type both in the mid-thickness of the specimen, as well as at the free surface, Fig. 3.33a. For low ΔK values, the fracture surface at the edge is brighter than that at the middle, hence suggesting a thicker oxide scale close to the free surfaces of the sample where oxidizing elements have an easier access to the microstructure. The SEM views given in Fig. 3.33 evidence the presence of secondary micro-cracks (indicated by red arrows) caused by grain boundary decohesion. Fatigue striations are less visible compared to the pure fatigue case, probably because of the deposited oxide layer on both crack surfaces upon dwell-holding. Fractographic observations at 550°C in the mid-thickness of the specimen evidence faceted-like surfaces for the larger ΔK values, see Fig. 3.33b. Such aspects may be associated with twin boundary decohesion and pseudo-cleavage fracture mode. At the edge of the sample and close to the final crack front, the presence of some matted surfaces has been reported, probably due to crack closure mechanisms leading to the contact of the crack lips or shearing mechanisms.

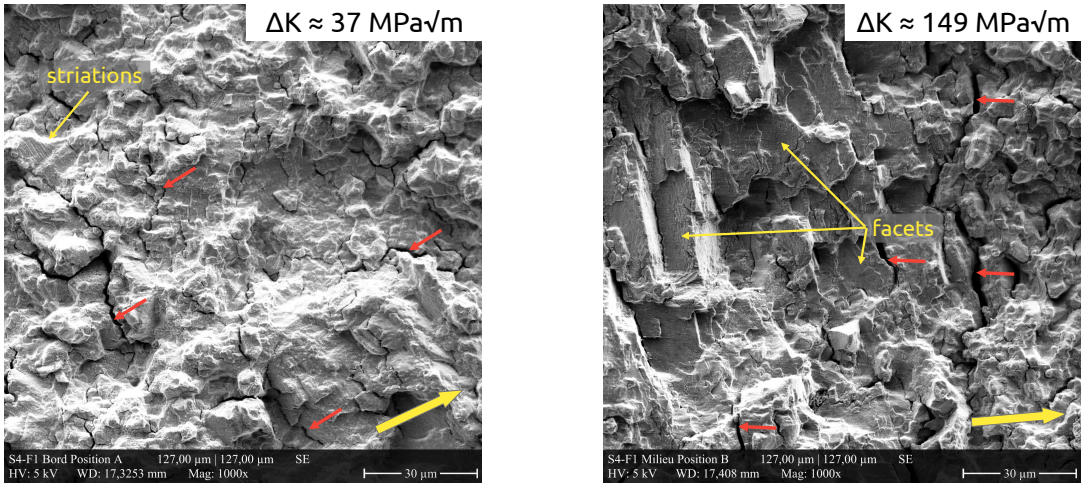

(a) $a \simeq 2.0$mm / $\Delta K \simeq 37\,\mathrm{MPa}\sqrt{\mathrm{m}}$ - egde. (b) $a \simeq 7.5$mm / $\Delta K \simeq 149\,\mathrm{MPa}\sqrt{\mathrm{m}}$ - middle.

Figure 3.33: SEM fracture surface analyses for the S4-F1 specimen subjected to dwell-fatigue at 550°C (10-300-10 s, 440 MPa, $R = 0.05$). Identification of the main cracking mechanisms during the *stage II* crack propagation regime.

Increasing the testing temperature from 550 to 700°C results in brighter images (see Fig. E.12 in the appendices, page 286), hence suggesting the preponderance of the oxide layer. Secondary cracking is also visible in both middle and edge zones, as indicated by red arrows. Grain boundary decohesion seems to occur, hence leading to intergranular cracking. For the highest ΔK values, Fig. E.12c & Fig. E.12d, intergranular fracture mode is clearly visible with a more disturbed topography (more ridges and valleys). The macroscopic crack growth data evidence an almost stable

stage II crack propagation regime, which in turn suggests the mode of rupture to be quasi-constant during the overall crack growth stage. Thus, intergranular fracture mode seems to be predominant throughout the crack growth process at 700°C under dwell-fatigue loading. For the sake of brevity, all the plots have not been detailed in the present chapter but are gathered in the appendices, see Fig. E.12 page 286.

3.1.3 Conclusions on the fatigue and dwell-fatigue crack growth tests

From the last sub-sect. 3.1.2.1 to sub-sect. 3.1.2.4, both the fatigue and dwell-fatigue crack growth tests have been analyzed using different length scales. Several aspects have been evidenced with the help of precise and targeted observations following a three-scales scheme. The macroscopic data have been compared to the morphology of both crack front and fracture surfaces at a mesoscopic scale, prior to final microscopic observations on dedicated zones. This way, the main failure modes within the FG AD730™ have been emphasized.
The main tendencies to be noticed for these two crack growth testing conditions are as follows:

- pure fatigue tests at 20, 550 or 700°C result in a nearly straight crack front, hence validating the use of the Johnson formula for crack length estimation. No crack front tortuosity has been observed for cycle-dependent crack growth, the latter resulting in even crack fronts;
- tunneling effect associated with a differential in terms of crack propagation rates between the bulk and the free surfaces of the specimen has been seen noticeable when introducing a dwell-period over pure fatigue loading conditions at the maximum load level. The resulting crack front exhibits a curved-shaped morphology as well with tortuosity;
- the longer the dwell-period, the more pronounced the crack front curvature and tortuosity. The latter is assumed to depend on local interactions between environmental effects, local stress state and microstructure;
- the introduction of a compressive dwell time over a pure fatigue loading signal disables the crack front tunneling effect as well as crack front tortuosity. Creep and oxidation processes hence seem to have been alleviated during the compressive dwell period;
- flat-to-slant transition arises from closure-induced shear lips development at the free edges of the specimen. The crack growth process hence evidences mixed mode loading associated with both normal opening and out-of-plane shear loadings;
- the three-dimensional topographical reconstruction of the fracture surfaces allows for the analysis of transverse crack front profiles and enables the computation of local twist angles, hence emphasizing on the flat-to-slant transition;
- from a microscopic point of view, pure fatigue loading conditions yield mixed mode crack propagation with both transgranular and intergranular features. Secondary cracking can be related to grain boundaries decohesion. At RT, fatigue striations typically representative of transgranular cracking can be observed. For the highest temperature of 700°C, intergranular fracture mode rules the crack propagation with faceted fracture surfaces, representative of pseudo-cleavage fracture for the highest ΔK values;
- dwell-fatigue loading schemes result in intergranular crack mode with secondary micro-

cracking related to grain boundary decohesion. Faceted-like surfaces reflect the pseudo-cleavage aspects of the fracture process.

Finally, one can notice that for a better visibility of both crack initiation and crack growth processes associated with grain boundary or primary precipitates decohesion, SEM observations using Back-Scattered Electron (BSE) should have been performed. Such a task remains left to do for further understanding of the underlying mechanisms leading to intergranular cracking.

Discussions on the occurrence of tunneling effect and crack front tortuosity

Even though the **tunneling effect** has been observed in numerous Ni-based crack growth problems at elevated temperatures, no clear explanation has yet been found to validate or invalidate the numerous hypotheses. This is probably due to the fact that such a phenomenon depends on several intrinsic and extrinsic parameters with possible interactions, making the problem even more complex.

In the present work, the database is not sufficiently exhaustive for clear conclusions to be drawn. However, possible explanations can be given. For dwell-fatigue loading conditions, the tunneling effect might be related to differing viscoplastic activity from the free edges of the specimen to its mid-thickness, hence suggesting varying crack driving forces. Indeed, tunneling effect has been shown to occur for the highest temperature of 700°C, which is also the temperature at which viscous properties of the material are predominant. Consequently, a larger plastic zone is assumed to occur at the free surfaces since plane stress conditions are met, as opposed to the mid-thickness of the sample (plane strain conditions). As a result, retardation effects may be the consequence of a higher plastic wake in the near surfaces, hence lowering the FCG rates. Moreover, the dwell-time causes the stress to relax due to the viscous properties of the material. It has been shown in Chap. 2 that the viscous properties of FG AD730™ seem to be dependent on the viscoplastic strain level, see sub-sect. 2.2.3.2. A possible scenario would be then to relate the viscoplastic behavior of the material with possible recovery of its hardening properties with increasing strain levels. The viscoplastic strain levels at the crack front extremities being high, this may lead to greater viscous-stress relaxation and recovery mechanisms (which could be significant above 550°C), and as a result favoring the crack driving forces in the vicinity of the crack-tip compared to the crack front extremities.

Nevertheless, oxidation effects also seem to play a role in tunneling process since a compressive dwell-period results in a vanishing tunneling effect. Once the crack is opened, the strong plasticity in the near surfaces may inhibit the environmental effects, lowering the crack growth rates in these zones and leading to a "pinned" crack front in the mid-thickness of the sample. On the contrary, once the crack is closed, there is no detrimental effects associated with the environment, leading to an almost similar crack front from the edges to the middle of the specimen.

As for the slight **tortuosity** effect observed at 700°C, the local mechanical state in close relation with the microstructure (C&W textured material) might be a probable explanation to the local differential in FCG rates leading to a tortuous crack front. However, further investigations on this point are required for a more comprehensive understanding to be accessed.

Contribution of the micrographic observations to the modeling work

The previously discussed points are mainly related to micro-mechanisms governing the fracture process. Even though such observations cannot be included in a phenomenological fatigue damage model dedicated to crack propagation, as intended in the present Ph.D. project, some information can nevertheless guide the modeling task. The prevalent transgranular crack mode at low temperature under pure fatigue loading conditions allows for the fatigue damage mechanism to be dominant. In such a case, creep mechanisms can be deactivated. There is no significant creep-fatigue interaction up to 550°C, as reported in sub-sect. 3.1.2.2. As long as temperature increases, creep mechanisms may start to play a role in the crack growth process since intergranular features have been revealed in sub-sect. 3.1.2.4. This trend has been observed under pure fatigue and is even more significant under dwell-fatigue. Thus, creep damage must start to be active and acts in close interaction with fatigue damage. Finally, for dwell-fatigue loading conditions, creep damage mechanisms of intergranular-type have been noticed to be prevalent and consequently must play a major role on the crack growth process. In addition, fatigue damage must remains active since a strong creep-fatigue interaction has been reported in sub-sect. 3.1.2.2. This way, a parallel can be made from a phenomenological point of view, between microscopic evidences and modeling features. This parallel is also to be considered in the calibration process for the damage model.
At last, ductile-like features (dimples, cavities) have been observed close to the final crack front. Since the crack length is sufficiently long at the end of the test, significant plasticity is expected to occur at the crack-tip, hence leading to ductile damage mechanisms. This latter mechanism, strongly influenced by the stress state, may also play a role on the fracture process, particularly for flat-to-slant transition. It is discussed in more details in the next sect. 3.2.

3.2 Cracking behavior of flat specimens of AD730™ under VLCF loading conditions

During fatigue crack growth, even if small scale yielding conditions are ensured, large plastic strains are assumed to occur at the crack-tip where the stress fields are (theoretically) singular. The stress state parameters, which are namely, the stress triaxiality ratio and the Lode parameter [Besson, 2010], [Danas and Ponte Castañeda, 2012], are assumed to play a role on both deformation and fracture modes. Owing to these aspects, mechanisms associated with ductile fracture are assumed to occur, in combination with both fatigue and creep processes. To get closer from the target of the present study focusing on cyclic crack propagation, and as a complementary result, it seems interesting to look at the ductile fracture behavior of AD730™ through *Very Low Cycle Fatigue* (VLCF) conditions. Such a loading scheme is assumed to be associated with large plastic strains occurring in the vicinity of the crack-tip during a very limited number of loading cycles [Dufailly and Lemaitre, 1995], [Voyiadjis et al., 2012].

In the current section, the quasi-static VLCF failure process in FG AD730™ is investigated. First, the selection of the specimens geometries is discussed in sub-sect. 3.2.1 with corresponding testing conditions and experimental set-up. Next, in the same manner as for the cyclic tests, macro-

scopic results are detailed in sub-sect. 3.2.2.1 prior to post-mortem fractographic observations, sub-sect. 3.2.2.2. In this way, the main crack driving mechanisms as well as fracture modes will be highlighted and discussed.

3.2.1 Experimental sample and set-up

Even though both monotonic and VLCF fracture tests have been performed on three distinct specimen geometries in this Ph.D. project, choice has been made here, for brevity reasons, to only focus on one flat specimen under VLCF conditions. Monotonic results might be given and discussed for comparison purposes only.

3.2.1.1 Selected geometry

In order to reach several levels of heterogeneity of the kinematic fields as well as differing stress states, the specimens geometries for crack initiation and propagation analysis should be carefully chosen. To this end, some guidelines provided by previous studies of [Karolak, 2016], [Bettonte, 2017], [Defaisse, 2018], [Davaze, 2019] dedicated to ductile fracture analysis helped on the choice of the dedicated specimens geometries. For mechanical testing, three flats specimens were designed in order to use a tensile machine with DIC for test monitoring. As said, and for the sake of brevity, only one specimen geometry will be discussed.

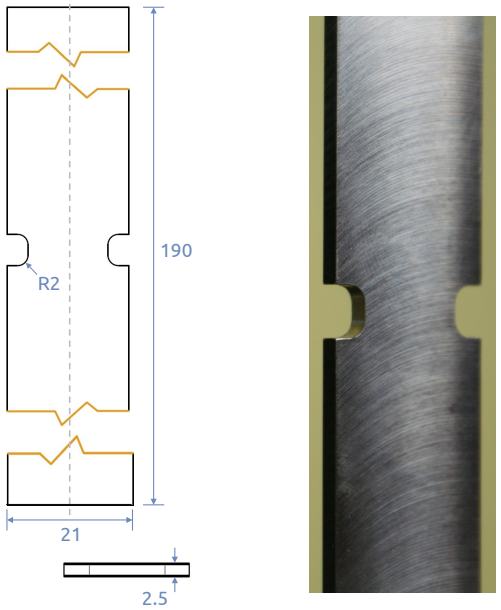

(a) FN2 spec. (b) As-machined specimens.

Figure 3.34: Flat FN2 specimens for monotonic cracking tests on FG AD730™.

Notched specimens, referred to as *FN2*, see Fig. 3.34, are relevant for stress triaxiality ratios analysis. It is assumed that the smaller the notch, the higher the stress triaxiality ratio [Davaze, 2019]. Such a specimen geometry has been considered in this work, with a 2.5 mm-thickness. No negative stress triaxiality ratios were investigated in order to avoid any buckling situations.

Some specific dimensions and relevant information about such a flat FN2 testing sample are given in Fig. 3.34. Notches and specific features were obtained through EDM process. The detailed sketch of this specimen is given in the appendices, see sect. B.3 page 272. Specimens were extracted from slices of the parallelepipeds through wire EDM, see the cutting plans in Fig. A.2.

3.2.1.2 Experimental facilities & procedures

Very Low Cycle Fatigue (VLCF) crack growth tests were performed within the ONERA facilities. To this end, a specific testing bench has been used. It consists in a *Losenhausen (LOS)* retrofitted servo-hydraulic testing machine with a load-cell capacity of 100 kN. During the testing process, sample was held via upper and lower *MTS 647* hydraulic wedge grips, see Fig. 3.35. For elevated temperature testing conditions, an induction-heating system was used. For this reason, the specimen was not in an enclosed environment, resulting in a greater variability of the specimen temperature along the useful zone (but homogeneous in the thickness). The inductor was made of two coils which were located on both sides of the useful zone of the specimen, allowing the Region of Interest (ROI) of the test-piece to be visible in order to perform DIC, see Fig. 3.35.

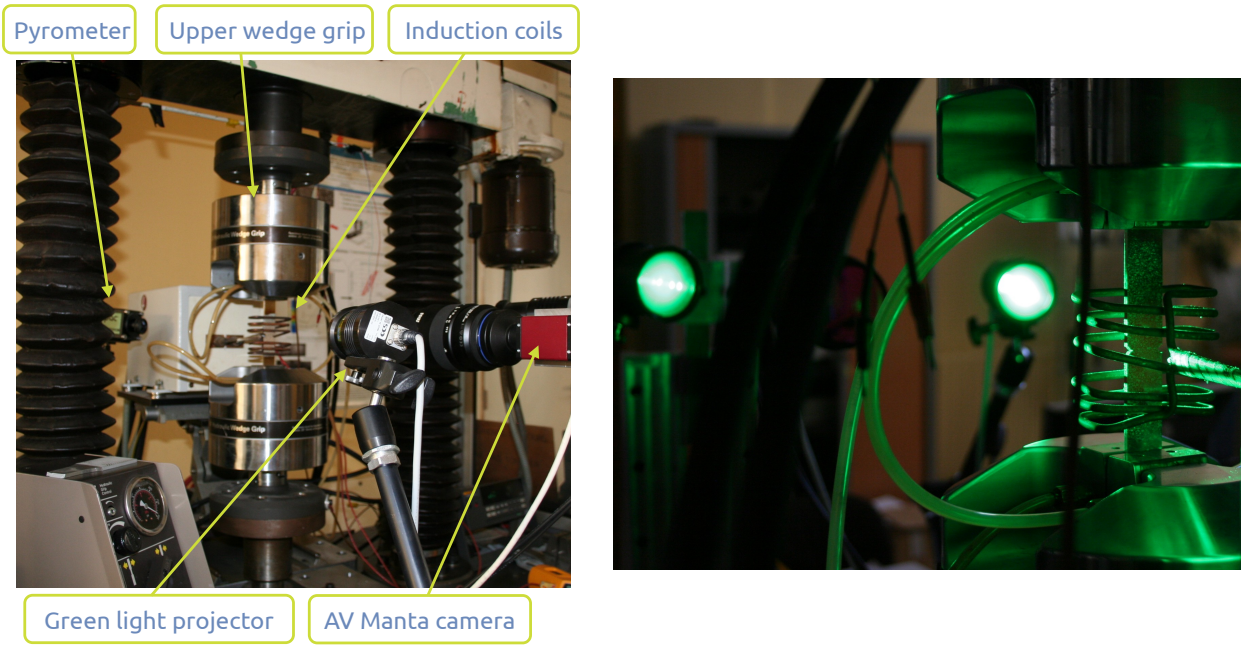

(a) Overall set-up for monotonic crack growth testing with associated monitoring equipment.

(b) Close-up view on the specimen upon high temperature testing using induction-heating system and DIC.

Figure 3.35: Testing bench for monotonic and VLCF crack growth testing in FG AD730™ flat specimens using a 100 kN *LOS* servo-hydraulic testing machine.

VLCF testing process:

For the loading conditions, a specific testing procedure has been designed for this study. Tests were performed under displacement control with a prescribed displacement rate of $dU/dt = 0.01\,\mathrm{mm.s^{-1}}$, which induced a local strain rate within the range $10^{-3} - 10^{-4}\,\mathrm{s^{-1}}$. The loading waveform for displacement U vs. time t was thus triangular. However, in order to prevent any buckling problem upon cycling, the specimen should be unloaded up to the zero force level. Due to the fact that the tests were displacement-controlled, the minimum U_{min} was given by the zero force level acquired by the load cell. Moreover, in order to settle incremental increasing loading cycles, the maximum prescribed displacement needed to be estimated from one cycle to the other. This was done using a dedicated procedure schematically represented in Fig. 3.36. Such a procedure

aimed at re-evaluating the maximum displacement U_{max} for each loading cycle from a deviation δU to the linear portion of the curve $F(U)$, see Fig. 3.36a & Fig. 3.36b. That way, several loading cycles can be performed with a displacement control to match with the corresponding monotonic loading curve.

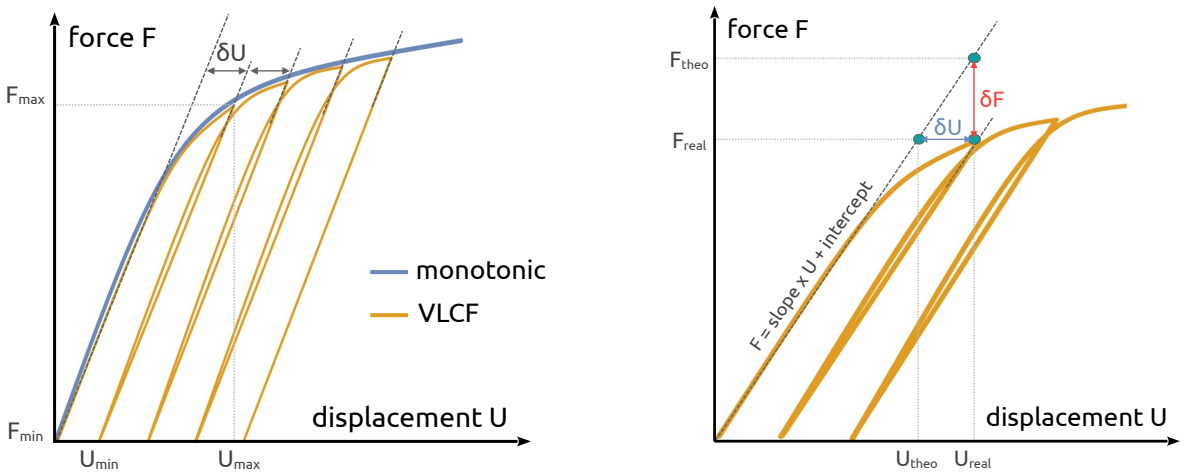

(a) Schematic view of the VLCF testing process.

(b) y-intercept updating process.

Figure 3.36: VLCF testing procedure on flat specimens based on monotonic response.

Such VLCF tests were only performed at 700°C, up to sample failure. The sampling frequency of the testing machine for data acquisition was set to 10 Hz. A synthesis of all the VLCF tests performed during this research work with corresponding loading conditions is given in Tab. 3.4.

	Loading conditions			**Images**		**Test data**	
Specimen	**Loading type**	**T**	**dU/dt**	**Sampling**	**Integration**	**Cycles**	**Failure**
		[°C]	[mm.s^{-1}]	[Hz]	[ms]	[-]	[-]
FN2-1	Monotonic	20	0.025	0.25	50 - 60	-	✓
FN2-6	Monotonic	700	0.01	1.	50 - 60	-	✓
FN2-5	VLCF	700	0.01	1.	50 - 60	7	✓
FN2-2	VLCF	700	0.01	1.	50 - 60	19	✓

Table 3.4: Synthesis of the monotonic and VLCF crack propagation tests performed on FN2 specimens made of fine-grained AD730™ for the present study.

3.2.2 VLCF fracture tests

The purpose of this sub-section is to discuss the tests on *FN2* flat specimens conducted under (quasi-static) VLCF loading conditions. The global material response is studied for one specific specimen geometry and the highest testing temperatures of 700°C. Fractographic observations using SEM images are then analyzed in order to highlight the main fracture modes.

3.2.2.1 Analysis of the macroscopic responses

In the present work, each test was performed only once, limiting the repeatability of the tests and the representativeness of the macroscopic response. The plots depicted in the following are given in terms of force vs. displacement, or if no particular mention is made, in stress vs. strain (associated with a **nominal measure**), see eq. (2.1).

The macroscopic stress-strain curves related to the VLCF tests on FN2 specimens at 700°C are plotted in Fig. 3.37. Note that the corresponding monotonic curve is also reported for comparison purposes. For the first test, the deviation from the linear slope was set to $\delta U = 0.1\,\text{mm}$, hence resulting in a macroscopic response involving 7 loading cycles, see Fig. 3.37a. It can be noticed that the monotonic curve represents a fairly accurate envelope curve of the VLCF test. The procedure allows to contain the crack propagation phase within a given number of loading cycles. The ductility of the material can be seen to be limited, with an insignificant strain-hardening phase. A plateau is evidenced in the curve prior to the softening process up to failure. This softening phase can be seen to be not so pronounced. Then, the crack propagation stage is very fast, even unstable, which does not allow for a progressive decrease of the curve to be seen, Fig. 3.37a. The strain at failure for the VLCF test can be seen to be lower than that of the monotonic test.

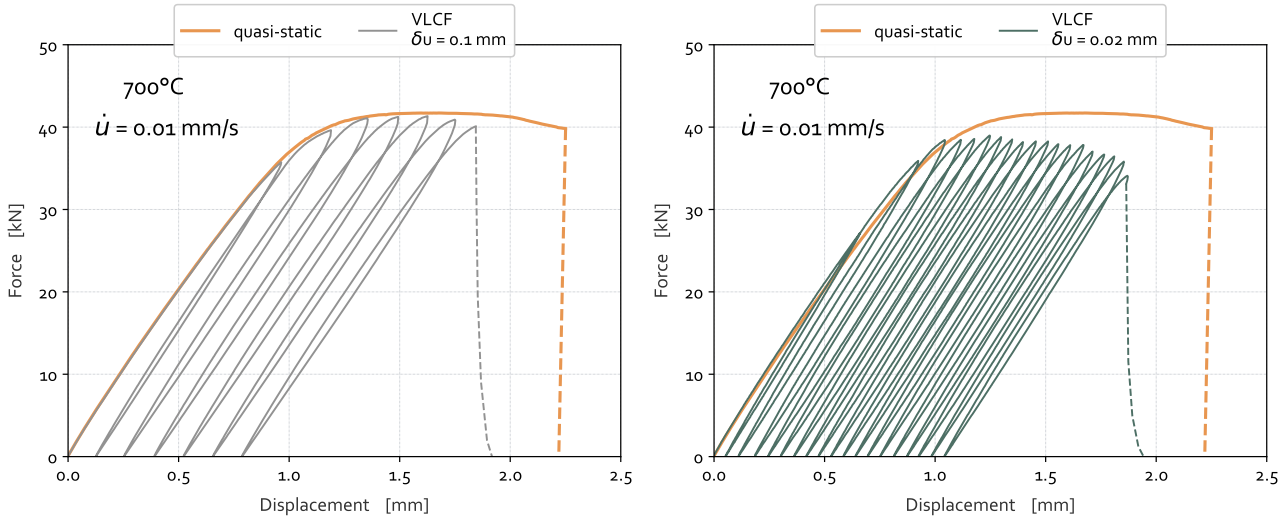

(a) VLCF tensile response for the FN2-5 specimen.

(b) VLCF tensile response for the FN2-2 specimen.

Figure 3.37: Test responses for the FN2 specimen under VLCF tensile loading conditions at 700°C (spec. FN2-5 & 2).

Decreasing the deviation from the linear slope up to $\delta U = 0.02\,\text{mm}$ resulted in an increased number of loading cycles up to 19, see Fig. 3.37b. The macroscopic response is still fairly well contained below the stress-strain monotonic envelope, but with a lower extent of work-hardening. Comparing Fig. 3.37a & Fig. 3.37b, the strain at failure can be seen to be close, no matter the chosen linear deviation δU.

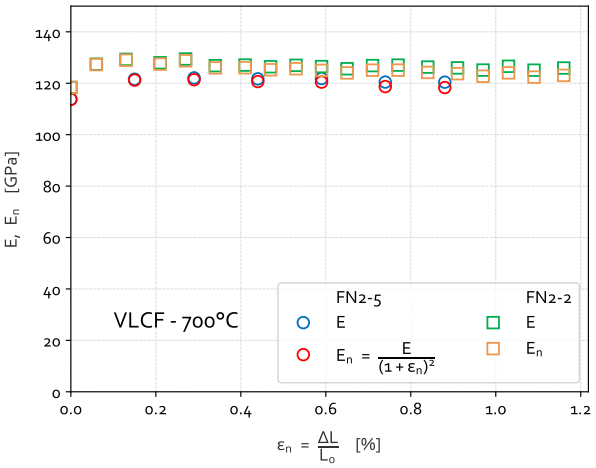

Figure 3.38: Elastic modulus evolution in FN2 subjected to VLCF loading conditions at 700°C.

An important point needs to be recalled: the slope of the linear curve is not updated upon testing. This means that the slope is always the same, which does not account for possible decrease with damage and/or specimen elongation. Such a point may lead to inaccurate estimates of the U_{max} value. However, as reported in Fig. 3.38, no clear evolution of the true stiffness is noticeable, hence suggesting the absence of damage on the elastic response of the material bur rather a damaging process associated with plasticity. Moreover, since the response is not so ductile, there is no significant difference between true and nominal measures associated with the reduction of cross-section.
A possible improvement of the testing procedure, although tricky, might rely on a continuous updating of the elastic slope, hence resulting in better estimates for the U_{max} value and consequently to an improved predictive capability of the method. A repeatability of the tests would be necessary to improve the testing procedure and thus draw more accurate conclusions. Nevertheless, it is to be recalled that the purpose of the present work was not to assess the scattering of the material behavior but to evidence the main failure (or damage) mechanisms related to crack propagation under various loading conditions.

3.2.2.2 Micro-graphic observations of the fracture surfaces

Fractographic observations of the VLCF testing specimens have been carried out at ONERA using a Mira3 Tescan scanning electron microscope. Such observations provide data about the rupture mechanisms within the material at the microstructural scale. On the considered FN2 specimen, the stress state at failure is supposed to be non-homogeneous on the whole fracture surface. Thus, by looking at the shape and size of the fracture features (rivers, cavities, dimples...), one can check which mechanism is dominant between shear and tension.

In Fig. 3.39, a typical reconstruction of the whole fracture surface of the FN2-2 specimen subjected to VLCF loading is given. Some observation zones with various magnitude are evidenced on it. Shear lips associated with slant zones are noticeable, particularly in *zones 2-4*. A chevron-shaped fracture surface is evidenced, as already demonstrated for the monotonic case, see Fig. E.13. In Fig. 3.40a, in the slant area of the *zone 5*, some porosities (indicated by red arrows) are visible in a transgranular-like pattern. In opposition, the Fig. 3.40b evidences two zones: the lower part consisting in some voids and transgranular features while the upper one reflects more intergranular

features. The close-up view on the *zone 3* given in Fig. 3.40c evidences a similar topographic aspect. Some secondary cracks are apparent but no distinct cavities.

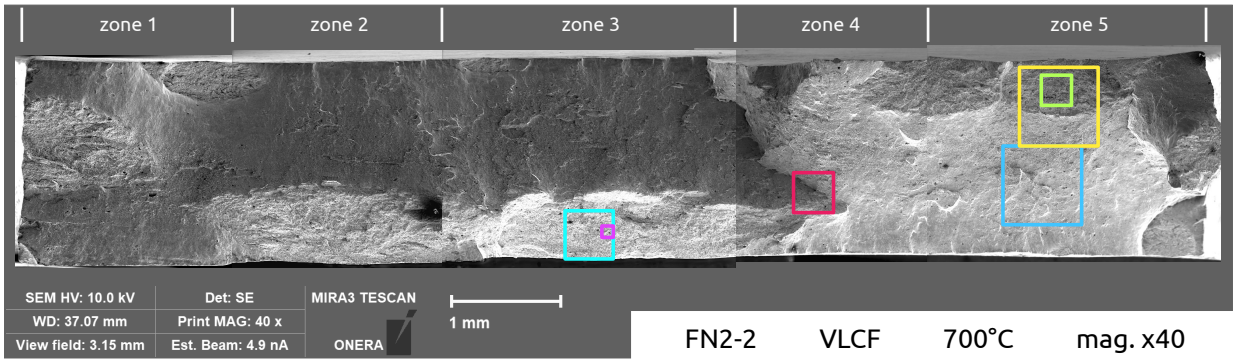

Figure 3.39: Assembly of successive SEM views of the fracture surface for the spec. FN2-2 subjected to VLCF loading conditions at 700°C with $\dot{U} = 0.01\,\text{mm.s}^{-1}$.

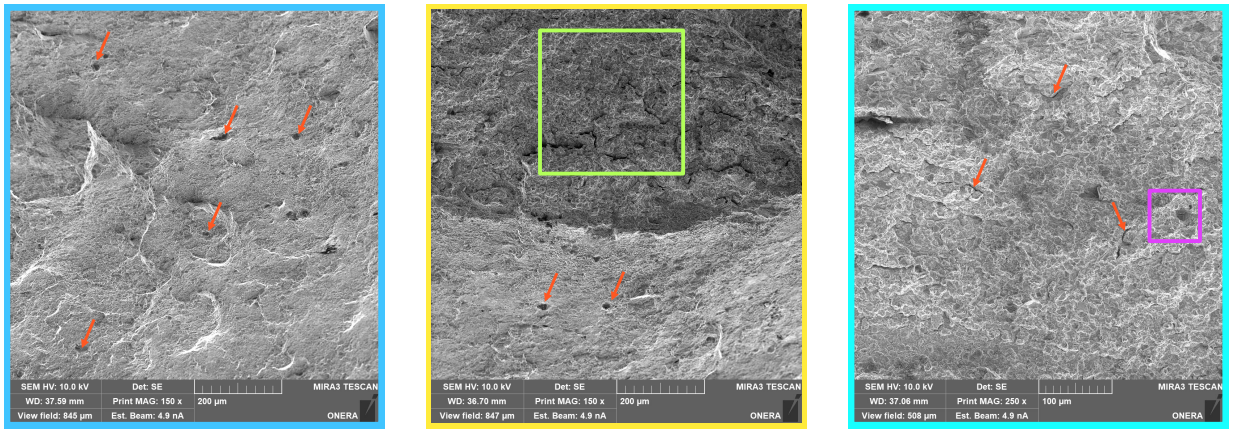

(a) FN2-2 - zone 5-1 - mag. ×150. (b) FN2-2 - zone 5-2 - mag. ×150. (c) FN2-2 - zone 3-1 - mag. ×250.

Figure 3.40: SEM fracture surface analyses for the FN2-2 specimen subjected to VLCF loading at 700°C ($\dot{U} = 0.01\,\text{mm.s}^{-1}$). Identification of the main cracking mechanisms.

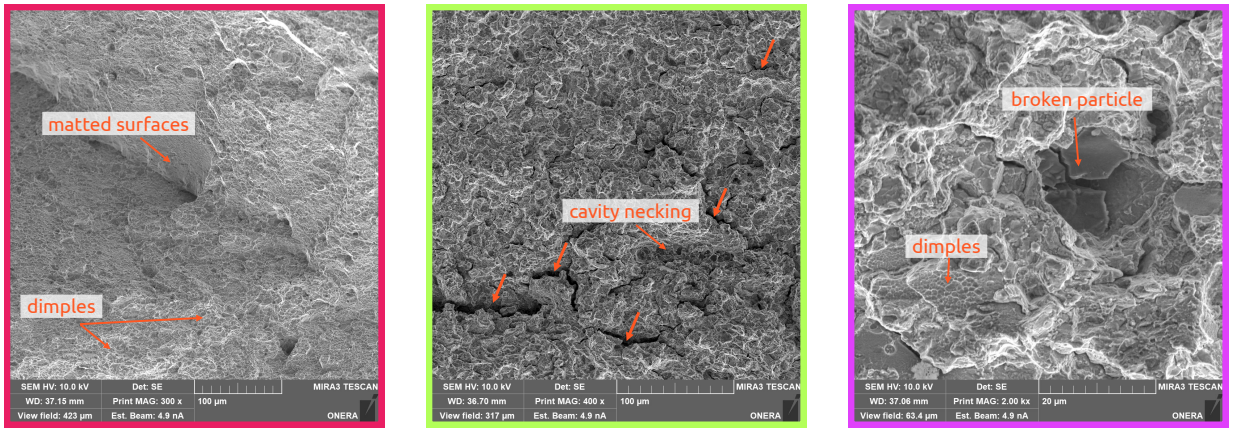

(a) FN2-2 - zone 4 - mag. ×300. (b) FN2-2 - zone 5-3 - mag. ×400. (c) FN2-2 - zone 3-2 - mag. ×2000.

Figure 3.41: SEM fracture surface analyses for the FN2-2 specimen subjected to VLCF loading at 700°C ($\dot{U} = 0.01\,\text{mm.s}^{-1}$). Identification of the main cracking mechanisms.

The analysis in Fig. 3.41a of the *zone 4* reveals some thin dimples as well with some matted surfaces probably due to halves specimen friction. The close-up view given in Fig. 3.41b evidences some secondary cracking, typical of intergranular mode, as well with some cavity necking. In Fig. 3.41c some small dimples are noticeable, in a really fine length scale while a broken particle is clearly noticeable. The fracture surface exhibits mixed fracture modes with both inter- and transgranular attributes, hence differing from the monotonic case (see Fig. E.15 in the appendices). The occurrence of broken particles and small cavities & dimples also evidences the presence of plasticity-related ductile mechanisms.

3.3 Conclusion of the chapter

In the present chapter, low-cycle fatigue and dwell-fatigue crack growth processes in fine-grained AD730™ at 20, 550 and 700°C have been investigated. Using SEN-T specimens subjected to sinusoidal and trapezoidal waveforms with varying loading conditions (in terms of extrinsic parameters: temperature, load ratio, dwell times, tensile/compressive hold...), fracture crack propagation tests have been performed. Macroscopic data completed with both mesoscopic and microscopic observations highlighted the main governing mechanisms and evidenced some crack propagation peculiarities. The smaller scale has enabled to identify the main fracture modes.
The same work has been further performed on flat notched specimens in order to assess the ductile capabilities of the material under very low-cycle fatigue (VLCF) conditions. Macroscopic data and fractographic observations have been considered in order to assess the crack growth behavior of AD730™ at 700°C under VLCF loading scheme.
To perform all these tests, dedicated testing benches and specific testing procedures have been developed. In addition, specific instrumentation such as a DCPD technique for crack growth monitoring or a camera for DIC purposes has been used.

Ni-based superalloys are known to be prone to crack front peculiarities including flat-to-slant transition and crack front tunneling effect. Up to now and thanks to the experimental work, these two aspects, including crack front tortuosities, have been evidenced in AD730™ under various loading conditions. Some differences seem to have arisen from the loading mode. However, the underlying mechanisms responsible for such effects are still not clear at the moment and deserve further investigation. Based on the literature review and the overall observations, closure-induced crack tunneling effect is assumed to trigger shear lips development along the crack path and favoring crack twisting. This aspect results in greater crack growth rates at the core of the material compared to its free surfaces.

Fracture modes for the fatigued and dwell-fatigued specimens have been studied thanks to SEM observations. Mixed cracking modes have been evidenced with both transgranular and intergranular features, the latter being related to grain boundary and precipitates interface decohesion. Specimens subjected to pure fatigue loading have exhibited a great extent of transgranular cracking mode whereas dwell-fatigued specimens were more susceptible to develop intergranular patterns. Temperature effect on time-related processes seem to have been triggered for a temperature above

550°C. This aspect was reported to be in accordance with the material mechanical response which has been proven to significantly change between 550 and 700°C.
Under VLCF loading conditions, the fracture process generally involves a mixed mode of crack growth with both tensile and shear stresses. The occurrence of shear lip(s) has been attributed to plane stress conditions at the free surfaces of the samples. Moreover, shear-dominated failure mode at 45° prevailed for the considered FN2 specimen.

The fracture process, not so ductile for the studied specimen geometry, needs to be related to some plastic instabilities associated with the localization of the plastic deformation within specific bands. Such a localization process, well known for thin sheets ductile tearing problems, is generally assumed to be responsible for the premature failure of the specimens [Besson, 2010], [Chen et al., 2022]. Due to high temperature testing (hence leading to the lack of adherence of the speckle to the specimen surface), the supposedly localization of the deformations as well with the brutality of the crack propagation, DIC process was not able to neither assess crack initiation locus in an accurate manner, nor to monitor the crack propagation stage through the whole specimen. However, due to the specimen geometry, crack initiation was assumed to occur at the notch roots.

Micro-graphic observations on flat specimens have evidenced the presence of dimples, cavities and quasi-cleavage facets. This suggests the occurrence of some ductile damaging mechanisms including matrix-particle and inclusion decohesion processes. Monotonic loading scheme has been proved to favor a ductile-like fracture pattern with voids and dimples whereas the VLCF signal seems to lead to mixed fracture modes with a mixture of intergranular and transgranular characteristics including secondary micro-cracking and dimples, respectively.

As a matter of fact, in order to assess as accurately as possible the fracture mechanisms, further SEM observations need to be considered. Such a task remains an outlook of the present study. Moreover, repeatability of each test still needs to be considered for the previous statements to be confirmed. The main conclusions related to the ductile fracture process can, to some extent, be considered valid.

In the context of the *local approach to fracture* which aims at relating the material behavior to some damage mechanisms, it can be concluded that material failure under complex loading schemes rely on several governing mechanisms. These mechanisms may intervene alone or simultaneously, depending on the loading schemes. In particular, one can mention the occurrence of *i)* transgranular cracking associated with LCF loading with moderate plastic yielding, *ii)* intergranular cracking generally occurring at elevated temperatures under holding-times, *iii)* ductile cracking under quasi-static monotonic tensile and VLCF loading conditions under higher plastic strain levels.
These mechanisms, though microstructurally and mechanically different, can be embedded in a phenomenological material model thanks to appropriate coupling, in order to make the material mechanical response dependent on the damaging effects. That is the purpose of the next chapter.

Résumé du chapitre en français

Dans ce chapitre, la réponse en fissuration de l'AD730™ à grains fins a été étudiée à plusieurs températures (20, 550 et 700°C). D'une part, des éprouvettes type SEN-T ont été utilisées pour étudier la propagation de fissure en fatigue et fatigue-fluage. Les paramètres extrinsèques des essais ont été modifiés afin d'étudier la ténacité du matériau pour des rapports de charge ou temps de maintien variables. D'autre part, des essais monotones et de fatigue à très faible nombre de cycles ont également été réalisés sur des éprouvettes plates à géométries variables. Pour tous ces tests, des bancs d'essais spécifiques ont été utilisés, alliant ainsi la méthode de la chute du potentiel électrique pour suivre l'avancée de fissure sous chargements cycliques, et une caméra pour réaliser de la corrélation d'images numériques sur mouchetis peints.
Pour l'analyse des essais, trois échelles ont été considérées. Les résultats macroscopiques ont d'abord été analysés, puis mis au regard des analyses à une échelle plus mésoscopique. A celle-ci, les faciès de rupture et l'analyse topographique du plan de fissuration ont été extraits et étudiés. Enfin, des observations au Microscope Electronique à Balayage (MEB) ont été réalisées afin de visualiser la topologie de la surface de rupture et identifier les mécanismes pilotant la propagation.
Pour les essais en fatigue pure, les faciès de rupture des éprouvettes révèlent un front de fissure relativement droit avec l'apparition de lèvres de cisaillement à mesure que la fissure croît. Le déversement se fait de manière systématique et de façon anti-symétrique par rapport au plan moyen de l'éprouvette. Un mode de propagation principalement transgranulaire a été mis en évidence à 20 et 550°C. Des mécanismes intergranulaires apparaissent néanmoins à 700°C via l'apparition d'effets thermiquement activés. Des stries de fatigue sont visibles à une échelle sub-granulaire, ce qui confirme le caractère transgranulaire en fatigue. En fatigue-fluage, le front de fissure apparaît courbé, traduisant alors la présence d'effet tunnel avec un différentiel de croissance de fissure le long du front de propagation. La propagation est majoritairement intergranulaire, et ce, en raison des temps de maintien en traction qui favorisent les processus d'oxydation et de fluage. Ce dernier, généralement associé à la décohésion au niveau des joints de grains ou à l'interface avec des précipités, semble opérer de par la présence de fissures secondaires.
En monotone, les essais sur éprouvette plate manifestent une rupture brutale de l'échantillon. Les essais, pilotés en effort, témoignent d'une absence de ductilité macroscopique du matériau, la rupture étant relativement rapide une fois le régime non-linéaire atteint. Les surfaces de rupture témoignent d'une mixité dans les modes de rupture avec l'apparition de lèvres de cisaillement en mode *I*. En fatigue à très faible nombre de cycles, les constats sont globalement identiques. La rupture brutale semble être associée à la présence d'instabilités plastiques dans le matériau, comme par exemple l'apparition de bandes de localisation de la déformation. La présence de cupules sur les faciès de rupture témoignent néanmoins d'un mécanisme de rupture ductile associé à une plasticité importante.
Dans le cadre de cette étude associée à l'utilisation de l'approche locale de la rupture pour simuler la propagation d'une fissure en fatigue, la présence de mécanismes d'endommagement de natures différentes semble être confirmée par cette analyse, certes partielle, mais qualitative. La rupture mixte trans- et intergranulaire en régime cyclique associée à des mécanismes de rupture ductile en fatigue à très faible nombre de cycles (pour la pointe de fissure très sollicitée) semblent tous deux définir les mécanismes d'endommagement pilotant la fissuration sous chargements complexes.

4 A local approach to fracture for fatigue crack propagation

This chapter is devoted to the development of a time-incremental damage model dedicated to fatigue crack propagation modeling. Such a model relies on the strong coupling between the damaging mechanisms and the mechanical behavior of the constitutive material. A multi-mechanism damage model is established considering the damage effects evidenced thanks to the experimental work carried on cyclic and monotonic crack growth specimens. To this end, the Continuum Damage Mechanics framework is used in association with the material model derived in the Chap. 2. Such a method is related to the so-called "local approach to fracture", allowing the assessment of structural failure in numerical simulations. Once derived, the fully coupled constitutive equations relating the elastic-viscoplastic material behavior of the material to its damage mechanisms is implemented within a FE subroutine. The implicit integration procedure at the integration point level is detailed prior to the assessment of the capabilities of the damage model .

Contents

In the last Chap. 3, fatigue, dwell-fatigue, monotonic and very low-cycle fatigue (VLCF) crack propagation analyses have been conducted. Such a work has highlighted the main crack growth mechanisms through multi-scale observations. As a consequence, the phenomenological introduction of damage mechanisms within the constitutive model derived in the Chap. 2 allows to model the crack growth process.

4.1 A time-incremental fatigue damage model for AD730™

As seen in the literature review, sect. 1.4, the local approach to fracture has known a great success in predicting brittle and ductile fracture over the last three decades. Nonetheless, such a method has been less investigated in the context of fatigue crack growth. Nowadays, computational performances together with the maturity of the FE method allow considering such an approach for fatigue crack advance analysis within non-linear media. In this section, a fatigue damage model of phenomenological- and incremental-type is proposed to cope with the fatigue crack growth concern in structural calculations. The properties of the model, in accordance with the target application for the research project, as well as the main assumptions leading to the constitutive equations are described.

4.1.1 Expected properties of the damage model

In this part, it seems important to present the main assumptions that made the skeleton of the model developed along the Ph.D. project. In order to clearly define the scope of the proposed fatigue damage model, its main properties are described.

Local approach to fracture

Fatigue crack growth in engineering fracture problems is generally split into *i)* micro-crack initiation and *ii)* macro-crack propagation. In the present Ph.D. project, we focus our analysis in the modeling of the crack growth stage. Thus, the proposed fatigue damage model is not intended to simulate the crack initiation process but only the subsequent propagation of a long crack, starting from a sufficiently long pre-crack.

As indicated in sub-sect. 1.1.3, a long fatigue crack is considered to be insensitive to the material microstructure and to have a greater length compared to the size of the plastic zone. A length greater than 500 µm can hence be assimilated to such long crack [Suresh, 1998].
In this study, the fatigue crack growth will be computed thanks to a damaged-based modeling (through a local approach) rather than a Fracture Mechanics model (global approach). The damage accumulation in the so-called *fracture process zone* (FPZ) at the crack-tip will be responsible for the stress-softening, and then, the material degradation will, in turn, enable the crack propagation, see Fig. 4.1. In the present formulation, it is assumed that damage is fully coupled to the behavior of the material, allowing the crack to propagate by itself taking into account the redistribution of the mechanical fields along the crack path. Such a calculation scheme needs some computational effort due to the step-by-step calculation of the stresses, strains and damage along the whole lifetime of the structure.

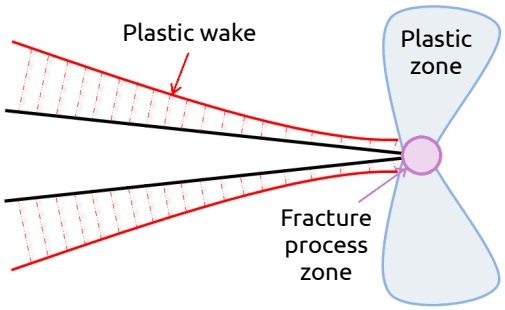

Figure 4.1: Cyclic process zone.

Time incremental approach

Loading sequences experienced by gas turbine components are complex, multiaxial and generally anisothermal, see Fig. 4.2. They are usually difficult to model and the resulting damage is generally misestimated since the use of cycle-counting methods, such as the well-known *Rainflow algorithm*, is required [Downing and Socie, 1982], [Bathias and Pineau, 2010] and leads to some approximations.
An overcoming method relies on the use of *time incremental* formulations which allow to follow the loading spectrum along its whole path without pre-defining a given loading cycle. In the present work, the choice has been made to consider a kinetic law in order to relate the fatigue damage rate $\dot{D}_f$ to current values of the stress tensor and accumulated plastic strain rate $\dot{p}$. The local approach proposed here is the most convenient framework to develop a time incremental model. Inelastic constitutive equations and damage evolution rule are hence fully coupled and both written in a time-dependent formalism in order to solve the whole problem at each time step in a unified manner. The time incremental formalism has already been considered for the modeling of LCF in metallic alloys [Lemaitre and Chaboche, 1990], specifically for fatigue crack initiation [Otin, 2007], [Barbier, 2009], [Kaminski, 2007], but fewer works have been dedicated to the modeling of fatigue crack propagation [Hamon, 2010].

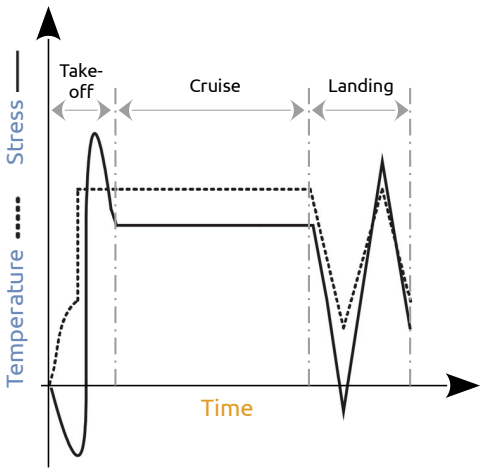

Figure 4.2: Complex loading cycles (adapted from [Rodriguez and Bhanu Sankara Rao, 1993]).

A phenomenological-type fatigue damage model

The material model derived in sect. 2.3 has been written in the framework of the unified viscoplasticity theory [Chaboche, 1986]. Such a cyclic material model was written according to a single potential describing both plastic and viscoplastic strains, hence allowing both time-independent (plastic) and time-dependent (*e.g.* creep) processes to be accounted for in a unified manner (see sub-sect. 1.2.1 on this point). The proposed material damage model belongs to the class of phenomenological models (as opposed to the micromechanical or crystallographic models). Established through a thermodynamically consistent approach using the local state method [Germain, 1973], such a model enables the possibility to take into account the stress triaxiality effects into the damage evolution [Lemaitre, 1985a], [Pandey et al., 2021].

The richness of the phenomenological models lies in the choice of the formulation of different state and dissipative potentials. Such a choice is somewhat heuristic and based on the knowledge one may have on the various phenomena, their evolution, their mutual interactions and possible couplings. This leads to predictive models valid on a specified domain defined by experimental data bases used for the proper identification. The derivation of the thermodynamics potentials will be discussed in the forthcoming sub-sect. 4.1.2.

Isotropic properties of both behavior and damage

The nature of the damage(s) variable(s) (scalar, vector, tensor...) still remains an open question since it directly depends on the underlying mechanisms governing the damage growth and its effect on material properties. For materials subjected to complex loading conditions (as in the present study), the direct measurement of damage is, if possible, a difficult task.
In the present work, for the sake of simplicity, isotropic properties are considered. Indeed, the purpose of the Ph.D. project consists in a first attempt to the crack growth modeling using such a local approach to fracture. Owing to the other underlying aspects to be faced for both the modeling and numerical tasks (discussed later on), I have chosen in the modeling to consider only isotropic variables. Indeed, the fatigue damage model has to be relevant without unnecessary complexities, at least in this primary study. Thus, in the following, the damage variable(s) will be of scalar-type in order to ease the material model numerical implementation.

A modular damage model

Apart from fatigue damage, material may be subjected to other degradation mechanisms. Such a point has been discussed in sect. 3.3. The present material model is hence expected to account for additional damage variables in order to encompass other plasticity- and time-dependent degradation processes. Such a point will be discussed later on in the sect. 4.2.
In addition, stress triaxiality levels has been proved to play a significant role in determining the fatigue life of a component [Pandey et al., 2021]. The stress triaxiality $T_X = \frac{\sigma_h}{\sigma_{eq}}$ (where $\sigma_h = \sigma_{ii}/3$ is the hydrostatic stress and $\sigma_{eq} = \sqrt{\frac{3}{2}\,\sigma_{ij}^D \sigma_{ij}^D}$ the equivalent Von Mises stress) should thus be incorporated in the damage law, as suggested in some strain-based fatigue damage models [Lemaitre and Plumtree, 1979], [Dufailly and Lemaitre, 1995], [Wang and Zhang, 2015].

4.1.2 State laws and effective variables

Considering crack propagation under LCF conditions, *i.e.* with sufficiently high plastic dissipation, the CDM framework is well adapted for fatigue damage evaluation [Lemaitre et al., 1999]. This is particularly true in the vicinity of the crack-tip where the material behavior is non-linear. As a result, (visco)plasticity and fatigue damage mechanisms involve large volumes at the mesoscale (RVE) and CDM can be used to model the local loss of stiffness [Lemaitre, 1985b], [Benallal et al., 1991].

State variables and effective variables

Since the constitutive equations of the Chap. 2 have been written using a consistent thermodynamics framework, the same applies for the fatigue damage model [Lemaitre et al., 2009].
The choice for the external variables is generally trivial because they are the ones from which the laws of conservation are derived. The choice for the internal variables is more tricky and is highly dependent on the physical phenomena to be accounted in the modeling process. The defined processes will be thermodynamically admissible, if, at each moment of the evolution, the *Clausius-Duhem Inequality* (CDI) is satisfied. More details about thermodynamics can be found in [Lemaitre and Desmorat, 2005].

For dissipative phenomena, the internal state variables are representative of the history of the system. The developed damage model dedicated to fatigue crack growth analysis hence encompass the following state variables, Tab. 4.1, in accordance with the material model calibrated in Chap. 2. Hence, each physical phenomenon is described by a set of: one state variable $\mathbf{a}_j$ in the strain space with its dual variable $\mathbf{A}_j$ in the stress space (seen as a conjugated force).

Mechanism	Internal variables	Conjugated variables
Elasticity	$\underset{\sim}{\varepsilon}^e$	$\underset{\sim}{\sigma}$
(Visco)Plasticity	$\underset{\sim}{\varepsilon}^{in}$	$-\underset{\sim}{\sigma}$
Kinematic hardening	$\underset{\sim}{\alpha}^k$	$\underset{\sim}{X}^k$
Isotropic hardening	r^i	R^i
Isotropic fatigue damage	D_f	$-Y_f$

Table 4.1: State variables and associated mechanisms for elastic-viscoplasticity and damage.

Accordingly to the calibration process performed in sect. 2.4, k refers to the k-th component of the total back stress tensor $\underset{\sim}{X}$ ($k \in [1-3]$) while i refers to the i-th component of the drag stress R ($i \in [1,2]$). Each component is associated with one internal variable.
It can also be precised that the "$-$" sign for the stress tensor $\underset{\sim}{\sigma}$ for plasticity modeling comes from the dissipative properties associated with plastic work. This is also the case for damage which is undoubtedly a dissipative process (Y_f being the energy release rate related to fatigue damage). On the contrary, work-hardening is considered as stored energy.

In the present study, choice has been made to rely on the *principle of strain equivalence* for the mapping between the virgin and damaged RVE [Lemaitre and Chaboche, 1978]. Such a choice mainly comes from simplicity and ease in numerical implementation [Egner et al., 2020]. Moreover, when isotropic damage is considered, which is the case here, the strain equivalence has been proved to be very efficient for behavior-damage coupling [Reckwerth and Tsakmakis, 2003]. Details on equivalence principles can be found in sub-sect. 1.4.2.

According to the strain equivalence hypothesis, all the stress-like variables should be written in the effective configuration, leading to the following effective stresses:

$$\underset{\sim}{\tilde{\sigma}} = \frac{\underset{\sim}{\sigma}}{f^e(D_f)}\,; \qquad \underset{\sim}{\tilde{X}}^k = \frac{\underset{\sim}{X}^k}{f^k(D_f)}\,; \qquad \tilde{R}^i = \frac{R^i}{f^i(D_f)} \tag{4.1}$$

where each stress-like variable possesses its own softening function defined hereafter.
In eq. (4.1), choice has been made to set a full coupling between the stress-like variables and damage. Following the effective stress concept and considering that damage growth should make the stress tend to zero, it seems physically acceptable to make the strain-hardening altered by damage [Saanouni et al., 1994], [Besson et al., 2010].

Softening functions

The chosen softening functions $f^*(D_f)$ (where "*" stands for "e", "k" or "i") must fulfill the following conditions [Dimitrijević and Hackl, 2008], [Brepols, 2018]:

- $f^*(D_f)$ should be continuous, at least twice-differentiable, positive and scalar-valued on $[0, D^{crit}]$;
- $f^*(0) = 1$ (virgin state) and $\lim_{D_f \to \infty} f^*(D_f) \simeq 0$ (broken state);
- f^* should be strictly decreasing on $[0, D^{crit}]$ (softening effect), *i.e.* : $f^{*\prime} < 0 \ \forall D_f \in [0, D^{crit}]$.

where D^{crit} represents a critical damage state for which the RVE is considered broken.
In the present case, the following exponential decaying damage effect function has been included in the model:

$$f^*(D_f) = \exp\left(-\beta_* \eta_D D_f\right) \tag{4.2}$$

where "*" in β_* of eq. (4.2) still stands for "e", "k" or "i" and enables coupling/decoupling properties between damage and stress variables. In case $\beta_* = 1$ there is a coupling between damage and stress component, while if $\beta_* = 0$, there is no coupling.
The choice of the exponential damage effect function in eq. (4.2) has already been made in the work of [Kaminski, 2007], [Yin et al., 2022] for fatigue crack initiation prediction, or in [Murakami and Liu, 1995], [Dimitrijević and Hackl, 2008] for general applications. It comes from this formulation the (theoretical) absence of critical value for D_f which may lead to numerical issues once getting closer to 1 (compared to the standard "$(1 - D_f)$" Lemaitre formulation). Indeed, the form given in eq. (4.2) approaches the state of complete damage in an asymptotic manner. This represents the advantage that the actual damage variable can take any value in $\mathbb{R}_0^+$ and therefore it is not necessary to algorithmically restrict this variable to the interval $[0, 1[$ as for the linear case.

Another interesting feature of the exponential form comes from the introduction of the exponential rate parameter η_D which allows for a weighting influence of damage on various physical mechanisms, *e.g.* the deviatoric and volumetric contributions of the strains, or the various strain-hardening as opposed to elasticity. A greater flexibility can also be gained thanks to the addition of a damage threshold parameter that may trigger the damage accumulation (not implemented in the present work), for details, see [Ostwald et al., 2019].

Remark: As a last point to be noticed, the exponential softening function, already used for creep crack growth prediction, is known to ease the mesh-independence of the numerical results thanks to the work of [Murakami and Liu, 1995]. This point will be discussed later on in Chap. 5.

State potentials and state relations

The *Generalized Standard Materials* (GSM) cover a number of inelastic material behaviors and hence constitute a robust modeling framework for the present study [Halphen and Nguyen, 1975]. The evolution of internal variables is governed by two potentials: the free energy and the dissipation potential [Hackl and Fischer, 2008]. The state variables given in Tab. 4.1 are sufficient to define the equilibrium state of the system (material) through the knowledge of a thermodynamic state potential (or free energy functional): the Helmholtz free energy. Such a potential is a convex function of the state variables and allows the thermodynamic forces associated with the state variables to be fully defined, thanks to the Coleman-Noll relations [Coleman and Noll, 1963].

Following the work of [Lemaitre et al., 2009] and [Bonora, 1997], the free energy is split into both elastic and inelastic contributions, thus implying that the elastic properties are not influenced by the plastic flow but only by damage:

$$\rho\psi\left(\underset{\sim}{\varepsilon}^e, \underset{\sim}{\alpha}^k, r^i, D_f\right) = \rho\psi_e\left(\underset{\sim}{\varepsilon}^e, D_f\right) + \sum_k \rho\psi_{in}^k\left(\underset{\sim}{\alpha}^k, D_f\right) + \sum_i \rho\psi_{in}^i\left(r^i, D_f\right) \tag{4.3}$$

and where a state decoupling exists between the two hardening mechanisms.
In eq. (4.3), each contribution is given by:

$$\rho\psi_e\left(\underset{\sim}{\varepsilon}^e, D_f\right) = \frac{1}{2}\,\underset{\sim}{\varepsilon}^e : f^e(D_f)\,\underset{\approx}{\Lambda} : \underset{\sim}{\varepsilon}^e = \frac{1}{2}\,\underset{\sim}{\varepsilon}^e : \underset{\approx}{\tilde{\Lambda}} : \underset{\sim}{\varepsilon}^e \tag{4.4}$$

$$\rho\psi_{in}^k\left(\underset{\sim}{\alpha}^k, D_f\right) = \sum_{k=1}^{3} \frac{1}{2}\,\underset{\sim}{\alpha}^k : f^k(D_f)\,\underset{\approx}{C}^k : \underset{\sim}{\alpha}^k = \sum_{k=1}^{3} \frac{1}{2}\,\underset{\sim}{\alpha}^k : \underset{\approx}{\tilde{C}}^k : \underset{\sim}{\alpha}^k \tag{4.5}$$

$$\rho\psi_{in}^i\left(r^i, D_f\right) = \sum_{i=1}^{2} \frac{1}{2}\, f^i(D_f)\, b^i\, Q^i {r^i}^2 = \sum_{i=1}^{2} \frac{1}{2}\, b^i\, \tilde{Q}^i {r^i}^2 \tag{4.6}$$

where $\underset{\approx}{\Lambda}$, $\underset{\approx}{C}^k$ and Q^i correspond to the moduli associated with elastic behavior, the k^{th} kinematic hardening and the i^{th} isotropic hardening, respectively. The tensor $\underset{\approx}{\Lambda}$ is given by:

$$\underset{\approx}{\Lambda} = \lambda_e\, \underset{\sim}{1} \otimes \underset{\sim}{1} + 2\,\mu_e\, \underset{\approx}{I}^s = \frac{\nu E}{(1+\nu)(1-2\nu)}\, \underset{\sim}{1} \otimes \underset{\sim}{1} + \frac{E}{2(1+\nu)}\, \underset{\approx}{I}^s \tag{4.7}$$

with λ_e & μ_e the Lame's coefficients for elasticity.
The second, assuming a pure deviatoric kinematic strain-hardening, is given by:

$$\underset{\approx}{C}^k = \frac{2}{3} C^k \underset{\approx}{P}^D \tag{4.8}$$

with C^k the modulus for the k-component of the back-stress and $\underset{\approx}{P}^D$ the 4$^{\text{th}}$-order deviatoric projector defined thanks to the 4$^{\text{th}}$-order hydrostatic projector:

$$\underset{\approx}{P}^S = \frac{1}{3}\left(\underset{\sim}{1} \otimes \underset{\sim}{1}\right) \qquad \leftrightarrow \qquad \underset{\approx}{P}^D = \underset{\approx}{I} - \underset{\approx}{P}^S \tag{4.9}$$

One can remark in eq. (4.3) - eq. (4.6) the presence of the softening functions $f^*(D_f)$ which define the coupling between the behavior of the material and damage. Effective moduli are given by:

$$\underset{\approx}{\tilde{\Lambda}} = f^e(D_f)\,\underset{\approx}{\Lambda} \qquad \underset{\approx}{\tilde{C}}^k = f^k(D_f)\,\underset{\approx}{C}^k \qquad \tilde{Q}^i = f^i(D_f)\,Q^i \tag{4.10}$$

In eq. (4.5) & eq. (4.6) choice has been made to relate the fatigue damage and the plastic hardening of the material, as done in *e.g.* [Billardon and Moret-Bailly, 1987], [Saanouni et al., 1994].

Thanks to the effective moduli defined in eq. (4.10), the effective variables can be redefined:

$$\underset{\sim}{\tilde{\sigma}} = \underset{\approx}{\Lambda} : \underset{\approx}{\tilde{\Lambda}}^{-1} : \underset{\sim}{\sigma} \qquad \underset{\sim}{\tilde{X}}^k = \underset{\approx}{C}^k : \underset{\approx}{\tilde{C}}^{k-1} : \underset{\sim}{X}^k \qquad \tilde{R}^i = Q^i\,\tilde{Q}^{i-1}\,R^i \tag{4.11}$$

According to the Clausius-Duhem inequality and the Coleman postulate [Coleman and Noll, 1963], [Truesdell, 1969], the associated thermodynamic forces related with the internal variables can be derived from the state potential eq. (4.3) as:

$$\underset{\sim}{\sigma} = \rho\frac{\partial \psi}{\partial \underset{\sim}{\varepsilon}^e} = \rho\frac{\partial \psi_e}{\partial \underset{\sim}{\varepsilon}^e} = f^e(D_f)\,\underset{\approx}{\Lambda} : \underset{\sim}{\varepsilon}^e = \underset{\approx}{\tilde{\Lambda}} : \underset{\sim}{\varepsilon}^e \tag{4.12}$$

$$\underset{\sim}{X}^k = \rho\frac{\partial \psi}{\partial \underset{\sim}{\alpha}^k} = \rho\frac{\partial \psi^k_{in}}{\partial \underset{\sim}{\alpha}^k} = f^k(D_f)\,\underset{\approx}{C}^k : \underset{\sim}{\alpha}^k = \underset{\approx}{\tilde{C}}^k : \underset{\sim}{\alpha}^k \tag{4.13}$$

$$R^i = \rho\frac{\partial \psi}{\partial r^i} = \rho\frac{\partial \psi^i_{in}}{\partial r^i} = f^i(D_f)\,b^i\,Q^i r^i = b^i \tilde{Q}^i r^i \tag{4.14}$$

The energy release rate associated with fatigue damage is given by:

$$Y_f = -\rho\frac{\partial \psi}{\partial D_f} = -\rho\frac{\partial\left(\psi_e + \sum_k \psi^k_{in} + \sum_i \psi^i_{in}\right)}{\partial D_f} = Y^e_f + \kappa_X \sum_k Y^k_f + \kappa_R \sum_i Y^i_f \tag{4.15}$$

with:

$$Y^e_f = -\rho\frac{\partial \psi_e}{\partial D_f} = -\frac{1}{2}\,\underset{\sim}{\varepsilon}^e : \frac{\partial f^e(D_f)}{\partial D_f}\,\underset{\approx}{\Lambda} : \underset{\sim}{\varepsilon}^e = -\frac{1}{2}\,\underset{\sim}{\varepsilon}^e : f^{e\,\prime}(D_f)\,\underset{\approx}{\Lambda} : \underset{\sim}{\varepsilon}^e \tag{4.16}$$

$$Y^k_f = -\rho\frac{\partial \psi^k_{in}}{\partial D_f} = -\frac{1}{2}\,\underset{\sim}{\alpha}^k : \frac{\partial f^k(D_f)}{\partial D_f}\,\underset{\approx}{C}^k : \underset{\sim}{\alpha}^k = -\frac{1}{2}\,\underset{\sim}{\alpha}^k : f^{k\,\prime}(D_f)\,\underset{\approx}{C}^k : \underset{\sim}{\alpha}^k \tag{4.17}$$

$$Y_f^i = -\rho \frac{\partial \psi_{in}^i}{\partial D_f} = -\frac{1}{2} \frac{\partial f^i(D_f)}{\partial D_f} b^i Q^i r^{i2} = -\frac{1}{2} f^{i\prime}(D_f) b^i Q^i r^{i2} \tag{4.18}$$

where κ_X and κ_R in eq. (4.15) are introduced to account or not for the inelastic contributions to the energy release rate in case of state decoupling between damage and work-hardening variables.

One can notice in eq. (4.15) the presence of two distinctive fatigue mechanisms:

- an elastic free energy contribution given in eq. (4.16) which, in the absence of plastic strains, drives the fatigue crack growth in the HCF regime;
- and inelastic terms given by eq. (4.17) & eq. (4.18) which corresponds to plastic energy (free and dissipated) associated with kinematic and isotropic hardening processes, respectively. Such contributions drive the FCG in the LCF regime by additively increasing the damage driving force Y_f through Y_f^k and Y_f^i.

It is also important to note that the elastic part of the fatigue damage driving force Y_f^e intrinsically contains the stress triaxiality effect, as eq. (4.16) can be re-written [Chaboche, 1977b], [Lemaitre and Desmorat, 2005]:

$$Y_f^e = -\frac{1}{2} \underset{\sim}{\varepsilon}^e : f^{e\prime}(D_f) \underset{\approx}{\Lambda} : \underset{\sim}{\varepsilon}^e = -\frac{1}{2} f^{e\prime}(D_f) \underset{\sim}{\tilde{\sigma}} : \underset{\sim}{\varepsilon}^e = -f^{e\prime}(D_f) \frac{\tilde{\sigma}_{eq}^2 R_\nu}{2E} \tag{4.19}$$

where E the elastic (Young) modulus, $\tilde{\sigma}_{eq}$ is the effective equivalent stress based on the effective stress given by eq. (4.1) and R_ν is a triaxiality factor derived from eq. (4.19) using the Von Mises equivalent stress:

$$R_\nu = \frac{2}{3}(1+\nu) + 3(1-2\nu)\left(\frac{\sigma_h}{\sigma_{eq}}\right)^2 = \frac{2}{3}(1+\nu) + 3(1-2\nu) T_X^2 \tag{4.20}$$

where ν is the Poisson's ratio.
As stated in the sub-sect. 4.1.1, the incorporation of the stress triaxiality effect in the fatigue damage law is of the first importance when dealing with lifetime evaluation of components using CDM-based models [Pandey et al., 2021].

4.1.3 Viscoplasticity criterion

The change in material behavior due to increasing damage has to be considered in the yield function. Up to now, it is assumed that irreversible deformations are connected with volume constancy which leads to the only dependence of the yield function on the second invariant of the stress tensor (the first invariant, pressure-dependent, is first neglected). Indeed, for ductile materials, the inelastic strains are generally known to result from irreversible slip along crystallographic planes, hence leading to the absence of volume variation.
In the present work dealing with Ni-based superalloys which can be assimilated to ductile mate-

rials, a Von Mises-type (visco)plastic yield function of the thermodynamic conjugated forces is first introduced. In order to account for damage in the inelastic regime, the effective stresses are introduced in this criterion thanks to the strain equivalence principle:

$$\mathcal{F}_y^{vp} = \mathcal{F}_y - \sigma_{ov} = \tilde{\sigma}_{eq} - \sum_i \tilde{R}^i - R_0 - \sigma_{ov} \leq 0 \tag{4.21}$$

where R_0 is the initial yield limit, σ_{ov} defines an over-stress which exceeds the elastic limit and that is defined by a given flow rule [Benallal, 1989], [Lemaitre and Desmorat, 2005], and $\tilde{\sigma}_{eq}$ is the *effective* equivalent stress which is influenced by damage through the introduction of the effective stresses:

$$\tilde{\sigma}_{eq} = \sqrt{\frac{3}{2}\left(\underset{\sim}{\tilde{\sigma}}^D - \sum_k \underset{\sim}{\tilde{X}}^k\right) : \left(\underset{\sim}{\tilde{\sigma}}^D - \sum_k \underset{\sim}{\tilde{X}}^k\right)} = \sqrt{\frac{3}{2}\,\underset{\sim}{\tilde{Z}} : \underset{\sim}{\tilde{Z}}} = \sqrt{\frac{3}{2}}\,\left\|\,\underset{\sim}{\tilde{Z}}\,\right\| \tag{4.22}$$

and where $\underset{\sim}{\tilde{Z}} = \left(\underset{\sim}{\tilde{\sigma}}^D - \underset{\sim}{\tilde{X}}\right)$ is the apparent stress tensor, $\underset{\sim}{\tilde{X}} = \sum_k \underset{\sim}{\tilde{X}}^k$ the total back-stress tensor, $\underset{\sim}{\tilde{\sigma}}^D$ the deviatoric part of the effective stress tensor ($\underset{\sim}{\tilde{\sigma}}^D = \underset{\approx}{P}^D : \underset{\sim}{\tilde{\sigma}}$) and $\left\|\,\underset{\sim}{\tilde{Z}}\,\right\|$ represents the norm of the apparent stress tensor $\underset{\sim}{\tilde{Z}}$. Note that in eq. (4.22), the back-stress components $\underset{\sim}{\tilde{X}}^k$ are already deviatoric thanks to their moduli, see eq. (4.8) & eq. (4.13).

The yield criterion hence defines the limit of the elastic domain in the stress space. The consistency condition is given by:

- $\mathcal{F}_y < 0$ for elasticity (the stress state lies inside the yield surface);
- $\mathcal{F}_y = 0,\ \dot{\mathcal{F}}_y = 0$ for plasticity (the stress state lies on the limit of the yield surface);
- $\mathcal{F}_y = \sigma_{ov} > 0$ for viscoplasticity (the stress state lies outside of the yield surface).

The loading/unloading conditions on the yield criterion $\mathcal{F}_y$ associated with the inelastic multiplier $\dot{\lambda}$ fulfill the so-called *Karush-Kuhn-Tucker* (KKT) conditions:

$$\dot{\lambda} \geq 0, \qquad \mathcal{F}_y \leq 0, \qquad \dot{\lambda}\,\mathcal{F}_y = 0 \tag{4.23}$$

4.1.4 Dissipation potentials

The intrinsic dissipation (*i.e.* the power dissipated by the production of heat during the irreversible processes) is directly gained from the Clausius-Duhem inequality (CDI), the latter needing to be unconditionally satisfied:

$$\begin{aligned}
\mathcal{D}_{int} &= \underset{\sim}{\sigma} : \dot{\underset{\sim}{\varepsilon}} - \rho\dot{\psi} \geq 0 \\
&= \underset{\sim}{\sigma} : \dot{\underset{\sim}{\varepsilon}} - \rho\left(\frac{\partial\psi}{\partial\underset{\sim}{\varepsilon}^e} : \dot{\underset{\sim}{\varepsilon}}^e + \sum_k \frac{\partial\psi}{\partial\underset{\sim}{\alpha}^k} : \dot{\underset{\sim}{\alpha}}^k + \sum_i \frac{\partial\psi}{\partial r^i}\dot{r}^i + \frac{\partial\psi}{\partial D_f}\dot{D}_f\right) \geq 0 \\
&= \underset{\sim}{\sigma} : \dot{\underset{\sim}{\varepsilon}}^{in} - \sum_k \underset{\sim}{X}^k : \dot{\underset{\sim}{\alpha}}^k - \sum_i R^i\dot{r}^i + Y_f\dot{D}_f \geq 0
\end{aligned} \tag{4.24}$$

In the Chap. 2, it has been demonstrated that AD730™ , when loaded at elevated temperatures, exhibits an elastic-viscoplastic behavior. Hence, for the present approach, choice has been made to mainly focus on the time-dependent modeling. Let us recall that time-independent case (*i.e.* plasticity) can be seen as a limiting situation of the time-dependent case, providing the existence of a yield domain [Chaboche, 2008]. A general form for the viscosity function is given by:

$$\phi_v\left(\mathcal{F}_y\right) = 0 \quad \text{if} \quad \mathcal{F}_y < 0 \qquad \text{and} \qquad \phi_v\left(\mathcal{F}_y\right) = \dot{\lambda} \quad \text{if} \quad \mathcal{F}_y \geq 0 \tag{4.25}$$

The fulfillment of the 2nd Principle of Thermodynamics through the CDI, eq. (4.24), can be automatically achieved if the evolution laws for the internal variables $\dot{\mathbf{a}}_j$ derive from a dissipative pseudo-potential with adequate mathematical properties [Germain et al., 1983], [Chaboche, 1999]. The pseudo-dissipation (or dual) potential, composed of contributions from strain-hardenings, recovery and damage, is given by:

$$\Omega^* = \Omega^*_{vp}\left(\tilde{\underset{\sim}{\sigma}},\, \tilde{\underset{\sim}{X}}^k,\, \tilde{R}^i,\, Y_f;\, \underset{\sim}{\alpha}^k,\, r^i,\, D_f\right) + \Omega^*_{D_f}\left(\tilde{\underset{\sim}{\sigma}},\, Y_f;\, D_f\right) \tag{4.26}$$

where internal variables $\underset{\sim}{\alpha}^k$, r^i and D_f are used as parameters [Lemaitre and Chaboche, 1990].

Viscoplastic contribution:

The viscoplastic contribution Ω^*_{vp} of Ω^* can be deduced from the chosen flow rule:

$$\Omega^*_{vp} = \int K\, \phi_v\left(\mathcal{F}_y\right) \mathrm{d}\mathcal{F}_y \tag{4.27}$$

where $\phi_v\left(\mathcal{F}_y\right)$ is the chosen viscosity function (or flow rule).
By adding and subtracting equal terms in the viscosity function, one can express the non-linear evolution for both strain-hardenings thanks to the following pseudo-potential:

$$\Omega^*_{vp} = \int K\, \phi_v \left[\frac{1}{K}\left(\mathcal{F}_y + \frac{1}{2}\sum_k \gamma^k\, \varphi^k(p)\, \tilde{\underset{\sim}{X}}^k : \underset{\approx}{C}^{k-1} : \tilde{\underset{\sim}{X}}^k - \frac{1}{2}\sum_k \gamma^k\, \varphi^k(p)\, \underset{\sim}{\alpha}^k : \underset{\approx}{C}^k : \underset{\sim}{\alpha}^k + \frac{1}{2}\sum_i \frac{\tilde{R}^{i\,2}}{Q^i} - \frac{1}{2}\sum_i Q^i (b^i r^i)^2\right)\right] \mathrm{d}\mathcal{F}_y \tag{4.28}$$

with K the drag stress for viscoplastic behavior and $\varphi^k(p)$ a softening/hardening function of p used to define the transients upon cyclic loading, according to [Marquis, 1979]. Such a point has already been discussed in the sub-sect. 2.3.5. In eq. (4.28), the last 4 terms in the parentheses represents the dynamic recovery terms for the kinematic and isotropic hardening variables, respectively. They vanish when the constitutive equations eq. (4.13) & eq. (4.14) are satisfied.

Such a formulation is said to be *normal* and *associated* in the stress space. Indeed, the more or less "artificial" introduction of terms whose sum is zero in equation eq. (4.28) allows to describe a non-linear evolution of the strain-hardening without imposing $\mathcal{F}_y \neq F_p$ (see eq. (4.29)) as it would have been the case for non-associated time-independent plasticity [Saanouni et al., 1994]:

$$F_p = \mathcal{F}_y + \frac{1}{2}\sum_k \gamma^k \varphi^k(p)\, \underset{\sim}{\tilde{X}}^k : \underset{\approx}{C}^{k-1} : \underset{\sim}{\tilde{X}}^k - \frac{1}{2}\sum_k \gamma^k \varphi^k(p)\, \underset{\sim}{\alpha}^k : \underset{\approx}{C}^k : \underset{\sim}{\alpha}^k + \frac{1}{2}\sum_i \frac{\tilde{R}^{i\,2}}{Q^i} - \frac{1}{2}\sum_i Q^i (b^i r^i)^2 \quad (4.29)$$

so that the viscoplastic part yields:

$$\Omega^*_{vp}\left(\underset{\sim}{\tilde{\sigma}},\, \underset{\sim}{\tilde{X}}^k,\, \tilde{R}^i;\, \underset{\sim}{\alpha}^k,\, r^i\right) = \frac{K\dot{\epsilon}_0}{2}\,\beta\left(\frac{1+N}{2};\, -\frac{N}{2};\, \left[\tanh\left\langle \frac{F_p}{K}\right\rangle_+\right]^2\right) \quad (4.30)$$

where the viscosity function defined in eq. (4.30) is the hyperbolic sine flow rule, first introduced in the work of [Sellars and McTegart, 1966], [Pétry, 2006]. In eq. (4.30), the parameter $\beta\,(a, b, x)$ is the so-called *incomplete beta function* [Spanier and Oldham, 1987]. Such a function admits real values, defined on the interval $]-\infty;\ 1[$ provided that a is positive. Its convexity in the case of $N \geq 0$ is automatically verified on the positive real domain as a primitive of an increasing function [Pétry, 2006]. The hyperbolic sine form in eq. (4.30) is particularly suited for applications with high thermomechanical loadings and for cases where the over-stress is highly non-linear at low strain rates [Pétry, 2006], [Vincent, 2010], [Bartošák et al., 2020]. As detailed in sub-sect. 2.2.3.2, AD730™ exhibits a highly non-linear evolution of its over-stress with respect to the viscoplastic strain rate over loading rates ranging in $\left[10^{-5} - 10^{-3}\right]$ s^{-1} down to 10^{-7} s^{-1} for stress relaxation (and possible recovery effects). The choice for an hyperbolic sine function, enabling to cover a wide range of strain rates, hence constitutes a good candidate.

Fatigue damage contribution:

The damage contribution $\Omega^*_{D_f}$ to the pseudo-potential of dissipation Ω^* depends on the nature of the degradation process. It is constructed thanks to the pioneer work of [Lemaitre, 1985a]:

$$\Omega^*_{D_f} = \dot{p}\,\frac{S_f}{m_f+1}\left\langle \frac{Y_f - Y_{f_0}}{S_f}\right\rangle_+^{m_f+1} \exp(\beta_f\,\eta_D\ D_f)\ f^e(D_f) \quad (4.31)$$

with $\langle\,.\,\rangle_+$ the Macauley brackets (returning the positive part of its argument, as defined in the notations page xxvii), S_f & m_f the resistance parameters associated with fatigue damage, Y_{f_0} a threshold value for the energy release rate Y_f (so that to delay fatigue damage growth, as done in, *e.g.* [Boudifa, 2006]) and β_f is a parameter controlling the non-linearity of the damage evolution. Note that all these material parameters could depend on temperature.

It can be noticed that the use of the effective variables in both the state and dissipation potentials, eq. (4.3) & eq. (4.26), leads to fully coupled constitutive equations which is known to improve and complete the coupled theory introduced by [Chaboche, 1978].
Indeed, according to [Saanouni et al., 1994] such a formalism leads to the three following properties:

- the use of the same pseudo-potential to characterize the dissipation of both viscoplasticity and damage eq. (4.28) & eq. (4.31) implicitly supposes that damage cannot initiate at any material point without plastic deformation [Lemaitre, 1985a]. Such an assumption seems

reasonable for crack propagation where plasticity in ductile materials (like the present Ni-based superalloy) is always present at the crack-tip;

- due to the strong coupling between damage and hardening mechanisms, the fully damaged RVE should be free from any remaining stress;
- the stored energy (through plastic work) is released by the initiation and growth of damage.

Finally, in order to satisfy the principle of irreversibility, the rate of dissipative energy has to be non-negative. Physically, it means preventing damage healing after the load is removed. The generalized normality rule associated with the dissipation pseudo-potential Ω^* allows for the intrinsic dissipation to be written:

$$\mathcal{D}_{int} = \left[\underset{\sim}{\sigma} : \frac{\partial \Omega^*}{\partial \underset{\sim}{\sigma}} + \sum_k \underset{\sim}{X}^k : \frac{\partial \Omega^*}{\partial \underset{\sim}{X}^k} + \sum_i R^i \frac{\partial \Omega^*}{\partial R^i} + Y_f \frac{\partial \Omega^*}{\partial D_f} \right] \geq 0 \tag{4.32}$$

The consistent validation of the positivity of the intrinsic dissipation related to both plastic power, work-hardening and damage is given in the appendices, see Chap. F page 289.

4.1.5 Evolution laws

According to the generalized normality rule associated with instantaneous dissipative phenomena [Chaboche, 2008], [Lemaitre and Chaboche, 1990], the following rate equation for the inelastic strain tensor is obtained through the derivative of the dissipative pseudo-potential:

$$\dot{\underset{\sim}{\varepsilon}}^{in} = \frac{\partial \Omega^*_{vp}}{\partial \underset{\sim}{\sigma}} = \frac{\partial \Omega^*_{vp}}{\partial F_p} \frac{\partial F_p}{\partial \underset{\sim}{\sigma}} = \phi_v(\mathcal{F}_y) \frac{\partial \mathcal{F}_y}{\partial \underset{\sim}{\sigma}} = \frac{3}{2} \frac{\phi_v(\mathcal{F}_y)}{f^e(D_f)} \frac{\left(\tilde{\underset{\sim}{\sigma}}^D - \tilde{\underset{\sim}{X}}\right)}{\sqrt{\frac{3}{2}\left(\tilde{\underset{\sim}{\sigma}}^D - \tilde{\underset{\sim}{X}}\right) : \left(\tilde{\underset{\sim}{\sigma}}^D - \tilde{\underset{\sim}{X}}\right)}} \tag{4.33}$$

where $\phi_v(\mathcal{F}_y)$ is a viscoplastic (Lagrange) multiplier given either by the consistency condition eq. (4.23) for plasticity or by a viscosity potential for viscoplasticity [Benallal, 1989]:

$$\dot{\lambda} = \frac{\partial \Omega^*_{vp}}{\partial F_p} = \phi_v(\mathcal{F}_y) = \dot{\epsilon}_0 \left[\sinh \left\langle \frac{\mathcal{F}_y}{K} \right\rangle_+^n \right]^m \tag{4.34}$$

and where the normal to the yield surface $\underset{\sim}{n}$ is given by:

$$\underset{\sim}{n} = \frac{\partial \mathcal{F}_y}{\partial \underset{\sim}{\sigma}} = \frac{1}{f^e(D_f)} \sqrt{\frac{3}{2}} \frac{\left(\tilde{\underset{\sim}{\sigma}}^D - \tilde{\underset{\sim}{X}}\right)}{\sqrt{\left(\tilde{\underset{\sim}{\sigma}}^D - \tilde{\underset{\sim}{X}}\right) : \left(\tilde{\underset{\sim}{\sigma}}^D - \tilde{\underset{\sim}{X}}\right)}} \tag{4.35}$$

Using the apparent stress $\tilde{\underset{\sim}{Z}} = \left(\tilde{\underset{\sim}{\sigma}}^D - \tilde{\underset{\sim}{X}}\right)$ and the viscoplastic multiplier eq. (4.34) together with the equivalent effective stress eq. (4.22), the inelastic strain rate tensor eq. (4.33) can be re-written:

$$\dot{\underset{\sim}{\varepsilon}}^{in} = \frac{3}{2} \frac{\dot{\lambda}}{f^e(D_f)} \frac{\left(\tilde{\underset{\sim}{\sigma}}^D - \tilde{\underset{\sim}{X}}\right)}{\sqrt{\frac{3}{2}\left(\tilde{\underset{\sim}{\sigma}}^D - \tilde{\underset{\sim}{X}}\right) : \left(\tilde{\underset{\sim}{\sigma}}^D - \tilde{\underset{\sim}{X}}\right)}} = \frac{3}{2} \frac{\dot{\lambda}}{f^e(D_f)} \frac{\tilde{\underset{\sim}{Z}}}{\tilde{\sigma}_{eq}} \tag{4.36}$$

The framework of the GSM [Halphen and Nguyen, 1975], [Germain et al., 1983] hence introduces the inelastic multiplier $\dot{\lambda}$ which turns out to be the accumulated plastic strain rate $\dot{p}$. This one is equal to the norm of the inelastic strain rate tensor, which from eq. (4.36) yields:

$$\dot{p} = \sqrt{\frac{2}{3}\,\underset{\sim}{\dot{\varepsilon}}^{in} : \underset{\sim}{\dot{\varepsilon}}^{in}} = \sqrt{\frac{2}{3}}\,\left\|\,\underset{\sim}{\dot{\varepsilon}}^{in}\,\right\| = \frac{\dot{\lambda}}{f^e\left(D_f\right)} \qquad \leftrightarrow \qquad p = \int_0^t \dot{p}\,\mathrm{d}\tau \tag{4.37}$$

Using the plastic work through the energetic equivalence also directly yields:

$$\dot{p}\,\tilde{\sigma}_{eq} = \left(\underset{\sim}{\tilde{Z}} : \underset{\sim}{\dot{\varepsilon}}^{in}\right) \qquad \leftrightarrow \qquad \dot{p} = \frac{\left(\underset{\sim}{\tilde{Z}} : \underset{\sim}{\dot{\varepsilon}}^{in}\right)}{\tilde{\sigma}_{eq}} \tag{4.38}$$

In order to lighten the notations as well as to facilitate the future implementation process, choice is made to introduce additional effective variables, namely the *effective inelastic strain rate* tensor:

$$\underset{\sim}{\dot{\tilde{\varepsilon}}}^{in} = \frac{\partial \Omega^*_{vp}}{\partial \underset{\sim}{\tilde{\sigma}}} = \phi_v\left(\mathcal{F}_y\right)\frac{\partial \mathcal{F}_y}{\partial \underset{\sim}{\tilde{\sigma}}} = \phi_v\left(\mathcal{F}_y\right)\sqrt{\frac{3}{2}}\,\frac{\underset{\sim}{\tilde{Z}}}{\left\|\,\underset{\sim}{\tilde{Z}}\,\right\|} = \phi_v\left(\mathcal{F}_y\right)\sqrt{\frac{3}{2}}\,\underset{\sim}{\tilde{n}} \tag{4.39}$$

with the *unit effective normal* to the inelastic limit surface $\underset{\sim}{\tilde{n}}$ (so that $\underset{\sim}{\tilde{n}} : \underset{\sim}{\tilde{n}} = 1$) defined by:

$$\underset{\sim}{\tilde{n}} = \sqrt{\frac{2}{3}}\,\frac{\partial F_p}{\partial \underset{\sim}{\tilde{\sigma}}} = \sqrt{\frac{2}{3}}\,\frac{\partial \mathcal{F}_y}{\partial \underset{\sim}{\tilde{\sigma}}} = \sqrt{\frac{2}{3}}\,\frac{\partial}{\partial \underset{\sim}{\tilde{\sigma}}}\left[\sqrt{\frac{3}{2}}\,\left\|\,\underset{\sim}{\tilde{Z}}\,\right\| - \sum_i \tilde{R}^i - R_0\right] = \frac{\underset{\sim}{\tilde{Z}}}{\left\|\,\underset{\sim}{\tilde{Z}}\,\right\|} \tag{4.40}$$

and the *effective accumulated plastic strain rate*:

$$\dot{\tilde{p}}\,\tilde{\sigma}_{eq} = \left(\underset{\sim}{\tilde{Z}} : \underset{\sim}{\dot{\tilde{\varepsilon}}}^{in}\right) \qquad \leftrightarrow \qquad \dot{\tilde{p}} = \frac{\left(\underset{\sim}{\tilde{Z}} : \underset{\sim}{\dot{\tilde{\varepsilon}}}^{in}\right)}{\tilde{\sigma}_{eq}} = \sqrt{\frac{2}{3}}\,\left\|\,\underset{\sim}{\dot{\tilde{\varepsilon}}}^{in}\,\right\| \tag{4.41}$$

In the case of viscoplasticity-damage coupling, the effective accumulated plastic strain rate eq. (4.41) equals the visco-plastic multiplier eq. (4.34):

$$\dot{\tilde{p}} = \phi_v\left(\mathcal{F}_y\right) = \sqrt{\frac{2}{3}}\,\left\|\,\underset{\sim}{\dot{\tilde{\varepsilon}}}^{in}\,\right\| = \dot{\lambda} \tag{4.42}$$

From eq. (4.42), it is evidenced the fact that the viscous stress is a function of the effective accumulated plastic strain rate $\dot{\tilde{p}}$ rather than the accumulated viscoplastic strain rate. Thus, damage also affects the viscous properties of the material [Saanouni et al., 1994], [Pétry, 2006], [Kaminski, 2007], [Vincent, 2010], [Cailletaud et al., 2018]:

$$\mathcal{F}_y^{vp} = \tilde{\sigma}_{eq} - \sum_i \tilde{R}^i - R_0 - \sigma_{ov}\left(\dot{\tilde{p}}\right) \leq 0 \tag{4.43}$$

According to eq. (4.40), the inelastic strain rate eq. (4.36) can be re-written:

$$\underset{\sim}{\dot{\varepsilon}}^{in} = \frac{3}{2}\,\frac{\dot{\lambda}}{f^e\left(D_f\right)}\,\frac{\underset{\sim}{\tilde{Z}}}{\tilde{\sigma}_{eq}} \qquad \leftrightarrow \qquad \underset{\sim}{\dot{\varepsilon}}^{in} = \frac{\dot{\lambda}}{f^e\left(D_f\right)}\sqrt{\frac{3}{2}}\,\underset{\sim}{\tilde{n}} = \dot{p}\sqrt{\frac{3}{2}}\,\underset{\sim}{\tilde{n}} \tag{4.44}$$

where the scalar term in eq. (4.44) gives the intensity of the inelastic flow, while the tensor term

defines its direction in the (effective) stress space.

Similarly to the eq. (4.33), the rates for the hardening variables are given by:

$$\dot{\underset{\sim}{\alpha}}^k = -\frac{\partial \Omega^*_{vp}}{\partial \underset{\sim}{X}^k} = -\frac{\partial \Omega^*_{vp}}{\partial F_p}\frac{\partial F_p}{\partial \underset{\sim}{X}^k} = \frac{\dot{\lambda}}{f^k(D_f)}\left(\sqrt{\frac{3}{2}}\,\tilde{\underset{\approx}{n}} - \gamma^k \varphi^k(p)\,\underset{\approx}{P}^D : \underset{\sim}{\alpha}^k\right) \tag{4.45}$$

$$\dot{r}^i = -\frac{\partial \Omega^*_{vp}}{\partial R^i} = -\frac{\partial \Omega^*_{vp}}{\partial F_p}\frac{\partial F_p}{\partial R^i} = -\dot{\lambda}\frac{\partial F_p}{\partial R^i} = \frac{\dot{\lambda}}{f^i(D_f)}\left(1 - b^i\, r^i\right) \tag{4.46}$$

The idea of a unified damage model for metallic alloys is to relate the damage rate to the main dissipative mechanism. For LCF conditions, cumulative plasticity can be considered as the fatigue damage driving force [Desmorat, 2006]. Such a choice is relatively common, especially for fatigue crack initiation prediction [Lemaitre, 1985b], [Besson and Desmorat, 2009], [Vincent, 2010]. Let us note that other mechanisms could have been considered to govern the fatigue damage process. This point is addressed is a dedicated discussion hereafter. The derivative of the dissipation potential yields:

$$\dot{D}_f = \frac{\partial \Omega^*_{D_f}}{\partial Y_f} = \dot{\lambda}\left\langle \frac{Y_f - Y_{f_0}}{S_f} \right\rangle_+^{m_f} \mathrm{e}^{(\beta_f\, \eta_D\, D_f)}\; \mathcal{H}(p - p_D) \tag{4.47}$$

The kinetic law of fatigue damage evolution, eq. (4.47), derives from the dissipation potential eq. (4.31) which is taken as a power function of the associated thermodynamic variable Y_f to the fatigue damage D_f. Such an evolution rule eq. (4.47) remains valid as long as $D_f \leq D^{crit}$.

→ Discussion on the fatigue damage driving force:

Apart from the cumulative plasticity $\dot{p}$ to govern the fatigue damage, other choices are possible:

i) The plastic work can be taken as the fatigue damage driving force, as suggested by [Jiang, 2000], [Banvillet et al., 2003] & [Yu et al., 2011] and exploited by [Ma and Yuan, 2017] for fatigue in sintered metals. This choice embeds a greater physical meaning but needs more material constants to be calibrated. Moreover, such a critical plane criterion seems to be more suited for fatigue crack initiation prediction rather than crack propagation analysis.

ii) Another approach for fatigue damage evolution is based on the phenomenological model of [Landgraf et al., 1969] dedicated to fatigue failure. Such a model assumes that large strain ranges are performed upon loading and that the total strain range $\Delta\varepsilon$ is related to the number of cycles at failure N_r. This approach was adopted by [Schwarz et al., 2011] who succeeded in transforming the Landgraf & Morrow's model to a continuous time-incremental damage evolution law, hence leading to a fewer number of damage-related material constants.

iii) Lastly, contrarily to the empirical CDM-based models, some recent studies have tried to relate the damage evolution to the dissipation associated with damage development through entropy creation [Egner et al., 2020]. Relying on the so-called *Unified Mechanics Theory* (UMT) [Lee

and Basaran, 2021], the approach consists in modifying the universal laws of motion of Newton by incorporating the 2nd Law of Thermodynamics directly into Newton's laws at the *ab initio* level. As a consequence, such an entropy-based formulation allows the fatigue damage to develop from the very beginning of the loading scheme compared to the classical approach of [Lemaitre, 1996] for which damage starts to accumulate once a specific threshold value is reached [Egner et al., 2020].

4.1.6 On micro-cracks closure effect for fatigue damage

Physical facts have shown that the damage evolution is amplified in tensile conditions whereas under compressive loads the rate of deterioration reduces. Such a phenomenon is due to *partial micro-crack closure*, also referred to as *quasi-Unilateral Conditions* (UC) [Lemaitre and Desmorat, 2005]. The stiffness of the material under compression is supposed to lie between the undamaged and the damaged stiffness. Taking into account this effect is important, especially for high mean stress loadings [Barbier, 2009]. In order to define the compressive stiffness of the damaged material, a crack closure parameter h was introduced [Lemaitre, 1996]. Thus, effective stresses are defined differently for tension and compression:

$$\tilde{\sigma}_{tension} = \frac{\sigma}{f^e(D_f)} \qquad \tilde{\sigma}_{compression} = \frac{\sigma}{f_h^e(h, D_f)} \tag{4.48}$$

For $h = 0$ the initial stiffness of the material is recovered whereas a value of $h = 1$ assumes that the stiffness under compression equals that under tension. For metallic alloys, in the absence of experimental evidences, a value of $h = 0.2$ is often assumed [Lemaitre, 1996].

For the 3-dimensional stress state it is difficult to determine the loading direction by means of a scalar quantity. To remedy this problem, several decomposition have been proposed in the literature, such as the elastic energy decomposition [Ladevèze, 1983], the Kelvin decomposition of the compliance tensor [Desmorat, 2000], the damage tensor decomposition [Halm and Dragon, 1996], or more classically the stress tensor decomposition [Lemaitre, 1996], [Zhang et al., 2021]. Following this last approach, the effective stress tensor $\tilde{\underline{\underline{\sigma}}}$ can be transformed into the principal values $\tilde{\underline{\underline{\sigma}}}^{diag}$ and then decomposed into its positive $\tilde{\underline{\underline{\sigma}}}_+$ and negative $\tilde{\underline{\underline{\sigma}}}_+$ parts. This can be done using the spectral decomposition technique which allows for the Cauchy stress tensor (nominal and effective) to be decomposed into two distinct parts, as first proposed by [Ladevèze, 1983] and applied in other studies, *e.g.* [Lemaitre, 1996], [Cicekli et al., 2007].

Hereafter, "+" and "-" stem for the tensile and compressive parts, respectively. Therefore, the decomposed nominal stress tensor can be written according to its principal unit vectors $\underline{e}_i$:

$$\underline{\underline{\sigma}}^{diag} = \sum_{i=1}^{3} \sigma_i \, \underline{e}_i \otimes \underline{e}_i = \underline{\underline{\sigma}}_+ + \underline{\underline{\sigma}}_- \tag{4.49}$$

$$\underline{\underline{\sigma}}_+ = \sum_{i=1}^{3} \langle \sigma_i \rangle_+ \, \underline{e}_i \otimes \underline{e}_i \qquad \underline{\underline{\sigma}}_- = \sum_{i=1}^{3} -\langle -\sigma_i \rangle_+ \, \underline{e}_i \otimes \underline{e}_i \tag{4.50}$$

where $\langle . \rangle_+$ is a weighted step function defined in the notations, page xxvii, $\underline{\underline{\sigma}}_+$ and $\underline{\underline{\sigma}}_-$ are the

positive and negative parts of the nominal stress tensor in the principal coordinate axes, respectively.

It results from this spectral decomposition the following nominal stress tensor of the damaged material written in terms of effective stress tensor and softening functions including closure effect:

$$\underset{\sim}{\sigma}^{diag} = \underset{\sim}{\tilde{\sigma}}_{+} f^{e}(D_f) + \underset{\sim}{\tilde{\sigma}}_{-} f_h^{e}(h, D_f) \tag{4.51}$$

where the softening functions in eq. (4.51) are re-defined as:

$$f^{e}(D_f) = \exp(-\beta_e \eta_D D_f) \qquad \text{and} \qquad f_h^{e}(h, D_f) = \exp(-\beta_e \eta_D h D_f) \tag{4.52}$$

Elasticity-damage coupling: In order to select stress as an independent variable and to operate the partition of the stress tensor between its tensile and compressive parts, it is required to work on the space of the stress-like variables rather than that of the strain-like forces. Such a change is more convenient while dealing with the state law of elasticity [Lemaitre and Desmorat, 2005]. Hence, a partial Legendre transform of the Helmholtz specific free energy ψ given in eq. (4.3) should be performed to get the Gibbs specific enthalpy ψ^*:

$$\psi^* = \psi_e^* + \psi_{in}^* = \psi_e^* + \frac{1}{\rho}\underset{\sim}{\sigma} : \underset{\sim}{\varepsilon}^{in} - \psi_{in} \tag{4.53}$$

where ψ_e^* is the elastic part of the Gibbs specific enthalpy and ψ_{in} is the inelastic contribution to the Helmholtz specific free energy given by eq. (4.5).

The elastic part of the Gibbs potential is given by:

$$\psi_e^* = \sup_{\varepsilon^e}\left[\frac{1}{\rho}\underset{\sim}{\sigma} : \underset{\sim}{\varepsilon}^{e} - \psi_e\right] = \frac{1}{2\rho}\underset{\sim}{\sigma} : \underset{\approx}{\tilde{\mathit{\Lambda}}}^{-1} : \underset{\sim}{\sigma} \tag{4.54}$$

in which the spectral decomposition of $\underset{\sim}{\sigma}$ can be performed so that to get unilateral conditions within the specific Gibbs enthalpy, see [Lemaitre and Desmorat, 2005] for more details.
The elastic part of the Gibbs potential finally reads:

$$\rho\,\psi_e^* = = \frac{1+\nu}{2E}\left[\frac{\underset{\sim}{\sigma}_{+} : \underset{\sim}{\sigma}_{+}}{f^{e}(D_f)} + \frac{\underset{\sim}{\sigma}_{-} : \underset{\sim}{\sigma}_{-}}{f_h^{e}(h, D_f)}\right] - \frac{\nu}{2E}\left[\frac{\langle \operatorname{tr}\underset{\sim}{\sigma}\rangle^2}{f^{e}(D_f)} + \frac{\langle -\operatorname{tr}\underset{\sim}{\sigma}\rangle^2}{f_h^{e}(h, D_f)}\right] \tag{4.55}$$

The introduction of the partial closure effects has been integrated in the modeling following two complementary ways:

- in the elasticity relations: $\underset{\sim}{\varepsilon}^{e} = \underset{\approx}{\tilde{\mathit{\Lambda}}}^{-1} : \underset{\sim}{\sigma}$ which may evidence a partial stiffness recovery once compressive stress state is reached, depending on the closure parameter h:

$$\underset{\sim}{\varepsilon}^{e} = \rho\frac{\partial \psi_e^*}{\partial \underset{\sim}{\sigma}} = \frac{1+\nu}{E}\left[\frac{\underset{\sim}{\sigma}_{+}}{f^{e}(D_f)} + \frac{\underset{\sim}{\sigma}_{-}}{f_h^{e}(h, D_f)}\right] - \frac{\nu}{E}\left[\frac{\langle \operatorname{tr}\underset{\sim}{\sigma}\rangle}{f^{e}(D_f)} - \frac{\langle -\operatorname{tr}\underset{\sim}{\sigma}\rangle}{f_h^{e}(h, D_f)}\right]\underset{\sim}{1} \tag{4.56}$$

thus defining the effective stress tensor with unilateral conditions $\tilde{\underset{\sim}{\sigma}}_{uc}$:

$$\tilde{\underset{\sim}{\sigma}}_{uc} = \frac{\underset{\sim}{\sigma}_+}{f^e(D_f)} + \frac{\underset{\sim}{\sigma}_-}{f_h^e(h, D_f)} + \frac{\nu}{1-2\nu}\left[\frac{\underset{\sim}{1} : \underset{\sim}{\sigma}_+ - \langle \operatorname{tr} \underset{\sim}{\sigma} \rangle}{f^e(D_f)} + \frac{\underset{\sim}{1} : \underset{\sim}{\sigma}_- + \langle -\operatorname{tr} \underset{\sim}{\sigma} \rangle}{f_h^e(h, D_f)}\right] \underset{\sim}{1} \tag{4.57}$$

- in the elastic part of the fatigue damage driving force Y_f^e, eq. (4.58): although the involvement of the energy release rate due to tensile principal stresses is complete, for compressive principal stresses it is only partial, where the extent of its contribution is scaled by the closure parameter h and which in turn yields a lower damage rate.

$$\begin{aligned} Y_f^e = \rho \frac{\partial \psi_e^*}{\partial D_f} = &-\frac{1+\nu}{2E}\left[\frac{\underset{\sim}{\sigma}_+ : \underset{\sim}{\sigma}_+}{f^{e2}(D_f)} \frac{\partial f^e(D_f)}{\partial D_f} + \frac{\underset{\sim}{\sigma}_- : \underset{\sim}{\sigma}_-}{f_h^{e2}(h, D_f)} \frac{\partial f_h^e(h, D_f)}{\partial D_f}\right] \\ &+ \frac{\nu}{2E}\left[\frac{\langle \operatorname{tr} \underset{\sim}{\sigma} \rangle^2}{f^{e2}(D_f)} \frac{\partial f^e(D_f)}{\partial D_f} + \frac{\langle -\operatorname{tr} \underset{\sim}{\sigma} \rangle^2}{f_h^{e2}(h, D_f)} \frac{\partial f_h^e(h, D_f)}{\partial D_f}\right] \end{aligned} \tag{4.58}$$

Such a second option is often chosen alone in order to avoid the problem of convexity loss due to the discontinuity of the potential depending on positive and negative parts [Ganczarski and Cegielski, 2010], [Lemaitre and Desmorat, 2005], [Saanouni, 2012]. Thus, only the decomposition into positive and negative parts can be accounted for the damage energy density rate Y_f so as to get higher values in tension than in compression. This modeling approach has been adopted, *e.g.* by [Diamantopoulou et al., 2017] in the context of ductile fracture modeling.

Viscoplasticity-damage coupling: The yield surface depends on the amount of strain-hardening and damage. However, it does not account for the influence of damage regarding the loading direction (as opposed to elasticity). Thus, in case of compression, hardening develops for stress states exceeding the yield surface, while the evolution of damage remains active but may be reduced (or even disabled) thanks to the introduction of micro-cracks closure effect within Y_f^e, see eq. (4.58). It is assumed that differences between the influence of damage on the description of the yield surface under tensile and compressive stress states are assumed to be negligible [Otin, 2007], [Desmorat and Cantournet, 2008]. Such an aspect relies on the nature of the mechanisms of plasticity itself controlled by slips and produced by shear stresses in the same manner regardless of their signs [Lemaitre and Desmorat, 2005]. For these reasons, in the following, the (standard) effective stress tensor $\tilde{\underset{\sim}{\sigma}}$ given in eq. (4.1) will be introduced within the yield criterion disregarding the tensile and compressive contributions.

→ **Remark about the mean stress effect:** It has been proved that a damage law ensuring a damage rate smaller in compression than in tension (at a given stress level) will naturally model the mean stress effect [Desmorat, 2006]. The introduction of the micro-defects closure effect into the energy release rate Y_f associated with damage represents one possibility for the modeling of the mean stress effect in metals plasticity [Lemaitre et al., 1999], [Barbier, 2009], [Desmorat et al., 2015a]. As can be seen in Fig. 4.3, the mean stress effect is noticeable when varying the micro-defects closure parameter h. Particularly, a value of $h = 1$ results in the absence of mean stress effect, while $h = 0.2$ leads to greater stress amplitude to reach the failure for negative mean stresses, see Fig. 4.3a.

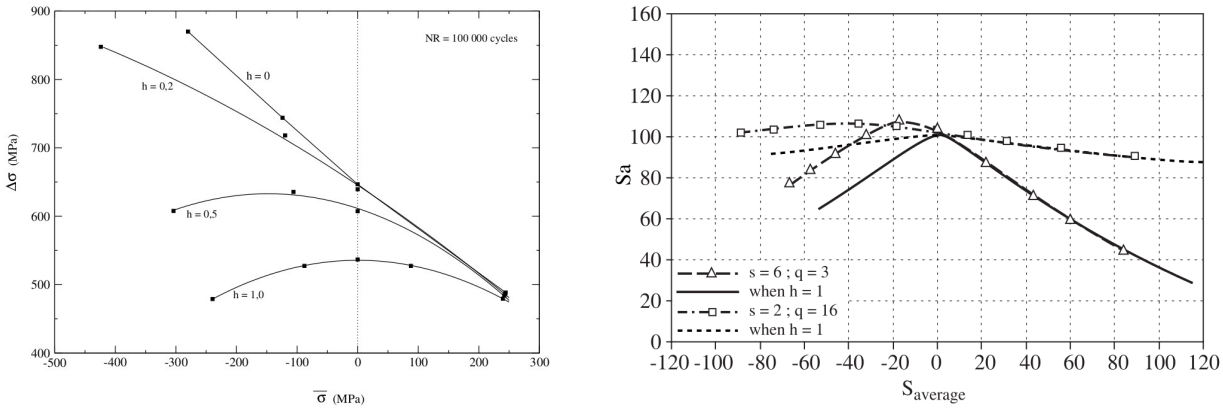

(a) 304L steel at 10^5 cycles (from [Barbier, 2009]). (b) Case for $h = 0.2$ (from [Chaboche, 2011]).

Figure 4.3: Influence of the micro-defects closure parameter h on Haigh diagrams for fatigue loadings.

The introduction of the micro-defects closure effect within the present fatigue damage model will enable the possibility to account for a slight mean stress effect thanks to a load ratio-dependent fatigue damage evolution. Such a point will be discussed in the sub-sect. 4.4.1.2 later on.

4.2 On a unified multi-mechanism damage model

In this Ph.D. project, the comprehensive material model for FG AD730™ has been derived and calibrated in the Chap. 2 while the coupling with damage has been formulated in the sect. 4.1 assuming a *local approach to fracture* associated with consistent thermodynamics- and CDM-based frameworks. Some particular aspects associated with complex loading schemes have already been included in the modeling, such as the micro-defects closure effect for fatigue damage, see sub-sect. 4.1.6. In order to take into account the whole failure modes, the present fatigue damage model needs to be improved for complex loading conditions and needs to account for various degradation processes. This point is the topic of the present section.

4.2.1 Ductile damage associated with porosity change

Experimental observations carried on FG AD730™ revealed some ductile dimples as well as micro-pores (*cf.* sect. 3.2). Such defects result in high stress concentrations and lead to final fracture.
In the present case, choice has been made to introduce a new damage variable D_v for volumetric change. This volumetric damage is associated with the growth of porosity and subsequent damage-induced plastic volume variation, also referred to as *plastic compressibility* [Chaboche et al., 2006], [Saanouni, 2012]. The introduction of this additional damage variable D_v comes from the change from initial to current material density. The volumetric damage is used to quantify the effects of

void growth and increase in crack density per unit volume in the material:

$$D_v = 1 - \frac{\rho_t}{\rho_0} \qquad \leftrightarrow \qquad \rho_t = \frac{1 - D_v}{1 - D_{v_0}} \tag{4.59}$$

where ρ_0 is the initial density associated with the bulk material. In eq. (4.59), D_{v_0} is a small valued phenomenological coefficient that triggers the plasticity-induced compressibility effects, even for initial conditions (prior to volumetric damage development) where $D_v = 0$, and which makes the criterion pressure-dependent, see eq. (4.61) hereafter [Chaboche et al., 2006].
Neglecting the elastic strain-induced volume variation, the mass conservation principle yields:

$$\dot{\rho}_t = -\rho_t \operatorname{tr} \underset{\sim}{\dot{\varepsilon}}^{in} \qquad \leftrightarrow \qquad \dot{D}_v = -\frac{\dot{\rho}_t}{\rho_0} = -\frac{\dot{\rho}_t}{\rho_t}(1 - D_v) = (1 - D_v) \operatorname{tr} \underset{\sim}{\dot{\varepsilon}}^{in} \tag{4.60}$$

which yields to the exact counterpart of the cavity growth equation in Gurson [Gurson, 1977] or Rousselier [Rousselier, 1987] models. The eq. (4.60) indicates that the inelastic strain rate tensor is no more purely deviatoric but also contains hydrostatic terms as long as plastic strain develops. Moreover, D_v is not considered as an (independent) internal state variable as it is the case for the fatigue damage D_f introduced in sub-sect. 4.1.2. The former is directly governed by inelastic strains which in turn makes D_v a non-dissipative variable as its evolution is already accounted for in the inelastic power. The theoretical derivation of the evolution of the model, not given here, follows the guidelines given in [Chaboche et al., 2006].

It is somewhat important to notice the change in the yield function $\mathcal{F}_y$ from the one given in eq. (4.21) to that of eq. (4.61) which, due to this additional damage variable D_v, combines the first and the second stress invariants. An elliptic form is chosen here, as suggested by [Green, 1972] for porous materials and as previously studied by [Besson and Guillemer-Neel, 2003], [Kaminski, 2007].

$$\mathcal{F}_y^{vp} = \mathcal{F}_y - \sigma_{ov} = \sqrt{\frac{3}{2}} \left\| \underset{\approx}{\tilde{Z}} \right\|_H - \sum_i \tilde{R}^i - R_0 - \sigma_{ov} \leq 0 \tag{4.61}$$

with the norm of the apparent stress tensor $\left\| \underset{\approx}{\tilde{Z}} \right\|_H$ defined by:

$$\left\| \underset{\approx}{\tilde{Z}} \right\|_H = \sqrt{\underset{\approx}{\tilde{Z}} : \underset{\approx}{H} : \underset{\approx}{\tilde{Z}}} = \sqrt{\underset{\approx}{\tilde{Z}} : \left[\underset{\approx}{P}^D + 2\,\varphi_c\, g_D(D_v)\, \underset{\approx}{P}^S \right] : \underset{\approx}{\tilde{Z}}} \tag{4.62}$$

in which φ_c is a material parameter allowing for the pressure sensitivity to be scaled, g_D is a function of the volumetric damage D_v, and $\underset{\approx}{P}^D$ & $\underset{\approx}{P}^S$ are the 4$^{\text{th}}$-order deviatoric and hydrostatic projection tensors, respectively, defined in eq. (4.9). Note that if we set $\varphi_c = 0$ in eq. (4.62), the elliptic yield criterion eq. (4.61) reduces to the standard pressure-independent Von Mises criterion given in eq. (4.21). In eq. (4.62), the function g_D, modular in nature, is simply chosen as the sum of the volumetric damage variables:

$$g_D(D_v) = D_v + D_{v_0} \tag{4.63}$$

Finally, the total damage rate $\dot{D}_{tot}$ can up to now be divided into a fatigue contribution due to

fluctuating loading and a volumetric contribution driven by the inelastic deformation:

$$\mathrm{d}D_{tot} \;=\; \mathcal{F}_f\left(\tilde{\underset{\sim}{\sigma}}, \tilde{\underset{\sim}{X}}, \tilde{R}, D_f, \dot{p}\right)\mathrm{d}t \;+\; \mathcal{F}_v\left(\underset{\sim}{\varepsilon}^{in}, D_v\right)\mathrm{d}t \tag{4.64}$$

A specific feature associated with the summation in eq. (4.64) is the direct coupling between damage and both elasticity and (visco)plasticity. Indeed, in the effective variables, eq. (4.1), as well as in the softening function given in eq. (4.2), introducing the total damage D_{tot} results in a strong coupling between the overall damage mechanisms and material behavior.

4.2.2 Extension to time-activated effects

Once subjected to long time exposure at elevated temperatures, most of the metallic materials lose their mechanical properties. This decrease in resistance is to be related (among others) to the creep process which is a thermally-activated phenomenon.
For polycrystalline alloys, like the present Ni-based superalloy AD730™, the creep degradation process occurs at the GB (*i.e.* at the intergranular level) through cavity initiation and expansion (typically by a diffusion process) [Thébaud, 2017], [Vultos, 2019]. The results obtained from the experimental work as detailed in Chap. 3 have evidenced the occurrence of mixed cracking modes under dwell-fatigue loading conditions in AD730™. As stated, dwell-fatigue loading schemes resulted in creep processes associated with holding periods and elevated temperatures. This led to creep pores nucleation at GB with intergranular cracking features.

In the present study, the aim is not to accurately model the creep process (since no proper creep tests have been performed in the experimental campaign), but to account for creep damage mechanisms to enable the simulation of complex loading conditions (see sub-sect. 4.1.1).
Since the pioneer works from [Kachanov, 1958] & [Rabotnov, 1969], a general CDM-based creep model has been suggested by [Leckie and Hayhurst, 1974] in order to generalize the classical uniaxial creep damage equation proposed by [Rabotnov, 1969] to multiaxial stress states. This was made possible thanks to the use of adequate stress invariants.

In order to introduce an additional creep damage variable D_c into the proposed fatigue damage model, one should postulate the existence of an additional pseudo-potential $\Omega^*_{D_c}$ to the dissipative pseudo-potential given in eq. (4.26). This is rather straightforward due to the obvious time-dependence of creep damage accumulation:

$$\Omega^*_{D_c} \;=\; Y_c \left\langle \frac{\chi_c\left(\underset{\sim}{\sigma}\right)}{S_c} \right\rangle^{m_c} \mathrm{e}^{\left(\beta_c\,\eta_D\,D_c\right)} \quad\leftrightarrow\quad \dot{D}_c \;=\; \frac{\partial \Omega^*_{D_c}}{\partial Y_c} \;=\; \left\langle \frac{\chi_c\left(\underset{\sim}{\sigma}\right)}{S_c} \right\rangle^{m_c} \mathrm{e}^{\left(\beta_c\,\eta_D\,D_c\right)} \tag{4.65}$$

where Y_c is the energy release rate related to creep damage, S_c & m_c are the creep damage resistance and exponent, respectively, and β_c controls the non-linearity of the creep damage evolution. Note that all these material constants may depend on temperature. In eq. (4.65), the $\chi_c\left(\underset{\sim}{\sigma}\right)$ is a multiaxiality function of the stress invariants as suggested by [Martin and Leckie, 1972]:

$$\chi_c\left(\underset{\sim}{\sigma}\right) \;=\; \alpha_c\, I_0\left(\underset{\sim}{\sigma}\right) \;+\; \delta_c\, I_1\left(\underset{\sim}{\sigma}\right) \;+\; \left(1-\alpha_c-\delta_c\right)\sqrt{3J_2\left(\underset{\sim}{\sigma}\right)} \tag{4.66}$$

with:

$$I_0\left(\underset{\sim}{\sigma}\right) = \max_i(\sigma_i) \quad ; \quad I_1\left(\underset{\sim}{\sigma}\right) = \operatorname{tr}\underset{\sim}{\sigma} \quad ; \quad \sqrt{3J_2\left(\underset{\sim}{\sigma}\right)} = \sqrt{\frac{3}{2}\,\underset{\sim}{\sigma}^{D} : \underset{\sim}{\sigma}^{D}} \tag{4.67}$$

where α_c and δ_c are temperature-dependent coefficients controlling the damage growth.
In eq. (4.66), the introduction of $I_0\left(\underset{\sim}{\sigma}\right)$ accounts for the maximum principal stress which opens the micro-cracks and makes them to grow (mode I crack opening). The invariant $I_1\left(\underset{\sim}{\sigma}\right)$ relates the hydrostatic stress which is known to greatly affect the cavities growth (through dilatation process) and $\sqrt{3J_2\left(\underset{\sim}{\sigma}\right)}$, known as the octahedral shear stress allows for the shear mechanisms to be accounted for [Arnold and Kruch, 1991].

Remark 1: It can be mentioned that the introduction of the effective stress $\underset{\sim}{\tilde{\sigma}}$ defined in eq. (4.1) into the creep damage evolution equation eq. (4.65) yields:

$$\dot{D}_c = \left\langle \frac{\chi_c\left(\underset{\sim}{\tilde{\sigma}}\right)}{S_c} \right\rangle^{m_c} f_D^{e\,m_c}\; \mathrm{e}^{(\beta_c\,\eta_D\,D_c)} \tag{4.68}$$

Owing to the introduction of an additional creep damage variable, the total damage rate $\dot{D}_{tot}$ defined in eq. (4.64) can be supplemented with a creep contribution due to dwell periods:

$$\mathrm{d}D_{tot} = \mathcal{F}_f\left(\underset{\sim}{\tilde{\sigma}}, \underset{\sim}{\tilde{X}}, \tilde{R}, D_f, D_c, \dot{p}\right)\mathrm{d}t \;+\; \mathcal{F}_c\left(\underset{\sim}{\sigma}, D_f, D_c, t\right)\mathrm{d}t \;+\; \mathcal{F}_v\left(\underset{\sim}{\dot{\varepsilon}}^{in}, D_v\right)\mathrm{d}t \tag{4.69}$$

where all the evolution equations are written in a time-incremental formalism, hence easing the numerical integration process. Moreover, one can remark through the eq. (4.69) that an increase in fatigue damage accelerates the creep one, and conversely. This corresponds to a simple *damage interaction effect* as suggested by [Blackmon et al., 1983] & [Chaboche, 1988b] and which is to be related to the introduction of the total damage D_{tot} in each single damage evolution equation. In the present work, for the sake of simplicity, choice has been made to consider an equally weighted linear combination of all the damage variables:

$$D_{tot} = D_f + D_c + D_v \tag{4.70}$$

Remark 2: Let us note that it is possible, in the modeling, to exacerbate the interaction effects between damage mechanisms through specific formulations. Details can be found in, *e.g.* [Dunne and Hayhurst, 1992], [Skelton and Gandy, 2008], [Jing et al., 2017] or [Tang et al., 2020].

Once the total damage has reached a critical value D_{tot}^{crit}, the material point is assumed to be broken. The evolution equations eq. (4.47), eq. (4.60) and eq. (4.65) remain valid as long as $D_{tot} \leq D_{tot}^{crit}$. Finally, other interaction effects of the damage mechanisms are neglected here for simplicity reasons.

Remark 3: Due to the summation of the damage variables as in eq. (4.70), the creep damage driving force Y_c admits the same form as the one from fatigue damage Y_f given in eq. (4.15) - eq. (4.18). As a consequence, the free energy functional (Helmholtz, eq. (4.3), or Gibbs, eq. (4.53)) is thus supplemented by an additional internal state variable D_c. In the same time, the effective variables eq. (4.1) and the softening function eq. (4.2) both include the total damage D_{tot} as

parameter, which in turn results in a strong coupling between total damage and the mechanical response (whereas damage interaction effects are first disregarded). Owing to the CDM framework, the condition $D_{tot} = 0$ still corresponds to the virgin (undamaged) state while $D_{tot} = D_{tot}^{crit}$ corresponds to the fully damaged state (*i.e.* crack initiation).

4.2.3 Overall equations of the multi-mechanism damage model

Mechanism	Constitutive equation
Strain partition	$\dot{\underset{\sim}{\varepsilon}} = \dot{\underset{\sim}{\varepsilon}}^{e} + \dot{\underset{\sim}{\varepsilon}}^{in}$
Elasticity	$\underset{\sim}{\varepsilon}^{e} = \tilde{\underset{\approx}{A}}^{-1} : \underset{\sim}{\sigma}$ or $\underset{\sim}{\varepsilon}^{e} = \underset{\approx}{A}^{-1} : \tilde{\underset{\sim}{\sigma}}_{uc}$ if U.C.
(Visco)Plasticity	$\dot{\underset{\sim}{\varepsilon}}^{in} = \dfrac{\dot{\lambda}}{f^{e}(D)} \sqrt{\dfrac{3}{2}}\, \tilde{\underset{\sim}{n}}$
Unit effective normal	$\tilde{\underset{\sim}{n}} = \sqrt{\dfrac{2}{3}} \dfrac{\partial \mathcal{F}_y}{\partial \tilde{\underset{\sim}{\sigma}}} = \dfrac{\underset{\approx}{H} : \tilde{\underset{\sim}{Z}}}{\left\| \tilde{\underset{\sim}{Z}} \right\|_{H}}$
Apparent stress	$\tilde{\underset{\sim}{Z}} = \tilde{\underset{\sim}{\sigma}}^{D} - \sum_{k} \tilde{\underset{\sim}{X}}^{k}$
Cumulated plasticity	$\dot{p} = \sqrt{\dfrac{2}{3}} \left\| \dot{\underset{\sim}{\varepsilon}}^{in} \right\|_{H} = \dfrac{\dot{\lambda}}{f^{e}(D)} = \dfrac{\left(\tilde{\underset{\sim}{Z}} : \dot{\underset{\sim}{\varepsilon}}^{in}\right)}{\tilde{\sigma}_{eq}}$
Viscoplastic multiplier	$\dot{\lambda} = \phi_v(\mathcal{F}_y) = \dot{\epsilon}_0 \left[\sinh \left\langle \dfrac{\mathcal{F}_y}{K} \right\rangle_{+}^{n} \right]^{m}$
Yield (visco-)surface	$\mathcal{F}_y^{vp} = \mathcal{F}_y - \sigma_{ov} = \sqrt{\dfrac{3}{2}} \left\| \tilde{\underset{\sim}{Z}} \right\|_{H} - \sum_{i} \tilde{R}^{i} - R_0 - \sigma_{ov}$
Isotropic hard.	$\dot{R} = \sum_{i}^{2} \dot{R}^{i} = b^{i} \tilde{Q}^{i} \dot{r}^{i}$ with $\dot{r}^{i} = \dfrac{\dot{\lambda}}{f^{i}(D)} \left(1 - b^{i} r^{i}\right)$
Kinematic hard.	$\dot{\underset{\sim}{X}} = \sum_{k}^{3} \dot{\underset{\sim}{X}}^{k} = \tilde{\underset{\approx}{C}}^{k} : \dot{\underset{\sim}{\alpha}}^{k}$ with $\dot{\underset{\sim}{\alpha}}^{k} = \dfrac{\dot{\lambda}}{f^{k}(D)} \left(\sqrt{\dfrac{3}{2}}\, \tilde{\underset{\sim}{n}} - \gamma^{k}\, \varphi^{k}(p)\, \underset{\approx}{P}^{D} : \underset{\sim}{\alpha}^{k} \right)$
Fatigue damage	$\dot{D}_f = \dot{\lambda} \left\langle \dfrac{Y_f - Y_{f_0}}{S_f} \right\rangle_{+}^{m_f} \mathrm{e}^{(\beta_f \eta_D D_{tot})}\, \mathcal{H}(p - p_D)$
Creep damage	$\dot{D}_c = \left\langle \dfrac{\chi_c(\underset{\sim}{\sigma})}{S_c} \right\rangle_{+}^{m_c} \mathrm{e}^{(\beta_c \eta_D D_{tot})}$
Volumetric damage	$\dot{D}_v = (1 - D_{tot})\, \mathrm{tr}\, \dot{\underset{\sim}{\varepsilon}}^{in}$
Total damage	$\dot{D}_{tot} = \dot{D} = \dot{D}_f + \dot{D}_c + \dot{D}_v$

Table 4.2: Three-dimensional form of the overall constitutive equations fully coupled to damage.

4.3 Numerical implementation into a Finite Element code

This section is dedicated to the numerical implementation and solving routines associated with the time-incremental fatigue damage model proposed in the last sect. 4.1 & sect. 4.2. Interested reader may have a look on this section, while the one who is more interested in the applications can directly refer to the sect. 4.4.

To perform FE calculations, the multi-mechanism damage model derived in the last sect. 4.2 needs to be implemented within a FE code. In the present study, as already stated in Chap. 2, this task is achieved in the multi-purposes Z-set static implicit FE solver through the *Z-front* utility which allows to write user-defined sub-routines [Foerch et al., 1997], [Besson and Foerch, 1997].

In order to solve the first order initial value problem (IVP) defined by the whole constitutive evolution equations, see Tab. 4.2, a relevant numerical integration algorithm should be considered. Indeed, thanks to the time-incremental formalism, the entire set of evolution equations governing the non-linear and damageable behavior of the material needs to be integrated with respect to time during the whole loading scheme. To achieve this task, both explicit and implicit resolution procedures can be considered. In the present work, for stability reasons, I have chosen an implicit scheme, despite its high-demanding implementation cost. As a consequence, the numerical integration of the above constitutive equations may be expressed via a fully-implicit stress update routine. Such a task was carried out following some guidelines given in, *e.g.* [Besson et al., 2010]. By performing the temporal discretization of the problem, the algorithm starts with an elastic trial step, and by reaching the prescribed yield limit, a solution strategy is applied to update the internal state variables. This section gives some details about such numerical procedures.

4.3.1 Local integration of the constitutive equations

Assuming the use of the standard FE method, the purpose of the numerical constitutive model is to compute the stress tensor $\underset{\sim}{\sigma}$ (as well with other internal variables) at the end of the load increment accordingly to the strain tensor increment $\Delta\underset{\sim}{\varepsilon}$ associated with the prescribed displacement of the structure $\Delta\underline{u}$, during a time step Δt. Such an integration scheme is applied locally at every integration (Gauss) point during each global iteration step.

For the present viscoplastic-damage model, the sets of degrees of freedom DOF, input variables $\mathcal{V}_{IN}$, output variables $\mathcal{V}_{OUT}$, integrated variables $\mathcal{V}_{int}$ and auxiliary variables $\mathcal{V}_{aux}$ for a standard (displacement-based) FE are given by:

$$DOF : \left\{ \underline{u} \right\}; \qquad \mathcal{V}_{IN} : \left\{ \underset{\sim}{\varepsilon} \right\}; \qquad \mathcal{V}_{OUT} : \left\{ \underset{\sim}{\sigma} \right\}; \tag{4.71a}$$

$$\mathcal{V}_{int} : \left\{ \underset{\sim}{\varepsilon}^{e},\ \underset{\sim}{\alpha}^{k},\ r^{i},\ \lambda,\ D_f,\ D_c,\ D_v \right\}; \qquad \mathcal{V}_{aux} : \left\{ \underset{\sim}{\varepsilon}^{in},\ \underset{\sim}{X}^{k},\ \underset{\sim}{Z},\ R^{i},\ p,\ Y_f,\ Y_c \right\} \tag{4.71b}$$

As stated in sub-sect. 4.1.3 for an elastic-viscoplastic behavior, two cases may be encountered:

- if $\mathcal{F}_y \leq 0$ then the material behaves elastically with a linear stress-strain response;
- while if $\mathcal{F}_y = \sigma_{ov} > 0$ the material behavior is non-linear with viscoplastic & damage properties.

The numerical procedure is hence split into two steps: *i)* an elastic prediction is realized so that to evaluate the yield criterion eq. (4.21), see sub-sect. 4.3.1.1; *ii)* in case of an inelastic response of the material, a local update of the internal variables is achieved, see sub-sect. 4.3.1.2.

4.3.1.1 Elastic trial

Assuming that the input strain increment $\Delta\underset{\sim}{\varepsilon}$ is purely elastic at the time step $n+1$, the trial stress tensor is given by:

$$\underset{\sim}{\sigma}^{tr}_{n+1} = \underset{\sim}{\sigma}_n + \Delta\underset{\sim}{\sigma} = \underset{\sim}{\sigma}_n + f^e\left(D_{tot\,n}\right)\underset{\approx}{\Lambda} : \Delta\underset{\sim}{\varepsilon} \tag{4.72}$$

Then a trial of the yield function $\mathcal{F}^{tr}_y$ is performed using the new trial stress $\underset{\sim}{\sigma}^{tr}$ as follows:

$$\mathcal{F}^{tr}_y = \sqrt{\frac{3}{2}}\left\|\left(\underset{\sim}{\tilde{\sigma}}^{D\,tr}_{n+1} - \sum_k \underset{\sim}{\tilde{X}}^k_n\right)\right\|_H - \sum_i \tilde{R}^i_n - R_0 \leq 0 \tag{4.73}$$

The two cases defined above can be distinguished:

- if $\mathcal{F}^{tr}_y \leq 0$ the material response is effectively linear elastic, only $\Delta\sigma$ is different from zero and the trial stress eq. (4.72) is kept as final stress tensor at t_{n+1}:

$$\underset{\sim}{\sigma}_{n+1} = \underset{\sim}{\sigma}^{tr}_{n+1} \tag{4.74}$$

and then both the int. and aux. variables are kept unchanged from their previous value at t_n:

$$\mathcal{V}_{int} : \left\{\underset{\sim}{\varepsilon}^e,\ \underset{\sim}{\alpha}^k,\ r^i,\ \lambda,\ D_f,\ D_c,\ D_v\right\}_{n+1} = \left\{\underset{\sim}{\varepsilon}^e,\ \underset{\sim}{\alpha}^k,\ r^i,\ \lambda,\ D_f,\ D_c,\ D_v\right\}_n \tag{4.75}$$

$$\mathcal{V}_{aux} : \left\{\underset{\sim}{\varepsilon}^{in},\ \underset{\sim}{X}^k,\ \underset{\sim}{Z},\ R^i,\ p,\ Y_f,\ Y_c\right\}_{n+1} = \left\{\underset{\sim}{\varepsilon}^{in},\ \underset{\sim}{X}^k,\ \underset{\sim}{Z},\ R^i,\ p,\ Y_f,\ Y_c\right\}_n \tag{4.76}$$

- if $\mathcal{F}^{tr}_y > 0$ then the material behavior is non-linear with inelastic & damage properties, hence requiring a inelastic correction to be performed to ensure the consistency condition eq. (4.23) as well with the proper update of the int. and aux. variables. Such an update procedure aims at evaluating the stress tensor as well as the integrated variables in order to ensure the condition $\mathcal{F}_y \simeq 0$. In such a case, one gets:

$$\underset{\sim}{\sigma}_{n+1} = \underset{\sim}{\sigma}^{tr}_{n+1} - \underset{\approx}{\tilde{\Lambda}} : \Delta\underset{\sim}{\varepsilon}^{in} \tag{4.77}$$

The internal and auxiliary variables also need to be updated consistently following the resolution procedure discussed in the following sub-sect. 4.3.2:

$$\left\{\mathcal{V}_{int/aux}\right\}_{n+1} = \left\{\mathcal{V}_{int/aux}\right\}_n + \left\{\Delta\mathcal{V}_{int/aux}\right\} \tag{4.78}$$

4.3.1.2 Correction for the internal variables

In order to update the integrated variables $\mathcal{V}_{int}$ as well with the stress tensor $\mathcal{V}_{OUT} = \underset{\sim}{\sigma}$ accordingly to the imposed total strain increment $\Delta\mathcal{V}_{IN} = \Delta\underset{\sim}{\varepsilon}$, an iterative numerical procedure aiming at solving the non-linear governing equations given in Tab. 4.2 is required. To do so, two numerical procedures can be considered: implicit & explicit schemes. In the present study, implicit numerical scheme has been chosen for particular reasons discussed below. Thus, for the sake of brevity, explicit schemes will not be discussed. Some information can be found in [Besson et al., 2010].

In this Ph.D. project, choice for an implicit numerical scheme mainly relies on the need to perform relatively large time steps. Indeed, owing to the loading schemes assessed in the present work dealing with LCF conditions, a large number of loading cycles needs to be simulated, hence requiring a huge number of time increments. In addition, stability properties were also required.
On the one hand, implicit methods are known to be unconditionally stable while preserving a good accuracy, providing that a convergence criterion is respected [Ortiz and Popov, 1985], [Besson et al., 2010], [de Souza Neto et al., 2011]. On the other hand, the convergence of the well-known gradient-based iterative scheme referred to as the *Newton-Raphson* (N-R) algorithm requires the estimation of the so-called *Jacobian matrix* (see sub-sect. 4.3.3) which size depends on the number of integrated variables.

In the following, the constitutive equations associated with the viscoplastic and damageable behavior of AD730™ are implemented using the N-R iterative scheme to solve the implicitly defined equations thanks to a backward-Euler numerical scheme.

4.3.2 Incremental formulation of the problem

As it can be observed from the constitutive equations of the model, summarized in Tab. 4.2, the strong coupling between damage and elastic-viscoplasticity, as well with the presence of a back-stress tensor, induce a highly non linear problem to be solved. Therefore, an iterative numerical scheme is required to update the state variables incrementally.

4.3.2.1 Time discretization

The material equations given in Tab. 4.2 are time-dependent ordinary differential equations of first order which are discretized in time thanks to a standard θ-method [Chaboche and Cailletaud, 1996]. We have the following initial value problem (IVP):

$$\dot{x} = f(t,x), \quad x(t_0) = x_0 \qquad \leftrightarrow \qquad x_{n+\theta} = x_n + \theta\,\Delta t\, f\left(t_{n+\theta}, x_{n+\theta}\right) \tag{4.79}$$

where the eq. (4.79) represents an implicit equation for any arbitrary unknown value $x_{n+\theta}\left(t_{n+\theta}\right)$. Defining a family of generalized mid-point integration rules parameterized in θ, as:

$$x_{n+1} = x_n + \Delta t\,\dot{x}_{n+\theta} \qquad \text{with} \qquad \dot{x}_{n+\theta} = (1-\theta)\,\dot{x}_n + \theta\,\dot{x}_{n+1} \tag{4.80}$$

Such a method is second order accurate for $\theta = 1/2$ [Mathews and Fink, 2002], whereas $\theta = 1$ gives account for the first order accurate and unconditionally stable backward-Euler method which is known to be highly efficient in the integration of $\underset{\sim}{\alpha}$ [Jirásek and Bažant, 2001].

When the implicit backward-Euler method is applied to plastic or viscoplastic equations, the method is recognized as the radial return method [Wilkins, 1964], [Besson et al., 2010]. Using the Z-set code allows for the fast and exact determination of the consistent tangent operator required for the evaluation of the elementary stiffness matrix (see later in sub-sect. 4.3.5) [Armines et al., 2020b]. To that extent, a **strain-based** formulation should be used in order to consistently derive the material tangents [Cai et al., 2019]. Thus, considering a **strain-driven** problem, that is, controlled by the total strain tensor $\underset{\sim}{\varepsilon}$, the time interval is given by $[t_n,\ t_{n+1}]$ whereas the time increment is $\Delta t = t_{n+1} - t_n$. For the strain-driven problem, the set of internal variables is chosen as:

$$\mathcal{V}_{int} = \left\{ \underset{\sim}{\sigma},\ \underset{\sim}{\varepsilon}^e,\ \underset{\sim}{\alpha}^k,\ r^i,\ \lambda,\ D_f, D_c, D_v \right\} \tag{4.81}$$

which corresponds to a number of equations to be solved of:

$$\mathcal{N} = \left\{ 6 + 6 + (k \times 6) + (i \times 1) + 1 + 1 + 1 + 1 \right\} = 36 \quad \text{with} \quad k = 3;\ i = 2 \tag{4.82}$$

On the one hand, the values of the state variables at t_n are known $\left\{ \mathcal{V}_{int/aux} \right\}_n$.
On the other hand, the prescribed variable is given at current time $t_{n+1} = t_n + \Delta t$ by $\left\{ \underset{\sim}{\varepsilon}_{n+1} \right\}$.

The updating procedure for the internal variables (see sub-sect. 4.3.1.2) restores the consistency condition eq. (4.21) by *returning* the trial stress eq. (4.72) to the yield surface through a radial return. Thus, such a method of corrector step is usually performed using an incremental formulation (implicit function). Thus, in case of a (visco)plastic yielding, the 11 independent internal state variables (*i.e.* 5 second order tensors and 6 scalars) given in eq. (4.81) need to be updated at the end of the time step, that is at $t_n + \Delta t$. The discretization in time transforms the differential equations into incremental (*i.e.* difference) formulation. In the following, any quantity evaluated at t_n will be denoted with a subscript n while, for the sake of clearness, those at t_{n+1} will have their subscript $n+1$ omitted:

$$\underset{\sim}{\varepsilon}^e = \underset{\sim}{\varepsilon}^e_n + \theta \Delta t \frac{\partial \underset{\sim}{\varepsilon}^e}{\partial t} = \underset{\sim}{\varepsilon}^e_n + \theta \Delta t\, \dot{\underset{\sim}{\varepsilon}}^e \tag{4.83a}$$

$$\underset{\sim}{\alpha}^k = \underset{\sim}{\alpha}^k_n + \theta \Delta t \frac{\partial \underset{\sim}{\alpha}^k}{\partial t} = \underset{\sim}{\alpha}^k_n + \theta \Delta t\, \dot{\underset{\sim}{\alpha}}^k \tag{4.83b}$$

$$r^i = r^i_n + \theta \Delta t \frac{\partial r^i}{\partial t} = r^i_n + \theta \Delta t\, \dot{r}^i \tag{4.83c}$$

$$\lambda = \lambda_n + \Delta t \frac{\partial \lambda}{\partial t} = \lambda_n + \theta \Delta t\, \dot{\lambda} \tag{4.83d}$$

$$D_f = D_{f\,n} + \theta \Delta t \frac{\partial D_f}{\partial t} = D_{f\,n} + \theta \Delta t\, \dot{D}_f \tag{4.83e}$$

$$D_c = D_{cn} + \theta \Delta t \frac{\partial D_c}{\partial t} = D_{cn} + \theta \Delta t \, \dot{D}_c \tag{4.83f}$$

$$D_v = D_{vn} + \theta \Delta t \frac{\partial D_v}{\partial t} = D_{vn} + \theta \Delta t \, \dot{D}_v \tag{4.83g}$$

It is worth noting that the implicit formulation of the constitutive equations implies that derivatives in eq. (4.83) are evaluated at the current time step $n+1$. Considering the rate form of the constitutive equations given in Tab. 4.2, the system eq. (4.83) can be re-written, using $\theta = 1$:

$$\underset{\sim}{\varepsilon}^e = \underset{\sim}{\varepsilon}^e_n + \Delta \underset{\sim}{\varepsilon}^e = \underset{\sim}{\varepsilon}^e_n + \Delta \underset{\sim}{\varepsilon} - \Delta \underset{\sim}{\varepsilon}^{in} = \underset{\sim}{\varepsilon}^e_n + \Delta \underset{\sim}{\varepsilon} - \frac{\Delta \lambda}{f^e(D)} \sqrt{\frac{3}{2}} \, \underset{\sim}{\tilde{n}} \tag{4.84a}$$

$$\underset{\sim}{\alpha}^k = \underset{\sim}{\alpha}^k_n + \Delta \underset{\sim}{\alpha}^k = \underset{\sim}{\alpha}^k_n + \frac{\Delta \lambda}{f^k(D)} \left(\sqrt{\frac{3}{2}} \, \underset{\sim}{\tilde{n}} - \gamma^k \, \varphi^k(p) \, \underset{\approx}{P}^D : \underset{\sim}{\alpha}^k \right) \tag{4.84b}$$

$$r^i = r^i_n + \Delta r^i = r^i_n + \frac{\Delta \lambda}{f^i(D)} \left(1 - b^i r^i\right) \tag{4.84c}$$

$$\lambda = \lambda_n + \Delta \lambda = \lambda_n + \Delta t \, \phi_v(\mathcal{F}_y) \tag{4.84d}$$

$$D_f = D_{fn} + \Delta D_f = D_{fn} + \Delta \lambda \left\langle \frac{Y_f - Y_{f_0}}{S_f} \right\rangle_+^{m_f} e^{(\beta_f \eta_D D_{tot})} \tag{4.84e}$$

$$D_c = D_{cn} + \Delta D_c = D_{cn} + \Delta t \left\langle \frac{\chi_c(\underset{\sim}{\sigma})}{S_c} \right\rangle_+^{m_c} e^{(\beta_c \eta_D D_{tot})} \tag{4.84f}$$

$$D_v = D_{vn} + \Delta D_v = D_{vn} + (1 - D_v) \frac{\Delta \lambda}{f^e(D)} \sqrt{\frac{3}{2}} \, \underset{\sim}{\tilde{n}} : \underset{\sim}{1} \tag{4.84g}$$

4.3.2.2 Residual expressions

Once the time discretization of the evolution equations is achieved, the expression of the residual equations to be solved is required. Using the θ-method, one gets at time $t + \theta \Delta t$:

$$\mathcal{R} = \Delta \mathcal{V}_{int} - \Delta \hat{\mathcal{V}}_{int} = \Delta \mathcal{V}_{int} - \Delta t \, \dot{\mathcal{V}}_{int}(t + \theta \Delta t) = 0 \tag{4.85}$$

$$\text{with} \qquad \dot{\mathcal{V}}_{int}(t + \theta \Delta t) = \frac{\mathcal{V}_{int}(t + \Delta t) - \mathcal{V}_{int}(t)}{\Delta t} = \frac{\Delta \mathcal{V}_{int}}{\Delta t} \tag{4.86}$$

where $\Delta \hat{\mathcal{V}}_{int}$ denotes the function resulting from the evolution rule for the integrated variable. Through time discretization of the evolution equations with $\theta = 1$, eq. (4.84), we obtain the corresponding residual equation system to be solved at t_{n+1}:

$$\mathcal{R} = \left\{ \mathcal{R}_{\underset{\sim}{\sigma}},\, \mathcal{R}_{\underset{\sim}{\varepsilon}^e},\, \mathcal{R}_{\underset{\sim}{\alpha}^k},\, \mathcal{R}_{r^i},\, \mathcal{R}_{\lambda},\, \mathcal{R}_{D_f},\, \mathcal{R}_{D_c},\, \mathcal{R}_{D_v} \right\}^T = 0 \tag{4.87}$$

where, for the sake of clearness, index for quantities at time $t_{n+1} = t_n + \Delta t$ is omitted and use is made of the increments of the internal variables, as defined in eq. (4.84):

$$\mathcal{R}_{\underset{\sim}{\sigma}} = \underset{\sim}{\varepsilon}^e - \underset{\approx}{A}^{-1} : \underset{\sim}{\tilde{\sigma}}_{uc} = \underset{\sim}{0} \tag{4.88a}$$

$$\mathcal{R}_{\underset{\sim}{\varepsilon}^e} = \Delta\underset{\sim}{\varepsilon}^e - \Delta\underset{\sim}{\varepsilon} + \frac{\Delta\lambda}{f^e(D)}\sqrt{\frac{3}{2}}\,\underset{\approx}{\tilde{n}} = \underset{\sim}{0} \tag{4.88b}$$

$$\mathcal{R}_{\underset{\sim}{\alpha}^k} = \Delta\underset{\sim}{\alpha}^k - \frac{\Delta\lambda}{f^k(D)}\left(\sqrt{\frac{3}{2}}\,\underset{\approx}{\tilde{n}} - \gamma^k\,\varphi^k(p)\,\underset{\approx}{P}^D : \underset{\sim}{\alpha}^k\right) = \underset{\sim}{0} \tag{4.88c}$$

$$\mathcal{R}_{r^i} = \Delta r^i - \frac{\Delta\lambda}{f^i(D)}\left(1 - b^i r^i\right) = 0 \tag{4.88d}$$

$$\mathcal{R}_{\lambda} = \Delta\lambda - \Delta t\,\phi_v\left(\mathcal{F}_y\right) = 0 \tag{4.88e}$$

$$\mathcal{R}_{D_f} = \Delta D_f - \Delta\lambda\left\langle \frac{Y_f - Y_{f_0}}{S_f} \right\rangle_+^{m_f} \mathrm{e}^{\beta_f\,\eta_D\,D_{tot}}\,\mathcal{H}(p - p_D) = 0 \tag{4.88f}$$

$$\mathcal{R}_{D_c} = \Delta D_c - \Delta t\left\langle \frac{\chi_c(\underset{\sim}{\sigma})}{S_c} \right\rangle_+^{m_c} \mathrm{e}^{\beta_c\,\eta_D\,D_{tot}} = 0 \tag{4.88g}$$

$$\mathcal{R}_{D_v} = \Delta D_v - (1 - D_v)\,\frac{\Delta\lambda}{f^e(D)}\sqrt{\frac{3}{2}}\,\underset{\approx}{\tilde{n}} : \underset{\sim}{1} = 0 \tag{4.88h}$$

where the eq. (5.54a) is not the incremental form of a differential equation. Such a supplementary equation is added in the Newton-Raphson iterative loop so as to solve for the implicitly defined stress-strain relationship strongly coupled with damage in case of micro-defects closure effect (*i.e.* UC) in the elasticity law, as in eq. (4.56). Such a point, already discussed in [Lemaitre and Desmorat, 2005], is also detailed in the appendices, see Chap. I. Of course, for the case without any UC, the eq. (5.54a) is omitted.

4.3.3 Linearization and iterative solving algorithm

In order to solve the system of non-linear equations eq. (4.88) through the N-R scheme, these equations first need to be linearized. Therein, a consistent linearization with respect to all basic unknowns describing the problem is essential [Simo and Taylor, 1985], [Simo and Hughes, 1998]. The general root finding problem from eq. (4.85) can be written:

$$\mathcal{R}(\mathcal{V}_{int}, t) = 0 \quad \in \mathbb{R}^n \tag{4.89}$$

Thus, the consistent linearization of eq. (4.89) (or eq. (4.87)) with respect to $\mathcal{V}_{int}$ leads to the

local resolution procedure realized at each Gauss point in order to update the internal state variables. This can be carried out with the following iterative scheme, considering a first order Taylor expansion:

$$\mathcal{R}\big|_{\mathcal{V}_{int0}} + \mathcal{J}\big|_{\mathcal{V}_{int0}}\,\delta\Delta\mathcal{V}_{int} \;=\; 0 \qquad \leftrightarrow \qquad \Delta\mathcal{V}_{int}^{(k+1)} \;=\; \Delta\mathcal{V}_{int}^{(k)} \;-\; \left[\mathcal{J}^{(k)}\right]^{-1}\,\mathcal{R}^{(k)} \tag{4.90}$$

where $\mathcal{V}_{int0}$ is the initial value of the variables at each iteration step, $\mathcal{J}$ is the algorithmic tangent operator, also known as material *Jacobian* matrix and $\delta\Delta\mathcal{V}_{int}^{(k+1)} = \Delta\mathcal{V}_{int}^{(k+1)} - \Delta\mathcal{V}_{int}^{(k)}$ denotes the corrections for the increments of unknowns. The Jacobian matrix [1] is therefore given by:

$$\mathcal{J} \;=\; \frac{\partial\mathcal{R}}{\partial\Delta\mathcal{V}_{int}} \;=\; 1 - \Delta t\,\frac{\partial\dot{\mathcal{V}}_{int}}{\partial\Delta\mathcal{V}_{int}}\bigg|_{t+\theta\Delta t} \;=\; \begin{bmatrix} \dfrac{\partial\mathcal{R}_{\underset{\sim}{\sigma}}}{\partial\Delta\underset{\sim}{\sigma}} & \cdots & \dfrac{\partial\mathcal{R}_{\underset{\sim}{\sigma}}}{\partial\Delta D_v} \\ \cdots & \cdots & \cdots \\ \dfrac{\partial\mathcal{R}_{D_v}}{\partial\Delta\underset{\sim}{\sigma}} & \cdots & \dfrac{\partial\mathcal{R}_{D_v}}{\partial\Delta D_v} \end{bmatrix} \tag{4.91}$$

Finally, the consistent linearization reads:

$$\begin{bmatrix} \dfrac{\partial\mathcal{R}_{\underset{\sim}{\sigma}}}{\partial\Delta\underset{\sim}{\sigma}} & \cdots & \dfrac{\partial\mathcal{R}_{\underset{\sim}{\sigma}}}{\partial\Delta D_v} \\ \cdots & \cdots & \cdots \\ \dfrac{\partial\mathcal{R}_{D_v}}{\partial\Delta\underset{\sim}{\sigma}} & \cdots & \dfrac{\partial\mathcal{R}_{D_v}}{\partial\Delta D_v} \end{bmatrix}^{(k)} \cdot \begin{bmatrix} \Delta\underset{\sim}{\sigma}^{(k+1)} - \Delta\underset{\sim}{\sigma}^{(k)} \\ \cdots \\ \Delta D_v^{(k+1)} - \Delta D_v^{(k)} \end{bmatrix} \;=\; -\begin{Bmatrix} \mathcal{R}_{\underset{\sim}{\sigma}} \\ \cdots \\ \mathcal{R}_{D_v} \end{Bmatrix}^{(k)} \tag{4.92}$$

In eq. (4.90) & eq. (4.92), the superscripts (k) & $(k+1)$ refer to the previous and current iteration number, respectively, owing to the fact that the approximation of the zero residual equation eq. (4.87) is realized in several iterations of the N-R scheme. The convergence of the algorithm is reached once a specific criterion is fulfilled, that is generally $\|\mathcal{R}\|_2 < \epsilon_{tol}^{loc}$ where ϵ_{tol}^{loc} is a tolerance to be defined, *e.g.* 10^{-8}. Note also that during the iterations, the total strain increment $\Delta\underset{\sim}{\varepsilon}$ remains constant. The matrix $\mathcal{J}$ in eq. (4.91), although cumbersome to calculate is highly necessary. Even if the accurate derivation of its terms is required, a good approximation can be sufficient. Such a matrix needs to be computed and inverted at each iteration so that the internal variables to be updated. Such a process demands a high computational effort during the local update procedure (the more the $\mathcal{V}_{int}$, the larger the required CPU-time).

Remark: For the sake of brevity, only the general procedure has been detailed. Since the model will be extended to non-local interactions in the next Chap. 5, a similar procedure will have to be performed. The values of each term of the Jacobian matrix are given in the appendix, see Chap. I page 301. When a distinction between both local and non-local models exists, it will be expressively indicated.

[1] The symbolic matrix representation is used for the Jacobian matrix, even though each element of this symbolic matrix can be either a scalar or a tensor of appropriate order.

4.3.4 Update algorithm

Once the residual equation system eq. (4.88) is solved (*i.e.* the N-R loop has reached the convergence criterion), the independent internal variables $\mathcal{V}_{int} = \left\{ \underset{\sim}{\sigma}, \underset{\sim}{\varepsilon}^e, \underset{\sim}{\alpha}^k, r^i, \lambda, D_f, D_c, D_v \right\}$ at time t_{n+1} can be determined.

$$\text{At convergence:} \qquad \Delta\mathcal{V}_{int} = -\left[\mathcal{J}\right]^{-1} \mathcal{R} \tag{4.93}$$

$$\mathcal{V}_{int} \Leftarrow \mathcal{V}_{int} + \Delta\mathcal{V}_{int} \qquad \text{and} \qquad \mathcal{V}_{aux} \Leftarrow \mathcal{V}_{aux} + \Delta\mathcal{V}_{aux} \tag{4.94}$$

Finally, thermodynamics associated variables (mostly defined by auxiliary variables) can be updated at the end of the time step following state relations eq. (4.12), eq. (4.13), eq. (4.14), eq. (4.15), eq. (4.16) (or eq. (4.58) in case of UC), eq. (4.17), eq. (4.18), eq. (4.37).

As a matter of synthesis, the numerical integration algorithm for the strain-driven problem is summarized in Tab. 4.3 page 170.

4.3.5 Consistent material tangent matrix

For the complete implementation of the fully coupled multi-mechanism damage model into the implicit FE code Z-set, the consistent tangent operator (CTO) which is consistent with the integration algorithm developed above in sub-sect. 4.3.3 should be implemented at the FE level to evaluate the elementary stiffness. According to [Simo and Taylor, 1985], the CTO is required in order to guarantee the convergence properties of the iterative N-R method. Hence, use of the CTO guarantees a quadratic convergence of the global Newton equilibrium iteration.

As said previously, the main advantage of the fully implicit integration scheme is the direct evaluation of the consistent tangent operator [Simo and Taylor, 1985], [Besson et al., 2010]. In the present work, the CTO is estimated from the incremental form of the constitutive equations, as suggested by [Besson et al., 2010] and applied in, *e.g.* [Besson et al., 2001], [Feld-Payet, 2010] and [Ling, 2017]. The residual equations eq. (4.88) are expressed in terms of increments of the integrated variables $\Delta\mathcal{V}_{int}$ and increments of the input variables $\mathcal{V}_{IN}$. The calculation of the consistent tangent matrix is hence performed after the integration of the constitutive equations which normally yields vanish residual equations:

$$\left\{ \mathcal{R}\left(\Delta\mathcal{V}_{IN}, \Delta\mathcal{V}_{int}\right) \right\} = \left\{ 0 \right\} \tag{4.95}$$

with imposed $\Delta\mathcal{V}_{IN}$ and calculated $\mathcal{V}_{int}$.
A perturbation analysis can then be achieved: by applying an infinitesimal variation to the increments $\mathcal{V}_{IN}$, one obtains a new $\Delta\mathcal{V}_{int}$ according to the requirement of null residual system. The variation of $\Delta\mathcal{V}_{int}$ resulting from the variation of $\Delta\mathcal{V}_{IN}$ should make the variation of $\left\{ \mathcal{R} \right\}$ to vanish, which is expressed as:

Inputs: Number of iteration steps k, time step $t_{n+1} = t + \Delta t$, and prescribed strain $\underset{\sim}{\varepsilon}_{n+1}$

Outputs: Updated stress $\underset{\sim}{\sigma}_{n+1}$ and int. variables $\mathcal{V}_{int_{n+1}}$ at current time step t_{n+1}

1. given $\left\{\underset{\sim}{\varepsilon}_n,\ \underset{\sim}{\sigma}_n,\ \underset{\sim}{\varepsilon}^e_n,\ \underset{\sim}{\varepsilon}^{in}_n,\ \underset{\sim}{\alpha}^k_n,\ r^i_n,\ \lambda_n,\ D_{fn},\ D_{cn}, D_{vn}\right\}$ at t_n and $\left\{\underset{\sim}{\varepsilon}\right\}$ at t_{n+1}
2. evaluate the trial stress $\underset{\sim}{\sigma}^{tr}_{n+1} = \underset{\sim}{\sigma}_n + \underset{\approx}{\tilde{\Lambda}} : \Delta\underset{\sim}{\varepsilon}$
3. check for the yield condition $\mathcal{F}^{pred}_y\left(\tilde{\underset{\sim}{\sigma}}^{tr}_{n+1}, \mathcal{V}_{int_n}\right) \leq 0$?

   yes $\rightarrow$ update variables $\underset{\sim}{\sigma}_{n+1} = \underset{\sim}{\sigma}^{tr}_{n+1}$, $\mathcal{V}_{int_{n+1}} = \mathcal{V}_{int_n}$ and **go to** 7.

   no $\rightarrow$ continue to 4.
4. initialize $\tilde{\underset{\sim}{Z}}_{n+1} = \left(\tilde{\underset{\sim}{\sigma}}^{tr}_{n+1} - \tilde{\underset{\sim}{X}}_{n+1}\right)$ and $\Delta\mathcal{V}_{int} = 0$
5. update stress $\underset{\sim}{\sigma}_{n+1}$ and internal variables $\mathcal{V}_{int_{n+1}}$ using the procedure in sub-sect. 4.3.3

   update of internal variables

   a) set the initial guess of the variables $\mathcal{V}^{(k)}_{int} = \left\{\underset{\sim}{\sigma}_n,\ \underset{\sim}{\varepsilon}^e_n,\ \underset{\sim}{\alpha}^k_n,\ r^i_n,\ \lambda_n,\ D_{fn},\ D_{cn},\ D_{vn}\right\}$

   b) **iterate** over $k \in \{0, \ldots, k_{max}\}$

   - compute the residual equation system $\mathcal{R}^{(k)}$
   - calculate the Jacobian matrix $\mathcal{J}^{(k)}$ and its inverse $\left[\mathcal{J}^{(k)}\right]^{-1}$
   - solve the linear system $\delta\Delta\mathcal{V}^{(k+1)}_{int} = -\left[\mathcal{J}^{(k)}\right]^{-1}\mathcal{R}^{(k)}$
   - update all variables:

     $$\Delta\mathcal{V}^{(k+1)}_{int} = \Delta\mathcal{V}^{(k)}_{int} + \delta\Delta\mathcal{V}^{(k+1)}_{int} \qquad \forall\,\mathcal{V}_{int} \in \left\{\underset{\sim}{\sigma},\ \underset{\sim}{\varepsilon}^e,\ \underset{\sim}{\alpha}^k,\ r^i,\ \lambda,\ D_f,\ D_c,\ D_v\right\}$$

   - check for convergence $\left\|\mathcal{R}^{(k)}\right\|_2 < \epsilon^{loc}_{tol}$?

     yes $\Rightarrow$ **exit** loop

     no $\Rightarrow$ $k \rightarrow k+1$ and **go to** step b)

     no and $k = k_{max}$ $\rightarrow$ **exit** algorithm with error $\rightarrow$ divergence

   c) extract variables' increment $\Delta\mathcal{V}_{int}$
6. update variables $\mathcal{V}_{int_{n+1}} \leftarrow \mathcal{V}_{int_n} + \Delta\mathcal{V}_{int}$ & $\underset{\sim}{\sigma}_{n+1} = \underset{\sim}{\sigma}_n + \underset{\approx}{\tilde{\Lambda}} : \left(\Delta\underset{\sim}{\varepsilon} - \Delta\underset{\sim}{\varepsilon}^{in}\right)$
7. calculate the consistent tangent operator $\mathcal{L} = \partial\Delta\underset{\sim}{\sigma}/\partial\Delta\underset{\sim}{\varepsilon}$
8. return updated stress $\underset{\sim}{\sigma}_{n+1}$ and CTO $\mathcal{L}$ to check for global equilibrium

exit

Table 4.3: Numerical integration procedure associated with the strain-driven problem applied to the local cyclic elastic-viscoplastic-damage model (local level).

$$\left\{\delta\mathcal{R}\right\} = \frac{\{\partial\mathcal{R}\}}{\{\partial\Delta\mathcal{V}_{IN}\}}\,\delta\Delta\mathcal{V}_{IN} + \frac{\{\partial\mathcal{R}\}}{\{\partial\Delta\mathcal{V}_{int}\}}\,\delta\Delta\mathcal{V}_{int} = \left\{0\right\} \tag{4.96}$$

which leads to:

$$\left\{ \delta \Delta \mathcal{V}_{int} \right\} = \left[- \left(\frac{\left\{ \partial \mathcal{R} \right\}}{\left\{ \partial \Delta \mathcal{V}_{int} \right\}} \right)^{-1} \frac{\left\{ \partial \mathcal{R} \right\}}{\left\{ \partial \Delta \mathcal{V}_{IN} \right\}} \right] \left\{ \delta \Delta \mathcal{V}_{IN} \right\} \tag{4.97}$$

where the term within the bracket in eq. (4.97) gives an evaluation of $\frac{\left\{ \delta \Delta \mathcal{V}_{int} \right\}}{\left\{ \delta \Delta \mathcal{V}_{IN} \right\}}$, *i.e.* $\frac{\partial \left\{ \Delta \mathcal{V}_{int} \right\}}{\partial \left\{ \Delta \mathcal{V}_{IN} \right\}}$.

Moreover, by looking at the constitutive equations in Tab. 4.2, it can be noticed that $\mathcal{V}_{OUT}$ depends not only on $\mathcal{V}_{int}$ but also on $\mathcal{V}_{IN}$, which yields:

$$\Delta \mathcal{V}_{OUT} = \mathcal{V}_{OUT} \left(\Delta \mathcal{V}_{int}, \Delta \mathcal{V}_{IN} \right) \tag{4.98}$$

Consequently, the variation of $\Delta \mathcal{V}_{OUT}$ should follow:

$$\delta \Delta \mathcal{V}_{OUT} = \frac{\partial \Delta \mathcal{V}_{OUT}}{\partial \Delta \mathcal{V}_{int}} \delta \Delta \mathcal{V}_{int} + \frac{\partial \Delta \mathcal{V}_{OUT}}{\partial \Delta \mathcal{V}_{IN}} \delta \Delta \mathcal{V}_{IN} \tag{4.99}$$

Substituting eq. (4.97) into eq. (4.99) reads:

$$\delta \Delta \mathcal{V}_{OUT} = \left\{ \frac{\partial \Delta \mathcal{V}_{OUT}}{\partial \Delta \mathcal{V}_{int}} \left[- \left(\frac{\left\{ \partial \mathcal{R} \right\}}{\left\{ \partial \Delta \mathcal{V}_{int} \right\}} \right)^{-1} \frac{\left\{ \partial \mathcal{R} \right\}}{\left\{ \partial \Delta \mathcal{V}_{IN} \right\}} \right] + \frac{\partial \Delta \mathcal{V}_{OUT}}{\partial \Delta \mathcal{V}_{IN}} \right\} \delta \Delta \mathcal{V}_{IN} \tag{4.100}$$

which finally leads to:

$$\delta \Delta \mathcal{V}_{OUT} = \left\{ \mathcal{L} \right\} \delta \Delta \mathcal{V}_{IN} \qquad \leftrightarrow \qquad \left\{ \mathcal{L} \right\} = \frac{\delta \Delta \underset{\sim}{\sigma}}{\delta \Delta \underset{\sim}{\varepsilon}} \tag{4.101}$$

with $\left\{ \mathcal{L} \right\}$ the consistent tangent matrix[1], which is calculated from four matrices: $\frac{\partial \Delta \mathcal{V}_{OUT}}{\partial \Delta \mathcal{V}_{int}}$, $\frac{\left\{ \partial \mathcal{R} \right\}}{\left\{ \partial \Delta \mathcal{V}_{int} \right\}}$, $\frac{\left\{ \partial \mathcal{R} \right\}}{\left\{ \partial \Delta \mathcal{V}_{IN} \right\}}$ and $\frac{\partial \Delta \mathcal{V}_{OUT}}{\partial \Delta \mathcal{V}_{IN}}$.

Due to the strong coupling between damage and behavior as well with non-associated viscoplasticity, it can be noticed that the CTO of the constitutive model is generally non-symmetric. Moreover, as already noticed, the inverse of the Jacobian matrix $\mathcal{J} = \frac{\partial \mathcal{R}}{\partial \Delta \mathcal{V}_{int}}$ is gained thanks to the numerical inversion of the residual system upon iterating, see eq. (4.90). For the sake of brevity, details for the derivation of each terms of the previous matrices are given in the appendices, see Chap. J page 309.

[1] Similarly to the Jacobian matrix, a symbolic matrix representation is considered for the consistent tangent matrix, even though each element of this symbolic matrix can be either a scalar or a tensor of appropriate order.

4.4 Validation of the implementation

In the present section, some numerical simulations are performed on the general FE solver *Zébulon* from the Z-set suite, using the classical Newton-Raphson fully implicit procedure both at the global (equilibrium equation) and local (constitutive damage model) levels. A short benchmark seems mandatory in order to validate the user-defined implementation.

4.4.1 Simulations on a single element

In order to assess the validity of the user-defined numerical damage model as implemented within the Z-set solver (see sect. 4.3), it seems first reasonable to validate the numerical time-integration procedure at the integration point level. To do so, a generic comparison between the present cyclic damage model and a standard cyclic model already implemented within the FE code (process "gen-evp", see [Armines et al., 2020a]) is performed. In order to check the material response, simulations are run on a single element, *i.e.* at the scale of the Representative Volume Element (RVE), see Fig. 4.4.

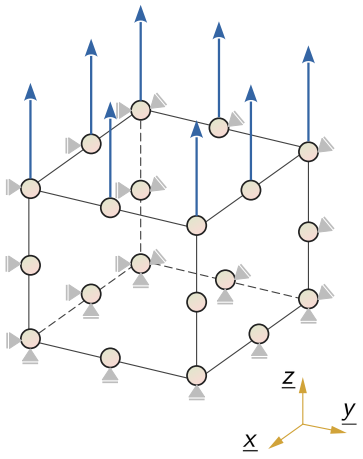

Figure 4.4: Uniaxial tension-compression test on an under-integrated c3d20r FE.

4.4.1.1 Convergence study

First of all, the damaging processes are disabled in our model to only check the cyclic elastic-viscoplastic behavior. A strain-controlled cyclic loading scheme with increasing strain levels is performed. The loading rate is fixed to $\dot{\varepsilon} = 10^{-3}\,\mathrm{s}^{-1}$. The material model is the one derived in Chap. 2 at 550°C with corresponding material constants given in Tab. H.1.

In Fig. 4.5, both the stress-strain hysteresis loops and the accumulated plasticity evolution are compared for each model: the "gen-evp" model integrated along time thanks to an explicit 2^{nd} order Runge-Kutta procedure (the hyperbolic sine function not being implemented with the θ-method and the "gen-evp" model) while the present material model is integrated using the standard fully implicit θ-method. The choice for $\theta = 1$ has been made to enforce the stability of the solving algorithm when the problem involves a back-stress tensor [Jirásek and Bažant, 2001].
One can easily see in Fig. 4.5a that the hysteresis loops match well, hence suggesting the accuracy of the numerical integration procedure. The cumulative plasticity p along the loading time is also well estimated, see Fig. 4.5b. As a matter of comparison, it can be noted that the local convergence of the numerical scheme, thanks to the criterion $\|\mathcal{R}\|_2 < \epsilon_{tol}^{loc}$ and for the same loading scheme, is reached in 4253 iterations for the explicit integration, while it requires 2786 iterations

for the implicit integration process. Thus, the present user-defined material model seems to be accurate enough to perform large time steps compared with a standard explicit resolution process.

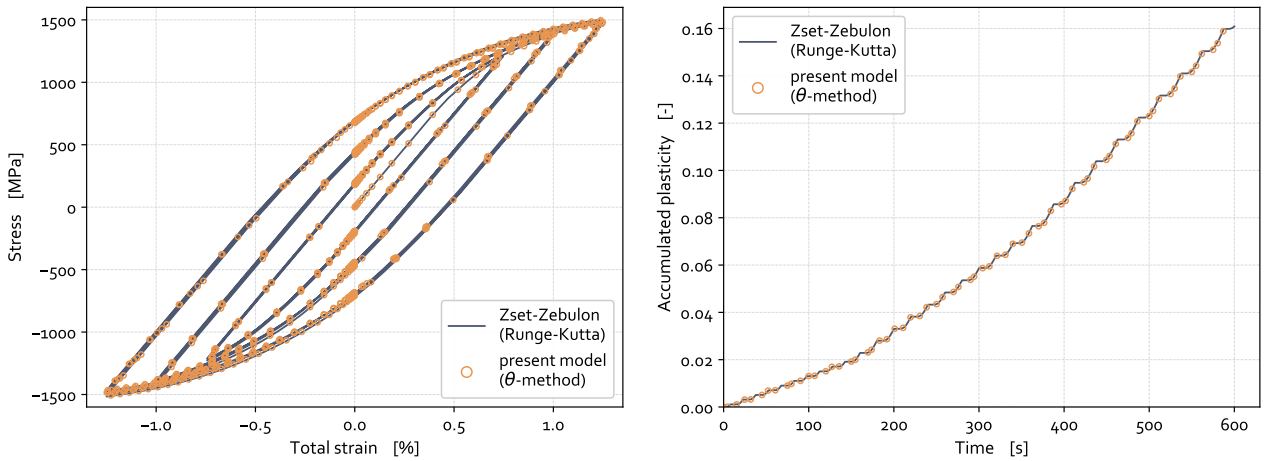

(a) Stress-strain loops.

(b) Time - accumulated plasticity.

Figure 4.5: Validation of the FE implementation over RVE simulations: comparison between implicit (user-defined model) and explicit (integrated) time-integration schemes within the *Z-set* solver ($D_{tot} = 0$).

4.4.1.2 Parametric study of the multi-mechanism damage model

The goal of this sub-section is tho assess the implemented model performing some FE simulations in order to analyze the capabilities of the proposed elastic-viscoplastic multi-mechanism damage material model. For the sake of briefness and simplicity, damage-related material constants were deliberately chosen to be severe in order to emphasize on the properties of the model. Their values are not intended to characterize the real response of the material.

4.4.1.2.a Damage-induced stress-softening response

At first, a simple loading signal is simulated with fatigue damage activated in order to assess the capability of the model to relate the loss of bearing capability of the material through the damage-induced drop in stiffness.

From the Fig. 4.6, one can check the damage-induced softening response of the material point. As long as the damage increases, the stress drop is evidenced, Fig. 4.6a. The resulting stress-strain loops are depicted in Fig. 4.6b. In the latter plot, the decrease in elastic stiffness of the material with increasing damage is clearly evidenced.

4.4.1.2.b Strain-hardenings and damage coupling

As discussed earlier, the present material model is intended to be as general as possible, with a great extent of flexibility regarding both the mechanisms and the couplings to be considered. One

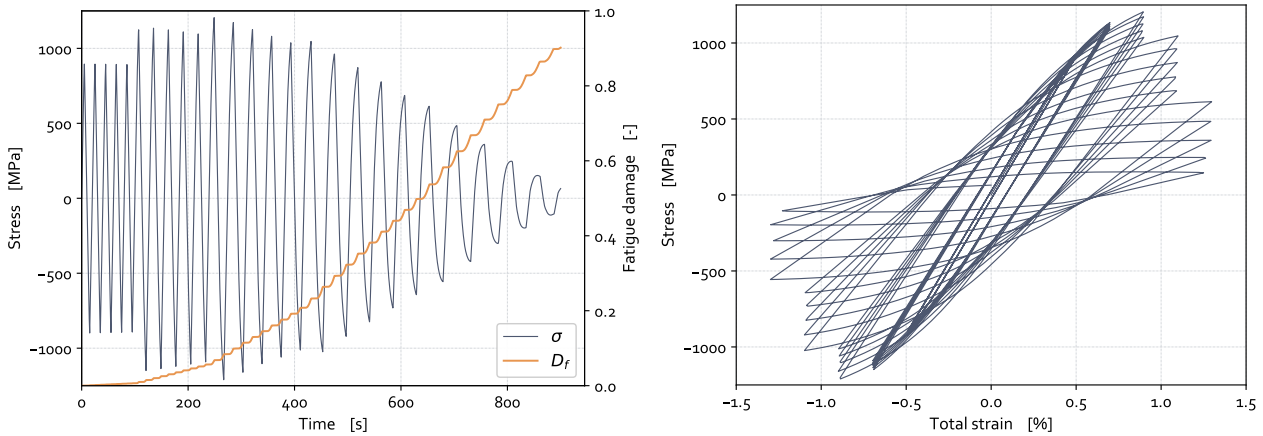

(a) Stress and fatigue damage along time. (b) Corresponding stress-strain loops.

Figure 4.6: Damage-induced stress-softening material response under cyclic loading conditions.

flexibility gained from the previous implementation comes from the possible decoupling between damage and kinematic hardening. Such a feature is illustrated in Fig. 4.7.

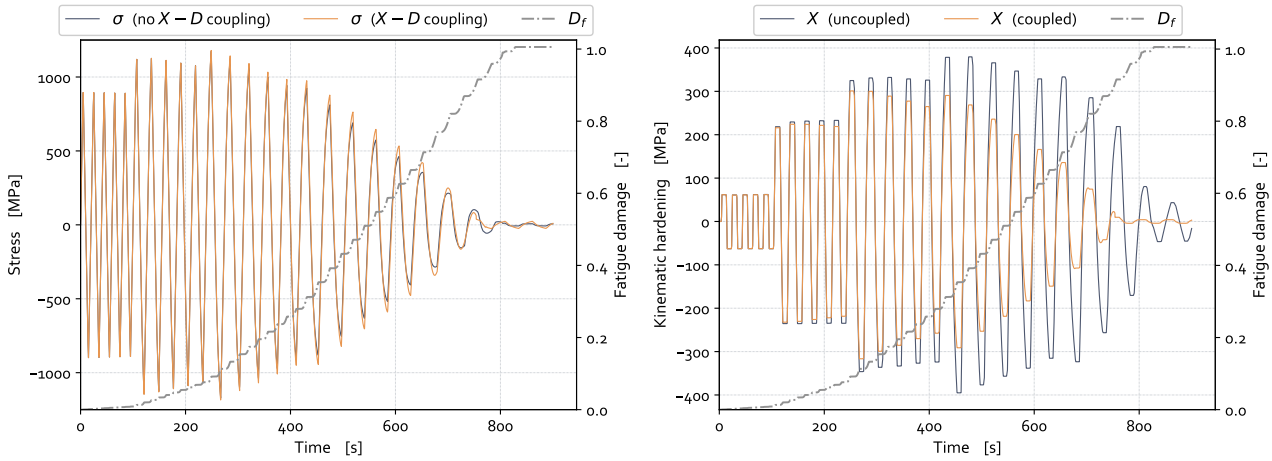

(a) Stress and fatigue damage along time. (b) Back-stress and fatigue damage along time.

Figure 4.7: Effect of kinematic hardening-damage coupling on the material response under cyclic loading conditions.

The Fig. 4.7a shows that the Cauchy stress decreases as long as the damage increases. On the contrary, a possible state decoupling (as opposed to the coupled case) between damaging effects and back stresses can be obtained, see Fig. 4.7b.
Using a local approach to fracture, the crack advance is governed by the complete deterioration of the material points at the crack-tip. The coupling between damage and elastic properties of the material is generally assumed since it relies on the initial formalism of the CDM framework. However, one question is still open to present days on the coupling assumptions for viscoplasticity (*i.e.* strain-hardening mechanisms). In the yield criterion, eq. (4.21), I have chosen a strong coupling assumption between total damage and each of the strain-hardening mechanisms ($\underset{\sim}{X}$ and R). This choice ensures that the stress drops to zero with increasing damage [Besson et al., 2010].

4.4.1.2.c Damage mechanisms

Pure fatigue

Let us analyze two pure fatigue loading spectra under strain control with differing loading ratios from alternate ($R_\epsilon = -1$), see Fig. 4.8, to non-symmetric case ($R_\epsilon = 0.1$), Fig. 4.9.

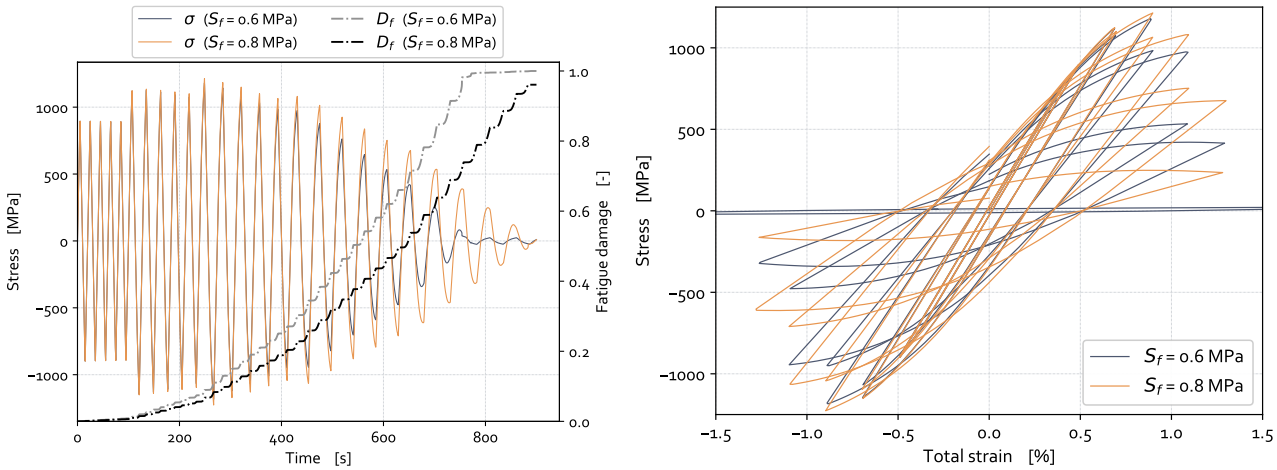

(a) Stress and fatigue damage along time. (b) Corresponding stress-strain loops.

Figure 4.8: Effect of fatigue damage parameter on the material response - cyclic conditions with $R_\epsilon = -1$.

In Fig. 4.8, the fact that the greater fatigue damage resistance S_f leads to the higher fatigue lifetime is clearly evidenced. Once a material point has reached its *broken* state, the damage variable is assumed to be constant with the critical value D^{crit}. The maximum value is chosen to be close to unity ($D = 1$) so as to conform with standard formulation associated with CDM (note that for the exponential softening function defined in eq. (4.2), the trend can be adjusted using the η_D parameter). Once a material point is *broken*, stiffnesses (elasticity and strain-hardenings) are drastically reduced inducing nearly vanishing stresses.

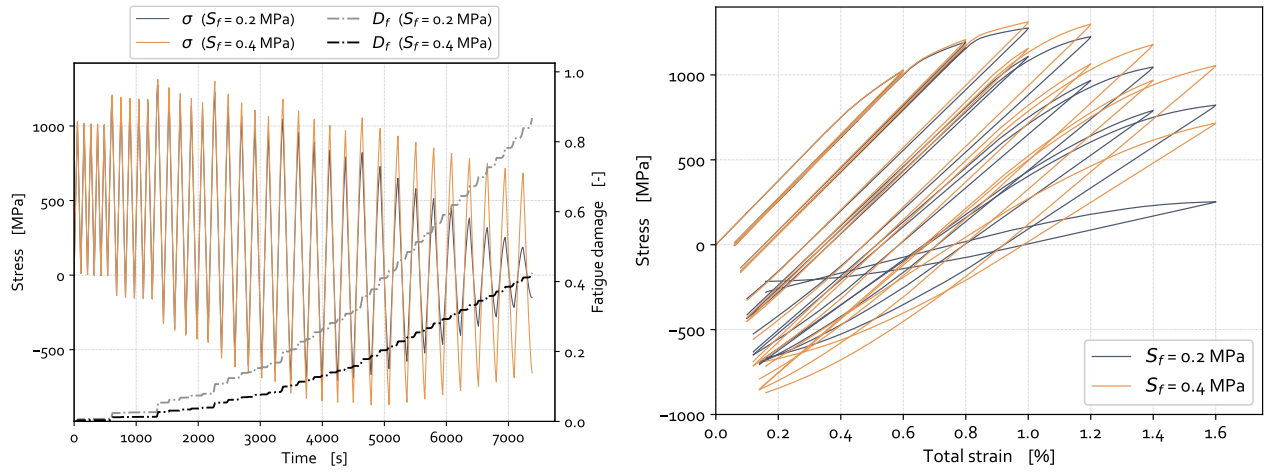

(a) Stress and fatigue damage along time. (b) Corresponding stress-strain loops.

Figure 4.9: Effect of fatigue damage parameter on the material response - cyclic conditions with $R_\epsilon = 0.1$.

For the case with non-symmetric loading, Fig. 4.9, the drop in stresses is also noticeable. The higher the fatigue damage resistance S_f, the lower the damage and the higher the corresponding actual stress. Moreover, the mean stress relaxation is also evidenced. Such a result is expected for asymmetric loading waveforms and is mainly related to the non-linearity of the back stress evolution rule. Details on this point can be found in, *e.g.* [Chaboche, 1991].

Analysis of frequency effect on fatigue damage

In this short paragraph, the idea is to assess the occurrence of loading rate effect on the pure fatigue response of the damage model. In Fig. 4.10, four loading rates are compared, ranging in $\dot{\varepsilon} \in [1.10^{-5} - 1.10^{-2}]\,\mathrm{s}^{-1}$. The material point is subjected to pure fatigue loading conditions at $\Delta\varepsilon/2 = 0.9\%$ under symmetric loading.

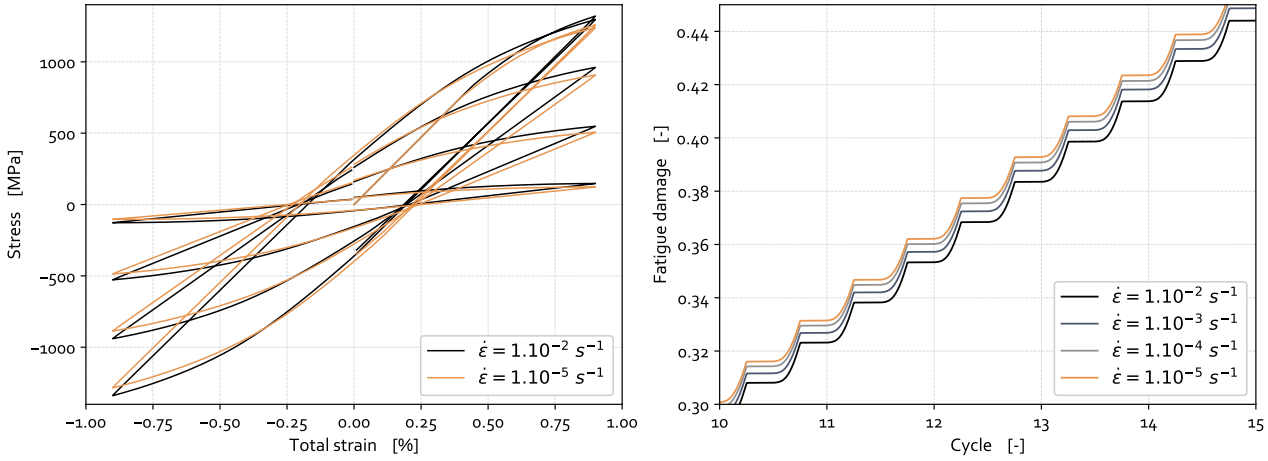

(a) Stress-strain hysteresis loops. (b) Corresponding fatigue damage evolution (zoom).

Figure 4.10: Influence of the loading rate on the fatigue damage evolution under pure fatigue conditions.

In Fig. 4.10a, for the sake of clarity, only a few cycles at both extreme loading rates are plotted. One can notice a difference between the highest loading rate $\dot{\varepsilon} = 1.10^{-2}\,\mathrm{s}^{-1}$ and the lowest one at $\dot{\varepsilon} = 1.10^{-5}\,\mathrm{s}^{-1}$. The shape of the hysteresis loops remains almost the same despite a slight difference in the size of the elastic domain. In Fig. 4.10b, a close-up view on the fatigue damage evolution during 5 loading cycles is reported. One can easily notice the slight difference in the fatigue damage evolution respective to the loading rate. As a result, the slower the loading rate, the faster the fatigue damage growth. The cyclic damage model hence includes a slight and intrinsic sensitivity to the loading frequency even if pure fatigue loading conditions are considered. This latter effect is to be related to the viscosity effects included in the constitutive equations (see sub-sect. 2.3.3).

Microcracks closure effect in fatigue

The unilateral conditions (UC) for elastic stiffnesses associated with the partial microcracks closure effect introduced in sub-sect. 4.1.6 can be evidenced from a pure fatigue loading with varying micro-defects closure parameter h, Fig. 4.11.

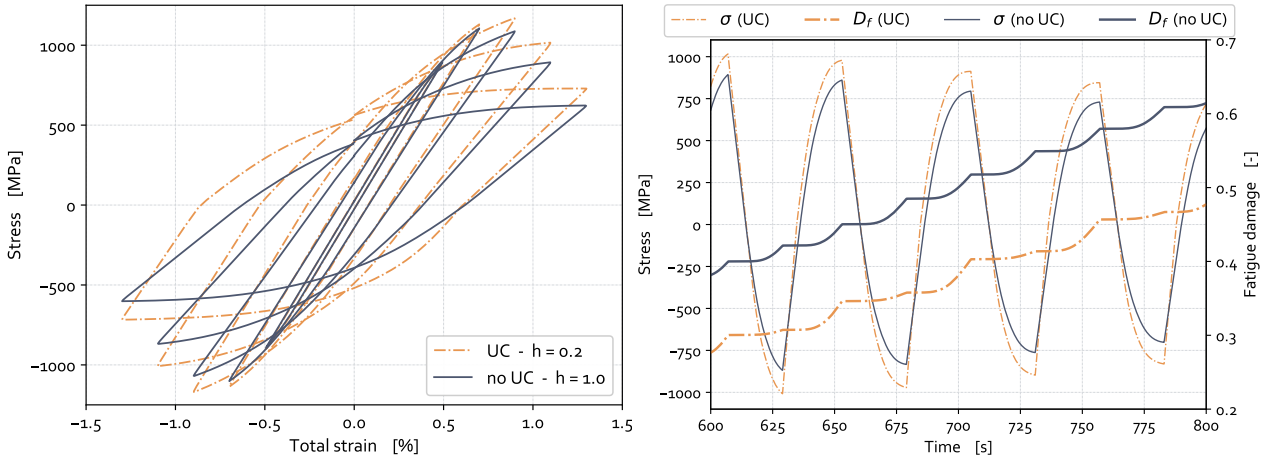

(a) Alternating loading scheme. (b) Fatigue damage evolution upon cycling.

Figure 4.11: Influence of the micro-defects closure parameter h on the fatigue damage evolution.

On the Fig. 4.11a, some characteristic hysteresis loops at given strain levels are plotted. One can see that as long as damage increases, the elastic stiffness tends to decrease. In the case there is no partial closure of the microcracks ($h = 1.0$), the elastic stiffness in compressive stress state is not recovered. It results in symmetric hysteresis loops with respect to both stress and strain axes. On the contrary, once micro-defects are supposed to partially close once compressed, elastic stiffness recovery is observed. Such a property yields in a greater compressive stress level for a given strain level, Fig. 4.11a.
On the Fig. 4.11b, a close-up view on the time evolution of stress σ and fatigue damage D_f is given. It can be noticed in the case of UC that the damage growth is lower for the compression levels than for the tension ones. This feature tends to delay the fatigue damage for low loading ratios.

Pure fatigue with plastic compressibility

In this part, the damage-induced plastic compressibility effect is evidenced as an additional damage mechanism. Hence, a volumetric damage variable D_v is added apart from fatigue damage D_f. Both the effect of the initial porosity D_{v_0} and that of the plastic compressibility coefficient φ_c on the overall damage evolution can be analyzed.

On the Fig. 4.12a, it can be noticed that the total damage D_{tot} exhibits different initial values at the beginning of the loading scheme. This is attributed to the differing value of the initial porosity D_{v_0}. This variable is assumed to trigger the volumetric damage growth which in turn influences the plastic compressibility effect of the material through the equivalent stress given by eq. (4.62) & eq. (4.63). As long as the loading cycles increase, the total damage ($D_{tot} = D_f + D_v + D_{v_0}$) tends to the same value, no matter the initial porosity D_{v_0}, see Fig. 4.12a. This can be explained by the fact that the initial porosity D_{v_0} only enforces the compressibility effect in the (elliptic) yield criterion. However, since the fatigue damage is predominant, Fig. 4.12b, the plastic compressibility effect and its resulting cavity growth process are in the minority compared to the fatigue damage increase. The global trend is hence almost unchanged.

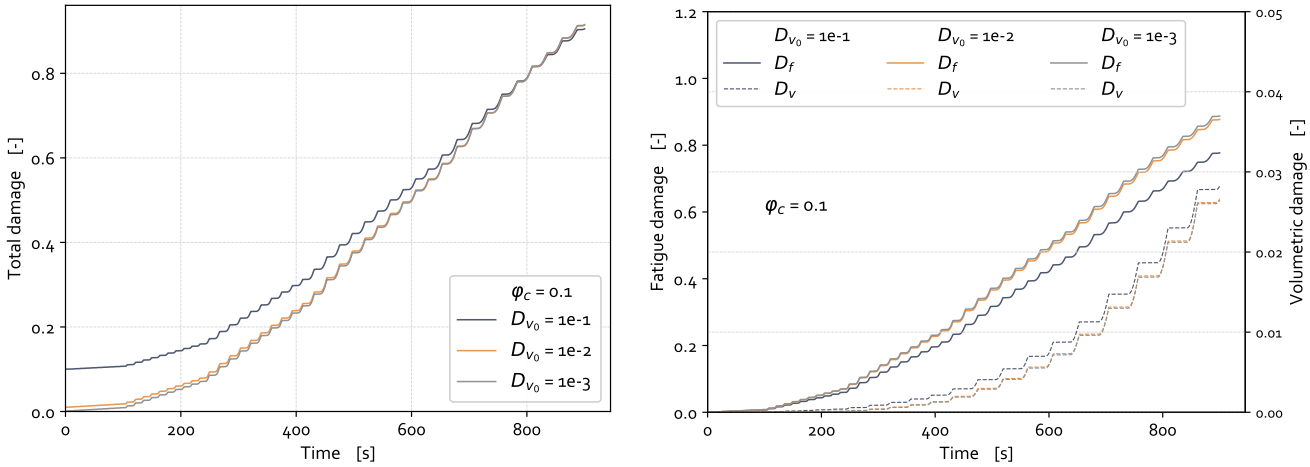

(a) Total damage w.r.t. time. (b) Fatigue and volumetric damages w.r.t. time.

Figure 4.12: Numerical response of a RVE subjected to fatigue loading conditions with plastic compressibility - effect of the initial porosity D_{v_0}.

In Fig. 4.12b, it can be observed that fatigue damage D_f is lower for the highest value of $D_{v_0} = 1.10^{-1}$ while the volumetric damage D_v is greater. However, the growth kinetic shows a similar trend regarding the three values of D_{v_0}. The volumetric damage growth also admits the same kinetics. One can explain the slight effect of the initial porosity D_{v_0} on the fatigue damage D_f from plastic compressibility effect which is directly related to volumetric damage D_v and acts on the equivalent stress of the viscoplastic yield surface, see eq. (4.61) & eq. (4.62). As a consequence, the plastic activity governing the fatigue damage through $\dot{p}$ is influenced by the deviatoric part of the viscoplastic strain rate tensor, itself influenced by compressibility effects (once plastic compressibility effects are active, the viscoplastic strain tensor is no more purely deviatoric). Finally, the higher the initial porosity, the higher the volumetric part of the strain tensor and the lower the fatigue damage driving force. In addition, the higher the initial porosity, the greater the volumetric damage development, Fig. 4.12b.

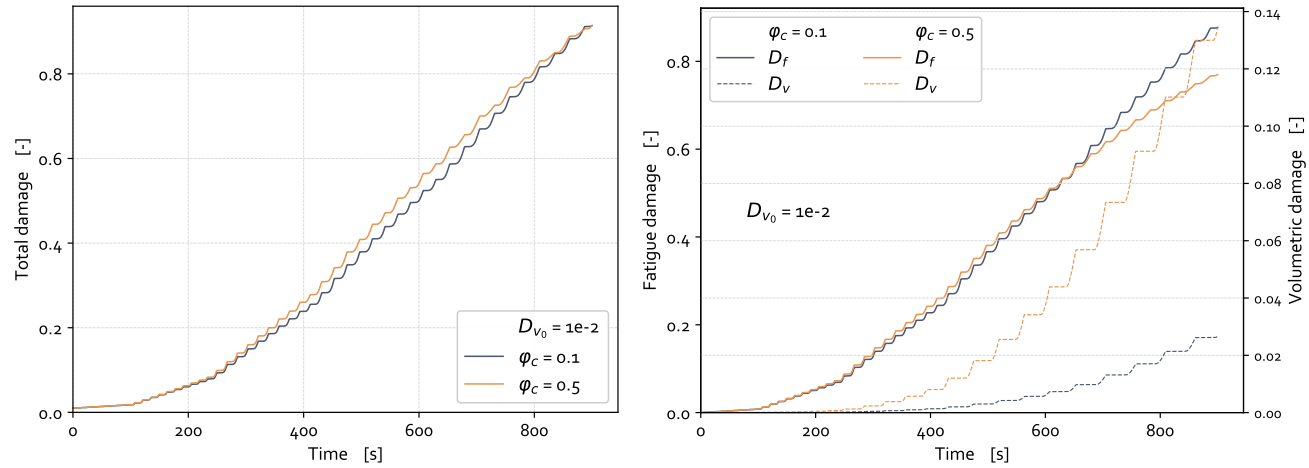

(a) Total damage w.r.t. time. (b) Fatigue and volumetric damages w.r.t. time.

Figure 4.13: Numerical response of a RVE subjected to fatigue loading conditions with plastic compressibility - effect of the compressibility coefficient φ_c.

On the Fig. 4.13a, the effect of the compressibility coefficient φ_c on the total damage growth is plotted. This parameter is assumed to control the pressure-dependence of the yield criterion, see eq. (4.61) & eq. (4.62). Obviously, the higher the value of φ_c, the greater the viscoplastic compressibility effect. A closer look at the partition between fatigue and volumetric damages is given in Fig. 4.13b. It is clearly evidenced the fact that a higher compressibility effect in the yield criterion results in a higher extent of volumetric damage, Fig. 4.13b. Such a result is nearly independent of the initial porosity D_{v_0} (taken as $D_{v_0} = 1.10^{-2}$ in Fig. 4.13).

Dwell-fatigue

In this paragraph, the effect of the loading signal on both the creep and fatigue damage evolution is studied. A trapezoidal waveform with some 360 and 240 s holding-periods is simulated upon pure fatigue cycling. The loading spectra and the resulting stress evolution are given in Fig. 4.14 while the creep-fatigue damage evolution and corresponding stress-strain loops are reported in Fig. 4.15.

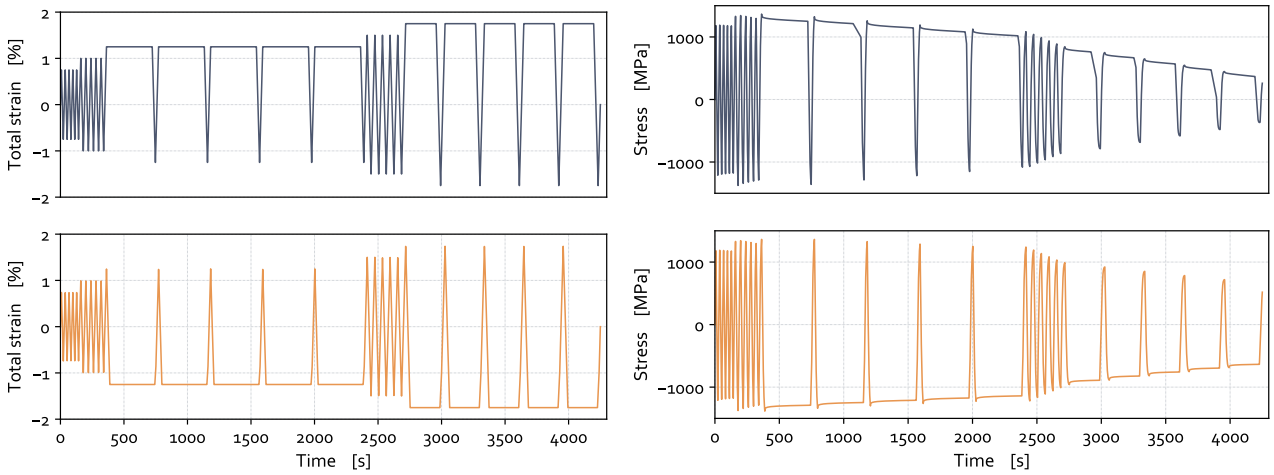

(a) Dwell-fatigue cyclic loading.

(b) Stress evolution along time.

Figure 4.14: Numerical response of a RVE subjected to dwell-fatigue loading conditions (1/2).

During the holding periods, the over-stress that relaxes can be observed, Fig. 4.14b. Moreover, the stress-softening is greater for positive holding-times compared to negative ones.

From the Fig. 4.15a it can be noticed, on the one hand, a significant change in the growth of creep damage depending whether the dwell-periods are performed upon tension (+) or compression (-). This is mainly related to the modeling aspects which assume a vanishing creep cavity growth under compression, hence resulting in the absence of damage rise. On the contrary, positive dwell-time favors the opening of cavities and thus yields in an increase of the creep damage.
On the other hand, the fatigue loading being subjected to the same stress amplitude at a given loading ratio, the fatigue damage increases approximately with the same trend no matter the sign of the dwell-periods. Owing to the fact that positive holding-periods yield in a greater extent of creep damage, the resulting hysteresis loops exhibit a greater stress-softening effect, Fig. 4.15b.

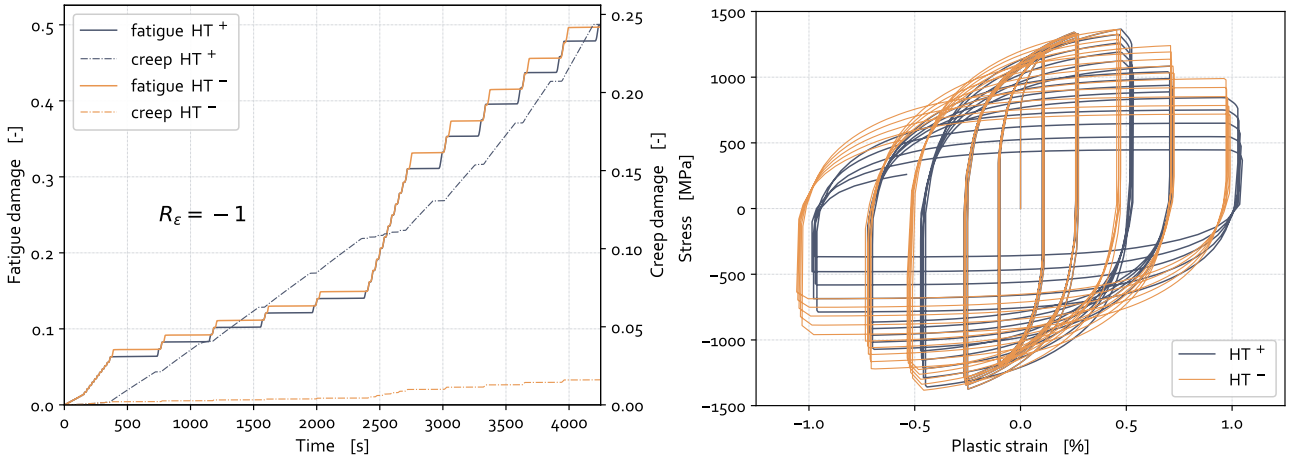

(a) Fatigue and creep damage evolution. (b) Stress evolution along time.

Figure 4.15: Numerical response of a RVE subjected to dwell-fatigue loading conditions (2/2).

4.4.1.2.d Mean stress effect

As already reported in [Lemaitre and Desmorat, 2005] and discussed in sub-sect. 4.1.6, the micro-cracks closure effect induces a mean stress effect in fatigue. By looking at a given stress-controlled cyclic loading scheme with constant stress amplitude and varying loading ratios, one can study the influence of the micro-defects closure effect on the fatigue lifetime, see Fig. 4.16:

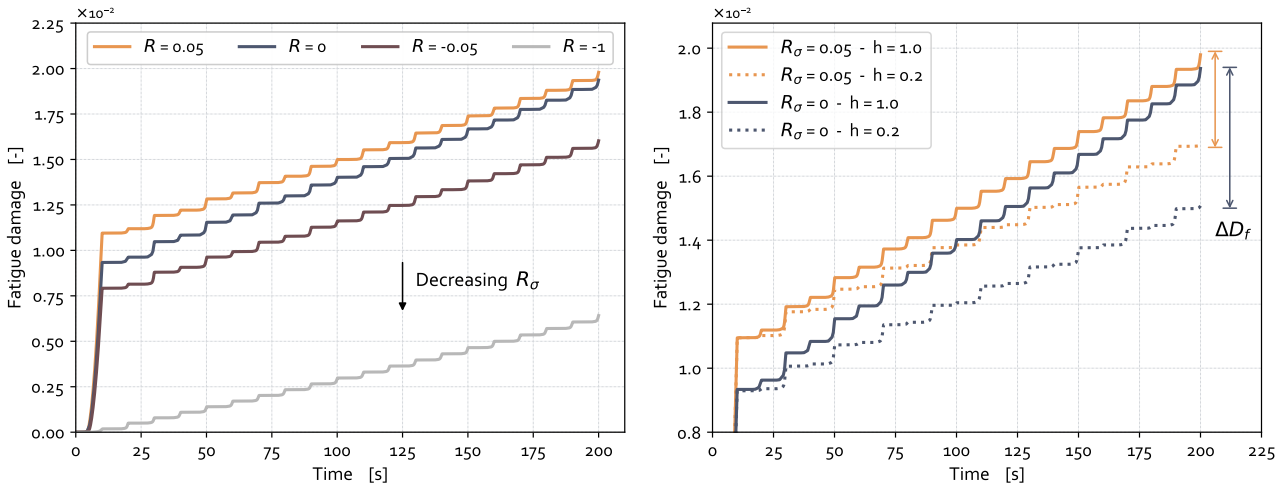

(a) Effect of decreasing load ratios on D_f ($h = 1.$). (b) Positive load ratios with micro-defects closure effect.

Figure 4.16: Influence of the loading ratio and the micro-defects closure parameter h on the fatigue damage evolution under cyclic loading.

From the Fig. 4.16a, it is obvious that the higher the loading ratio (with $h = 1.0$), the more detrimental it is for the lifetime of the material point. Then, the proposed fatigue damage model includes an intrinsic sensitivity to the mean stress. Looking at the Fig. 4.16b, the effect of the micro-defects closure parameter on the positive load ratios can be analyzed. Specifically for this sub-section, the plain line corresponds to the case without micro-cracks closure ($h = 1.0$), whereas the dotted line referred to the case with closure effect ($h = 0.2$). One can see from Fig. 4.16 that:

- without any closure effect ($h = 1$), the lower the loading ratio, the smaller the fatigue damage, Fig. 4.16a;
- for the lowest load ratio, the micro-defects closure parameter h has a greater influence on the fatigue damage evolution compared to the case with the highest load ratio, Fig. 4.16b;
- the fatigue damage drop ΔD_f with/without taking into account micro-cracks closure is greater as long as the load ratio is decreasing. This can be attributed to the higher proportion of compressive stresses for the lower load ratio, Fig. 4.16b.

Finally, one can conclude from a qualitative analysis that the lower the load ratio, the smaller the elastic energy release rate associated with fatigue damage growth, and subsequently, the lower the resulting damage. In turn, the lower the fatigue damage, the greater the fatigue lifetime, hence suggesting an additional mean-stress sensitivity effect obtained through such a partial closure mechanism [Desmorat, 2006], [Otin, 2007], [Barbier, 2009].

4.4.2 Structural analysis: a shear-dominated loading case

In this paragraph, a simple 2D structural tensile example is considered in order to assess the computational capability of the previously implemented damage model. A double-notched specimen is analyzed following the work of [Mediavilla Varas, 2005], [Feld-Payet, 2010] or [Khoei et al., 2013a]. To this end, a specimen with two asymmetrically circular notches in the upper right and lower left parts of the square specimen is considered, as shown in Fig. 4.17. This figure also presents the boundary conditions of the problem. The specimen is considered in plane strain conditions and the loading rate is assumed to be equal to $\dot{u} = 10^{-2}\,\text{mm.s}^{-1}$. A benchmark simulation has been performed in order to assess the capability of the computations for different mesh sizes and on the overall load-displacement responses. The material parameters are reported in sect. H.2.

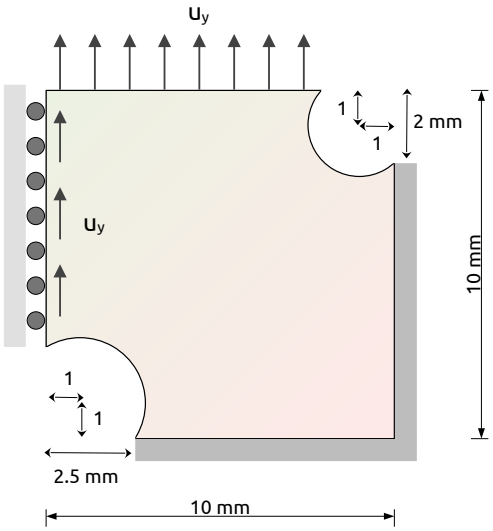

Figure 4.17: Geometry of the double-notched specimen subjected to tensile loading with corresponding dimensions and associated boundary conditions (after [Mediavilla Varas, 2005]).

In Fig. 4.18, two over the three considered spatial discretizations of the structure are given, namely the extrema, with an average element size of 0.3 mm for the first one (Fig. 4.18a) and 0.1 mm for the second one (Fig. 4.18b). The structure is meshed with 6-nodes quadratic triangular elements with reduced integration points (c2d6r FE in the Z-set suite). The properties of the three discretizations are reported in Tab. 4.4.

Meshes	**0.3 mm**	**0.2 mm**	**0.1 mm**
Elements	4 650	10 890	23 867
Nodes	9 459	22 023	48 134

Table 4.4: Properties of the FE meshes for the double-notched specimen.

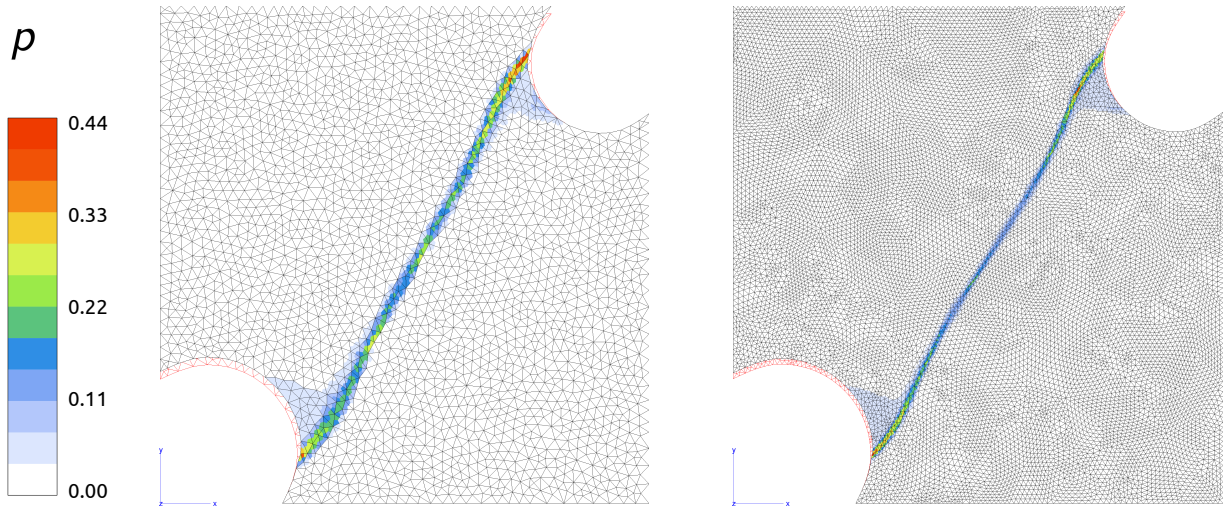

(a) Coarse mesh (0.3 mm) - p. (b) Fine mesh (0.1 mm) - p.

Figure 4.18: Accumulated plasticity field obtained in the double-notched specimen subjected to tensile loading with the local damage model.

Looking at the accumulated plasticity in Fig. 4.18 and the total damage fields in Fig. 4.19, allows to evidence both the strain and damage localization process. It can be seen that plasticity and damage tend to localize in a narrow band, called the *localization band*. As long as the load increases and once the damage-induced stress-softening effect is triggered, the localization process is amplified while the rest of the structure undergoes elastic unload.
The comparison of the two mesh sizes evidence the fact that the damaged zone tends to decrease as long as the mesh size is refined. Such a phenomenon, well-known for stress-softening damage models based on the *local state principle*, is referred to as the *mesh-dependency effect* [Besson et al., 2003], [Feld-Payet, 2010]. The strain and damage localize within the smallest band that can be represented by the spatial discretization, which in turn may be a single row of elements or integration points.

As previously seen, the localization process is fairly rapid, just after the peak, Fig. 4.20, and then the calculation diverges. One can notice that the three load-displacement curves show different results at crack initiation. The finest mesh (0.1 mm) evidences an earlier crack initiation when compared to the two other mesh sizes (0.2 & 0.3 mm). The displacement at crack initiation (and

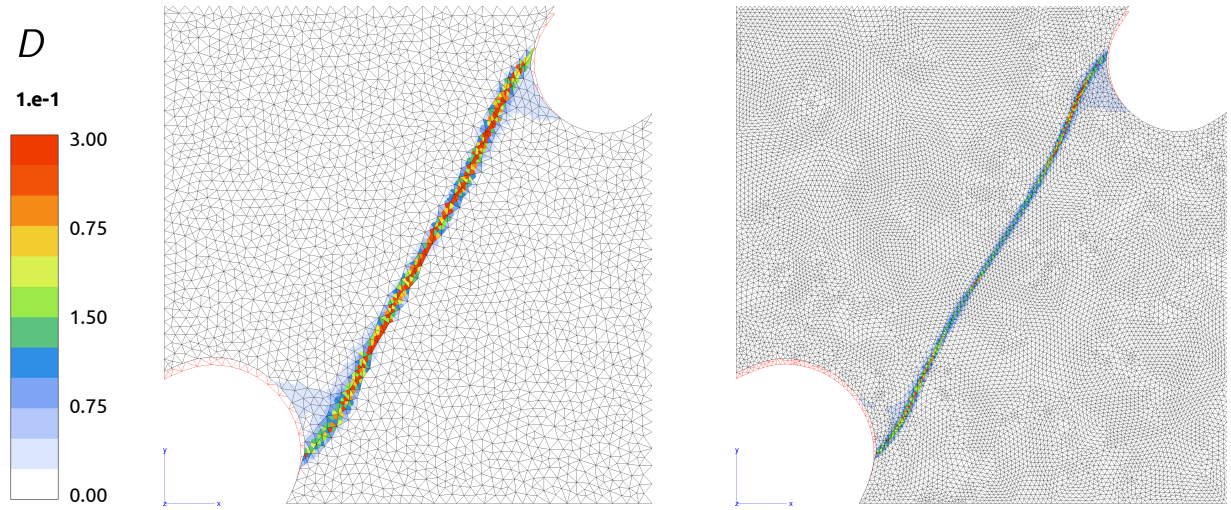

(a) Coarse mesh (0.3 mm) - D_{tot}. (b) Fine mesh (0.1 mm) - D_{tot}.

Figure 4.19: Total damage field obtained in the double-notched specimen subjected to tensile loading with the local damage model.

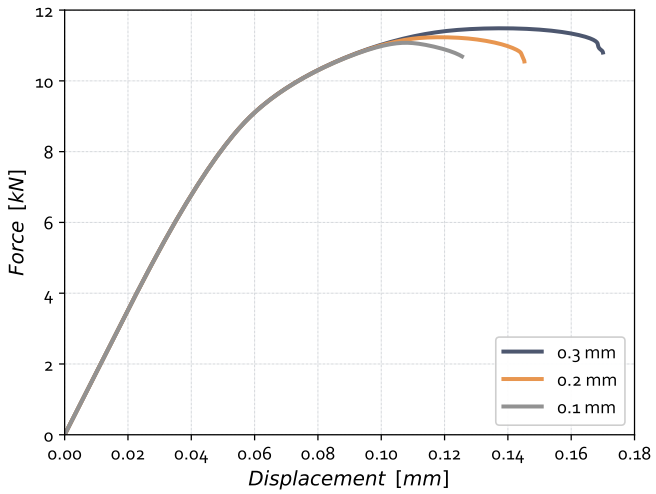

Figure 4.20: Force-displacement curves for the double-notched specimen with three mesh sizes illustrating the mesh dependency of the mechanical response.

consequently the associated dissipated energy) tends to increase with increasing the mesh size. Such a result seems to make sense: the larger the finite elements, the greater the energy they need to reach the failure. However, this is not in agreement with the physical fracture process which needs to be treated in an objective manner, no matter the choice of the spatial discretization (mesh size) of the considered structure for FE analyses. Thus, to overcome such a spurious effect, a regularization technique should be considered to induce mesh-independent results upon mesh refinement during FE analyses. Such a point is discussed in the following Chap. 5.

4.5 Conclusion of the chapter

In this chapter, a time-incremental fatigue damage model has been derived. Such a model belongs to the class of the *phenomenological damage models* owing to its consistent formulation using the Thermodynamics of Irreversible Processes (TIP) and the local state method. Some internal variables describing the degradation processes within the material under complex loading schemes have been chosen to be fully coupled to the mechanical response of the material. In this study, the small strain framework has been adopted as a starting point for an easier modeling process (extension to finite strains remains an outlook for further investigations). Then, the cyclic constitutive equations derived and calibrated in Chap. 2 have been adapted in order to alter the stiffnesses of the material in the CDM framework.

The consistent development of such a damage model has been detailed as well with its numerical implementation into a FE code thanks to a in-house subroutine. A parametric study has been performed in order to assess the capabilities of this cyclic damage model.
A two-dimensional structural calculation under plane strain conditions has been simulated in order to highlight the mesh-dependence effects.

Damage models relying on the *local state principle* allow getting rid of the transferability issues from one geometry to another and to calculate in a fine and accurate manner the mechanical fields at the tip of a crack. Such points hence represent the main improvements gained from the *local approach to fracture* compared to energetic analyses offered by the *global* one.
Also, fully coupled CDM-based damage formalisms lead to the non-convergence of the FE calculations due to both the damage-induced stress-softening effect and the presence of broken elements in the mesh. Some remeshing or node elimination techniques have been proposed in recent years to remove such elements, but these methods lead to energy losses that distort the final solution. Another weakness of this approach is related to the mesh-dependency. For this reason, regularization techniques have been developed to overcome an important part of such a mesh-dependency. This point constitutes the main topic of the next Chap. 5 devoted to the non-local extension of the proposed local damage model.

Résumé du chapitre en français

Dans ce chapitre, l'approche locale de la rupture a été mise en place pour prédire la croissance de fissure en fatigue. Pour ce faire, un couplage comportement-endommagement a été formulé, reliant les équations constitutives décrites au Chap. 2 avec les mécanismes d'endommagement présents sous chargements complexes et identifiés au Chap. 3. Un modèle d'endommagement par fatigue, phénoménologique et macroscopique, écrit sous une forme incrémentale en temps a été développé à l'aide des concepts de la Mécanique de l'Endommagement Continu et la Thermodynamique des Processus Irréversibles. Les potentiels d'état et de dissipation associés aux variables internes et à leur évolution temporelle ont été décrits. Le couplage fort entre la réponse matériau et l'endommagement est réalisé à l'aide du concept de contrainte effective associé à l'hypothèse d'équivalence en déformation. Le critère de (visco)plasticité fortement couplé à l'endommagement tenant compte des variables d'écrouissages isotropes et cinématiques effectives a été détaillé. Les effets de refermeture partielle des micro-défauts pour des chargements en compression ont ensuite été intégrés au modèle. Ainsi, la loi d'évolution du dommage de fatigue a été améliorée pour tenir compte des effets de refermeture et conduire à une croissance moindre de l'endommagement sous chargement de compression. En complément, une restauration partielle des propriétés élastiques du matériau a également été prise en compte dans la modélisation. Ces deux effets contribuent à l'introduction dans le modèle d'un effet de contrainte moyenne sur la croissance de l'endommagement de fatigue.
Le modèle de fatigue a ensuite été étendu à des mécanismes d'endommagement additionnels. Ainsi, la compressibilité plastique du critère d'écoulement a été ajoutée via la croissance d'une variable d'endommagement liée à la conservation de la masse et à la croissance de cavité. En complément, comme attendu pour les chargements à hautes tempréatures avec temps de maintien, une variable d'endommagement de fluage associée à la croissance de cavités aux joints de grains a été ajoutée. Toutes ces variables, phénoménologiques par nature, viennent s'additionner pour former une variable d'endommagement total venant dégrader les propriétés matériau et ainsi piloter la croissance de fissure.
L'implémentation numérique du modèle complet dans le code Element Finis Z-set a ensuite été réalisée. Pour ce faire, un effort particulier a été mis sur l'intégration temporelle du système différentiel couplé. La résolution de ce problème est effectuée à l'aide d'un schéma itératif de type Euler implicite (θ-méthode). Bien que fastidieux dans sa partie imlémentation, ce type de résolution pour des cas de chargement cycliques permet la résolution du système sur de larges pas de temps. L'écriture incrémentale du problème différentiel est ensuite discuté, avant l'écriture des résidus à minimiser pour résoudre le système d'équations non-linéaires couplées. Enfin, le calcul de la matrice tangente, consistante avec le schéma de résolution, est détaillé. Cette dernière est nécessaire pour garantir la bonne convergence de la boucle de résolution de l'équilibre global via la construction des matrices de rigidité élémentaires. Le processus de résolution d'un point de vue algorithmique est finalement rappelé.
En fin de chapitre, l'implémentation du modèle est validée sur des cas tests simples à l'échelle de l'élément de volume. Les propriétés du modèle sont testées et la sensibilité à certains paramètres est éprouvée. Pour finir, un cas structurel en 2D est donné. Il s'agit d'une plaque à double encoches, sollicitée en cisaillement, et soumise à un chargement monotone. Ce problème met alors en évidence le problème de dépendance au maillage associé à la perte d'unicité de la solution. La dissipation mécanique du problème n'est plus unique et le problème doit être régularisé.

5 Towards a non-local cyclic elastic-viscoplastic multi-mechanism damage model for fatigue crack growth

In the present chapter, a non-local formulation of the cyclic elastic-viscoplastic multi-mechanism damage model is proposed. Such an extension of the local damage model proposed in the Chap. 4 aims, from a numerical point of view, at obtaining mesh-objective numerical results during FE calculations. First, the strain localization process is briefly described and numerical methods allowing the regularization of the mesh-size dependence are detailed with both their potentialities and limitations in the scope of FCG applications. Then, a non-local formulation of the damage model is suggested with a discussion on the choice of the variable endorsing the non-locality. The extension to locking-free elements regarding the volumetric properties of the model is also discussed. Once the non-local extension is settled, the numerical implementation of the whole model is discussed prior to the numerical validation through benchmark tests.

Contents

Although the FEM is known to be relevant for the prediction of strain-hardening in continuous media within the small strain framework, some numerical problems have been reported for the fracture prediction using the local state method:

- finite elements (FE) can undergo possible locking issues associated with some deformation modes;
- some FE of the structure could reach a null stiffness due to the strong coupling with damage;
- the mechanical response of the problem is highly dependent on the spatial discretization, *i.e.* the mesh size, as evidenced in the previous structural example, see sub-sect. 4.4.2.

In the following, aspects related to numerical issues in stress-softening problems are briefly discussed and overcoming methods are presented prior to the proper enhancement of the cyclic damage model to counteract such drawbacks.

5.1 Strain localization phenomenon in quasi-static problems

When subjected to severe loadings, most of the engineering metals exhibit a progressive damage failure due to distributed micro-cracking and thus result in a loss of apparent stiffness after reaching the peak stress. In structural analyses, such a typical behavior is generally termed as *strain-softening*. The implementation in FEM codes of local CDM-based damage models, as the one suggested in Chap. 4, causes numerical difficulties such as ill-posedness of the boundary value problem. Indeed, the differential equations controlling the material response may lose their ellipticity for quasi-static problems ([Bigoni and Zaccaria, 1992], [Ottosen and Ristinmaa, 2005]). This leads to damage localization to an evanescent volume upon mesh refinement, and consequently to vanishing dissipation of energy and mesh-dependency. This issue has been addressed in numerous studies, see *e.g.* [Billardon and Moret-Bailly, 1987], [Besson et al., 2003], [Feld-Payet, 2010], [Davaze, 2019] for monotonic crack growth, [Saanouni et al., 1989], [Kruch et al., 1991] for creep crack growth and [Marchal, 2006], [Aslan, 2010] for fatigue crack growth problems.

The loss of ellipticity is attributed to the violation of the stability criterion. The condition for local stability based on Drucker's principle on the positiveness of the second order work [Drucker, 1950] was postulated by [Hill, 1958] and mathematically formulated for FE applications by [de Borst et al., 1993]:

$$\dot{\underset{\sim}{\varepsilon}} : \dot{\underset{\sim}{\sigma}} = \dot{\underset{\sim}{\varepsilon}} : \frac{\partial \underset{\sim}{\sigma}}{\partial \underset{\sim}{\varepsilon}} : \dot{\underset{\sim}{\varepsilon}} > 0 \qquad \forall \dot{\underset{\sim}{\varepsilon}} \quad \text{adm.} \tag{5.1}$$

Mathematically, the condition for the onset of material instability for a material having a tangent

stiffness tensor $\underset{\approx}{H}(D)$, which in general could be non-symmetric, and an isotropic damage D, can be written as:

$$\dot{\underset{\sim}{\varepsilon}} : \underset{\approx}{H}(D) : \dot{\underset{\sim}{\varepsilon}} = 0 \tag{5.2}$$

Uniqueness of the solution is therefore guaranteed as long as the material tangent modulus remains positive-definite [de Borst et al., 1993]. In the case of a localization band with a jump of the deformation gradient, an acoustic tensor can be defined in terms of the vector $\underline{n}$, normal to the localization surface as follows:

$$\underset{\approx}{A} = \underline{n} \,.\, \underset{\approx}{H}(D) \,.\, \underline{n} > 0 \qquad \forall \underline{n} \tag{5.3}$$

Loss of ellipticity of the governing equations occurs when the acoustic tensor $\underset{\approx}{A}$ becomes singular.

The incorporation of a characteristic internal length in the classical (local) continuum damage models is known to allow the strain/damage localization process to occur without losing the well-posedness of the rate boundary value problem. Such a process is mainly associated with the *non-local* extension of the classical local models, using a so-called *regularization* treatment [Forest and Lorentz, 2004], [Zhu, 2017]. With a non-local model, the material state is no longer characterized by point-wise state variables and an interaction distance appears through the so-called *internal length*.

5.2 Choice of a regularization method and related aspects

5.2.1 Choice of a non-local approach

The past decades provided some understanding on the mathematical implications of non-local integral and gradient models, particularly in avoiding pathological localization, see sect. 1.5, but fundamental questions still remain. For instance, the role of the enhancement in crack growth modeling and the associated treatment of boundaries have not yet been fully clarified [Samal, 2007].

Besides, all the studies listed in the literature review, see sub-sect. 1.5.2, have highlighted the fact that fatigue (as well as creep) crack growth analysis using non-local models still remains a narrow area of research. To the best of the author's knowledge, there have been little attempts (if any) in assessing the performance of non-local models under LCF loading conditions for the growth of long cracks in structural calculations.

Implicit-gradient approaches are nowadays generally favored. This is notably due to their strong analogy with the integral-type formulations [Askes and Sluys, 2002], which are both truly non-local, and to their easiest numerical implementation in standard multi-purpose FE codes. The critical comparison conducted by [César de Sá et al., 2006] also tends to confirm the superiority of implicit gradient-enhanced formulations over integral ones for solving the mesh-dependency effect while preserving a reasonable CPU-time demand. Besides, they allow the simultaneous resolution of

both the global and the non-local problems (see sect. 5.4 later on). The only requirement comes from the introduction of an additional nodal DoF.

The work from [Peerlings et al., 2000] has reported, in a study where inelastic strains are prevented, that a gradient-type non-local regularization is effective as localization limiter for HCF conditions. Moreover, CDM-based non-local cyclic damage models assuming a strong coupling between damage and behavior, together with a non-linear constitutive model in fatigue situations, have been very little discussed, except in [Maniar et al., 2017] (integral formulation) or [Yin et al., 2022] (implicit gradient formulation). The present non-local extension of the cyclic elastic-viscoplastic multi-mechanism damage model for fatigue crack growth prediction hence represents a key point for this Ph.D. project.

All these aspects at hand, I have chosen to use in the present Ph.D. project an **implicit gradient-enhancement** of the local damage model dedicated to cyclic crack growth [Peerlings et al., 2001], [Engelen et al., 2003]. The implicit gradient regularization technique has already been used at the ONERA in the context of damage evolution in composites structures [Germain, 2006], [Médeau, 2019] as well as for ductile fracture in various metallic alloys [Feld-Payet, 2010], [Davaze, 2019]. Obviously, the choice of the nature of the non-local variable is of primary importance and will be discussed in the following.

5.2.2 Choice of the non-local variable

The choice of the non-local variable constitutes a **delicate** decision process since the non-local effect is related to both the regularization technique and the considered material model. A non-exhaustive review is given in the Tab. 5.1 so as to support the choice.

Non-local variable	Framework	References
Displacement field	CDM	[Jirásek and Marfia, 2005], [Rodríguez-Ferran et al., 2005], [Tamayo-Mas and Rodríguez-Ferran, 2014]
	GTN	[Huespe et al., 2012]
Total strain	CDM	[Belytschko and Lasry, 1989], [Simo and Ju, 1989]
Cauchy stress	CDM	[Bažant, 1994], [Giry et al., 2011]
Equivalent plastic strain	CDM	[Pijaudier-Cabot and Bažant, 1987], [Peerlings, 1999], [Liebe and Steinmann, 2001], [Peerlings et al., 2002], [Geers et al., 2003], [Engelen et al., 2003], [Boers et al., 2005], [Mediavilla et al., 2006a], [Belnoue et al., 2010], [Feld-Payet et al., 2011], [Khoei et al., 2013a], [Seupel and Kuna, 2019]
	GTN	[Gologanu et al., 1997], [Linse et al., 2012], [Hütter et al., 2013], [Linse et al., 2014], [Zhang, 2016], [Zhang et al., 2018], [Davaze, 2019], [El Ouazani Tuhami et al., 2021]
Energy release rate	CDM	[Pijaudier-Cabot and Bažant, 1987], [Bažant and Pijaudier-Cabot, 1988], [Liebe et al., 2001], [Germain, 2006], [Sornin, 2007]

Damage	**CDM**	[Pijaudier-Cabot and Bažant, 1987], [Lorentz and Andrieux, 1999], [Areias et al., 2003], [Simone et al., 2003], [César de Sá et al., 2006], [Sornin, 2007], [Fayolle, 2008], [El Khaoulani El Idrissi, 2010], [Velde, 2010], [Kowalsky et al., 2012], [Almansba et al., 2012], [Alessi et al., 2015], [Brepols et al., 2015]
Porosity	**GTN**	[Leblond et al., 1994], [Tvergaard and Needleman, 1995], [Reusch et al., 2003], [Jackiewicz and Kuna, 2003], [Brunet et al., 2005], [Enakoutsa et al., 2007], [Samal et al., 2009b]
	Rousselier	[Samal et al., 2009a], [Seidenfuss et al., 2011]
Damage rate	**CDM**	[Saanouni et al., 1989], [Andrade et al., 2011], [Seabra et al., 2013], [Maniar et al., 2017]
Porosity rate	**GTN**	[Enakoutsa et al., 2007]
Volume change	**GTN**	[El Ouazani Tuhami et al., 2021]
	Rousselier	[Lorentz and Cano, 2005], [Lorentz et al., 2008], [Bargellini et al., 2009]

Table 5.1: Global review on the non-local variables and related publications (CDM: Continuum Damage Mechanics, GTN: Gurson-Tvergaard-Needleman).

Non-locality can in practice be applied indifferently to a dissipation or state variable [Sornin, 2007]. This is the reason why the energy release rate Y can, for instance, be used as the non-local variable. Most of the time, the regularization of the variable responsible for the stress-softening process remains sufficient [Bažant and Pijaudier-Cabot, 1988]. However, some works investigated the regularization of the whole set of internal state variables [Voyiadjis and Al-Rub, 2005], [Dorgan, 2006], [Diamantopoulou et al., 2017]. Such a choice still remains highly dependent on the constitutive equations and the nature of the state couplings between the non-local variable(s) and the others problem variables. In the work at hand, choice has been made to first assess the capabilities of a non-local model with a **single** non-local quantity.

No matter the chosen underlying variable, authors agree to either interpret the delocalization of the source of damage by choosing $\underset{\sim}{\varepsilon}$, ε^p_{eq} or Y, or to delocalize the effects of damage by choosing D. Although there exists some flexibility in the choice of the non-local variable $\overline{\mathcal{V}}$, as no consensus seems valid at this time, some restrictions still need to be ensured [Bažant and Jirásek, 2002]:

- the candidate variable must not be bounded (*e.g.* a damage variable ranging from 0 to 1 should be avoided);
- it should be related to the dissipative mechanism.

However, [Jirásek, 1998] in his work, reported that different types of non-local averaging lead to different computational costs and material responses. Besides, some non-local formulations give rise to unreasonable behavior as they are inherently flawed. Moreover, vanishing stress is not always ensured, even for total damage which may be problematic [Jirásek, 1998]. Some other studies, thanks to a comparative analysis on the regularized variable, also pointed out unsatisfying results when the choice of the non-local variable is not suitable [Jirásek and Rolshoven, 2003a], [Andrade et al., 2014]. Most of the time, the variable which is responsible for the stress-softening process

(damage D) is used as the support for the non-local interaction with neighboring points [Pijaudier-Cabot and Bažant, 1987], [Sornin, 2007], [Fayolle, 2008]. Such an approach seems to yield the best results, according to [Andrade et al., 2014]. It has also been noticed that the delocalization of damage, rather than that of strain, stress or accumulated plasticity, results in improved convergence and consistency of FE solutions [Maniar et al., 2017].

In the present study, the choice for the **non-local total damage** variable $\overline{D}_{tot}$ (simply referred to as $\overline{D}$) to regularize the mathematical problem under strain-softening conditions is, in this case, also supported by the following arguments:

- as seen in Chap. 4, and more particularly in the sect. 4.2, the local cyclic damage model has been designed so as to embed several damage mechanisms, namely the fatigue, creep and volumetric damages. Since a simple summation has been considered, see eq. (4.70), using one single non-local damage variable $\overline{D}$ is more efficient than computing non-local variables for all the different damage mechanisms. In particular, this choice is more practical than the choice of a non-local accumulated plasticity, since time-dependent creep processes have been integrated in the cyclic damage model through a dedicated damage variable not depending on viscoplasticity ($\dot{p}$ for D_f & D_v, and t for D_c);
- thanks to the exponential softening functions given in eq. (4.2), the total damage does not need to be bounded.

Consequently, I have favored the total damage $\overline{D}$ as non-local variable in this Ph.D. project.

Remark: As a preliminary work, a first non-local model considering the accumulated plasticity p as the non-local variable has been derived. Such a formulation, though finally not suitable for cyclic loading conditions, has still been implemented within the Z-set code and assessed in structural calculations. For the sake of brevity, the corresponding results, though mainly associated with the validation of the non-local strategy, are not given in the present chapter but are reported in the appendices, see sect. G.1 and sect. G.2 in Chap. G page 293.

5.2.3 Choice of the characteristic length

Nowadays, the choice of the characteristic length-scale ℓ_c governing the non-local interaction with neighboring points still remains a tricky point. The physical interpretation of the length-scale parameter in metallic materials can be related to microstructural features such as the void spacing, distance between distributed cracks and the density of Geometrically Necessary Dislocations (GND). Such a parameter can be estimated using a combination of experiments and FE inverse analyses [Bažant and Jirásek, 2002], [Andrade, 2011].
In ductile fracture problems, the inter-voids distance or the voids radius is usually taken as the internal length [Tvergaard and Needleman, 1997], [Bargellini et al., 2009] [Hütter et al., 2014]. The maximum aggregate size can also be considered [Bažant and Pijaudier-Cabot, 1989] as well as, in a smaller length-scale, the mean free-path for dislocation motion or the order of grain and particle size [Abu Al-Rub and Voyiadjis, 2004]. The internal length is known to be close to 10 µm for steels [Pommier et al., 2011]. For creep crack growth problems, the volume (or surface) in which

takes place the process of nucleation, growth and coalescence of defects can also be experimentally determined and related to the characteristic length [Kruch et al., 1991].

Standard non-local integral / gradient-enhanced damage models with constant internal length (*i.e.* ℓ_c) may suffer from the problem that the damaged zone artificially widens after complete failure of the structure [Geers et al., 1998], [Simone et al., 2004], [Feld-Payet, 2010]. To solve this problem, it has been proposed to consider an evolving internal length instead of a constant one [Poh and Sun, 2017], [Nguyen et al., 2018]. For instance, in the case of gradient plasticity, it can be expressed as a variable dependent on the accumulated plastic strain, dislocation spacing or grain size, etc. [Abu Al-Rub and Voyiadjis, 2004], [Voyiadjis and Al-Rub, 2005], [Dorgan, 2006]. Motivated by micromechanical analyses and experimental facts indicating that interactions between cracks and voids change in the course of failure, [Pijaudier-Cabot et al., 2004] suggested to make the internal length-scale to depend on the equivalent strain or damage. In the same context, [Desmorat et al., 2015b], [Rastiello et al., 2018] suggested the use of an internal length evolving with the damage field. Many authors examined such a feature in non-local models, *e.g.* [Geers et al., 1998], [Simone et al., 2003], [Nguyen, 2011], [Giry et al., 2011]. This allows to model a progressive transition from diffuse damage to strain localization, hence making a bridge between Damage Mechanics and Fracture Mechanics as the non-local interactions vanish [Rastiello et al., 2018]. Particularly, [Geers et al., 1998] and [Pijaudier-Cabot et al., 2004] studied the effect of a vanishing length scale as a function of the strain level in order to alleviate the widening of the damage zone normal to the crack growth direction. Despite some experimental evidences indicating the need for an evolving internal length, use is generally made of a constant one, at least for simplicity reasons.

As stated by [Besson, 2010], two populations of cavities could be involved in the so-called *flat-to-slant* fracture process. In such a case, at least two characteristic length scales should then be embedded in the modeling. However, the precise identification of the characteristic length scale in the context of cyclic crack growth problems still remains little studied to date, due to both the absence of further understanding on the fracture process under complex loading conditions (fatigue and creep-fatigue) and the inherent complexity of multiple non-local variables numerical modeling. In the present work, choice has been made to use a **single constant non-local parameter** ℓ_c to validate the considered regularization method. Its order of magnitude is chosen based on practical considerations: from a practical and FE numerical point of view, the characteristic length ℓ_c needs to be greater than the maximum FE size, *i.e.* $\ell_c \geq h_e$ according to the recommendations from, *e.g.* [Feld-Payet, 2010], [Linse et al., 2012], [Seupel et al., 2020], [Davaze et al., 2021].

5.3 On the adaption of the viscoplastic-damage formulation

5.3.1 A gradient-enhancement based on the total damage

Spatial localization limiters are known to be mathematically robust and to provide excellent results regarding the mesh-objectivity of the FE simulation results [Hamon, 2010]. That is why the

implicit gradient formulation has been chosen for the present damage model, see sub-sect. 5.2.1. The total damage variable has been chosen as the support for the non-local interaction:

$$D_{tot} = D_f + D_c + D_v \tag{5.4}$$

$$\dot{D}_{tot} = \dot{\lambda} \left\langle \frac{Y_f - Y_{f_0}}{S_f} \right\rangle_+^{m_f} e^{(\beta_f \eta_D D_{tot})} + \left\langle \frac{\chi_c(\underset{\sim}{\sigma})}{S_c} \right\rangle_+^{m_c} e^{(\beta_c \eta_D D_{tot})} + (1 - D_{tot}) \operatorname{tr} \underset{\sim}{\dot{\varepsilon}}^{in} \tag{5.5}$$

A total non-local damage variable $\overline{D}_{tot}$ is introduced, in which, for the sake of clarity, the subscript *"tot"* is deliberately omitted. The diffusion equation (related to a non-constitutive variable $\overline{D}_{tot}$) to be solved is given by:

$$\overline{D}_{tot} - c \nabla^2 \overline{D}_{tot} = D_{tot} \quad \text{in } \Omega \quad \textit{and} \quad \nabla \overline{D}_{tot} \cdot \underline{n} = 0 \quad \text{on } \partial\Omega \tag{5.6}$$

while the non-local constitutive model $\mathbb{B}$ reads:

$$(\underset{\sim}{\sigma}, D_{tot}) = \mathbb{B} (\Delta \underset{\sim}{\varepsilon}, \Delta \overline{D}_{tot}, \mathcal{V}_{int}) \tag{5.7}$$

Still assuming a strong coupling between damage and elastic-viscoplastic behavior, the local effective variables eq. (4.1) are re-written in a non-local format:

$$\underset{\sim}{\tilde{\sigma}} = \frac{\underset{\sim}{\sigma}}{f^e(\overline{D})} \qquad \underset{\sim}{\tilde{X}}^k = \frac{\underset{\sim}{X}^k}{f^k(\overline{D})} \qquad \tilde{R}^i = \frac{R^i}{f^i(\overline{D})} \tag{5.8}$$

The viscoplastic yield criterion eq. (4.61), strongly coupled to non-local damage, is defined by:

$$\mathcal{F}_y^{vp} = \sqrt{\frac{3}{2}} \left\| \left(\frac{\underset{\sim}{\sigma}^D}{f^e(\overline{D})} - \sum_k \frac{\underset{\sim}{X}^k}{f^k(\overline{D})} \right) \right\|_H - \sum_i \frac{R^i}{f^i(\overline{D})} - R_0 - \sigma_{ov}(\dot{\lambda}) \leq 0 \tag{5.9}$$

while the loading/unloading conditions (KKT) eq. (4.23) remain valid. In addition, both the state and the evolution equations eq. (4.12), eq. (4.13), eq. (4.14), eq. (4.44), eq. (4.45), eq. (4.46), eq. (4.47), eq. (4.60), eq. (4.65), eq. (4.37) are reformulated:

$$\underset{\sim}{\sigma} = f^e(\overline{D}) \underset{\approx}{\Lambda} : \underset{\sim}{\varepsilon}^e \qquad \underset{\sim}{X}^k = f^k(\overline{D}) \underset{\approx}{C}^k : \underset{\sim}{\alpha}^k \qquad R^i = b^i f^i(\overline{D}) Q^i r^i \tag{5.10}$$

$$\underset{\sim}{\dot{\varepsilon}}^{in} = \frac{\dot{\lambda}}{f^e(\overline{D})} \sqrt{\frac{3}{2}} \underset{\sim}{\tilde{n}} \tag{5.11}$$

$$\underset{\sim}{\dot{\alpha}}^k = \frac{\dot{\lambda}}{f^k(\overline{D})} \left(\sqrt{\frac{3}{2}} \underset{\sim}{\tilde{n}} - \gamma^k \varphi^k(p) \underset{\approx}{P}^D : \underset{\sim}{\alpha}^k \right) \tag{5.12}$$

$$\dot{r}^i = \frac{\dot{\lambda}}{f^i(\overline{D})} (1 - b^i r^i) \tag{5.13}$$

$$\dot{D} = \dot{\lambda} \left\langle \frac{Y_f - Y_{f_0}}{S_f} \right\rangle_+^{m_f} e^{(\beta_f \eta_D \overline{D})} + \left\langle \frac{\chi_c(\underset{\sim}{\sigma})}{S_c} \right\rangle_+^{m_c} e^{(\beta_c \eta_D \overline{D})} + (1 - \overline{D}) \operatorname{tr} \underset{\sim}{\dot{\varepsilon}}^{in} \tag{5.14}$$

$$\dot{p} = \frac{\phi_v(\mathcal{F}_y)}{f^e(\overline{D})} \tag{5.15}$$

From eq. (5.9) to eq. (5.15), one can observe that the whole constitutive equations are fully coupled to the non-local damage thanks to the effective variables. A similar approach was adopted by [Sornin, 2007] and [Velde, 2010]. Such a modeling framework assumes that $\overline{D}$ may evolve independently of the local plasticity. The non-local variable coming from the resolution of the diffusion equation, see eq. (5.6), is estimated at each node of the non-local FE. This extra nodal information is then interpolated to the IP thanks to dedicated (linear) shape functions in order to be introduced in the constitutive relations. In order to ensure a positive dissipation along the whole loading path, a decreasing evolution for $\overline{D}$ must be precluded. To this end, healing effects should be excluded, which can be, in an analytical and incremental manner, be achieved by setting:

$$\mathrm{d}\overline{D} \geq 0 \qquad \leftrightarrow \qquad \overline{D}(t) = \max\left[\,\overline{D}(\tau)\,\right],\ 0 \leq \tau \leq t \tag{5.16}$$

The performance of this non-local extension will be discussed later on, in sect. 5.4. Prior to the assessment, some numerical aspects related to the FE implementation of this gradient-enhanced damage model should be discussed.

5.3.2 Thermodynamic consistency

During the material modeling process, it is of primary importance to ensure the positivity of the intrinsic dissipation. As a result of the introduction of the non-local variable $\overline{D}$ in the constitutive relations, the rate of change of the free energy expressed in eq. (4.24) here becomes:

$$\begin{aligned}\mathcal{D}_{int} &= \underset{\sim}{\sigma} : \dot{\underset{\sim}{\varepsilon}} - \rho\dot{\psi} \geq 0 \\ &= \underset{\sim}{\sigma} : \dot{\underset{\sim}{\varepsilon}}^{in} - \sum_k \underset{\sim}{X}^k : \dot{\underset{\sim}{\alpha}}^k - \sum_i R^i \dot{r}^i + Y\dot{\overline{D}} \geq 0\end{aligned} \tag{5.17}$$

The thermodynamic state potential ψ from eq. (4.3) needs to be adapted according to the coupling with the non-local damage, which yields:

$$\rho\psi\left(\underset{\sim}{\varepsilon}^e, \underset{\sim}{\alpha}^k, r^i, \overline{D}\right) = \rho\psi_e\left(\underset{\sim}{\varepsilon}^e, \overline{D}\right) + \sum_k \rho\psi^k_{in}\left(\underset{\sim}{\alpha}^k, \overline{D}\right) + \sum_i \rho\psi^i_{in}\left(r^i, \overline{D}\right) \tag{5.18}$$

Consequently, the definition of the energy release rate:

$$Y = -\rho\frac{\partial\psi}{\partial\overline{D}} = -\rho\frac{\partial\left(\psi_e + \sum_k \psi^k_{in} + \sum_i \psi^i_{in}\right)}{\partial\overline{D}} \tag{5.19}$$

along with the need for a strictly increasing $\mathrm{d}\overline{D} \geq 0$ (see eq. (5.16)) allow for the damage-related intrinsic dissipation to be positive $Y\dot{\overline{D}} \geq 0$. The consistent validation of the positivity of the intrinsic dissipation related to both plastic power, work-hardening and damage has already been discussed in sub-sect. 4.1.4 and is detailed in the appendices, see Chap. F page 289.

5.4 Finite Element formulation of the enriched non-local cyclic damage model

The following sections address the main necessary steps for building an enhanced FE model including both linearization and solving procedures. Details on the whole modeling process can be found in, *e.g.* [Simo and Hughes, 1998], [de Souza Neto et al., 2011]. Let us note that this non-linear problem will be solved using the static implicit Z-set solver.

5.4.1 Governing equations

The classical mechanical problem to solve reads:

$$\nabla . \underset{\sim}{\sigma}(\underline{u}) + \underline{f}_b = \underline{0} \qquad \text{in} \quad \Omega \tag{5.20}$$

$$\underset{\sim}{\sigma} = \underset{\sim}{\sigma}^T \qquad \text{in} \quad \Omega \tag{5.21}$$

$$[\![\underset{\sim}{\sigma} . \underline{n}]\!] = \underline{0} \qquad \text{on} \quad \Gamma_{int} \tag{5.22}$$

$$\underline{u} = \underline{u}^p \qquad \text{on} \quad \partial\Omega_u \qquad \text{and} \qquad \underset{\sim}{\sigma} . \underline{n}_t = \underline{t}^p \qquad \text{on} \quad \partial\Omega_t \tag{5.23}$$

In eq. (5.20), $\underset{\sim}{\sigma}$ is the Cauchy stress tensor, $\underline{f}_b$ is the body force per unit volume, whereas inertia is neglected. The eq. (5.22) is referred to as the interior continuity condition, which ensures the continuity on all the interfaces Γ_{int} between subdomains of Ω. In eq. (5.23), $\underline{u}$ is the displacement vector, $\underline{u}^p$ and $\underline{t}^p$ are the prescribed boundary values on $\partial\Omega$ for the displacement and traction fields, respectively (with $\partial\Omega_u \cup \partial\Omega_t = \partial\Omega$ and $\partial\Omega_u \cap \partial\Omega_t = \emptyset$) and $\underline{n}_t$ the outward unit normal to $\partial\Omega_t$.

With the implicit gradient enhancement, an additional diffusion equation of Helmholtz-type also needs to be solved along with the single-field equilibrium problem described by eq. (5.20) - eq. (5.23):

$$\left(\overline{\mathcal{V}} - \mathcal{V} \right) - c\,\nabla^2 \overline{\mathcal{V}} = 0 \qquad \leftrightarrow \qquad \overline{\mathcal{V}} - c\,\nabla^2 \overline{\mathcal{V}} = \mathcal{V} \qquad \text{in} \quad \Omega \tag{5.24}$$

where $\overline{\mathcal{V}}$ and $\mathcal{V}$ are the non-local and local quantities, respectively, $\nabla^2 = \sum_i \partial^2/\partial x_i^2$ the Laplacian operator with respect to the current configuration and $c = \frac{1}{2}\ell_c^2$ is related to the characteristic internal length [Peerlings et al., 2000].
Following the standard process of adopting homogeneous BC for $\nabla\overline{\mathcal{V}}$ in the boundary normal direction, in agreements with [Peerlings et al., 1996b], one gets:

$$\nabla \overline{\mathcal{V}} . \underline{n}_{\overline{\mathcal{V}}} = 0 \qquad \text{on} \quad \partial\Omega \tag{5.25}$$

where $\underline{n}_{\overline{\mathcal{V}}}$ denotes the outward unit normal to the boundary $\partial\Omega$ of the problem domain.

The whole set of eq. (5.20) - eq. (5.23) & eq. (5.24) - eq. (5.25) is known as the strong form of

the equilibrium and non-local equations.

5.4.2 Weak formulations of the 2-fields non-local finite element

5.4.2.1 Variational formulation of the equilibrium equation

The governing equations given in sub-sect. 5.4.1 have to be satisfied in every material point at each (discrete) moment of the loading process. In order to be implemented within a FE code, such a mechanical problem has to be reformulated in weak form so as to use a variational formulation. This can be done using the principle of virtual work, multiplying eq. (5.20) & eq. (5.24) with the test functions $\delta\underline{u}^*$ and integrating the product over the domain Ω. This way, the eq. (5.20) can be written:

$$\int_\Omega \delta\underline{u}^* \left(\nabla . \underset{\sim}{\sigma} + \underline{f}_b \right) \mathrm{d}\Omega = \underline{0} \qquad \forall\, \delta\underline{u}^* \in \mathcal{U}^0 \tag{5.26}$$

where $\mathcal{U}^0$ is the vector space of kinematically admissible fields at zero. Using $\underset{\sim}{\varepsilon}^* = \nabla^s \underline{u}^*$, including the BC given by eq. (5.23), and applying partial integration together with the Green-Gauss divergence theorem, eq. (5.26) can be written [Zienkiewicz and Taylor, 2000]:

$$\int_\Omega \underset{\sim}{\sigma} : \delta\underset{\sim}{\varepsilon}^*(\underline{u}^*) \,\mathrm{d}\Omega = \int_\Omega \underline{f}_b \,.\, \delta\underline{u}^* \,\mathrm{d}\Omega + \int_{\partial\Omega} \underline{t}^p \,.\, \delta\underline{u}^* \,\mathrm{d}\partial\Omega \qquad \forall\, \delta\underline{u}^* \in \mathcal{U}^0 \tag{5.27}$$

In eq. (5.27), the integral on the left-hand side of eq. (5.27) represents the work of the internal forces associated with the virtual displacement, while the integrals on the right-hand side describe the work of the external loading associated with the virtual displacement.

5.4.2.2 Variational formulation of the gradient equation

As for the non-local enhancement, in a similar fashion, the weak form of eq. (5.24) reads:

$$\int_\Omega \delta\overline{\mathcal{V}}^* \left(\overline{\mathcal{V}} - c\,\nabla^2 \overline{\mathcal{V}} - \mathcal{V} \right) \mathrm{d}\Omega = \underline{0} \tag{5.28}$$

which is obtained using the virtual quantity $\delta\overline{\mathcal{V}}^*$. Including the boundary condition eq. (5.25) and employing the partial integration together with the Green-Gauss divergence theorem into eq. (5.28), the resulting weak form becomes:

$$\int_\Omega \left(\overline{\mathcal{V}} - \mathcal{V}\right) \delta\overline{\mathcal{V}}^* \,\mathrm{d}\Omega + c \int_\Omega \nabla\overline{\mathcal{V}} \,.\, \nabla\left(\delta\overline{\mathcal{V}}^*\right) \mathrm{d}\Omega = 0 \tag{5.29}$$

The equation eq. (5.29) exhibits the balance between internal and (vanishing) external non-local forces. The difference between the local variable $\mathcal{V}$ and its non-local counterpart $\overline{\mathcal{V}}$ in eq. (5.29) serves as source term for the non-local interaction (diffusion) process.

5.4.3 Spatial discretization using Finite Element method

5.4.3.1 Shape functions for the interpolations

The problem at hand involves two unknowns at the nodal level, that are the displacement fields and the non-local variable, gathered within the vector $\underline{q} = \left\{\underline{u},\, \overline{\mathcal{V}}\right\}$. In the standard FE framework, the strain field $\underset{\sim}{\varepsilon}$ follows from the gradient of displacement field which is given by:

$$\underset{\sim}{\varepsilon}\left(\underline{x}\right) = \sum_{a=1}^{n_a} \nabla^s \underline{N}_u^a\left(\underline{x}\right) \underline{u}^a = \sum_{a=1}^{n_a} \underline{B}_u^a\left(\underline{x}\right) \underline{u}^a \tag{5.30}$$

$$\delta\underset{\sim}{\varepsilon}^*\left(\underline{x}\right) = \sum_{a=1}^{n_a} \nabla^s \underline{N}_u^a\left(\underline{x}\right) \delta\underline{u}^{a,*} = \sum_{a=1}^{n_a} \underline{B}_u^a\left(\underline{x}\right) \delta\underline{u}^{a,*} \tag{5.31}$$

where n_a is the number of nodes in the FE, $\underline{u}^a$ are the unknown nodal values for the displacement, $\underline{N}_u^a$ (resp. $\underline{B}_u^a$) are the elementary matrices containing interpolation functions for the DoF associated with the displacements (resp. their derivatives).
Note that eq. (5.30) & eq. (5.31) are also true for virtual quantities $\delta\underline{u}^*$ and $\delta\overline{\mathcal{V}}^*$.
In a similar fashion, the gradient of the non-local field is given by the product of the nodal values and the shape functions, so that:

$$\nabla\overline{\mathcal{V}}\left(\underline{x}\right) = \sum_{a=1}^{n_a} \nabla\underline{N}_{\overline{\mathcal{V}}}^a\left(\underline{x}\right) \overline{\mathcal{V}}^a = \sum_{a=1}^{n_a} \underline{B}_{\overline{\mathcal{V}}}^a\left(\underline{x}\right) \overline{\mathcal{V}}^a \tag{5.32}$$

$$\nabla\delta\overline{\mathcal{V}}^*\left(\underline{x}\right) = \sum_{a=1}^{n_a} \nabla\underline{N}_{\overline{\mathcal{V}}}^a\left(\underline{x}\right) \delta\overline{\mathcal{V}}^{a,*} = \sum_{a=1}^{n_a} \underline{B}_{\overline{\mathcal{V}}}^a\left(\underline{x}\right) \delta\overline{\mathcal{V}}^{a,*} \tag{5.33}$$

where $\overline{\mathcal{V}}^a$ are the unknown nodal values for the non-local variable, $\underline{N}_{\overline{\mathcal{V}}}^a$ (resp. $\underline{B}_{\overline{\mathcal{V}}}^a$) are the elementary matrices containing interpolation functions for the DoF associated with the non-local variable (resp. their derivatives).

5.4.3.2 Elementary reactions

The substitution of the FE approximations from the sub-sect. 5.4.3.1 into the weak forms of the sub-sect. 5.4.2 yields the respective virtual works over the element as follows:

$$\delta A_u^e = \delta\underline{d}_u^* \left[\int_{\Omega_e} \underline{B}_u^T \,\underset{\sim}{\sigma}\, \mathrm{d}\Omega_e - \int_{\Omega_e} \underline{N}_u^T \,\underline{f}_b \,\mathrm{d}\Omega_e - \int_{\partial\Omega_e} \underline{N}_u^T \,\underline{t}^p \,\mathrm{d}\partial\Omega_e\right] \tag{5.34}$$

$$\delta A_{\overline{\mathcal{V}}}^e = \delta\underline{d}_{\overline{\mathcal{V}}}^* \left[\int_{\Omega_e} \left(\underline{N}_{\overline{\mathcal{V}}}^T \underline{N}_{\overline{\mathcal{V}}}\, \overline{\mathcal{V}} - \underline{N}_{\overline{\mathcal{V}}}^T\, \mathcal{V} + c\, \underline{B}_{\overline{\mathcal{V}}}^T \underline{B}_{\overline{\mathcal{V}}}\, \overline{\mathcal{V}}\right) \mathrm{d}\Omega_e - c \int_{\partial\Omega_e} \underline{N}_{\overline{\mathcal{V}}}^T\, t_{\overline{\mathcal{V}}} \,\mathrm{d}\partial\Omega_e\right] \tag{5.35}$$

where the superscript e refers to a quantity belonging to element e.
Due to the fact that the virtual work of the element vanishes for the arbitrary values of the

virtual quantities $\delta \underline{d}_u^*$ and $\delta \underline{d}_{\overline{\mathcal{V}}}^*$, the residuals of equilibrium and gradient equations follows from eq. (5.34) & eq. (5.35), respectively:

$$\underline{r}_u^e = \int_{\Omega_e} \underline{B}_u^T \underset{\sim}{\sigma} \, \mathrm{d}\Omega_e - \int_{\Omega_e} \underline{N}_u^T \underline{f}_b \, \mathrm{d}\Omega_e - \int_{\partial\Omega_e} \underline{N}_u^T \underline{t}^p \, \mathrm{d}\partial\Omega_e = \underline{0} \tag{5.36}$$

$$\underline{r}_{\overline{\mathcal{V}}}^e = \int_{\Omega_e} \left(\underline{N}_{\overline{\mathcal{V}}}^T \underline{N}_{\overline{\mathcal{V}}} \, \overline{\mathcal{V}} - \underline{N}_{\overline{\mathcal{V}}}^T \mathcal{V} + c \, \underline{B}_{\overline{\mathcal{V}}}^T \underline{B}_{\overline{\mathcal{V}}} \, \overline{\mathcal{V}} \right) \mathrm{d}\Omega_e - c \int_{\partial\Omega_e} \underline{N}_{\overline{\mathcal{V}}}^T \, t_{\overline{\mathcal{V}}} \, \mathrm{d}\partial\Omega_e = \underline{0} \tag{5.37}$$

And thus, the element vectors of internal and external nodal forces can be devised as follows:

$$\underline{f}_{u,\,int}^e = \int_{\Omega_e} \underline{B}_u^T \underset{\sim}{\sigma} \, \mathrm{d}\Omega_e \tag{5.38}$$

$$\underline{f}_{u,\,ext}^e = \int_{\Omega_e} \underline{N}_u^T \underline{f}_b \, \mathrm{d}\Omega_e + \int_{\partial\Omega_e} \underline{N}_u^T \underline{t}^p \, \mathrm{d}\partial\Omega_e \tag{5.39}$$

$$\underline{f}_{\overline{\mathcal{V}},\,int}^e = \int_{\Omega_e} \left(\underline{N}_{\overline{\mathcal{V}}}^T \underline{N}_{\overline{\mathcal{V}}} \, \overline{\mathcal{V}} - \underline{N}_{\overline{\mathcal{V}}}^T \mathcal{V} + c \, \underline{B}_{\overline{\mathcal{V}}}^T \underline{B}_{\overline{\mathcal{V}}} \, \overline{\mathcal{V}} \right) \mathrm{d}\Omega_e \tag{5.40}$$

$$\underline{f}_{\overline{\mathcal{V}},\,ext}^e = c \int_{\partial\Omega_e} \underline{N}_{\overline{\mathcal{V}}}^T \, t_{\overline{\mathcal{V}}} \, \mathrm{d}\partial\Omega_e = \underline{0} \tag{5.41}$$

For the sake of clarity, the elementary residuals forms eq. (5.36) and eq. (5.37) are expressed by the following compact form:

$$\underline{r}^e = \begin{bmatrix} \underline{r}_u^e \\ \underline{r}_{\overline{\mathcal{V}}}^e \end{bmatrix} = \begin{bmatrix} \underline{f}_{u,\,int}^e - \underline{f}_{u,\,ext}^e \\ \underline{f}_{\overline{\mathcal{V}},\,int}^e - \underline{f}_{\overline{\mathcal{V}},\,ext}^e \end{bmatrix} = \begin{bmatrix} \underline{0} \\ \underline{0} \end{bmatrix} \tag{5.42}$$

5.4.3.3 Assembly

The last step to define the whole system is to achieve the assembly of all the elementary reactions so that to get the global system. To this end, the virtual works of all the elements resulting from eq. (5.34) and eq. (5.35) are thereafter assembled:

$$\delta A_u = \sum_{e=1}^{n_e} \delta A_u^e \qquad \text{and} \qquad \delta A_{\overline{\mathcal{V}}} = \sum_{e=1}^{n_e} \delta A_{\overline{\mathcal{V}}}^e \tag{5.43}$$

In an analogous way, the residuals of equilibrium and gradient equations of the global system are gained through:

$$\underline{R}_u = \bigcup_{e=1}^{n_e} \underline{r}_u^e \qquad \text{and} \qquad \underline{R}_{\overline{\mathcal{V}}} = \bigcup_{e=1}^{n_e} \underline{r}_{\overline{\mathcal{V}}}^e \tag{5.44}$$

As a result, after assembling all the element residual vectors $\underline{r}^e$ from eq. (5.42), the global residual vector $\underline{R}$ of the system is gained:

$$\underline{R} = \begin{bmatrix} \underline{R}_u \\ \underline{R}_{\overline{\mathcal{V}}} \end{bmatrix} = \bigcup_{e=1}^{n_e} \begin{bmatrix} \underline{f}^{e}_{u,int} - \underline{f}^{e}_{u,ext} \\ \underline{f}^{e}_{\overline{\mathcal{V}},int} - \underline{f}^{e}_{\overline{\mathcal{V}},ext} \end{bmatrix} = \begin{bmatrix} \underline{F}_{u,int} - \underline{F}_{u,ext} \\ \underline{F}_{\overline{\mathcal{V}},int} - \underline{F}_{\overline{\mathcal{V}},ext} \end{bmatrix} = \begin{bmatrix} \underline{0} \\ \underline{0} \end{bmatrix} \tag{5.45}$$

The reader is referred to [Besson et al., 2010] for the description of the assembly procedure.
It can also be noticed that the residual equation eq. (5.45) results from the weak forms of the equations of the problem and are, in the present case, owing to the non-linear behavior of the material as well with the coupling with damage, highly non-linear.

5.4.4 Global implicit resolution scheme

This paragraph details the numerical implementation of the non-local model. Some aspects, particularly at the integration point (or local) level follow the developments detailed in sect. 4.3. Again, the reader more interested in the application of this numerical part can directly go to paragraph sect. 5.5 which presents the validation of the proposed improvements.

5.4.4.1 Consistent linearization

We seek for the solution for which $\underline{R} = \underline{0}$. In order to be numerically solved thanks to incremental-iterative techniques (*e.g.* the Newton-Raphson algorithm), the non-linear system of equations eq. (5.45) needs to be consistently linearized [Zienkiewicz and Taylor, 2000]. To this end, the residual equations have to be differentiated w.r.t. the unknown nodal DoF $\underline{q} = \left\{\underline{q}_u, \underline{q}_{\overline{\mathcal{V}}}\right\}^T$. This can be achieved by the Taylor expansion of the residual vector function eq. (5.45) in the neighborhood of a better approximated solution of unknown DoF $\underline{q}$ at the $(r+1)^{th}$ iteration step within the time step t_{n+1}:

$$\underline{R}\left(\underline{q}_{n+1}^{(r+1)}\right) = \underline{R}\left(\underline{q}_{n+1}^{(r)}\right) + \left.\frac{\partial \underline{R}\left(\underline{q}_{n+1}\right)}{\partial \underline{q}}\right|_{\underline{q}^{(r)}} \delta\Delta\underline{q}_{n+1}^{(r+1)} = \underline{0} \tag{5.46}$$

in which $\Delta\underline{q}_{n+1}^{(r+1)} = \Delta\underline{q}_{n+1}^{(r)} + \delta\Delta\underline{q}_{n+1}^{(r+1)}$ is the approximated solution obtained at the $(r+1)^{th}$ iteration step after convergence. Then, rearranging and simplifying eq. (5.46) leads to a linearized system of equations within the time step t_{n+1}:

$$\underline{\underline{K}}^{(r)}\, \delta\Delta\underline{q}_{n+1}^{(r+1)} = -\underline{R}^{(r)} \tag{5.47}$$

where $\underline{\underline{K}}^{(r)}$ is the tangential stiffness matrix of the structural system, $\Delta\underline{q}_{n+1}^{(r+1)}$ is the iterative solution of the system of non-linear equations upon convergence, and $\underline{R}^{(r)}$ refers to the vector of residuals. In addition, the inner terms in the linearized equation eq. (5.47) are given by:

$$\underline{\underline{K}}^{(r)} = \bigcup_{e=1}^{n_e} \begin{bmatrix} \underline{\underline{k}}^{e,(r)}_{uu} & \underline{\underline{k}}^{e,(r)}_{u\overline{\mathcal{V}}} \\ \underline{\underline{k}}^{e,(r)}_{\overline{\mathcal{V}}u} & \underline{\underline{k}}^{e,(r)}_{\overline{\mathcal{V}}\overline{\mathcal{V}}} \end{bmatrix} \qquad \Delta\underline{q}^{(r+1)} = \bigcup_{e=1}^{n_e} \begin{bmatrix} \Delta\underline{q}_u^{e,(r+1)} \\ \Delta\underline{q}_{\overline{\mathcal{V}}}^{e,(r+1)} \end{bmatrix} \qquad \underline{R}^{(r)} = \bigcup_{e=1}^{n_e} \begin{bmatrix} \underline{r}_u^{e,(r)} \\ \underline{r}_{\overline{\mathcal{V}}}^{e,(r)} \end{bmatrix} \tag{5.48}$$

where the sub-matrices of eq. (5.48)-a are given by:

$$\underline{\underline{k}}^{e,(r)}_{uu} = \left.\frac{\partial \underline{r}^{e}_{u}}{\partial \underline{q}^{e}_{u}}\right|_{\underline{q}^{(r)}} = \int_{\Omega_e} \underline{B}^{T}_{u} \underset{\approx}{C}_{uu} \underline{B}_{u} \, \mathrm{d}\Omega_e \tag{5.49a}$$

$$\underline{\underline{k}}^{e,(r)}_{u\overline{\mathcal{V}}} = \left.\frac{\partial \underline{r}^{e}_{u}}{\partial \underline{q}^{e}_{\overline{\mathcal{V}}}}\right|_{\underline{q}^{(r)}} = \int_{\Omega_e} \underline{B}^{T}_{u} \underset{\sim}{C}_{u\overline{\mathcal{V}}} \underline{N}_{\overline{\mathcal{V}}} \, \mathrm{d}\Omega_e \tag{5.49b}$$

$$\underline{\underline{k}}^{e,(r)}_{\overline{\mathcal{V}}u} = \left.\frac{\partial \underline{r}^{e}_{\overline{\mathcal{V}}}}{\partial \underline{q}^{e}_{u}}\right|_{\underline{q}^{(r)}} = -\int_{\Omega_e} \underline{N}^{T}_{\overline{\mathcal{V}}} \underset{\sim}{C}_{\overline{\mathcal{V}}u} \underline{B}_{u} \, \mathrm{d}\Omega_e \tag{5.49c}$$

$$\underline{\underline{k}}^{e,(r)}_{\overline{\mathcal{V}}\overline{\mathcal{V}}} = \left.\frac{\partial \underline{r}^{e}_{\overline{\mathcal{V}}}}{\partial \underline{q}^{e}_{\overline{\mathcal{V}}}}\right|_{\underline{q}^{(r)}} = \int_{\Omega_e} \left(\underline{N}^{T}_{\overline{\mathcal{V}}} \left(1 - C_{\overline{\mathcal{V}}\overline{\mathcal{V}}}\right) \underline{N}_{\overline{\mathcal{V}}} + c\, \underline{B}^{T}_{\overline{\mathcal{V}}} \underline{B}_{\overline{\mathcal{V}}} \right) \mathrm{d}\Omega_e \tag{5.49d}$$

in which one can notice the appearance in eq. (5.49a) - eq. (5.49d) of the material tangents, consistent with the incremental discretization of the problem so that to ensure a good convergence. They need to be evaluated at each Gauss points of the elements. They are given by:

$$\underset{\approx}{C}_{uu} = \frac{\partial \Delta \underset{\sim}{\sigma}}{\partial \Delta \underset{\sim}{\varepsilon}} \qquad \underset{\sim}{C}_{u\overline{\mathcal{V}}} = \frac{\partial \Delta \underset{\sim}{\sigma}}{\partial \Delta \overline{\mathcal{V}}} \qquad \underset{\sim}{C}_{\overline{\mathcal{V}}u} = \frac{\partial \Delta \mathcal{V}}{\partial \Delta \underset{\sim}{\varepsilon}} \qquad C_{\overline{\mathcal{V}}\overline{\mathcal{V}}} = \frac{\partial \Delta \mathcal{V}}{\partial \Delta \overline{\mathcal{V}}} \tag{5.50}$$

One should keep in mind that $\underset{\approx}{C}_{uu}$ (4^{th}-order tensor) is non-symmetric due to the fact that the coupled damage model employs the non-associative flow rule. Indeed, the coupled cyclic damage model presented in Chap. 4 is said to be associative w.r.t $\underset{\sim}{\sigma}$ as long as $\partial F_p / \partial \underset{\sim}{\sigma} = \partial \mathcal{F}_y / \partial \underset{\sim}{\sigma}$ but is non-associative w.r.t. $\underset{\sim}{X}^{k}$ owing to the fact that $\partial F_p / \partial \underset{\sim}{X}^{k} \neq \partial \mathcal{F}_y / \partial \underset{\sim}{X}^{k}$. Moreover, the strong coupling between damage (local or non-local) and behavior, together with the use of a non-associated viscoplasticity framework generally lead to a non-symmetric tangent operator. Moreover, the (possible) coupling between the non-local variable with the equilibrium equation eventually results in non-symmetric element matrices, that is $\underline{\underline{k}}^{e,r}_{u\overline{\mathcal{V}}} \neq \underline{\underline{k}}^{e,r}_{\overline{\mathcal{V}}u}$, which in turn results, after assembly, in a non-symmetric global stiffness matrix $\underline{\underline{K}}$. In such a case, specific solvers able to cope with non-symmetric tangential stiffness matrices should be employed [Gosselet, 2003].

Finally, one can write in a matrix form the local consistent tangent matrix which is evaluated at the Gauss point level $\underset{\approx}{\mathcal{L}}$:

$$\underset{\approx}{\mathcal{L}} = \begin{pmatrix} \underset{\approx}{C}_{uu} & \underset{\sim}{C}_{u\overline{\mathcal{V}}} \\ \underset{\sim}{C}_{\overline{\mathcal{V}}u} & C_{\overline{\mathcal{V}}\overline{\mathcal{V}}} \end{pmatrix} = \begin{pmatrix} \dfrac{\partial \Delta \underset{\sim}{\sigma}}{\partial \Delta \underset{\sim}{\varepsilon}} & \dfrac{\partial \Delta \underset{\sim}{\sigma}}{\partial \Delta \overline{\mathcal{V}}} \\ \dfrac{\partial \Delta \mathcal{V}}{\partial \Delta \underset{\sim}{\varepsilon}} & \dfrac{\partial \Delta \mathcal{V}}{\partial \Delta \overline{\mathcal{V}}} \end{pmatrix} \tag{5.51}$$

For the sake of brevity, details for the derivation of each terms of the previous local consistent tangent matrix are given in the appendix, see Chap. J page 309.

5.4.4.2 Solving procedure

The problem in eq. (5.47) is solved thanks to the global Newton-Raphson algorithm. At increment $n+1$, the change in DoF $\delta\Delta\underline{q}_{n+1}^{(r+1)} = \Delta\underline{q}_{n+1}^{(r+1)} - \Delta\underline{q}_{n}^{(r)}$ at iteration $(r+1)$ is given thanks to the resolution of the matrix system:

$$\underline{\underline{K}}\left(\underline{q}_{n+1}^{(r)}\right)\left[\Delta\underline{q}_{n+1}^{(r+1)} - \Delta\underline{q}_{n+1}^{(r)}\right] = -\underline{R}\left(\underline{q}_{n+1}^{(r)}\right) \tag{5.52}$$

Once the residuals associated with each unknown variable have been minimized, the following convergence criteria are checked:

$$\frac{\left\|\underline{R}_u\right\|}{\left\|\underline{F}_{u,\,ext}\right\|} = \frac{\left\|\underline{F}_{u,\,int} - \underline{F}_{u,\,ext}\right\|}{\left\|\underline{F}_{u,\,ext}\right\|} < \epsilon_u \qquad \text{and} \qquad \left\|\underline{R}_{\overline{\mathcal{V}}}\right\| = \left\|\underline{F}_{\overline{\mathcal{V}}}\right\| < \epsilon_{\overline{\mathcal{V}}} \tag{5.53}$$

where the L_2-norm has been used for the residual of $\underline{u}$ and the L_∞-norm for that of $\overline{\mathcal{V}}$. Due to the absence of external forces for the non-local variable, see eq. (5.41), the criterion for $\overline{\mathcal{V}}$ has been chosen to rely on an absolute value for the residual, see the right-hand side of eq. (5.53).

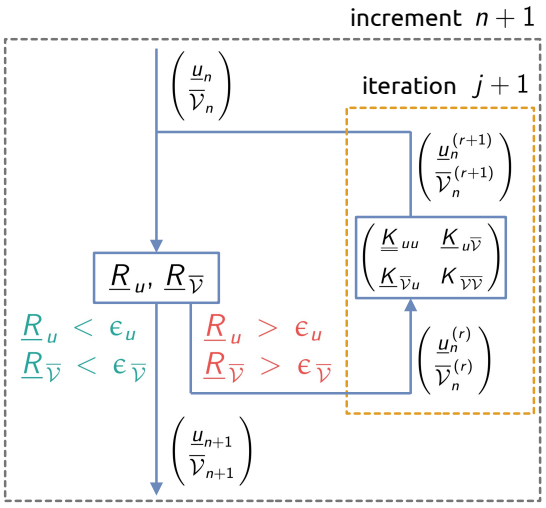

Figure 5.1: Monolithic solving algorithm for the coupled equilibrium / non-local problem.

In the present case, a *monolithic* solving procedure is adopted so all the unknown residuals in eq. (5.45) are solved simultaneously with a *strong* coupling. Thus, all the terms of $\underline{\underline{K}}$ (global level) and $\underline{\underline{\underline{\underline{\mathcal{L}}}}}$ (local level) are required to ensure the good convergence of the solving algorithm, see Fig. 5.1. Such a solving process is inherent to the multi-purposes Z-set implicit solver used in this work, which is known to be unconditionally stable.

5.4.5 Numerical algorithm at the Gauss point level

Once the evolution equations related to the internal state variables have been modified, see sub-sect. 5.3.1, the gradient enhanced cyclic damage mode needs to be implemented within the

Z-set suite thanks to a user-defined routine.

5.4.5.1 Time discretization of the evolution equations

At the integration point level, the constitutive equations need to be integrated with respect to time. In a similar fashion as for the local model, the material residual equations coming from the incremental form of the evolution equations are given by:

$$\mathcal{R}_{\underset{\sim}{\sigma}} = \underset{\sim}{\varepsilon}^e - \underset{\approx}{A}^{-1} : \underset{\sim}{\tilde{\sigma}}_{uc}(\overline{D}) = \underset{\sim}{0} \tag{5.54a}$$

$$\mathcal{R}_{\underset{\sim}{\varepsilon}^e} = \Delta\underset{\sim}{\varepsilon}^e - \Delta\underset{\sim}{\varepsilon} + \frac{\Delta\lambda}{f^e(\overline{D})}\sqrt{\frac{3}{2}}\,\underset{\approx}{\tilde{n}} = \underset{\sim}{0} \tag{5.54b}$$

$$\mathcal{R}_{\underset{\sim}{\alpha}^k} = \Delta\underset{\sim}{\alpha}^k - \frac{\Delta\lambda}{f^k(\overline{D})}\left(\sqrt{\frac{3}{2}}\,\underset{\approx}{\tilde{n}} - \gamma^k(p)\,\underset{\approx}{P}^D : \underset{\sim}{\alpha}^k\right) = \underset{\sim}{0} \tag{5.54c}$$

$$\mathcal{R}_{r^i} = \Delta r^i - \frac{\Delta\lambda}{f^i(\overline{D})}\left(1 - b^i r^i\right) = 0 \tag{5.54d}$$

$$\mathcal{R}_{\lambda} = \Delta\lambda - \Delta t\,\phi_v(\mathcal{F}_y) = 0 \tag{5.54e}$$

$$\begin{aligned}\mathcal{R}_D = \Delta D - \Delta\lambda\left\langle\frac{Y_f - Y_{f_0}}{S_f}\right\rangle_+^{m_f} e^{\beta_f \eta_D \overline{D}} - \Delta t\left\langle\frac{\chi_c(\underset{\sim}{\sigma})}{S_c}\right\rangle_+^{m_c} e^{\beta_c \eta_D \overline{D}} \\ - (1-\overline{D})\frac{\Delta\lambda}{f^e(\overline{D})}\sqrt{\frac{3}{2}}\,\underset{\approx}{\tilde{n}} : \underset{\sim}{1} = 0\end{aligned} \tag{5.54f}$$

where the system eq. (5.54) needs to be linearized and solved by an iterative N-R process.

5.4.5.2 Local update of internal state variables

Not willing, for the sake of brevity, to describe the whole solving procedure at the (local) GP level in case of viscoplastic loading (*i.e.* when a correction for the internal variables is required), which is close to that for the local model, see sub-sect. 4.3.3, we restrict ourselves to the main algorithm given in Tab. 5.2.

5.4.5.3 Material sensitivities for the monolithic resolution scheme

In order to compute the global tangential stiffness matrix $\underline{\underline{K}}$ given by eq. (5.48), in the case of the present gradient-enhanced damage model, the consistent tangent matrix (composed of the material tangents, see eq. (5.51)) is required to be evaluated at each Gauss point. On the one

Inputs: Increment of gradient variables $\Delta\underset{\sim}{\varepsilon}$ and $\Delta\overline{D}$ at current time step t_{n+1}

Outputs: Updated flux variables $\underset{\sim}{\sigma}_{n+1}$, $\mathcal{V}_{n+1}$ and $\mathcal{V}_{int_{n+1}}$ at current time step t_{n+1}

1) elastic predictor with $\underset{\sim}{\sigma}^{tr}_{n+1}\left(\Delta\underset{\sim}{\varepsilon}, \Delta\overline{D}, \mathcal{V}_{int_n}\right)$ and $\overline{D}_{n+1} = \overline{D}_n + \Delta\overline{D}$

2) check yield criterion $\mathcal{F}^{tr}_y\left(\underset{\sim}{\sigma}^{tr}_{n+1}, \Delta\overline{D}, \mathcal{V}_{int_n}\right) > 0$?

no

update stress $\underset{\sim}{\sigma}_{n+1} = \underset{\sim}{\sigma}^{tr}_{n+1}$

compute the updated variables $\mathcal{V}_{int_{n+1}} \leftarrow \mathcal{V}_{int_n}$ and **go to** step 4)

yes

a) set initial values at $k = 0$: $\mathcal{V}^{(0)}_{int_{n+1}} = \mathcal{V}_{int_n}$

b) iterate over $k \in [0, ..., k_{max}]$

compute the residual equations $\mathcal{R}^{(k)}$, the Jacobian matrix $\mathcal{J}^{(k)}$

solve the linearized residual system $\delta\Delta\mathcal{V}^{(k+1)}_{int} = -\left[\mathcal{J}^{(k)}\right]^{-1}\mathcal{R}^{(k)}$

compute the updated variables $\Delta\mathcal{V}^{(k+1)}_{int} = \Delta\mathcal{V}^{(k)}_{int} + \delta\Delta\mathcal{V}^{(k+1)}_{int}$

check for convergence $\left\|\mathcal{R}^{(k)}\right\|_2 < \epsilon^{loc}_{tol}$?

yes $\Rightarrow$ **exit** loop

no $\Rightarrow$ $k \leftarrow k+1$ and **go to** step b)

c) extract variables' increment $\Delta\mathcal{V}_{int}$

3) update variables $\mathcal{V}_{int_{n+1}} \leftarrow \mathcal{V}_{int_n} + \Delta\mathcal{V}_{int}$ & $\underset{\sim}{\sigma}_{n+1}\left(\underset{\sim}{\sigma}^{tr}_{n+1}, \Delta\underset{\sim}{\varepsilon}, \Delta\overline{\mathcal{V}}, \Delta\mathcal{V}_{int}\right)$

4) compute the material tangents $\underset{\approx}{\mathcal{C}}_{uu}$, $\underset{\sim}{\mathcal{C}}_{u\overline{D}}$, $\underset{\sim}{\mathcal{C}}_{\overline{D}u}$, $\mathcal{C}_{\overline{DD}}$

exit

Table 5.2: Numerical integration procedure associated with the strain-driven problem applied to the non-local cyclic elastic-viscoplastic-damage model (local level).

hand, in case of gradient-enhanced elastic-damage model, these material tangents can be explicitly computed from the algorithmic update functions of $\underset{\sim}{\sigma}_{n+1}$ and $\underset{\sim}{\varepsilon}_{n+1}$.
On the other hand, for the gradient-enhanced elastic-viscoplastic-damage model, it is necessary to find out the total derivation of material residual equations. Practically, the material tangent operators can be obtained by linearizing the output of the material law $(\underset{\sim}{\sigma}, \mathcal{V})$ with respect to the input $(\underset{\sim}{\varepsilon}, \overline{\mathcal{V}})$.

Similarly to the case with the local material model, sub-sect. 4.3.5, the consistent tangent operators can be found in an "easy" way thanks to the implicit backward-Euler scheme used for the incremental resolution at the GP level. For the present non-local viscoplastic-damage model, the sets of degrees of freedom DOF, input variables $\mathcal{V}_{IN}$, output variables $\mathcal{V}_{OUT}$, integrated variables $\mathcal{V}_{int}$ and auxiliary variables $\mathcal{V}_{aux}$ for an enhanced FE (displacement-based + non-local variable) are given by:

$$DOF : \left\{\underline{u}, \overline{\mathcal{V}}\right\}; \qquad \mathcal{V}_{IN} : \left\{\underset{\sim}{\varepsilon}, \overline{\mathcal{V}}\right\}; \qquad \mathcal{V}_{OUT} : \left\{\underset{\sim}{\sigma}, \mathcal{V}\right\}; \tag{5.55a}$$

$$\mathcal{V}_{int} : \left\{ \underset{\sim}{\varepsilon}^{e}, \underset{\sim}{\alpha}^{k}, r^{i}, \lambda, D_{tot} \right\}; \qquad \mathcal{V}_{aux} : \left\{ \underset{\sim}{\varepsilon}^{in}, \underset{\sim}{X}^{k}, \underset{\sim}{Z}, R^{i}, p, Y \right\} \tag{5.55b}$$

where the residual system eq. (5.54) reads:

$$\left\{ \mathcal{R}\left(\Delta\mathcal{V}_{IN}, \Delta\mathcal{V}_{int}\right) \right\} = \left\{ 0 \right\} \tag{5.56}$$

Using the chain rule and tensorial calculus, the problem can be expressed in terms of the derivatives of the internal variables $\mathcal{V}_{int}$:

$$\left\{ \delta\mathcal{R} \right\} = \frac{\{\partial\mathcal{R}\}}{\{\partial\Delta\mathcal{V}_{IN}\}} \delta\Delta\mathcal{V}_{IN} + \frac{\{\partial\mathcal{R}\}}{\{\partial\Delta\mathcal{V}_{int}\}} \delta\Delta\mathcal{V}_{int} = \left\{ 0 \right\} \tag{5.57}$$

As previously described, the material residuals $\mathcal{R}$ are obtained by time integration with the implicit backward-Euler approach, see eq. (5.54). After transformation, the unknown material tangents can be calculated from the linear equation system:

$$\frac{\{\partial\mathcal{R}\}}{\{\partial\Delta\mathcal{V}_{int}\}} \frac{\{\partial\Delta\mathcal{V}_{int}\}}{\{\partial\Delta\mathcal{V}_{IN}\}} = -\frac{\{\partial\mathcal{R}\}}{\{\partial\Delta\mathcal{V}_{IN}\}} \tag{5.58}$$

As already done in the case of the local model, and for the sake of brevity, details for the derivation of each term of the previous matrices are given in the appendices, see Chap. I page 301.

5.4.6 Overall scheme of solving algorithm

By way of summary, the whole numerical procedure of solving the non-linear system of equations eq. (5.20) - eq. (5.25) is given in the present section. The global solution of the problem is the unknown field variables (DoF) $\underline{q}_{n+1}$ satisfying both the equilibrium problem and BC. Within one time step, the entire computational process consists in two levels of numerical computations, the global and the local levels. The global computation implies the solution of both the equilibrium and gradient equations which are obtained by spatial discretization with the FEM, see sub-sect. 5.4.3, and which is discretized in time thanks to an implicit Euler-backward scheme. The unknown increments of the field variables $\underline{u}$ and $\overline{\mathcal{V}}$ can be obtained from a linearized system of equations using the Newton-Raphson approach. The linearized system of equations consists of the consistent stiffness matrix $\underline{\underline{K}}$ and the residuals $\underline{R}$. The consistent tangential stiffness matrix, as indicated in sub-sect. 5.4.4 includes the material tangents. With the current solutions of the field variables, the associated internal state variables of the material $\mathcal{V}_{int}$ can be computed within a local iteration loop. The evolution equations related to material behavior are solved using an implicit backward-Euler scheme and the Newton-Raphson method in order to consider material non-linearities. The consistent stiffness matrix for the subsequent global iterations includes the updated material variables. The iterations within a time-step end as soon as the norms of both local and global residuals $\mathcal{R}$ and $\underline{R}$ fall below the stop criteria ϵ_{tol}^{loc} and ϵ_{tol}^{glob}, respectively.

The general scheme of solving algorithm is summarized in Tab. 5.3:

Inputs: number of global iteration steps $r \in [0, ..., r_{max}]$ and time steps $t_{n+1} = t_n + \Delta t$
and material tangents $\underset{\approx}{\underset{\approx}{C}}_{uu}$, $\underset{\approx}{C}_{u\overline{\mathcal{V}}}$, $\underset{\approx}{C}_{\overline{\mathcal{V}}u}$, $C_{\overline{\mathcal{V}}\overline{\mathcal{V}}}$

Outputs: nodal values $\underline{q}_{n+1}$ at current time step t_{n+1}

Loop over time increments

A) $t_{n+1} = t_n + \Delta t$

B) compute $\underline{f}_b$ and $\underline{t}^p$ from the input data and BC at $t_{n+1} = t_n + \Delta t$

Global level computations

initialize global iteration step $r = 0$

Loop over elements

1. compute $\Delta \underset{\approx}{\varepsilon} = \underline{\underline{B}}_u \Delta \underline{u}$ and $\nabla \overline{\mathcal{V}} = \underline{\underline{B}}_{\overline{\mathcal{V}}} \overline{\mathcal{V}}$ from the approx. of $\Delta \underline{u}$ and $\overline{\mathcal{V}}$

Local level computations

Loop over Gauss points

a) call for the constitutive law

b) update of internal variables with N-R iterative process, see Tab. 5.2

c) check for convergence criterion $\| \mathcal{R} \|_2 \leq \epsilon_{tol}^{loc}$

yes $\rightarrow$ **continue to** d)

no $\rightarrow$ **go to** b)

d) update stress $\underset{\approx}{\sigma}_{n+1}$, local variable $\mathcal{V}_{n+1}$ and internal variables $\mathcal{V}_{int_{n+1}}$

e) compute material tangents $\underset{\approx}{\underset{\approx}{C}}_{uu}$, $\underset{\approx}{C}_{u\overline{\mathcal{V}}}$, $\underset{\approx}{C}_{\overline{\mathcal{V}}u}$, $C_{\overline{\mathcal{V}}\overline{\mathcal{V}}}$

exit

2. compute reactions $\underline{F}^{(r)} = \left[\underline{F}_{u,\,int} - \underline{F}_{u,\,ext},\ \underline{F}_{\overline{\mathcal{V}},\,int} - \underline{F}_{\overline{\mathcal{V}},\,ext} \right]^T$
3. compute residuals $\underline{R}^{(r)} = \left[\underline{R}_u,\ \underline{R}_{\overline{\mathcal{V}}} \right]^T$
4. check for convergence criterion $\| \underline{R}^{(r)} \|_2 \leq \epsilon_{tol}^{glob}$

yes

$\underline{q}_{n+1} = \underline{q}_{n+1}^{(r)}$, $\underline{\underline{K}}_{n+1} = \underline{\underline{K}}^{(r)}$, $\underline{R}_{n+1} = \underline{R}^{(r)}$

$\underset{\approx}{\sigma}_n \leftarrow \underset{\approx}{\sigma}_{n+1}$ $\mathcal{V}_{int_n} \leftarrow \mathcal{V}_{int_{n+1}}$ $\mathcal{V}_n \leftarrow \mathcal{V}_{n+1}$ $\underline{u}^{(r)} \leftarrow \underline{u}^{(r)} + \Delta \underline{u}^{(r)}$

$t_n \leftarrow t_n + \Delta t$ and **go to** B)

no

compute consistent stiffness matrix $\underline{\underline{K}}^{(r)}$ at the rth iteration step

solve the system of equations $\underline{\underline{K}}^{(r)} \delta \Delta \underline{q}^{(r+1)} = -\underline{R}^{(r)}$

update nodal values $\Delta \underline{q}_{n+1}^{(r+1)} = \Delta \underline{q}_{n+1}^{(r)} + \delta \Delta \underline{q}_{n+1}^{(r+1)}$

update global iteration $r = r + 1$ and **go to** 1.

exit

exit

Table 5.3: General flowchart of the solving algorithm for the non-linear coupled problem using the FEM.

5.5 Validation of the non-local model implementation

5.5.1 On a single element

In order to valide the numerical implementation of the non-local model, a simple tension-compression test on a single element has been simulated, see Fig. 5.2. The resulting stress-strain curves are given in Fig. 5.3a while the local damage growth is reported in Fig. 5.3b.
One can see in Fig. 5.3 that the numerical implementation of the gradient-enhanced damage model ensures a good convergence towards the limit case of vanishing length-scale $\ell_c \to 0\,\text{mm}$ (*i.e.* when the non-local model degenerates into a local one). Moreover, due to the strong coupling between damage and elastic-viscoplastic constitutive equations, as long as damage increases, the stiffnesses decrease hence leading to a stress-softening cyclic response, see Fig. 5.3a.

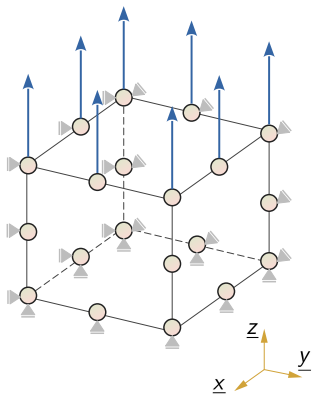

Figure 5.2: Uniaxial tension-compression test on an under-integrated non-local c3d20r FE.

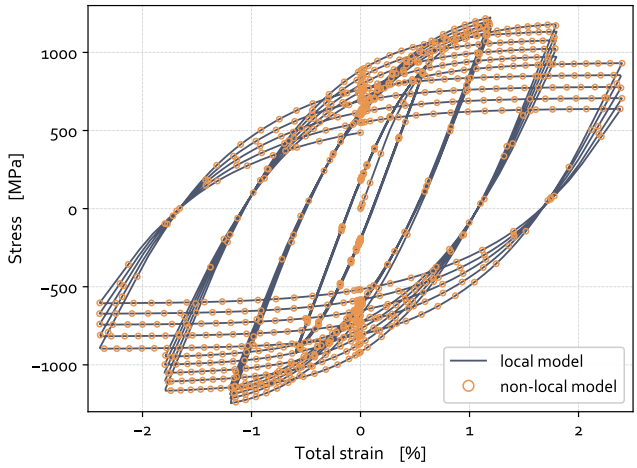

(a) Stress-strain loops.

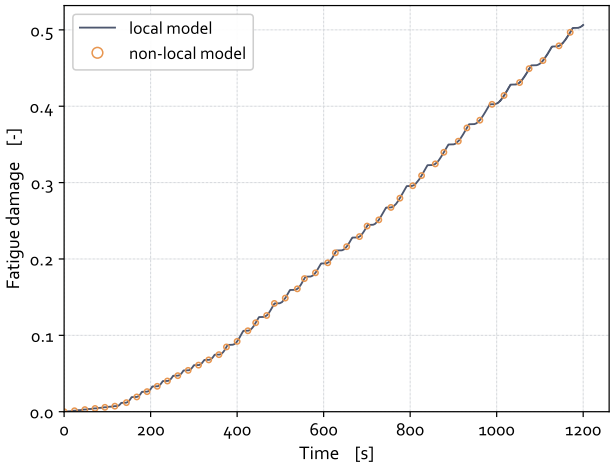

(b) Time - fatigue damage.

Figure 5.3: Validation of the FE implementation over RVE simulations: comparison between local and non-local damage model ($\ell_c = 0\,\text{mm}$) using an implicit time-integration scheme within the *Z-set* solver.

5.5.2 2D structural cases under monotonic loading

In this sub-section, the purpose is to assess the capability of the non-local enhancement of the damage model to cope with mesh-dependency and volumetric locking issues in 2D structural calculations. To this end, two examples will be considered using the 4-fields mixed non-local FE, see Fig. 1.17a, which is described in the sect. 1.6. In the present work, since an implicit

gradient formulation has been considered for the non-local extension, use is made of quadratic elements [Peerlings et al., 1996b], [Simone et al., 2004].
As only monotonic tests will be considered, the fatigue damage parameters will be adjusted in order to evidence a quasi-ductile behavior in structural calculations. Related parameters are reported in Chap. H.

5.5.2.1 Shear-dominated loading case 1: double-notched specimen

The double-notched specimen studied in the previous chapter considering the local damage model, see sub-sect. 4.4.2, is again investigated. The prescribed loading rate of $\dot{u}_y = 10^{-2}\,\text{mm.s}^{-1}$ is imposed at the top and left edges of the specimen in the y-direction, see Fig. 4.17. The lower and right edges are fixed. Three different mesh sizes are considered in the following calculations: $h_{e_i} \in [0.3,\, 0.2,\, 0.1]$ mm. The internal length is taken as $\ell_c = 0.4\,\text{mm}$ while material parameters are reported in the appendices, see Tab. H.2 page 299.

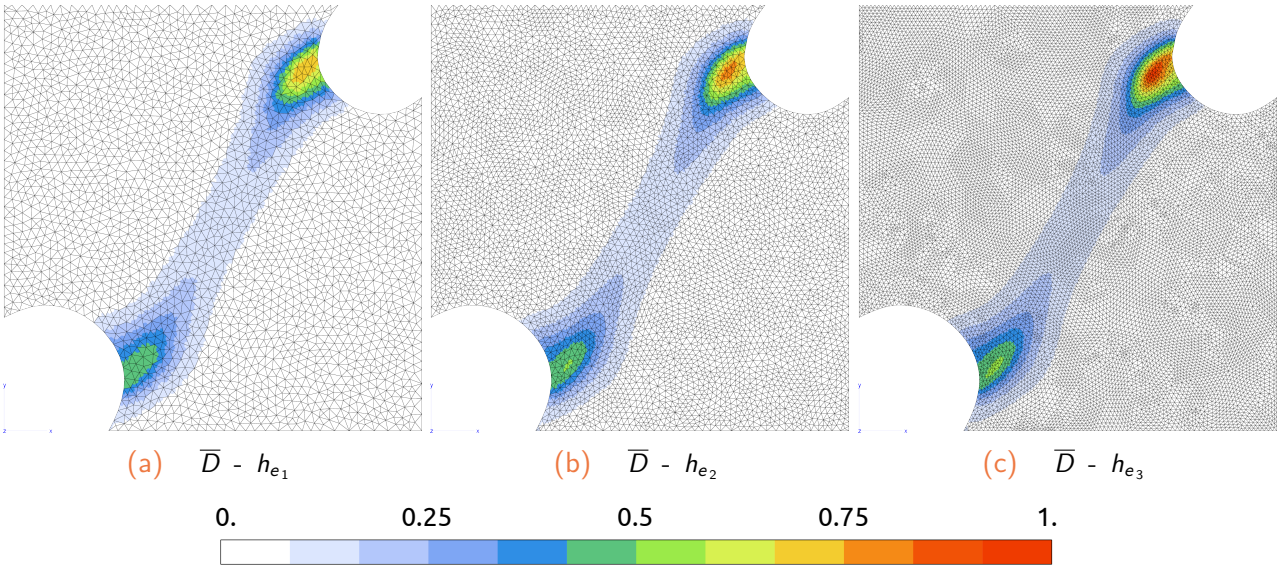

Figure 5.4: Non-local damage field for the double-notched specimen (4-fields FE, deformed state, mag. factor $\times 1.$) at $u = 0.1689\,\text{mm}$ for the three mesh sizes: $h_e = 0.3,\, 0.2,\, 0.1\,\text{mm}$.

In Fig. 5.4a to Fig. 5.4c, the non-local damage is plotted. One can see that the regularization process ensures a control of the width of the localization band thanks to the internal length ℓ_c. The results are given at the same simulation time, but some small variations can be noticed in the upper notch where damage process is predominant. Since shortly before the crack initiation process the local damage increases significantly, the finer the spatial discretization, the greater the non-local damage field, see Fig. 5.4c.

Looking at the macroscopic curves, Fig. 5.5, one can notice that results are nearly similar. Moreover, mesh convergence seems verified since the progressive mesh refinement results in closer curves, see Fig. 5.5b. The slight differences observed in Fig. 5.5b are induced by the classical influence of the mesh discretization on the FE results. Globally, the non-local formulation seems to be able to solve for the mesh-dependence in FE calculations.

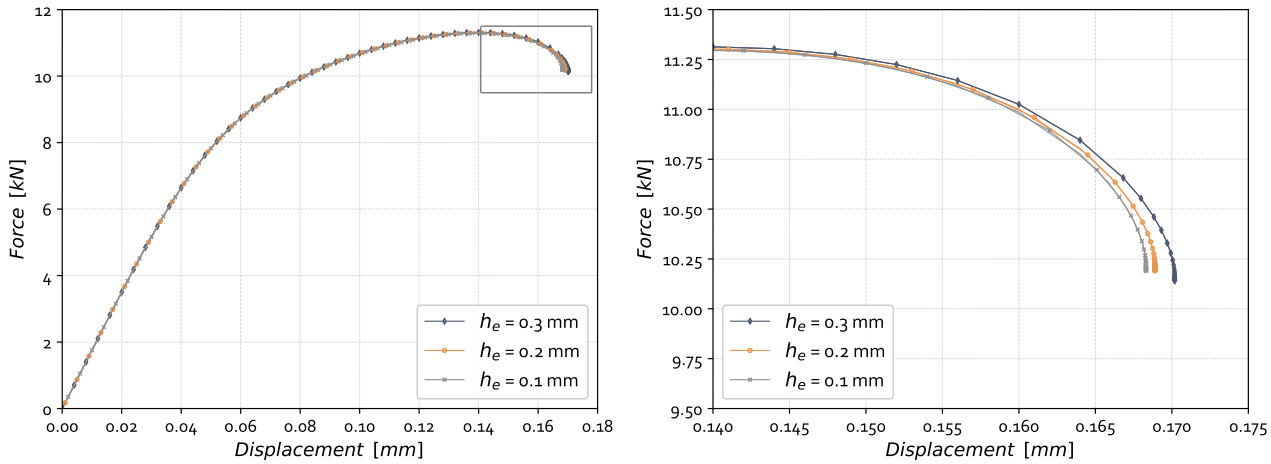

(a) Effect of the mesh size on the mechanical response. (b) Close-up view on the stress-softening phase.

Figure 5.5: Comparison of the force-displacement curves for the double-notched specimen. Effect of the mesh size on the overall mechanical response.

5.5.2.2 Shear-dominated loading case 2: 2-holes specimen

Lastly, a rectangular specimen with two holes inspired by the work of [Broumand and Khoei, 2015] is studied. It is fixed at the bottom edge and subjected to a prescribed displacement at the top edge. The geometry and associated BC are given in Fig. 5.6. The calculation is performed under the plane strain assumption. The considered material is AD730™ with the parameters given in Tab. H.2. The characteristic length ℓ_c is equal to 0.9 mm.

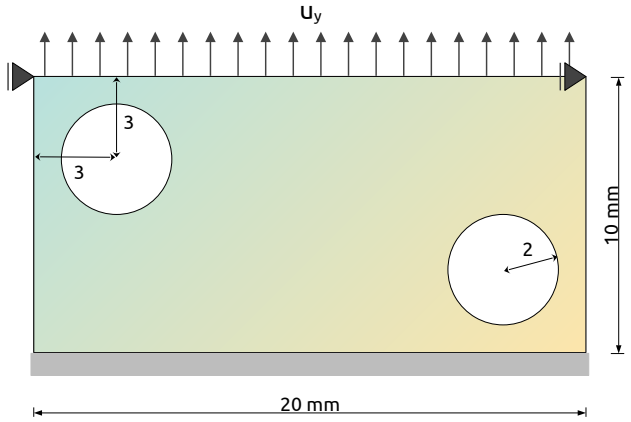

Figure 5.6: Geometry of the rectangular specimen with two holes specimen subjected to tensile loading with corresponding dimensions and associated BC (after [Broumand and Khoei, 2015]).

In Fig. 5.7, the non-local damage distribution is reported. Considering three different mesh sizes, namely $h_e = 0.45$, 0.36 and 0.18 mm, one can observe the nearly-similar non-local damage field distributions. The width of the localization band is almost the same in each case, demonstrating the ability of the non-local regularization procedure to solve the mesh-dependency problem.

One can notice in Fig. 5.8a the mesh-convergence of the numerical results. Indeed, for different spatial discretizations, the resulting mechanical response is nearly the same.

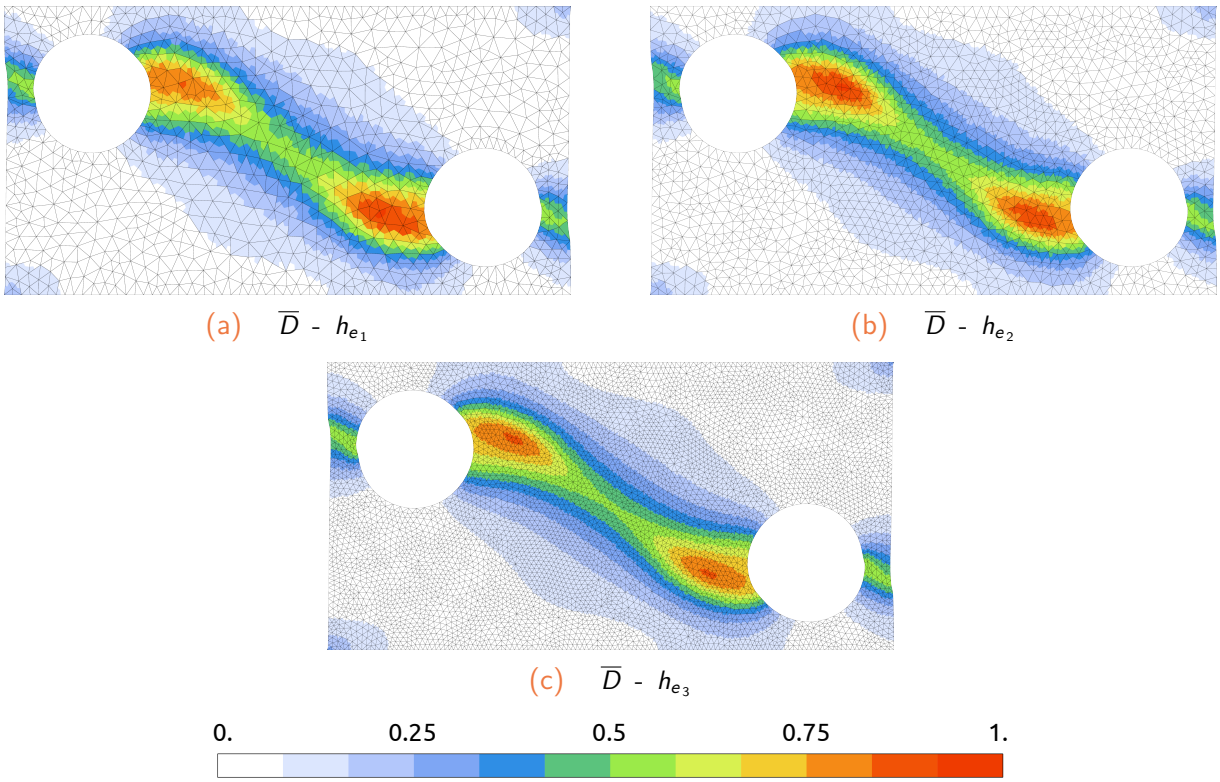

Figure 5.7: Non-local damage field for the plane-strain rectangular specimen with two holes (4-fields FE, deformed state, mag. factor $\times 0.5$) at $u = 0.3455$ mm for the three mesh sizes: $h_e = 0.45,\ 0.36,\ 0.18$ mm.

According to the Fig. 5.8b, one can see that the regularization parameter ℓ_c has a great influence on the overall mechanical responses. Moreover, the higher the regularization parameter, the higher the macroscopic ductility of the material. Indeed, as long as ℓ_c increases, the non-local interaction is extended, hence resulting in a larger localization band-width and a slower damaging process. In this case, the material response is more ductile with a delayed crack initiation step.

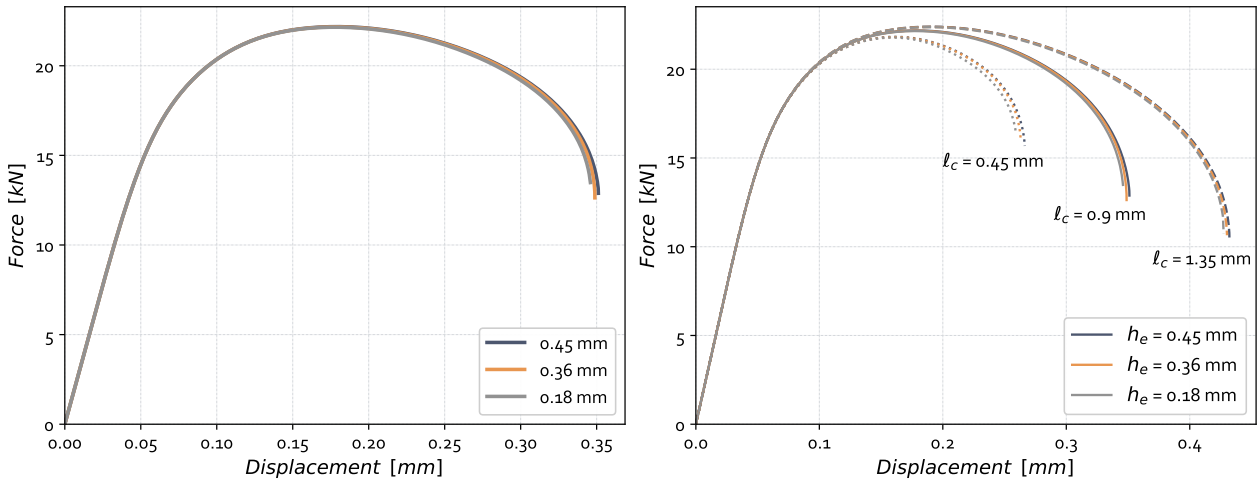

(a) Effect of the mesh size h_e on the mechanical response.

(b) Effect of the characteristic length ℓ_c on the mechanical response.

Figure 5.8: Comparison of the force-displacement curves for the rectangular plate with two holes. Effect of both the mesh size and the characteristic length on the overall mechanical response.

5.5.3 2D Single Edge Notched specimen under cyclic loading conditions

The aim of this sub-section is to validate the non-local model under cyclic loading conditions. This can be done while analyzing the evolution of some mechanical fields close to the crack-tip and along the crack path upon cycling. Thus, focus is put here on pure fatigue conditions. A sinusoidal stress-controlled loading scheme has been applied to a SEN-T specimen with a current crack length of $\sim 2\,\text{mm}$ (which corresponds to $\Delta K = 36.8\,\text{MPa}\sqrt{m}$). The specimen dimensions and associated boundary conditions are depicted in Fig. 5.9a, while the prescribed loading signal is given in Fig. 5.9b. The specimen is modeled with plane strain conditions. The simulations are run with material parameters calibrated for AD730™ at 550°C, see Tab. D.1, with 4-fields FE.

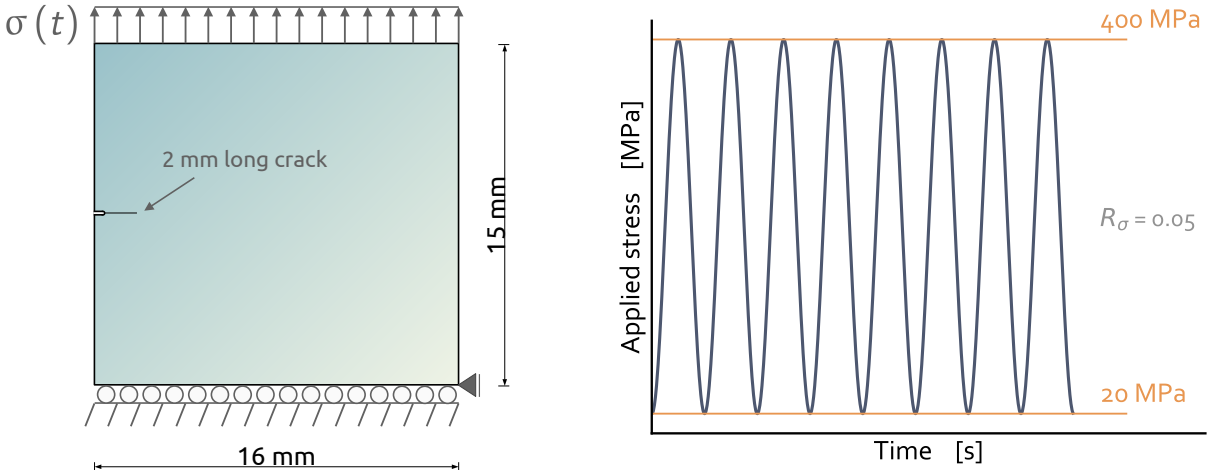

(a) Prescribed boundary conditions. (b) Test loading signal (stress- or displacement-controlled).

Figure 5.9: Schematic representation of the SEN-T specimen and corresponding periodic loading signal.

5.5.3.1 Analysis of the mechanical fields at the crack-tip

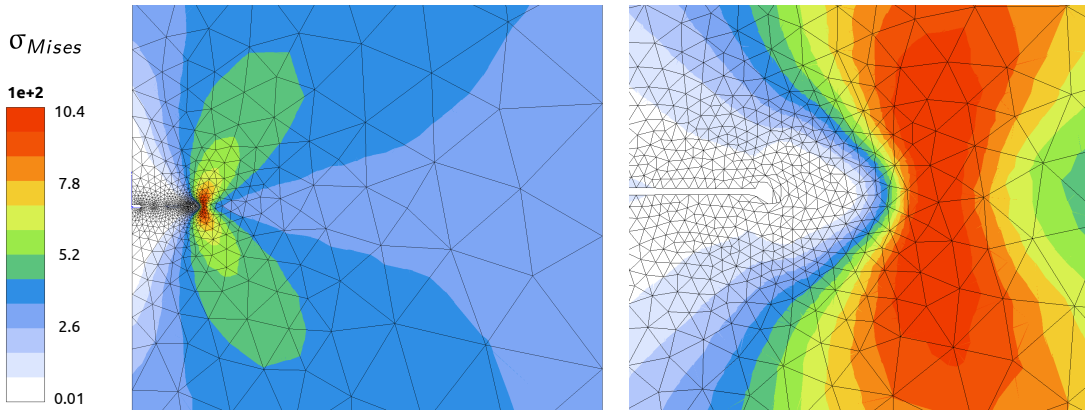

(a) σ_{Mises} at max. load. (b) σ_{Mises} at max. load (close-up view).

Figure 5.10: Distribution of the Von Mises stress at maximum load (c2d6r 4-fields FE - view at contours).

In Fig. 5.10a, the Von Mises stress field is plotted at the maximum load, with a close-up view on the crack-tip stress zone in Fig. 5.10b. As we get closer to the crack-tip, the effect of damage

on the stress fields leads to a vanishing Von Mises stress. This means that ahead of the crack-tip there is no more material resistance and a crack can be inserted since there is no more energy to dissipate (the methodology will be explained in the next Chap. 6).
In the same manner as for the Cauchy stress, the back-stress, which is also fully coupled to damage, vanishes in the fully damaged elements, see Fig. 5.11a and Fig. 5.11b.

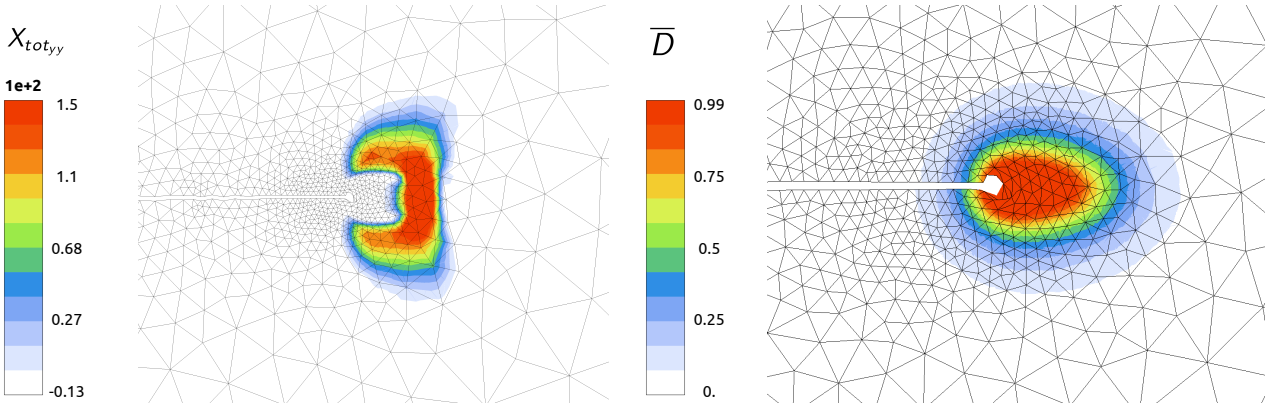

(a) $X_{tot_{22}}$ at max. load (close-up view). (b) $\overline{D}$ at max. load (close-up view).

Figure 5.11: Distribution of the total back-stress $X_{tot_{22}}$ and the non-local damage $\overline{D}$ at maximum load (c2d6r 4-fields FE - view at contours).

One can observe that the localization band is spread over several elements, which indicates an effective regularization. Let us note that the elements at the crack-tip are excessively distorted due to their degraded stiffnesses, see Fig. 5.11b, in close relation with the strong coupling between damage and both elasticity and strain-hardenings. It can be noted that distorted elements may prevent to achieve the local convergence and consequently may lead to numerical issues. Dealing with these highly distorted elements will be achieved thanks to remeshing procedures introduced in Chap. 6.

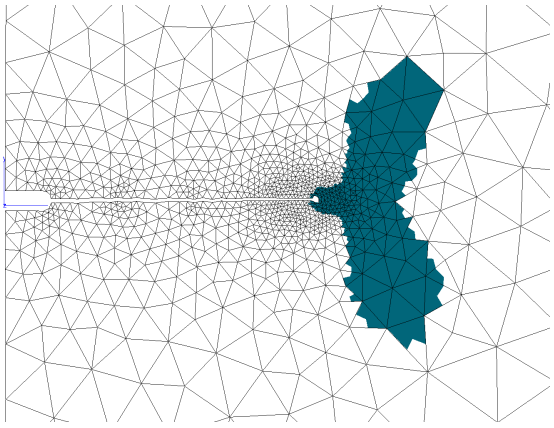

Figure 5.12: Viscoplastic activity at max. load.

Elements exhibiting a non-linear viscoplastic response upon loading are reported in Fig. 5.12 with a dark blue color, while those with a linear elastic behavior remain uncolored. One can observe a typical "butterfly shape" for the viscoplastic zone, as expected to occur for plane strain conditions [Zhao et al., 2020].

5.5.3.2 Local evolution at integration points

An advantage of this local approach to fracture is the possibility to analyze local fields at the scale of the integration points. The evolution of certain mechanical fields at some specific integration points (IP) will be analyzed as a function of time. Along the crack ligament (where the crack is assumed to propagate), 5 integration points have been considered in elements located at various distances from the crack-tip, see Fig. 5.13, namely IP_1 at 0.01 mm, IP_2 at 0.12 mm, IP_3 at 0.25 mm, IP_4 at 0.62 mm and IP_5 at 1.32 mm. In Fig. 5.13b, the selected elements from which one single Gauss point is studied are highlighted in blue.

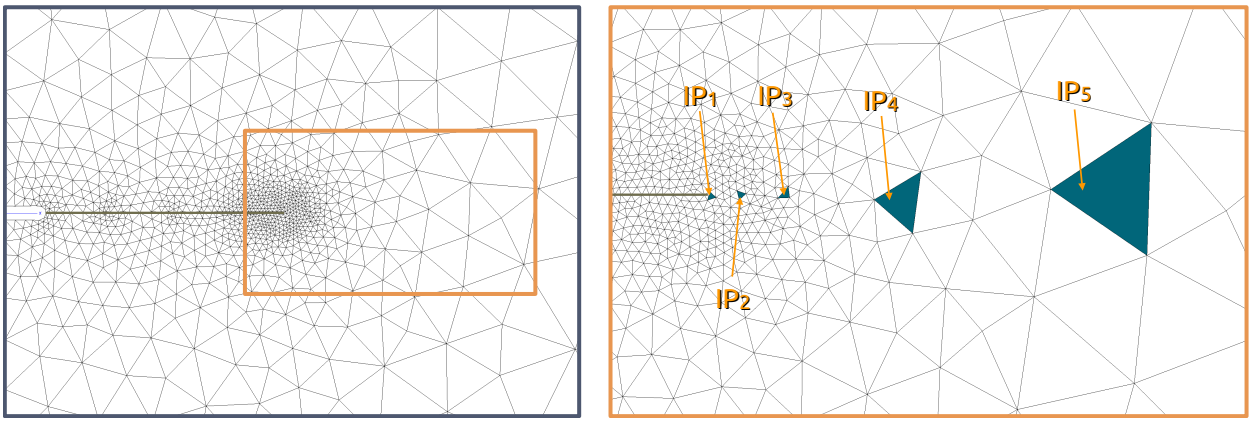

(a) 2 mm pre-cracked SEN-T specimen. (b) Close-up view on the selected FE for GP analyzes.

Figure 5.13: Mesh of the 2 mm pre-cracked SEN-T specimen and corresponding selection of integration points on the crack path ligament.

Crack-tip far-fields:

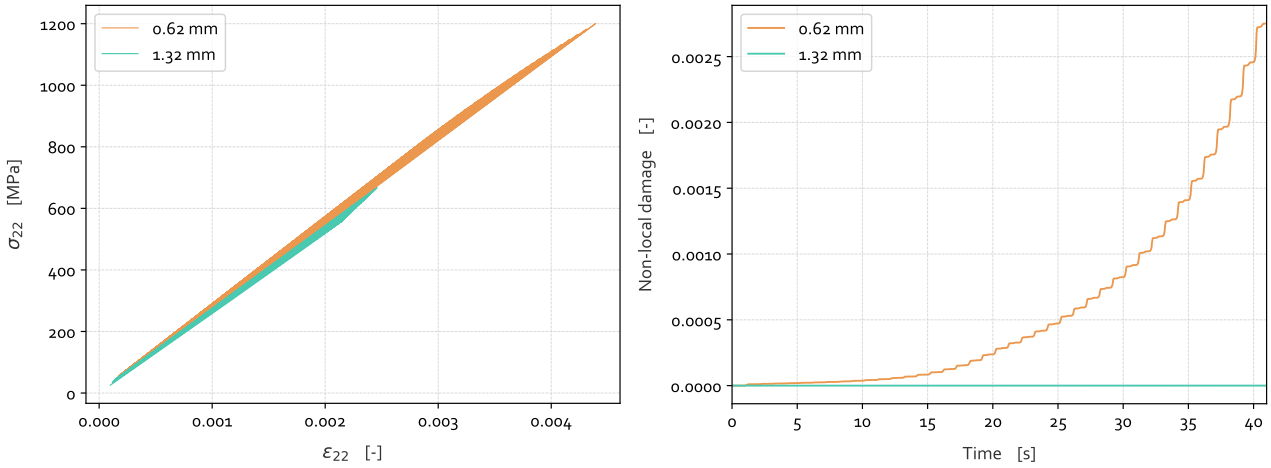

(a) Stress-strain curves at IP 4 & 5. (b) Non-local damage at IP 4 & 5.

Figure 5.14: Stress-strain curves and evolution of the non-local damage far from the crack-tip for IP_4 (0.62 mm) & IP_5 (1.32 mm) (c2d6r 4-fields FE).

Paying attention to IP_4 & IP_5, far from the crack-tip (see Fig. 5.13b), the material behavior is assumed to be linear elastic with no clear cyclic hysteresis: see Fig. 5.14a. The corresponding

non-local damage at these IP is null or extremely low, see Fig. 5.14b, since there is no source term (*i.e.* no local damage) for the non-local damage to be calculated.

Crack-tip close-fields:

IP_1, IP_2 & IP_3 are located close to the crack-tip, in the FPZ, Fig. 5.13b. Consequently, mechanical fields in these zones are expected to be non-linear with both viscoplasticity and damage. For each IP, the mechanical response exhibits more or less open hysteresis viscoplastic loops, see Fig. 5.15. The high stress level obtained at IP_1 is induced by an important over-stress. Indeed, since the viscoplastic strain rate at the very close vicinity of the crack-tip is extremely high, the resulting estimated over-stress is high. A saturation effect of the viscosity function could be a precondition for the over-stress to be well limited for high strain rates. Nevertheless, the fast increase in damage at crack-tip easily counterbalances such an effect by making the stress to drop due to the damage effect on the stiffness.

One can also remark that the stress-plastic strain curves are non-symmetric w.r.t. strain, hence exhibiting cyclic ratcheting effects, that is the accumulation of strain with increasing loading cycles. Another point to be noticed is the progressive decrease of the stress level induced by the damage evolution with increasing loading cycles. For IP_1 and IP_2, the stress drop is almost complete while for IP_3 the damage is not high enough to cause a vanishing stress state yet (blue curve in Fig. 5.15b).

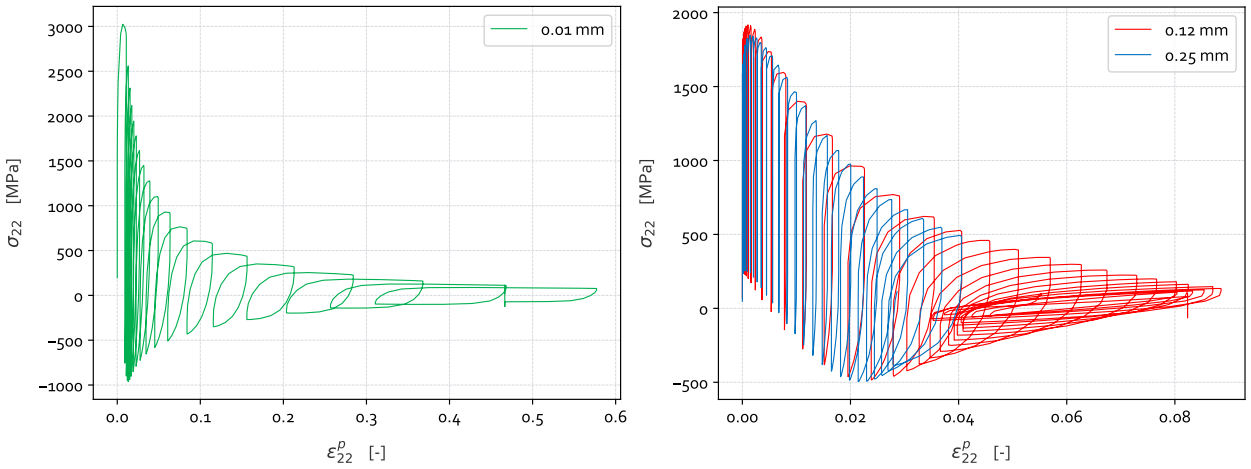

(a) Stress-plastic strain curves at IP 1.

(b) Stress-plastic strain curves at IP 2 & 3.

Figure 5.15: Stress-plastic strain curves close to the crack-tip for IP_1 (0.01 mm), IP_2 (0.12 mm) & IP_3 (0.25 mm) (c2d6r 4-fields FE).

The evolution of the accumulated viscoplastic strain is reported in Fig. 5.16a. As expected, viscoplasticity is more pronounced as the IP is located close to the crack-tip. Moreover, once the broken state is reached in the IP, the variable is forced to remain constant (so as for the viscoplastic multiplier) in order to avoid any excessive accumulation of strain in elements that no longer contribute to the rigidity of the structure.
The evolution of the non-local damage is reported in Fig. 5.16b. A fast increase is noticeable in IP_1 with a steady-state value once the broken state is reached. As evidenced, the non-local damage evolution is, in the present case, unbounded.

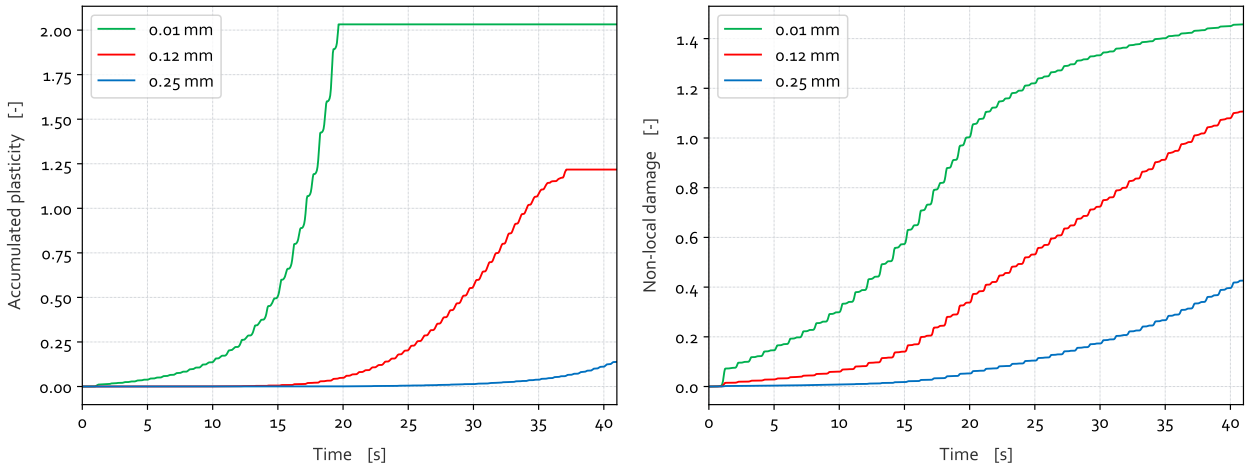

(a) Accumulated viscoplasticity at IP 1, 2 & 3. (b) Non-local damage at IP 1, 2 & 3.

Figure 5.16: Evolution of the accumulated viscoplastic strain and non-local damage close to the crack-tip for IP_1 (0.01 mm), IP_2 (0.12 mm) & IP_3 (0.25 mm) (c2d6r 4-fields FE).

The temporal evolution of both the Cauchy stress and the kinematic hardening are given in Fig. 5.17a and Fig. 5.17b, respectively. One can notice the progressive decrease of these components as time (or non-local damage) increases. The strong coupling between the constitutive equations and damage induces a progressive decrease until a complete cancellation of mechanical fields when (non-local) damage has reached a sufficiently high value, $\overline{D}^{crit}$.

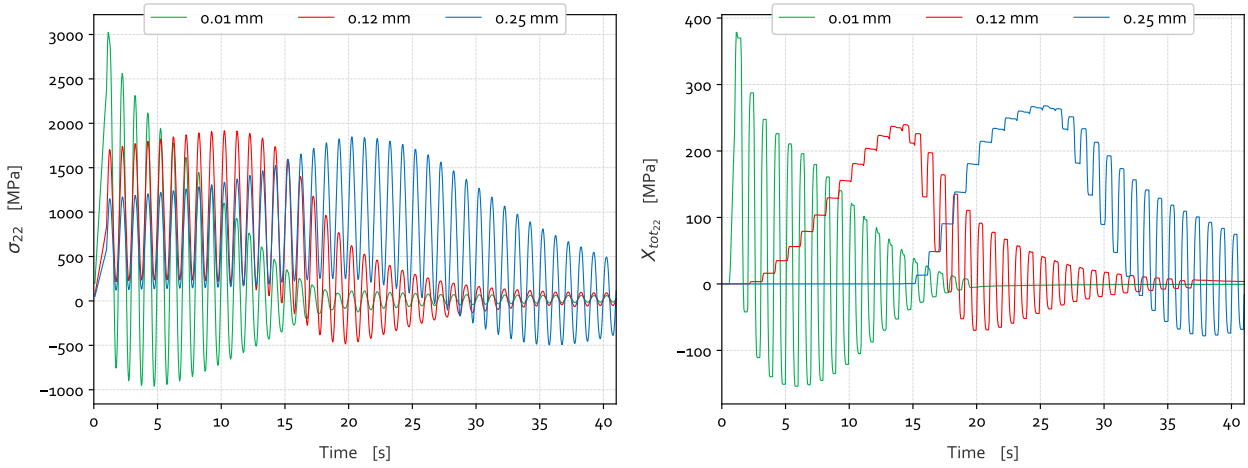

(a) Stress w.r.t. time at IP 1, 2 & 3. (b) Back-stress w.r.t. time at IP 1, 2 & 3.

Figure 5.17: Temporal evolution of both Cauchy stress and total back-stress close to the crack-tip (c2d6r 4-fields FE).

5.6 Conclusion of the chapter

Since the local cyclic multi-mechanism damage model developed in the Chap. 4 suffers from spurious mesh-dependency (see sub-sect. 4.4.2), a non-local extension of the model with an implicit gradient formulation has been proposed. Such a regularization technique has proven to be efficient since the resolution of a diffusion equation is relatively fast and the value of the introduced characteristic length does not influence the resolution time. As far as the constitutive equations are concerned, the non-locality has been achieved by exchanging in every equation of the model the local total damage variable D by its non-local counterpart $\overline{D}$. All the other equations of the non-local gradient-enhanced damage model remain unchanged compared to the local one.

The non-local model has been implemented within the general purposes Z-set FE solver, Both the global and local solving schemes have been detailed. Implicit resolution procedure has been considered for the global equilibrium problem. Meanwhile, the local resolution of the constitutive relations at the Gauss point level has been achieved thanks to a fully implicit backward-Euler algorithm associated with an elastic trial / local update procedure for the internal state variables. Several numerical tests of increasing complexity have illustrated the ability of this non-local formulation to efficiently control damage localization and subsequently to ensure convergence of the numerical results upon mesh refinement. In particular, local mechanical fields have been analyzed in a SEN-T specimen subjected to pure fatigue loading. The damage-induced stress softening response has been exhibited, as well with the spatial averaging of the damage field through the implicit gradient formulation.

As a conclusion, the proposed damage model is able to efficiently predict damage growth and resulting stress-softening response due to micro-cracking up to the onset of fracture in 2D structural calculations, both under monotonic and cyclic loading conditions.
But, even if the fully damaged elements in the FPZ allow to roughly estimate the crack path, they do not enable to properly represent the kinetics of the crack advance. Besides, the presence of distorted elements can deteriorate the accuracy of the computation. The continuous description of the fracture process has thus reached its limitations and a discrete representation of the crack is required in order to describe entirely the whole fracture process.
The insertion of a real discontinuity in the spatial discretization of the structure to represent the crack advance is finally another option that is discussed in the following Chap. 6.

Let us note that the proper calibration with experimental results for the considered material would be necessary in order to be able to draw accurate comparisons between numerical simulations and experimental results. In particular, a microstructure-related internal length scale would be necessary in order to give a better physical meaning to this non-local modeling approach. Both the proper calibration of the damage model and the experimental estimation of the characteristic length represent major outlooks for the present work.

Résumé du chapitre en français

Le modèle d'endommagement cyclique local développé au Chap. 4 a montré une sensibilité à la dépendance en maillage, entraînant la non-convergence des résultats numériques. Afin de résoudre ce problème, une approche non-locale a été proposée qui introduit une longueur interne dans les équations du problème. Après un tour d'horizon des méthodes employées pour régulariser les problèmes d'endommagement couplé en fatigue et fluage, il est apparu que la technique la plus appropriée dans le cas présent est la méthode à gradient implicite. Il s'agit alors de résoudre de manière simultanée l'équilibre de la structure et une équation de diffusion reliant la variables non-locale à son pendant non-local. Dans ce contexte, le choix d'une seule variable régularisée a été fait de sorte à limiter les temps de calculs et les couplages associés dans le modèle d'endommagement cyclique. Une seule longueur interne a donc été considérée, utilisée ici comme paramètre numérique pour contrôler la largeur de la bande de localisation. Ainsi, la régularisation de la variable d'endommagement total a été favorisée (par rapport à la plasticité cumulée), offrant alors la possibilité de rendre non-locaux tous les mécanismes d'endommagement (fatigue, fluage, volumique) de manière unifiée. De plus, ce choix a permis de ne pas impacter le comportement cyclique du matériau déjà calibré et ainsi laisser indépendants les mécanismes d'adoucissement régis par la plasticité cyclique (écrouissages isotropes négatifs) et ceux en lien avec l'endommagement. Le couplage fort comportement-endommagement nécessite l'introduction de l'endommagement non-local dans les lois d'évolution de chaque variable interne du problème.

Le modèle non-local proposé dans ce chapitre a été intégré dans la suite Z-set à l'aide d'une loi utilisateur dédiée. L'utilisation d'un élément fini multi-champs (déplacement et variable non-locale) permet la résolution monolithique du problème couplé. Un schéma de résolution implicite a été utilisé pour résoudre l'équilibre global et l'équation non-locale. Au niveau des points d'intégration, la loi de comportement est intégrée en temps suivant un schéma d'Euler implicite (θ-méthode), ce qui permet de réaliser des pas de temps relativement grands tout en conservant une bonne stabilité du solveur. Le calcul des termes des matrices tangentes consistantes avec le schéma de résolution temporel a été détaillé.

Enfin, des calculs sur un élément fini et sur structures 2D ont été réalisés de sorte à vérifier l'implémentation du modèle et sa capacité à régler la dépendance au maillage. Les courbes macroscopiques et les iso-valeurs des champs montrent la capacité de l'approche à permettre la convergence en maillage.
Les calculs structuraux en fatigue ont finalement montré les limites de l'approche continue qui doit alors être complétée d'une représentation discrète de la fissure afin de bien représenter la cinétique de croissance de fissure et éviter la distorsion des éléments endommagés.

6 A damage to fracture transition for fatigue crack growth prediction

Using the proposed cyclic non-local damage model, the width of the localization band, where non-linear phenomena occur, can be controlled thanks to the internal length scale parameter. Such a localization band is of primary importance and a sufficiently fine discretization is required. This implies either meshing finely the area covered by the crack (the fracture process zone and its wake) all along its growth (but it supposes that the crack path is a priori known). In this work, we favored using adaptive remeshing techniques based on error indication. Then, the calculation can be conducted up to the onset of failure. This step is performed in a continuous manner thanks to the gradient extended damage model. Once crack initiation is achieved at the crack-tip, crack could grow. Thus, a continuous-to-discontinuous transition must be performed to model the real crack and to capture the kinetics of the crack advance. In the present work, such a damage-to-fracture transition is achieved using successive remeshing steps to allow the crack to propagate thanks to discrete crack increments insertion within a damage-induced softening material. In order to predict the crack increment orientation from damage distribution, a dedicated crack path tracking algorithm is used, namely the Marching Ridges algorithm. Besides, at each remeshing step, the mesh size in the fracture process zone close to the crack-tip is refined using an error-based mesh adaption strategy in order to achieve accurate numerical simulations. Once the new mesh is created, fields are transferred from the old mesh to the new one and a re-equilibrium procedure is performed before the next load increment.

The aim of this chapter is to detail the different elements required for the continuous-discontinuous approach (see sect. 6.1 to sect. 6.3) and to evaluate the ability of this approach, when combined with the non-local damage model, to capture crack propagation under cyclic fatigue loading conditions (see sect. 6.3). The sensitivity of the model to both the prescribed loading conditions and material parameters are assessed. Finally, the overall capabilities of the present cyclic damage model will be discussed as well with suggestions for further works.

Contents

6.1 Mesh adaption strategy

6.1.1 Interest of h-remeshing

Keeping in mind that the present work relies on the previous developments from [Feld-Payet, 2010] and [Chiaruttini et al., 2010], choice is made to consider a **global h-remeshing** procedure for the optimization of the mesh topology (see [Ladevèze and Pelle, 2005] for details). Such a method has been proved to be the most efficient one (compared to p- or r-adaptivity strategies), particularly when a singularity exists within the mesh and when the total number of elements in the mesh must be decreased [Babuška et al., 1983], [Díez and Huerta, 1999]. Moreover, global h-remeshing can be easily used thanks to the recent development of numerous robust 2D automatic mesh generators [George, 1991].

Mesh refinement around the crack-tip enables the possibility to keep a good precision in the vicinity of the crack [Bouchard et al., 2003]. While it is fairly easy to model the fracture process whose final pattern is *a priori* known by using an appropriately pre-refined mesh, using fixed uniform mesh would generally lead to too high computational cost. In the present work, since the crack path is unknown, it is beneficial to rely on mesh adaption methods so that to get a refined mesh in the region of interest (ROI), *i.e.* the FPZ, and a coarse one in the zones where non-linearities are

non-existent (*i.e.* elastic or fully damaged zones). As the crack-tip moves along during the loading process, the areas which need to be refined will change. Thus, a new mesh is created and refined only in the areas where it is needed in order to save calculation time [Bouchard et al., 2000]. In fracture modeling problems, more particularly, due to the localized material deterioration in the damaged zones, many elements will be severely distorted producing unacceptably inaccurate solutions, hence making a mesh optimization strategy necessary.

Applications of mesh adaption methods to ductile fracture prediction can be found in, *e.g.* [Mediavilla et al., 2006b], [Feld-Payet, 2010], [El Khaoulani and Bouchard, 2012]. However, to the author's knowledge, applications to cyclic loading conditions – with a non-linear material behavior fully coupled to damage – have not been published. This represents a challenging point for the present Ph.D. project.

The mesh adaption process can be either driven by a criterion based on physical phenomena (see *e.g.* [Andrade Pires et al., 2004], [El Khaoulani and Bouchard, 2012]), or by the reduction of an error (see [Ladevèze and Pelle, 2005]). In this last case, an error indicator estimates the error between the (unknown) exact solution and the solution provided by the solver. A new mesh is then generated in order to reduce the error to an acceptable level. Error-based mesh adaption methods are quite popular as they allow to perform calculations with a predefined numerical accuracy at optimized computational cost [Boussetta et al., 2006], [Zhang et al., 2012].

In the present study, for mesh adaption purposes, I have retained an error-based approach. Such an *a posteriori* error estimator relies on the lack of regularity of the FE solution. It assumes that a smoother estimation of the FE solution should be a better approximation of the exact solution and uses it to provide an error estimation. Different fields can be considered to evaluate the error [Zienkiewicz et al., 1999], [Boroomand and Zienkiewicz, 1999].

6.1.2 Error-estimation

6.1.2.1 ZZ2 error indicator

The recovery-based error indicators have proven to be widely used, especially for linear [Zienkiewicz and Zhu, 1987] and non-linear [Boroomand and Zienkiewicz, 1999] 2D problems, as well as for 3D elastic [Boussetta and Fourment, 2003] and viscoplastic [Boussetta and Fourment, 2004] problems. The comparative study of [Ladevèze and Rougeot, 1997] evidences the fact the recovery-based error estimator is a good compromise between efficiency and computational cost. The *ZZ2* error estimator [Zienkiewicz and Zhu, 1992] is said to be robust as admitting an asymptotically accuracy [Babuška et al., 1994], but it may suffer from lack of accuracy close to the boundaries. Although recovery-based estimates only give a magnitude of the error, the latter is preferable in this context as an exact error estimation would be too costly for a mesh adaption strategy [Feld-Payet, 2010]. This *a posteriori* error estimator relies on the lack of regularity of the FE solution. It assumes that a smoother estimation of the FE solution should be a better approximation of the exact one and uses it to provide an error estimation. Different fields can be considered for error evaluation [Zienkiewicz et al., 1999], [Boroomand and Zienkiewicz, 1999].

6.1.2.2 Choice of the underlying variable(s)

In order to save computational time, it is interesting to consider a scalar variable as the support for the error estimation. The choice for the underlying variable [1] must endorse a particular relevance associated with the studied mechanisms. As the damage variable governs the crack initiation and crack growth processes, in my analysis, the error estimation will be based on this variable [Moslemi and Khoei, 2010].

6.1.2.3 Error definition

Since all the damage mechanisms are embedded in the same scalar variable, choice for the non-local total damage $\overline{D}$ as support for the error estimation is relevant. A smoother field $\overline{D}^{\star}$ must then be computed in order to provide an estimation for the error $\theta_{\overline{D}}$:

$$\theta_{\overline{D}} = \overline{D}^{\star} - \overline{D}_h \tag{6.1}$$

which represents a point-wise error.
Following the extension of the *ZZ2* estimator initiated by [Perić et al., 1994], [Feld-Payet, 2010] to non-linear problems, an *incremental* form for the L_2 norm of the global error can be defined:

$$\| \theta_{\overline{D}} \|_{\Omega} = \left| \int_{\Omega} \left(\overline{D}^{\star} - \overline{D}_h \right) \times \left(\Delta\overline{D}^{\star} - \Delta\overline{D}_h \right) \mathrm{d}\Omega \right|^{1/2} = \left(\sum_{e=1}^{n_e} \| \theta^e_{\overline{D}} \|^2_{\Omega^e} \right)^{1/2} \tag{6.2}$$

which is the sum of the elementary contributions to the error:

$$\| \theta^e_{\overline{D}} \|_{\Omega^e} = \left| \int_{\Omega^e} \left(\overline{D}^{\star e} - \overline{D}^e_h \right) \times \left(\Delta\overline{D}^{\star e} - \Delta\overline{D}^e_h \right) \mathrm{d}\Omega^e \right|^{1/2} \tag{6.3}$$

Global and local relative errors are given respectively by:

$$\eta_{\overline{D}} = \frac{\| \theta_{\overline{D}} \|_{\Omega}}{E} \times 100 \qquad \text{and} \qquad \eta^e_{\overline{D}} = \frac{\| \theta^e_{\overline{D}} \|_{\Omega^e}}{E} \times 100 \tag{6.4}$$

where E is given by:

$$E = \left| \int_{\Omega} \overline{D}^{\star} \times \Delta\overline{D}^{\star} \, \mathrm{d}\Omega \right|^{1/2} \tag{6.5}$$

6.1.2.4 Superconvergent Patch Recovery (SPR) procedure

Using the SPR technique, a continuous field (defined at the nodes of the mesh) is reconstructed from the discontinuous state variable field (defined at the integration points). The nodal value

[1] Let us note that the degree for the interpolation of the chosen variable must be lower than that of the displacement field so as to get a better approximation through the smoothing process.

of the field can be approximated thanks to a polynomial function on patches of elements. This polynomial function is close (in the least-squares' sense) to the gradient evaluated in some sampling points which are chosen to be *superconvergent* points whenever possible (*i.e.* points where the FE solution is more accurate). The polynomial function can be evaluated at each node:

$$\widehat{\overline{D}}^{k}\left(x_k, y_k, z_k\right) = \underline{P}\left(x_k, y_k, z_k\right) . \underline{a}^{k} \tag{6.6}$$

where $\widehat{\overline{D}}^{k}$ denotes the continuous recovered value of the non-local damage at node k and $\underline{a}^{k}$ denotes a vector of unknowns in the patch assumed as:

$$\underline{a}^{k} = \left\{ a_0^k,\ a_1^k,\ a_2^k,\ a_3^k,\ a_4^k,\ a_5^k \right\}^T \tag{6.7}$$

and $\underline{P}(M)$ is the basis of the polynomial expansion given in point $M\left(x_k, y_k, z_k\right)$ for 6-node triangles by:

$$\underline{P}(M) = \left\{ 1,\ x,\ y,\ x^2,\ xy,\ y^2 \right\} \tag{6.8}$$

From the evaluation of this polynomial functions at the nodes, the FE shape functions of degree p are used in order to get an approximation of the local fields (at GP) with a superior degree to that at the integration points $(p-1)$:

$$\overline{D}^{\star}(M) = \underline{N}(M) . \widehat{\underline{\overline{D}}}^{\star} \tag{6.9}$$

where $\underline{N}$ is a vector containing the shape functions and $\widehat{\underline{\overline{D}}}^{\star}$ another one containing the nodal contributions of the recovered non-local damage. Let us note that the contributions of non-vertex nodes are averaged between the patches sharing these nodes.
A complete presentation of the method can be found in [Feld-Payet, 2010] and [Zeramdini, 2018].

6.1.3 Generation of a new mesh

6.1.3.1 When to remesh?

After each load (time) increment, using the resulting FE solutions, the errors are estimated. The global relative error $\eta_{\overline{D}}$ defined in eq. (6.4) serves as an indicator to trigger the mesh adaption process. When a prescribed global tolerance $\epsilon^h_{\overline{D}}$ is exceeded, *i.e.* $\eta_{\overline{D}} \leq \epsilon^h_{\overline{D}}$, the remeshing process is performed.

6.1.3.2 How to remesh?

For optimizing the mesh refinement, several local mesh adaption criteria have been proposed in the literature, namely: the uniform distribution of the error [Oñate and Castro, 1991], [Ladevèze and Pelle, 2005], the uniform distribution of the specific error [Oñate and Castro, 1991] and the limitation of the number of elements in the mesh [Li and Bettes, 1995], [Ladevèze and Pelle, 2005]

to name a few. Let us note that these methods have been proposed initially for linear problems with a sufficiently regular solution [Feld-Payet, 2010]. A critical review of these criteria has been published by [Díez and Huerta, 1999].

In the present work, it is chosen to impose that the error contributions of the elements are equally distributed over the mesh [Ladevèze and Pelle, 2005]. For this criterion to be met, the ratio between the new element size and the old one must be:

$$r_e = \frac{h'_e}{h_e} = \frac{\epsilon^{\frac{h}{D}^{1/q}}}{\eta^{\frac{e}{D}^{2/(2q+d)}} \left[\sum_{\Omega^e} \eta^{\frac{e}{D}^{2d/(2q+d)}} \right]^{1/2q}} \tag{6.10}$$

with d the problem's dimension and q the convergence rate depending on the element size and the regularity of the exact solution. According to [Ciarlet, 1978], a value of $q = 2$ can be assumed for 6-nodes triangles. Note that for sufficiently smoothed solutions, such a criterion is equivalent to the minimization of the number of FE [Li and Bettes, 1995].

6.1.3.3 Final map size for the mesh generator

In this work, to generate the new (optimized) mesh, a fully automatic mesh generator, namely MeshGems has been used [Frey and George, 2008]. This tool has been developed at the INRIA by the Distene work-team for mesh generation purposes. The MeshGems mesh generator requires a map size to generate the optimized mesh.

Nodal sizes determination:

As recommended by [Feld-Payet, 2010] and [Zeramdini, 2018], a map of new mesh sizes defined at each node is computed:

$$h'_i = \frac{1}{n_e} \sum_{e \subset \Omega_i} h'_e \tag{6.11}$$

where Ω_i is the union of the n_e elements of e connected to node i and h'_e is the element size obtained from eq. (6.10).
More details on mesh generation can be found in [Frey and George, 2008] and [Feld-Payet, 2010].

Mesh size limitation:

In order to prevent the creation of too large or too small elements, upper and lower limits for the element size in the new mesh can be specified at nodes [Moslemi and Khoei, 2009]:

$$h_{min} \leq h'_i \leq h_{max} \tag{6.12}$$

Choice for an element size in fatigue situations:

The choice of a minimum element size h_{min} in cyclic situations is not trivial. It is some-

how admitted that the size of the finite elements needs to be small enough to well discretize the monotonic (MPZ) and cyclic plastic zones (CPZ) [McClung and Sehitoglu, 1989], [Pommier, 2003], [González-Herrera and Zapatero, 2005], [Gardin et al., 2016b]. The plastic zone size seems to represent the scale reference to relate to the minimum element size in FEA (in terms of number of divisions of the size of r_{mpz}) [McClung et al., 1991], [González-Herrera and Zapatero, 2005]. It is clear that the size of the monotonic plastic zone r_{mpz} is influenced by the maximum load level.

In order to estimate the appropriate element size in the vicinity of the crack-tip, [McClung and Sehitoglu, 1989] & [Dougherty et al., 1997] proposed the following criterion:

$$h_{min} = \frac{1}{10} r_{mpz} = \frac{1}{10} \left[\frac{\alpha}{\pi} \left(\frac{K_{max}}{\sigma_y} \right)^2 \right] \tag{6.13}$$

where r_{mpz} defines the radius of the monotonic plastic zone (in Irwin's sense [Irwin, 1960]), α a constraint factor ($\alpha = 1$ for plane stress and $\alpha = (1-2\nu)^2$ for plane strain conditions) and K_{max} is the maximum applied level reached upon FCG testing.

Based on the literature survey and on our own experience, the criterion defined in eq. (6.13) is considered in my study. This criterion is also the most restrictive with respect to the existing ones. For the material under concern and the SEN-T specimen subjected to fatigue loading as described in sub-sect. 5.5.3 and corresponding to the experimental tests in sect. 3.1, the estimated minimum element size derives from the two limiting situations: $a = 1.0\,\text{mm}$ ($K_{max} = 25.6\,\text{MPa}\sqrt{\text{m}}$) and $a = 8.0\,\text{mm}$ ($K_{max} = 179.4\,\text{MPa}\sqrt{\text{m}}$) which induce respectively $h_{min} \simeq 4.0\,\mu\text{m}$ and $h_{min} \simeq 186.0\,\mu\text{m}$ at 550°C. In order to ensure reliability of numerical results, an intermediate refinement from $h_{min} = 10.0$ up to $20.0\,\mu\text{m}$ has been considered in most of the simulations of sect. 6.3 & sect. 6.4.

6.1.4 Fields transfer

When changing the mesh topology, history-dependent variables for non-linear and dissipative processes as well as nodal variables (DoF) must be transferred from the old to the new mesh. Such a projection is not an easy task since a transfer operator should preserve the consistency of the constitutive relations, the compatibility conditions, the boundary conditions and the equilibrium of the structure [Perić et al., 1996]. Meanwhile, the so-called *numerical diffusion* should be avoided or minimized. It goes without saying that the mapping procedure must also represent a minimal computational cost. Most of the time, all these constraints cannot be ensured simultaneously.

In the present work, the most important requirement is to limit the numerical diffusion which may induce numerical errors and non-convergence of the next balancing step [Chen, 2019]: more particularly, the damage localization band should not change. In case of elastic-viscoplastic behavior, all the mechanical fields, which are generally history-dependent, need to be known at each load increment and consequently are to be transferred.

Nodal variables:

In the literature, there are only a few methods dedicated to the transfer of nodal variables. We can cite the direct transfer using nodal interpolation functions, the transfer using a L_2 norm [Bernardi et al., 1989], [Combescure et al., 2003] and the use of an auxiliary mesh [Espinosa et al., 1998]. "Standard" nodal interpolation is the most commonly used transfer operator [Perić et al., 1996], [Feld-Payet et al., 2015]. It is assumed to yield satisfactory results [Ladevèze and Pelle, 2005], [Kumar et al., 2015] and has been already implemented in the Z-set code. This is why this transfer operator has been selected for this work.

Internal variables:

Several methods can be considered for the transfer of internal variables. Description and critical discussions of these methods can be found in [Perić et al., 1996], [Feld-Payet, 2010], [Zeramdini, 2018]. In the present work, a direct transfer of the smoothed fields evaluated at the old IP to the new ones using a moving (weighted) least-squares (MLS) method is considered. Such a procedure has already been implemented within the Z-set code [Feld-Payet, 2010]. Such a direct transfer method has proven to limit numerical diffusion [Andrade Pires et al., 2004]. Moreover, with a MLS-based method, the transferred results are not influenced by the quality of the elements in the old mesh and any type of elements can be used [Yang, 2017].

The idea is to built locally a polynomial approximation s' of the field to transfer s. Considering the coordinates $\underline{x}$ of a given IP of the old mesh $\mathcal{M}$, and those of an IP $\underline{x}'$ in the new mesh $\mathcal{M}'$, the goal is to find the vector of coefficients $\underline{a}$ which minimize the following quantity:

$$\mathcal{J}_{\underline{x}'}(\underline{a}) = \frac{1}{2} \sum_{i \subset V(\underline{x}')} \mathcal{W}(\underline{x}_i, \underline{x}') \left[\underline{P}^T (\underline{x}_i - \underline{x}') \cdot \underline{a} - s(\underline{x}_i) \right]^2 \tag{6.14}$$

in which:

$$\underline{P}^T (\underline{x}_i - \underline{x}') \cdot \underline{a} = s' \tag{6.15}$$

In eq. (6.14) the term $V(\underline{x}')$ corresponds to the region around $\underline{x}'$ in which the approximation is performed, $\mathcal{W}(\underline{x}_i, \underline{x}')$ is a weight function defined below in eq. (6.16), $\underline{x}_i$ the coordinates of the i^{th} IP from the old mesh where the field s is known and that is used to build the approximation. By minimizing the quantity $\mathcal{J}_{\underline{x}'}(\underline{a})$ in eq. (6.14), one can solve for the unknown vector $\underline{a}$ which in turn allows (using the eq. (6.15)) for the value of the field at $\underline{x}'$ to be estimated.

$$\mathcal{W}(m) = \begin{cases} \frac{2}{3} - 4m^2 + 4m^3 & \text{if} \quad m \leq 0.5 \\ \frac{4}{3} - 4m + 4m^2 - \frac{4}{3}m^3 & \text{else} \end{cases} \qquad \text{with} \quad m = \frac{\| \underline{x}_i - \underline{x}' \|}{\max_i (\| \underline{x}_i - \underline{x}' \|)} \tag{6.16}$$

Once the local approximation s' is known, it is directly projected to the new IP of $\mathcal{M}'$. The number of sampling points i from the old mesh is user-defined and should be limited in order to avoid numerical diffusion. Moreover, it should be compatible with the rank of the polynomial basis $\underline{P}$ [Labergere et al., 2014]. In the present work, 13 integration points belonging to the old mesh $\mathcal{M}$ are chosen in case of 6-node triangular elements, as suggested in [Feld-Payet, 2010].

6.1.5 Equilibrium recovery

After transfer, the different fields are out of equilibrium and special measures can be taken in order to ease the re-equilibrium. The simplest one consists in dividing the next loading step, as suggested by [Boroomand and Zienkiewicz, 1999], [Yang et al., 2018] in order to ease the convergence (reloading is then more gradual and the loading conditions are nearly the same). However, when introducing a discontinuity, additional equilibrium recovery procedures prior to the next loading increment can be very helpful to prevent convergence issues.
Several methods are proposed in the literature: those transferring only a reduced number of variables to then compute the remaining ones [Javani, 2011], those performing a stabilization treatment of the transferred fields [Mediavilla et al., 2006d], and those introducing extra residual forces [Broumand and Khoei, 2013].

To restore the equilibrium once a crack increment has been inserted, a specific procedure is added to the calculation chain. To this end, I have chosen to use developments from the recent Ph.D. work of [El Ouazani Tuhami, 2022]: an additional re-equilibrium step is performed with fixed BC, Fig. 6.1. Contrarily to the division of the time step method, the BC correspond here to the instant t_n (and not t_{n+1}). Besides, contrarily to the elastic step of [Mediavilla et al., 2006d], [El Ouazani Tuhami, 2022] proposes to consider the full non-linear (and time-dependent) behavior during a prescribed (user-defined) small time increment (*e.g.* $\Delta t_{req} = 10^{-5}$ s). Using such a small time increment enables the viscoplasticity and damage variables to evolve, but in a negligible manner since BC are kept constant. The process starts with a very small time increment of 10^{-12} s. If convergence is reached, the time increment is increased by a ratio 0.01 (*i.e.* multiplied by a factor 100) until Δt_{req} has elapsed. A succession of $\sim$5-6 converged small increments suffices to restore the equilibrium. After this re-equilibrium step, the frozen BC are relaxed and the calculation can resume with a good convergence rate.

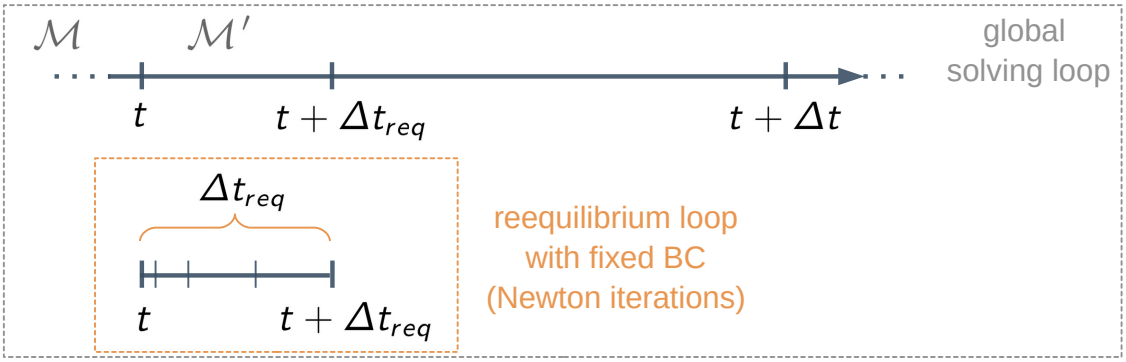

Figure 6.1: Schematic representation of the balancing step.

6.1.6 Overview of the error-based mesh adaption strategy

Finally, the overall *ZZ2* error estimation method and mesh adaption process can be resumed to the flowchart given in Fig. 6.2:

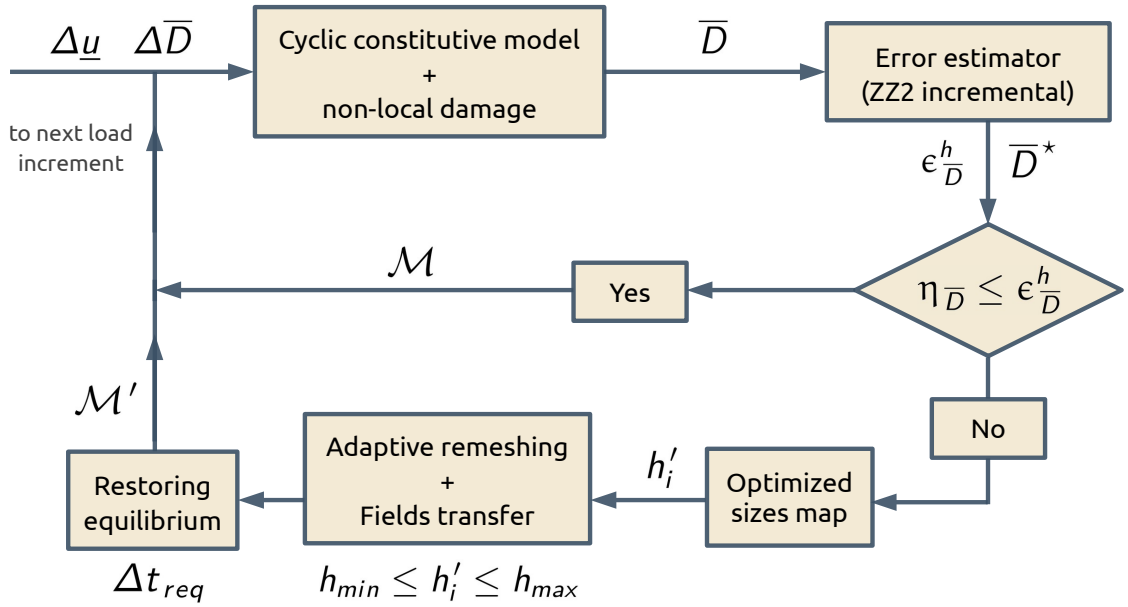

Figure 6.2: Overall flowchart for the error estimation and mesh adaption strategy during FE calculations using a mixed gradient-enhanced regularized cyclic elastic-viscoplastic damage model.

6.1.7 Illustration on an example

The strategy for the mesh adaption relying on an *a posteriori ZZ2* error estimator is illustrated in this section on a quasi-static loading. The specimen studied in the sub-sect. 5.5.2.1 is considered.

6.1.7.1 Error-based mesh adaption

In the present example the prescribed relative accuracy for the error on $\overline{D}$ was fixed to $\eta_{\overline{D}} = 0.5\%$. The *ZZ2* incremental error estimation only starts when a significant non-local damage level has been reached, *i.e.* $\overline{D}^{ZZ2}_{th} = 0.001$. Then, remeshing is triggered if the sum of the elementary contributions to the global error $\eta_{\overline{D}}$ exceeds the global tolerance $\epsilon^h_{\overline{D}}$. In practice, it is useful to trigger remeshing for a global relative error that is slightly greater than the prescribed tolerance on the new mesh in order to limit the number of successive remeshing steps. Indeed, the map sizes were estimated based on the hypothesis of a linear and sufficiently regular solution. The considered problem being non-linear, the resulting global error on the new mesh might by slightly greater than expected. Finally, in order to save computational time by avoiding the generation of very small elements, a minimum element size of $h_{min} = 0.05\,\text{mm}$ has been provided to the automatic mesher, as discussed above in sub-sect. 6.1.3.2.

In the Fig. 6.3a, the non-local damage field is reported at the beginning of the loading process, when $u_y = 0.024\,\text{mm}$. Next, in Fig. 6.3b, the corresponding non-local damage-based *ZZ2* error is also depicted. As expected, the non-local damage (and the corresponding error) first initiates at the notches of the specimen. This enables to detect the elements that are potentially too large to capture large gradients of damage.

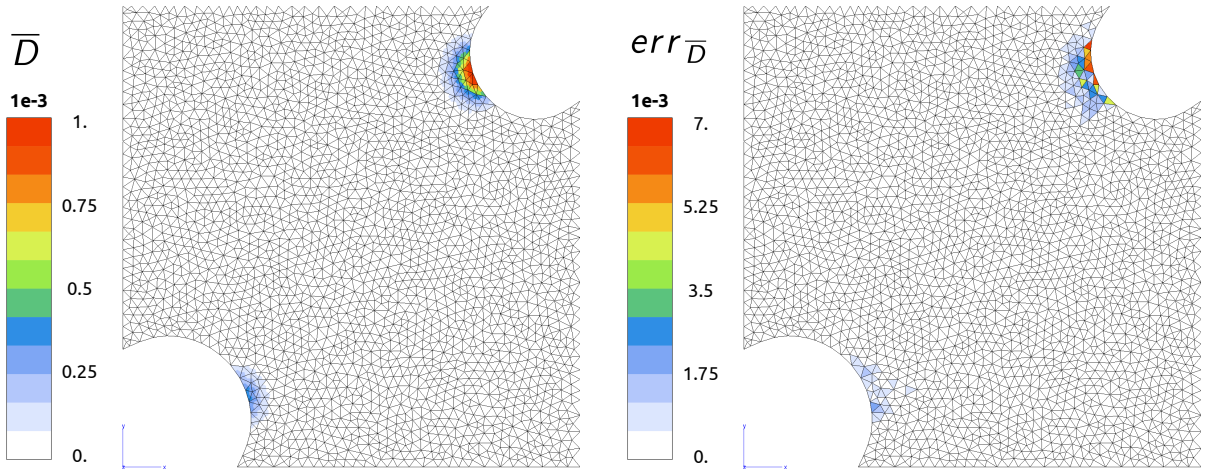

(a) Non-local damage distribution. (b) *ZZ2* error distribution.

Figure 6.3: Error-estimation on a the double-notched specimen meshed with 0.3 mm FE and subjected to prescribed tensile loading at $u_y = 0.024\,\text{mm}$ ($\overline{\mathcal{V}} = \overline{D}$, c2d6r 4-fields FE).

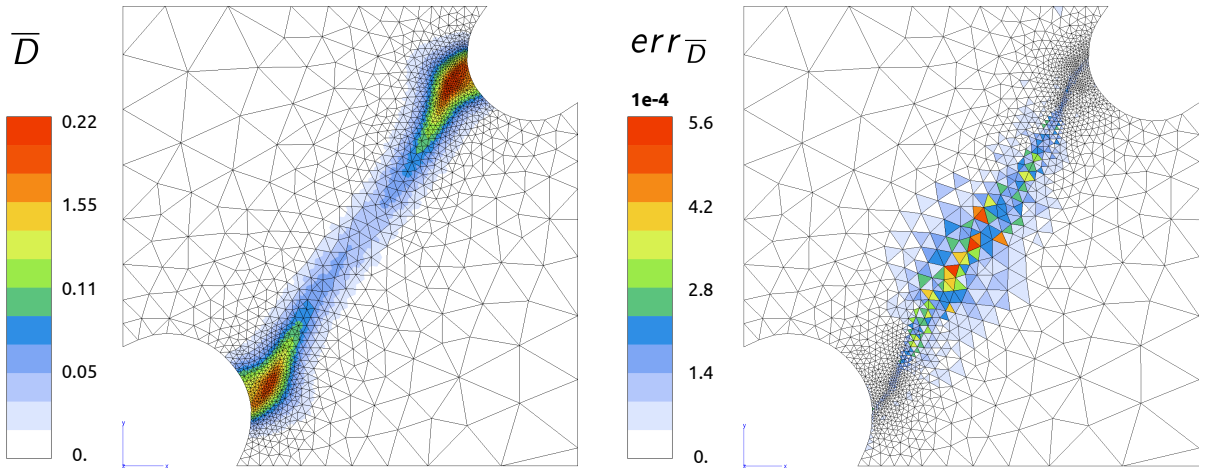

(a) Non-local damage distribution. (b) *ZZ2* error distribution.

Figure 6.4: Error-estimation on double-notched specimen subjected to prescribed tensile loading at $u_y = 0.078\,\text{mm}$ ($\overline{\mathcal{V}} = \overline{D}$, c2d6r 4-fields FE).

By comparing the meshes before and after the remeshing step, Fig. 6.3a and Fig. 6.4a, it can be clearly seen that the mesh is refined in the zones where the non-local damage field exhibits significant gradients. Since the chosen local criterion requires the uniform distribution of the error over the whole domain, the zones where the error is significant are refined, while those where it is non-significant are coarsened, see Fig. 6.3b to Fig. 6.4b.

The resulting adapted meshes are depicted in Fig. 6.5. The properties for each FE mesh are reported in Tab. 6.1. The numerical solving procedure has enabled a reduction of $\sim$47% of the number of nodes during the first remeshing step, and of $\sim$36% for the second remeshing step (compared to the regular 0.3 mm mesh) while allowing the use of smaller elements (0.05 vs. 0.3 mm for more accuracy) in the localization band.

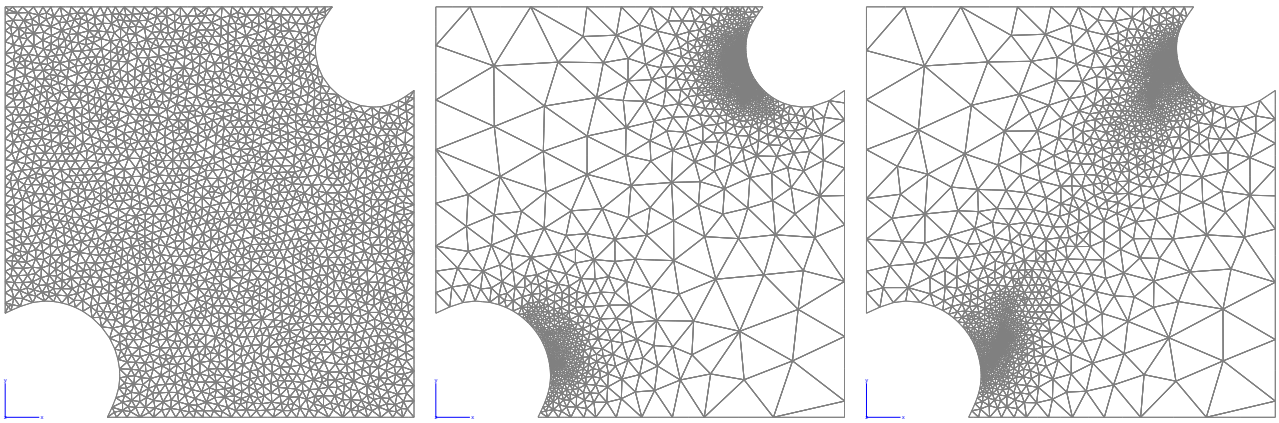

(a) Mesh 1 (initial 0.3 mm). (b) Mesh 2. (c) Mesh 3.

Figure 6.5: Successive error-based adapted meshes.

Meshes	0.3 mm	Adapted 1	Adapted 2
Elements	4 650	**2 459**	**2 981**
Nodes	9 459	**5 046**	**6 080**

Table 6.1: Properties of the FE meshes for the monotonic loading case.

6.1.7.2 Fields transfer

Once the mesh has been adapted, the fields are transferred from the old to the new mesh.

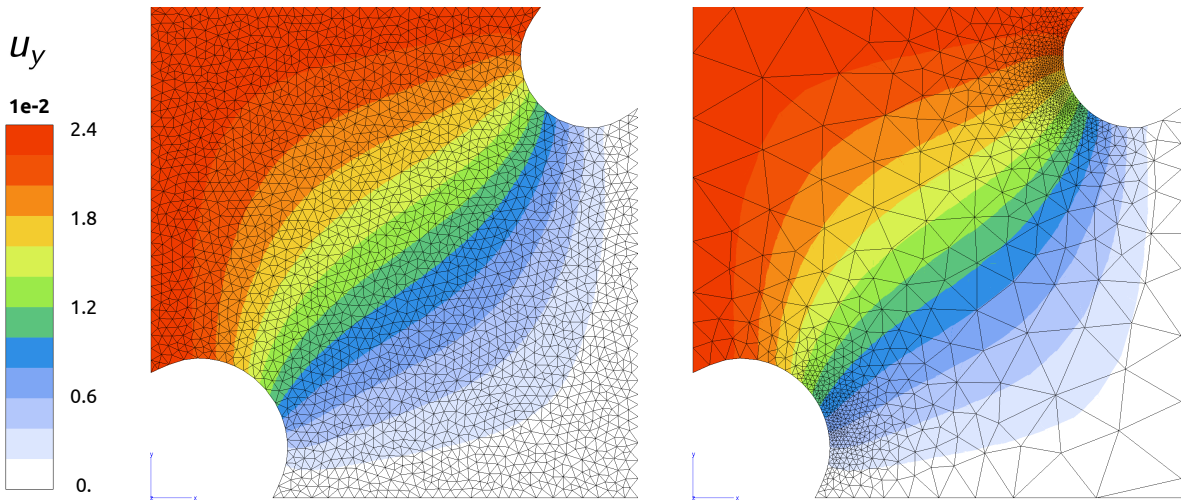

(a) u_y - $\mathcal{M}_1$ (before). (b) u_y - $\mathcal{M}_2$ (after).

Figure 6.6: First transfer of nodal variables u_y from mesh 1 to 2 at $u_y = 0.024$ mm.

Fig. 6.6 & Fig. 6.7 exhibit the displacement field u_y before and after two remeshing steps with significant topology changes. In both cases, one can notice an excellent correlation between the former and the new continuous (nodal) field distribution.

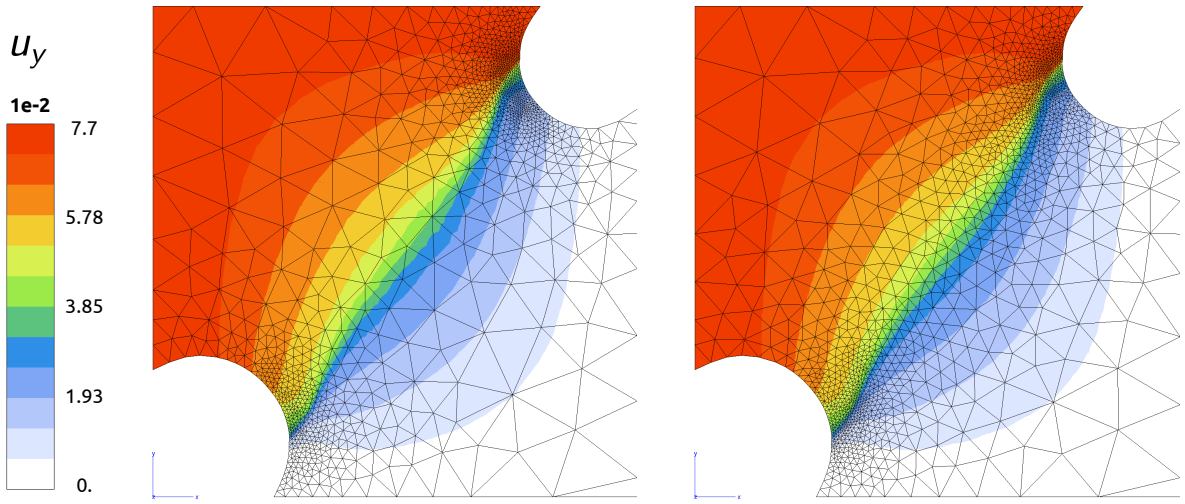

(a) u_y - $\mathcal{M}_2$ (before). (b) u_y - $\mathcal{M}_3$ (after).

Figure 6.7: Second transfer of nodal variables u_y from mesh 2 to 3 at $u_y = 0.077\,\text{mm}$.

The non-local damage during the first and second transfers are depicted in Fig. 6.8 & Fig. 6.9, respectively. Due to the significant refinement during the first remeshing step, the transfer of the local data is much more affected than for the second transfer. However, the very low damage values (*i.e.* about 10^{-3}) make the discrepancy insignificant. For the second transfer, the 3$^{\text{rd}}$ mesh is close to the 2$^{\text{nd}}$ one and the transfer does not significantly change the data distribution, Fig. 6.9.

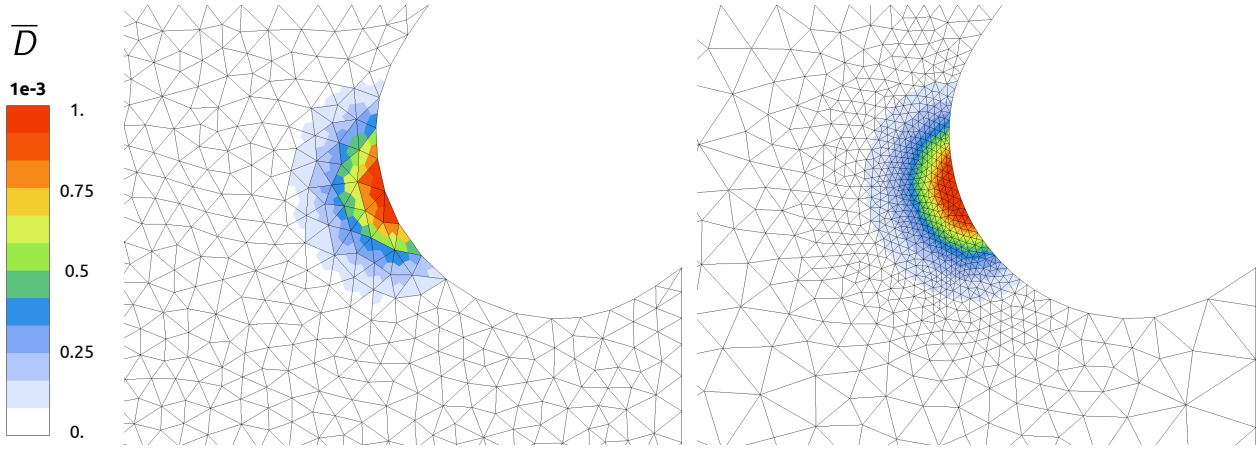

(a) $\overline{D}$ - $\mathcal{M}_1$ (before). (b) $\overline{D}$ - $\mathcal{M}_2$ (after).

Figure 6.8: First transfer of local (internal) variables $\overline{D}$ from mesh 1 to 2 at $u_y = 0.024\,\text{mm}$.

This quasi-static example has enabled to evidence the capabilities of the *ZZ2* incremental error estimator to effectively control the mesh refinement process. The choice of the non-local damage variable as the underlying variable for mesh refinement has been confirmed. Besides, it has also been shown that the selected transfer operators enable to avoid numerical diffusion. Finally, up to this point, the proposed strategy gives the possibility to perform structural calculations up to the onset of fracture (*i.e.* some IP have reached their critical damaged state) with a controlled accuracy.

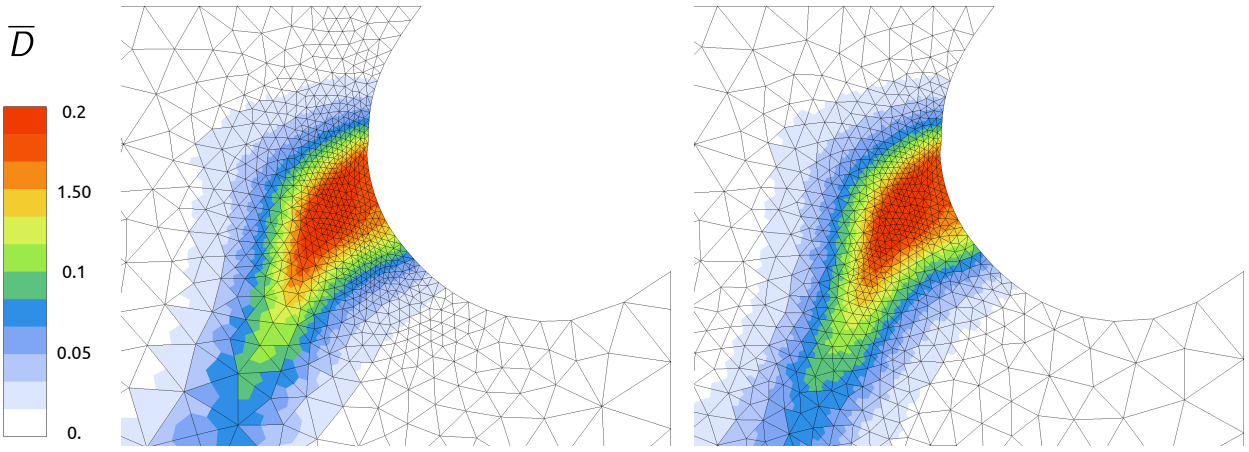

(a) $\overline{D}$ - $\mathcal{M}_2$ (before). (b) $\overline{D}$ - $\mathcal{M}_3$ (after).

Figure 6.9: Second transfer of local (internal) variables $\overline{D}$ from mesh 2 to 3 at $u_y = 0.077\,\text{mm}$.

6.2 Continuous-discontinuous transition

6.2.1 Motivation and elements of a continuous-discontinuous transition

One of the most significant limitations of the continuous approaches relies on their inability to represent surface decohesion associated with crack propagation in structures. Indeed, when considering pure non-local damage models without introducing an explicit fracture surface in the numerical model:

- the real crack lips cannot be visualized as lines (2D computations) or surfaces (3D);
- the effect of crack opening/closure, crack-lips contact and friction cannot be assessed;
- the proper definition of the crack-tip, *i.e.* a point (2D) or a line (3D) is not trivial, which in turn leads to the absence of a precise crack growth rate estimation;
- excessive straining arises since the material across the damaged zone remains kinematically connected to almost null stress levels [Geers et al., 1998], [Simone et al., 2004], [Feld-Payet, 2010], [Rastiello et al., 2018].

In order to overcome such drawbacks, some numerical methods, mainly referred to as *continuous-discontinuous transition* (CDT) techniques (or sometimes denoted as *hybrid crack approaches* [Saloustros et al., 2019]) have been proposed lately, Fig. 6.10.

While such CDT methods have been initially suggested for fracture prediction in quasi-static conditions, one of the goals of the present Ph.D. project is to assess their ability to deal with fatigue (cyclic) conditions.

When using a continuous-to-discontinuous transition technique for the modeling of fracture process, some questions always need to be considered [Feld-Payet, 2022]:

1. where to locate the discrete crack?
2. when to insert the crack, *i.e.* when to switch from a diffuse damage to a sharp crack?
3. how to model a discrete crack?

These three questions are answered in the following sub-sections.

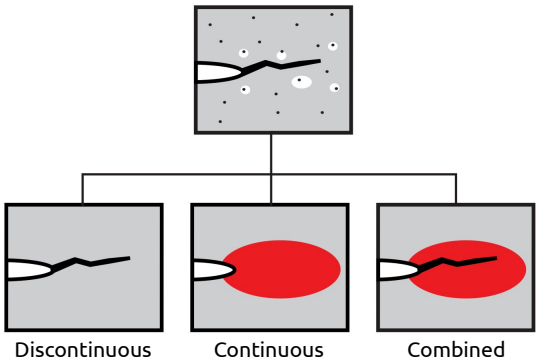

Figure 6.10: Different approaches to fracture (adapted from [Mediavilla Varas, 2005]).

6.2.2 Where to locate the discrete crack?

6.2.2.1 Crack orientation criteria

For non-linear material behaviors, orientation criteria have been suggested over the past two decades. The loss of material stability (*i.e.* bifurcation analysis), as used by [Besson et al., 2003], [Huespe et al., 2009], [Wolf et al., 2018], [Nikolakopoulos et al., 2021], can only be considered for local (*i.e.* non regularized) stress-softening material behaviors. For non-linear material models (plastic or viscoplastic), [Jirásek and Zimmermann, 2001] have proposed to propagate the crack in the direction normal to the maximum principal non-local strain. Similarly, [Simone et al., 2003] suggested to consider for the crack growth direction the one where the non-local equivalent strain accumulation is the greatest.
Finally, in a natural way, the direction in which the degradation process is maximum (*i.e.* the direction corresponding to maximum damage or porosity) can obviously be considered [Könke, 1995], [Brokken, 1999]. This has the advantage that both crack initiation and propagation can be dealt with using the same (continuum) equations and no separate fracture criterion is necessary [Javani, 2011]. This concept has been successfully applied to 2D crack growth problems in metal forming processes for both uncoupled [Brokken et al., 2000] or coupled damage models [Mediavilla et al., 2006c], [Feld-Payet, 2010], [Broumand and Khoei, 2013].
Taking into account this literature survey, I made the choice to model the crack growth in the direction where the smoothed non-local damage field $\overline{D}^{\star}$ is maximum.

6.2.2.2 Crack path tracking algorithms

To determine where the next crack increment should be, according to the chosen orientation criterion, it is then necessary to resort to a practical method. These methods are referred to as *crack path tracking algorithms* [Saloustros et al., 2019], [Feld-Payet, 2022]. Their original goal was to ensure continuity of the crack path but they have evolved to also ensure a sufficient regularity.

Among the algorithms relying solely on a degradation-related field, there are notably:

- the **maximum projected ridge** approach of [Bottoni et al., 2015], which searches for the maximum of the projected value of a damage-related field on a segment perpendicular to the previous crack increment. Let us note that this method has only been applied to 2D problems;
- the **medial axis** method suggested by [Tamayo-Mas, 2013], [Tamayo-Mas and Rodríguez-Ferran, 2015]. This algorithm is a geometrical one defining the crack-tip positions along the successive centers of bi-tangent interior spheres to a regularized damage field level set. This algorithm was applied for both 2D and 3D problems. However, it allows cracks only to initiate on a boundary of the structure;
- the **marching ridges** technique proposed by [Feld-Payet, 2010], [Feld-Payet et al., 2015] for ductile fracture prediction. This tracking algorithm is based on the local approximation of the ridge by a segment. The direction of the segment is determined thanks to the evaluation of a scalar product involving the gradient of a regularized degradation-related field and the orthoradial vector defined in a polar grid centered on the crack-tip or crack initiation spot. This algorithm was applied for both 2D and 3D problems and allows crack initiation anywhere in the structure. Besides, this algorithm is already implemented within the Z-set suite. For all these reasons, this crack path tracking algorithm has been selected for this work.

6.2.2.3 Theoretical aspects of the *Marching Ridges* algorithm

This algorithm is termed as "marching" since the search for the crack-tip position is a local gradual process. Starting from a point $\underline{x}_0$ on the ridge, and assuming that the ridge line can be locally approximated by a linear segment, the eq. (6.17) can be used to find the next point(s) on the ridge at a given distance R (and so on in an incremental manner) [Feld-Payet et al., 2015]:

$$\begin{cases} \underline{e}_\theta\left(\theta - \Delta\theta/2\right).\underline{\nabla} f\left(\underline{x}_0 + R\underline{e}_r(\theta - \Delta\theta/2)\right) > 0 \\ \underline{e}_\theta\left(\theta + \Delta\theta/2\right).\underline{\nabla} f\left(\underline{x}_0 + R\underline{e}_r(\theta + \Delta\theta/2)\right) < 0 \end{cases} \tag{6.17}$$

In this eq. (6.17), R defines an evaluation radius, $\Delta\theta$ is an angular step (or precision) enabling to test a finite number of directions $\underline{e}_\theta$ (tangential to the radius), $\underline{x}_0$ the starting point (*i.e.* the last position of the crack front), and f a sufficiently smoothed degradation-related scalar field (estimated thanks to the SPR procedure, see sub-sect. 6.1.2.4), see Fig. 6.11.

For each tested direction θ, the scalar product $\underline{e}_\theta.\underline{\nabla} f$ is evaluated. If this scalar product changes its sign from positive to negative for a given direction θ, then a ridge is identified. The angle θ hence defines the ridge orientation, with an angular precision of $\Delta\theta$.

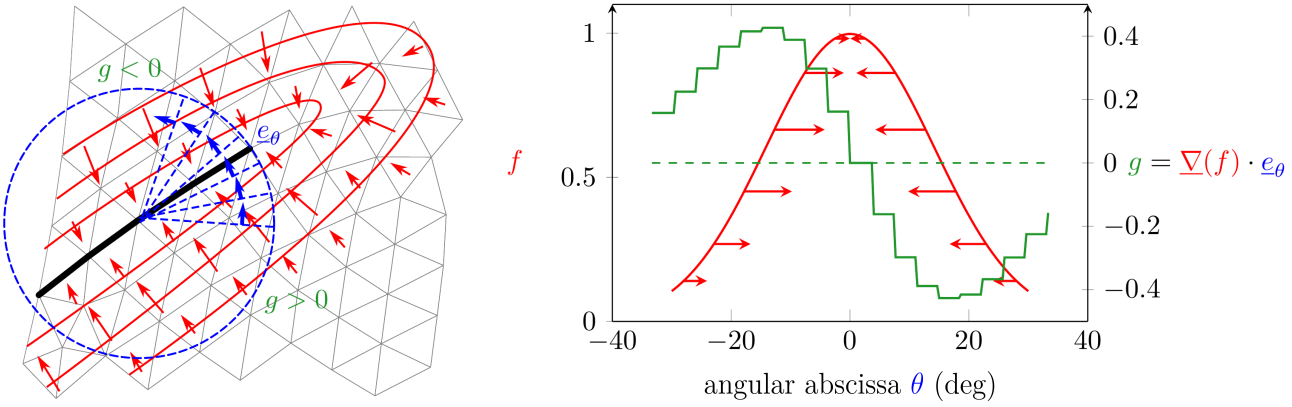

(a) Polar grid (blue) located on the crack (bold black line) with contour plots of the f function and corresponding gradient vectors $\underline{\nabla} f$ (red arrows).

(b) Evolution of the f function along the angular abscissa θ and corresponding scalar product g. The angular discretization along θ yields a piece-wise constant scalar (dot) product g whose sign change allows for the crack path to be identified.

Figure 6.11: Schematic view of the underlying concepts of the *Marching Ridges* crack path tracking algorithm (after [Feld-Payet, 2022]).

It should be mentioned that in the present study, the smoothed non-local damage field $\overline{D}^\star$ will be used by the *Marching Ridges* algorithm as the support for the ridge search process.

6.2.3 When to insert a crack?

6.2.3.1 Magnitude of the crack increment

The length of the discontinuity increment remains to be defined. This length ℓ_{inc} can be a constant length prescribed by the user or it can depend on the damage evolution in the considered direction as in [Seabra et al., 2013]. Besides, one has the choice to only insert one crack increment or to resume the procedure until the insertion criterion is no longer verified. This last strategy is known as the *exhaustion* method and it has been used by [Mediavilla Varas, 2005], [Wolf et al., 2018], [Javanmardi and Maheri, 2019]. The choice is made in this work to only insert one increment of fixed length at a time in order to restore the equilibrium of the system before any further crack propagation. Such a procedure aims at obtaining a better robustness by avoiding divergence issues.

6.2.3.2 When to insert a crack?

A crack increment is inserted in the mesh when a critical damaged state is reached in the fracture process zone. This ensures that the material has nearly lost its whole load-bearing capacity and that no residual energy remains to be dissipated. To be more specific, a crack can only be inserted if $\overline{D} \geq \overline{D}^{crit}$ along the considered crack increment. Let us note that to ensure a good estimation of the crack insertion criterion given above, the non-local damage $\overline{D}$ is considered rather than its smoothed value $\overline{D}^\star$. Indeed, the latter, although more regular in the bulk, may exhibit a poor quality close to the edges. Moreover, such a smoothed field is not physically-based and the positivity of its evolution is not necessarily ensured [Feld-Payet, 2010].

6.2.4 How to insert the crack increment?

Since mesh adaption is already used to locally refine the mesh up to the onset of fracture, and since the present work follows the developments from [Feld-Payet, 2010], it is natural to also use mesh adaption to represent the discrete crack too. This choice also represents the advantage of providing a very accurate description of the crack (see the review on discontinuous crack modeling in sub-sect. 1.7.2). It is obviously more complex than a simple element deletion technique (also considered in the appendices, see Chap. K). However, with element deletion, in order to get relatively "smooth" crack lips and avoid too large mass loss, a very fine mesh should be considered.

Once the geometry of the crack increment has been evaluated by the MR algorithm and the insertion criterion is verified, mesh intersection techniques developed by [Chiaruttini et al., 2013] are used to represent the discontinuity. The auxiliary surfacic mesh of the crack increment (see Fig. 6.12) is used to intersect the structural mesh. Then, a mesh is generated from the contour of the structure with new boundaries associated with the updated crack thanks to the MeshGems tools.

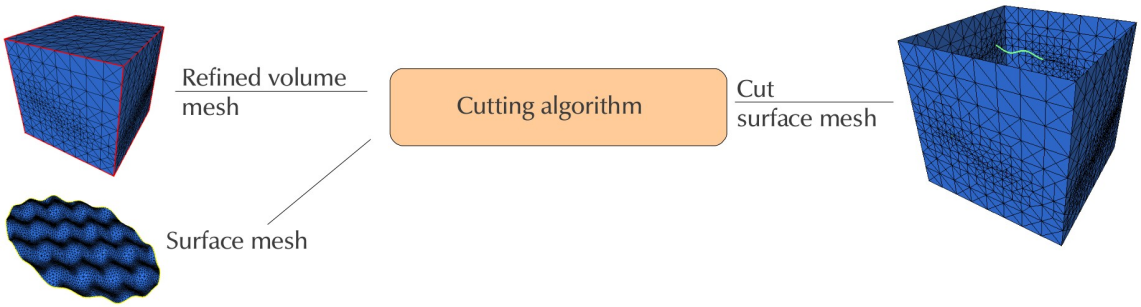

Figure 6.12: General cutting surface process for mesh intersection (from [Chiaruttini et al., 2013]).

Let us remark that the insertion of the new crack is done by splitting the nodes generated on the new crack lips by the surfacic mesher. This implies that for each node, a corresponding node with the same coordinates is generated.

6.2.5 Overview of the remeshing-based crack growth modeling

Once the non-local damage field has been smoothed using the *ZZ2* error estimator, see sub-sect. 6.1.2, this latter field and its spatial gradient are provided in a post-processing step to the MR algorithm which conducts the search for possible ridges in order to locate the position of the crack increment, see sub-sect. 6.2.2.3. Then, an auxiliary mesh is built to define the discontinuity surface. This one is provided to the Z-cracks tool which performs the mesh intersection process, see sub-sect. 6.2.4. A new meh is hence generated and properly refined using the fully automatic mesh generator MeshGems. Then, both nodal and local fields are transferred from the old to the new mesh, see sub-sect. 6.1.4. Finally, the equilibrium is retrieved according to a specific procedure described in sub-sect. 6.1.5 and the next load increment can be solved.
As a matter of synthesis, the whole numerical procedure for the crack growth modeling can be summarized in the flowchart given in Fig. 6.13:

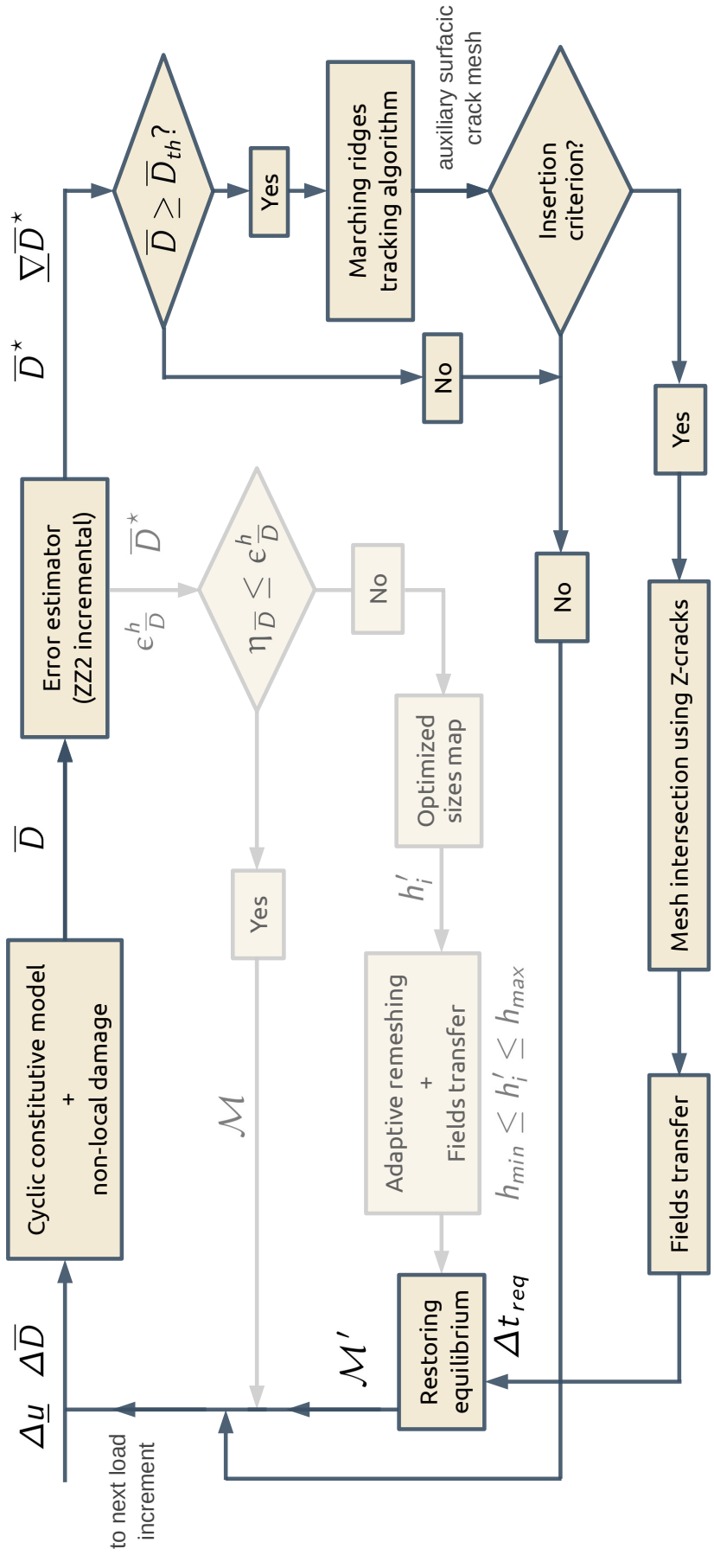

Figure 6.13: Overall flowchart for the error-based mesh adaption strategy and crack propagation modeling through mesh adaption steps during FE calculations using a mixed gradient-enhanced regularized cyclic elastic-viscoplastic damage model.

6.3 Application of the continuous-discontinuous strategy for fatigue crack growth

In the remaining of this Chap. 6, various numerical calculations will be discussed. All of them derive from a standard cyclic test case on a SEN-T specimen as the one introduced in sub-sect. 5.5.3 which corresponds to the experimental test described in the sect. 3.1.
In this section, **only pure fatigue crack growth** testing conditions will be discussed. The crack insertion strategy needs to be validated on cyclic cases. The aim of this section is to evaluate the performance of the continuous-discontinuous strategy for LCF propagation by confronting the numerical results with the experimental observations.

6.3.1 Description of the test case

6.3.1.1 Specimen geometry and boundary conditions

Only the central zone of the SEN-T specimen is studied, see Fig. 6.14. An initial pre-crack of 0.6 mm has been introduced in the initial mesh to approximate the experimental conditions for the propagation stage with a sufficiently long crack. The edges of the considered zone are assumed to be far enough from the notch to assume locally homogeneous boundary conditions. For the same reason, the zone is meshed with a coarse spatial discretization away from the notch root, while in the vicinity of the notch root, the mean element size is decreased. Both the geometry and the prescribed boundary conditions of the considered problem are depicted in Fig. 6.15a. The displacement on the lower boundary of the specimen along the y-direction is fixed. The displacements along the x-direction on both upper and lower edges are free. A node is fixed to prevent the rigid body motion (a similar procedure was conducted by [Lu et al., 2019], [Kirkesaether Brun et al., 2020]). A uniform stress (or displacement) load is applied continuously on the upper boundary in a cyclic manner. A sinusoidal stress-controlled cyclic loading waveform is considered with a 1 Hz frequency, an applied stress level of 400 MPa and a load ratio of $R_\sigma = 0.05$, see Fig. 6.15b. A displacement-controlled signal will also be considered.

6.3.1.2 Numerical aspects related to the FE calculations

Two-dimensional structural calculations have been performed assuming plane strain loading conditions (the specimen thickness being 4.0 mm). Quadratic triangular elements are used to obtain satisfactory mesh quality after automatic 2D mesh adaption [Bouchard et al., 2000], [Bouchard et al., 2003], [Besson and Desmorat, 2004]. Consequently, similarly to Chap. 4 and Chap. 5, c2d6r (quadratic triangular) elements have been considered using either the mixed gradient-enhanced formulation (p2-p1-p1-p1), see Fig. 1.17a, or solely the gradient-enhanced formulation (p2-p1), see Fig. 1.17b. During the FE calculations, in order to reduce the solving time, especially at the local level where the non-linear regularized cyclic damage model needs to be integrated (see sub-sect. 5.4.5), a sequential multi-threaded procedure has been considered using 4 to 6 threads. The

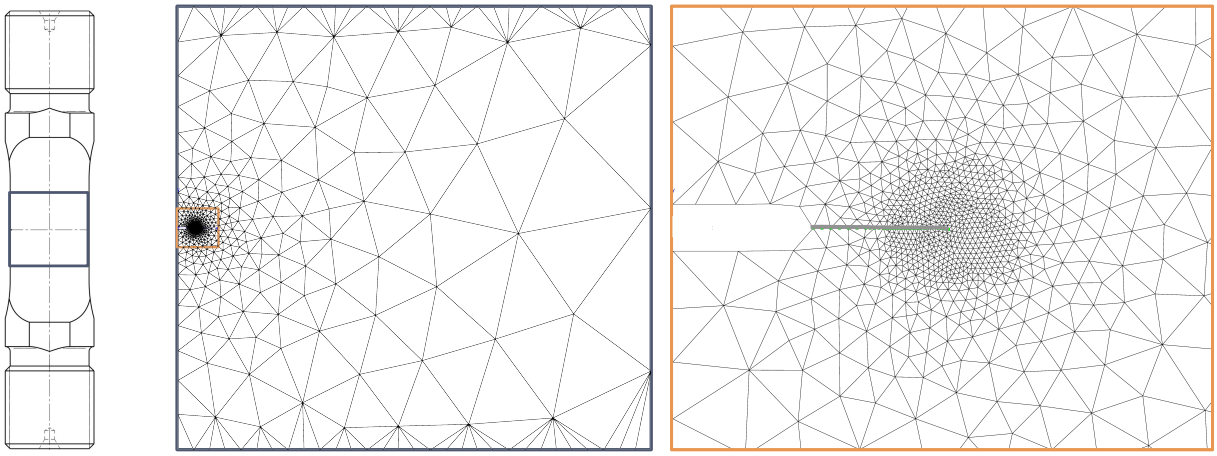

(a) SEN-T spec. (b) FE mesh of the useful zone. (c) Close-up view around the crack-tip.

Figure 6.14: Mesh of the useful zone of a SEN-T specimen subjected to cyclic loading in the 2D case.

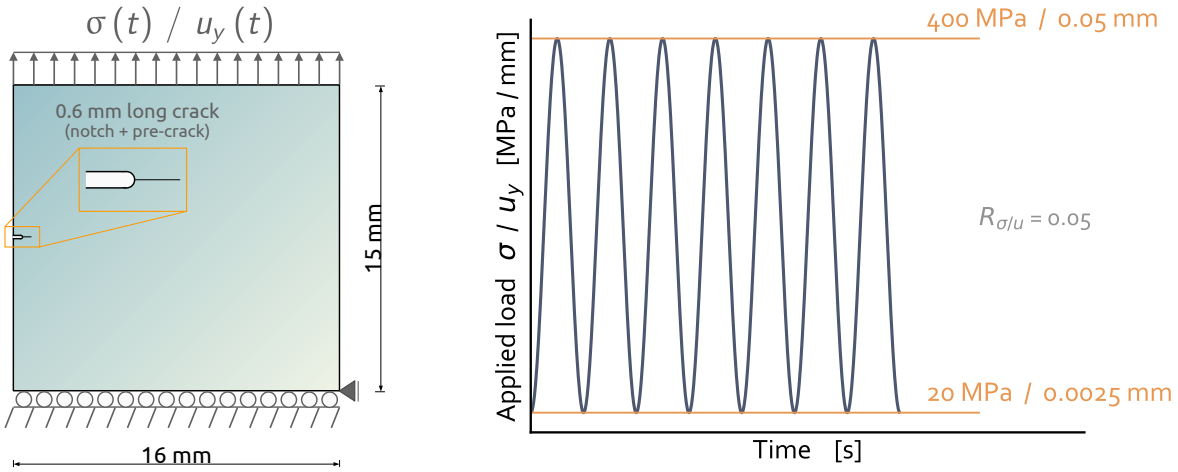

(a) Prescribed boundary conditions. (b) Test loading signal (stress- or displacement-controlled).

Figure 6.15: Schematic representation of the useful zone of the SEN-T specimen under cyclic loading and corresponding loading signal.

so-called *MUltifrontal Massively Parallel sparse direct Solver* (MUMPS) was used for sequential computations. This solver, already implemented within the Z-set suite, is known to be particularly suitable in case of non-symmetric problems like the one considered here.

6.3.1.3 Numerical parameters

Before running the FE calculation, the basic ingredients to be provided to the *ZZ2* incremental error-estimator are as follows:

- the supporting scalar field: the non-local damage field $\overline{D}$
- the threshold value triggering the *ZZ2* error estimation: $\overline{D}_{th}^{ZZ2}$
- the global error on the mesh triggering the remeshing process: $\eta_{\overline{D}}$
- the (global) target error (accuracy): $\epsilon_{\overline{D}}^{h}$

- the min. and max. element sizes: $h_{min/max}$

while those controlling the MR crack path tracking algorithm are:

- the supporting scalar degradation-related field: the smoothed non-local damage field $\overline{D}^{\star}$
- the threshold value triggering the ridge search and validating the direction: $\overline{D}_{th}^{MR}$
- the threshold value for the gradient estimation: $\underline{\nabla}\overline{D}_{th}^{\star}$
- the angular precision for the discretization of the evaluation space: $\Delta\theta = \frac{360^{\circ}}{m}$ where $m \in \mathbb{N}$
- the critical value triggering the crack insertion through remeshing: $\overline{D}^{crit}$
- the length of the crack increment: $\ell_{inc} = \lambda_{inc} \times h_{min}$ where $\lambda_{inc} \in \mathbb{R}$

Thus, parameters considered for the simulation are reported in Tab. 6.2 together with the material parameters for AD730™ calibrated at 550 and 700°C, see Tab. D.1.

Parameters	ℓ_c	$\overline{D}_{th}^{ZZ2}$	$\eta_{\overline{D}}$	$\epsilon_{\overline{D}}^{h}$	h_{min}	h_{max}	$\overline{D}_{th}^{MR}$	$\underline{\nabla}\overline{D}_{th}^{\star}$	$\Delta\theta$	$\overline{D}^{crit}$	ℓ_{inc}
	[mm]	[-]	[-]	[-]	[mm]	[mm]	[-]	[-]	[°]	[mm]	[mm]
Value	0.03	0.001	0.02	0.01	0.015	10.	0.9	0.001	10.	0.95	0.06

Table 6.2: Parameters for the simulations of a standard crack insertion strategy.

6.3.2 Strategy evaluation

6.3.2.1 Global results analysis

The fatigue crack growth simulation for the SEN-T specimen resulted in 86 crack increment insertions to obtain a final crack length of $\approx 2.01\,\text{mm}$. The corresponding contour plots for the non-local damage and the Von Mises stress field are depicted in Fig. 6.16 at two distinct crack lengths of $a = 0.71\,\text{mm}$ and $a = 2.01\,\text{mm}$.

The contour plots of the Von Mises equivalent stress field, Fig. 6.16c & Fig. 6.16d, can be seen to be conform to the theoretical repartition starting from the crack-tip. As expected, as long as the crack grows, the gradients are more pronounced and the stress level is increased. Let us also note that at the end of the simulation, the assumption of homogeneous BC at the edges may be no longer verified, Fig. 6.16d. Indeed, with increasing crack length, the Von Mises equivalent stress field is larger and the meshed area of the SEN-T specimen might be too narrow compared to the resulting stress fields (Fig. 6.16c vs. Fig. 6.16d). A larger structural mesh might have been necessary to ensure homogeneous far-field stress levels. This point has been first disregarded in order to save computational cost for this methodology validation phase.

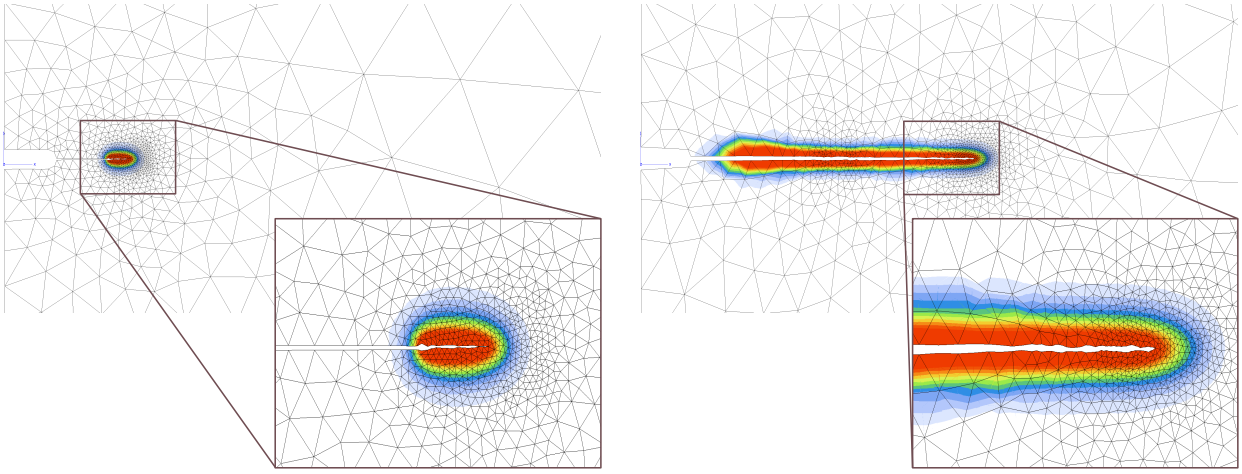

(a) Non-local damage field for $a = 0.71\,\text{mm}$. (b) Non-local damage field for $a = 2.01\,\text{mm}$.

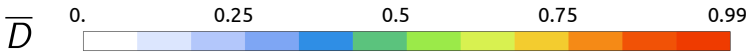

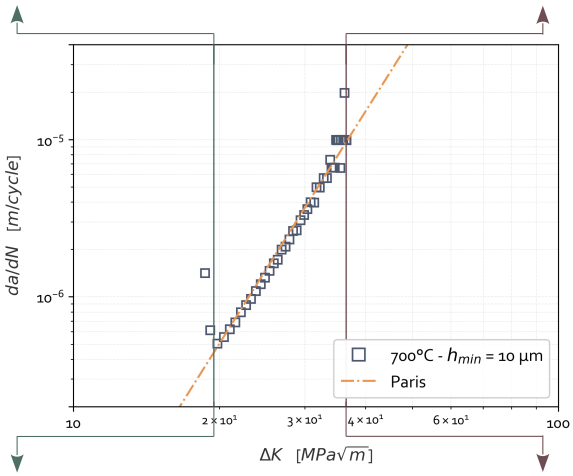

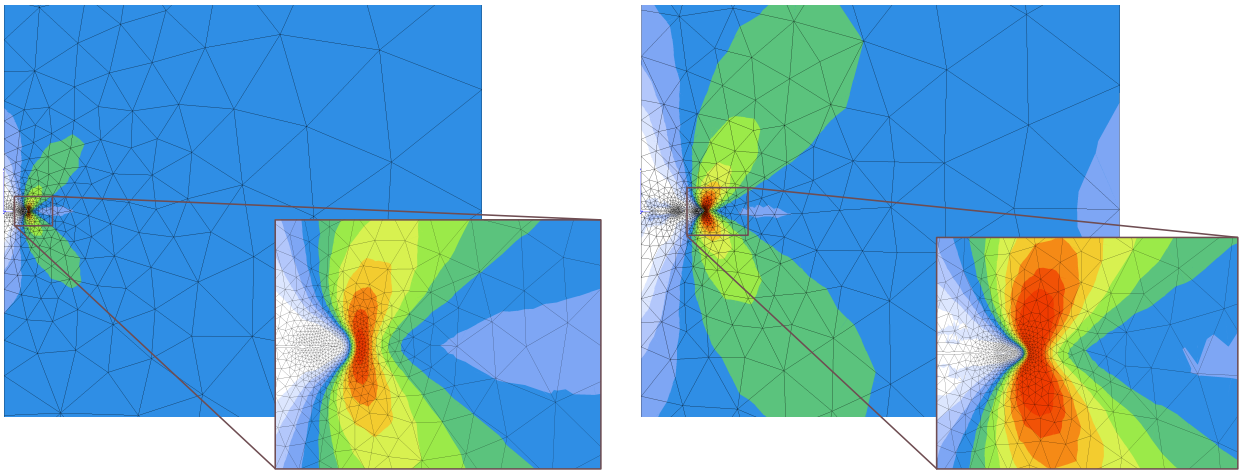

(c) Von Mises stress field for $a = 0.71\,\text{mm}$. (d) Von Mises stress field for $a = 2.01\,\text{mm}$.

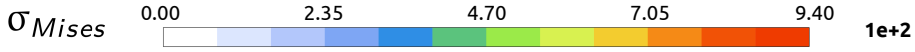

Figure 6.16: Overall fatigue crack growth curve for the FE calculation with some mechanical fields during a standard fatigue loading at 700°C (sinus 1 Hz, $\sigma = 400\,\text{MPa}$, $R_\sigma = 0.05$, c2d6r 2-fields FE).

In close relation with the stress field, the fact that a plastic zone exists at the level of the singularity, *i.e.* at the crack-tip in an elastic-plastic (work-hardening) material, has been extensively studied in the past decades [Irwin, 1960], [Rice, 1967]. Such a plastic zone is known to be responsible (among other mechanisms) for crack closure effects as well as for the modification of both the kinetics and the crack's orientation [Pommier, 2007]. Moreover, it is well established that crack growth is largely influenced by the effect of this plastic zone at the front of the crack. The latter, upon growing, leaves a wake of yielded material, also referred to as the *plastic wake*.

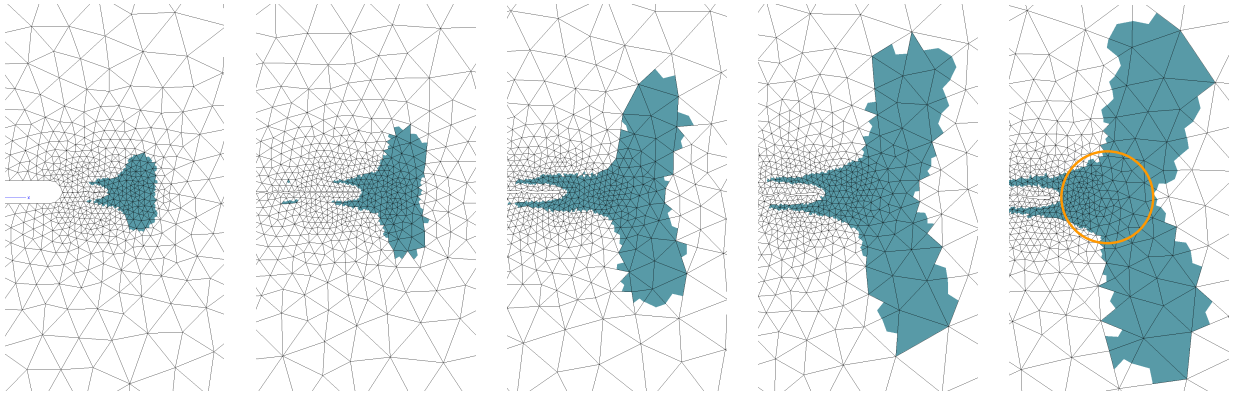

(a) $a = 0.49\,\text{mm}$ (b) $a = 1.03\,\text{mm}$ (c) $a = 1.99\,\text{mm}$ (d) $a = 2.99\,\text{mm}$ (e) $a = 4.14\,\text{mm}$

Figure 6.17: Evolution of the size of the plastic zone at the tip of an advancing fatigue crack at maximum load (550°C, sinus 1 Hz, $u_y = 0.05\,\text{mm}$, $R_{u_y} = 0.05$, plane strain conditions, c2d6r 2-fields FE).

In Fig. 6.17, the (visco)plastic zone at the tip of the growing crack is reported for the present fatigue damage model. One can easily observe from Fig. 6.17a to Fig. 6.17e the increase in size of the (visco)plastic zone with the increase in crack length. As the crack advances, the range of stress intensity factors ΔK also increases from 16.9 to 66.2 $\text{MPa.m}^{1/2}$. Moreover, the "butterfly" shape of the plastic zone is also noticeable, as expected in pure fatigue loading under plane strain conditions [Zhao et al., 2020]. According to [McClung, 1991], the cyclic plastic zone size is assumed to be equal to the radius of the zone starting from the crack-tip to the boundary of the plastic zone along the crack direction, see Fig. 6.17e. Such a plastic zone is finally expected to leave behind a plastic wake of increasing size as long as the crack grows.

In order to track the crack length and evaluate the corresponding crack growth rate, the position of the crack-tip after each remeshing step is recorded (based on its coordinates w.r.t. to the initial configuration). In parallel, the displacements and resulting efforts at the upper boundary of the specimen with corresponding time are also recorded at each time increment in order to plot the FCG curve in Fig. 6.16.

A noticeable result is the quasi-linear trend of the FCG curve with increasing ΔK. This evidences a stable propagation regime that can be assimilated to a Paris regime. This assimilation is supported by the fact that the crack is sufficiently long ($a \geq 500\,\mu\text{m}$). The process hence belongs to the fatigue crack propagation of long cracks, as discussed in sub-sect. 1.1.3.

Finally, one can notice that the use of this continuous-discontinuous transition (CDT) method for crack growth modeling through remeshing needs to be well controlled before any conclusion to be

drawn. Apart from the proper calibration of the parameters for the damage model, the specific choice for the parameters associated with the MR algorithm, see sub-sect. 6.3.1.3 (ℓ_{inc}, $\overline{D}_{th}^{MR}$, $\underline{\nabla}\overline{D}_{th}^{\star}$, $\overline{D}^{crit}$, $\Delta\theta$) also needs to be carefully handled. The use of such a complex modeling approach hence requires sufficient confidence in the parameters to ensure robustness and consistency of the numerical results, since several sources of error can affect the overall result. However, the proposed CDT strategy seems appropriate to model FCG. The inclusion of discontinuities into a regularized strain-softening continuum model allows the entire failure process, from the onset of inelastic strain to complete failure, to be modeled effectively.

6.3.2.2 Mesh-convergence analysis for long fatigue crack growth

In the present sub-section, a mesh convergence analysis is first performed. The same FCG problem has been simulated for three minimum element sizes, namely $h_{min} = 0.015$, 0.01 and 0.005 mm.

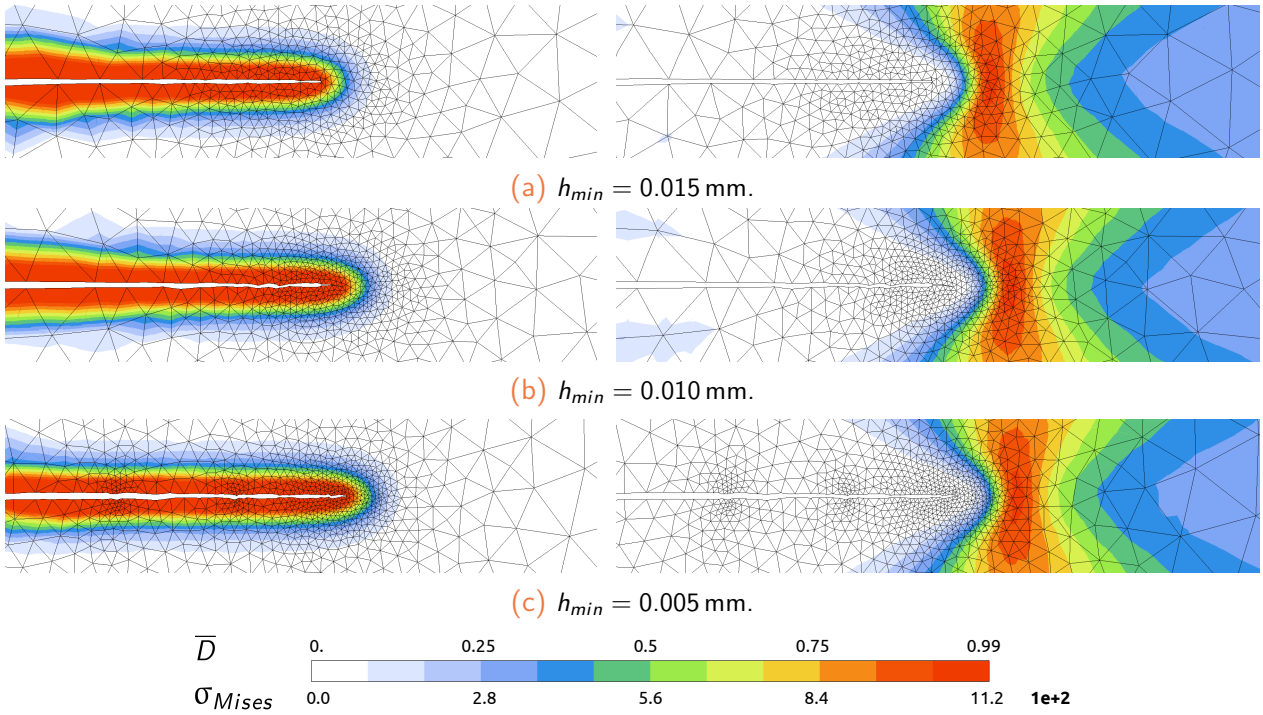

Figure 6.18: Distribution of the non-local damage for the three different mesh sizes at maximum load of the 700th cycle (c2d6r 4-fields FE - view at contours).

In Fig. 6.18 & Fig. 6.19, the contours of the non-local damage and Von Mises stress fields for the three discretizations are reported (on the left and on the right images, respectively) at cycle 700 and 850. One can see that the non-local damage admits comparable iso-contours at the 700th cycle. The coarser mesh exhibits a slight delay, Fig. 6.18a, compared to the two finest discretizations, Fig. 6.18b & Fig. 6.18c. The equivalent stress profiles are nearly the same, with a vanishing level in the wake of the crack. Let us also note the change in mesh size has a slight effect of the predicted gradients at the crack-tip, Fig. 6.18a - Fig. 6.18c (right hand-side images).
For the cycle 850, since the crack is longer, the Von Mises stress levels are correspondingly higher, Fig. 6.19a - Fig. 6.19c (right hand-side images). The difference in terms of crack length is a little

bit more noticeable, see Fig. 6.19. The two finest mesh size (10 & 5 µm) exhibit almost the same crack length while the delay of the coarser mesh is more pronounced.

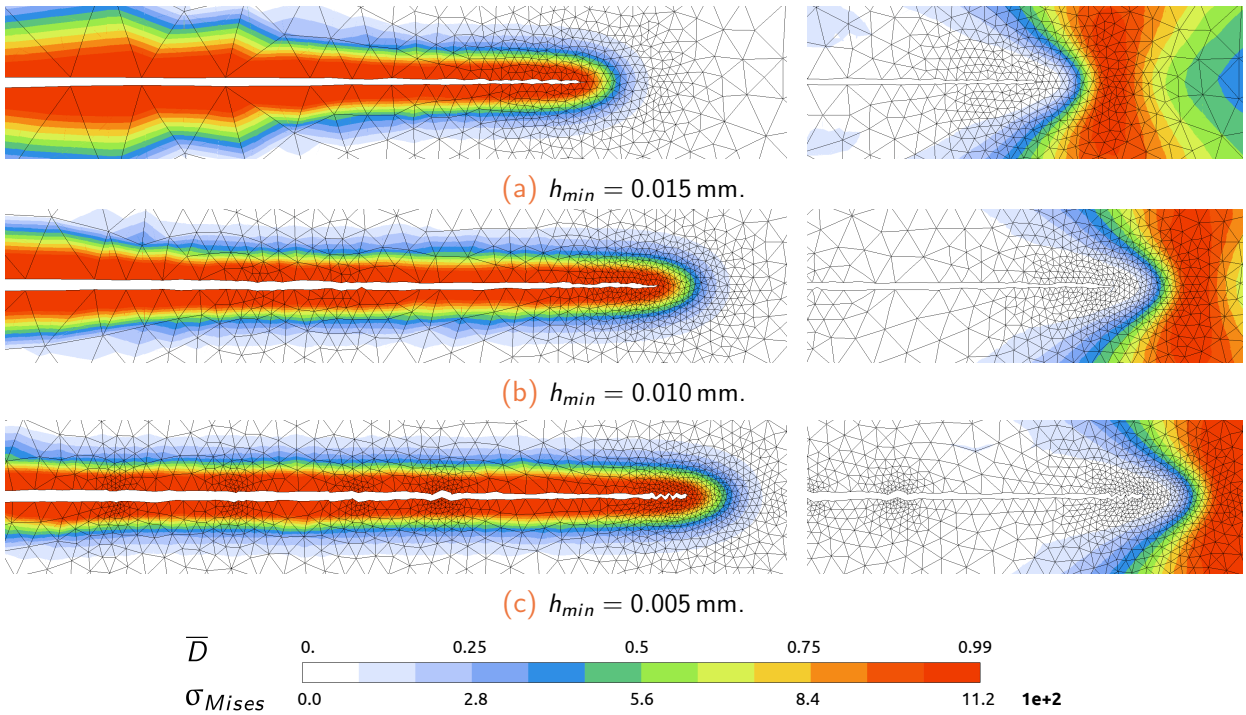

Figure 6.19: Distribution of the non-local damage for the three different mesh sizes at maximum load of the 850th cycle (c2d6r 4-fields FE - view at contours).

These last observations are consistent with the evolution of the crack length for the three simulations given in Fig. 6.20. Let us note that each point of the plots Fig. 6.20a & Fig. 6.20b corresponds to a single remeshing procedure associated with a crack increment, since the crack length remains constant between two remeshing steps. In Fig. 6.20a, one can observe that the crack lengths are very close for the different minimal sizes and seem to converge upon mesh refinement, Fig. 6.20b. The difference in the number of loading cycles to reach the same crack length (between the two smallest element sizes) is approximately of ~ 10 cycles, which is reasonable compared to the large number of loading cycles that are considered in LCF conditions. Moreover, one can notice in Fig. 6.20c that the smaller the imposed mesh size in the FPZ, the shorter the fatigue life, which seems physically acceptable since the energy required to break large elements is necessarily higher than that required to break small ones.
In Fig. 6.20c, the FCG curves are reported in a da/dN vs. ΔK diagram. One can easily see in this plot a quasi-linear evolution of the FCG rates, which seems to indicate a stable crack growth regime. The Paris lines are also reported. The fact that they exhibit almost the same slope confirms that similar crack growth rates are obtained for the three mesh sizes.

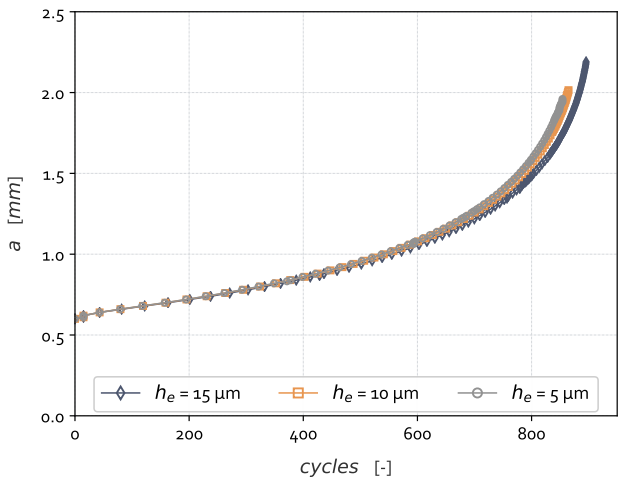

(a) Crack lengths.

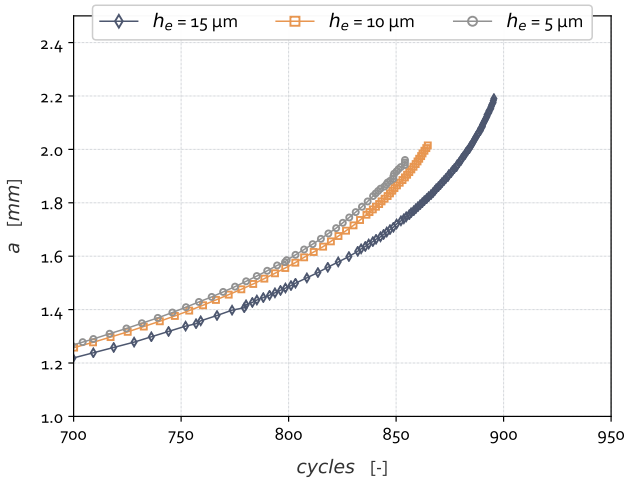

(b) Crack lengths (close-up view).

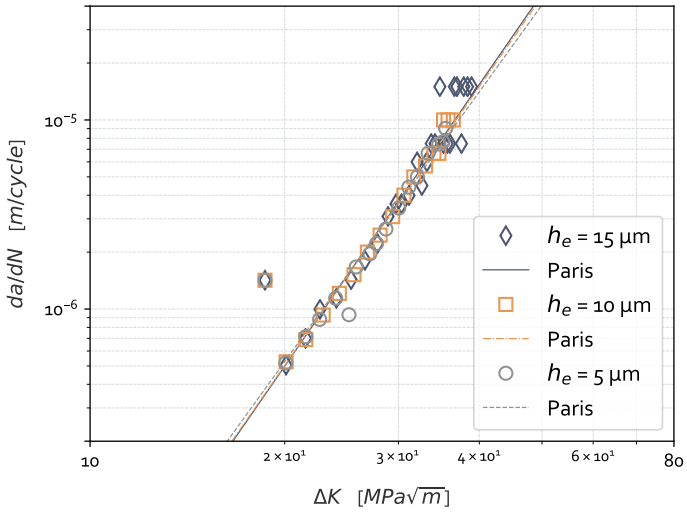

(c) Fatigue crack growth curves.

Figure 6.20: Mesh convergence analysis on a SEN-T specimen under fatigue loading conditions at 700°C (sinus 1 Hz, 400 MPa, $R_\sigma = 0.05$, plane strain conditions, p2-p1 FE).

6.3.2.3 Mesh coarsening process

In Fig. 6.21, the distribution of accumulated plasticity in the wake of the crack at several instants is reported. One can notice the accumulation of plasticity along the lips of the crack. As long as crack advances, the mesh is refined ahead of its tip, while the wake is progressively coarsened thanks to the error-based mesh adaption strategy. This coarsening is due to the absence of damage evolution: the error is thus not significant in these areas. One can notice that the successive coarsening procedures together with field transfer steps have made the distribution less regular in the wake of the crack. However, since there is no more evolution of the mechanical fields in these areas and the material has lost almost all its carrying capacity, the incidence on the overall energy of the structure is minimal.

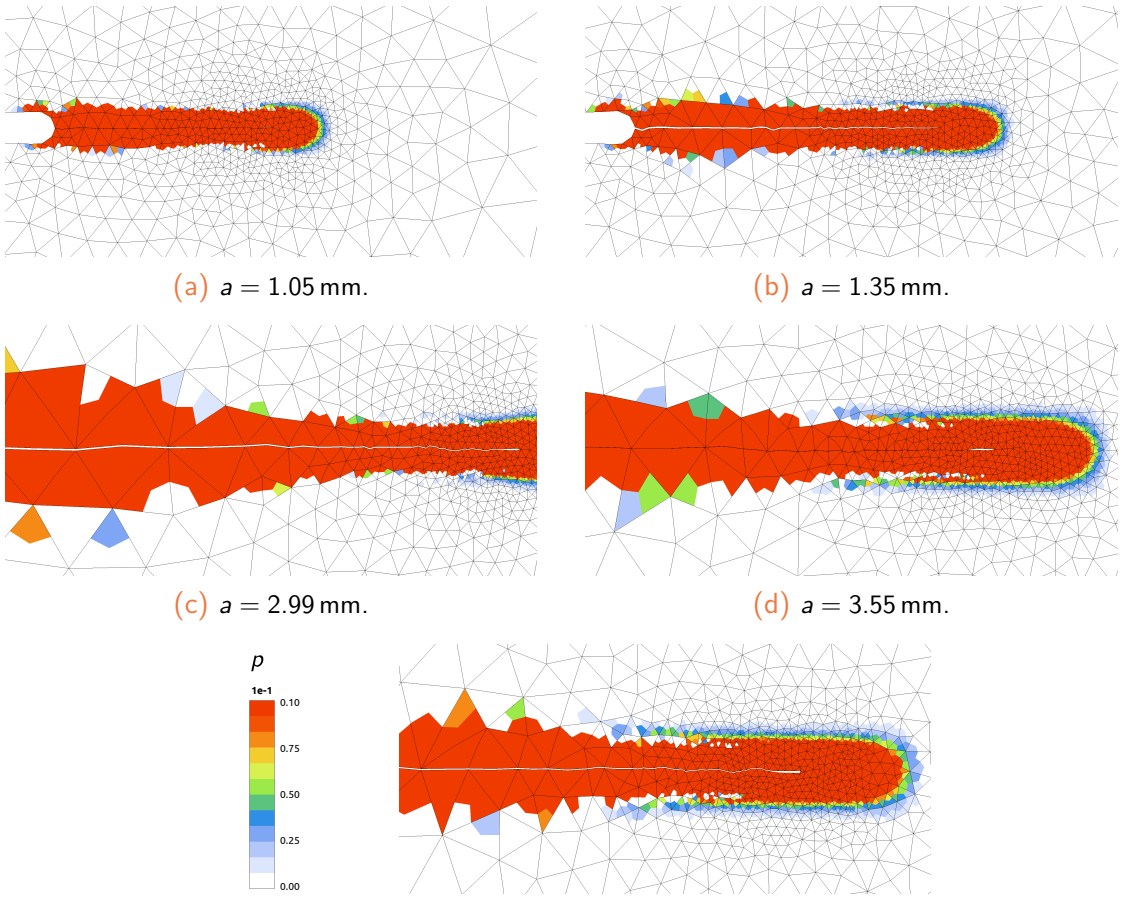

(a) $a = 1.05\,\text{mm}$. (b) $a = 1.35\,\text{mm}$.

(c) $a = 2.99\,\text{mm}$. (d) $a = 3.55\,\text{mm}$.

(e) $a = 4.07\,\text{mm}$.

Figure 6.21: Accumulated plasticity in the wake of a growing crack at several instants of a pure fatigue loading scheme (c2d6r 2-fields FE).

6.4 Sensitivity analysis for the fatigue model

The aim of this section is to assess the predictive capabilities of the fatigue damage model and its sensitivity to extrinsic parameters, that are: the temperature, the load ratio, the loading frequency and the over-load effect. Such a sensitivity analysis is performed on a structural calculation similar to that described in sub-sect. 6.3.1 which served for the validation of the approach in sub-sect. 6.3.2.

The damage model has been seen in sub-sect. 4.2.3 to be governed by some material parameters (*e.g.* S_f, m_f and β_f for fatigue damage, eq. (4.47)). A change in one of these parameters should result in a change in the FCG process. Such a point will be assessed in sub-sect. 6.4.2.
Moreover, the fatigue crack growth response of the material upon testing revealed a sensitivity to the loading conditions, also referred to as the *extrinsic parameters* (see also the sub-sect. 1.3.1 in the literature review). Thus, in the following, the change of temperature, load ratio, loading frequency, or prescribed boundary conditions are assessed in a qualitative manner. Moreover, a testing loading scheme including some overloads is also discussed. To this end, either material parameters (in sub-sect. 6.4.2) or loading modes will be varying in the calculations (in sub-sect. 6.4.3).

At last, let us note that some parameters related to either the mesh-adaptivity procedure or to the *Marching Ridges* algorithm may change in the following sub-sections. This point, independent from any physical aspect, comes from the numerical assessment of the method and possible encountered convergence issues. Since the model has been proved to provide mesh-converged results, sub-sect. 6.3.2.2, a change in these numerical parameters (*e.g.* ℓ_c, h_{min} or ℓ_{inc}) should not result in a significant change in the overall response of the model.

6.4.1 Preliminary remarks

Before discussing numerical calculation results, it is important to point out the fact that the simulations exposed in what follows have been run with arbitrary parameters for the damage model. Indeed, the consistent calibration of the damage model parameters associated with each damage mechanism (fatigue, creep and ductile) have not been yet calibrated.
There are two reasons for this lack of calibration: the first comes from the necessity to cope with long calculations to simulate 10^4 to 10^5 cycles, which is out of the present capabilities of the numerical work. For this purpose, some specific numerical tools need to be addressed in order to accelerate the analysis, like cycle-jump techniques. This could be done in further developments.
Moreover, the robustness of the present FCG modeling had to be first evaluated and improved prior to the "automatic" use of the whole strategy. The error-based mesh-adaption strategy together with the crack insertion strategy through mesh intersection also rely on user-defined parameters which additionally had to be assessed through benchmark tests. This took a significant time, explaining the absence of a proper calibration for constants of the damage model. Nevertheless, the proposed modeling approach can still be assessed in FE calculations to evaluate the predictive capabilities of the non-local model together with the CDT method under cyclic loading cases, at least in a qualitative manner.
A critical discussion and suggestions for the calibration strategy of the non-local damage model will be given in sect. 6.6.

6.4.2 Fatigue damage parameters sensitivity analysis

When considering pure fatigue loading conditions, the variable which is responsible for the FCG process is the fatigue damage, through its non-local form $\overline{D}$. As indicated in eq. (4.47), the fatigue damage evolution is closely related to the resistance parameter S_f and the viscoplastic activity through $\dot{p}$. In this paragraph, the effect of the fatigue damage resistance parameter S_f on the overall FCG rate is quantitatively assessed.

In Fig. 6.22a, the evolution of the crack length w.r.t. the loading cycles is reported for two values of S_f. As expected, the lower the fatigue damage resistance S_f, the faster the crack advance and consequently the lower the fatigue lifetime. Paying attention to the FCG curves in Fig. 6.22b, one can see that a linear regime is evidenced for both cases ($S_f = 0.3$ or $0.5\,\text{MPa}$). Looking at the Paris lines, a higher slope is noticeable for $S_f = 0.3\,\text{MPa}$ which results in a faster crack growth at a given ΔK.

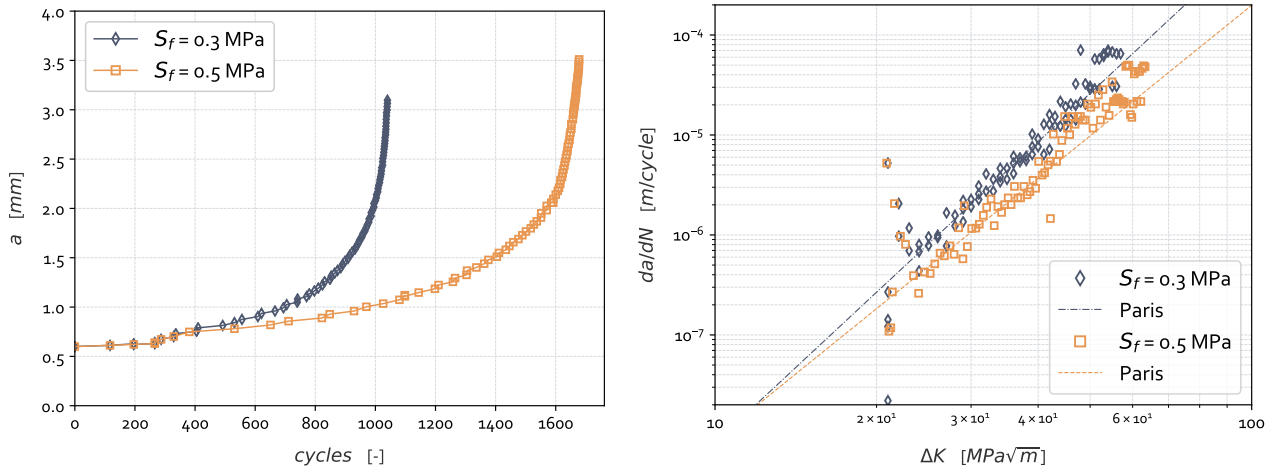

(a) Crack lengths. (b) Fatigue crack growth curves.

Figure 6.22: Effect of the fatigue damage resistance S_f on the FCG on a SEN-T specimen under pure fatigue loading conditions at 550°C (sinus 1 Hz, $u_y = 0.05$ mm, $R_{u_y} = 0.05$, plane strain conditions, p2-p1 FE).

Once this feature of the model has been assessed, let us note that in the remaining of this work, a sufficiently low value of S_f has been intentionally chosen. Such a choice comes from the requirement to perform FCG numerical simulations over a limited number of loading cycles ($N < 2000$) in order to limit computational demand.

6.4.3 Sensitivity of the model to extrinsic parameters

In this sub-section, the influence of temperature, load ratios, loading frequencies, prescribed boundary conditions and over-loads are discussed in accordance with the model capabilities.

6.4.3.1 Temperature effect on FCG

As detailed in sect. 2.4, the cyclic material model has been calibrated for three target temperatures, namely 20, 550 and 700°C. Consequently, in the following, a cyclic FCG simulation has been run for each testing temperature with the same numerical parameters, see Tab. L.1 in the appendix. In order to study the effect of temperature on the FCG, only the material behavior parameters are changed (while the material damage parameters are kept constant). The smallest FE size has been set to $h_{min} = 0.05$ mm and the internal length to $\ell_c = 0.15$ mm.

In the Fig. 6.23a, the crack lengths are reported. One can notice a significant distinction between each loading temperature. As expected, lower temperatures induce longer crack fatigue lives. This result was expected. Indeed, as discussed in Chap. 2, the material's stiffnesses (elastic modulus and kinematic hardening moduli) tend to decrease as the temperature increases. As a consequence, the mechanical resistance of the material decreases. Moreover, strain-hardening mechanisms are

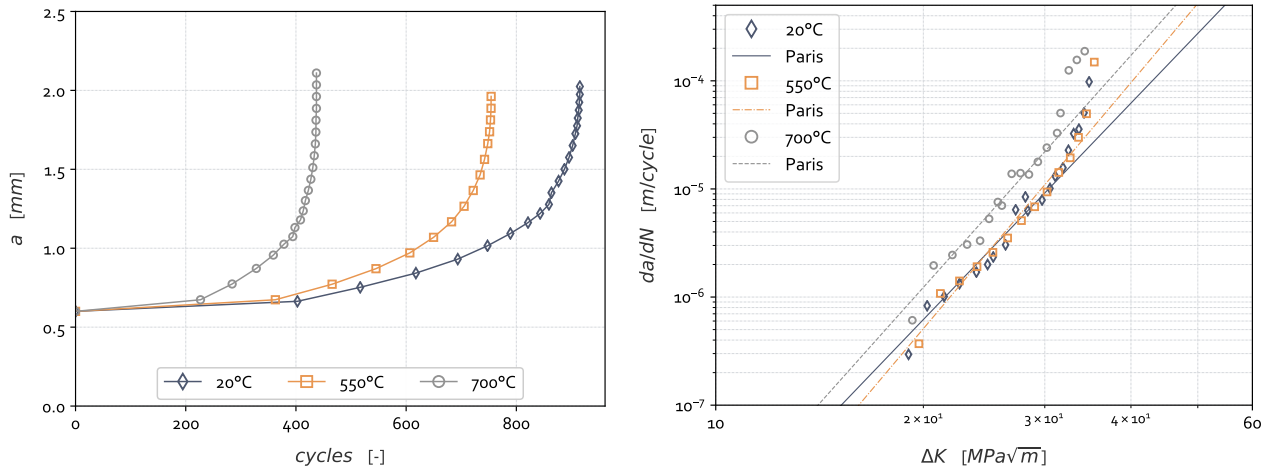

(a) Crack lengths. (b) Fatigue crack growth curves.

Figure 6.23: Temperature effect on the FCG on a SEN-T specimen under pure fatigue loading conditions (sinus 1 Hz, 400 MPa, $R_\sigma = 0.05$, plane strain conditions, p2-p1 FE).

also less important with temperature increase.

In Fig. 6.24, experimental results on the FCG behavior of FG AD730™ are depicted. The temperature effect in pure fatigue conditions is clearly evidenced. The difference in terms of FCG rates is even more pronounced, since in real conditions, time-related effects are (obviously) accounted for, while they are not in the simulation. However, the slope of the Paris line in each case can be seen to be almost identical, as also evidenced in Fig. 6.23b.

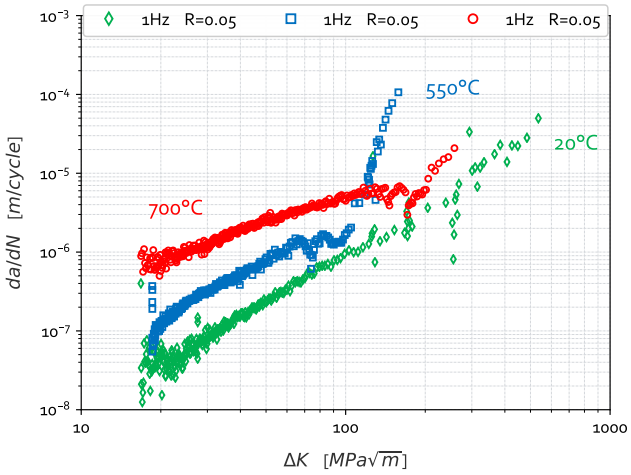

Figure 6.24: Effect of temperature on the pure fatigue crack growth behavior of FG AD730™.

Remark: The present study is meant to be only qualitative. Indeed, in the present case, only the fatigue damage effect has been accounted for in the calculation. At high temperatures, especially 700°C, time-driven processes (creep, oxidation...) should enforce damage growth, consequently yielding to higher crack growth rates and lower fatigue lives. Damage parameters are also not supposed to be the same for each temperature.

6.4.3.2 Effect of applied boundary conditions on FCG

In the present sub-section, the effect of the different load control (either in stress or displacement control) is assessed. Corresponding parameters are reported in Tab. L.2. The min. element size was set to $h_{min} = 0.01\,\text{mm}$ and the internal length scale to $\ell_c = 0.03\,\text{mm}$.
In Fig. 6.25a, the evolution of the crack length as a function of the loading cycles is reported. One can see that the displacement-controlled test yields a longer fatigue life. In the Fig. 6.25b, the FCG curves are reported in a da/dN vs. ΔK frame. One can see that the stress-controlled exhibits a higher slope in the Paris regime, which is consistent with the previously observed faster crack growth rate.

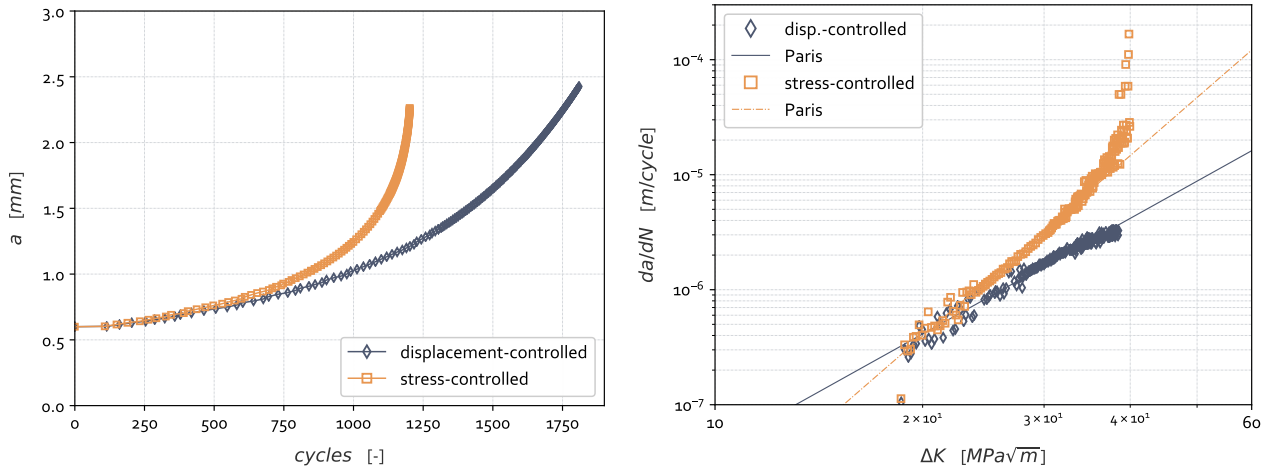

(a) Crack lengths. (b) Fatigue crack growth curves.

Figure 6.25: Effect of the prescribed boundary conditions on the FCG on a SEN-T specimen under pure fatigue loading conditions at 550°C (sinus 1 Hz, $R_{\sigma/u_y} = 0.05$, plane strain conditions, p2-p1 FE).

A possible explanation for the difference in FCG rates can be that when loading is stress-controlled (*i.e.* force-controlled), the SIF is always increasing, hence leading to a faster crack growth with increasing ΔK. This is not the case with displacement-controlled loading which may allow a deceleration of the crack advance.

Finally, as a prospective point, it should be interesting in forthcoming works to use the real kinematics fields obtained, *e.g.* through Digital Image Correlation (DIC), as prescribed boundary conditions to the structural case. This way, the simulation should reach a higher degree of fidelity with respect to the real applied BC and the crack advance should be predicted with an improved accuracy.

Remark: one can remark for the highest ΔK an asymptotic tendency of the curve (which is generally known to be related to the fracture toughness ΔK_c). In the present case, the real fracture toughness of the material that represents a threshold before unstable crack propagation has not been reached. The instability of the calculation comes from a too significant damage rate in the FPZ (coming from a too low fatigue damage resistance parameter S_f). The damage parameters have been lowered so as to enforce a faster crack propagation and to limit the CPU time. However, the global trends before unstable crack growth are well transcribed.

6.4.3.3 Effect of load ratio on FCG

In this sub-section, the load ratio effect is studied. The same loading case has been simulated with three different positive loading ratios, namely $R_\sigma = 0.05$, 0.07 and 0.12. These load ratios can be seen to be close each others. Such a choice comes from the necessity to perform FCG calculation over a reasonable number of loading cycles. To do so, fatigue damage parameters have been intentionally set low, as previously said in sub-sect. 6.4.3.2. This low values for the damage parameters have resulted in convergence issues since damage increases fast. This explains why almost similar load ratios have been considered in this preliminary step.
Let us note that negative load ratios have not been considered in this work since crack-lips closure mechanisms could intervene (not considered in the present study). The stress amplitude is kept unchanged and corresponds to $\Delta\sigma/2 = 190\,\text{MPa}$. Consequently, the minimum and maximum stress levels evolve ($\sigma_{max} = 400$, 410 and 430 MPa, respectively), and since the load ratio is increased, the mean stress follows the same trend. Simulations are run with material parameters of AD730™ at 550°C, $h_{min} = 0.01\,\text{mm}$ and $\ell_c = 0.03\,\text{mm}$. The others material parameters are reported in Tab. L.3.

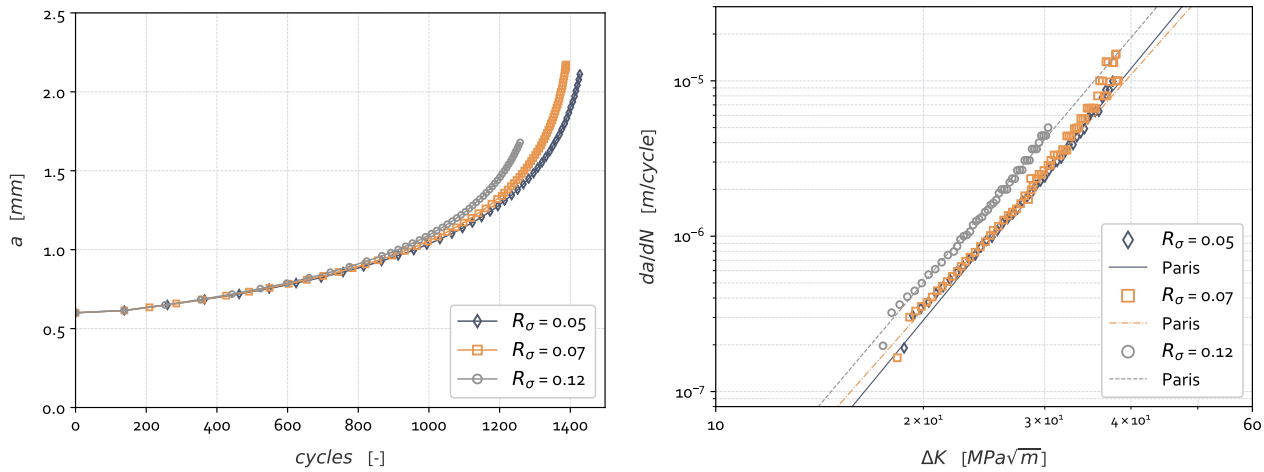

(a) Crack lengths.

(b) Fatigue crack growth curves.

Figure 6.26: Load ratio effect on the FCG on a SEN-T specimen under pure fatigue loading conditions at 550°C (sinus 1 Hz, $\Delta\sigma/2 = 190\,\text{MPa}$, plane strain conditions, p2-p1 FE).

As expected, a higher load ratio yields a lower fatigue lifetime, Fig. 6.26a. Indeed, the mean stress being higher in case of high load ratio, material is more prone to develop plastic strains and then to degrade. Let us also note that since there is only a slight difference between the case with $R_\sigma = 0.05$ and that of 0.07, there is no significant difference in the FCG curves, see Fig. 6.26b. The slope for each Paris regime is almost similar.

6.4.3.4 Effect of the loading frequency on FCG

In this sub-section, the effect of the loading frequency on the FCG is investigated. Simulations are run with material parameters of AD730™ at 550°C, with $h_{min} = 0.05\,\text{mm}$ and $\ell_c = 0.15\,\text{mm}$. The loading is stress-controlled with an applied stress of 400 MPa at the upper boundary (see

Fig. 6.15). Three loading frequencies are prescribed, that are 0.1, 1 and 5 Hz. The others material parameters are reported in Tab. L.4.

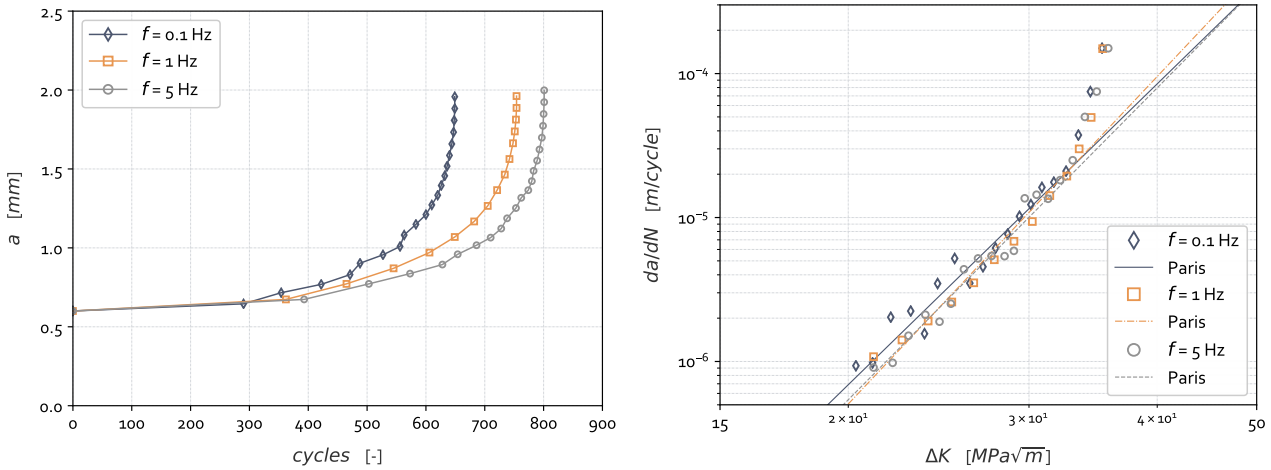

(a) Crack lengths.

(b) Fatigue crack growth curves.

Figure 6.27: Effect of loading frequency on the FCG on a SEN-T specimen under pure fatigue loading conditions at 550°C (sinus 0.1, 1 & 5 Hz, $\sigma = 400$ MPa, $R_\sigma = 0.05$, plane strain conditions, p2-p1 FE).

One can remark in Fig. 6.27a that the lower the loading frequency, the shorter the fatigue lifetime. However, looking at the FCG curves in Fig. 6.27b, one can notice that there is no significant difference in the slopes of the $da/dN - \Delta K$ curves in the Paris regime. The crack growth rates seem to be almost equivalent. Thus, it seems there is no clear difference in FCG rates with evolving loading frequency.

Normally, under pure fatigue loading conditions, the frequency effect is not that pronounced as long as the frequency is sufficiently high (so as for time-dependent processes not to occur) [Fessler, 2017]. In the present study, only the fatigue damage D_f is active and contributes to the total non-local damage $\overline{D}$. It has been reported page 176 during the parametric study related to the cyclic damage model, more particularly in Fig. 4.10, that a slight frequency effect is intrinsically included in the model since the unified viscoplasticity theory enables the introduction of an over-stress which is responsible for a time-dependency of the mechanical response. In addition, since the inelastic flow is responsible for the fatigue damage evolution, the change in loading rate results in a change in the viscoplasticity activity and a change in the fatigue damage evolution.

In order to evidence the difference in material response with the change in loading frequency, the Von Mises stress fields for the three loading frequencies are depicted in Fig. 6.28. One can remark a higher stress level for the lowest loading frequency, which induces a longer crack length.

This effect could be also illustrated by the evolution of the viscoplastic multiplier $\dot{\lambda}$ (and consequently the viscoplastic zone at the crack-tip) as reported in Fig. 6.29. One can notice a larger viscoplastic zone for the lowest loading frequency of 0.1 Hz. As a result, the increment of non-local damage $\dot{\overline{D}}$ is larger in this case, Fig. 6.30, hence leading to a higher FCG rate and a lower fatigue lifetime.

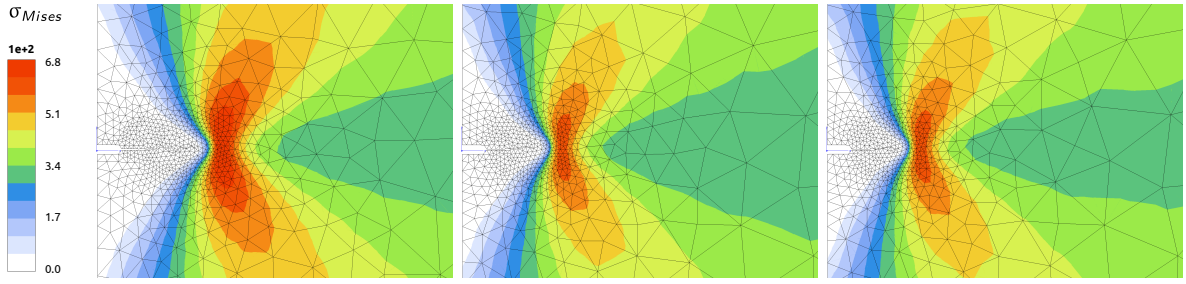

(a) 0.1 Hz - $a = 1.21$ mm. (b) 1.0 Hz - $a = 0.87$ mm. (c) 5.0 Hz - $a = 0.83$ mm.

Figure 6.28: Von Mises stress level at peak level of the 600$^{\text{th}}$ cycle for the three different loading frequencies (c2d6r 2-fields FE).

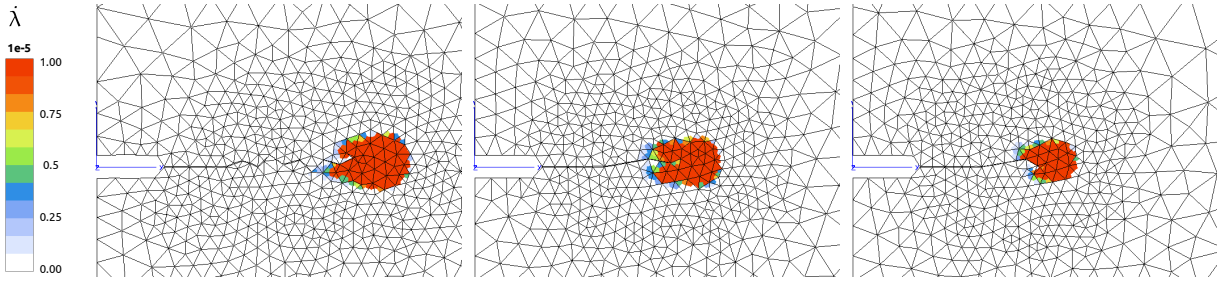

(a) 0.1 Hz - $a = 1.21$ mm. (b) 1.0 Hz - $a = 0.87$ mm. (c) 5.0 Hz - $a = 0.81$ mm.

Figure 6.29: Increment of the viscoplastic multiplier at peak level of the 600$^{\text{th}}$ cycle for the three different loading frequencies (c2d6r 2-fields FE).

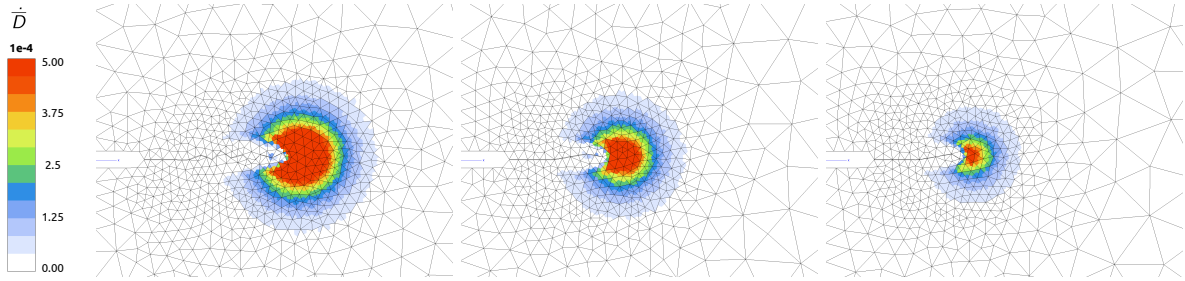

(a) 0.1 Hz - $a = 1.21$ mm. (b) 1.0 Hz - $a = 0.87$ mm. (c) 5.0 Hz - $a = 0.81$ mm.

Figure 6.30: Increment of non-local damage at peak level of the 600$^{\text{th}}$ cycle for the three different loading frequencies (c2d6r 2-fields FE).

6.4.3.5 Overload effect on FCG

In this sub-section, an attempt to simulate the effect of several over-loads (OL) on the FCG in pure fatigue loading conditions is investigated. Simulations have been run with material parameters of AD730$^{\text{TM}}$ at 550°C, with $h_{min} = 0.01$ mm and $\ell_c = 0.03$ mm. The loading is stress-controlled with an applied stress of 400 MPa and two successive 20% over-loads every 20 loading cycles. A schematic view of the loading scheme is reported in Fig. 6.31. The others material parameters are reported in Tab. L.5.

Generally, it is commonly observed in metallic materials that application of a (moderate) over-load gives rise to a so-called *long range effect*, that is, a retardation of the crack advance. Such a mechanism has been extensively studied in the literature [Willenborg et al., 1971], [Wheeler, 1972]. This effect is generally attributed to crack-closure mechanisms associated with compressive stresses in the plastic zone that has been generated during the over-load and left in the wake of a growing crack [Bathias and Pineau, 2010].

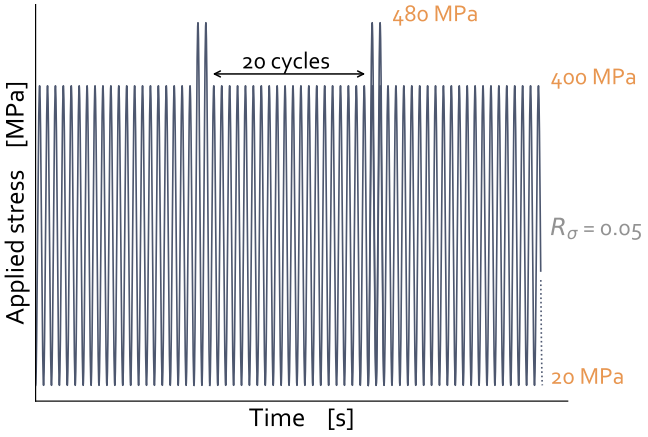

Figure 6.31: Loading signal with successive over-loads.

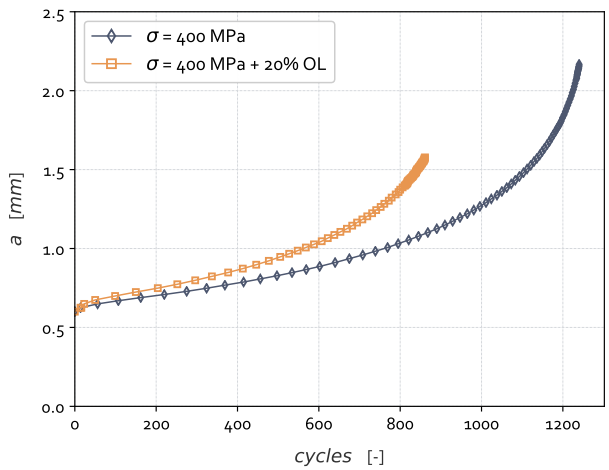

(a) Crack lengths.

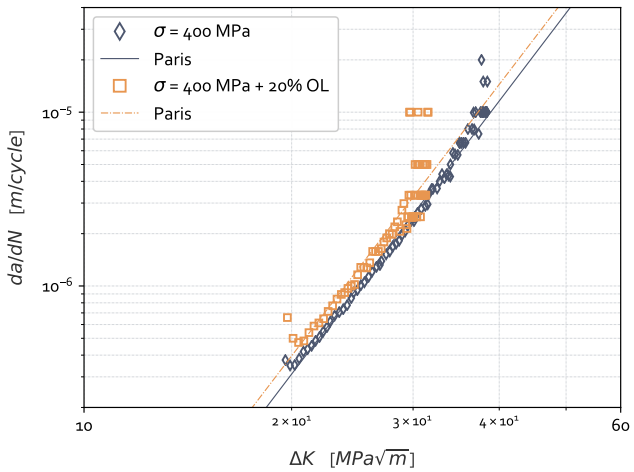

(b) Fatigue crack growth curves.

Figure 6.32: Effect of several overloads on a nominal FCG test on a SEN-T specimen under pure fatigue loading conditions at 550°C (sinus 1 Hz, $\sigma = 400$ MPa, OL 20%, $R_\sigma = 0.05$, plane strain conditions, p2-p1 FE).

In the present case, an unexpected effect is observed, since as one can notice in Fig. 6.32, a shorter fatigue lifetime is obtained if material has experienced some OL. In my model, this can be explained by the fact that the fatigue damage is governed by the accumulated plasticity. The occurrence of over-loads automatically results in much more yielded (plastic) material points in the FPZ. Even if strain-hardening mechanisms are favored in these zones, fatigue damage is more prone to increase, hence resulting in more degraded elements and faster crack growth. The Fig. 6.33 - Fig. 6.35 illustrate the increase in damage induced by the over-loads. In Fig. 6.33, the iso-contours for the Von Mises equivalent stress are depicted. A higher stress level is reached once an OL is applied, Fig. 6.33b. As a consequence, the viscoplastic activity at the crack-tip is slightly higher in this case, Fig. 6.34b, and the resulting non-local damage increment follows the same trend, Fig. 6.35b.

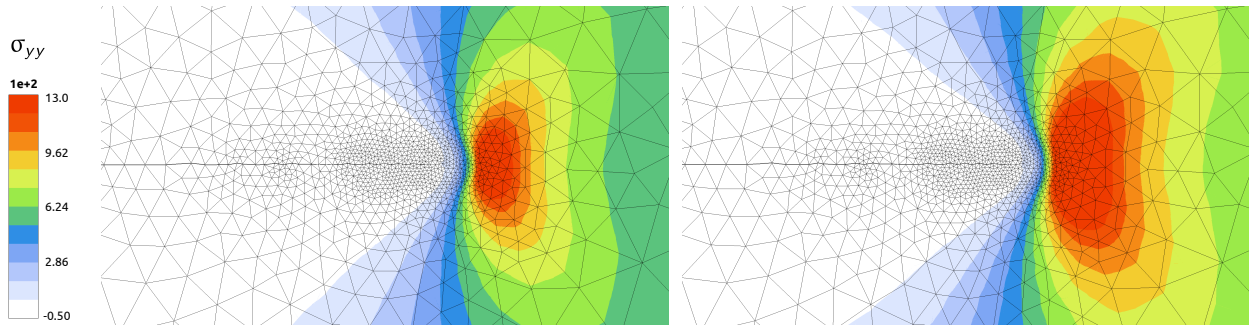

(a) nominal loading - cycle 775. (b) 20% over-load - cycle 776.

Figure 6.33: Distribution of the stress σ_{yy} during the nominal loading (cycle 775) and a 20% over-load (cycle 776) of a pure fatigue loading scheme (c2d6r 2-fields FE).

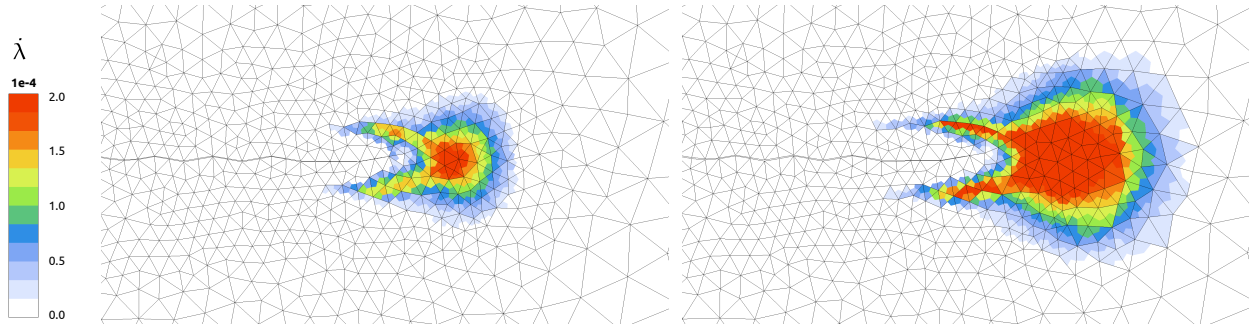

(a) nominal loading - cycle 775. (b) 20% over-load - cycle 776.

Figure 6.34: Increment of the viscoplastic multiplier $\dot{\lambda}$ during the nominal loading (cycle 775) and a 20% over-load (cycle 776) of a pure fatigue loading scheme (c2d6r 2-fields FE).

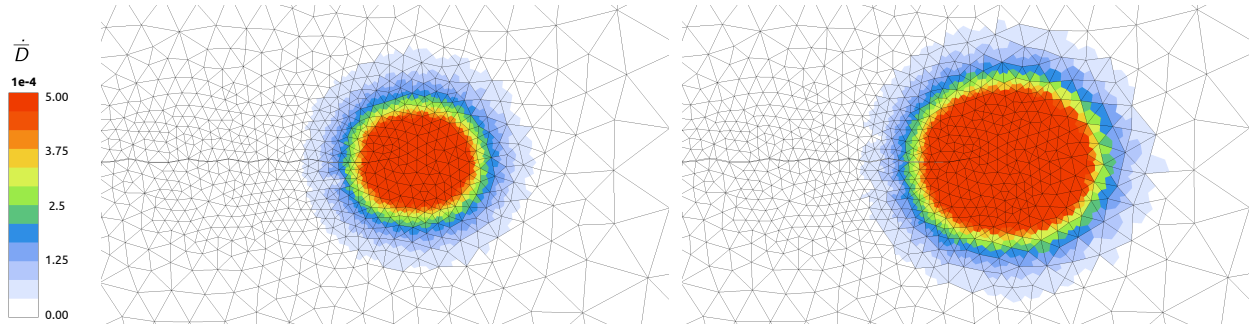

(a) nominal loading - cycle 775. (b) 20% over-load - cycle 776.

Figure 6.35: Increment of the non-local damage $\dot{\overline{D}}$ during the nominal loading (cycle 775) and a 20% over-load (cycle 776) of a pure fatigue loading scheme (c2d6r 2-fields FE).

This deficiency of the model to reproduce the over-loads effect on the crack propagation must be corrected in order to be able to simulate complex loads, but this will require a reassessment of some choices that have been made on the variables that drive the fatigue damage.

6.5 Creep-fatigue loading case

In the present sub-section, the SEN-T specimen is now subjected to tension at the upper edge, fixed at the bottom and assumed under plane strain conditions, as depicted in Fig. 6.15a. The loading scheme consists in a trapezoidal waveform at $R_\sigma = 0.05$ with $\sigma_{max} = 400\,\text{MPa}$, loading ramps of 10 s and dwell-periods of $\Delta t = 300\,\text{s}$, see Fig. 6.36. The purpose of this final calculation is the assessment of the predictive response of the model to the introduction of dwell-times. Here, both fatigue and creep damage mechanisms are activated (still with arbitrary values for the evolution laws). Few loading cycles have been simulated, but general trends can nevertheless be analyzed. In addition, because of convergence issues when starting from a pre-crack (due to excessive distortion of elements at crack-tip during crack onset), calculation has been performed starting from the notch of the SEN-T specimen (*i.e.* not from a pre-crack as in the previous examples). Numerical parameters have been set to $h_{min} = 0.05\,\text{mm}$ and $\ell_c = 0.15\,\text{mm}$.

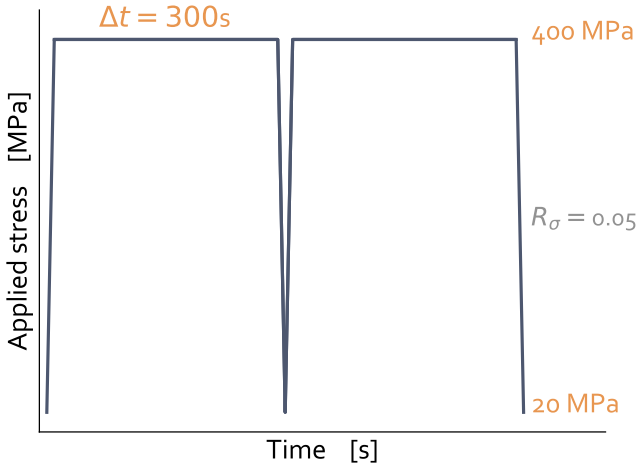

Figure 6.36: Creep-fatigue test loading signal

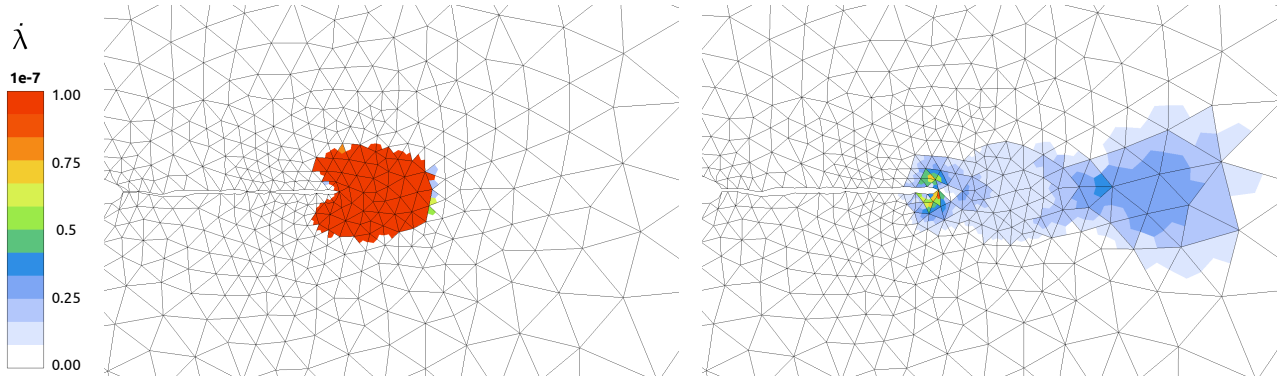

(a) Transient phase (loading). (b) Dwell-period.

Figure 6.37: Increment of the viscoplastic multiplier during the transient and dwell periods of a creep-fatigue loading scheme (cycle 56) at 550°C (c2d6r 2-fields FE).

In Fig. 6.37 increments of the viscoplastic multiplier during both the loading ramp (transient) and the dwell-period are presented. The crack length is of about $a \approx 1.43\,\text{mm}$. One can notice higher plasticity levels during the transient, Fig. 6.37a, compared to that during the dwell-period, Fig. 6.37b. In addition, for the loading ramp, the viscoplasticity is more localized close to the crack-tip while it is diffuse during the holding period. This is consistent with experimental observations evidencing a larger contribution to fatigue mechanisms during the transients and creep ones during the dwell periods [Fessler, 2017].

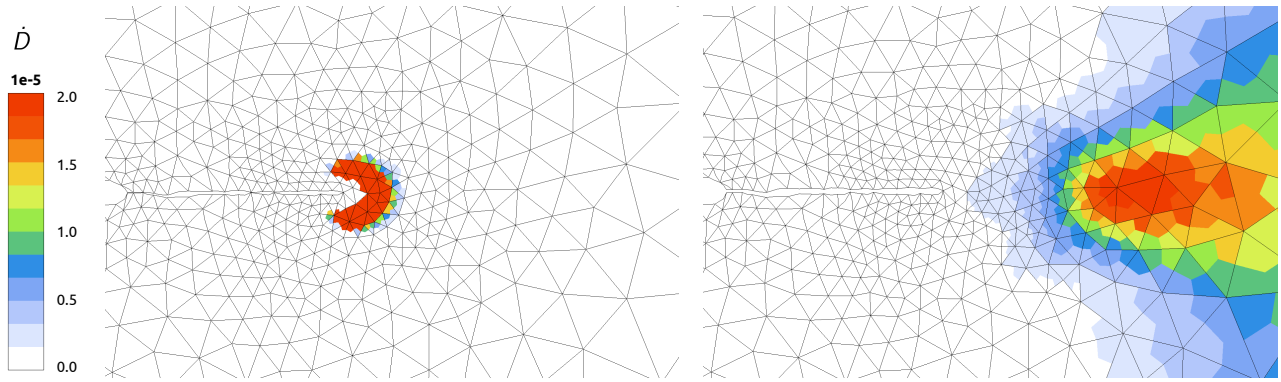

(a) Transient phase (loading). (b) Dwell-period.

Figure 6.38: Increment of local total damage during the transient and dwell periods of a creep-fatigue loading scheme (cycle 56) at 550°C (c2d6r 2-fields FE).

In Fig. 6.38, the increments of local total damage (fatigue + creep) are depicted, for the transient and the dwell-period. Consistently with the increment of viscoplasticity, the local damage increases significantly in the vicinity of the crack-tip, Fig. 6.38a. On the contrary, during the holding-time, damage is predominant in a larger zone, along the crack growth direction, Fig. 6.38b.

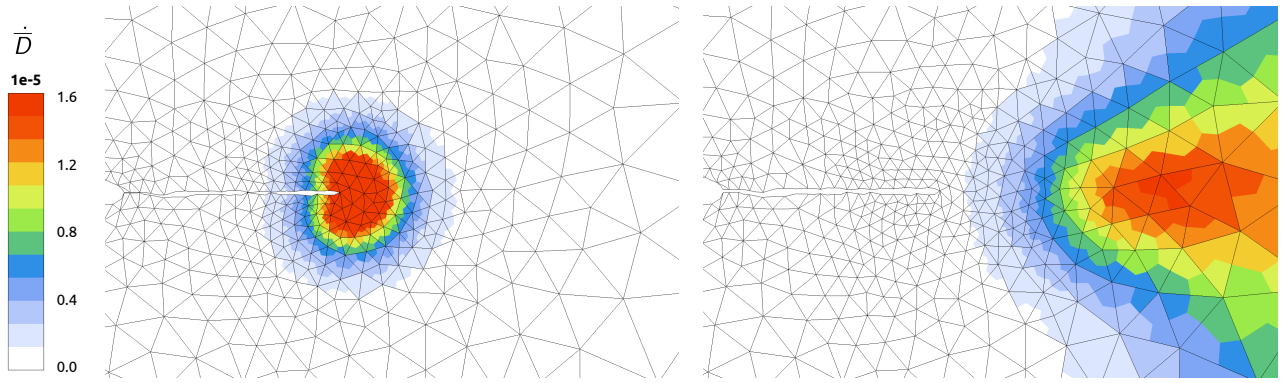

(a) Transient phase (loading). (b) Dwell-period.

Figure 6.39: Increment of non-local damage during the transient and dwell periods of a creep-fatigue loading scheme (cycle 56) at 550°C (c2d6r 2-fields FE).

Contour plots of the increment of the non-local damage are reported in Fig. 6.39. One point should be mentioned: owing to the unified formalism for the non-local extension, *i.e.* the use of a single internal length scale, the rate of change of the non-local damage follows the same trend as the source term (*i.e.* the local damage), no matter the governing mechanism. As a consequence, it is difficult to distinguish the fatigue contribution to the total damage and that of creep. The use of distinct auxiliary (output) variables associated with each damage increment would provide insight on this point.

Nevertheless, one can notice a significant increase of $\overline{D}$ during the dwell period, Fig. 6.39b, compared to that during the transient, Fig. 6.39a. Moreover, there is a slight difference between the increment of local and non-local damage during the hold-time, Fig. 6.38b & Fig. 6.39b respectively. This comes from two aspects: *i)* the absence of mesh refinement in the bulk which prevents

the non-local interaction from being well accounted for, and *ii)* the more diffuse aspect of creep processes relying on the stress field rather than plasticity.

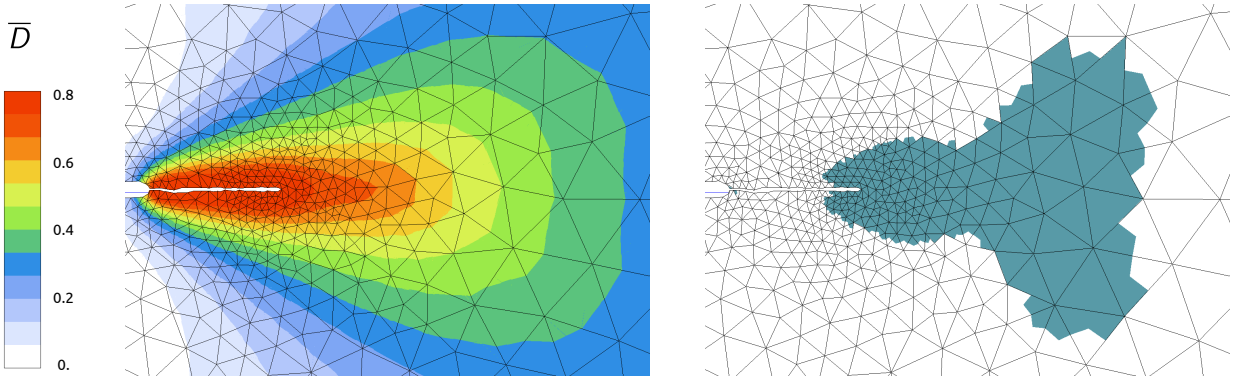

(a) $\overline{D}$ during the dwell-period. (b) Viscoplastic activity during the dwell-period.

Figure 6.40: Non-local damage field and viscoplastic zone during the dwell-period of a creep-fatigue loading scheme (cycle 56) at 550°C (c2d6r 2-fields FE).

The resulting non-local total damage field is plotted in Fig. 6.40a. It can be observed that the structure is largely affected by the damage field and mechanical properties start to degrade in a much larger zone than the crack-tip. The FPZ is no more localized in front of the crack-tip. In Fig. 6.40b, the viscoplastic zone size is reported. One can notice a larger zone size, also offset from the crack-tip, compared to the pure fatigue case (see *e.g.* Fig. 6.17), loosing the characteristic "butterfly" shape.

One comment can be given on the remeshing procedure. One can notice in Fig. 6.39 the absence of mesh-refinement ahead of the crack-tip. Even if damage increases in the bulk material, mainly due to creep damaging processes, the rate of change, and consequently the non-local damage level, are not sufficiently high to trigger a remeshing step. This may be a limit to the method which relies on a single non-local total damage threshold triggering mesh-adaption: depending on the main governing mechanism (creep or fatigue), the spatial distribution won't be the same (fatigue is more localized at the tip while creep is more diffuse). An extension of the error-based remeshing procedure could be to use a dual criterion to trigger remeshing: one relying on the non-local total damage, and the other one relying on the creep (local) damage contribution. This way, the mesh adaptivity could be more robust. Let us note that such a multi-criteria for the ZZ2 error estimation has already been implemented in Z-set [Feld-Payet, 2010] and can be assessed in short term works.

This last calculation evidences that the use of a single internal length is not as appropriate as expected since damage mechanisms are of differing nature and do not evolve in the same manner. Creep damage already being of diffusive-type as opposed to localized plasticity-induced fatigue (or ductile) damage seems to require the introduction of a dedicated characteristic length. The localizing aspect of creep damage mechanism in structural calculation still remains unstudied and represents a prospective issue to the present study.

6.6 Conclusion of the chapter

In this chapter, a continuous-discontinuous approach for fracture modeling in FE calculations in the context of fatigue loading has been proposed.
A FE strategy involving error-controlled adaptive mesh refinement has been considered. More specifically, h-adaptive remeshing steps aimed at producing smaller elements in areas where non-linearities (plasticity, damage...) evolve significantly and larger elements in linear regions or those where the damage does not evolve (notably in the wake of the crack). A better refinement of the FPZ throughout its evolution has provided a better description of the non-local damage field. Meanwhile, the coarsening of areas of vanishing stresses has allowed for CPU time to be saved.

In order for the crack advance to be suitably captured, a local crack path tracking algorithm has been used. It enabled to define a discrete and continuous crack path from the distribution of the non-local damage. Crack characteristics have hence been directly determined from the continuous model and therefore there was no need of identifying additional material parameters for fracture apart from those associated with the cyclic damage model.

Once the crack increment geometry has been estimated, a continuous-to-discontinuous transition is performed thanks to remeshing operations. A discrete crack is introduced once the damage has reached a critical value in some points of the structure. Thus, crack advance is a natural result of the material gradual degradation. In opposition to some existing exhaustion methods, crack increments of fixed length are introduced one at a time with intermediate equilibrium recovery steps so as to promote numerical robustness.

It has been shown that using this strategy in combination with the proposed non-local cyclic damage model enables to qualitatively capture some features associated with fatigue loading. This Ph.D. project has thus offered the possibility to make a bridge between the *Fracture Mechanics* and the *Continuum Damage Mechanics* frameworks. Global fatigue crack growth curves have been obtained thanks to long fatigue crack growth calculations using the FEM. Such results are worth highlighting since the use of continuous-to-discontinuous approaches in the context of fatigue still remains a tenuous field of research.

Besides, it has been shown that the global strategy for fatigue crack growth leads to mesh convergence upon mesh refinement. Then, consistent evolution of the cyclic plastic zone size has been evidenced. In addition, the sensitivity of the model to the extrinsic parameters (temperature, load ratio, loading frequency, over-load) has been assessed in sect. 6.4 and globally validates the strategy, although some points require further investigations. The model has been tested on a more complex loading scheme of dwell-fatigue type, hence including both fatigue and creep damages. Calculations have evidenced some limitations of the modeling approach, particularly in relation with the non-local interactions.

Finally, the proper calibration still remains to be achieved but this Ph.D. work has already provided some very encouraging results.

Résumé du chapitre en français

Dans ce dernier chapitre, une méthode de transition endommagement-rupture a été proposée pour simuler la propagation d'une fissure longue en fatigue. La loi d'endommagement non-locale développée au chapitre précédent a en effet permis de simuler la croissance de l'endommagement jusqu'à amorçage d'une macro-fissure, et ce, de manière continue. Néanmoins, afin de rendre compte du caractère discret du processus de fissuration, une fissure réelle doit être insérée dans le maillage de la structure de sorte à reproduire fidèlement la cinétique d'avancée de fissure.
Dans cette optique, un processus de raffinement de maillage a été mis en oeuvre afin d'optimiser les coûts de calcul associés à la simulation de spectres de chargements cycliques complexes. Basé sur le contrôle de l'erreur de discrétisation élément finis, ce processus de raffinement du maillage se veut adaptatif et agit en post-traitement du calcul. Il permet alors de raffiner le maillage dans les zones présentant de fortes non-linéarités matérielles (viscoplasticité, endommagement...), à savoir la zone d'élaboration en point de fissure, tandis que les zones élastiques sont discrétisées de façon plus grossière. Une fois le maillage optimisé et l'erreur de discrétisation contrôlée, la géométrie de l'incrément de fissure doit être estimée. Pour ce faire, un algorithme de suivi du chemin de fissure, le *Marching Ridges* déjà implémenté dans la suite *Z-set*, a été utilisé. Cet algorithme permet de suivre l'avancée de la pointe de fissure à l'aide de la recherche du front sur une ligne de crête. Une crête est composée des lieux successifs des maximums globaux d'un champ scalaire lissé associé à l'endommagement non-local. Ce dernier étant localisé dans la bande de localisation, dont la largeur est elle-même contrôlée par la longueur interne non-locale, l'algorithme de suivi de crête, utilisé en post-traitement du calcul, permet alors, d'une part, d'estimer la position du front de fissure suivant. D'autre part, un critère d'insertion basé sur un endommagement non-local critique permet, lui, de valider l'insertion de l'incrément de fissure. Lorsque ces conditions sont assurées, des outils d'intersection de maillage, développés à l'ONERA et disponibles dans *Z-set* via les outils *Z-cracks*, sont utilisés pour insérer l'incrément de fissure dans le maillage de la structure fissurée. Ensuite, une opération de transfert de champs est opérée. Le transfert des variables nodales s'effectue par interpolation standard, tandis que les variables internes, en lien avec l'histoire du chargement, sont transférées de manière directe à l'aide d'une approximation diffuse (sur un patch d'éléments) associée à une méthode des moindres carrés mobiles. Ces deux méthodes de transfert ont été choisies de sorte à minimiser la diffusion numérique. Suite à cette étape, la structure, alors hors-équilibre de par le transfert des champs de l'ancien vers le nouveau maillage, doit retrouver une solution à l'équilibre afin de garantir la convergence du solveur. Pour cela, une étape de rééqulibrage de la structure est réalisée avant la poursuite du calcul au pas de temps suivant.
La boucle de simulation complète est alors éprouvée sur des cas de chargements variés. Ainsi, des calculs cycliques 2D sont réalisés sur éprouvette SEN-T en état de déformation plane. Ces simulations sont réalisées en faisant varier les paramètres extrinsèques (température, fréquence, rapport de charge, conditions limites, surcharges, ...). Les résultats démontrent les possibilités offertes par l'approche proposée, ainsi que ses limites, inhérentes à la formulation du modèle, ou en lien avec des artefacts numériques. L'approche proposée démontre notamment sa capacité à relier les outils de la Mécanique de la Rupture à ceux de la Mécanique de l'Endommagement Continu. Des courbes de fissuration globales da/dN vs. ΔK et les tendances associées sont finalement extraites de ces calculs et discutées.

General conclusion, discussions and outlooks

This Ph.D. project intended to assess the capabilities of the so-called *local approach to fracture* to simulate the fatigue propagation of an existing crack in structural problems using the Finite Element method. To address such a problem, the present work – detailed in the previous six chapters – has been articulated around three major axes:

- an **experimental** work dedicated to both the characterization of the cyclic behavior of the material and its cracking resistance under complex loading conditions at several temperatures;
- a **modeling** task including the derivation of the (local) constitutive equations for the cyclic behavior and the strong coupling with damage mechanisms. A non-local enhancement of the model has also been proposed to solve the mesh-dependency of the FE results;
- a **numerical** work intending at the simulation of fatigue crack growth in 2D structural calculations using both the FEM and a damage-to-fracture transition method.

First, an **experimental** campaign has been conducted on the Nickel-based superalloy AD730™. Due to its recent development, the modeling of the cyclic non-linear response of this material had not been yet investigated. Consequently, I proposed to build an experimental campaign to characterize the cyclic elastic-viscoplastic behavior of the material. In order to ease the examination of these experimental data, an existing tool, initiated at the ONERA and based on multiple *Python* programs, has been improved. Relying on the Cottrell's partition method of the stress, I modified this numerical tool in order to extract the main information from the raw data and to obtain relevant plots (in view of a calibration process). In addition, corrective procedures for the detection of the onset of plasticity have been integrated in order to render the estimation more accurate. This *Python* tool has proven to be valuable in extracting the strain-hardening mechanisms as well as analyzing the shape of hysteresis loops, particularly in the way to exhibit particular effects associated with cyclic plasticity. It has then been possible to perform the calibration of a unified viscoplasticity model to reproduce the cyclic non-linear behavior of AD730™ from low to high temperatures. A fairly good match between both the simulated and the experimental behavior has been observed. An improvement of this analysis can be mentioned. In case of high temperature testing (550 & 700°C), hysteresis loops exhibit a change in shape due to the influence of viscosity effects. As a result, since the elastic domain is less well-defined when viscosity effects are present, the program, which relies on the choice of a plastic strain offset δ_{pl}, has been shown to yield poor quality estimation of the work-hardenings. Possible overcoming methods to this point could be:

- to consider an extension of the *Python* program to automatically detect and account for the over-stress [Feaugas, 1999], [Ahmed, 2013]. This would be of great benefit, especially for Ni-based superalloys which are mainly exposed to high temperatures where thermally-activated viscous effects are significant;

- to base the analysis either on *Statistical Process Control* [Fournier et al., 2006] or on Polak's method [Polák et al., 2001].

This way, a better estimation of linear parts of hysteresis loops could be achieved, obtaining consequently better estimates of the viscous, effective and internal stresses.

Still in the **experimental** work, complex fatigue crack growth (FCG) tests have been performed during the Ph.D. work. Macroscopic fatigue and dwell-fatigue crack growth results have enabled to evidence the loading mode effects. Specific extrinsic effects have been discussed and the strong creep-fatigue interaction on the FCG regime has been evidenced. The mesoscopic scale analysis, mainly relying on the observation of the crack front and the crack surface topology, has enabled to discuss the crack growth anomalies observed in AD730™ under complex loading cases. At high temperature with dwell-periods, the crack front loses its linearity, causing a differential in propagation rates along the crack front. The Direct Potential Drop Technique (DCPD) used to monitor the crack advance relies on the assumption of a straight crack front in the through-thickness of the specimen. As a result, I suggested a corrective procedure to the evaluation of the crack length. This method provided a better agreement between real and estimated crack lengths in case of tunneling effect. Finally, for the first time in the lab, Very Low-Cycle Fatigue (VLCF) crack growth tests have been performed to investigate the ductile fracture modes in AD730™. To this purpose, specific flat specimens have been designed. In close relation, a specific force-controlled VLCF testing procedure has been proposed and assessed at high temperatures in order to design the test accordingly to the crack growth process obtained under monotonic loading conditions. The method proved to control the fatigue crack growth process in a limited number of loading cycles. However, the assumption of a constant elastic slope might have been too severe in some cases and yielded to crack arrest. This point deserves further developments, for instance, through the recursive updating of the elastic slope.

Regarding the **modeling** aspects, several tasks have been achieved in this Ph.D. research project. In a first step, the knowledge of the cyclic non-linear behavior of AD730™ gained from the experimental campaign has enabled to propose and calibrate a set of constitutive equations. In the context of the local approach to fracture, a strong coupling between the damage mechanisms and the constitutive equations has been proposed. The formalism being by itself very complex, isotropic damage properties have been favored, but an extension to anisotropic damage could also be beneficial since the damage process at the crack-tip is clearly of anisotropic nature.
It is also worth noting that I made the choice to rely on a strong coupling between damage and elasticity (classical) as well with all the strain-hardening mechanisms (less classical). This approach enables a complete stress drop in the damaged points, favoring the consistent energy-free transition between damage and crack insertion.
In order to ensure stability and robustness of the numerical solving process at the integration point level, a fully implicit resolution procedure relying on the backward-Euler scheme has been favored. Despite a burdensome implementation (full coupling assumptions, high number of internal state variables, mainly of tensorial-type) and a high numerical demand (large matrix inversion, iterative procedure), the implicit resolution of the local damage model has offered a good accuracy. It can be mentioned that a condensation of the equations of the non-linear model could provide a smaller problem to be solved (in the numerical sense). However, such a task is not trivial since strong coupling assumptions prevails and since the model relies on a non-associated theory [Malcher and

Mamiya, 2014]. Furthermore, such a reduction may not lead to the direct estimation of the consistent tangent operator, as considered in the present work and required for the element formulation. This may penalize the global implicit resolution procedure, which is not reasonable owing to the considered cyclic loading schemes.
The unified viscoplasticity formalism has proven to be responsible for the slight strain rate effect in the fatigue damage evolution under pure cyclic conditions. In addition, even if creep-fatigue interaction effects have been reported in AD730™ under dwell-fatigue loading at high temperatures, these effects have not been completely accounted for and analyzed, since a simple linear summation of the damage mechanisms has been considered in a first attempt. Nonetheless, there is no doubt that damages interact each others in a greater extent, which would require further investigations, both on the experimental and numerical prospects. For instance, this could be done in conducting specific tests to complete the database, notably for pure creep loading conditions. Suggestions for improvements of the damage evolution rules and integration of creep-fatigue interaction in the modeling can be found, as a starting point, in the work of [Cai et al., 2019] and [Tang et al., 2020].

In a second step, a non-local extension of the local damage model has been proposed in order to solve the spurious mesh-dependency effect associated with strain-softening mechanical response. To do this, an internal length scale has been introduced within the local model through a gradient-enhanced formulation. In order to regularize the whole set of damage variables (fatigue, creep and volumetric damages), choice for the regularization of the total damage has then been favored. A consistent modification of the local model has been achieved. All the non local theoretical formalism has been implemented in the Z-set FE solver. Again, I chose an implicit resolution scheme in order to perform relatively large time steps and, as a result, improve the convergence of the local step (integration) and accelerate the global one (equilibrium). The dual problem involving the equilibrium and the (implicit) gradient equations have been solved using a monolithic resolution scheme. As a consequence, the derivation of the consistent tangent operators has been achieved in order to determine the elementary stiffness matrices.
The proposed non-local damage model has proven to provide converged results upon mesh refinement under both monotonic and cyclic conditions. In any case, the internal length scale has been chosen as a numerical parameter related to the width of the localization band. Still today, there is no clear consensus on the calibration of the non-local length scale which is, in the vast majority, used as a numerical parameter. Attaching a physical meaning to one (or several) length scale(s) remains an interesting and open question. In case of dwell-fatigue crack growth problems, such an approach is, to the best of the author's knowledge, still not yet investigated by researchers due to the complexity of the problem relying on a non-linear material behavior fully coupled to damage.
Finally, it can be mentioned that for both the local and non-local models, small strain assumptions have been considered. An extension of the problem to the finite strain framework could be beneficial since finite deformations could evolve in the fracture process zone close to the crack-tip. However, since the present modeling work relies on a gradient-enhanced formulation, the change for a finite strain framework is not that trivial since the gradient term may depend on the initial or current configuration. In addition, to the author's knowledge, fatigue crack growth modeling using a finite strain framework is not that common and thus requires further investigations.

Finally, in the **numerical** scope, this Ph.D. work has succeeded in bringing together a whole range of pre-existing numerical tools. The complete chain from the proposal of an error-based mesh adaption strategy (in order to properly describe the localization bands), the definition of the

crack increment (thanks to the *Marching Ridges* crack path tracking algorithm), to the physical insertion of a crack (with the mesh adaption, fields transfer and equilibrium recovery steps) has been made operative on complex fatigue and dwell-fatigue loading conditions.
Regarding the numerical developments, even though the computational tools used in this work were already implemented into the Z-set suite, this Ph.D. project has assessed the capabilities and robustness of these tools in the above-mentioned complex calculation chain. Specific adjustments to cyclic loading cases have been proposed, *e.g.* the addition of the re-equilibrium procedure, in order to ease the convergence after crack advance through mesh intersection.
The proposed numerical chain has been assessed in structural calculations and yielded encouraging results. The main tendencies of the Fracture Mechanics framework have been evidenced, namely the presence of a quasi-stable Paris' regime and an asymptotic trend. However, due to long computations, the fatigue crack growth process has only be achieved over moderate crack lengths in 2D cases. The qualitative analysis of the proposed model highlighted the capability of the local approach to fracture to analyze the local fields and their evolution with time. The knowledge of these fields as well with the stress redistribution throughout the cyclic cracking process are already of great interest since more accurate fracture or crack growth bifurcation criteria could be defined in future works. Crack propagation anomalies under cyclic conditions associated with Nickel-based superalloys still have to be modeled. An interesting prospect of the proposed approach would be to switch to 3D computations and to benefit from local mechanical fields close to the crack-tip to use specific local criteria, particularly for flat-to-slant modeling [Besson et al., 2003], [Xue and Wierzbicki, 2009] or tunneling effect [Antunes et al., 2001].
In order to limit computational cost in LCF conditions, use could be made of *cycle jump techniques* enabling to skip some cycles, provided the evolution of the internal variables is sufficiently low [Nesnas and Saanouni, 2000], [Foerch et al., 2000].
In any case, the proposed approach has been proved to qualitatively relate some loading modes effects during FCG computations. Namely, the temperature, load ratio and frequency effects have been reported. Effect of applied boundary conditions has also been addressed. The non-conventional trend observed in cases of over-loads requires further analysis and possible changes in the model. Additionally, the proper calibration of the damage model, *e.g.* through a *point-by-point* method [Hamon, 2010] should provide better insights on the FCG modeling.
Finally, the acquisition of the real boundary conditions of the problem as well with local stress-strain fields at the crack-tip, *e.g.* through Digital Image Correlation, would also be beneficial in order to improve both the understanding and calculations.

At last, this Ph.D. project constitutes a first contribution to the overall complex problem of simulating the propagation of a crack in structural problems under cyclic loading conditions with a local approach to fracture. This study has evidenced the possibility to consider a continuous-to-discontinuous description of the fatigue and dwell-fatigue crack growth process and, consequently, pushes back the boundaries associated with CDM, mainly restricted either to ductile/brittle fracture problems under quasi-static loading conditions or fatigue crack initiation cases.
The proposed modeling approach can hence be seen as a bridge between Damage and Fracture Mechanics frameworks, with promising results.

Part III - Supplements

A Extraction of the specimens from the raw material of AD730™

(a) As-received raw material of AD730™ in the form of two Ø 204 mm cylinders.

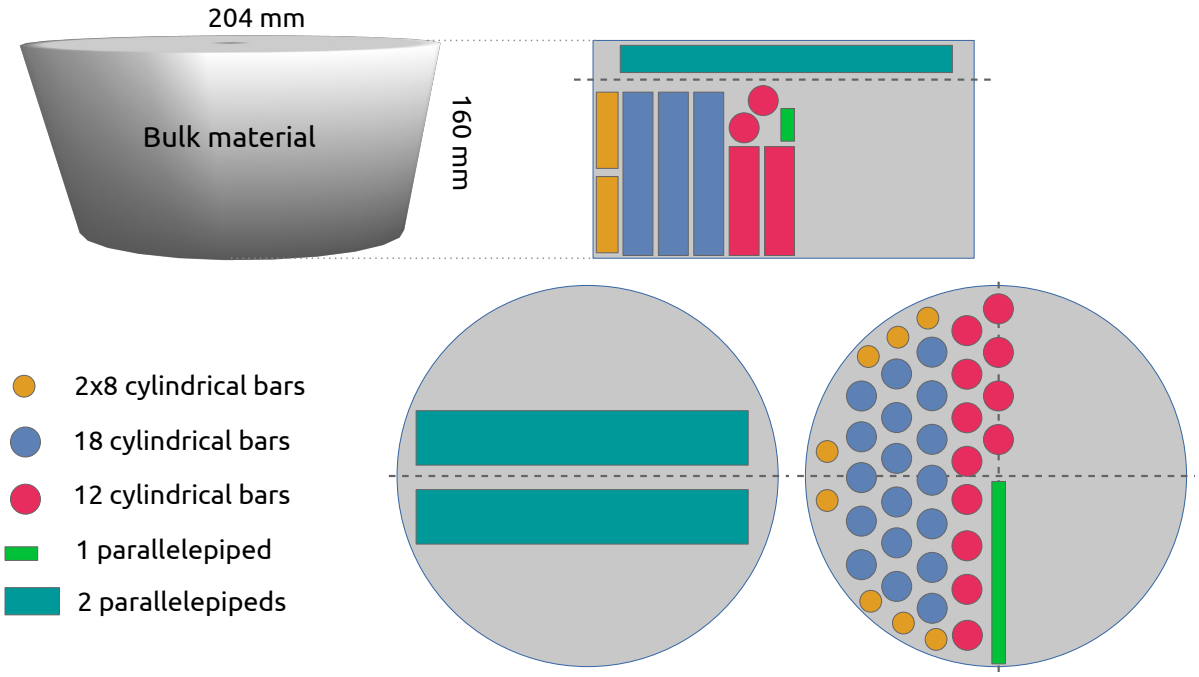

(b) Specimens sampling plans from the bulk material of AD730™.

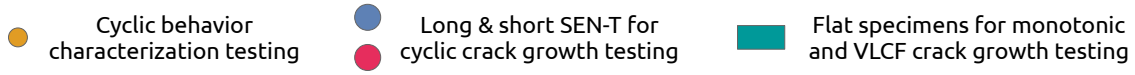

(c) Correspondence between samples and specimens.

Figure A.1: Sampling plans for the specimens made of AD730™ dedicated to cyclic behavior characterization testing and both cyclic and monotonic crack growth testing.

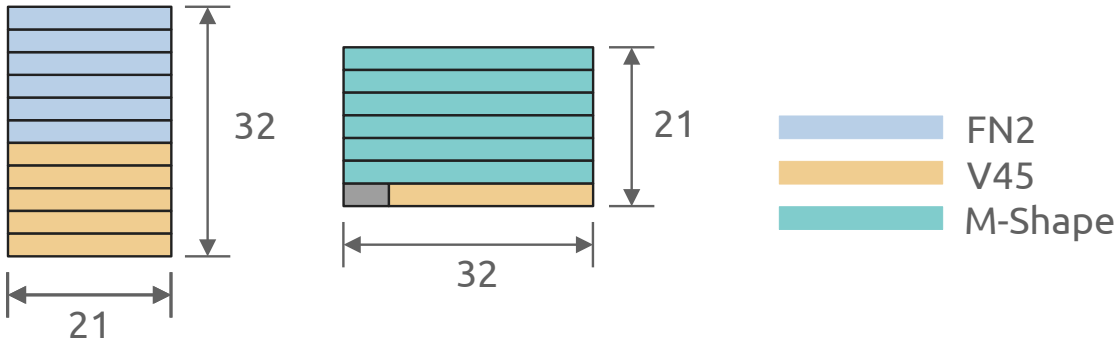

Figure A.2: Parallelepipeds sampling plans for monotonic & VLCF testing flat specimens.

Extraction of the cyclic behavior characterization specimens:

Cyclic and monotonic characterization samples consist of a batch of 16 cylindrical specimens, see Fig. A.1b, with a diameter of 6 mm (for a corresponding section of 28.27 mm^2), with a length of the useful zone in the middle area equal to 12.328 mm. Once dedicated heat-treatments have been carried out, see sub-sect. 2.1.2.3, the final specimen geometry was finally obtained from the extracted cylindrical bars through Electrical Discharge Machining (EDM). A final surface grounding with a specification of $R_a = 0.2$ was achieved.

Extraction of the fatigue crack growth specimens:

Starting from the bulk material, 12 $\varnothing 20 \times 94\,mm^3$ and 18 $\varnothing 20 \times 137\,mm^3$ cylinders have been extracted, see Fig. A.1b. Once the raw cylinders were machined from the material log, heat-treatments were applied, see sub-sect. 2.1.2.3, prior to the final machining of the specimens (through turning-milling processes) with corresponding specific items (*e.g.* U-notch) added through EDM. After machining, the surface of the specimens was ground to a specification of average roughness $R_a = 0.8$.

B Geometries for the testing specimens

B.1 Cyclic behavior characterization specimen

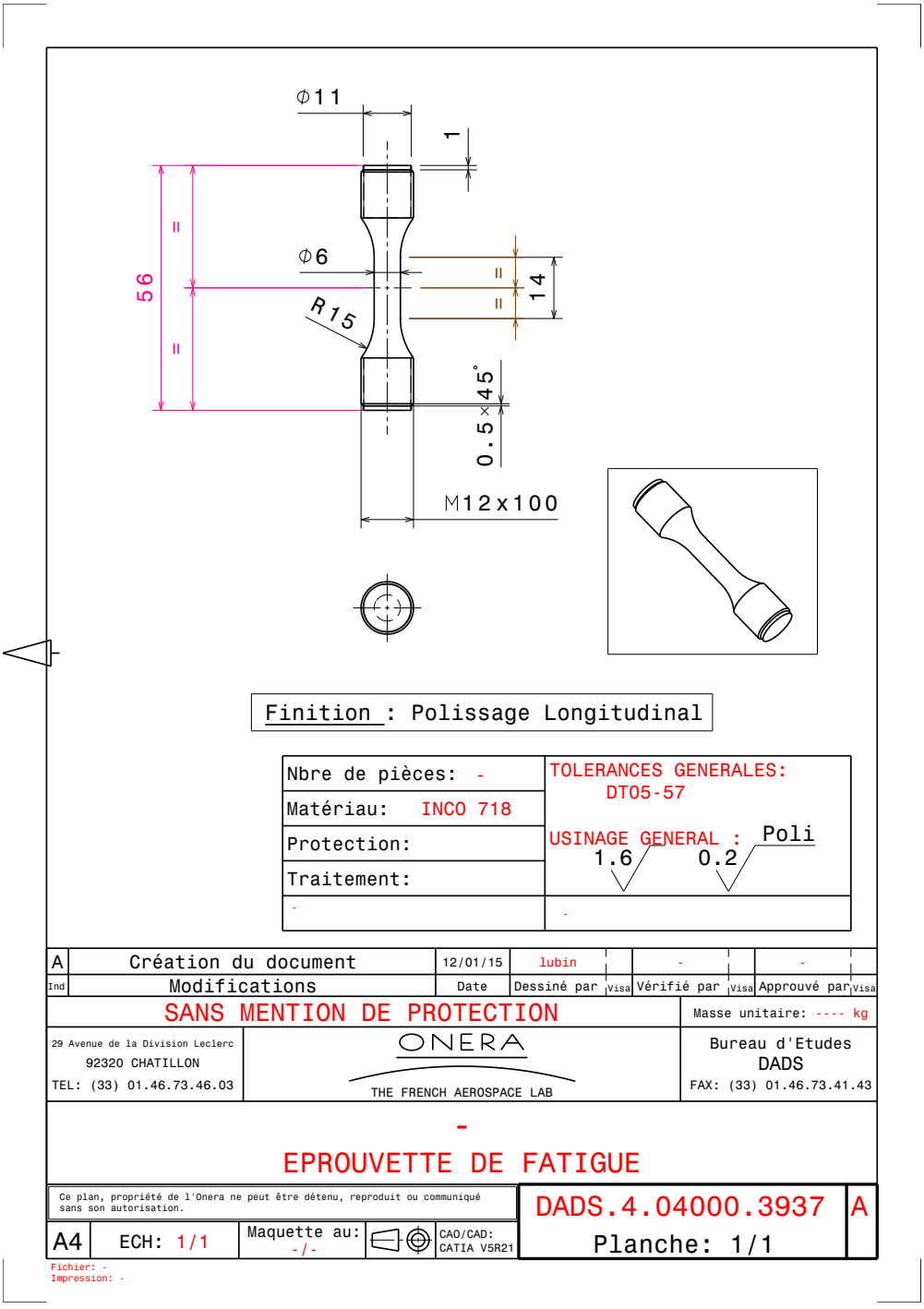

Figure B.1: Cylindrical specimen for cyclic behavior characterization process.

B.2 Cyclic crack propagation specimens

B.2.1 SEN for clamshell furnace

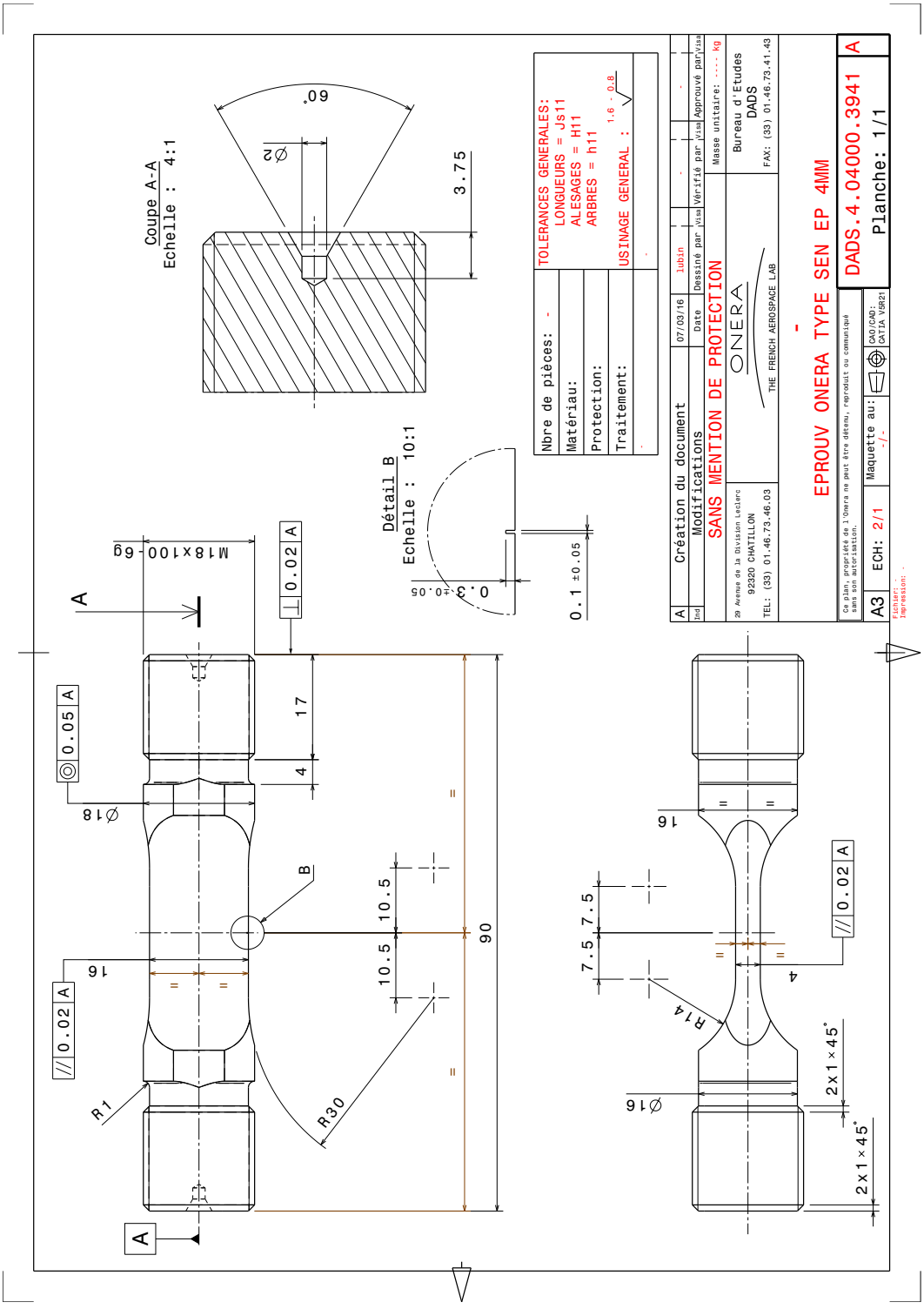

Figure B.2: Single-Edge Notched (SEN) specimen for crack propagation analysis under clamshell furnace (thickness 4 mm).

B.2.2 SEN for induction-heating - 4 mm

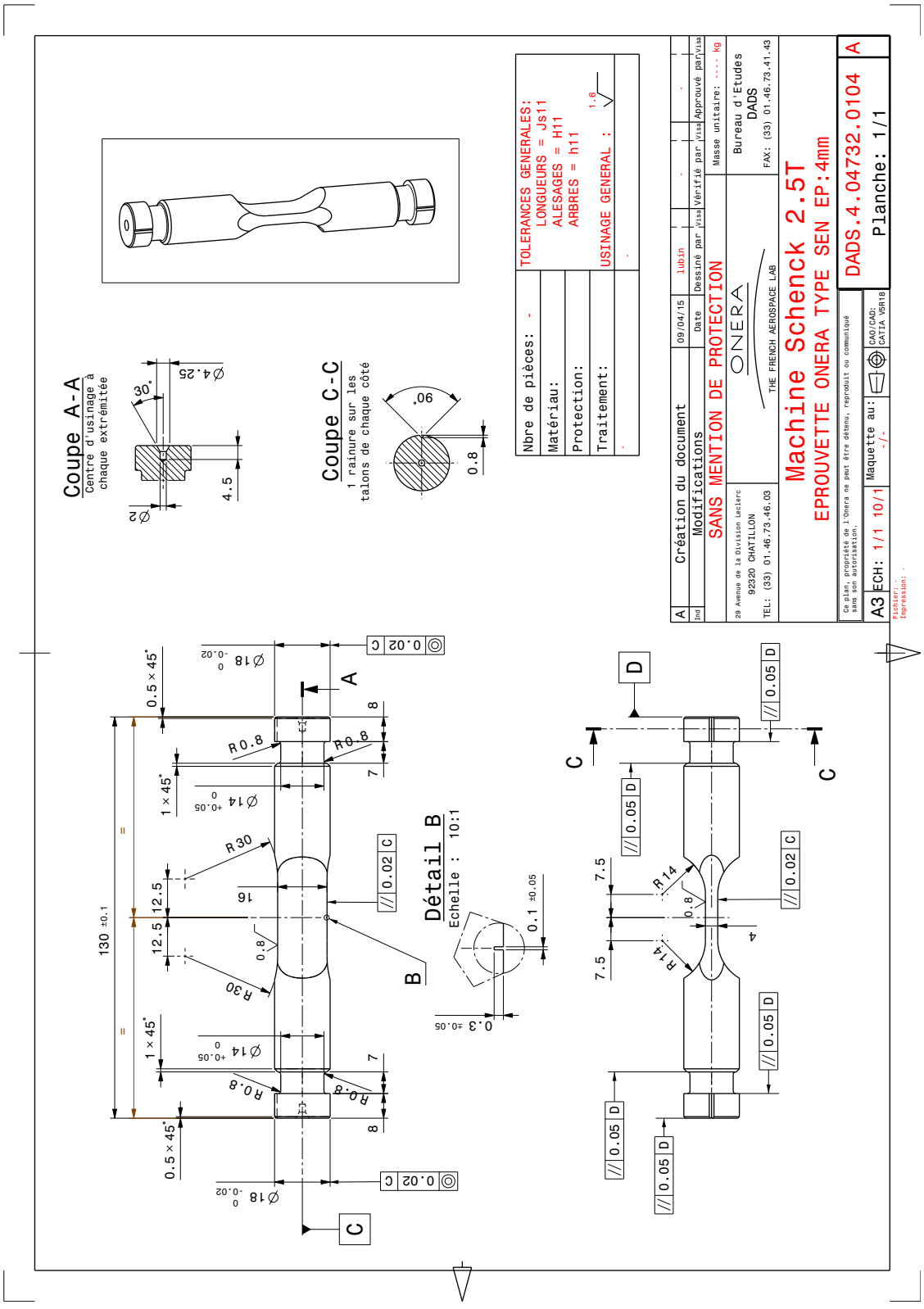

Figure B.3: Single-Edge Notched (SEN) specimen for crack propagation analysis with inductor (thickness 4 mm).

B.3 Flat specimen for VLCF ductile fracture testing

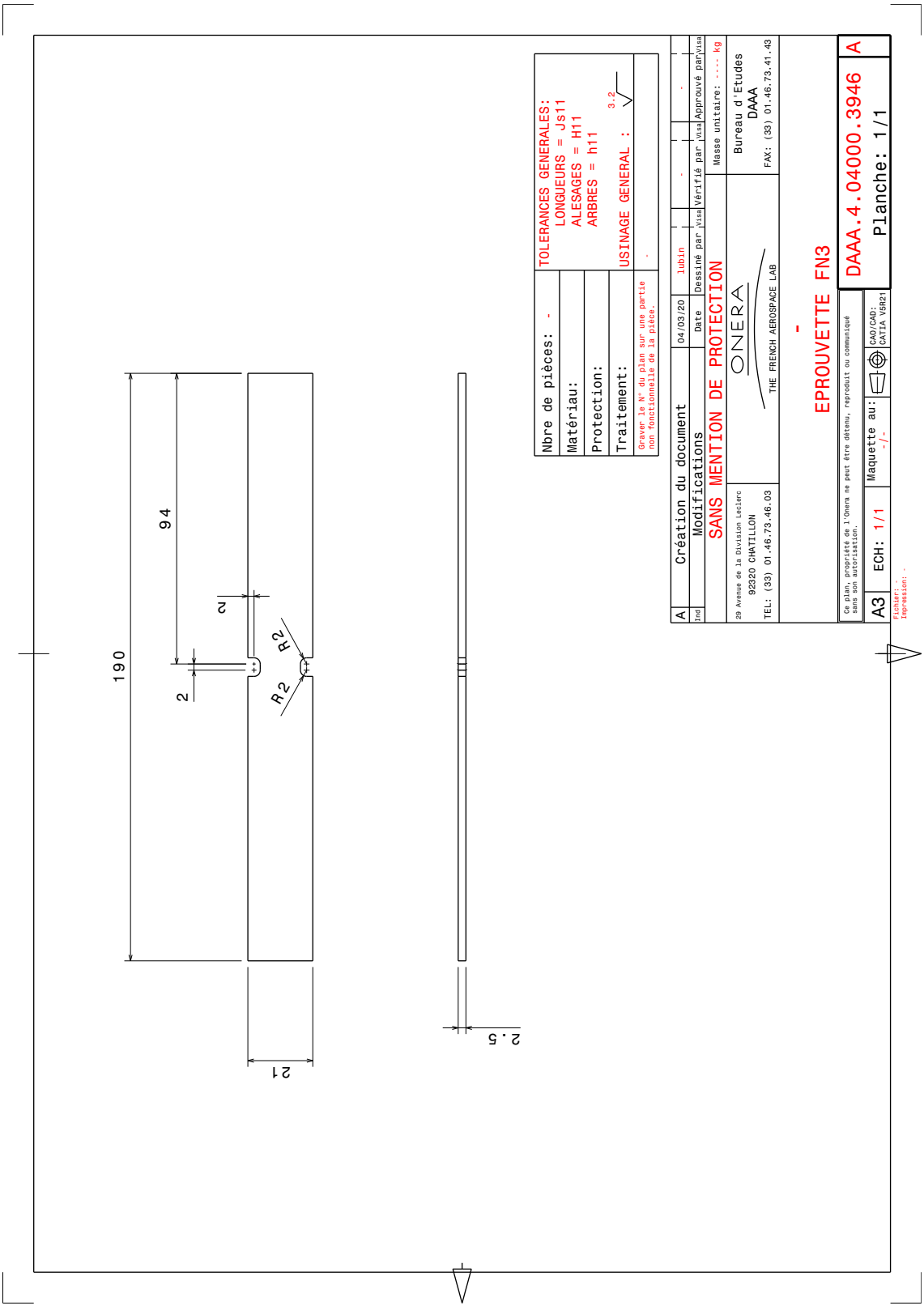

Figure B.4: "FN2" flat specimen (thickness 2.5 mm).

C Supplementary results for Chap. 2

C.1 Plasticity / Strain-hardening

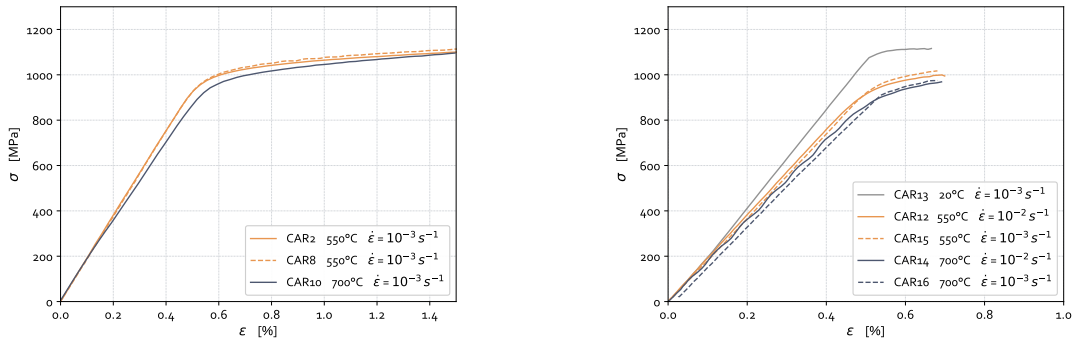

(a) Monotonic tensile curves at 550 and 700°C. (b) Cyclic tensile curves at 20, 550 and 700°C.

Figure C.1: Tensile curves for both monotonic and cyclic (1st 1/4 loop) loadings.

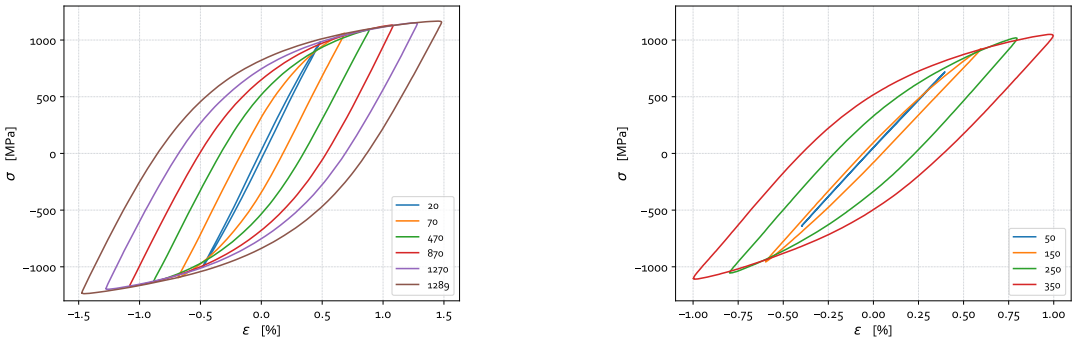

(a) 20°C / $\dot{\varepsilon} = 10^{-3}$ s^{-1} (spec. CAR1). (b) 650°C / $\dot{\varepsilon} = 10^{-3}$ s^{-1} (spec. CAR6).

Figure C.2: Last hysteresis loops for each strain amplitude at 20 and 650°C with $\dot{\varepsilon} = 10^{-3}$ s^{-1} and $R_\varepsilon = -1$ (spec. CAR1 & 6).

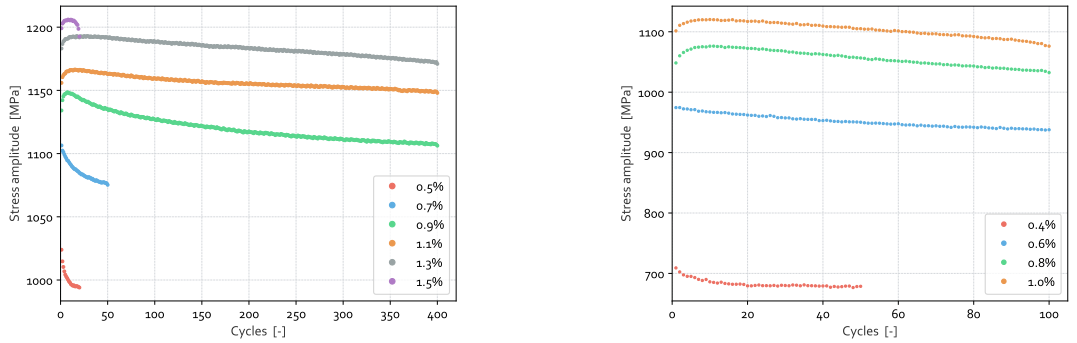

(a) Cyclic softening at 20°C at 10^{-3} s^{-1} (CAR1). (b) Cyclic softening at 650°C at 10^{-3} s^{-1} (CAR6).

Figure C.3: Evolution of the stress amplitude at 20 and 650°C at $\dot{\varepsilon} = 10^{-3}$ s^{-1}, $R_\varepsilon = -1$ (spec. CAR 1 & 6).

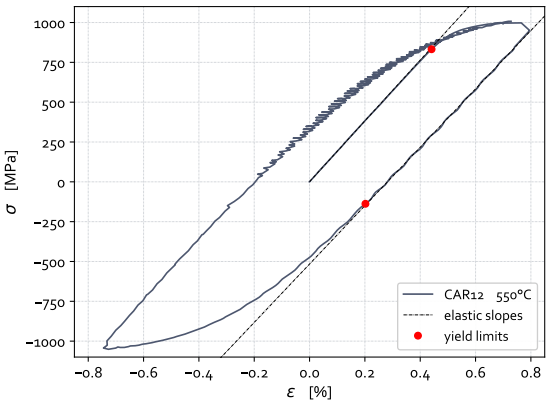

(a) Bauschinger effect: 1st hysteresis loop at 550°C at 10^{-2} s^{-1} (CAR12).

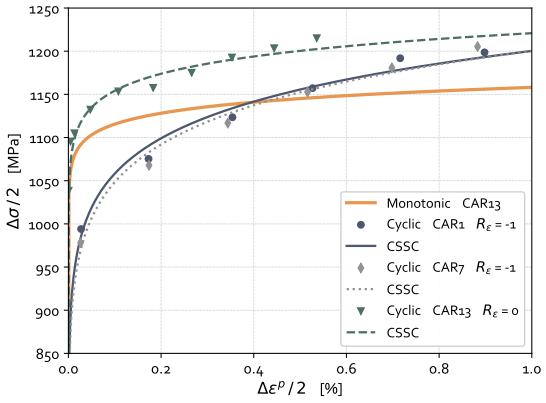

(b) Cyclic hardening curves of AD730™ at 20°C for $\dot{\varepsilon} = 10^{-3}$ s^{-1}, $R_\varepsilon = -1$.

Figure C.4: Bauschinger effect at 550°C and cyclic hardening curve at 20°C of AD730™.

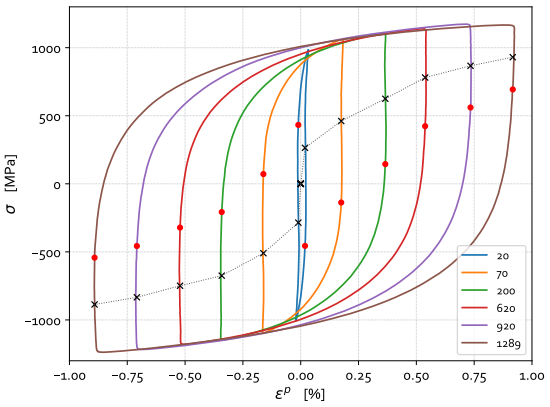

(a) Stabilized hysteresis loops at 20°C.

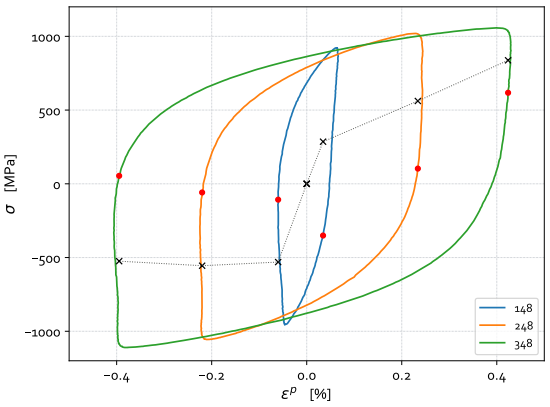

(b) Stabilized hysteresis loops at 650°C.

Figure C.5: Stabilized hysteresis loops for type-1 cyclic tests at 20 & 650°C, R_ε = -1 with $\dot{\varepsilon} = 10^{-3}$ s^{-1} (spec. CAR 1 & 6). ● : yield limits; ✖ : yield surface's center.

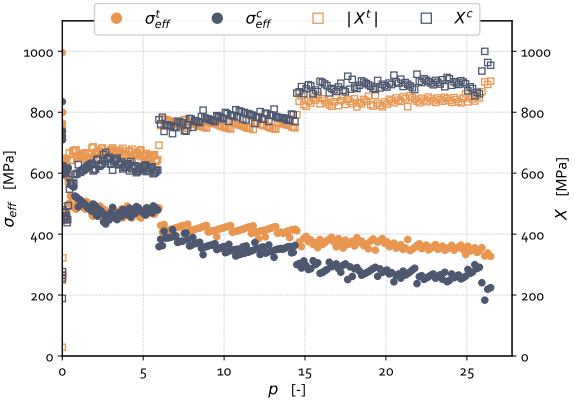

(a) Effective and internal stresses evolution w.r.t. p.

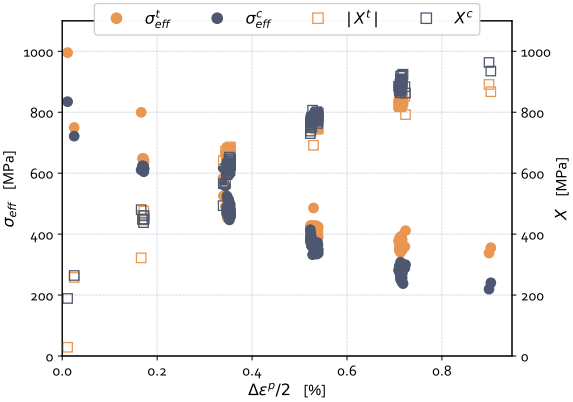

(b) Effective and internal stresses evol. w.r.t. $\Delta\varepsilon_p/2$.

Figure C.6: Effective and internal stresses evolution with respect to plastic strain amplitude and accumulated plasticity for type-1 cyclic tests at 20°C, R_ε = -1, $\dot{\varepsilon} = 10^{-3}$ s^{-1} (spec. CAR1). ● : effective stress = radius of yield surface; □ : internal stress = yield surface's center.

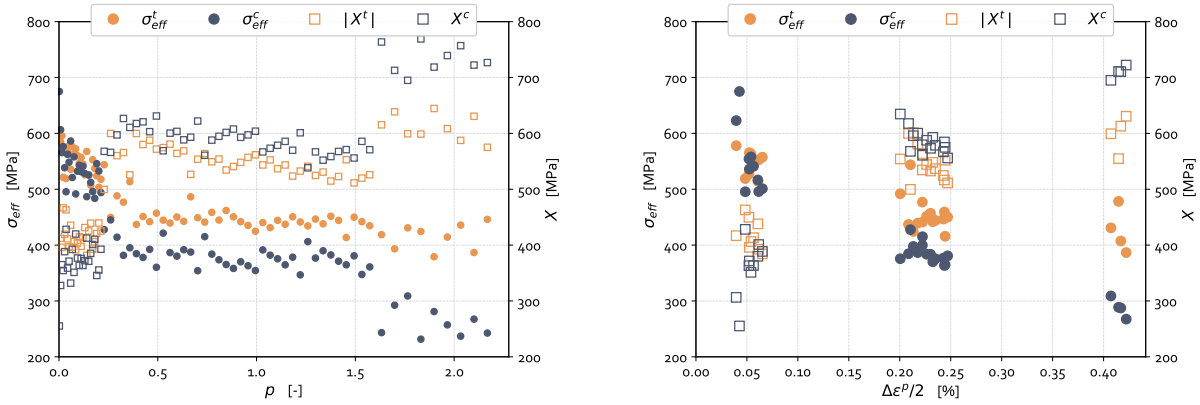

(a) Effective and internal stresses evolution w.r.t. p. (b) Effective and internal stresses evol. w.r.t. $\Delta\varepsilon_p/2$.

Figure C.7: Effective and internal stresses evolution with respect to plastic strain amplitude and accumulated plasticity for type-1 cyclic tests at 700°C, R_ε = -1, $\dot{\varepsilon} = 10^{-3}$ s^{-1} (spec. CAR5). ● : effective stress = radius of yield surface; □ : internal stress = yield surface's center.

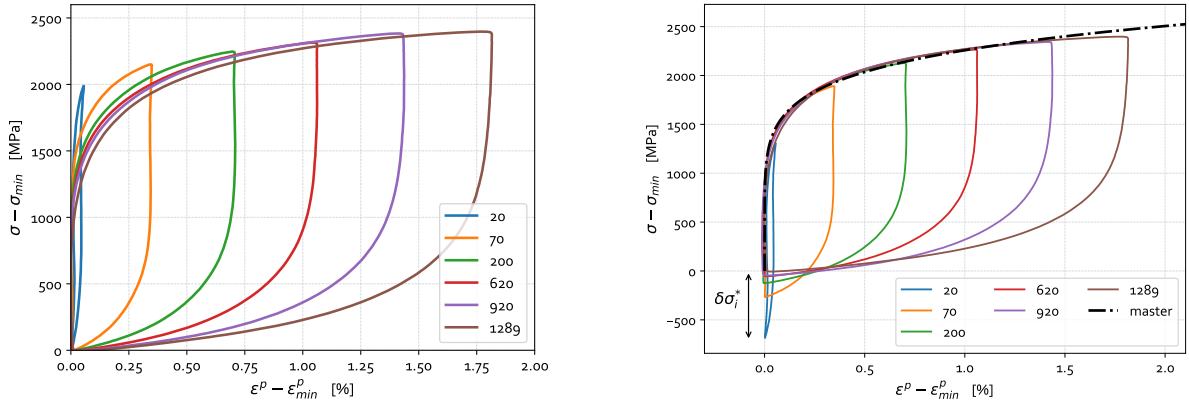

(a) Shifted quasi-saturated hysteresis loops. (b) Shifted hysteresis loops with master curve.

Figure C.8: Shifted hysteresis loops for Masing-type behavior analysis at 20°C, $R_\varepsilon = -1$, $\dot{\varepsilon} = 10^{-3}$ s^{-1} (spec. CAR1).

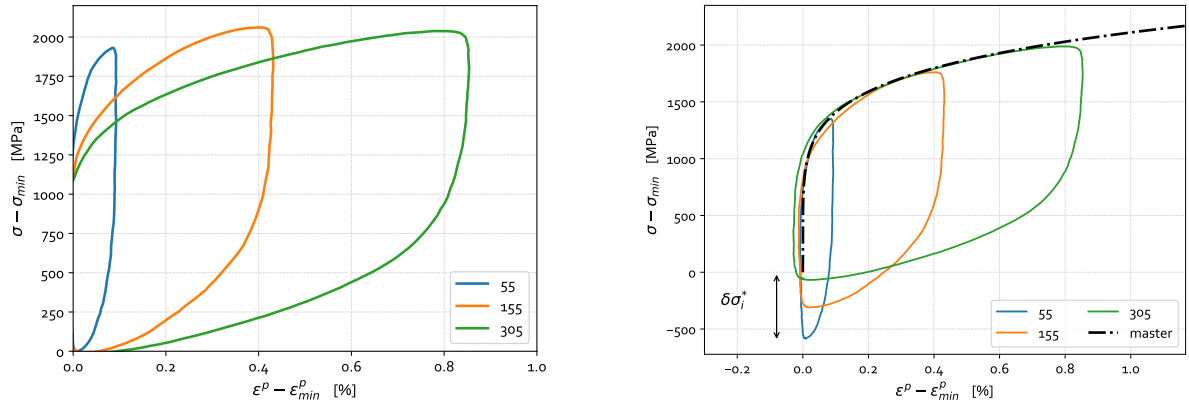

(a) Shifted quasi-saturated hysteresis loops. (b) Shifted hysteresis loops with master curve.

Figure C.9: Shifted hysteresis loops for Masing-type behavior analysis at 700°C, $R_\varepsilon = -1$, $\dot{\varepsilon} = 10^{-3}$ s^{-1} (spec. CAR5).

C.2 Time-related effects

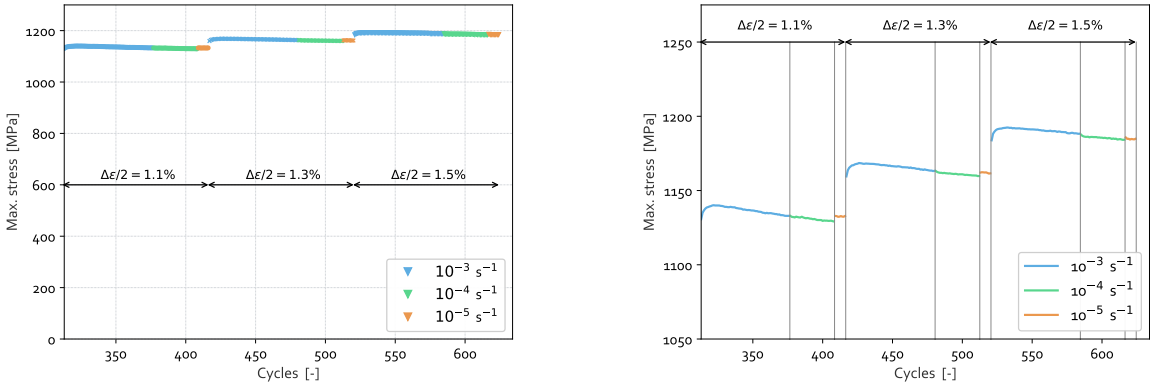

(a) Stress jumps for varying strain rates. (b) Close-up view.

Figure C.10: Strain-rate sensitivity analysis under cyclic loading at 20°C, $R_\varepsilon = -1$, strain levels 4-6 (spec. CAR7).

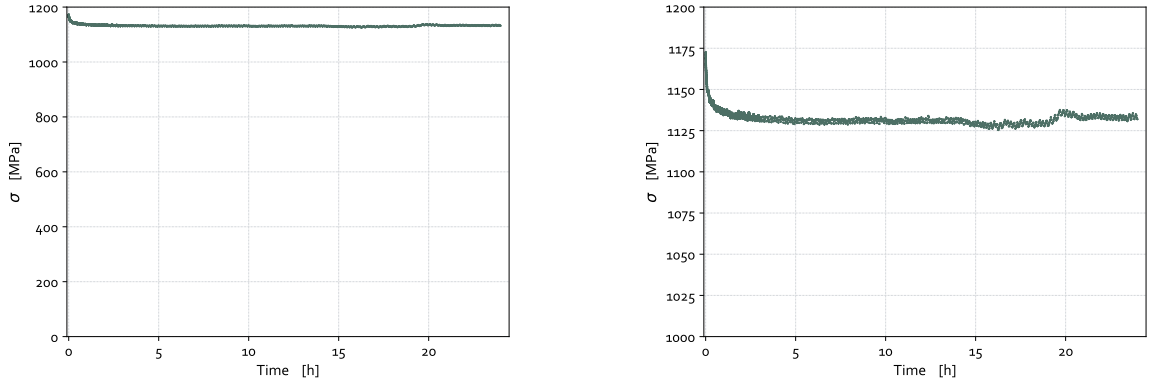

(a) 24h stress relaxation test after cyclic loading. (b) Close-up view on the stress drop.

Figure C.11: Stress relaxation test after cyclic loading conditions at 20°C, with $\Delta\varepsilon/2 = 1.5\%$ (spec. CAR7).

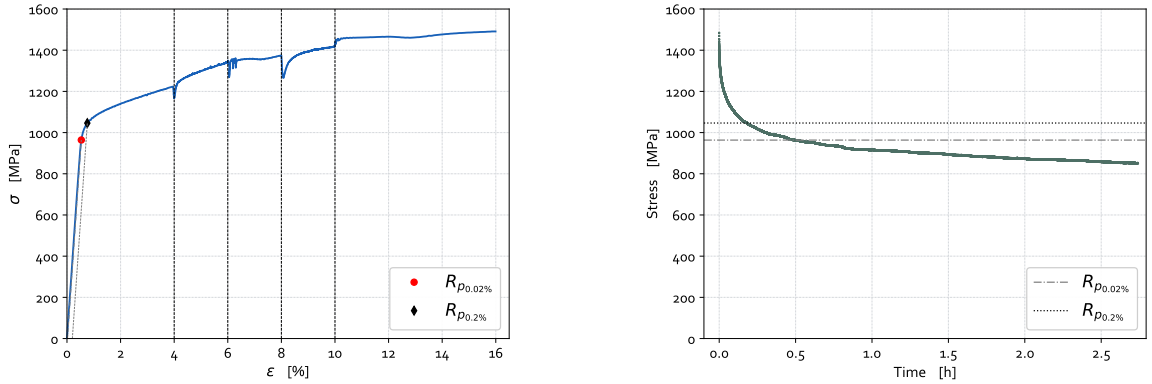

(a) Stress-strain curve of the MS test at 550°C. (b) Stress-time curve of the relaxation at 550°C.

Figure C.12: Tensile stress-strain and stress-time curves for the MS tests at 550°C at $\dot{\varepsilon} = 10^{-3}$ s^{-1} with 2.8h relaxation phase at the end at $\varepsilon = 16.0\%$ (spec. CAR8). Vertical dotted lines correspond to the change in loading strain rates.

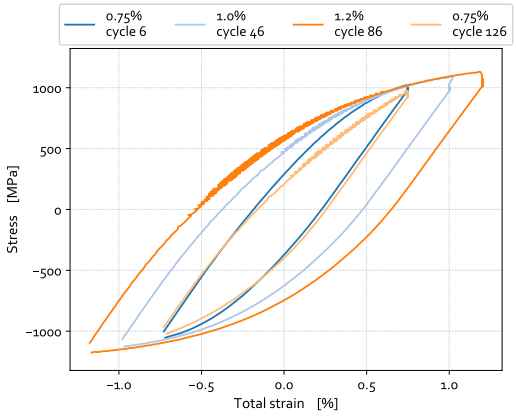

(a) Hysteresis loop with a 720 s holding time.

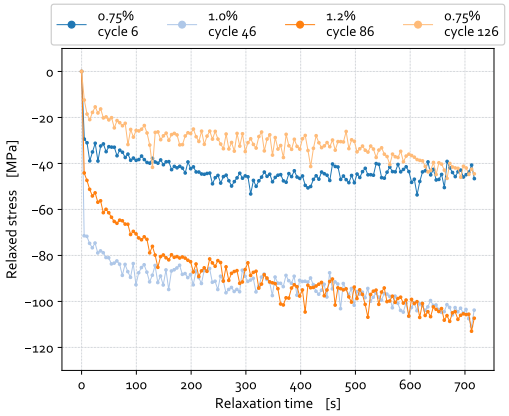

(b) Stress relax. during $HT_3 = 720$ s.

Figure C.13: Hysteresis loops and corresponding stress relaxation profiles during the 1st holding period of the type-4 cyclic test at $T = 550°C$, $\dot{\varepsilon} = 1.\ 10^{-2}\ s^{-1}$, $HT_3 = 720$ s (spec. CAR12).

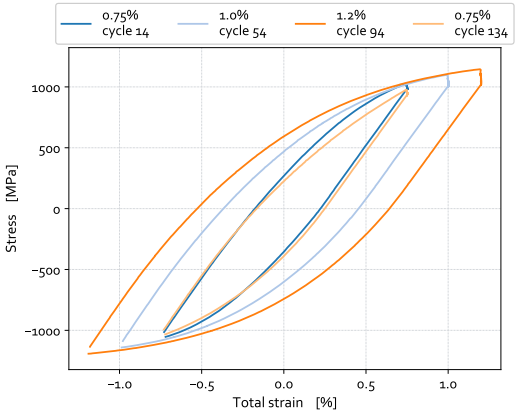

(a) Hysteresis loop with a 720 s holding time.

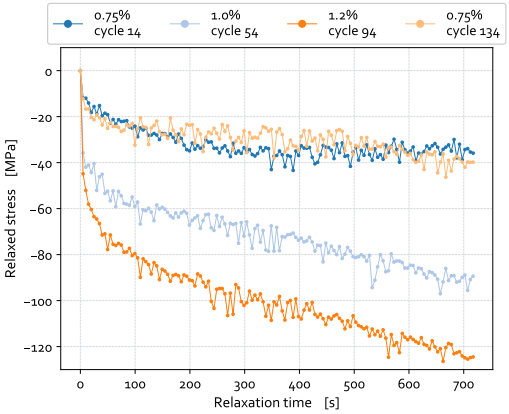

(b) Stress relax. during $HT_3 = 720$ s.

Figure C.14: Hysteresis loops and corresponding stress relaxation profiles during the 1st holding period of the type-4 cyclic test at $T = 550°C$, $\dot{\varepsilon} = 2.5\ 10^{-3}\ s^{-1}$, $HT_3 = 720$ s (spec. CAR12).

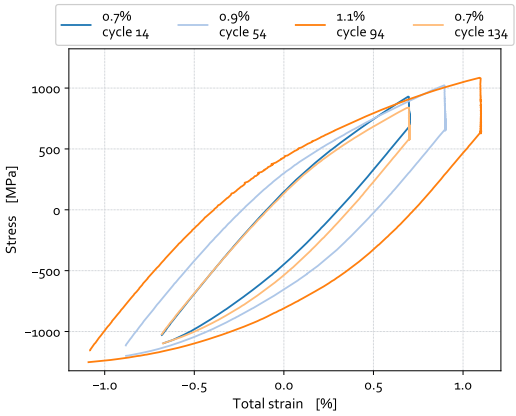

(a) Hysteresis loop with a 720 s holding time.

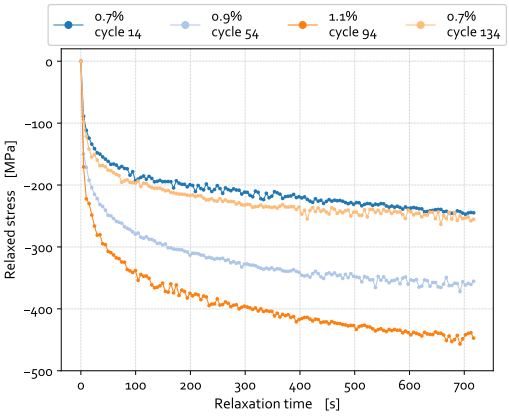

(b) Stress relax. during $HT_3 = 720$ s.

Figure C.15: Hysteresis loops and corresponding stress relaxation profiles during the 1st holding period of the type-4 cyclic test at $T = 700°C$, $\dot{\varepsilon} = 2.5\ 10^{-3}\ s^{-1}$, $HT_3 = 720$ s (spec. CAR14).

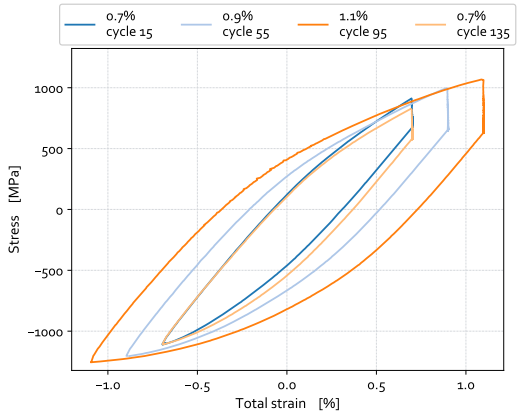

(a) Hysteresis loop with a 720 s holding time.

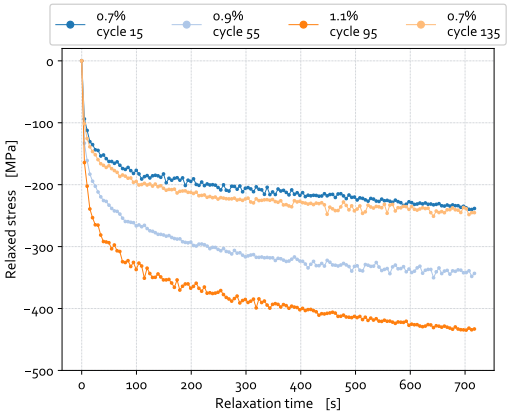

(b) Stress relax. during $HT_3 = 720$ s.

Figure C.16: Hysteresis loops and corresponding stress relaxation profiles during the 2nd holding period of the type-4 cyclic test at $T = 700°C$, $\dot{\varepsilon} = 2.5\ 10^{-3}\ s^{-1}$, $HT_3 = 720$ s (spec. CAR14).

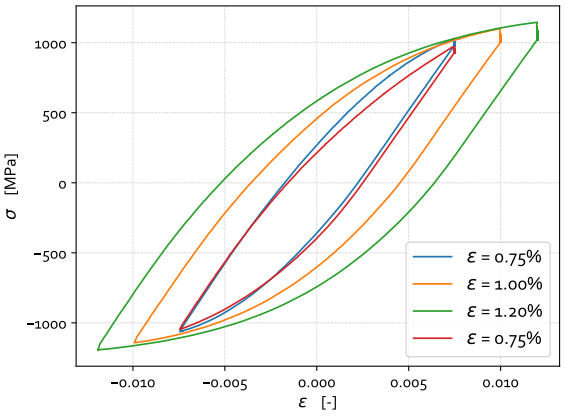

(a) Stress-strain hysteresis loops at 550°C.

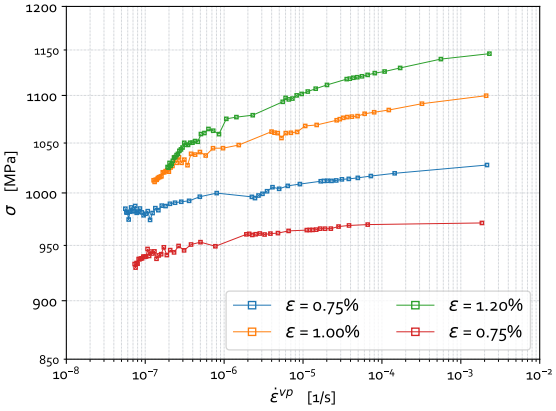

(b) Tensile holding periods at 550°C.

Figure C.17: Stress evolution with strain and viscoplastic strain rate during the 2nd tensile holding period of each strain range of the type-4 cyclic-dwell tests at 550°C with $\dot{\varepsilon} = 2.5\ 10^{-3}\ s^{-1}$ (spec. CAR 12).

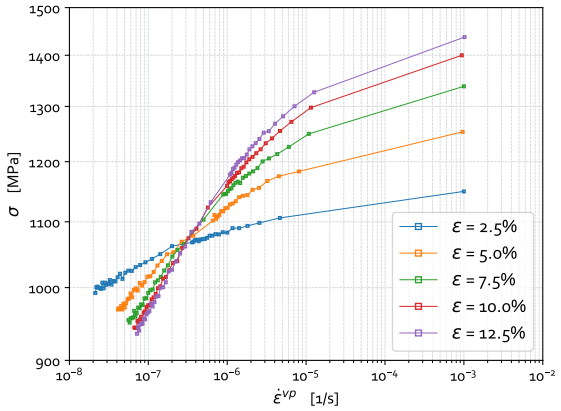

(a) Stress evolution during MHR test at 550°C.

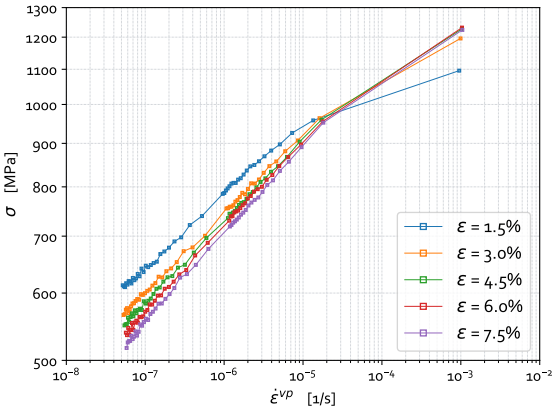

(b) Stress evolution during MHR test at 700°C.

Figure C.18: Stress evolution with viscoplastic strain rate during dwell-sequences of MHR tests at 550 and 700°C at $\dot{\varepsilon} = 10^{-3}\ s^{-1}$ (spec. CAR 2 & 10).

D Material constants for the unified elastic-viscoplastic model of FG AD730™

Mechanism	Material constants	Units	20°C	550°C	700°C
Elasticity	E	MPa	Confidential		
	ν	-			
Viscoplasticity	$\dot{\varepsilon}_0$	s^{-1}			
	K_{vp}	MPa			
	n_{vp}	-			
	m_{vp}	-			
Initial yield limit	R_0	MPa			
Isotropic hardening	Q^1	MPa			
	Q^2	MPa			
	b^1	-			
	b^2	-			
Kinematic hardening	C^1	MPa			
	C^2	MPa			
	C^3	MPa			
	γ_0^1	-			
	γ_0^2	-			
	γ_0^3	-			
Marquis' effect	φ_∞^1	-			
	φ_∞^2	-			
	φ_∞^3	-			
	ω^1	-			
	ω^2	-			
	ω^3	-			

Table D.1: Calibrated parameters for the unified viscoplastic material model for FG AD730™.

E Supplementary results for Chap. 3

E.1 Fatigue crack growth analysis

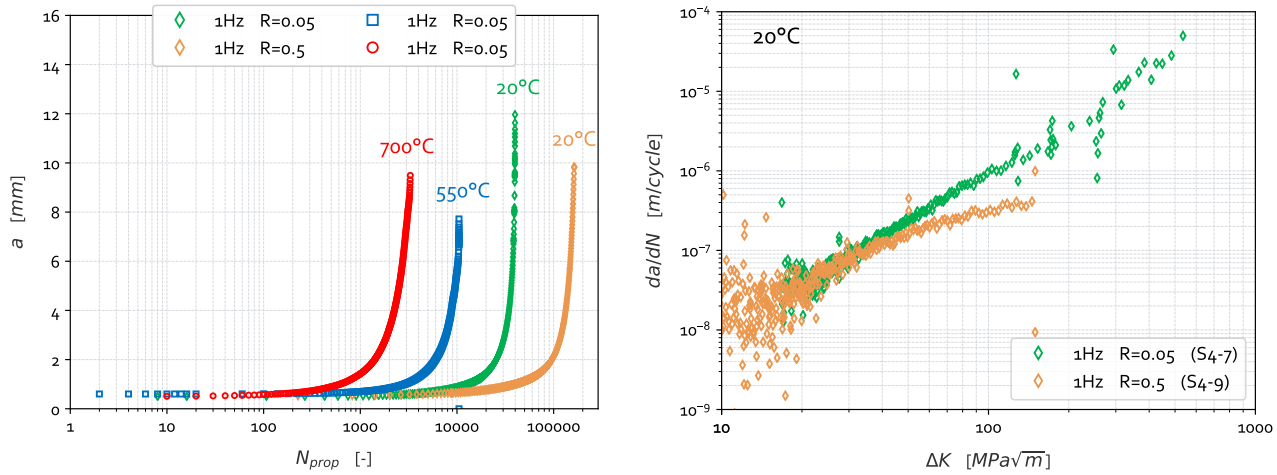

(a) Crack length evolution with increasing temperature.

(b) FCG rates with respect to ΔK at 20°C.

Figure E.1: Temperature and load ratio effects in pure fatigue loading.

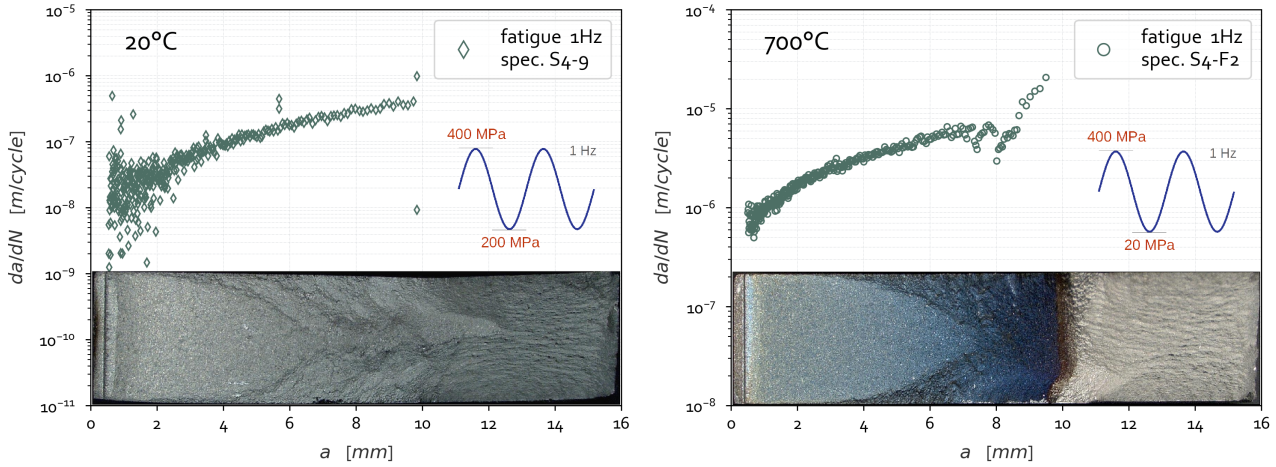

(a) Crack growth test data and corresponding fracture surface (spec. S4-9).

(b) Crack growth test data and corresponding fracture surface (spec. S4-F2).

Figure E.2: Macroscopic data as opposed to the mesoscopic analysis of the fracture surface in pure fatigue loading (spec. S4-9 & S4-F2).

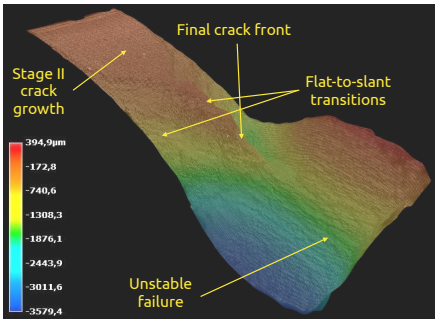

(a) 3D reconstruction of the fracture surface of the spec. S4-9 at 20°C.

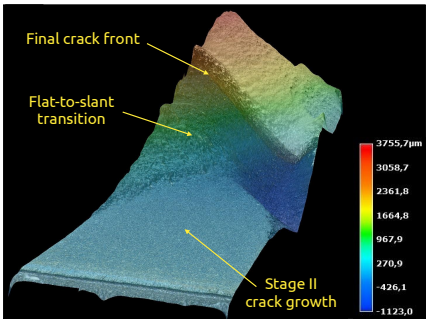

(b) 3D reconstruction of the fracture surface of the spec. S4-F2 at 700°C.

Figure E.3: Topographic analysis of the fractured surfaces of the spec. S4-9 (resp. S4-F2) under pure fatigue loading conditions at 20°C (resp. 700°C) with $R = 0.5$ (resp. $R = 0.05$) - $f = 1\,\text{Hz}$.

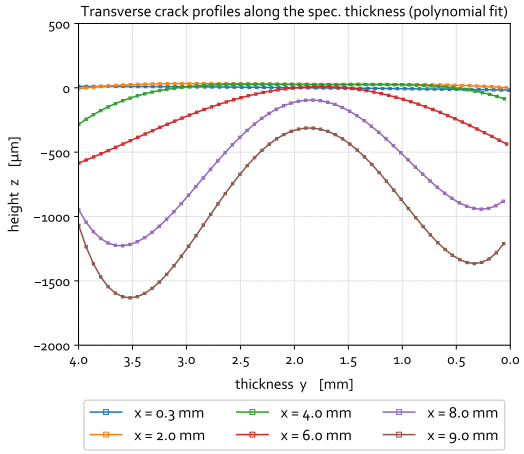

(a) Transverse profiles along the spec. thickness (fitted).

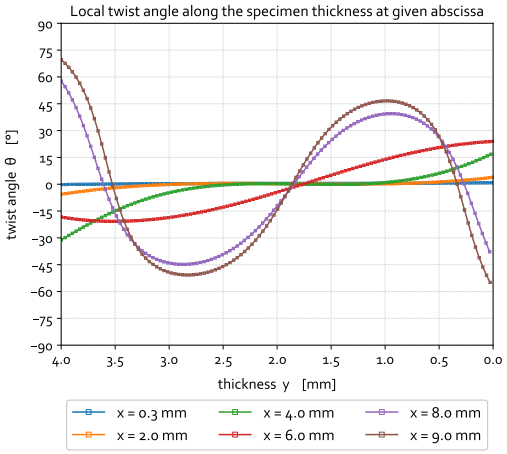

(b) Local twist angles along the spec. thickness.

Figure E.4: Transverse crack profiles $z(y)$ and corresponding twist angles $\theta(y)$ at given through-thickness positions for SEN-T specimens under pure fatigue conditions at 20°C (spec. S4-9).

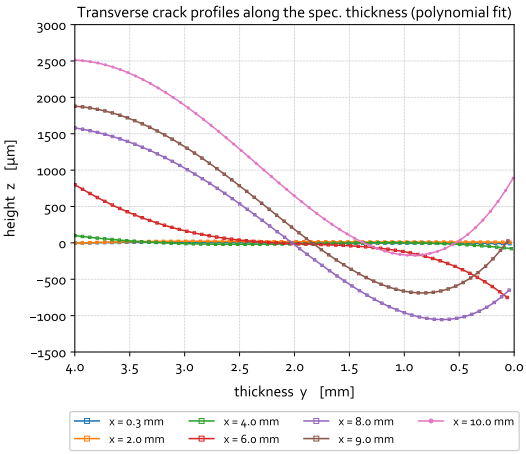

(a) Transverse profiles along the spec. thickness (fitted).

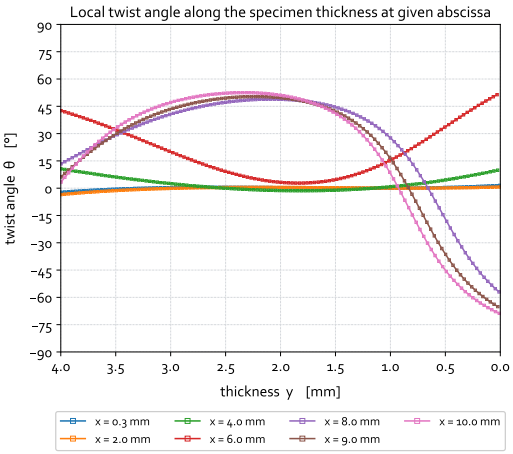

(b) Local twist angles along the spec. thickness.

Figure E.5: Transverse crack profiles $z(y)$ and corresponding twist angles $\theta(y)$ at given through-thickness positions for SEN-T specimens under pure fatigue conditions at 700°C (spec. S4-F2).

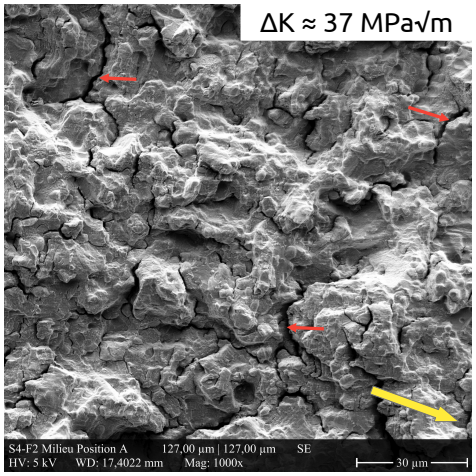

(a) $a \simeq 2.0$mm / $\Delta K \simeq 37\,\mathrm{MPa}\sqrt{\mathrm{m}}$ - middle.

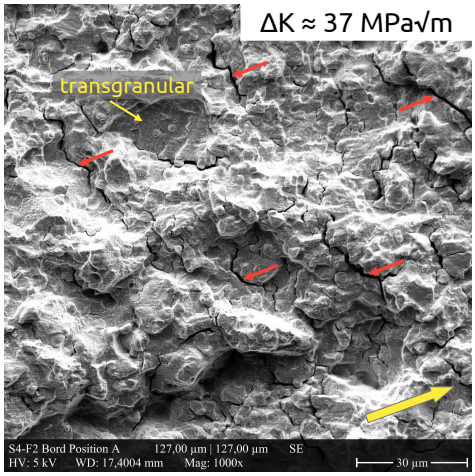

(b) $a \simeq 2.0$mm / $\Delta K \simeq 37\,\mathrm{MPa}\sqrt{\mathrm{m}}$ - egde.

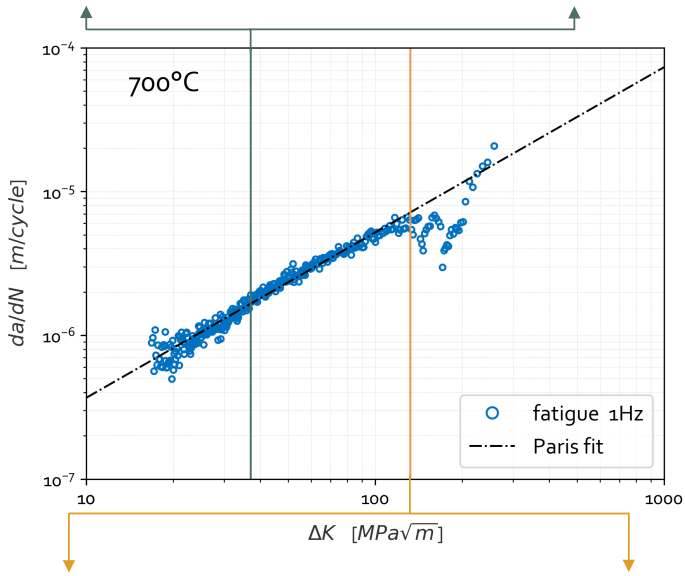

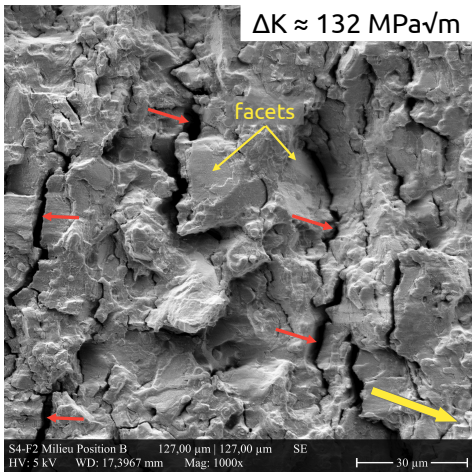

(c) $a \simeq 7.0$mm / $\Delta K \simeq 132\,\mathrm{MPa}\sqrt{\mathrm{m}}$ - middle.

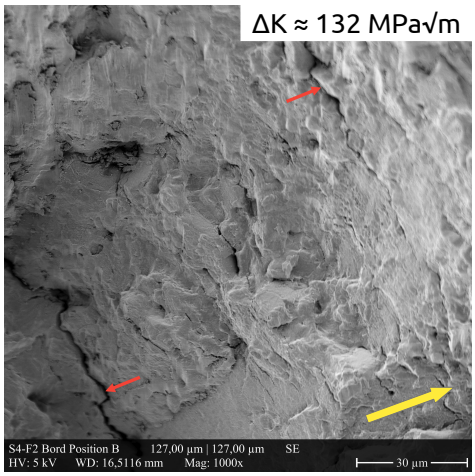

(d) $a \simeq 7.0$mm / $\Delta K \simeq 132\,\mathrm{MPa}\sqrt{\mathrm{m}}$ - edge.

Figure E.6: SEM fracture surface analyses for the S4-F2 specimen subjected to pure fatigue at 700°C (1 Hz, 400 MPa, $R = 0.05$). Identification of the main cracking mechanisms during the *stage II* crack propagation regime.

E.2 Dwell-fatigue crack growth analysis

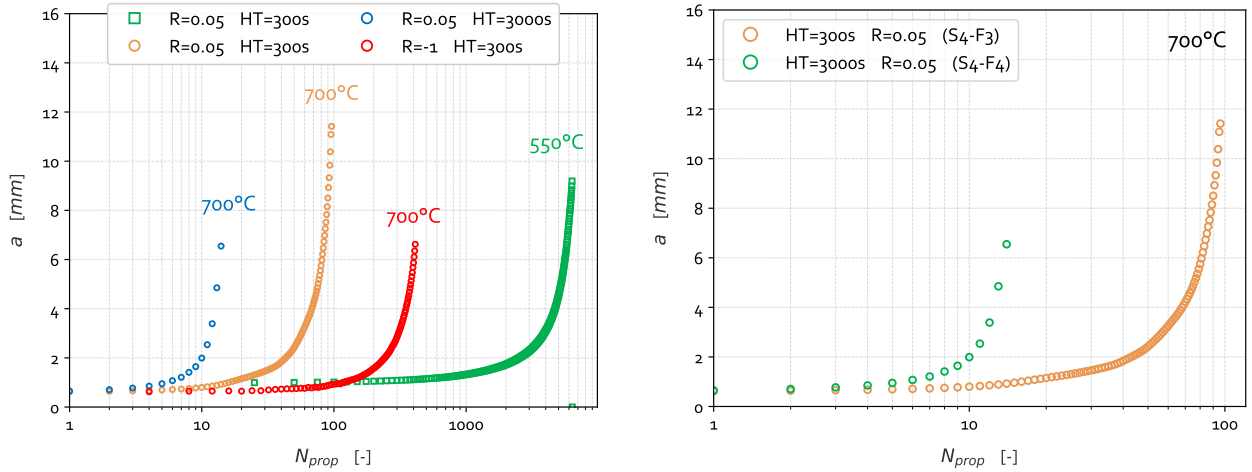

(a) Crack length evolution with increasing temperature. (b) Crack length evolution with decreasing holding-time.

Figure E.7: Temperature and dwell-time effects in creep-fatigue loading.

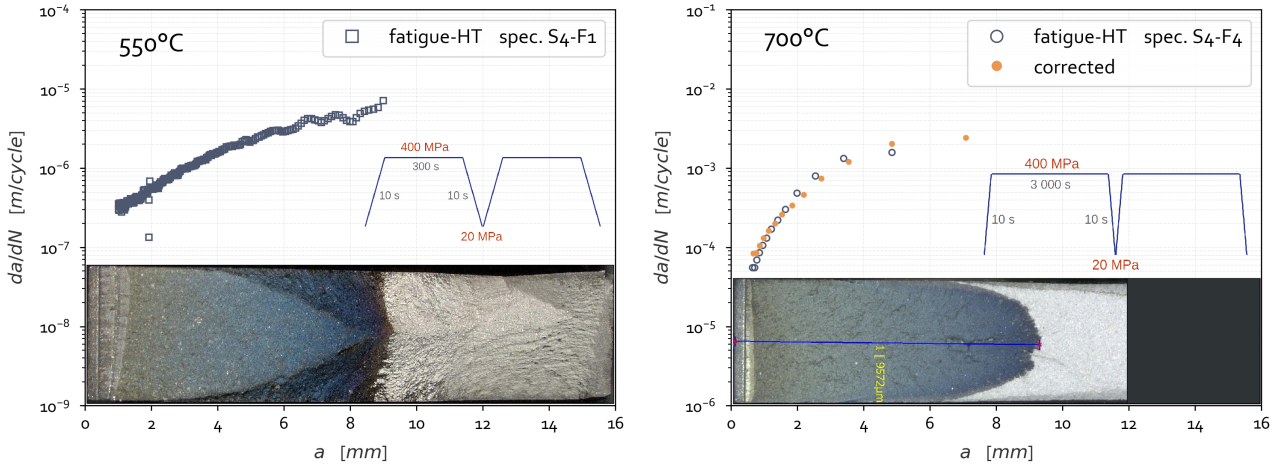

(a) Crack growth test data and corresponding fracture surface (spec. S4-F1).

(b) Crack growth test data and corresponding fracture surface (spec. S4-F4).

Figure E.8: Macroscopic data as opposed to the mesoscopic analysis of the fracture surface in pure fatigue loading (spec. S4-F1 & S4-F4).

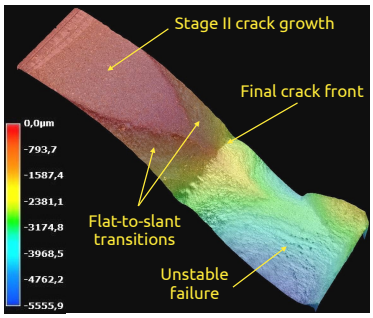

(a) 3D reconstruction of the fracture surface of the spec. S4-F1 at 550°C.

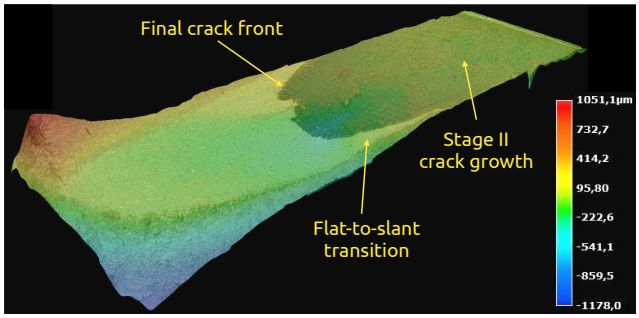

(b) 3D reconstruction of the fracture surface of the spec. S4-F4 at 700°C.

Figure E.9: Topographic analysis of the fractured surfaces of the spec. S4-F1 (resp. S4-F4) under dwell-fatigue loading conditions at 550°C (resp. 700°C) with $R = 0.05$ and HT = 300 s (resp. 3000 s).

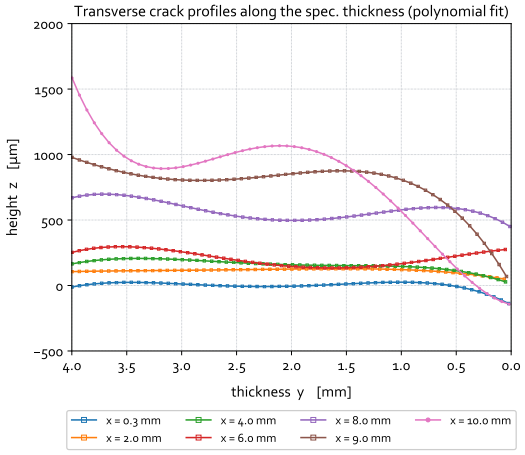

(a) Transverse profiles along the spec. thickness (fitted).

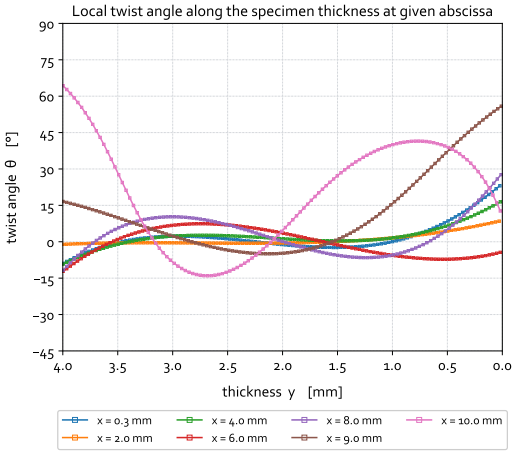

(b) Local twist angles along the spec. thickness.

Figure E.10: Transverse crack profiles $z(y)$ and corresponding twist angles $\theta(y)$ at given through-thickness positions for SEN-T specimens under dwell-fatigue conditions at 700°C (spec. S4-F3).

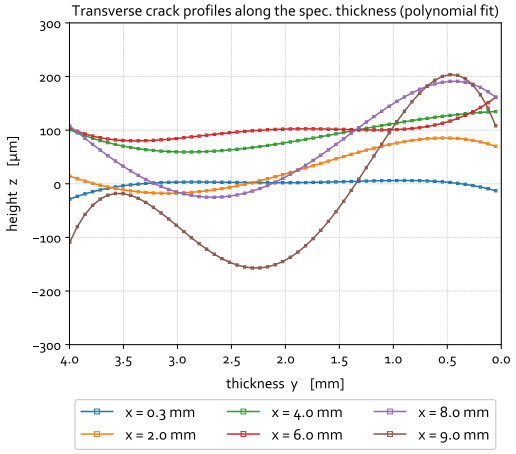

(a) Transverse profiles along the spec. thickness (fitted).

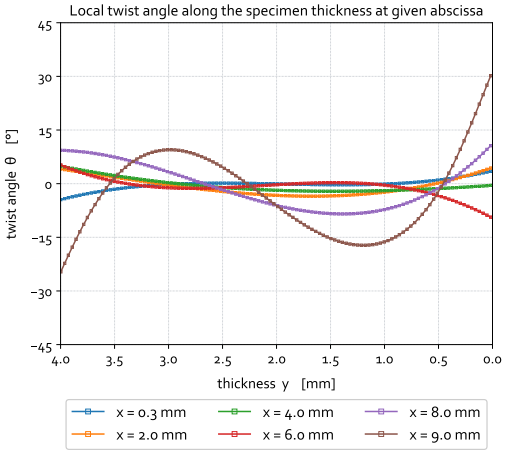

(b) Local twist angles along the spec. thickness.

Figure E.11: Transverse crack profiles $z(y)$ and corresponding twist angles $\theta(y)$ at given through-thickness positions for SEN-T specimens under dwell-fatigue conditions at 700°C (spec. S4-F4).

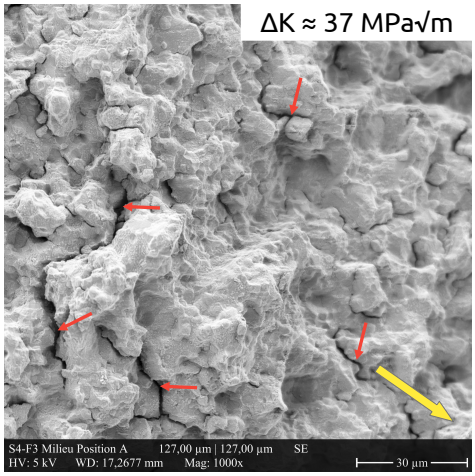

(a) $a \simeq 2.0$mm / $\Delta K \simeq 37\,\mathrm{MPa}\sqrt{\mathrm{m}}$ - middle.

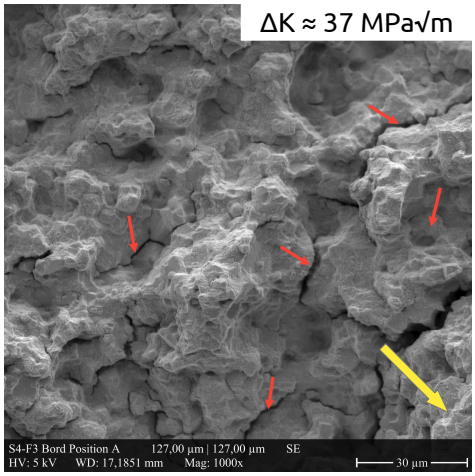

(b) $a \simeq 2.0$mm / $\Delta K \simeq 37\,\mathrm{MPa}\sqrt{\mathrm{m}}$ - egde.

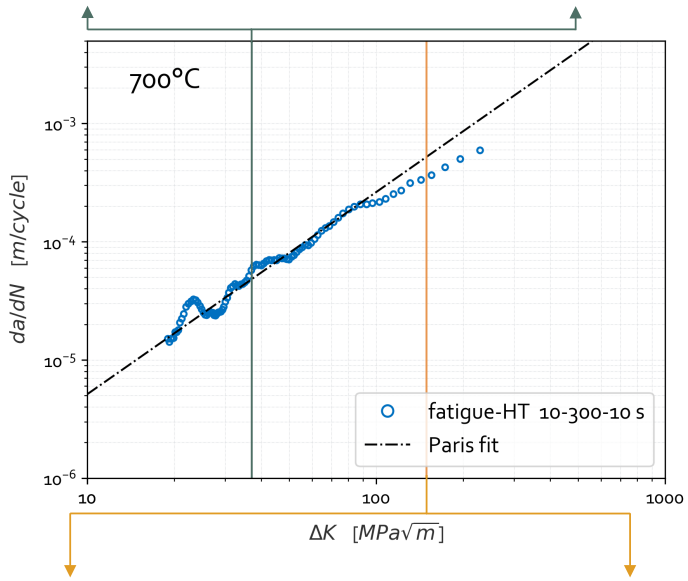

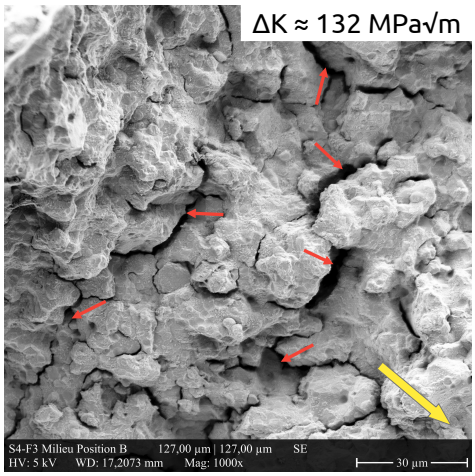

(c) $a \simeq 7.0$mm / $\Delta K \simeq 132\,\mathrm{MPa}\sqrt{\mathrm{m}}$ - middle.

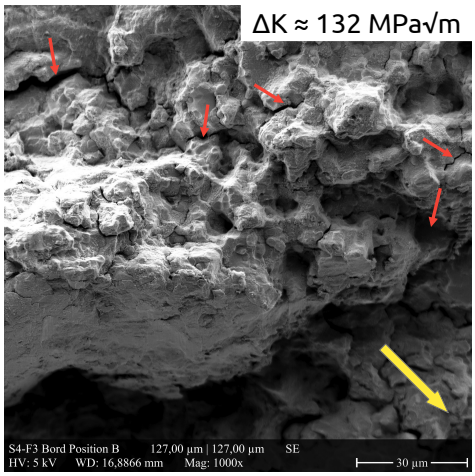

(d) $a \simeq 7.0$mm / $\Delta K \simeq 132\,\mathrm{MPa}\sqrt{\mathrm{m}}$ - edge.

Figure E.12: SEM fracture surface analyses for the S4-F3 specimen subjected to dwell-fatigue at 700°C (10-300-10 s, 400 MPa, $R = 0.05$). Identification of the main cracking mechanisms during the *stage II* crack propagation regime.

E.3 Monotonic and VLCF crack growth analysis

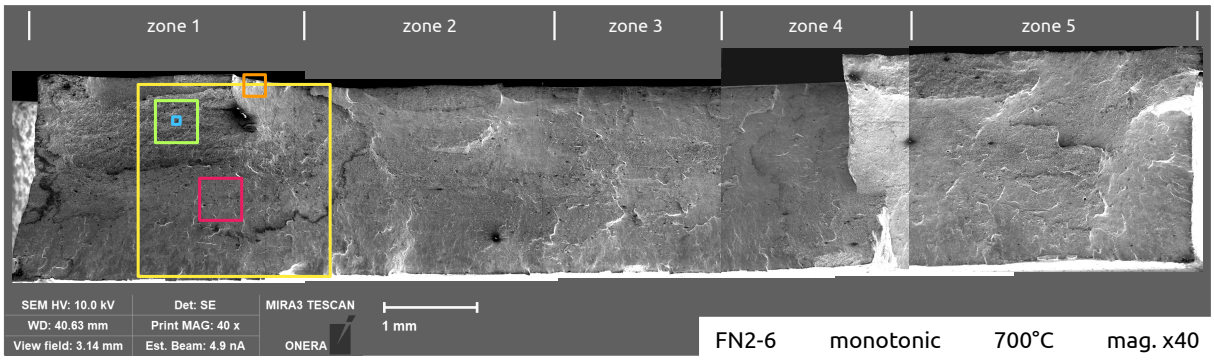

Figure E.13: Assembly of successive SEM views of the fracture surface for the spec. FN2-6 subjected to monotonic loading conditions at 700°C with $\dot{U} = 0.01\,\text{mm.s}^{-1}$.

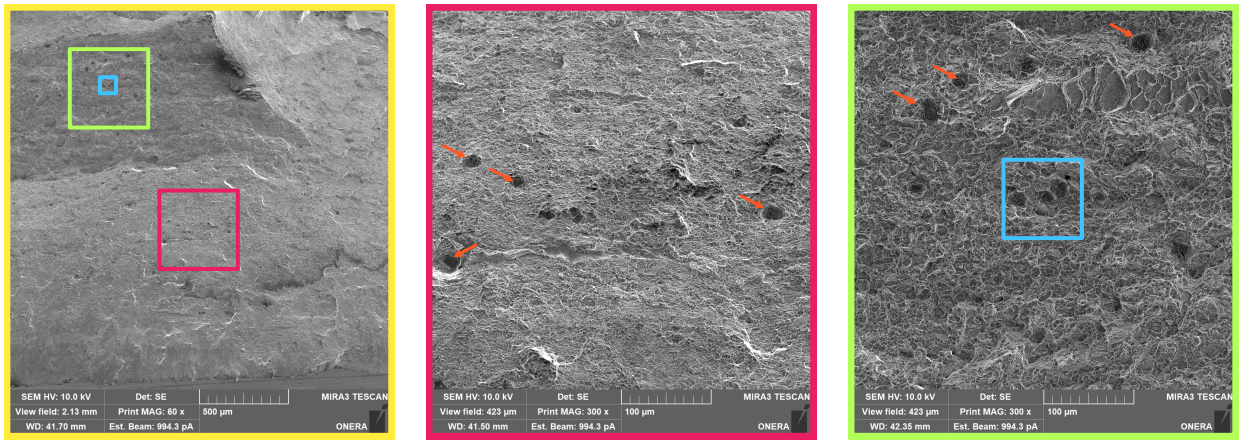

(a) FN2-6 - zone 1 - mag. ×60. (b) FN2-6 - zone 1-1 - mag. ×300. (c) FN2-6 - zone 1-2 - mag. ×300.

Figure E.14: SEM fracture surface analyses for the FN2-6 specimen subjected to monotonic loading at 700°C ($\dot{U} = 0.01\,\text{mm.s}^{-1}$). Identification of the main cracking mechanisms.

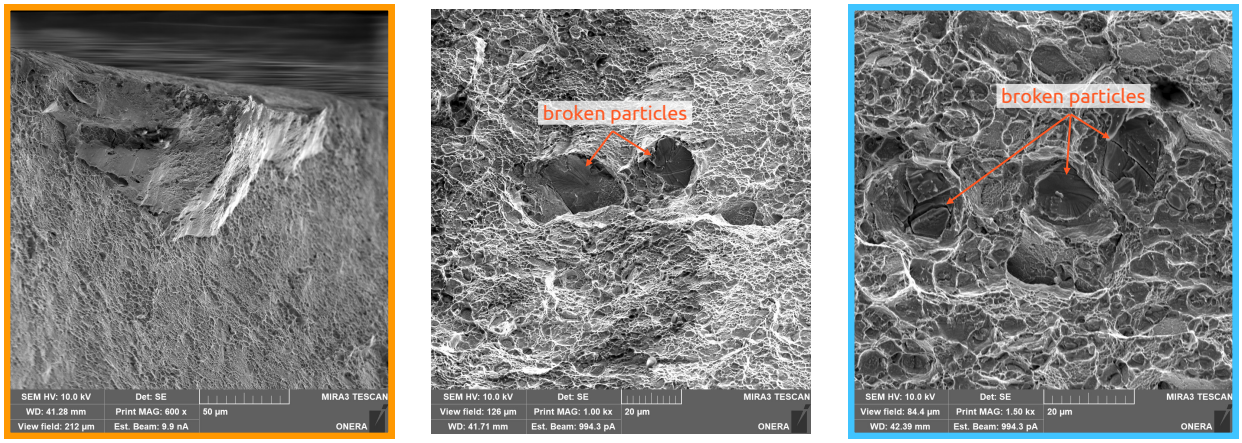

(a) FN2-6 - zone 1-3 - mag. ×600. (b) FN2-6 - mag. ×1000. (c) FN2-6 - zone 1-4 - mag. ×1500.

Figure E.15: SEM fracture surface analyses for the FN2-6 specimen subjected to monotonic loading at 700°C ($\dot{U} = 0.01\,\text{mm.s}^{-1}$). Identification of the main cracking mechanisms.

F Thermodynamical consistency of the cyclic elastic-viscoplastic-damage model

In order to satisfy the 2nd Law of Thermodynamics (*Clausius-Duhem inequality* - CDI), it must be shown that the energy dissipated due to damage and work-hardening (*i.e.* the intrinsic dissipation) is positive or zero. The CDI is given by eq. (4.24) and corresponds to:

$$\mathcal{D}_{int} = \underbrace{\underset{\sim}{\sigma} : \dot{\underset{\sim}{\varepsilon}}^{in}}_{inelastic\ power} - \underbrace{\sum_k \underset{\sim}{X}^k : \dot{\underset{\sim}{\alpha}}^k - \sum_i R^i \dot{r}^i}_{stored\ energy} + \underbrace{Y_f \dot{D}_f}_{damage\ dissipation} \geq 0 \tag{F.1}$$

$$\mathcal{D}_{int} = \dot{\lambda} \left[\underset{\sim}{\sigma} : \frac{\partial F_p}{\partial \underset{\sim}{\sigma}} - \sum_k \underset{\sim}{X}^k : \frac{\partial F_p}{\partial \underset{\sim}{X}^k} - \sum_i R^i \frac{\partial F_p}{\partial R^i} \right] + Y_f \frac{\partial \Omega^*_{D_f}}{\partial Y_f} \geq 0 \tag{F.2}$$

where $F_p\left(\underset{\sim}{\sigma}, \underset{\sim}{X}^k, R^i, D_f\right)$ is a non negative convex (real-valued) function of its arguments $\underset{\sim}{\sigma}$, $\underset{\sim}{X}^k$, R^i with $F_p\left(\underset{\sim}{0}, \underset{\sim}{0}, 0; D_f\right) = 0$ and where the fatigue damage D_f acts as a parameter. Similarly, the pseudo-potential $\Omega^*_{D_f}\left(Y_f; D_f\right)$ is a non negative function of its argument Y_f with $\Omega^*_{D_f}\left(0; D_f\right) = 0$ and D_f also acts as parameter.

Such a condition requires the damage rate to be positive or zero $\left(\dot{D}_f \geq 0\right)$ and the stored energy rate $\left(\sum_k \underset{\sim}{X}^k : \dot{\underset{\sim}{\alpha}}^k + \sum_i R^i \dot{r}^i\right)$ to remain smaller or equal to the inelastic strain power $\left(\underset{\sim}{\sigma} : \dot{\underset{\sim}{\varepsilon}}^{in}\right)$.

Inelastic power:

Using the evolution law eq. (4.44), the inelastic power can hence be rewritten:

$$\underset{\sim}{\sigma} : \dot{\underset{\sim}{\varepsilon}}^{in} = \frac{\left(\underset{\sim}{\sigma} : \underset{\sim}{\tilde{Z}}\right)}{\|\underset{\sim}{\tilde{Z}}\|} \sqrt{\frac{3}{2}} \frac{\dot{\lambda}}{f^e\left(D_f\right)} \tag{F.3}$$

Stored energy:

Evolution laws for the back strain variables eq. (4.45) & eq. (4.46) allow the stored energy related to kinematic hardening to be written:

$$\begin{aligned} \sum_k \underset{\sim}{X}^k : \dot{\underset{\sim}{\alpha}}^k &= \sum_k \underset{\sim}{X}^k : \left[\frac{\dot{\lambda}}{f^k\left(D_f\right)} \left(\sqrt{\frac{3}{2}} \underset{\sim}{\tilde{n}} - \gamma^k \varphi^k(p) \underset{\approx}{P}^D : \underset{\sim}{\alpha}^k \right) \right] \\ &= \sum_k \left[\frac{\left(\underset{\sim}{X}^k : \underset{\sim}{\tilde{Z}}\right)}{\|\underset{\sim}{\tilde{Z}}\|} \sqrt{\frac{3}{2}} - \underset{\sim}{X}^k : \underset{\sim}{X}^k \frac{\gamma^k \varphi^k(p)}{\underset{\approx}{\tilde{C}}^k} \right] \frac{\dot{\lambda}}{f^k\left(D_f\right)} \end{aligned} \tag{F.4}$$

Evolution laws for the drag strain variables eq. (4.46)allows the stored energy related to isotropic hardening to be written:

$$\sum_i R^i \dot{r}^i = \sum_i R^i \left[\frac{\dot{\lambda}}{f^i(D_f)} \left(1 - b^i r^i\right) \right] = \sum_i \left[R^i - \frac{R^{i2}}{\tilde{Q}^i} \right] \frac{\dot{\lambda}}{f^i(D_f)} \tag{F.5}$$

Global inelastic dissipation:

Combining the eq. (F.3) to eq. (F.5) and assuming for the sake of clearness equal damage-induced softening functions $f^e(D_f) = f^k(D_f) = f^i(D_f) = f(D_f)$ enable the writing of the global inelastic contribution to the intrinsic dissipation as:

$$\begin{aligned} \mathcal{D}_{int}^{in} &= \underset{\sim}{\sigma} : \dot{\underset{\sim}{\varepsilon}}^{in} - \sum_k \underset{\sim}{X}^k : \dot{\underset{\sim}{\alpha}}^k - \sum_i R^i \dot{r}^i = \frac{(\underset{\sim}{\sigma} : \tilde{\underset{\sim}{Z}})}{\|\tilde{\underset{\sim}{Z}}\|} \sqrt{\frac{3}{2}} \frac{\dot{\lambda}}{f(D_f)} \\ &- \sum_k \left[\frac{(\underset{\sim}{X}^k : \tilde{\underset{\sim}{Z}})}{\|\tilde{\underset{\sim}{Z}}\|} \sqrt{\frac{3}{2}} - \underset{\sim}{X}^k : \underset{\sim}{X}^k \frac{\gamma^k \varphi^k(p)}{\underset{\approx}{C}^k} \right] \frac{\dot{\lambda}}{f(D_f)} - \sum_i \left[R^i - \frac{R^{i2}}{\tilde{Q}^i} \right] \frac{\dot{\lambda}}{f(D_f)} \end{aligned} \tag{F.6}$$

$$\begin{aligned} \mathcal{D}_{int}^{in} &= \left[\sqrt{\frac{3}{2}} \frac{\left(\tilde{\underset{\sim}{\sigma}} - \sum_k \tilde{\underset{\sim}{X}}^k\right) : \tilde{\underset{\sim}{Z}}}{\|\tilde{\underset{\sim}{Z}}\|} + \sum_k \tilde{\underset{\sim}{X}}^k : \tilde{\underset{\sim}{X}}^k \frac{\gamma^k \varphi^k(p)}{\underset{\approx}{C}^k} - \sum_i \tilde{R}^i + \sum_i \frac{\tilde{R}^{i2}}{Q^i} \right] \dot{\lambda} \\ &= \left[\sqrt{\frac{3}{2}} \frac{\left(\tilde{\underset{\sim}{\sigma}} - \sum_k \tilde{\underset{\sim}{X}}^k\right) : \tilde{\underset{\sim}{Z}}}{\|\tilde{\underset{\sim}{Z}}\|} - \sum_i \tilde{R}^i \right] \dot{\lambda} + \left[\sum_k \tilde{\underset{\sim}{X}}^k : \tilde{\underset{\sim}{X}}^k \frac{\gamma^k \varphi^k(p)}{\underset{\approx}{C}^k} + \sum_i \frac{\tilde{R}^{i2}}{Q^i} \right] \dot{\lambda} \end{aligned} \tag{F.7}$$

Which, considering the yield function eq. (4.21), finally leads to:

$$\mathcal{D}_{int}^{in} = \left[\sigma_{ov} + R_0 \right] \dot{\lambda} + \left[\sum_k \tilde{\underset{\sim}{X}}^k : \tilde{\underset{\sim}{X}}^k \frac{\gamma^k \varphi^k(p)}{\underset{\approx}{C}^k} + \sum_i \frac{\tilde{R}^{i2}}{Q^i} \right] \dot{\lambda} \tag{F.8}$$

The viscoplastic multiplier $\dot{\lambda}$ in eq. (F.8) is always positive or zero. The first term on the right hand-side of the eq. (F.8) is always positive. As usually observed for macroscopic material models, it corresponds to the sum of the over-stress σ_{ov} and the initial yield limit R_0 whose corresponding energies are dissipated as heat, while the hardening-related energies are stored. The second term in the right hand-side of eq. (F.8) corresponds to the recovery terms in the nonlinear hardening equations. They are always positive and dissipated as heat [Chaboche, 1999].

Damage dissipation:

Finally, the fatigue damage dissipation is given thanks to eq. (4.47) as:

$$Y_f \dot{D}_f = \left(Y_f^e + \sum_k Y_f^k + \sum_i Y_f^i \right) \left[\dot{\lambda} \left\langle \frac{Y_f - Y_{f_0}}{S_f} \right\rangle_+^{m_f} e^{(\beta_f \eta_D D_f)} \mathcal{H}(p - p_D) \right] \tag{F.9}$$

where eq. (4.16) - eq. (4.18) allow to write:

$$Y_f^e = -\frac{1}{2}\frac{\partial f^e(D_f)}{\partial D_f}\,\underset{\sim}{\varepsilon}^e : \underset{\approx}{\Lambda} : \underset{\sim}{\varepsilon}^e \geq 0 \tag{F.10}$$

$$Y_f^k = -\frac{1}{2}\frac{\partial f^k(D_f)}{\partial D_f}\,\underset{\sim}{\alpha}^k : \underset{\approx}{C}^k : \underset{\sim}{\alpha}^k \geq 0 \tag{F.11}$$

$$Y_f^i = -\frac{1}{2}\frac{\partial f^i(D_f)}{\partial D_f}\, b^i\, Q^i r^{i2} \geq 0 \tag{F.12}$$

The damage rate $\dot{D}_f$ is always positive or zero due to the form of the evolution equation (see eq. (4.47)) and due to the fact that damage is an irreversible process. The damage-related energy Y_f is always positive as composed of elastic and inelastic contributions which are both quadratic forms of their arguments with positive coefficients.
Finally, the damage dissipation is always positive or zero:

$$Y_f\,\dot{D}_f \geq 0 \tag{F.13}$$

Remark: it seems important to notice that in the case of cyclic softening behavior, the coefficients Q^i in the isotropic hardening evolution rule eq. (4.46) might be negative, hence leading to a non-positive dissipation associated to D_f through the fatigue damage driving force Y_f, itself containing an inelastic contribution from both isotropic (Y_f^i) and kinematic (Y_f^k) hardenings.
This is the reason why the coefficients κ_X and κ_R have been introduced in the eq. (4.15) so as to enable/disable the inelastic contribution to Y_f when necessary.

G Supplementary results for Chap. 5

G.1 A gradient-enhancement based on the accumulated plastic strain

As a complementary analysis to the case with the non-local damage $\overline{D}$ (see sub-sect. 5.3.1), choice has been made to solve for a non-local accumulated plasticity, that is $\overline{p}$. The additional gradient equation to be solved along with the IBPV yields:

$$\overline{p} - c\,\nabla^2\overline{p} = p \quad \text{in } \Omega \quad \textit{and} \quad \nabla\overline{p}\,.\,\underline{n} = 0 \quad \text{on } \partial\Omega \tag{G.1}$$

while the non-local constitutive model, denoted $\mathbb{B}$, reads:

$$\left(\underset{\sim}{\sigma},\, p\right) = \mathbb{B}\left(\Delta\underset{\sim}{\varepsilon},\, \Delta\overline{p},\, \mathcal{V}_{int}\right) \tag{G.2}$$

Then, the constitutive equations given in Tab. 4.2 must be adapted so that to account for the non-local variable in the softening-related variables: D_f and D_v. Let's recall that along this task, creep damage mechanisms are deactivated from the material model so that D_c can be disregarded (as it does not explicitly depends on the accumulated plasticity). Hence, $D_{tot} = D_f + D_v$.
Following the technique suggested by [Geers et al., 1998] to develop non-local damage models, also used by [Engelen et al., 2003], [Feld-Payet et al., 2011], [Davaze et al., 2021], the *non-local accumulated plastic strain* $\overline{p}$ is used in the rate equations of the softening variables. The local forms of the damage evolution equations eq. (4.47) & eq. (4.60) are recalled:

$$\dot{D}_f = \dot{\lambda}\left\langle \frac{Y_f - Y_{f_0}}{S_f}\right\rangle_+^{m_f} \mathrm{e}^{(\beta_f\,\eta_D\,D_{tot})}\;\mathcal{H}\left(p - p_D\right) \tag{G.3}$$

$$\dot{D}_v = (1 - D_{tot})\;\mathrm{tr}\,\underset{\sim}{\dot{\varepsilon}}^{in} = (1 - D_{tot})\,\frac{\dot{\lambda}}{f^e\left(D_{tot}\right)}\,\sqrt{\frac{3}{2}}\;\underset{\sim}{\tilde{\eta}}^S : \underset{\sim}{1} \tag{G.4}$$

along with the accumulated plastic strain rate eq. (4.37):

$$\dot{p} = \sqrt{\frac{2}{3}}\left\|\,\underset{\sim}{\dot{\varepsilon}}^{in}\,\right\|_H = \frac{\dot{\lambda}}{f^e\left(D_{tot}\right)} = \frac{\left(\underset{\approx}{H}^{-1} : \underset{\sim}{\tilde{Z}}\right) : \underset{\sim}{\dot{\varepsilon}}^{in}}{\tilde{\sigma}_{eq}} \tag{G.5}$$

Then, the damage rate equations eq. (G.3) & eq. (G.4) can be rewritten in an incremental form according to the increment of non-local plasticity $\Delta\overline{p} = \overline{p}_{n+1} - \overline{p}_n$, which reads:

$$\Delta D_f = \Delta\overline{p}\;f^e\left(D_{tot}\right)\left\langle \frac{Y_f - Y_{f_0}}{S_f}\right\rangle_+^{m_f} \mathrm{e}^{(\beta_f\,\eta_D\,D_{tot})}\;\mathcal{H}\left(p - p_D\right) \tag{G.6}$$

$$\Delta D_v = (1 - D_{tot})\;\Delta\overline{p}\;\sqrt{\frac{3}{2}}\;\underset{\sim}{\tilde{\eta}}^S : \underset{\sim}{1} \tag{G.7}$$

where eq. (G.6) & eq. (G.7) can now be referred to as *non-local damage* increments. It is to be noticed that, similarly to [Engelen et al., 2003], [Davaze et al., 2021], the strain-hardening and the rate-dependency (*i.e.* the over-stress) in the yield criterion still remain controlled by the local plasticity (through r or $\dot{\lambda}$) while only the damage variables evolve according to its non-local counterpart:

$$\mathcal{F}_y^{vp} = \sqrt{\frac{3}{2}} \left\| \tilde{\tilde{Z}} \right\|_H - \sum_i b^i Q^i r^i - R_0 - \sigma_{ov}(\dot{\lambda}) \leq 0 \tag{G.8}$$

The performance of this approach and the main conclusions to be drawn are illustrated in the following section, in sect. G.2.

G.2 Validation of the model with non-local plasticity

As previously said, the non-local accumulated plasticity has been considered in a first attempt as the non-local variable to regularize the stress-softening problem (see sect. G.1). Use is made of the 4-fields c2d6r mixed non-local elements (see Fig. 1.17a).

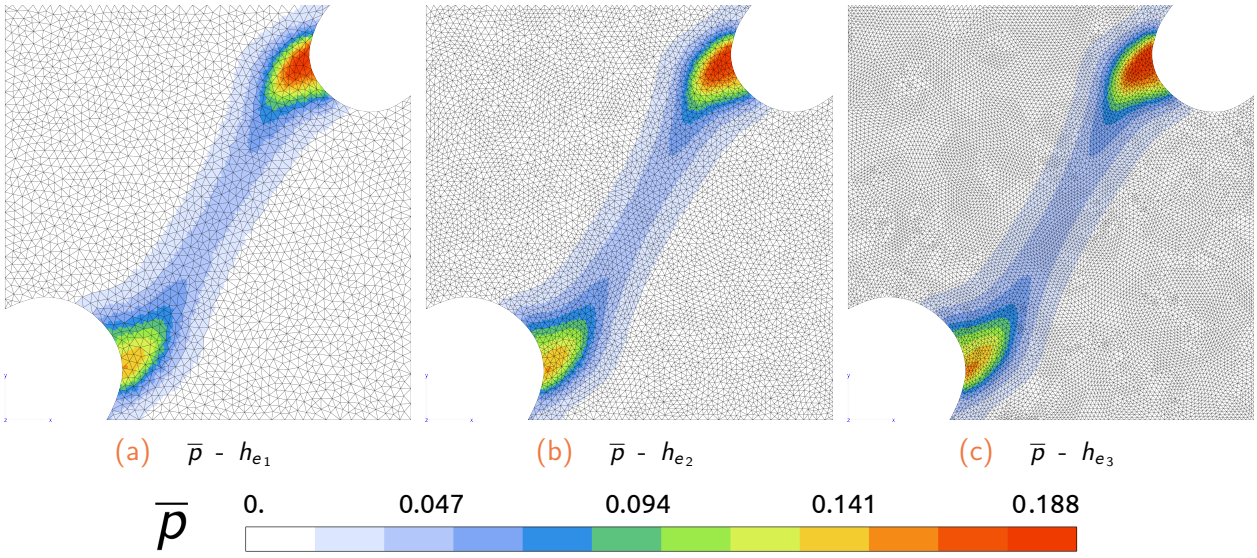

Figure G.1: Non-local accumulated plasticity field for the double-notched specimen (4-fields FEs, deformed state, mag. factor $\times 1.$) at $u = 0.1823\,\text{mm}$ for the three mesh sizes: $h_e = 0.3,\ 0.2,\ 0.1\,\text{mm}$.

In Fig. G.1 the non-local accumulated plastic strain for the three spatial discretizations is reported. Plots are given at the same displacement, that is for $u = 0.1823\,\text{mm}$. One can notice in Fig. G.1a to Fig. G.1c that the non-local accumulated plastic strain field is equivalent regardless the mesh-size.

In Fig. G.2a to Fig. G.2c, the non-local damage is plotted for the same displacement as in Fig. G.2 and it appears to follow the same trend. Thus, such a non-local method allows for the strain and damage localization process to be accounted for while preserving the well-posedness of the IBVP.

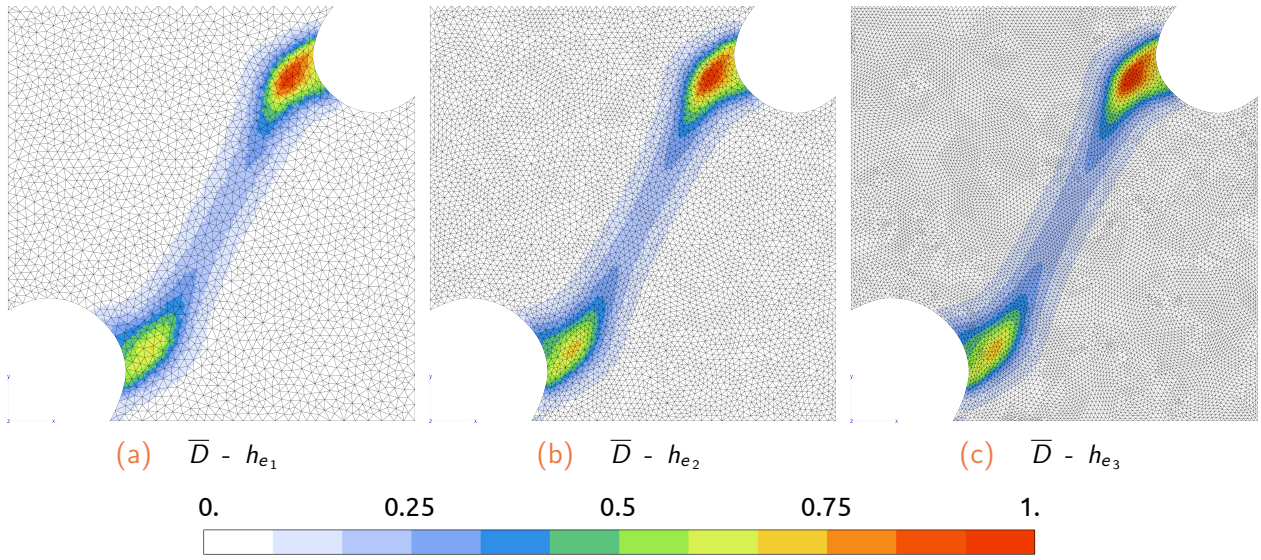

Figure G.2: Non-local damage field for the double-notched specimen (4-fields FEs, deformed state, mag. factor $\times 1.$) at $u = 0.1823\,\text{mm}$ for the three mesh sizes: $h_e = 0.3,\ 0.2,\ 0.1\,\text{mm}$.

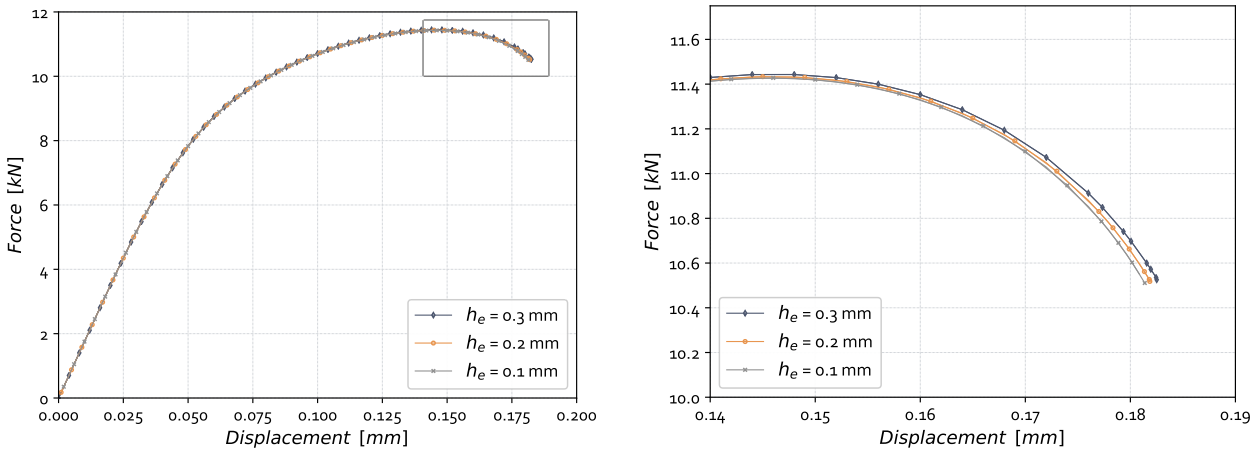

(a) Effect of the mesh size on the mechanical response.

(b) Zoom on the stress-softening phase.

Figure G.3: Comparison of the force-displacement curves for the double-notched specimen. Effect of the mesh size on the overall mechanical response. Regularization of the accumulated plasticity.

Paying attention to the macroscopic resulting load-displacement curves enables the possibility to check that the mesh-dependency has been significantly reduced thanks to the non-local approach. Indeed, for tensile loading, the dissipated energy can be estimated using the integral of the product between the effort and the imposed displacement. The macroscopic load-displacement curve is hence a good indicator for the dissipated energy upon loading. Each curve hence exhibits a strain-hardening phase which is not influenced by damage, Fig. G.3a, up to the peak stress, and then the damage-induced softening phase is clearly noticeable.
One can see in Fig. G.3a that when decreasing the mesh-size, the numerical results tend toward mesh-convergence. Thus, the spatial discretization does not influence the numerical approximation of the mechanical problem. A closer look to the stress-softening phase, Fig. G.3b, evidences small differences in the macroscopic dissipation from one mesh to another. These slight differences may

come from the numerical accuracy of the solving procedure which depends on convergence criteria for both the local and global resolution loops (see Tab. 5.3). Moreover, it is well acknowledged that decreasing the mesh size generally leads to fewer discretization errors and consequently to a better numerical approximation. Hence, such a rule remains valid for the present non-local damage model: the finer the mesh size, the better the non-local interaction and subsequently the better the numerical approximation.

Comparison of the two regularized variables:

In the last paragraph, as well with the sub-sect. 5.5.2.1, results obtained with a regularization on p and D have been discussed. Looking at Fig. G.3 & Fig. 5.5, one can notice slightly different results in the macroscopic force-displacement curves. Both regularized variables give well converged results since the smaller the mesh size, the closer the macroscopic results. Nonetheless, solving the mechanical problem for $\overline{D}$ represents a larger number of coupling cases in the equations, as well as a larger number of cross-derivative terms in the non-local cyclic elastic-viscoplastic damage model. The consistent material tangents matrices hence exhibit slightly more complex forms. Consequently, the resolution process is a bit more slower since more complex matrix inversions operations are required. Moreover, the extent of non-linearity to the problem is generally increased since D is fully coupled to all the elastic and viscoplastic properties. Despite these aspects, and as said in sub-sect. 5.2.2 page 190, the regularization through $\overline{D}$ has been favored in this work due to the cyclic properties of the considered loading schemes.

G.3 Validation of the model with non-local total damage

G.3.1 Linear bar with imperfection

In order to simply assess the regularization capability of the proposed damage model, a strip test is simulated. It consists in a 2D bar in tension where there exists a zone of fixed width where material properties are artificially weakened so that to prompt strain localization, see red elements in Fig. G.4b. The mesh density along the length of the strip is assumed to change from one simulation to another. The characteristic length was set to $\ell_c = 0.55\,\text{mm}$ while the other material parameters are kept unchanged for all the tests.

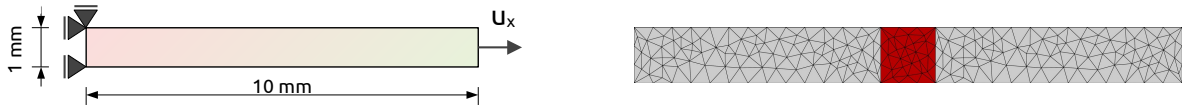

(a) Geometry and BC. (b) One FE discretization with weakened zone.

Figure G.4: Geometry of the strip model subjected to tensile loading with corresponding dimensions and associated BC (after [Sabnis, 2012]).

It can be seen in Fig. G.5 that, as expected, the damage tends to develop in the weakened zone. Moreover, the size of the regularization zone remains almost unchanged, irrespective of the spatial

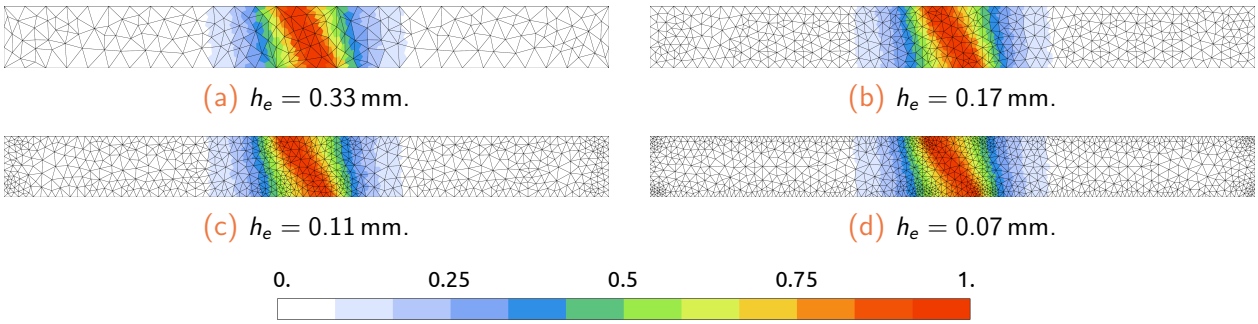

(a) $h_e = 0.33\,\text{mm}$. (b) $h_e = 0.17\,\text{mm}$.

(c) $h_e = 0.11\,\text{mm}$. (d) $h_e = 0.07\,\text{mm}$.

Figure G.5: Non-local damage in the strip bar subjected to monotonic tensile loading (c2d6r FE).

discretization, see Fig. G.5a to Fig. G.5d. Finally, regardless the mesh fineness, the regularization process seems to operate so that to get a spatial distribution of the non-local damage field. In the following, more complex cases are discussed so that to validate the regularization procedure.

G.3.2 Tensile test (rectangular plate)

This geometry is inspired by the work of [Saanouni and Chaboche, 2003] and [El Khaoulani and Bouchard, 2012]. The material is assumed to be under plane strain conditions. This example aims at illustrating the capability of the modeling approach to exhibit the well-known plastic flow localization mode (shear bands). The specimen is given in Fig. G.6a as well with corresponding BC. The considered non-local variable is $\overline{D}$ while material parameters are reported in the appendices, see Tab. H.3 page 300.

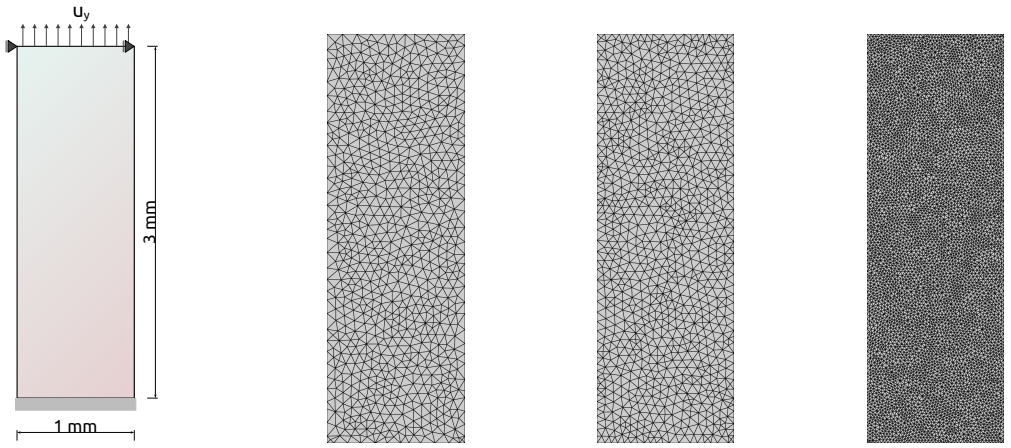

(a) Geometry and BC. (b) $h_e = 0.1\,\text{mm}$. (c) $h_e = 0.05\,\text{mm}$. (d) $h_e = 0.025\,\text{mm}$.

Figure G.6: Geometry of the rectangular tensile plate specimen subjected to tensile loading with corresponding dimensions, associated BC and mesh discretizations (after [Saanouni and Chaboche, 2003]).

In Fig. G.7, the results for the plane-strain tensile plate are reported. The corresponding displacement is $u = 0.323\,\text{mm}$. One can easily see that the non-local damage field is similar for each mesh size. Moreover, the strong coupling between damage and behavior allows for the realistic localization mode, *i.e.* the double shear bands, to be exhibited.

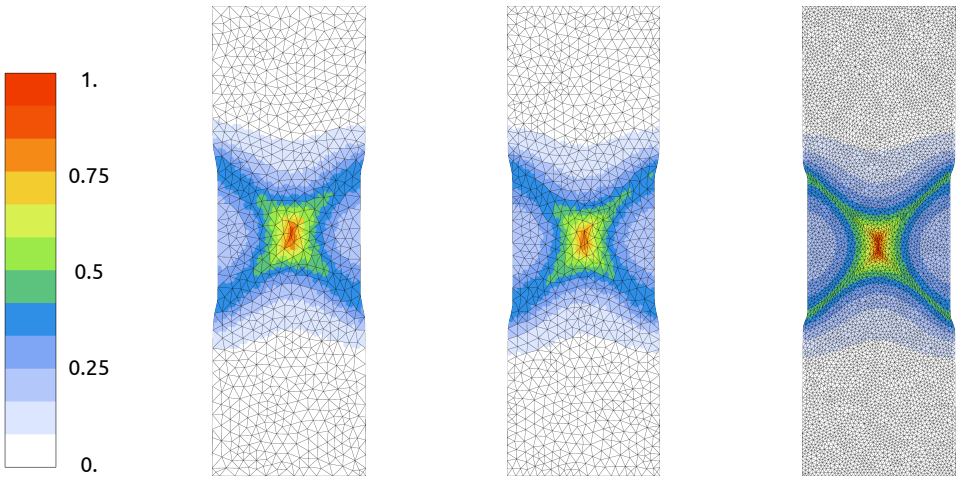

Figure G.7: Non-local damage field for the plane-strain rectangular tensile specimen (4-fields FEs, deformed state, mag. factor $\times 0.25$) at $t = 32.3\,\mathrm{s}$ for the three mesh sizes: $h_e = 0.1,\ 0.05,\ 0.025\,\mathrm{mm}$.

Moreover, one can notice in Fig. G.8a that the Von Mises stress tends to zero as long as damage increases, hence causing the stress-softening response of the material. In the nearly fully damaged zone, in the center of the specimen, the stresses vanish. The use of 4-fields mixed and non-local FEs in the calculation allows for the volumetric locking and the mesh-dependence to be alleviated. Indeed, the stress fields in Fig. G.8a and Fig. G.8b seem to be well defined without locking-related spurious oscillations. It can also be noticed in Fig. G.8c that the accumulated plastic strain remains localized in a thin band of FEs which consequently results in a local damage field, Fig. G.8d. Nonetheless, the strong coupling between non-local damage and material behavior enables to solve for the ill-posedness of the IBVP so that to get mesh-objective results, see Fig. G.7. The non-local enhancement hence allows for the dissipation process to be controlled.

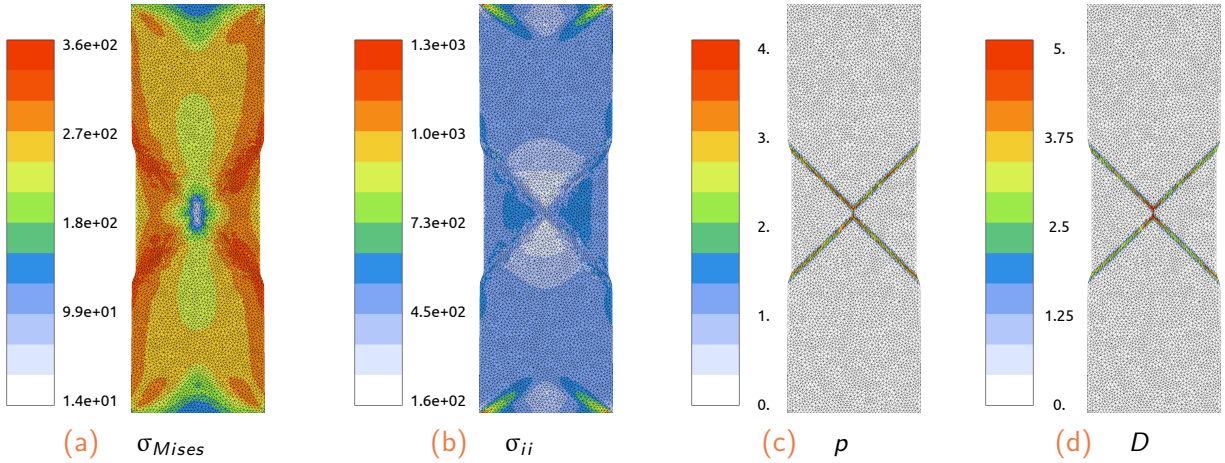

Figure G.8: Stress, plasticity and local damage fields for the plane-strain rectangular tensile specimen (4-fields FEs, deformed state, mag. factor $\times 0.25$) at $u = 0.323\,\mathrm{mm}$ for the mesh size $h_{e_3} = 0.025\,\mathrm{mm}$.

H Material model parameters for structural calculations

H.1 Material constants for the RVE simulations

For the simulations on a Representative Volume Element (c3d20r FE in Z-set), sub-sect. 4.4.1 page 172, material constants have been chosen to values defined in Tab. H.1. Saturated state for the hardening mechanisms is also assumed.

E	Confidential	MPa	m_f		-	S_f		MPa
ν		-	β_f		-	Y_{f_0}		MPa
R_0		MPa	p_D		-	h		-
$Q^i \quad i \in [1-2]$		MPa	m_c		-	S_c		MPa
$b^i \quad i \in [1-2]$		-	β_c		-	D^{crit}		-
$C^k \quad k \in [1-3]$		MPa	α_c		-	δ_c		-
$\gamma^k \quad k \in [1-3]$		-	φ_c		-	D_{v_0}		-
$\varphi^k_\infty \quad k \in [1-3]$		-	$\dot{\epsilon}_0$		s^{-1}	K		MPa
$\omega^k \quad k \in [1-3]$		-	n		-	m		-
Exponential damage function		η_D	0.22	-				

Table H.1: Material parameters for the RVE simulations.

H.2 Material constants for the double-notched square and the 2-holes rectangular specimens

In the calculations of the double-notched square specimen, sub-sect. 5.5.2.1 page 208, as well as for those for the rectangular plate with 2 holes, sub-sect. 5.5.2.2 page 209, the creep and volumetric damage are not accounted for. Hence parameters related to these damaging processes are set to null values. Saturated state for the hardening mechanisms is also assumed.

E	Confidential	MPa	m_f	Confidential	-	S_f	Confidential	MPa
ν		-	β_f		-	Y_{f_0}		MPa
R_0		MPa	p_D		-	h		-
$Q^i \quad i \in [1-2]$		MPa	m_c		-	S_c		MPa
$b^i \quad i \in [1-2]$		-	β_c		-	D^{crit}		-
$C^k \quad k \in [1-3]$		MPa	α_c		-	δ_c		-
$\gamma^k \quad k \in [1-3]$		-	φ_c		-	D_{v_0}		-
$\varphi^k_\infty \quad k \in [1-3]$		-	$\dot{\epsilon}_0$		s^{-1}	K		MPa
$\omega^k \quad k \in [1-3]$		-	n		-	m		-
Exponential damage function		η_D	0.22	-				

Table H.2: Material parameters for the double-notched square and the 2-holes rectangular specimens.

H.3 Material constants for the tensile rectangular specimen

In the calculation of the tensile plate specimen, sub-sect. G.3.2 page 297, the creep and volumetric damage are not accounted for. Hence parameters related to these damaging processes are set to null values. The other material parameters come from the example of [Saanouni and Chaboche, 2003]. Saturated state for the hardening mechanisms is also assumed, while a simple Norton-Perzyna flow rule is considered.

E	2.00e+05	MPa	m_f	1.0	-	S_f	0.8	MPa
ν	0.3	-	β_f	1.0	-	Y_{f_0}	0.	MPa
R_0	400.0	MPa	p_D	0.	-	h	1.0	-
$Q^i \quad i \in [1-2]$	20.0; 0.0	MPa	φ_c	0.	-	D_{v_0}	1.0e-5	-
$b^i \quad i \in [1-2]$	50.; 0.0	-	K_N	10.0	MPa	n_N	50.	-
$C^k \quad k \in [1-3]$	1.00e+04; 0.0; 0.0	MPa	D^{crit}	0.99	-			
$\gamma^k \quad k \in [1-3]$	1.00e+02; 1.00e+01; 1.00e+01	-						
$\varphi^k_\infty \quad k \in [1-3]$	1.0; 1.0; 1.0	-						
$\omega^k \quad k \in [1-3]$	1.00e+3; 1.00e+3; 1.00e+3	-						
Lemaitre damage function								

Table H.3: Material parameters for the tensile plate specimen.

Material Jacobian matrix (non-local model)

In the implicit implementation of the multi-mechanism cyclic constitutive model presented in Chap. 5, a system of residual equations has been defined, see eq. (5.54). All these equations should vanish in case of inelastic load increment. Hence, in this appendix, the material Jacobian matrix associated with the **local** cyclic viscoplastic-damage model is detailed. Such a matrix is composed of the derivatives of each residual equation with respect to each internal variable of the system. Let's first recall the problem's variables:

$$DoF : \left\{ \underline{u}\,, \overline{D} \right\}; \qquad \mathcal{V}_{IN} : \left\{ \underset{\sim}{\varepsilon}\,, \overline{D} \right\}; \qquad \mathcal{V}_{OUT} : \left\{ \underset{\sim}{\sigma}\,, D \right\}; \qquad \mathcal{V}_{int} : \left\{ \underset{\sim}{\sigma}\,, \underset{\sim}{\varepsilon}^{e}\,, \underset{\sim}{\alpha}^{k}\,, r^{i}\,, \lambda\,, D \right\}$$

Let us note that the presence of the stress tensor $\underset{\sim}{\sigma}$ in the internal state variables directly follows from the introduction of the micro-cracks closure effect within the model, see sub-sect. 4.3.2.2. In case this effect is not included in the model, this variable is disabled, hence leaving the elastic strain tensor $\underset{\sim}{\varepsilon}^{e}$ to rule the additive strain decomposition.

I.1 Differential equations to be integrated

$$\underset{\sim}{\varepsilon}^{e} = \underset{\approx}{\Lambda}^{-1} : \tilde{\underset{\sim}{\sigma}}_{uc}(\overline{D}) = \underset{\sim}{0} \quad \text{(if quasi-unilateral conditions)} \tag{I.1a}$$

$$\dot{\underset{\sim}{\varepsilon}}^{e} = \dot{\underset{\sim}{\varepsilon}} - \dot{\underset{\sim}{\varepsilon}}^{in} = \dot{\underset{\sim}{\varepsilon}} - \frac{\dot{\lambda}}{f^{e}(\overline{D})}\sqrt{\frac{3}{2}}\,\tilde{\underset{\sim}{n}} = \underset{\sim}{0} \tag{I.1b}$$

$$\dot{\underset{\sim}{\alpha}}^{k} = \frac{\dot{\lambda}}{f^{k}(\overline{D})}\left(\sqrt{\frac{3}{2}}\,\tilde{\underset{\sim}{n}} - \gamma^{k}\varphi^{k}(p)\,\underset{\approx}{P}^{D} : \underset{\sim}{\alpha}^{k}\right) = \underset{\sim}{0} \tag{I.1c}$$

$$\dot{r}^{i} = \frac{\dot{\lambda}}{f^{i}(\overline{D})}\left(1 - b^{i} r^{i}\right) = 0 \tag{I.1d}$$

$$\dot{\tilde{p}} = \dot{\lambda} = \phi_{v}(\mathcal{F}_{y}) = 0 \tag{I.1e}$$

$$\begin{aligned} \dot{D} = \dot{\lambda}\left\langle \frac{Y_{f} - Y_{f_0}}{S_{f}} \right\rangle_{+}^{m_f} \mathrm{e}^{\beta_f \eta_D \overline{D}}\; \mathcal{H}(p - p_D) - \left\langle \frac{\chi_c(\underset{\sim}{\sigma})}{S_{c}} \right\rangle_{+}^{m_c} \mathrm{e}^{\beta_c \eta_D \overline{D}} \\ - (1 - \overline{D})\,\frac{\dot{\lambda}}{f^{e}(\overline{D})}\sqrt{\frac{3}{2}}\,\langle\, \tilde{\underset{\sim}{n}}^{S} : \underset{\sim}{1} \,\rangle_{+} = 0 \end{aligned} \tag{I.1f}$$

with:

$$\mathcal{F}_y^{vp} = \mathcal{F}_y - \sigma_{ov} = \sqrt{\frac{3}{2}}\left\|\tilde{\underset{\sim}{Z}}\right\|_H - \sum_i \tilde{R}^i - R_0 - \sigma_{ov} \leq 0 \tag{I.2a}$$

$$\underset{\sim}{\tilde{n}} = \frac{\underset{\approx}{H} : \tilde{\underset{\sim}{Z}}}{\left\|\tilde{\underset{\sim}{Z}}\right\|_H}; \qquad \underset{\sim}{\tilde{n}}^S = \frac{\underset{\approx}{H}^S : \tilde{\underset{\sim}{Z}}}{\left\|\tilde{\underset{\sim}{Z}}\right\|_H} \tag{I.2b}$$

$$\underset{\approx}{H} = \underset{\approx}{P}^D + 2\,\varphi_c\, g_D(\overline{D})\,\underset{\approx}{P}^S; \qquad \underset{\approx}{H}^S = 2\,\varphi_c\, g_D(\overline{D})\,\underset{\approx}{P}^S \tag{I.2c}$$

$$\underset{\approx}{H}^{-1} = \underset{\approx}{P}^D + \frac{1}{2\,\varphi_c\, g_D(\overline{D})}\,\underset{\approx}{P}^S \tag{I.2d}$$

$$\tilde{\underset{\sim}{Z}} = \tilde{\underset{\sim}{\sigma}}^D - \sum_k \tilde{\underset{\sim}{X}}^k \tag{I.2e}$$

$$\left\|\tilde{\underset{\sim}{Z}}\right\|_H = \sqrt{\tilde{\underset{\sim}{Z}} : \underset{\approx}{H} : \tilde{\underset{\sim}{Z}}} \tag{I.2f}$$

$$\phi_v(\mathcal{F}_y) = \dot{\epsilon}_0 \left[\sinh\left\langle \frac{\mathcal{F}_y}{K}\right\rangle_+^n\right]^m \qquad \text{or} \qquad \sigma_{ov} = K\left[\operatorname{arcsinh}\left(\frac{\dot{\lambda}}{\dot{\epsilon}_0}\right)^{\frac{1}{m}}\right]^{\frac{1}{n}} \tag{I.2g}$$

$$\chi_c(\underset{\sim}{\sigma}) = \alpha_c\, I_0(\underset{\sim}{\sigma}) + \delta_c\, I_1(\underset{\sim}{\sigma}) + (1-\alpha_c-\delta_c)\sqrt{3J_2(\underset{\sim}{\sigma})} \tag{I.2h}$$

I.2 Residual equations for local update of the internal variables

$$\mathcal{R}_{\underset{\sim}{\sigma}} = \underset{\sim}{\varepsilon}^e - \underset{\approx}{\Lambda}^{-1} : \tilde{\underset{\sim}{\sigma}}_{uc}(\overline{D}) = \underset{\sim}{0} \quad \text{(if quasi-unilateral conditions)} \tag{I.3a}$$

$$\mathcal{R}_{\underset{\sim}{\varepsilon}^e} = \Delta\underset{\sim}{\varepsilon}^e - \Delta\underset{\sim}{\varepsilon} + \frac{\Delta\lambda}{f^e(\overline{D})}\sqrt{\frac{3}{2}}\,\underset{\sim}{\tilde{n}} = \underset{\sim}{0} \tag{I.3b}$$

$$\mathcal{R}_{\underset{\sim}{\alpha}^k} = \Delta\underset{\sim}{\alpha}^k - \frac{\Delta\lambda}{f^k(\overline{D})}\left(\sqrt{\frac{3}{2}}\,\underset{\sim}{\tilde{n}} - \gamma^k\varphi^k(p)\,\underset{\approx}{P}^D : \underset{\sim}{\alpha}^k\right) = \underset{\sim}{0} \tag{I.3c}$$

$$\mathcal{R}_{r^i} = \Delta r^i - \frac{\Delta\lambda}{f^i(\overline{D})}\left(1 - b^i r^i\right) = 0 \tag{I.3d}$$

$$\mathcal{R}_\lambda = \Delta\lambda - \Delta t\,\phi_v(\mathcal{F}_y) = 0 \tag{I.3e}$$

$$\begin{aligned}\mathcal{R}_D = \Delta D - \Delta\lambda\left\langle\frac{Y_f - Y_{f_0}}{S_f}\right\rangle_+^{m_f} \mathrm{e}^{\beta_f\,\eta_D\,\overline{D}}\;\mathcal{H}(p-p_D) - \Delta t\left\langle\frac{\chi_c(\underset{\sim}{\sigma})}{S_c}\right\rangle_+^{m_c}\mathrm{e}^{\beta_c\,\eta_D\,\overline{D}} \\ -(1-\overline{D})\,\frac{\Delta\lambda}{f^e(\overline{D})}\sqrt{\frac{3}{2}}\left\langle\,\underset{\sim}{\tilde{n}} : \underset{\sim}{1}\,\right\rangle = 0\end{aligned} \tag{I.3f}$$

where the eq. (I.3a) is not the incremental form of a differential equation. Such an equation is added in order to solve the elastic law in an implicit manner in the case where micro-defects closure effect on the elasticity law is activated [Lemaitre and Desmorat, 2005], [Otin, 2007].
Indeed, the effective stress defined in eq. (4.57) appearing in the elasticity law eq. (I.3a) is not used for the viscoplastic-damage coupling but only for that of elastic-damage. The relationship $\underset{\sim}{\sigma}(\underset{\sim}{\varepsilon}^e, \overline{D})$ is now implicit and given by the numerical inverting of the elasticity law upon iterating at the local (integration point) level. The stress tensor in eq. (4.56) cannot be written explicitly as a function of the strain tensor. Thus, given the input $\underset{\sim}{\varepsilon}$, the corresponding stress tensor $\underset{\sim}{\sigma}$ required as an output in the local integration loop can be obtained as the solution of the non-linear tensorial equation for $\underset{\sim}{\sigma}$, eq. (I.3a). This solution can be obtained by means of the Newton-Raphson algorithm [de Souza Neto et al., 2011].

Material Jacobian matrix

The Jacobian matrix relating the derivatives of the material residual equations with respect to the integrated variables is organized as follows:

$$\mathcal{J} = \frac{\partial \mathcal{R}}{\partial \Delta \mathcal{V}_{int}} = \begin{bmatrix} \frac{\partial \mathcal{R}_{\underset{\sim}{\sigma}}}{\partial \Delta \underset{\sim}{\sigma}} & \frac{\partial \mathcal{R}_{\underset{\sim}{\sigma}}}{\partial \Delta \underset{\sim}{\varepsilon}^e} & \frac{\partial \mathcal{R}_{\underset{\sim}{\sigma}}}{\partial \Delta \underset{\sim}{\alpha}^k} & \frac{\partial \mathcal{R}_{\underset{\sim}{\sigma}}}{\partial \Delta r^i} & \frac{\partial \mathcal{R}_{\underset{\sim}{\sigma}}}{\partial \Delta \lambda} & \frac{\partial \mathcal{R}_{\underset{\sim}{\sigma}}}{\partial \Delta D} \\ \frac{\partial \mathcal{R}_{\underset{\sim}{\varepsilon}^e}}{\partial \Delta \underset{\sim}{\sigma}} & \frac{\partial \mathcal{R}_{\underset{\sim}{\varepsilon}^e}}{\partial \Delta \underset{\sim}{\varepsilon}^e} & \frac{\partial \mathcal{R}_{\underset{\sim}{\varepsilon}^e}}{\partial \Delta \underset{\sim}{\alpha}^k} & \frac{\partial \mathcal{R}_{\underset{\sim}{\varepsilon}^e}}{\partial \Delta r^i} & \frac{\partial \mathcal{R}_{\underset{\sim}{\varepsilon}^e}}{\partial \Delta \lambda} & \frac{\partial \mathcal{R}_{\underset{\sim}{\varepsilon}^e}}{\partial \Delta D} \\ \frac{\partial \mathcal{R}_{\underset{\sim}{\alpha}^k}}{\partial \Delta \underset{\sim}{\sigma}} & \frac{\partial \mathcal{R}_{\underset{\sim}{\alpha}^k}}{\partial \Delta \underset{\sim}{\varepsilon}^e} & \frac{\partial \mathcal{R}_{\underset{\sim}{\alpha}^k}}{\partial \Delta \underset{\sim}{\alpha}^k} & \frac{\partial \mathcal{R}_{\underset{\sim}{\alpha}^k}}{\partial \Delta r^i} & \frac{\partial \mathcal{R}_{\underset{\sim}{\alpha}^k}}{\partial \Delta \lambda} & \frac{\partial \mathcal{R}_{\underset{\sim}{\alpha}^k}}{\partial \Delta D} \\ \frac{\partial \mathcal{R}_{r^i}}{\partial \Delta \underset{\sim}{\sigma}} & \frac{\partial \mathcal{R}_{r^i}}{\partial \Delta \underset{\sim}{\varepsilon}^e} & \frac{\partial \mathcal{R}_{r^i}}{\partial \Delta \underset{\sim}{\alpha}^k} & \frac{\partial \mathcal{R}_{r^i}}{\partial \Delta r^i} & \frac{\partial \mathcal{R}_{r^i}}{\partial \Delta \lambda} & \frac{\partial \mathcal{R}_{r^i}}{\partial \Delta D} \\ \frac{\partial \mathcal{R}_{\lambda}}{\partial \Delta \underset{\sim}{\sigma}} & \frac{\partial \mathcal{R}_{\lambda}}{\partial \Delta \underset{\sim}{\varepsilon}^e} & \frac{\partial \mathcal{R}_{\lambda}}{\partial \Delta \underset{\sim}{\alpha}^k} & \frac{\partial \mathcal{R}_{\lambda}}{\partial \Delta r^i} & \frac{\partial \mathcal{R}_{\lambda}}{\partial \Delta \lambda} & \frac{\partial \mathcal{R}_{\lambda}}{\partial \Delta D} \\ \frac{\partial \mathcal{R}_{D}}{\partial \Delta \underset{\sim}{\sigma}} & \frac{\partial \mathcal{R}_{D}}{\partial \Delta \underset{\sim}{\varepsilon}^e} & \frac{\partial \mathcal{R}_{D}}{\partial \Delta \underset{\sim}{\alpha}^k} & \frac{\partial \mathcal{R}_{D}}{\partial \Delta r^i} & \frac{\partial \mathcal{R}_{D}}{\partial \Delta \lambda} & \frac{\partial \mathcal{R}_{D}}{\partial \Delta D} \end{bmatrix} \tag{I.4}$$

In the following, each term of the Jacobian matrix is derived consistently with the implicit relations between internal state variables.

Derivatives of $\mathcal{R}_{\underset{\sim}{\sigma}}$ (in case of quasi-unilateral conditions)

$$\mathcal{R}_{\underset{\sim}{\sigma}} = \underset{\sim}{\varepsilon}^e - \underset{\approx}{\Lambda}^{-1} : \tilde{\underset{\sim}{\sigma}}_{uc} = \underset{\sim}{\varepsilon}^e - \frac{1+\nu}{E}\left[\frac{\underset{\sim}{\sigma}_+}{f^e(\overline{D})} + \frac{\underset{\sim}{\sigma}_-}{f_h^e(h,\overline{D})}\right] + \frac{\nu}{E}\left[\frac{\langle \operatorname{tr}\underset{\sim}{\sigma}\rangle}{f^e(\overline{D})} - \frac{\langle -\operatorname{tr}\underset{\sim}{\sigma}\rangle}{f_h^e(h,\overline{D})}\right]\underset{\sim}{1} = \underset{\sim}{0}$$

- $\dfrac{\partial \mathcal{R}_{\underset{\sim}{\sigma}}}{\partial \Delta \underset{\sim}{\sigma}} = \theta\, \underset{\approx}{I}$
- $\dfrac{\partial \mathcal{R}_{\underset{\sim}{\sigma}}}{\partial \Delta \underset{\sim}{\varepsilon}^e} = -\theta\left[\dfrac{1+\nu}{E}\left(\underset{\approx}{P}^+_{\sigma}\dfrac{1}{f^e(\overline{D})} + \underset{\approx}{P}^-_{\sigma}\dfrac{1}{f_h^e(h,\overline{D})}\right) - \dfrac{\nu}{E}\left(\dfrac{\mathcal{H}(\underset{\sim}{\sigma}:\underset{\sim}{1})}{f^e(\overline{D})} + \dfrac{\mathcal{H}(-\underset{\sim}{\sigma}:\underset{\sim}{1})}{f_h^e(h,\overline{D})}\right)\underset{\sim}{1}\otimes\underset{\sim}{1}\right]$
- $\dfrac{\partial \mathcal{R}_{\underset{\sim}{\sigma}}}{\partial \Delta \underset{\sim}{\alpha}^k} = \underset{\approx}{0}$
- $\dfrac{\partial \mathcal{R}_{\underset{\sim}{\sigma}}}{\partial \Delta \lambda} = \underset{\sim}{0}$
- $\dfrac{\partial \mathcal{R}_{\underset{\sim}{\sigma}}}{\partial \Delta r^i} = \underset{\sim}{0}$
- $\dfrac{\partial \mathcal{R}_{\underset{\sim}{\sigma}}}{\partial \Delta D} = \underset{\sim}{0}$

Derivatives of $\mathcal{R}_{\underset{\sim}{\varepsilon}^e}$

$$\mathcal{R}_{\underset{\sim}{\varepsilon}^e} = \Delta\underset{\sim}{\varepsilon}^e - \Delta\underset{\sim}{\varepsilon} + \frac{\Delta\lambda}{f^e(\overline{D})}\sqrt{\frac{3}{2}}\,\underset{\sim}{\tilde{n}} = \underset{\sim}{0}$$

- $\dfrac{\partial \mathcal{R}_{\underset{\sim}{\varepsilon}^e}}{\partial \Delta \underset{\sim}{\sigma}} = \theta\dfrac{\Delta\lambda}{f^{e2}(\overline{D})}\sqrt{\dfrac{3}{2}}\dfrac{\partial \underset{\sim}{\tilde{n}}}{\partial \underset{\sim}{\tilde{\sigma}}} : \underset{\approx}{I}$
- $\dfrac{\partial \mathcal{R}_{\underset{\sim}{\varepsilon}^e}}{\partial \Delta \underset{\sim}{\varepsilon}^e} = \underset{\approx}{I} + \theta\dfrac{\Delta\lambda}{f^e(\overline{D})}\sqrt{\dfrac{3}{2}}\dfrac{\partial \underset{\sim}{\tilde{n}}}{\partial \underset{\sim}{\tilde{\sigma}}} : \underset{\approx}{\Lambda}$
- $\dfrac{\partial \mathcal{R}_{\underset{\sim}{\varepsilon}^e}}{\partial \Delta \underset{\sim}{\alpha}^k} = \theta\dfrac{\Delta\lambda}{f^e(\overline{D})}\sqrt{\dfrac{3}{2}}\left[\dfrac{2}{3}C^k\dfrac{\partial \underset{\sim}{\tilde{n}}}{\partial \underset{\sim}{\tilde{X}}^k} : \underset{\approx}{P}^D\right]$
- $\dfrac{\partial \mathcal{R}_{\underset{\sim}{\varepsilon}^e}}{\partial \Delta r^i} = \underset{\sim}{0}$
- $\dfrac{\partial \mathcal{R}_{\underset{\sim}{\varepsilon}^e}}{\partial \Delta \lambda} = \sqrt{\dfrac{3}{2}}\dfrac{1}{f^e(\overline{D})}\underset{\sim}{\tilde{n}}$
- $\dfrac{\partial \mathcal{R}_{\underset{\sim}{\varepsilon}^e}}{\partial \Delta D} = \underset{\sim}{0}$

Derivatives of $\mathcal{R}_{\underset{\sim}{\alpha}^k}$

$$\mathcal{R}_{\underset{\sim}{\alpha}^k} = \Delta\underset{\sim}{\alpha}^k - \frac{\Delta\lambda}{f^k(\overline{D})}\left(\sqrt{\frac{3}{2}}\,\underset{\sim}{\tilde{n}} - \gamma^k\,\varphi^k(p)\,\underset{\approx}{P}^D : \underset{\sim}{\alpha}^k\right) = \underset{\sim}{0}$$

- $\dfrac{\partial \mathcal{R}_{\underset{\sim}{\alpha}^k}}{\partial \Delta \underset{\sim}{\sigma}} = -\theta \dfrac{\Delta\lambda}{f^k(\overline{D})\, f^e(\overline{D})} \sqrt{\dfrac{3}{2}}\, \dfrac{\partial \tilde{\underset{\sim}{n}}}{\partial \tilde{\underset{\sim}{\sigma}}} : \underset{\approx}{I}$
- $\dfrac{\partial \mathcal{R}_{\underset{\sim}{\alpha}^k}}{\partial \Delta \underset{\sim}{\varepsilon}^e} = -\theta \dfrac{\Delta\lambda}{f^k(\overline{D})} \sqrt{\dfrac{3}{2}}\, \dfrac{\partial \tilde{\underset{\sim}{n}}}{\partial \tilde{\underset{\sim}{\sigma}}} : \underset{\approx}{\Lambda}$
- $\dfrac{\partial \mathcal{R}_{\underset{\sim}{\alpha}^k}}{\partial \Delta \underset{\sim}{\alpha}^k} = \underset{\approx}{I} \left[1 + \theta\, \dfrac{\Delta\lambda}{f^k(\overline{D})}\, \gamma^k\, \varphi^k(p) \right] - \theta\, \dfrac{\Delta\lambda}{f^k(\overline{D})} \sqrt{\dfrac{3}{2}} \left[\dfrac{2}{3}\, C^k\, \dfrac{\partial \tilde{\underset{\sim}{n}}}{\partial \tilde{\underset{\sim}{X}}^k} : \underset{\approx}{P}^D \right]$
- $\dfrac{\partial \mathcal{R}_{\underset{\sim}{\alpha}^k}}{\partial \Delta\lambda} = \dfrac{1}{f^k(\overline{D})} \left[\gamma^k\, \varphi^k(p)\, \underset{\approx}{P}^D : \underset{\sim}{\alpha}^k - \sqrt{\dfrac{3}{2}}\, \tilde{\underset{\sim}{n}} \right]$
- $\dfrac{\partial \mathcal{R}_{\underset{\sim}{\alpha}^k}}{\partial \Delta r^i} = \underset{\sim}{0}$
- $\dfrac{\partial \mathcal{R}_{\underset{\sim}{\alpha}^k}}{\partial \Delta D} = \underset{\sim}{0}$

Derivatives of $\mathcal{R}_{r^i}$

$$\mathcal{R}_{r^i} = \Delta r^i - \frac{\Delta\lambda}{f^i(\overline{D})} \left(1 - b^i r^i\right) = 0$$

- $\dfrac{\partial \mathcal{R}_{r^i}}{\partial \Delta \underset{\sim}{\sigma}} = \underset{\sim}{0}$
- $\dfrac{\partial \mathcal{R}_{r^i}}{\partial \Delta \underset{\sim}{\varepsilon}^e} = \underset{\sim}{0}$
- $\dfrac{\partial \mathcal{R}_{r^i}}{\partial \Delta \underset{\sim}{\alpha}^k} = \underset{\sim}{0}$
- $\dfrac{\partial \mathcal{R}_{r^i}}{\partial \Delta r^i} = 1 + \theta\, \dfrac{\Delta\lambda}{f^i(\overline{D})}\, b^i$
- $\dfrac{\partial \mathcal{R}_{r^i}}{\partial \Delta\lambda} = \dfrac{1}{f^i(\overline{D})} \left[b^i r^i - 1 \right]$
- $\dfrac{\partial \mathcal{R}_{r^i}}{\partial \Delta D} = 0$

Derivatives of $\mathcal{R}_\lambda$

$$\mathcal{R}_\lambda = \Delta\lambda - \Delta t\, \phi_v(\mathcal{F}_y) = 0$$

- $\dfrac{\partial \mathcal{R}_\lambda}{\partial \Delta \underset{\sim}{\sigma}} = -\theta\, \Delta t\, \dfrac{\partial \phi_v(\mathcal{F}_y)}{\partial \mathcal{F}_y}\, \dfrac{\partial \mathcal{F}_y}{\partial \underset{\sim}{\sigma}}$
- $\dfrac{\partial \mathcal{R}_\lambda}{\partial \Delta \underset{\sim}{\varepsilon}^e} = -\theta\, \Delta t\, \dfrac{\partial \phi_v(\mathcal{F}_y)}{\partial \mathcal{F}_y}\, \dfrac{\partial \mathcal{F}_y}{\partial \underset{\sim}{\varepsilon}^e}$
- $\dfrac{\partial \mathcal{R}_\lambda}{\partial \Delta \underset{\sim}{\alpha}^k} = -\theta\, \Delta t\, \dfrac{\partial \phi_v(\mathcal{F}_y)}{\partial \mathcal{F}_y}\, \dfrac{\partial \mathcal{F}_y}{\partial \underset{\sim}{\alpha}^k}$
- $\dfrac{\partial \mathcal{R}_\lambda}{\partial \Delta r^i} = -\theta\, \Delta t\, \dfrac{\partial \phi_v(\mathcal{F}_y)}{\partial \mathcal{F}_y}\, \dfrac{\partial \mathcal{F}_y}{\partial r^i}$
- $\dfrac{\partial \mathcal{R}_\lambda}{\partial \Delta\lambda} = 1 - \theta\, \Delta t\, \dfrac{\partial \phi_v(\mathcal{F}_y)}{\partial \mathcal{F}_y}\, \dfrac{\partial \mathcal{F}_y}{\partial \lambda}$
- $\dfrac{\partial \mathcal{R}_\lambda}{\partial \Delta D} = 0$

Derivatives of $\mathcal{R}_D$

$$\mathcal{R}_D \;=\; \Delta D \;-\; \Delta D_f \;-\; \Delta D_c \;-\; \Delta D_v \;=\; 0$$

with:

$$\Delta D_f \;=\; \Delta\lambda \left\langle \frac{Y_f - Y_{f_0}}{S_f} \right\rangle_+^{m_f} \mathrm{e}^{\beta_f \eta_D \overline{D}}\; \mathcal{H}\left(p - p_D\right)$$

$$\Delta D_c \;=\; \Delta t \left\langle \frac{\chi_c(\underset{\sim}{\sigma})}{S_c} \right\rangle_+^{m_c} \mathrm{e}^{\beta_c \eta_D \overline{D}}; \qquad \Delta D_v \;=\; (1-\overline{D})\, \frac{\Delta\lambda}{f^e(\overline{D})} \sqrt{\frac{3}{2}}\, \langle\, \underset{\sim}{\tilde{n}}^S : \underset{\sim}{1} \,\rangle_+$$

- $$\frac{\partial \mathcal{R}_D}{\partial \Delta \underset{\sim}{\sigma}} \;=\; -\,\theta\,\Delta\lambda\, \frac{m_f}{Y_f} \left\langle \frac{Y_f - Y_{f_0}}{S_f} \right\rangle_+^{m_f} \mathrm{e}^{\beta_f \eta_D \overline{D}}\; \frac{\partial Y_f^e}{\partial \underset{\sim}{\sigma}}\; \mathcal{H}\left(p - p_D\right)$$
$$- \frac{\theta\,\Delta t\, m_c}{\chi_c\left(\underset{\sim}{\sigma}\right)} \left\langle \frac{\chi_c\left(\underset{\sim}{\sigma}\right)}{S_c} \right\rangle_+^{m_c} \mathrm{e}^{\beta_c \eta_D \overline{D}}\; \frac{\partial \chi_c\left(\underset{\sim}{\sigma}\right)}{\partial \underset{\sim}{\sigma}} \;-\; \frac{\theta\,\Delta\lambda}{f^{e2}(\overline{D})}\,(1-\overline{D})\, \sqrt{\frac{3}{2}} \left\langle \frac{\partial \underset{\sim}{\tilde{n}}^S}{\partial \underset{\sim}{\tilde{\sigma}}} : \underset{\sim}{1} \right\rangle_+$$

- $$\frac{\partial \mathcal{R}_D}{\partial \Delta \underset{\sim}{\varepsilon}^e} \;=\; -\,\theta\,\Delta\lambda\, \frac{m_f}{Y_f} \left\langle \frac{Y_f - Y_{f_0}}{S_f} \right\rangle_+^{m_f} \mathrm{e}^{\beta_f \eta_D \overline{D}}\; \frac{\partial Y_f^e}{\partial \underset{\sim}{\varepsilon}^e}\; \mathcal{H}\left(p - p_D\right)$$
$$- \frac{\theta\,\Delta t\, m_c}{\chi_c\left(\underset{\sim}{\sigma}\right)} \left\langle \frac{\chi_c\left(\underset{\sim}{\sigma}\right)}{S_c} \right\rangle_+^{m_c} \mathrm{e}^{\beta_c \eta_D \overline{D}}\; \frac{\partial \chi_c\left(\underset{\sim}{\sigma}\right)}{\partial \underset{\sim}{\sigma}} : \underset{\approx}{\Lambda}\, f^e\left(\overline{D}\right)$$
$$- \frac{\theta\,\Delta\lambda}{f^e(\overline{D})}\,(1-\overline{D})\, \sqrt{\frac{3}{2}} \left\langle \left(\frac{\partial \underset{\sim}{\tilde{n}}^S}{\partial \underset{\sim}{\tilde{\sigma}}} : \underset{\approx}{\Lambda} \right) : \underset{\sim}{1} \right\rangle_+$$

- $$\frac{\partial \mathcal{R}_D}{\partial \Delta \underset{\sim}{\alpha}^k} \;=\; -\,\kappa_X\,\theta\,\Delta\lambda\, \frac{m_f}{Y_f} \left\langle \frac{Y_f - Y_{f_0}}{S_f} \right\rangle_+^{m_f} \mathrm{e}^{\beta_f \eta_D \overline{D}}\; \frac{\partial Y_f^k}{\partial \underset{\sim}{\alpha}^k}\; \mathcal{H}\left(p - p_D\right)$$
$$- \theta\, \frac{\Delta\lambda}{f^e(\overline{D})}\,(1-\overline{D})\, \sqrt{\frac{3}{2}} \left\langle \left(\frac{2}{3}\, C^k\, \frac{\partial \underset{\sim}{\tilde{n}}^S}{\partial \underset{\sim}{\tilde{X}}^k} : \underset{\approx}{P}^D \right) : \underset{\sim}{1} \right\rangle_+$$

- $$\frac{\partial \mathcal{R}_D}{\partial \Delta r^i} \;=\; -1\,\kappa_R\,\theta\,\Delta\lambda\, \frac{m_f}{Y_f} \left\langle \frac{Y_f - Y_{f_0}}{S_f} \right\rangle_+^{m_f} \mathrm{e}^{\beta_f \eta_D \overline{D}}\; \frac{\partial Y_f^i}{\partial r^i}\; \mathcal{H}\left(p - p_D\right)$$

- $$\frac{\partial \mathcal{R}_D}{\partial \Delta \lambda} \;=\; -1 \left[\left\langle \frac{Y_f - Y_{f_0}}{S_f} \right\rangle_+^{m_f} \mathrm{e}^{\beta_f \eta_D \overline{D}} \;+\; (1-\overline{D})\, \sqrt{\frac{3}{2}}\, \frac{1}{f^e(\overline{D})}\, \langle\, \underset{\sim}{\tilde{n}}^S : \underset{\sim}{1} \,\rangle_+ \right]$$

- $$\frac{\partial \mathcal{R}_D}{\partial \Delta D} \;=\; 1$$

Auxiliary derivatives

with:

- $\dfrac{\partial f^*(\overline{D})}{\partial \overline{D}} = -\beta_* \eta_D \exp(-\beta_* \eta_D \overline{D})$ where "*" stands for "e", "k" or "i"
- $\dfrac{\partial^2 f^*(\overline{D})}{\partial \overline{D}^2} = (\beta_* \eta_D)^2 \exp(-\beta_* \eta_D \overline{D})$ where "*" stands for "e", "k" or "i"
- $\dfrac{\partial f_h^e(h,\overline{D})}{\partial \overline{D}} = -h\,\beta_e \eta_D \exp(-h\,\beta_e \eta_D \overline{D})$ for elasticity with micro-cracks closure effect
- $\dfrac{\partial^2 f_h^e(h,\overline{D})}{\partial \overline{D}^2} = (h\,\beta_e \eta_D)^2 \exp(-h\,\beta_e \eta_D \overline{D})$ for elasticity with micro-cracks closure effect
- $$\frac{\partial Y_f^e}{\partial \underset{\sim}{\sigma}} = -\frac{1+\nu}{E}\left[\frac{\underset{\sim}{\sigma}_+}{f^{e2}(\overline{D})}\frac{\partial f^e(\overline{D})}{\partial \overline{D}} + \frac{\underset{\sim}{\sigma}_-}{f_h^{e2}(h,\overline{D})}\frac{\partial f_h^e(h,\overline{D})}{\partial \overline{D}}\right] + \frac{\nu}{E}\left[\frac{\langle\, \underset{\sim}{\sigma} : \underset{\sim}{1}\,\rangle}{f^{e2}(\overline{D})}\frac{\partial f^e(\overline{D})}{\partial \overline{D}} - \frac{\langle\, -\underset{\sim}{\sigma} : \underset{\sim}{1}\,\rangle}{f_h^{e2}(h,\overline{D})}\frac{\partial f_h^e(h,\overline{D})}{\partial \overline{D}}\right]\underset{\sim}{1}$$
- $\dfrac{\partial Y_f^e}{\partial \underset{\sim}{\varepsilon}^e} = -\dfrac{\partial f^e(\overline{D})}{\partial \overline{D}}\,\underset{\sim}{\tilde{\sigma}}$
- $\dfrac{\partial Y_f^k}{\partial \underset{\sim}{\alpha}^k} = -\dfrac{\partial f^k(\overline{D})}{\partial \overline{D}}\,\underset{\sim}{\tilde{X}}^k$
- $\dfrac{\partial Y_f^i}{\partial r^i} = -\dfrac{\partial f^i(\overline{D})}{\partial \overline{D}}\,\tilde{R}^i$
- $\dfrac{\partial \mathcal{F}_y}{\partial \underset{\sim}{\varepsilon}^e} = \sqrt{\dfrac{3}{2}}\,\underset{\sim}{\tilde{n}} : \underset{\approx}{\Lambda}$
- $\dfrac{\partial \mathcal{F}_y}{\partial \underset{\sim}{\sigma}} = \dfrac{1}{f^e(\overline{D})}\sqrt{\dfrac{3}{2}}\,\underset{\sim}{\tilde{n}}$
- $\dfrac{\partial \mathcal{F}_y}{\partial \underset{\sim}{\alpha}^k} = -\sqrt{\dfrac{2}{3}}\,C^k\,\underset{\sim}{\tilde{n}} : \underset{\approx}{P}^D$
- $\dfrac{\partial \mathcal{F}_y}{\partial r^i} = -b^i\,Q^i$
- $\dfrac{\partial \mathcal{F}_y}{\partial \lambda} = 0$
- $\dfrac{\partial \mathcal{F}_y}{\partial D} = 0$
- $\dfrac{\partial \phi_v(\mathcal{F}_y)}{\partial \mathcal{F}_y} = \dot{\epsilon}_0\, m \left[\sinh\left(\left\langle \dfrac{\mathcal{F}_y}{K}\right\rangle_+^n\right)\right]^{m-1} \dfrac{n}{\mathcal{F}_y}\cosh\left(\left\langle \dfrac{\mathcal{F}_y}{K}\right\rangle_+^n\right)\left\langle \dfrac{\mathcal{F}_y}{K}\right\rangle_+^n$
- $\dfrac{\partial \chi_c(\underset{\sim}{\sigma})}{\partial \underset{\sim}{\sigma}} = \alpha_c \dfrac{\partial I_0(\underset{\sim}{\sigma})}{\partial \underset{\sim}{\sigma}} + \delta_c \dfrac{\partial I_1(\underset{\sim}{\sigma})}{\partial \underset{\sim}{\sigma}} + (1-\alpha_c-\delta_c)\dfrac{\partial \sqrt{3J_2(\underset{\sim}{\sigma})}}{\partial \underset{\sim}{\sigma}}$
- $\dfrac{\partial I_0(\underset{\sim}{\sigma})}{\partial \underset{\sim}{\sigma}} \rightarrow$ solved by perturbation analysis over the principal values of $\underset{\sim}{\sigma}$

- $\dfrac{\partial I_1(\underset{\sim}{\sigma})}{\partial \underset{\sim}{\sigma}} = \underset{\sim}{1}$
- $\dfrac{\partial \underset{\sim}{\tilde{n}}}{\partial \underset{\sim}{\tilde{\sigma}}} = \dfrac{1}{\left\| \underset{\sim}{\tilde{Z}} \right\|_H} \left[\underset{\approx}{H} - \underset{\sim}{\tilde{n}} \otimes \underset{\sim}{\tilde{n}} \right]$
- $\dfrac{\partial \underset{\sim}{\tilde{n}}}{\partial \underset{\sim}{\tilde{X}}^k} = \dfrac{-1}{\left\| \underset{\sim}{\tilde{Z}} \right\|_H} \left[\underset{\approx}{H} - \underset{\sim}{\tilde{n}} \otimes \underset{\sim}{\tilde{n}} \right]$
- $\dfrac{\partial \sqrt{3J_2(\underset{\sim}{\sigma})}}{\partial \underset{\sim}{\sigma}} = \dfrac{3}{2} \dfrac{\underset{\sim}{\sigma}^D}{\sqrt{3J_2(\underset{\sim}{\sigma})}}$
- $\dfrac{\partial \underset{\sim}{\tilde{n}}^S}{\partial \underset{\sim}{\tilde{\sigma}}} = \dfrac{1}{\left\| \underset{\sim}{\tilde{Z}} \right\|_H} \left[\underset{\approx}{H}^S - \underset{\sim}{\tilde{n}}^S \otimes \underset{\sim}{\tilde{n}}^S \right]$
- $\dfrac{\partial \underset{\sim}{\tilde{n}}^S}{\partial \underset{\sim}{\tilde{X}}^k} = \dfrac{-1}{\left\| \underset{\sim}{\tilde{Z}} \right\|_H} \left[\underset{\approx}{H}^S - \underset{\sim}{\tilde{n}}^S \otimes \underset{\sim}{\tilde{n}}^S \right]$

J Details on the consistent tangent operator (non-local model)

In this appendix, the matrices related to the derivation of the consistent tangent operator (CTO) associated with the **non-local** cyclic viscoplastic-damage model are detailed.
In the sub-sect. 4.3.5, and particularly in eq. (4.101), it has been shown that the CTO can be derived by:

$$\{\mathcal{L}\} = \frac{\delta\Delta\mathcal{V}_{OUT}}{\delta\Delta\mathcal{V}_{IN}} = \left\{\frac{\partial\Delta\mathcal{V}_{OUT}}{\partial\Delta\mathcal{V}_{int}}\left[-\left(\frac{\{\partial\mathcal{R}\}}{\{\partial\Delta\mathcal{V}_{int}\}}\right)^{-1}\frac{\{\partial\mathcal{R}\}}{\{\partial\Delta\mathcal{V}_{IN}\}}\right] + \frac{\partial\Delta\mathcal{V}_{OUT}}{\partial\Delta\mathcal{V}_{IN}}\right\} \tag{J.1}$$

which involves several matrices that need to be defined.
As a recall, the DoF, input and output, as well as the internal and auxiliary variables are:

$$DoF : \left\{\underset{\sim}{u}, \overline{D}\right\}; \qquad \mathcal{V}_{IN} : \left\{\underset{\sim}{\varepsilon}, \overline{D}\right\}; \qquad \mathcal{V}_{OUT} : \left\{\underset{\sim}{\sigma}, D\right\}; \qquad \mathcal{V}_{int} : \left\{\underset{\sim}{\sigma}, \underset{\sim}{\varepsilon}^{e}, \underset{\sim}{\alpha}^{k}, r^{i}, \lambda, D\right\}$$

while the local residuals associated with the internal state variables are given in eq. (I.3).

◇ The matrix $\dfrac{\partial\Delta\mathcal{V}_{OUT}}{\partial\Delta\mathcal{V}_{int}}$ is given by:

$$\frac{\partial\Delta\mathcal{V}_{OUT}}{\partial\Delta\mathcal{V}_{int}} = \frac{\partial\mathcal{V}_{OUT}}{\partial\mathcal{V}_{int}} = \begin{bmatrix} \dfrac{\partial\underset{\sim}{\sigma}}{\partial\underset{\sim}{\sigma}} & \dfrac{\partial\underset{\sim}{\sigma}}{\partial\underset{\sim}{\varepsilon}^{e}} & \dfrac{\partial\underset{\sim}{\sigma}}{\partial\underset{\sim}{\alpha}^{k}} & \dfrac{\partial\underset{\sim}{\sigma}}{\partial r^{i}} & \dfrac{\partial\underset{\sim}{\sigma}}{\partial\lambda} & \dfrac{\partial\underset{\sim}{\sigma}}{\partial D} \\ \dfrac{\partial D}{\partial\underset{\sim}{\sigma}} & \dfrac{\partial D}{\partial\underset{\sim}{\varepsilon}^{e}} & \dfrac{\partial D}{\partial\underset{\sim}{\alpha}^{k}} & \dfrac{\partial D}{\partial r^{i}} & \dfrac{\partial D}{\partial\lambda} & \dfrac{\partial D}{\partial D} \end{bmatrix} = \begin{bmatrix} \underset{\approx}{I} & \underset{\approx}{\Lambda}\, f^{e}(\overline{D}) & \underset{\approx}{0} & \underset{\sim}{0} & \underset{\sim}{0} & \underset{\sim}{0} \\ \underset{\sim}{0} & \underset{\sim}{0} & \underset{\sim}{0} & 0 & 0 & 1 \end{bmatrix} \tag{J.2}$$

◇ The matrix $\dfrac{\{\partial\mathcal{R}\}}{\{\partial\Delta\mathcal{V}_{IN}\}}$ is given by:

$$\frac{\{\partial\mathcal{R}\}}{\{\partial\Delta\mathcal{V}_{IN}\}} = \begin{bmatrix} \dfrac{\partial\mathcal{R}_{\underset{\sim}{\sigma}}}{\partial\Delta\underset{\sim}{\varepsilon}} & \dfrac{\partial\mathcal{R}_{\underset{\sim}{\varepsilon}^{e}}}{\partial\Delta\underset{\sim}{\varepsilon}} & \dfrac{\partial\mathcal{R}_{\underset{\sim}{\alpha}^{k}}}{\partial\Delta\underset{\sim}{\varepsilon}} & \dfrac{\partial\mathcal{R}_{r^{i}}}{\partial\Delta\underset{\sim}{\varepsilon}} & \dfrac{\partial\mathcal{R}_{\lambda}}{\partial\Delta\underset{\sim}{\varepsilon}} & \dfrac{\partial\mathcal{R}_{D}}{\partial\Delta\underset{\sim}{\varepsilon}} \\ \dfrac{\partial\mathcal{R}_{\underset{\sim}{\sigma}}}{\partial\Delta\overline{D}} & \dfrac{\partial\mathcal{R}_{\underset{\sim}{\varepsilon}^{e}}}{\partial\Delta\overline{D}} & \dfrac{\partial\mathcal{R}_{\underset{\sim}{\alpha}^{k}}}{\partial\Delta\overline{D}} & \dfrac{\partial\mathcal{R}_{r^{i}}}{\partial\Delta\overline{D}} & \dfrac{\partial\mathcal{R}_{\lambda}}{\partial\Delta\overline{D}} & \dfrac{\partial\mathcal{R}_{D}}{\partial\Delta\overline{D}} \end{bmatrix} = \begin{bmatrix} \underset{\approx}{0} & -\underset{\approx}{I} & \underset{\approx}{0} & \underset{\sim}{0} & \underset{\sim}{0} & \underset{\sim}{0} \\ \dfrac{\partial\mathcal{R}_{\underset{\sim}{\sigma}}}{\partial\Delta\overline{D}} & \dfrac{\partial\mathcal{R}_{\underset{\sim}{\varepsilon}^{e}}}{\partial\Delta\overline{D}} & \dfrac{\partial\mathcal{R}_{\underset{\sim}{\alpha}^{k}}}{\partial\Delta\overline{D}} & \dfrac{\partial\mathcal{R}_{r^{i}}}{\partial\Delta\overline{D}} & \dfrac{\partial\mathcal{R}_{\lambda}}{\partial\Delta\overline{D}} & \dfrac{\partial\mathcal{R}_{D}}{\partial\Delta\overline{D}} \end{bmatrix} \tag{J.3}$$

with:

- $\dfrac{\partial \mathcal{R}_{\underset{\sim}{\sigma}}}{\partial \Delta \overline{D}} = -\dfrac{1+\nu}{E}\left[-\dfrac{\underset{\sim}{\sigma}_{+}}{f^{e2}(\overline{D})}\dfrac{\partial f^{e}(\overline{D})}{\partial \overline{D}} - \dfrac{\underset{\sim}{\sigma}_{-}}{f_h^{e2}(h,\overline{D})}\dfrac{\partial f_h^{e}(h,\overline{D})}{\partial \overline{D}}\right] + \dfrac{\nu}{E}\left[-\dfrac{\langle\, \underset{\sim}{\sigma} : \underset{\sim}{1}\,\rangle}{f^{e2}(\overline{D})}\dfrac{\partial f^{e}(\overline{D})}{\partial \overline{D}} + \dfrac{\langle\, -\underset{\sim}{\sigma} : \underset{\sim}{1}\,\rangle}{f_h^{e2}(h,\overline{D})}\dfrac{\partial f_h^{e}(h,\overline{D})}{\partial \overline{D}}\right]\underset{\sim}{1}$
- $\dfrac{\partial \mathcal{R}_{\underset{\sim}{\varepsilon}^{e}}}{\partial \Delta \overline{D}} = \dfrac{\Delta\lambda}{f^{e}(\overline{D})}\sqrt{\dfrac{3}{2}}\left(\dfrac{\partial \tilde{\underset{\sim}{n}}}{\partial \overline{D}} - \tilde{\underset{\sim}{n}}\,\dfrac{1}{f^{e}(\overline{D})}\dfrac{\partial f^{e}(\overline{D})}{\partial \overline{D}}\right)$
- $\dfrac{\partial \mathcal{R}_{\underset{\sim}{\alpha}^{k}}}{\partial \Delta \overline{D}} = \dfrac{\Delta\lambda}{f^{k}(\overline{D})}\sqrt{\dfrac{3}{2}}\left(\tilde{\underset{\sim}{n}}\,\dfrac{1}{f^{k}(\overline{D})}\dfrac{\partial f^{k}(\overline{D})}{\partial \overline{D}} - \dfrac{\partial \tilde{\underset{\sim}{n}}}{\partial \overline{D}}\right)$
- $\dfrac{\partial \mathcal{R}_{r^{i}}}{\partial \Delta \overline{D}} = \dfrac{\Delta\lambda}{f^{i2}(\overline{D})}\left(1 - b^{i}r^{i}\right)\dfrac{\partial f^{i}(\overline{D})}{\partial \overline{D}}$
- $\dfrac{\partial \mathcal{R}_{\lambda}}{\partial \Delta \overline{D}} = -\Delta t\,\dfrac{\partial \phi_{v}(\mathcal{F}_{y})}{\partial \mathcal{F}_{y}}\dfrac{\partial \mathcal{F}_{y}}{\partial \overline{D}}$
- $\dfrac{\partial \mathcal{R}_{D}}{\partial \Delta \overline{D}} = -\Delta\lambda\left(\dfrac{\partial \hat{Y}_{f}}{\partial \overline{D}} + \dfrac{\partial \hat{Y}_{v}}{\partial \overline{D}}\right) - \Delta t\,\dfrac{\partial \hat{Y}_{c}}{\partial \overline{D}}$

◇ The matrix $\dfrac{\{\,\partial \mathcal{R}\,\}}{\{\,\partial \Delta \mathcal{V}_{int}\,\}} = \mathcal{J}$ is given by the material Jacobian matrix, already defined in Chap. I.

◇ The matrices $\dfrac{\partial \Delta \mathcal{V}_{OUT}}{\partial \Delta \mathcal{V}_{IN}}$ are given by:

$$\frac{\partial \Delta \mathcal{V}_{OUT}}{\partial \Delta \mathcal{V}_{IN}} = \begin{pmatrix} \dfrac{\partial \Delta \underset{\sim}{\sigma}}{\partial \Delta \underset{\sim}{\varepsilon}} & \dfrac{\partial \Delta \underset{\sim}{\sigma}}{\partial \Delta \overline{D}} \\ \dfrac{\partial \Delta D}{\partial \Delta \underset{\sim}{\varepsilon}} & \dfrac{\partial \Delta D}{\partial \Delta \overline{D}} \end{pmatrix} \tag{J.4}$$

- $\dfrac{\partial \Delta \underset{\sim}{\sigma}}{\partial \Delta \underset{\sim}{\varepsilon}} = \dfrac{\partial \underset{\sim}{\sigma}}{\partial \underset{\sim}{\varepsilon}} = \underset{\approx}{\Lambda}\; f^{e}(\overline{D})$
- $\dfrac{\partial \Delta D}{\partial \Delta \underset{\sim}{\varepsilon}} = \underset{\sim}{0}$
- $\dfrac{\partial \Delta \underset{\sim}{\sigma}}{\partial \Delta \overline{D}} = \dfrac{\partial \underset{\sim}{\sigma}}{\partial \overline{D}} = \underset{\approx}{\Lambda} : \underset{\sim}{\varepsilon}^{e}\,\dfrac{\partial f^{e}(\overline{D})}{\partial \overline{D}} = \tilde{\underset{\sim}{\sigma}}\,\dfrac{\partial f^{e}(\overline{D})}{\partial \overline{D}}$
- $\dfrac{\partial \Delta D}{\partial \Delta \overline{D}} = 0$

Auxiliary derivatives

with auxiliary derivatives given in Chap. I page 307 and:

- $$\frac{\partial Y_f^e}{\partial \overline{D}} = -\frac{1+\nu}{2E}\left(\frac{\underset{\sim}{\sigma}_+ : \underset{\sim}{\sigma}_+}{f^{e2}(\overline{D})}\,\beta_e\,\eta_D\frac{\partial f^e(\overline{D})}{\partial \overline{D}} + \frac{\underset{\sim}{\sigma}_- : \underset{\sim}{\sigma}_-}{f_h^{e2}(h,\overline{D})}\,h\,\beta_e\,\eta_D\frac{\partial f_h^e(h,\overline{D})}{\partial \overline{D}}\right) + \frac{\nu}{2E}\left(\frac{\langle \underset{\sim}{\sigma} : \underset{\sim}{1}\rangle^2}{f^{e2}(\overline{D})}\,\beta_e\,\eta_D\frac{\partial f^e(\overline{D})}{\partial \overline{D}} + \frac{\langle -\underset{\sim}{\sigma} : \underset{\sim}{1}\rangle^2}{f_h^{e2}(h,\overline{D})}\,h\,\beta_e\,\eta_D\frac{\partial f_h^e(h,\overline{D})}{\partial \overline{D}}\right) \quad \text{(UC)}$$

- $$\frac{\partial Y_f^e}{\partial \overline{D}} = -\frac{1}{2}\frac{\partial^2 f^e(\overline{D})}{\partial \overline{D}^2}\,\underset{\sim}{\varepsilon}^e : \underset{\sim}{\tilde{\sigma}} \quad \text{(no UC)}$$
- $$\frac{\partial Y_f^k}{\partial \overline{D}} = -\frac{1}{2}\frac{\partial^2 f^k(\overline{D})}{\partial \overline{D}^2}\,\underset{\sim}{\alpha}^k : \underset{\sim}{\tilde{X}}^k$$
- $$\frac{\partial Y_f^i}{\partial \overline{D}} = -\frac{1}{2}\frac{\partial^2 f^i(\overline{D})}{\partial \overline{D}^2}\,r^i\,\tilde{R}^i$$
- $$\frac{\partial \underset{\sim}{\tilde{\sigma}}}{\partial \overline{D}} = -\frac{1}{f^{e2}(\overline{D})}\frac{\partial f^e(\overline{D})}{\partial \overline{D}}\,\underset{\sim}{\sigma}$$
- $$\frac{\partial \underset{\sim}{\tilde{X}}^k}{\partial \overline{D}} = -\frac{1}{f^{k2}(\overline{D})}\frac{\partial f^k(\overline{D})}{\partial \overline{D}}\,\underset{\sim}{X}^k$$
- $$\frac{\partial \underset{\sim}{\tilde{Z}}}{\partial \overline{D}} = \frac{\partial \underset{\sim}{\tilde{\sigma}}}{\partial \overline{D}} - \sum_k \frac{\partial \underset{\sim}{\tilde{X}}^k}{\partial \overline{D}}$$
- $$\frac{\partial \tilde{R}^i}{\partial \overline{D}} = -\frac{1}{f^{i2}(\overline{D})}\frac{\partial f^i(\overline{D})}{\partial \overline{D}}\,R^i$$
- $$\frac{\partial \underset{\approx}{H}}{\partial \overline{D}} = 2\,\varphi_c\frac{\partial g_D(\overline{D})}{\partial \overline{D}}\,\underset{\approx}{P}^s = 2\,\varphi_c\,\underset{\approx}{P}^s$$
- $$\frac{\partial \underset{\approx}{H}^{-1}}{\partial \overline{D}} = \frac{-2\,\varphi_c}{\left(2\,\varphi_c\,g_D(\overline{D})\right)^2}\frac{\partial g_D(\overline{D})}{\partial \overline{D}}\,\underset{\approx}{P}^s$$
- $$\frac{\partial \mathcal{F}_y}{\partial \underset{\sim}{\sigma}} = \sqrt{\frac{3}{2}}\frac{1}{f^e(\overline{D})}\,\underset{\sim}{\tilde{n}}$$

- $$\frac{\partial \mathcal{F}_y}{\partial \overline{D}} = \sqrt{\frac{3}{2}}\frac{\partial \left\|\underset{\sim}{\tilde{Z}}\right\|_H}{\partial \overline{D}} + \sum_i \frac{R^i}{f^{i2}(\overline{D})}\frac{\partial f^i(\overline{D})}{\partial \overline{D}}$$
- $$\frac{\partial \left\|\underset{\sim}{\tilde{Z}}\right\|_H}{\partial \overline{D}} = \left[\frac{\partial \underset{\sim}{\tilde{Z}}}{\partial \overline{D}} : \underset{\sim}{\tilde{n}}\right] + \left[\frac{1}{2}\frac{1}{\left\|\underset{\sim}{\tilde{Z}}\right\|_H}\left(\underset{\sim}{\tilde{Z}} : \frac{\partial \underset{\approx}{H}}{\partial \overline{D}} : \underset{\sim}{\tilde{Z}}\right)\right]$$
- $$\frac{\partial \underset{\sim}{\tilde{n}}}{\partial \overline{D}} = \frac{1}{\left\|\underset{\sim}{\tilde{Z}}\right\|_H}\left[\frac{\partial \underset{\approx}{H}}{\partial D} : \underset{\sim}{\tilde{Z}} + \underset{\approx}{H} : \frac{\partial \underset{\sim}{\tilde{Z}}}{\partial \overline{D}} - \underset{\sim}{\tilde{n}}\frac{\partial \left\|\underset{\sim}{\tilde{Z}}\right\|_H}{\partial \overline{D}}\right]$$
- $$\frac{\partial \underset{\sim}{\tilde{n}}^s}{\partial \overline{D}} = \frac{1}{\left\|\underset{\sim}{\tilde{Z}}\right\|_H}\left[\frac{\partial \underset{\approx}{H}}{\partial D} : \underset{\sim}{\tilde{Z}} + \underset{\approx}{H}^s : \frac{\partial \underset{\sim}{\tilde{Z}}}{\partial \overline{D}} - \underset{\sim}{\tilde{n}}^s\frac{\partial \left\|\underset{\sim}{\tilde{Z}}\right\|_H}{\partial \overline{D}}\right]$$
- $$\frac{\partial \hat{Y}_f}{\partial \overline{D}} = \frac{\partial}{\partial \overline{D}}\left[\left\langle \frac{Y_f - Y_{f_0}}{S_f}\right\rangle_+^{m_f} \mathrm{e}^{\beta_f \eta_D \overline{D}}\right] = \hat{Y}_f\left[\frac{m_f}{Y_f}\left(\frac{\partial Y_f^e}{\partial \overline{D}} + \kappa_X\frac{\partial Y_f^k}{\partial \overline{D}} + \kappa_R\frac{\partial Y_f^i}{\partial \overline{D}}\right) + \beta_f\,\eta_D\right]$$

- $\dfrac{\partial \hat{Y}_v}{\partial \overline{D}} = \dfrac{\partial}{\partial \overline{D}} \left[(1-\overline{D}) \sqrt{\dfrac{3}{2}} \dfrac{1}{f^e(\overline{D})} \left\langle \tilde{\underset{\sim}{n}}^S : \underset{\sim}{1} \right\rangle_+ \right]$

$$= (1-\overline{D}) \sqrt{\frac{3}{2}} \frac{1}{f^e(\overline{D})} \left[\left\langle \frac{\partial \tilde{\underset{\sim}{n}}^S}{\partial \overline{D}} : \underset{\sim}{1} \right\rangle_+ - \frac{1}{f^e(\overline{D})} \frac{\partial f^e(\overline{D})}{\partial \overline{D}} \left\langle \tilde{\underset{\sim}{n}}^S : \underset{\sim}{1} \right\rangle_+ \right]$$

$$- \sqrt{\frac{3}{2}} \frac{1}{f^e(\overline{D})} \left\langle \tilde{\underset{\sim}{n}}^S : \underset{\sim}{1} \right\rangle_+$$

- $\dfrac{\partial \hat{Y}_c}{\partial \overline{D}} = \dfrac{\partial}{\partial \overline{D}} \left[\left\langle \dfrac{\chi_c(\underset{\sim}{\sigma})}{S_c} \right\rangle_+^{m_c} \mathrm{e}^{\beta_c \eta_D \overline{D}} \right] = \hat{Y}_c \left[\dfrac{m_c}{\chi_c(\underset{\sim}{\sigma})} \dfrac{\partial \chi_c(\underset{\sim}{\sigma})}{\partial \overline{D}} + \beta_c \eta_D \right]$

- $\dfrac{\partial \chi_c(\underset{\sim}{\sigma})}{\partial \overline{D}} = \alpha_c \dfrac{\partial I_0(\underset{\sim}{\sigma})}{\partial \overline{D}} + \delta_c \dfrac{\partial I_1(\underset{\sim}{\sigma})}{\partial \overline{D}} + (1-\alpha_c-\delta_c) \dfrac{\partial \sqrt{3J_2(\underset{\sim}{\sigma})}}{\partial \overline{D}}$

- $\dfrac{\partial I_0(\underset{\sim}{\sigma})}{\partial \overline{D}} = \dfrac{\partial I_0(\underset{\sim}{\sigma})}{\partial \underset{\sim}{\sigma}} : \dfrac{\partial \underset{\sim}{\sigma}}{\partial \overline{D}}$ $\rightarrow$ solved by perturbation analysis over the principal values of $\underset{\sim}{\sigma}$

- $\dfrac{\partial I_1(\underset{\sim}{\sigma})}{\partial \overline{D}} = \dfrac{\partial \underset{\sim}{\sigma}}{\partial \overline{D}} : \underset{\sim}{1}$

- $\dfrac{\partial \sqrt{3J_2(\underset{\sim}{\sigma})}}{\partial \overline{D}} = \left(\dfrac{3}{2} \dfrac{\underset{\sim}{\sigma}^D}{\sqrt{3J_2(\underset{\sim}{\sigma})}} \right) : \left(\underset{\approx}{P}^D : \dfrac{\partial \underset{\sim}{\sigma}}{\partial \overline{D}} \right)$

- $\dfrac{\partial \underset{\sim}{\sigma}}{\partial \overline{D}} = \underset{\approx}{\Lambda} : \underset{\sim}{\varepsilon}^e \dfrac{\partial f^e(\overline{D})}{\partial \overline{D}} = \tilde{\underset{\sim}{\sigma}} \dfrac{\partial f^e(\overline{D})}{\partial \overline{D}}$

K On the use of a controlled element-deletion method for FCG prediction

In this additional section, we briefly discuss the use of an enhanced element-deletion method for the crack growth modeling. Such an approach can be seen as an alternative to the remeshing procedure considered before in sect. 6.3 & sect. 6.4. The main idea consists in using both a crack insertion criterion and a crack path tracking algorithm, altogether ensuring the removal of FEs which necessarily lie on the crack path. That is the reason why such a method is referred to as *controlled element-deletion* method, contrarily to the element removal technique that only removes elements in which a critical damage state has been reached in a finite number of IP (see [Besson and Desmorat, 2004]). Using this method hence enables the possibility to control the removal of adjacent elements whose membership to the crack path has been validated thanks to the MR algorithm dedicated to crack path tracking (see sub-sect. 6.2.2.3). As a consequence, the crack path is guaranteed to be continuous. A related method can also be found in [Yun et al., 2019].

A similar pure fatigue loading case is applied to a SEN-T specimen, as done for the mesh intersection procedure in sect. 6.3, following the standard test case described in sub-sect. 6.3.1. In the Fig. K.1, the non-local damage field is plotted for a crack length of $a = 1.49\,\text{mm}$. One can notice the removal of elements following a continuous path defined thanks to the MR algorithm. The crack-path is well constrained in the localization band, since the MR follows the ridge defined by the successive points of maximum damage. Compared to the case with mesh intersection process (see sect. 6.3), one can notice that the crack-path is dependent of the mesh fineness, that is, the finer the mesh in the FPZ, the more accurate the crack path and the less the volume removal. One aspect to be noted is the fact that mesh-adaption procedure described in sect. 6.1 reduces the artificial mass loss due to element-deletion, since the elements within the damage localization regions are automatically refined prior to deletion, hence minimizing the lost volume. Such a point has also be noticed by [El Khaoulani and Bouchard, 2012], [Feld-Payet, 2022] where authors have used a so-called *adaptive element erosion* method through the coupling between element erosion and mesh adaption. This dual approach is assessed in the present appendix.

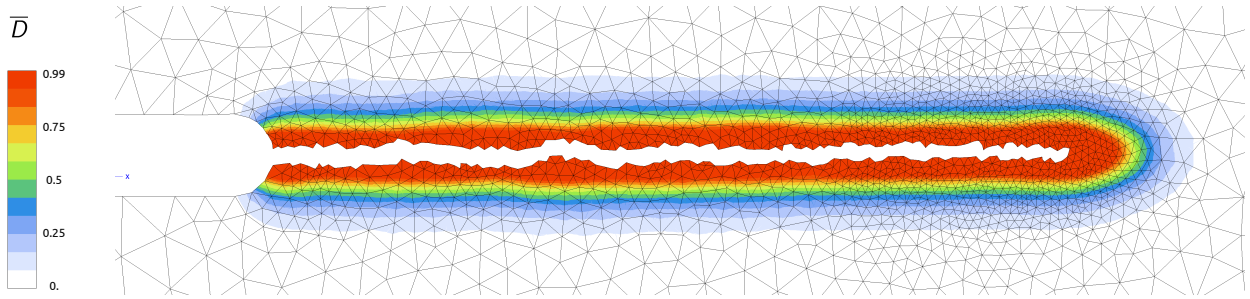

(a) Non-local damage for $a = 1.49\,\text{mm}$.

Figure K.1: Distribution of the non-local damage in the wake and FPZ of a fatigue crack in a SEN-T specimen (plane strain assumptions, c2d6r 4-fields FE).

In the Fig. K.2, the real and effective stress fields are depicted. One can notice in Fig. K.2a an almost vanishing stress level along the crack path and in the FPZ where damage evolution is

maximum. Similarly to the case with mesh intersection procedure, the crack insertion is performed in a consistent manner regarding energetic aspects since there is no rigidity where crack increment is inserted. Moreover, in Fig. K.2b, the effective stress (used for the strain equivalence principle) can be seen to be maximum ahead of the crack-tip in the FPZ. Obviously, since damage growth is mainly localized in the FPZ, the effective stress level is intended to be the largest in this zone.

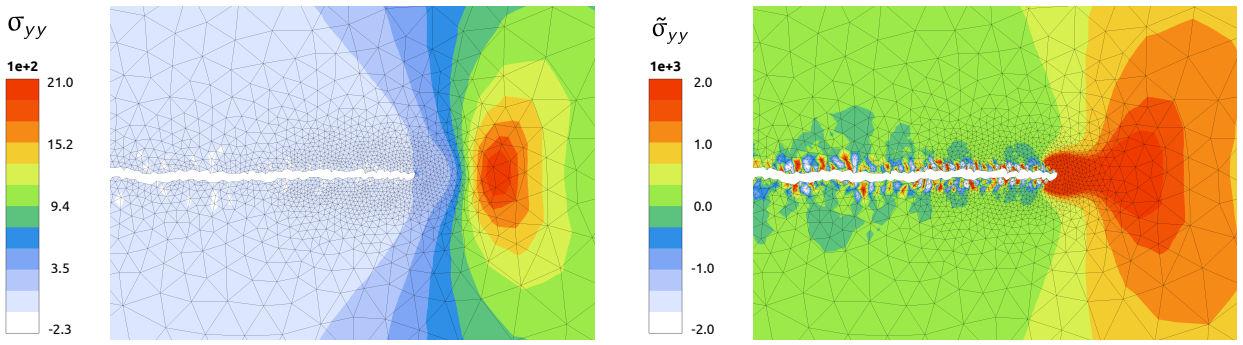

(a) Cauchy stress field in y-direction. (b) Effective Cauchy stress field in y-direction.

Figure K.2: Distribution of the real and effective stress fields in the wake and FPZ of a fatigue crack in a SEN-T specimen for $a = 1.49\,\text{mm}$ (plane strain assumptions, c2d6r 4-fields FE).

In Fig. K.3, the controlled element-removal technique is illustrated. The zone of influence where damage has reached (at least) the threshold value $\overline{D}_{th}^{MR}$ is shown in darker FE in the FPZ, see Fig. K.3a. The crack growth direction (CGD) estimated by the MR algorithm is also depicted. In Fig. K.3b, the crack insertion criterion has been validated along a prescribed crack increment of length $\ell_c = 5. \times h_{min}$ so as for the crack to extend in the estimated CGD.

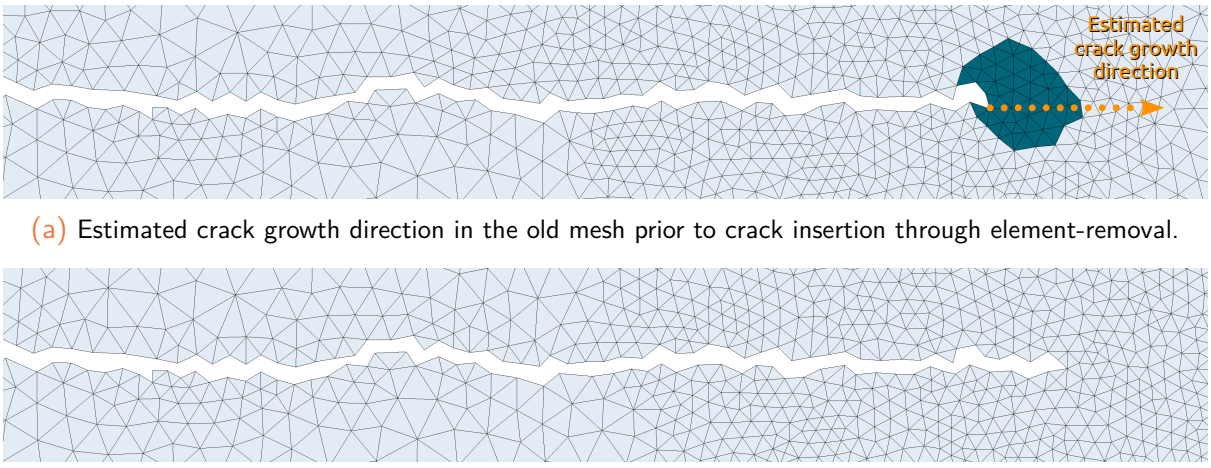

(a) Estimated crack growth direction in the old mesh prior to crack insertion through element-removal.

(b) Crack increment inserted through controlled erosion technique upon cycling.

Figure K.3: Controlled element-removal technique in a SEN-T specimen subjected to pure fatigue loading conditions (plane strain assumptions, c2d6r FE).

Remark: The previously described CDT method through controlled-erosion has not been extensively used. Indeed, such a technique consists in an alternative method to the mesh intersection procedure which was favored in this Ph.D. project. It was assessed to highlight the versatility of the MR algorithm to deal with crack path tracking, no matter the desired CDT method.

L Numerical parameters for FCG simulations

Temperature effect on FCG

Parameters	ℓ_c	$\overline{D}_{th}^{ZZ2}$	$\eta_{\overline{D}}$	$\epsilon_{\overline{D}}^{h}$	h_{min}	h_{max}	$\overline{D}_{th}^{MR}$	$\nabla\overline{D}_{th}^{\star}$	$\Delta\theta$	$\overline{D}^{crit}$	ℓ_{inc}
Value	0.15	0.001	0.02	0.01	0.05	10.	0.75	0.001	10.	0.8	0.1

Table L.1: Parameters for the simulations of the temperature effect on FCG.

Effect of prescribed boundary conditions on FCG

Parameters	ℓ_c	$\overline{D}_{th}^{ZZ2}$	$\eta_{\overline{D}}$	$\epsilon_{\overline{D}}^{h}$	h_{min}	h_{max}	$\overline{D}_{th}^{MR}$	$\nabla\overline{D}_{th}^{\star}$	$\Delta\theta$	$\overline{D}^{crit}$	ℓ_{inc}
Value	0.03	0.001	0.02	0.01	0.01	10.	0.9	0.001	10.	0.95	0.025

Table L.2: Parameters for the simulations of the effect of prescribed BC on FCG.

Effect of load ratio on FCG

Parameters	ℓ_c	$\overline{D}_{th}^{ZZ2}$	$\eta_{\overline{D}}$	$\epsilon_{\overline{D}}^{h}$	h_{min}	h_{max}	$\overline{D}_{th}^{MR}$	$\nabla\overline{D}_{th}^{\star}$	$\Delta\theta$	$\overline{D}^{crit}$	ℓ_{inc}
Value	0.03	0.001	0.02	0.01	0.01	10.	0.9	0.001	10.	0.95	0.02

Table L.3: Parameters for the simulations of the effect of load ratio on FCG.

Effect of loading frequency on FCG

Parameters	ℓ_c	$\overline{D}_{th}^{ZZ2}$	$\eta_{\overline{D}}$	$\epsilon_{\overline{D}}^{h}$	h_{min}	h_{max}	$\overline{D}_{th}^{MR}$	$\nabla\overline{D}_{th}^{\star}$	$\Delta\theta$	$\overline{D}^{crit}$	ℓ_{inc}
Value	0.15	0.05	0.02	0.01	0.05	10.	0.75	0.001	10.	0.8	0.1

Table L.4: Parameters for the simulations of the effect of loading frequency on FCG.

Overload effect on FCG

Parameters	ℓ_c	$\overline{D}_{th}^{ZZ2}$	$\eta_{\overline{D}}$	$\epsilon_{\overline{D}}^{h}$	h_{min}	h_{max}	$\overline{D}_{th}^{MR}$	$\nabla\overline{D}_{th}^{\star}$	$\Delta\theta$	$\overline{D}^{crit}$	ℓ_{inc}
Value	0.03	0.001	0.02	0.01	0.01	10.	0.9	0.001	10.	0.95	0.025

Table L.5: Parameters for the simulations of the overload effect on FCG.

References

[Abecassis, 2017] Abecassis, M. (2017). *Fissuration de matériaux soudés en condition de fatigue multi-axiale*. Ph.D. thesis, PSL Research University, Paris, France.

[Abecassis et al., 2019] Abecassis, M., Köster, A., Esin, V. A., Chiaruttini, V., and Maurel, V. (2019). Crack growth behavior in dissimilar welded Ti based alloys under biaxial fatigue loading. *International Journal of Fatigue*, 118:209–224.

[Abu Al-Rub and Voyiadjis, 2004] Abu Al-Rub, R. K. and Voyiadjis, G. Z. (2004). Analytical and experimental determination of the material intrinsic length scale of strain gradient plasticity theory from micro- and nano-indentation experiments. *International Journal of Plasticity*, 20(6):1139–1182.

[Adeli, 2019] Adeli, E. (2019). *Viscoplastic-Damage Model Parameter Identification via Bayesian Methods*. Ph.D. thesis, Technische Universität Braunschweig, Braunschweig, Germany. ISBN: 9781672824071.

[Aero and Kuvshinskii, 1961] Aero, E. and Kuvshinskii, E. (1961). Fundamental equations of the theory of elastic media with rotationally interacting particles. *Soviet Physics-Solid State*, 2(7):1272–1281.

[AFNOR, 1991] AFNOR (1991). Pratique des essais de vitesse de propagation de fissure en fatigue. Technical Report A03-404, Association Française de Normalisation (AFNOR).

[Ahmed, 2013] Ahmed, R. (2013). *Constitutive Modeling for Very High Temperature Thermo-Mechanical Fatigue Responses*. Ph.D. thesis, North Carolina State University, Raleigh, North Carolina.

[Aldakheel, 2017] Aldakheel, F. (2017). Micromorphic approach for gradient-extended thermo-elastic–plastic solids in the logarithmic strain space. *Continuum Mechanics and Thermodynamics*, 29(6):1207–1217.

[Alessi et al., 2018a] Alessi, R., Marigo, J.-J., Maurini, C., and Vidoli, S. (2018a). Coupling damage and plasticity for a phase-field regularisation of brittle, cohesive and ductile fracture: One-dimensional examples. *International Journal of Mechanical Sciences*, 149:559–576.

[Alessi et al., 2015] Alessi, R., Marigo, J.-J., and Vidoli, S. (2015). Gradient damage models coupled with plasticity: Variational formulation and main properties. *Mechanics of Materials*, 80:351–367.

[Alessi et al., 2018b] Alessi, R., Vidoli, S., and De Lorenzis, L. (2018b). A phenomenological approach to fatigue with a variational phase-field model: The one-dimensional case. *Engineering Fracture Mechanics*, 190:53–73.

[Algarni et al., 2017] Algarni, M., Choi, Y., and Bai, Y. (2017). A unified material model for multiaxial ductile fracture and extremely low cycle fatigue of Inconel 718. *International Journal of Fatigue*, 96:162–177.

[Aliabadi, 1997] Aliabadi, M. H. (1997). Boundary Element Formulations in Fracture Mechanics. *Applied Mechanics Reviews*, 50(2):83–96.

[Aliabadi, 2002] Aliabadi, M. H. (2002). *The Boundary Element Method, Volume 2: Applications in Solids and Structures*. John Wiley & Sons.

[Allix and Deü, 1997] Allix, O. and Deü, J.-F. (1997). Delayed-Damage Modelling for Fracture Prediction of Laminated Composites under Dynamic Loading. *Engineering Transactions*, 45(1):29–46.

[Allix et al., 2019] Allix, O., Lindner, D., and Paulien-Camy, O. (2019). Towards objective simulation of quasi-static failure using a bounded rate local model with damage. *International Journal of Fracture*, 220(2):167–179.

[Almansba et al., 2012] Almansba, M., Saanouni, K., and Hannachi, N. E. (2012). A simple damage-gradient enhanced elastoplastic formulation and its numerical implementation. *Mechanics & Industry*, 13(2):97–110. Publisher: EDP Sciences.

[Anderson, 2017] Anderson, T. L. (2017). *Fracture Mechanics - Fundamentals and Applications*. CRC Press, 4th edition edition.

[Andrade et al., 2011] Andrade, F., César de Sá, J., and Andrade Pires, F. (2011). A Ductile Damage Nonlocal Model of Integral-type at Finite Strains: Formulation and Numerical Issues. *International Journal of Damage Mechanics*, 20(4):515–557.

[Andrade et al., 2014] Andrade, F., César de Sá, J., and Andrade Pires, F. (2014). Assessment and comparison of non-local integral models for ductile damage. *International Journal of Damage Mechanics*, 23(2):261–296.

[Andrade, 2011] Andrade, F. X. C. (2011). *Non-local Modelling of Ductile Damage: Formulation and Numerical Issues*. Ph.D. thesis, Universidade do Porto, Porto, Portugal.

[Andrade Pires et al., 2004] Andrade Pires, F., de Souza Neto, E., and Owen, D. (2004). On the finite element prediction of damage growth and fracture initiation in finitely deforming ductile materials. *Computer Methods in Applied Mechanics and Engineering*, 193(48):5223–5256.

[Antunes et al., 2001] Antunes, F. V., Ferreira, J. M., Branco, C. M., and Byrne, J. (2001). Influence of stress state on high temperature fatigue crack growth in Inconel 718. *Fatigue & Fracture of Engineering Materials & Structures*, 24(2):127–135.

[Areias et al., 2003] Areias, P., César de Sá, J., and Conceição António, C. (2003). A gradient model for finite strain elastoplasticity coupled with damage. *Finite Elements in Analysis and Design*, 39(13):1191–1235.

[Armines et al., 2020a] Armines, ONERA, and Northwest Numerics and Modeling, Inc. (2020a). *Zset - Materials manual - Version 9.1*. Material and Structure Analysis Suite. Armines, ONERA, Northwest Numerics and Modeling, Inc., Evry, France.

[Armines et al., 2020b] Armines, ONERA, and Northwest Numerics and Modeling, Inc. (2020b). *Zset - User commands - Version 9.1*. Material and Structure Analysis Suite. Armines, ONERA, Northwest Numerics and Modeling, Inc., Evry, France.

[Arnold and Kruch, 1991] Arnold, S. and Kruch, S. (1991). Differential Continuum Damage Mechanics Models for Creep and Fatigue of Unidirectional Metal Matrix Composites. NASA Technical Memorandum NASA TM-105213, NASA & ONERA, Lewis Research Center, Cleveland, Ohio, USA.

[Arnold and Kruch, 1994] Arnold, S. and Kruch, S. (1994). A Differential CDM Model for Fatigue of Unidirectional Metal Matrix Composites. *International Journal of Damage Mechanics*, 3(2):170–191.

[Arora et al., 2021] Arora, P., Samal, M. K., Gupta, S. K., and Chattopadhyay, J. (2021). Proposing an improved cyclic plasticity material model for assessment of multiaxial response of low C-Mn steel. *International Journal of Fatigue*, 142:105888.

[Askes and Sluys, 2002] Askes, H. and Sluys, L. J. (2002). Explicit and implicit gradient series in damage mechanics. *European Journal of Mechanics - A/Solids*, 21(3):379–390.

[Aslan, 2010] Aslan, O. (2010). *Simulation numérique de la fissuration par fatigue dans les monocristaux de superalliages à base de nickel*. Ph.D. thesis, Ecole Nationale Supérieure des Mines de Paris, Paris, France.

[Aslan et al., 2011] Aslan, O., Quilici, S., and Forest, S. (2011). Numerical Modeling of Fatigue Crack Growth in Single Crystals Based on Microdamage Theory. *International Journal of Damage Mechanics*, 20(5):681–705.

[ASTM, 2015] ASTM (2015). Standard Test Method for Measurement of Fatigue Crack Growth Rates. Technical Report ASTM E647-15, ASTM International, West Conshohocken, PA, USA.

[ASTM, 2019] ASTM (2019). Standard Test Method for Measurement of Creep Crack Growth Times in Metals. Technical Report ASTM E1457-19e1, ASTM International, West Conshohocken, PA, USA.

[Aubert&Duval, 2017] Aubert&Duval (2017). AD730 - New Ni-based Superalloy for High Temperature Applications. Rapport technique, Aubert & Duval.

[Azinpour, 2020] Azinpour, E. (2020). *Phase field and gradient damage models in ductile failure*. Ph.D. thesis, University of Porto, Porto, Portugal.

[Babuška, 1971] Babuška, I. (1971). Error-bounds for finite element method. *Numerische Mathematik*, 16(4):322–333.

[Babuška and Melenk, 1997] Babuška, I. and Melenk, J. M. (1997). The Partition of Unity Method. *International Journal for Numerical Methods in Engineering*, 40(4):727–758.

[Babuška et al., 1983] Babuška, I., Miller, A., and Vogelius, M. (1983). Adaptive methods and error estimation for elliptic problems of structural mechanics. In Babuška, I., Chandra, J., and Flaherty, J., editors, *Adaptive Computational Methods for Partial Differential Equations*, pages 57–73. SIAM, Philadelphia, PA, USA, 1st edition.

[Babuška et al., 1994] Babuška, I., Strouboulis, T., Upadhyay, C. S., Gangaraj, S. K., and Copps, K. (1994). Validation of a posteriori error estimators by numerical approach. *International Journal for Numerical Methods in Engineering*, 37(7):1073–1123.

[Bai and Wierzbicki, 2015] Bai, Y. and Wierzbicki, T. (2015). A comparative study of three groups of ductile fracture loci in the 3D space. *Engineering Fracture Mechanics*, 135(Supplement C):147–167.

[Banvillet et al., 2003] Banvillet, A., Palin-Luc, T., and Lasserre, S. (2003). A volumetric energy based high cycle multiaxial fatigue citerion. *International Journal of Fatigue*, 25(8):755–769.

[Barbier, 2009] Barbier, G. (2009). *Fatigue biaxiale à grand nombre de cycles : étude expérimentale et modèle d'endommagement à deux échelles probabiliste*. Ph.D. thesis, ENS, Cachan, France.

[Bargellini et al., 2009] Bargellini, R., Besson, J., Lorentz, E., and Michel-Ponnelle, S. (2009). A non-local finite element based on volumetric strain gradient: Application to ductile fracture. *Computational Materials Science*, 45(3):762–767.

[Bari and Hassan, 2000] Bari, S. and Hassan, T. (2000). Anatomy of coupled constitutive models for ratcheting simulation. *International Journal of Plasticity*, 16(3):381–409.

[Barrett et al., 2014] Barrett, R. A., Farragher, T. P., Hyde, C. J., O'Dowd, N. P., O'Donoghue, P. E., and Leen, S. B. (2014). A Unified Viscoplastic Model for High Temperature Low Cycle Fatigue of Service-Aged P91 Steel. *Journal of Pressure Vessel Technology*, 136(2).

[Bartošák et al., 2020] Bartošák, M., Španiel, M., and Doubrava, K. (2020). Unified viscoplasticity modelling for a SiMo 4.06 cast iron under isothermal low-cycle fatigue-creep and thermo-mechanical fatigue loading conditions. *International Journal of Fatigue*, 136:105566.

[Basquin, 1910] Basquin, O. (1910). The exponential law of endurance tests. In *Proceedings of the Annual Meeting of the American Society For Testing and Materials*, volume 10, pages 625–630.

[Bathias and Pineau, 2010] Bathias, C. and Pineau, A. (2010). *Fatigue of Materials and Structures: Fundamentals*. ISTE Ltd. & John Wiley & Sons, London & New-York.

[Bauschinger, 1881] Bauschinger, J. (1881). Ueber die Veränderung der Elasticitätsgrenze und des Elasticitätmodulus verschiedener Metalle (On the changes of the elastic limit and elastic modulus of various metals). *Civiling N.F.*, 27(19):289–348.

[Bažant and Pijaudier-Cabot, 1988] Bažant, Z. and Pijaudier-Cabot, G. (1988). Nonlocal Continuum Damage, Localization Instability and Convergence. *Journal of Applied Mechanics*, 55(2):287–293.

[Bažant, 1994] Bažant, Z. P. (1994). Nonlocal Damage Theory Based on Micromechanics of Crack Interactions. *Journal of Engineering Mechanics*, 120(3):593–617. Publisher: American Society of Civil Engineers.

[Bažant and Jirásek, 2002] Bažant, Z. P. and Jirásek, M. (2002). Nonlocal Integral Formulations of Plasticity and Damage: Survey of Progress. *Journal of Engineering Mechanics*, 128(11):1119–1149.

[Bažant and Oh, 1983] Bažant, Z. P. and Oh, B. H. (1983). Crack band theory for fracture of concrete. *Matériaux et Construction*, 16(3):155–177.

[Bažant and Pijaudier-Cabot, 1989] Bažant, Z. P. and Pijaudier-Cabot, G. (1989). Measurement of Characteristic Length of Nonlocal Continuum. *Journal of Engineering Mechanics*, 115(4):755–767.

[Belattar et al., 2016] Belattar, A., Keller, C., and Taleb, L. (2016). Multiscale analysis of the prehardening effect on the cyclic behavior and fatigue life of 304L stainless steel. *Materials Science and Engineering: A*, 662:468–480.

[Bellet, 1999] Bellet, M. (1999). Finite element analysis of compressible viscoplasticity using a three-field formulation: Application to metal powder hot compaction. *Computer Methods in Applied Mechanics and Engineering*, 175(1):19–40.

[Belnoue et al., 2010] Belnoue, J. P., Garnham, B., Bache, M., and Korsunsky, A. M. (2010). The use of coupled nonlocal damage-plasticity to predict crack growth in ductile metal plates. *Engineering Fracture Mechanics*, 77(11):1721–1729.

[Belytschko and Black, 1999] Belytschko, T. and Black, T. (1999). Elastic crack growth in finite elements with minimal remeshing. *International Journal for Numerical Methods in Engineering*, 45(5):601–620.

[Belytschko et al., 2009] Belytschko, T., Gracie, R., and Ventura, G. (2009). A review of extended/generalized finite element methods for material modeling. *Modelling and Simulation in Materials Science and Engineering*, 17(4):043001.

[Belytschko and Lasry, 1989] Belytschko, T. and Lasry, D. (1989). A study of localization limiters for strain-softening in statics and dynamics. *Computers & Structures*, 33(3):707–715.

[Belytschko et al., 1994] Belytschko, T., Lu, Y. Y., and Gu, L. (1994). Element-free Galerkin methods. *International Journal for Numerical Methods in Engineering*, 37(2):229–256.

[Belytschko et al., 1995] Belytschko, T., Lu, Y. Y., and Gu, L. (1995). Crack propagation by element-free Galerkin methods. *Engineering Fracture Mechanics*, 51(2):295–315.

[Benaarbia et al., 2018] Benaarbia, A., Rouse, J. P., and Sun, W. (2018). A thermodynamically-based viscoelastic-viscoplastic model for the high temperature cyclic behaviour of 9–12% Cr steels. *International Journal of Plasticity*, 107:100–121.

[Benallal, 1989] Benallal, A. (1989). *Thermoviscoplasticité et endommagement des structures*. Ph.D. thesis, Université Paris 6, Cachan, France.

[Benallal et al., 1991] Benallal, A., Billardon, R., and Lemaitre, J. (1991). Continuum damage mechanics and local approach to fracture: Numerical procedures. *Computer Methods in Applied Mechanics and Engineering*, 92(2):141–155.

[Benallal and Marquis, 1987] Benallal, A. and Marquis, D. (1987). Constitutive equations for nonproportional cyclic elasto-viscoplasticity. *Journal of Engineering Materials and Technology*, 109(4):326–336.

[Berdin, 2004] Berdin, C. (2004). Damage evolution laws and fracture criteria. In *Local Approach to Fracture*, pages 147–174. Les Presses de l'Ecole des Mines, Paris, France, 1st edition.

[Bernardi et al., 1989] Bernardi, C., Maday, Y., and Patera, A. (1989). A new non-conforming approach to domain decomposition - the mortar method. Nonlinear Partial Differential Equations and Their Applications. Pitman Advanced Pub. Program.

[Besson, 2010] Besson, J. (2010). Continuum Models of Ductile Fracture: A Review. *International Journal of Damage Mechanics*, 19(1):3–52.

[Besson et al., 2004] Besson, J., Berdin, C., Bugat, S., Desmorat, R., Feyel, F., Forest, S., Lorentz, E., Maire, E., Pardoen, T., Pineau, A., and Tanguy, B. (2004). *Local Approach to Fracture*. Les Presses de l'Ecole des Mines, Paris, France, 1st edition.

[Besson et al., 2010] Besson, J., Cailletaud, G., Chaboche, J.-L., and Forest, S. (2010). *Non-Linear Mechanics of Materials*. Springer, Dordrecht, 2nd edition edition.

[Besson and Desmorat, 2004] Besson, J. and Desmorat, R. (2004). Numerical implementation of constitutive models. In *Local Approach to Fracture*, pages 279–310. Les Presses de l'Ecole des Mines, Paris, France, 1st edition.

[Besson and Desmorat, 2009] Besson, J. and Desmorat, R. (2009). Lois de comportement pour les matériaux endommageables. In Clavel, M. and Bompard, P., editors, *Endommagement et rupture des matériaux 1*, volume 1, pages 295–338. Hermès Science Publications, Paris, France, 1st edition.

[Besson and Foerch, 1997] Besson, J. and Foerch, R. (1997). Large scale object-oriented finite element code design. *Computer Methods in Applied Mechanics and Engineering*, 142(1):165–187.

[Besson and Guillemer-Neel, 2003] Besson, J. and Guillemer-Neel, C. (2003). An extension of the Green and Gurson models to kinematic hardening. *Mechanics of Materials*, 35(1):1–18.

[Besson and Lorentz, 2006] Besson, J. and Lorentz, E. (2006). Calcul de dommages: Simuler et prédire le vieillissement mécanique des installations de production et de transport d'énergie. Rapport annuel ACI/ARMINES 42240, Ecole des Mines de Paris, Centre des Matériaux, Evry.

[Besson et al., 2013] Besson, J., McCowan, C. N., and Drexler, E. S. (2013). Modeling flat to slant fracture transition using the computational cell methodology. *Engineering Fracture Mechanics*, 104:80–95.

[Besson et al., 2001] Besson, J., Steglich, D., and Brocks, W. (2001). Modeling of crack growth in round bars and plane strain specimens. *International Journal of Solids and Structures*, 38(46):8259–8284.

[Besson et al., 2003] Besson, J., Steglich, D., and Brocks, W. (2003). Modeling of plane strain ductile rupture. *International Journal of Plasticity*, 19(10):1517–1541.

[Bettonte, 2017] Bettonte, F. (2017). *Développement d'une stratégie d'identification des paramètres par recalage de modèle éléments finis à partir de mesures par corrélation d'images: vers l'application à un modèle d'endommagement non local*. Ph.D. thesis, PSL Research University, Paris, France.

[Bigoni and Zaccaria, 1992] Bigoni, D. and Zaccaria, D. (1992). Loss of strong ellipticity in non-associative elastoplasticity. *Journal of the Mechanics and Physics of Solids*, 40(6):1313–1331.

[Billardon and Moret-Bailly, 1987] Billardon, R. and Moret-Bailly, L. (1987). Fully coupled strain and damage finite element analysis of ductile fracture. *Nuclear Engineering and Design*, 105(1):43–49.

[Billot, 2010] Billot, T. (2010). *Comportement et endommagement en fatigue et fatigue - fluage à haute température de différents états microstructuraux du superalliage base-nickel Udimet 720*. Ph.D. thesis, ISAE-ENSMA, Poitiers, France.

[Blackmon et al., 1983] Blackmon, D., Socie, D., and Leckie, F. (1983). Application of continuum damage concepts to creep-fatigue interactions. In *Proceedings of the ASME Symposium on Thermal and Environmental Effects on Fatigue*, pages 45–47, Portland, USA. ASME. Publisher: Royal Society.

[Boers et al., 2005] Boers, S. H. A., Schreurs, P. J. G., and Geers, M. G. D. (2005). Operator-split damage-plasticity applied to groove forming in food can lids. *International Journal of Solids and Structures*, 42(14):4154–4178.

[Bonnand et al., 2019] Bonnand, V., Pacou, D., Voreux, O., Kruch, S., Kanouté, P., and Feld-Payet, S. (2019). Rapport d'avancement 1ère année du PR Meandres. Rapport technique RT 1/26582 DMAS, ONERA, DMAS, Châtillon, France.

[Bonora, 1997] Bonora, N. (1997). A nonlinear CDM model for ductile failure. *Engineering Fracture Mechanics*, 58(1):11–28.

[Bonora et al., 2005] Bonora, N., Gentile, D., Pirondi, A., and Newaz, G. (2005). Ductile damage evolution under triaxial state of stress: theory and experiments. *International Journal of Plasticity*, 21(5):981–1007.

[Boroomand and Zienkiewicz, 1999] Boroomand, B. and Zienkiewicz, O. C. (1999). Recovery procedures in error estimation and adaptivity. Part II: Adaptivity in nonlinear problems of elasto-plasticity behaviour. *Computer Methods in Applied Mechanics and Engineering*, 176(1):127–146.

[Bottoni et al., 2015] Bottoni, M., Dufour, F., and Giry, C. (2015). Topological search of the crack pattern from a continuum mechanical computation. *Engineering Structures*, 99:346–359.

[Bouchard, 2000] Bouchard, P.-O. (2000). *Contribution a la modelisation numerique en mecanique de la rupture et structures multimateriaux*. Ph.D. thesis, Ecole Nationale Supérieure des Mines de Paris, Paris, France.

[Bouchard, 2005] Bouchard, P.-O. (2005). Damage and Discrete Crack Propagation Modelling : Some Results and Challenges For 2d And 3d Configurations. In *Proceedings of ICF11*, page 6, Torino, Italia.

[Bouchard et al., 2003] Bouchard, P. O., Bay, F., and Chastel, Y. (2003). Numerical modelling of crack propagation: automatic remeshing and comparison of different criteria. *Computer Methods in Applied Mechanics and Engineering*, 192(35):3887–3908.

[Bouchard et al., 2000] Bouchard, P. O., Bay, F., Chastel, Y., and Tovena, I. (2000). Crack propagation modelling using an advanced remeshing technique. *Computer Methods in Applied Mechanics and Engineering*, 189(3):723–742.

[Bouchard et al., 2011] Bouchard, P.-O., Bourgeon, L., Fayolle, S., and Mocellin, K. (2011). An enhanced Lemaitre model formulation for materials processing damage computation. *International Journal of Material Forming*, 4(3):299–315.

[Boudifa, 2006] Boudifa, M. (2006). *Modélisation macro et micro-macro des matériaux polycristallins endommageables avec compressibilité induite*. Ph.D. thesis, UTT, Troyes, France.

[Bourdin et al., 2000] Bourdin, B., Francfort, G. A., and Marigo, J.-J. (2000). Numerical experiments in revisited brittle fracture. *Journal of the Mechanics and Physics of Solids*, 48(4):797–826.

[Boussetta, 2005] Boussetta, R. (2005). *Estimateurs d'erreur et remaillage adaptatif : application à la simulation 3D des procédés de mise en forme des matériaux*. Ph.D. thesis, Ecole Nationale Supérieure des Mines de Paris, Paris, France.

[Boussetta et al., 2006] Boussetta, R., Coupez, T., and Fourment, L. (2006). Adaptive remeshing based on a posteriori error estimation for forging simulation. *Computer Methods in Applied Mechanics and Engineering*, 195(48):6626–6645.

[Boussetta and Fourment, 2003] Boussetta, R. and Fourment, L. (2003). Study of various 3D element patches for a posteriori error estimation based on recovery techniques. In *Proceedings of ADMOS 2003*, Götteborg, Sweden.

[Boussetta and Fourment, 2004] Boussetta, R. and Fourment, L. (2004). A Posteriori Error Estimation And Three-dimensional Adaptive Remeshing: Application To Error Control Of Non-Steady Metal Forming Simulations. *AIP Conference Proceedings*, 712(1):2246–2251. Publisher: American Institute of Physics.

[Bouvard, 2006] Bouvard, J.-L. (2006). *Modélisation de la propagation de fissure dans les aubes de turbines monocristallines*. Ph.D. thesis, Ecole Nationale Supérieure des Mines de Paris, Paris, France.

[Bouvard et al., 2009] Bouvard, J. L., Chaboche, J. L., Feyel, F., and Gallerneau, F. (2009). A cohesive zone model for fatigue and creep–fatigue crack growth in single crystal superalloys. *International Journal of Fatigue*, 31(5):868–879.

[Branco et al., 1999] Branco, C., Baptista, J., and Byrne, J. (1999). Crack growth under constant sustained load at elevated temperature in IN718 superalloy. *Materials at High Temperatures*, 16(1):27–35.

[Branco and Byrne, 1995] Branco, C. M. and Byrne, J. (1995). Elevated Temperature Fatigue on IN718 Effects of Stress Ratio and Frequency. In *Proceedings of the 81st Meeting of the AGARD/SMP*, pages 6.1–12. North Atlantic Treaty Organization.

[Branco et al., 2012] Branco, R., Antunes, F. V., Ricardo, L. C. H., and Costa, J. D. (2012). Extent of surface regions near corner points of notched cracked bodies subjected to mode-I loading. *Finite Elements in Analysis and Design*, 50:147–160.

[Branco et al., 2008] Branco, R., Rodrigues, D. M., and Antunes, F. V. (2008). Influence of through-thickness crack shape on plasticity induced crack closure. *Fatigue & Fracture of Engineering Materials & Structures*, 31(2):209–220.

[Brepols, 2018] Brepols, T. (2018). *Theory and numerics of gradient-extended damage coupled with plasticity*. Ph.D. thesis, Rheinisch-Westfälischen Technischen Hochschule Aachen, Aachen, Germany.

[Brepols et al., 2015] Brepols, T., Wulfinghoff, S., and Reese, S. (2015). Examination of an implicit gradient-enhanced damage model coupled to elastoplasticity. In *Proceedings of the 3rd ECCOMAS Young Investigators Conference and 6th GACM Colloquium on Computational Mechanics*, Aachen, Germany. RWTH Aachen University.

[Brezzi, 1974] Brezzi, F. (1974). On the existence, uniqueness and approximation of saddle-point problems arising from Lagrangian multipliers. *Publications mathématiques et informatique de Rennes*, 4:1–26.

[Brighenti and Carpinteri, 2013] Brighenti, R. and Carpinteri, A. (2013). Damage Mechanics and Critical Plane Approach to Multiaxial Fatigue. *Key Engineering Materials*, 592-593:239–245.

[Brokken, 1999] Brokken, D. (1999). *Numerical modelling of ductile fracture in blanking*. Ph.D. thesis, Technische Universiteit Eindhoven, Eindhoven, The Netherlands.

[Brokken et al., 2000] Brokken, D., Brekelmans, W. A. M., and Baaijens, F. P. T. (2000). Predicting the shape of blanked products: a finite element approach. *Journal of Materials Processing Technology*, 103(1):51–56.

[Brooks and Rainforth, 1999] Brooks, R. R. and Rainforth, W. M. (1999). Fatigue damage mechanisms associated with 'tear-drop' cracking in UDIMET 720®. *Fatigue & Fracture of Engineering Materials & Structures*, 22(9):821–829.

[Brooks and Rainforth, 2000] Brooks, R. R. and Rainforth, W. M. (2000). The effect of microstructure on the morphology of fatigue cracks in UDIMET® 720. *Fatigue & Fracture of Engineering Materials & Structures*, 23(9):725–736.

[Broumand and Khoei, 2013] Broumand, P. and Khoei, A. R. (2013). The extended finite element method for large deformation ductile fracture problems with a non-local damage-plasticity model. *Engineering Fracture Mechanics*, 112-113:97–125.

[Broumand and Khoei, 2015] Broumand, P. and Khoei, A. R. (2015). X-FEM modeling of dynamic ductile fracture problems with a nonlocal damage-viscoplasticity model. *Finite Elements in Analysis and Design*, 99:49–67.

[Brunet et al., 2005] Brunet, M., Morestin, F., and Walter-Leberre, H. (2005). Failure analysis of anisotropic sheet-metals using a non-local plastic damage model. *Journal of Materials Processing Technology*, 170(1):457–470.

[Bucher, 2004] Bucher, L. (2004). *Etude de l'endommagement en fatigue thermique des aciers inoxydables F17TNb et R20-12 pour application automobile*. Ph.D. thesis, Ecole Nationale Supérieure des Mines de Paris, Paris, France.

[Cai et al., 2019] Cai, X., Steinmann, P., Yao, X., and Wang, J. (2019). Thermodynamic formulation of a unified multi-mechanism continuum viscoplastic damage model with application to high-Cr steels. *International Journal of Plasticity*, 114:15–39.

[Cailletaud and Saï, 1995] Cailletaud, G. and Saï, K. (1995). Study of plastic/viscoplastic models with various inelastic mechanisms. *International Journal of Plasticity*, 11(8):991–1005.

[Cailletaud et al., 2018] Cailletaud, G., Saï, K., and Taleb, L. (2018). *Multi-mechanism Modeling of Inelastic Material Behavior*. ISTE Ltd and John Wiley & Sons, Inc., 1st edition.

[Carbou, 2000] Carbou, C. (2000). *Interactions fatigue-fluage sur le comportement en fissuration à haute température des superalliages pour disques de turbine. Effets d'oxydation*. Ph.D. thesis, ISAE-ENSMA, Poitiers, France.

[Chaboche, 1974] Chaboche, J.-L. (1974). Une loi différentielle d'endommagement de fatigue avec cumulation non linéaire. *Revue Française de Mécanique*, pages 50–51.

[Chaboche, 1977a] Chaboche, J.-L. (1977a). Sur l'utilisation des variables d'état interne pour la description du comportement viscoplastique et de la rupture par endommagement. *Problèmes Non-Linéaires de Mécanique*, pages 137–159.

[Chaboche, 1977b] Chaboche, J.-L. (1977b). Viscoplastic constitutive equations for the description of cyclic and anisotropic behaviour of metals. *Bulletin de l'Académie Polonaise des Sciences - Série des Sciences Techniques*, XXV(1):33–39.

[Chaboche, 1978] Chaboche, J.-L. (1978). *Description thermodynamique et phénoménologique de la viscoplasticité cyclique avec endommagement*. Ph.D. thesis, Paris 6, ONERA - Châtillon, France.

[Chaboche, 1981] Chaboche, J.-L. (1981). Continuous damage mechanics - A tool to describe phenomena before crack initiation. *Nuclear Engineering and Design*, 64(2):233–247.

[Chaboche, 1986] Chaboche, J.-L. (1986). Time-independent constitutive theories for cyclic plasticity. *International Journal of Plasticity*, 2(2):149–188.

[Chaboche, 1987] Chaboche, J. L. (1987). Continuum damage mechanics: Present state and future trends. *Nuclear Engineering and Design*, 105(1):19–33.

[Chaboche, 1988a] Chaboche, J. L. (1988a). Continuum Damage Mechanics: Part I - General Concepts. *Journal of Applied Mechanics*, 55(1):59–64.

[Chaboche, 1988b] Chaboche, J. L. (1988b). Continuum Damage Mechanics: Part II - Damage Growth, Crack Initiation, and Crack Growth. *Journal of Applied Mechanics*, 55(1):65–72.

[Chaboche, 1989] Chaboche, J.-L. (1989). Constitutive equations for cyclic plasticity and cyclic viscoplasticity. *International Journal of Plasticity*, 5(3):247–302.

[Chaboche, 1991] Chaboche, J.-L. (1991). On some modifications of kinematic hardening to improve the description of ratchetting effects. *International Journal of Plasticity*, 7(7):661–678.

[Chaboche, 1999] Chaboche, J.-L. (1999). Thermodynamically Founded CDM Models for Creep and Other Conditions. In *Creep and Damage in Materials and Structures*, International Centre for Mechanical Sciences, pages 209–283. H. Haltenbach, J.J. Skrzypek, Vienna, springer edition.

[Chaboche, 2008] Chaboche, J.-L. (2008). A review of some plasticity and viscoplasticity constitutive theories. *International Journal of Plasticity*, 24(10):1642–1693.

[Chaboche, 2011] Chaboche, J.-L. (2011). Cumulative Damage. In Bathias, C. and Pineau, A., editors, *Fatigue of Materials and Structures: Application to Design and Damage*, volume 1, pages 47–110. ISTE Ltd. & John Wiley & Sons, London & New-York, 1st edition.

[Chaboche et al., 2006] Chaboche, J.-L., Boudifa, M., and Saanouni, K. (2006). A CDM Approach of Ductile Damage with Plastic Compressibility. *International Journal of Fracture*, 137(1-4):51–75.

[Chaboche and Cailletaud, 1996] Chaboche, J. L. and Cailletaud, G. (1996). Integration methods for complex plastic constitutive equations. *Computer Methods in Applied Mechanics and Engineering*, 133(1):125–155.

[Chaboche et al., 2013] Chaboche, J.-L., Gaubert, A., Kanouté, P., Longuet, A., Azzouz, F., and Mazière, M. (2013). Viscoplastic constitutive equations of combustion chamber materials including cyclic hardening and dynamic strain aging. *International Journal of Plasticity*, 46(Supplement C):1–22.

[Chaboche and Jung, 1997] Chaboche, J. L. and Jung, O. (1997). Application of a kinematic hardening viscoplasticity model with thresholds to the residual stress relaxation. *International Journal of Plasticity*, 13(10):785–807.

[Chaboche et al., 2012] Chaboche, J.-L., Kanouté, P., and Azzouz, F. (2012). Cyclic inelastic constitutive equations and their impact on the fatigue life predictions. *International Journal of Plasticity*, 35(Supplement C):44–66.

[Chaboche et al., 1998] Chaboche, J.-L., Lesné, O., and Pottier, T. (1998). Continuum damage mechanics of composites: Towards a unified approach. In Voyiadjis, G. Z., Ju, J.-W. W., and Chaboche, J.-L., editors, *Studies in Applied Mechanics*, volume 46 of *Damage Mechanics in Engineering Materials*, pages 3–26. Elsevier.

[Chaboche and Nouailhas, 1989] Chaboche, J. L. and Nouailhas, D. (1989). Constitutive Modeling of Ratchetting Effects - Part II: Possibilities of Some Additional Kinematic Rules. *Journal of Engineering Materials and Technology*, 111(4):409–416.

[Chaboche et al., 1991] Chaboche, J.-L., Pacou, D., Paulmier, P., and Nouailhas, D. (1991). Modeling of the cyclic response and ratchetting effects on Inconel-718 alloy. *European Journal of Mechanics - A/Solids*, 10(1):101–121.

[Chaboche and Rousselier, 1983] Chaboche, J.-L. and Rousselier, G. (1983). On the Plastic and Viscoplastic Constitutive Equations - Part I: Rules Developed With Internal Variable Concept. *Journal of Pressure Vessel Technology*, 105(2):153–158.

[Chang and Liu, 2001] Chang, K.-M. and Liu, X. (2001). Effect of γ' content on the mechanical behavior of the WASPALOY alloy system. *Materials Science and Engineering: A*, 308(1):1–8.

[Chen, 2019] Chen, Y. (2019). *Modélisation de la rupture ductile par approche locale : simulation robuste de la déchirure*. Ph.D. thesis, PSL Research University, Paris, France.

[Chen et al., 2022] Chen, Y., Lorentz, E., Dahl, A., and Besson, J. (2022). Simulation of ductile tearing during a full size test using a non local Gurson–Tvergaard–Needleman (GTN) model. *Engineering Fracture Mechanics*, 261:108226.

[Chiaruttini et al., 2010] Chiaruttini, V., Feyel, F., and Chaboche, J.-L. (2010). A robust meshing algorithm for complex 3D crack growth simulation. In *Proceedings of the IV European Conference on Computational Mechanics*, volume IV, Paris, France.

[Chiaruttini et al., 2012] Chiaruttini, V., Geoffroy, D., Riolo, V., and Bonnet, M. (2012). An adaptive algorithm for cohesive zone model and arbitrary crack propagation. *Revue Européenne de Mécanique Numérique/European Journal of Computational Mechanics*, 21:208–218.

[Chiaruttini et al., 2011] Chiaruttini, V., Guilie, J., Feyel, F., Bonnet, M., and Le Tallec, P. (2011). Approches par maillage conforme en mécanique non-linéaire de la rupture : méthode G-theta et modèle de zone cohésive. In *Proceedings of the 10ème Colloque National en Calcul des Structures*, page 8, Giens, France. CSMA.

[Chiaruttini et al., 2013] Chiaruttini, V., Riolo, V., and Feyel, F. (2013). Advanced remeshing techniques for complex 3D crack propagation. In *Proceedings of the 13th International Conference on Fracture*, Beijing, China.

[Chow and Lu, 1992] Chow, C. and Lu, T. (1992). An Analytical and Experimental Study of Mixed-Mode Ductile Fracture under Nonproportional Loading. *International Journal of Damage Mechanics*, 1(2):191–236. Publisher: SAGE Publications Ltd STM.

[Chowdhury and Sehitoglu, 2016] Chowdhury, P. and Sehitoglu, H. (2016). Mechanisms of fatigue crack growth – a critical digest of theoretical developments. *Fatigue & Fracture of Engineering Materials & Structures*, 39(6):652–674.

[Chu and Needleman, 1980] Chu, C. C. and Needleman, A. (1980). Void Nucleation Effects in Biaxially Stretched Sheets. *Journal of Engineering Materials and Technology*, 102(3):249–256.

[Ciarlet, 1978] Ciarlet, P. G. (1978). *The Finite Element Method for Elliptic Problems*, volume 4 of *Studies in Mathematics and Its Applications*. North-Holland Publishing Company, Amsterdam, The Netherlands, 1st edition.

[Cicekli et al., 2007] Cicekli, U., Voyiadjis, G. Z., and Abu Al-Rub, R. K. (2007). A plasticity and anisotropic damage model for plain concrete. *International Journal of Plasticity*, 23(10):1874–1900.

[Coleman and Noll, 1963] Coleman, B. D. and Noll, W. (1963). The Thermodynamics of Elastic Materials with Heat Conduction and Viscosity. *Archive for Rational Mechanics and Analysis*, 13(1):167–178.

[Combescure et al., 2003] Combescure, A., Gravouil, A., and Herry, B. (2003). An algorithm to solve transient structural non-linear problems for non-matching time-space domains. *Computers & Structures*, 81(12):1211–1222.

[Comi and Perego, 1996] Comi, C. and Perego, U. (1996). A generalized variable formulation for gradient dependent softening plasticity. *International Journal for Numerical Methods in Engineering*, 39(21):3731–3755.

[Cordebois and Sidoroff, 1979] Cordebois, J.-P. and Sidoroff, F. (1979). Anisotropie élastique induite par endommagement. In *Proceedings of Colloque Euromech 115*, Grenoble, France.

[Cosserat and Cosserat, 1909] Cosserat, E. and Cosserat, F. (1909). *Théorie des corps déformables*. Librairie Scientifique A. Hermann et Fils, Paris.

[Cottrell, 1953] Cottrell, A. H. (1953). *Dislocations and plastic flow in crystals*. Oxford, oxford university press edition.

[César de Sá et al., 2006] César de Sá, J., Areias, P., and Zheng, C. (2006). Damage modelling in metal forming problems using an implicit non-local gradient model. *Computer Methods in Applied Mechanics and Engineering*, 195(48):6646–6660.

[César de Sá et al., 2015] César de Sá, J., Pires, F., Andrade, F., Malcher, L., and Seabra, M. (2015). Ductile Failure Modelling: Stress Dependence, Non-locality and Damage to Fracture Transition. In Voyiadjis, G. Z., editor, *Handbook of Damage Mechanics: Nano to Macro Scale for Materials and Structures*, pages 877–937. Springer New York, New York, NY.

[Dahal et al., 2012] Dahal, J., Maciejewski, K., and Ghonem, H. (2012). Grain boundary deformation and fracture mechanisms in dwell fatigue crack growth in turbine disk superalloy ME2. In *Superalloys 2012*, pages 149–158. The Minerals, Metals and Materials Society.

[Danas and Ponte Castañeda, 2012] Danas, K. and Ponte Castañeda, P. (2012). Influence of the Lode parameter and the stress triaxiality on the failure of elasto-plastic porous materials. *International Journal of Solids and Structures*, 49(11):1325–1342.

[Davaze, 2019] Davaze, V. (2019). *Modélisation numérique de l'amorçage, la propagation et l'arrêt des fissures dans les matériaux ductiles*. Ph.D. thesis, PSL Research University, Paris, France.

[Davaze et al., 2020] Davaze, V., Vallino, N., Feld-Payet, S., Langrand, B., and Besson, J. (2020). Plastic and fracture behavior of a dual phase steel sheet under quasi-static and dynamic loadings. *Engineering Fracture Mechanics*, 235:107165.

[Davaze et al., 2021] Davaze, V., Vallino, N., Langrand, B., Besson, J., and Feld-Payet, S. (2021). A non-local damage approach compatible with dynamic explicit simulations and parallel computing. *International Journal of Solids and Structures*, 228:110999.

[de Borst et al., 1993] de Borst, R., Sluys, L., Mühlhaus, H., and Pamin, J. (1993). Fundamental issues in finite element analysis of localization of deformation. *Engineering Computations*, 10(2):99–121.

[De Lorenzis and Gerasimov, 2020] De Lorenzis, L. and Gerasimov, T. (2020). Numerical Implementation of Phase-Field Models of Brittle Fracture. In De Lorenzis, L. and Düster, A., editors, *Modeling in Engineering Using Innovative Numerical Methods for Solids and Fluids*, CISM International Centre for Mechanical Sciences, pages 75–101. Springer International Publishing, Cham.

[de Matos and Nowell, 2008] de Matos, P. F. P. and Nowell, D. (2008). Numerical simulation of plasticity-induced fatigue crack closure with emphasis on the crack growth scheme: 2D and 3D analyses. *Engineering Fracture Mechanics*, 75(8):2087–2114.

[de Souza Neto et al., 2011] de Souza Neto, E., Perić, D., and Owen, D. (2011). *Computational Methods for Plasticity: Theory and Applications*. John Wiley & Sons, Ltd, 2nd edition. Google-Books-ID: 21Q0oLGFZuoC.

[Defaisse, 2018] Defaisse, C. (2018). *Étude de la rupture ductile d'un acier à très haute résistance pour des applications aéronautiques*. Ph.D. thesis, PSL Research University, Paris, France.

[Deshpande et al., 2010] Deshpande, A. A., Leen, S. B., and Hyde, T. H. (2010). Finite Element Prediction of Creep-Plastic Ratchetting and Low Cycle Creep-Fatigue for a Large SPF Tool. *Journal of Materials Engineering and Performance*, 19(4):452–466.

[Desmorat, 2000] Desmorat, R. (2000). Quasi-unilateral conditions in anisotropic elasticity. *Comptes Rendus de l'Académie des Sciences - Series II - Fascicule B - Mechanics*, 328(6):445–450.

[Desmorat, 2004] Desmorat, R. (2004). Phenomenological constitutive damage models. In *Local Approach to Fracture*, pages 193–220. Les Presses de l'Ecole des Mines, Paris, France, 1st edition.

[Desmorat, 2006] Desmorat, R. (2006). Damage and fatigue - Continuum damage mechanics modeling for fatigue of materials and structures. *Revue Européenne de Génie Civil*, 10(6-7):849–877.

[Desmorat et al., 2015a] Desmorat, R., Angrand, L., Gaborit, P., Kaminski, M., and Rakotoarisoa, C. (2015a). On the introduction of a mean stress in kinetic damage evolution laws for fatigue. *International Journal of Fatigue*, 77:141–153.

[Desmorat and Cantournet, 2008] Desmorat, R. and Cantournet, S. (2008). Modeling Microdefects Closure Effect with Isotropic/Anisotropic Damage. *International Journal of Damage Mechanics*, 17(1):65–96.

[Desmorat et al., 2015b] Desmorat, R., Gatuingt, F., and Jirásek, M. (2015b). Nonlocal models with damage-dependent interactions motivated by internal time. *Engineering Fracture Mechanics*, 142:255–275.

[Desmorat et al., 2007] Desmorat, R., Ragueneau, F., and Pham, H. (2007). Continuum damage mechanics for hysteresis and fatigue of quasi-brittle materials and structures. *International Journal for Numerical and Analytical Methods in Geomechanics*, 31(2):307–329.

[Devaux et al., 2011] Devaux, A., Georges, E., and Héritier, P. (2011). Development of New C&W Superalloys for High Temperature Disk Applications. *Advanced Materials Research*, 278:405–410.

[Devaux et al., 2014] Devaux, A., Helstroffer, A., Cormier, J., Villechaise, P., Douin, J., Hantcherli, M., and Pettinari-Sturmel, F. (2014). Effect of Aging Heat-Treatment on Mechanical Properties of AD730™ Superalloy. In *8th International Symposium on Superalloy 718 and Derivatives*, pages 521–535. Wiley-Blackwell.

[Devaux et al., 2012] Devaux, A., Picqué, B., Gervais, M., Georges, E., Poulain, T., and Héritier, P. (2012). AD730 - A new nickel-based superalloy for high temperature engine rotative parts. *Superalloys 2012 - 12th International Symposium on Superalloys*, (12):911–919.

[Diamantopoulou et al., 2017] Diamantopoulou, E., Liu, W., Labergere, C., Badreddine, H., Saanouni, K., and Hu, P. (2017). Micromorphic constitutive equations with damage applied to metal forming. *International Journal of Damage Mechanics*, 26(2):314–339.

[Dimitrijević and Hackl, 2008] Dimitrijević, B. and Hackl, K. (2008). A method for gradient enhancement of continuum damage models. *Technische Mechanik*, 28(1):43–52.

[Doherty et al., 1969] Doherty, W., Wilson, E., and Taylor, R. (1969). Stress analysis of axisymmetric solids utilizing higher-order quadrilateral finite elements. Technical report, University of California, Structural Engineering Laboratory.

[Doll et al., 2000] Doll, S., Schweizerhof, K., Hauptmann, R., and Freischläger, C. (2000). On volumetric locking oflow-order solid andsolid-shell elements for finite elastoviscoplastic deformations and selective reduced integration. *Engineering Computations*, 17(7):874–902. Publisher: MCB UP Ltd.

[Donachie and Donachie, 2002] Donachie, M. J. and Donachie, S. J. (2002). *Superalloys: A Technical Guide, 2nd Edition*. ASM International.

[Doremus, 2014] Doremus, L. (2014). *Etude expérimentale et modélisaton de la micro-propagation à partir d'anomalies de surface dans l'Inconel 718DA*. Ph.D. thesis, ISAE-ENSMA, Poitiers, France.

[Dorgan, 2006] Dorgan, R. J. (2006). *A nonlocal model for coupled damage-plasticity incorporating gradients of internal state variables at multiscales*. Ph.D. thesis, Louisiana State University, Baton Rouge, LA, USA.

[Dougherty et al., 1997] Dougherty, J. D., Padovan, J., and Srivatsan, T. S. (1997). Fatigue crack propagation and closure behavior of modified 1070 steel: Finite element study. *Engineering Fracture Mechanics*, 56(2):189–212.

[Downing and Socie, 1982] Downing, S. D. and Socie, D. F. (1982). Simple rainflow counting algorithms. *International Journal of Fatigue*, 4(1):31–40.

[Drucker, 1950] Drucker, D. C. (1950). Some implications of work hardening and ideal plasticity. *Quarterly of Applied Mathematics*, 7(4):411–418.

[Duddu and Waisman, 2013] Duddu, R. and Waisman, H. (2013). A nonlocal continuum damage mechanics approach to simulation of creep fracture in ice sheets. *Computational Mechanics*, 51(6):961–974.

[Dufailly and Lemaitre, 1995] Dufailly, J. and Lemaitre, J. (1995). Modeling Very Low Cycle Fatigue. *International Journal of Damage Mechanics*, 4(2):153–170.

[Dunne and Hayhurst, 1992] Dunne, F. P. E. and Hayhurst, D. R. (1992). Continuum damage based constitutive equations for copper under high temperature creep and cyclic plasticity. *Proceedings of the Royal Society of London. Series A: Mathematical and Physical Sciences*, 437(1901):545–566. Publisher: Royal Society.

[Durand et al., 2020] Durand, M., Cormier, J., Villechaise, P., Franchet, J.-M., Dumont, C., and Bozzolo, N. (2020). Metallurgical Mechanisms upon Stress Relaxation Annealing of the AD730TM Superalloy. In Tin, S., Hardy, M., Clews, J., Cormier, J., Feng, Q., Marcin, J., O'Brien, C., and Suzuki, A., editors, *Superalloys 2020*, The Minerals, Metals & Materials Series, pages 546–558, Cham. Springer International Publishing.

[Díez and Huerta, 1999] Díez, P. and Huerta, A. (1999). A unified approach to remeshing strategies for finite element h-adaptivity. *Computer Methods in Applied Mechanics and Engineering*, 176(1):215–229.

[Egner et al., 2020] Egner, W., Sulich, P., Mroziński, S., and Egner, H. (2020). Modelling thermo-mechanical cyclic behavior of P91 steel. *International Journal of Plasticity*, 135:102820.

[El Khaoulani and Bouchard, 2012] El Khaoulani, R. and Bouchard, P. O. (2012). An anisotropic mesh adaptation strategy for damage and failure in ductile materials. *Finite Elements in Analysis and Design*, 59:1–10.

[El Khaoulani and Bouchard, 2013] El Khaoulani, R. and Bouchard, P. O. (2013). Efficient numerical integration of an elastic-plastic damage law within a mixed velocity-pressure formulation. *Mathematics and Computers in Simulation*, 94:145–158.

[El Khaoulani El Idrissi, 2010] El Khaoulani El Idrissi, R. (2010). *Prédiction fiable de l'endommagement ductile par la méthode des éléments finis mixtes : endommagement non local et adaptation de maillage*. Ph.D. thesis, Ecole Nationale Supérieure des Mines de Paris, Sophia Antipolis, France.

[El Ouazani Tuhami, 2022] El Ouazani Tuhami, A. (2022). *Simulation of ductile failure over long distances with a non-local GTN model*. Ph.D. thesis, PSL Research University, Paris, France.

[El Ouazani Tuhami et al., 2021] El Ouazani Tuhami, A., Feld-Payet, S., Quilici, S., Osipov, N., and Besson, J. (2021). A two characteristic length non local GTN model: application to cup-cone and slant fracture. *(preprint)*.

[Elber, 1970] Elber, W. (1970). Fatigue crack closure under cyclic tension. *Engineering Fracture Mechanics*, 2(1):37–45.

[Eldahshan et al., 2021] Eldahshan, H., Bouchard, P.-O., Alves, J., Perchat, E., and Munoz, D. P. (2021). Phase field modeling of ductile fracture at large plastic strains using adaptive isotropic remeshing. *Computational Mechanics*, 67(3):763–783.

[Ellyin, 1997] Ellyin, F. (1997). *Fatigue Damage, Crack Growth and Life Prediction*. Springer, Dordrecht.

[Ellyin and Kujawski, 1984] Ellyin, F. and Kujawski, D. (1984). Plastic Strain Energy in Fatigue Failure. *Journal of Pressure Vessel Technology*, 106(4):342–347.

[Enakoutsa et al., 2007] Enakoutsa, K., Leblond, J. B., and Perrin, G. (2007). Numerical implementation and assessment of a phenomenological nonlocal model of ductile rupture. *Computer Methods in Applied Mechanics and Engineering*, 196(13):1946–1957.

[Engelen et al., 2003] Engelen, R. A. B., Geers, M. G. D., and Baaijens, F. P. T. (2003). Nonlocal implicit gradient-enhanced elasto-plasticity for the modelling of softening behaviour. *International Journal of Plasticity*, 19(4):403–433.

[Erdogan and Sih, 1963] Erdogan, F. and Sih, G. C. (1963). On the Crack Extension in Plates Under Plane Loading and Transverse Shear. *Journal of Basic Engineering*, 85(4):519–525.

[Eringen and Edelen, 1972] Eringen, A. C. and Edelen, D. G. B. (1972). On nonlocal elasticity. *International Journal of Engineering Science*, 10(3):233–248.

[Eringen and Suhubi, 1964] Eringen, A. C. and Suhubi, E. S. (1964). Nonlinear theory of simple micro-elastic solids—I. *International Journal of Engineering Science*, 2(2):189–203.

[Esnault, 2014] Esnault, J.-B. (2014). *Etude experimentale et numerique en trois dimensions du developpement en fatigue d'une fissure deversee dans une tole mince*. Ph.D. thesis, Ecole Polytechnique X, Palaiseau, France.

[Espinosa et al., 1998] Espinosa, H. D., Zavattieri, P. D., and Emore, G. L. (1998). Adaptive FEM computation of geometric and material nonlinearities with application to brittle failure. *Mechanics of Materials*, 29(3):275–305.

[Fayolle, 2008] Fayolle, S. (2008). *Modélisation numérique de la mise en forme et de la tenue mécanique des assemblages par déformation plastique : application au rivetage auto-poinçonneur*. Ph.D. thesis, Ecole Nationale Supérieure des Mines de Paris, Sophia Antipolis, France.

[Feaugas, 1999] Feaugas, X. (1999). On the origin of the tensile flow stress in the stainless steel AISI 316L at 300 K: back stress and effective stress. *Acta Materialia*, 47(13):3617–3632.

[Feld-Payet, 2010] Feld-Payet, S. (2010). *Amorçage et propagation de fissures dans les milieux ductiles non locaux*. Ph.D. thesis, Ecole Nationale Supérieure des Mines de Paris, Paris, France.

[Feld-Payet, 2022] Feld-Payet, S. (2022). Transition endommagement-fissure. Personal Notes.

[Feld-Payet et al., 2011] Feld-Payet, S., Besson, J., and Feyel, F. (2011). Finite element analysis of damage in ductile structures using a nonlocal model combined with a three-field formulation. *International Journal of Damage Mechanics*, 20:655–680.

[Feld-Payet et al., 2015] Feld-Payet, S., Chiaruttini, V., Besson, J., and Feyel, F. (2015). A new marching ridges algorithm for crack path tracking in regularized media. *International Journal of Solids and Structures*, 71:57–69.

[Fessler, 2017] Fessler, E. (2017). *Etude des interactions fatigue-fluage-environnement lors de la propagation de fissure dans l'Inconel 718 DA*. Ph.D. thesis, Institut National Polytechnique de Toulouse, Toulouse, France.

[Fessler et al., 2017] Fessler, E., Andrieu, E., Bonnand, V., Chiaruttini, V., and Pierret, S. (2017). Relation between crack growth behaviour and crack front morphology under hold-time conditions in DA Inconel 718. *International Journal of Fatigue*, 96:17–27.

[Fiordalisi, 2014] Fiordalisi, S. (2014). *Modélisation tridimensionelle de la fermeture induite par plasticité lors de la propagation d'une fissure de fatigue dans l'acier 304L*. Thèse, ISAE-ENSMA, Poitiers, France.

[Fish and Oskay, 2005] Fish, J. and Oskay, C. (2005). A Nonlocal Multiscale Fatigue Model. *Mechanics of Advanced Materials and Structures*, 12(6):485–500.

[Flageolet, 2005] Flageolet, B. (2005). *Effet du vieillissement du superalliage base nickel N18 pour disques de turbines sur sa durabilité en fatigue et en fatigue-fluage à 700°C*. Ph.D. thesis, ISAE-ENSMA, Poitiers, France.

[Foerch et al., 1997] Foerch, R., Besson, J., Cailletaud, G., and Pilvin, P. (1997). Polymorphic constitutive equations in finite element codes. *Computer Methods in Applied Mechanics and Engineering*, 141(3):355–372.

[Foerch et al., 2000] Foerch, R., Gros, V., Mounoury, V., Quilici, S., and Cailletaud, G. (2000). Cyclic calculations and life prediction in thermomechanical fatigue using the Zmat library. In *ABAQUS Users' Conference–Proceedings*, pages 289–303, Rhode Island, USA.

[Forbes Jones and Jackman, 1999] Forbes Jones, R. M. and Jackman, L. A. (1999). The structural evolution of superalloy ingots during hot working. *JOM*, 51(1):27–31.

[Forest, 2009] Forest, S. (2009). Micromorphic Approach for Gradient Elasticity, Viscoplasticity, and Damage. *Journal of Engineering Mechanics*, 135(3):117–131.

[Forest and Lorentz, 2004] Forest, S. and Lorentz, E. (2004). Localization phenomena and regularization methods. In *Local Approach to Fracture*, pages 311–372. Les Presses de l'Ecole des Mines, Paris, France, 1st edition.

[Forman et al., 1967] Forman, R. G., Kearney, V. E., and Engle, R. M. (1967). Numerical Analysis of Crack Propagation in Cyclic-Loaded Structures. *Journal of Basic Engineering*, 89(3):459–463.

[Fournier et al., 2006] Fournier, B., Sauzay, M., Caës, C., Noblecourt, M., and Mottot, M. (2006). Analysis of the hysteresis loops of a martensitic steel: Part I: Study of the influence of strain amplitude and temperature under pure fatigue loadings using an enhanced stress partitioning method. *Materials Science and Engineering: A*, 437(2):183–196.

[Fournier et al., 2001] Fournier, L., Delafosse, D., and Magnin, T. (2001). Oxidation induced intergranular cracking and Portevin–Le Chatelier effect in nickel base superalloy 718. *Materials Science and Engineering: A*, 316(1):166–173.

[Francfort and Marigo, 1998] Francfort, G. A. and Marigo, J. J. (1998). Revisiting brittle fracture as an energy minimization problem. *Journal of the Mechanics and Physics of Solids*, 46(8):1319–1342.

[Frederick and Armstrong, 1966] Frederick, C. and Armstrong, P. (1966). A mathematical representation of the multiaxial Bauschinger effect. *CEGB report RD/B/N731*.

[Frey and George, 2008] Frey, P. and George, P.-L. (2008). *Mesh Generation: Application to Finite Elements, 2nd Edition | Wiley*. ISTE Ltd. & John Wiley & Sons.

[Gabb et al., 2013] Gabb, T. P., Gayda, J., Telesman, J., Ghosn, L. J., and Garg, A. (2013). Factors influencing dwell fatigue life in notches of a powder metallurgy superalloy. *International Journal of Fatigue*, 48:55–67.

[Ganczarski and Cegielski, 2010] Ganczarski, A. and Cegielski, M. (2010). Continuous damage deactivation in modeling of cycle fatigue of engineering materials. *Procedia Engineering*, 2(1):1057–1066.

[Gardin et al., 2016a] Gardin, C., Fiordalisi, S., Sarrazin-Baudoux, C., Gueguen, M., and Petit, J. (2016a). Numerical prediction of crack front shape during fatigue propagation considering plasticity-induced crack closure. *International Journal of Fatigue*, 88(Supplement C):68–77.

[Gardin et al., 2016b] Gardin, C., Fiordalisi, S., Sarrazin-Baudoux, C., and Petit, J. (2016b). Numerical simulation of fatigue plasticity-induced crack closure for through cracks with curved fronts. *Engineering Fracture Mechanics*, 160(Supplement C):213–225.

[Gaudin et al., 2001] Gaudin, C., Guillemer-Neel, C., and Feaugas, X. (2001). Hardening rate under reverse loading in 316 L : Back stress and effective stress evolutions. *Le Journal de Physique IV*, 11(PR5):Pr5–Pr5–292. Publisher: EDP Sciences.

[Gayda et al., 1988] Gayda, J., Gabb, T. P., and Miner, R. V. (1988). Fatigue Crack Propagation of Nickel-Base Superalloys at 650°C. In Solomon, H. D., Halford, G. R., G. R., Kaisand, L. R., and Leis, N. B., editors, *Low Cycle Fatigue*, number 942 in ASTM Special Technical Publication, pages 293–309. American Society for Testing and Materials, Philadelphia, PA. Publisher: ASTM International.

[Geers et al., 1998] Geers, M. G. D., de Borst, R., Brekelmans, W. A. M., and Peerlings, R. H. J. (1998). Strain-based transient-gradient damage model for failure analyses. *Computer Methods in Applied Mechanics and Engineering*, 160(1):133–153.

[Geers et al., 2003] Geers, M. G. D., Ubachs, R. L. J. M., and Engelen, R. a. B. (2003). Strongly non-local gradient-enhanced finite strain elastoplasticity. *International Journal for Numerical Methods in Engineering*, 56(14):2039–2068.

[George, 1991] George, P. L. (1991). *Génération automatique de maillages. Applications aux méthodes d'éléments finis*. Number 16 in Recherches en Mathématiques Appliquées. Masson, Paris, France, 1st edition.

[Germain, 2006] Germain, N. (2006). *Modélisation non locale de l'endommagement dans les structure composites*. Ph.D. thesis, Ecole Nationale Supérieure des Mines de Paris, ONERA - Châtillon, France.

[Germain, 1973] Germain, P. (1973). *Mécanique des milieux continus*, volume Tome 1 - Théorie générale. Masson, Paris.

[Germain et al., 1983] Germain, P., Nguyen, Q. S., and Suquet, P. (1983). Continuum Thermodynamics. *Journal of Applied Mechanics*, 50(4b):1010–1020.

[Gingold and Monaghan, 1977] Gingold, R. A. and Monaghan, J. J. (1977). Smoothed particle hydrodynamics: theory and application to non-spherical stars. *Monthly Notices of the Royal Astronomical Society*, 181(3):375–389.

[Giry et al., 2011] Giry, C., Dufour, F., and Mazars, J. (2011). Stress-based nonlocal damage model. *International Journal of Solids and Structures*, 48(25):3431–3443.

[Gologanu et al., 1997] Gologanu, M., Leblond, J.-B., Perrin, G., and Devaux, J. (1997). Recent Extensions of Gurson's Model for Porous Ductile Metals. In *Continuum Micromechanics*, International Centre for Mechanical Sciences, pages 61–130. Springer, Vienna.

[González-Herrera and Zapatero, 2005] González-Herrera, A. and Zapatero, J. (2005). Influence of minimum element size to determine crack closure stress by the finite element method. *Engineering Fracture Mechanics*, 72(3):337–355.

[González-Herrera and Zapatero, 2008] González-Herrera, A. and Zapatero, J. (2008). Tri-dimensional numerical modelling of plasticity induced fatigue crack closure. *Engineering Fracture Mechanics*, 75(15):4513–4528.

[Gosselet, 2003] Gosselet, P. (2003). *Méthodes de décomposition de domaine et méthodes d'accélération pour les problèmes multichamps en mécanique non-linéaire*. Ph.D. thesis, Université Pierre et Marie Curie - Paris VI, Paris, France.

[Goulmy, 2017] Goulmy, J.-P. (2017). *Modélisation de l'impact du grenaillage sur le comportement et l'endommagement en fatigue de l'Inconel 718*. Ph.D. thesis, UTT, Troyes, France.

[Gourdin, 2015] Gourdin, S. (2015). *Etude expérimentale et modélisation de la propagation de fissures à partir d'anomalies de surface dans le René 65*. Ph.D. thesis, ISAE-ENSMA, Poitiers, France.

[Govaere, 2020] Govaere, A. (2020). *Impact des carbures sur la variabilité des propriétés en fatigue de superalliages pour disques*. Ph.D. thesis, ISAE-ENSMA Ecole Nationale Supérieure de Mécanique et d'Aérotechique, Poitiers, France.

[Goyal et al., 2017] Goyal, S., Mandal, S., Parameswaran, P., Sandhya, R., Athreya, C. N., and Laha, K. (2017). A comparative assessment of fatigue deformation behavior of 316 LN SS at ambient and high temperature. *Materials Science and Engineering: A*, 696:407–415.

[Green, 1972] Green, R. J. (1972). A plasticity theory for porous solids. *International Journal of Mechanical Sciences*, 14(4):215–224.

[Gross et al., 1964] Gross, B., Srawley, J., and Brown, W. (1964). Stress intensity factors for a single-edge-notch tension specimen by boundary collocation of a stress function. Technical Note NASA TN D-2395, NASA - National Aeronautics and Space Administration, Lewis Research Center, Cleveland, Ohio, USA.

[Guillemer et al., 2011] Guillemer, C., Clavel, M., and Cailletaud, G. (2011). Cyclic behavior of extruded magnesium: Experimental, microstructural and numerical approach. *International Journal of Plasticity*, 27(12):2068–2084.

[Guillemer-Neel et al., 2000] Guillemer-Neel, C., Feaugas, X., and Clavel, M. (2000). Mechanical behavior and damage kinetics in nodular cast iron: Part II. Hardening and damage. *Metallurgical and Materials Transactions A*, 31(12):3075–3085.

[Gurson, 1975] Gurson, A. (1975). *Plastic flow and fracture behaviour of ductile materials: incorporating void nucleation, growth, and interaction*. Ph.D. thesis, Brown University, Providence, Rhode Island.

[Gurson, 1977] Gurson, A. L. (1977). Continuum Theory of Ductile Rupture by Void Nucleation and Growth: Part I—Yield Criteria and Flow Rules for Porous Ductile Media. *Journal of Engineering Materials and Technology*, 99(1):2–15.

[Gustafsson, 2012] Gustafsson, D. (2012). *High temperature fatigue crack propagation behaviour of Inconel 718*. Ph.D. thesis, Linköping University - Institute of Technology, Linköping, Sweden.

[Gustafsson et al., 2011a] Gustafsson, D., Moverare, J., Simonsson, K., Johansson, S., Hörnqvist, M., Månsson, T., and Sjöström, S. (2011a). Fatigue crack growth behaviour of Inconel 718 – the concept of a damaged zone caused by high temperature hold times - ScienceDirect. *Procedia Engineering*, 10:2821–2826.

[Gustafsson et al., 2011b] Gustafsson, D., Moverare, J. J., Johansson, S., Simonsson, K., Hörnqvist, M., Månsson, T., and Sjöström, S. (2011b). Influence of high temperature hold times on the fatigue crack propagation in Inconel 718. *International Journal of Fatigue*, 33(11):1461–1469.

[Gustafsson et al., 2011c] Gustafsson, D., Moverare, J. J., Simonsson, K., and Sjöström, S. (2011c). Modeling of the Constitutive Behavior of Inconel 718 at Intermediate Temperatures. *Journal of Engineering for Gas Turbines and Power*, 133(9):094501–094501–4.

[Hackl and Fischer, 2008] Hackl, K. and Fischer, F. D. (2008). On the relation between the principle of maximum dissipation and inelastic evolution given by dissipation potentials. *Proceedings of the Royal*

Society A: Mathematical, Physical and Engineering Sciences, 464(2089):117–132. Publisher: Royal Society.

[Haddag, 2007] Haddag, B. (2007). *Contribution à la modélisation de la mise en forme des tôles métalliques : application au retour élastique et à la localisation*. Ph.D. thesis, ENSAM, Metz, France.

[Hall and Hayhurst, 1991] Hall, F. and Hayhurst, D. (1991). Modelling of grain size effects in creep crack growth using a non-local continuum damage approach. *Proceedings of the Royal Society of London. Series A: Mathematical and Physical Sciences*, 433:405–421. Publisher: The Royal Society London.

[Halm and Dragon, 1996] Halm, D. and Dragon, A. (1996). A Model of Anisotropic Damage by Mesocrack Growth; Unilateral Effect. *International Journal of Damage Mechanics*, 5(4):384–402.

[Halphen and Nguyen, 1974] Halphen, B. and Nguyen, Q. S. (1974). Plastic and visco-plastic materials with generalized potential. *Mechanics Research Communications*, 1(1):43–47.

[Halphen and Nguyen, 1975] Halphen, B. and Nguyen, Q. S. (1975). Sur les matériaux standards généralisés. *Journal de Mécanique*, 14:39–63.

[Hamon, 2010] Hamon, F. (2010). *Modélisation du comportement mécanique en fissuration d'alliages aéronautiques*. Ph.D. thesis, ISAE-ENSMA, Poitiers, France.

[Hamon et al., 2012] Hamon, F., Henaff, G., Halm, D., Gueguen, M., and Billaudeau, T. (2012). A damage model for fatigue crack propagation from moderate to high DeltaK levels. *Fatigue & Fracture of Engineering Materials & Structures*, 35(2):160–172.

[Hamon et al., 2010] Hamon, F., Hénaff, G., Halm, D., Gueguen, M., and Billaudeau, T. (2010). CDM approach applied to fatigue crack propagation on airframe structural alloys. *Procedia Engineering*, 2(1):1403–1412.

[Harth and Lehn, 2007] Harth, T. and Lehn, J. (2007). Identification of Material Parameters for Inelastic Constitutive Models Using Stochastic Methods. *GAMM-Mitteilungen*, 30(2):409–429.

[Hasan and Baxevanis, 2021] Hasan, M. M. and Baxevanis, T. (2021). A phase-field model for low-cycle fatigue of brittle materials. *International Journal of Fatigue*, 150:106297.

[Heinrich et al., 2013] Heinrich, S., Kowalsky, U., and Dinkler, D. (2013). Evolution of nonlocal damage in steel under cyclic straining. In *Proc. of COMPLAS2013*, Barcelona, Spain. CIMNE.

[Hill, 1958] Hill, R. (1958). A general theory of uniqueness and stability in elastic-plastic solids. *Journal of the Mechanics and Physics of Solids*, 6(3):236–249.

[Hillerborg et al., 1976] Hillerborg, A., Modéer, M., and Petersson, P. E. (1976). Analysis of crack formation and crack growth in concrete by means of fracture mechanics and finite elements. *Cement and Concrete Research*, 6(6):773–781.

[Hosseini et al., 2018] Hosseini, Z. S., Dadfarnia, M., Somerday, B. P., Sofronis, P., and Ritchie, R. O. (2018). On the theoretical modeling of fatigue crack growth. *Journal of the Mechanics and Physics of Solids*, 121:341–362.

[Huang and Xue, 2009] Huang, H. and Xue, L. (2009). Prediction of slant ductile fracture using damage plasticity theory. *International Journal of Pressure Vessels and Piping*, 86(5):319–328.

[Huber and Tsakmakis, 2001] Huber, N. and Tsakmakis, C. (2001). A neural network tool for identifying the material parameters of a finite deformation viscoplasticity model with static recovery. *Computer Methods in Applied Mechanics and Engineering*, 191(3):353–384.

[Huespe et al., 2009] Huespe, A. E., Needleman, A., Oliver, J., and Sánchez, P. J. (2009). A finite thickness band method for ductile fracture analysis. *International Journal of Plasticity*, 25(12):2349–2365.

[Huespe et al., 2012] Huespe, A. E., Needleman, A., Oliver, J., and Sánchez, P. J. (2012). A finite strain, finite band method for modeling ductile fracture. *International Journal of Plasticity*, 28(1):53–69.

[Hughes, 1980] Hughes, T. J. R. (1980). Generalization of selective integration procedures to anisotropic and nonlinear media. *International Journal for Numerical Methods in Engineering*, 15(9):1413–1418.

[Hütter et al., 2013] Hütter, G., Linse, T., Mühlich, U., and Kuna, M. (2013). Simulation of ductile crack initiation and propagation by means of a non-local Gurson-model. *International Journal of Solids and Structures*, 50(5):662–671.

[Hütter et al., 2014] Hütter, G., Zybell, L., and Kuna, M. (2014). Size effects due to secondary voids during ductile crack propagation. *International Journal of Solids and Structures*, 51(3):839–847.

[Irwin, 1960] Irwin, G. (1960). Plastic zone near a crack and fracture toughness. In *Proceedings of the 7th Sagamore Ordnance Materials Research Conference*, volume 4, pages 63–78, New York, Syracuse University.

[Jackiewicz and Kuna, 2003] Jackiewicz, J. and Kuna, M. (2003). Non-local regularization for FE simulation of damage in ductile materials. *Computational Materials Science*, 28(3):684–695.

[Javani, 2011] Javani, H. R. (2011). *A computational damage approach towards three-dimensionalductile fracture*. Ph.D. thesis, Technische Universiteit Eindhoven, Eindhoven, The Netherlands.

[Javani et al., 2009] Javani, H. R., Peerlings, R. H. J., and Geers, M. G. D. (2009). Three dimensional modelling of non-local ductile damage: element technology. *International Journal of Material Forming*, 2(1):923.

[Javani et al., 2016] Javani, H. R., Peerlings, R. H. J., and Geers, M. G. D. (2016). Three-dimensional finite element modeling of ductile crack initiation and propagation. *Advanced Modeling and Simulation in Engineering Sciences*, 3(1):19.

[Javanmardi and Maheri, 2019] Javanmardi, M. R. and Maheri, M. R. (2019). Extended finite element method and anisotropic damage plasticity for modelling crack propagation in concrete. *Finite Elements in Analysis and Design*, 165:1–20.

[Jiang, 2000] Jiang, Y. (2000). A fatigue criterion for general multiaxial loading. *Fatigue & Fracture of Engineering Materials & Structures*, 23(1):19–32.

[Jiang and Zhang, 2008] Jiang, Y. and Zhang, J. (2008). Benchmark experiments and characteristic cyclic plasticity deformation. *International Journal of Plasticity*, 24(9):1481–1515.

[Jing et al., 2017] Jing, H., Su, D., Xu, L., Zhao, L., Han, Y., and Sun, R. (2017). Finite element simulation of creep-fatigue crack growth behavior for P91 steel at 625°C considering creep-fatigue interaction. *International Journal of Fatigue*, 98:41–52.

[Jirásek, 1998] Jirásek, M. (1998). Nonlocal models for damage and fracture: Comparison of approaches. *International Journal of Solids and Structures*, 35(31):4133–4145.

[Jirásek, 2007] Jirásek, M. (2007). Nonlocal damage mechanics. *Revue Européenne de Génie Civil*, 11(7-8):993–1021.

[Jirásek and Bažant, 2001] Jirásek, M. and Bažant, Z. P. (2001). *Inelastic Analysis of Structures*. John Wiley & Sons, England.

[Jirásek and Belytschko, 2002] Jirásek, M. and Belytschko, T. (2002). Computational Resolution of Strong Discontinuities. In Mang, H., Rammerstorfer, F., and Eberhardsteiner, J., editors, *Proceedings of the WCCM V*, Vienna, Austria.

[Jirásek and Marfia, 2005] Jirásek, M. and Marfia, S. (2005). Non-local damage model based on displacement averaging. *International Journal for Numerical Methods in Engineering*, 63(1):77–102.

[Jirásek and Rolshoven, 2003a] Jirásek, M. and Rolshoven, S. (2003a). Comparison of integral-type nonlocal plasticity models for strain-softening materials. *International Journal of Engineering Science*, 41(13):1553–1602.

[Jirásek and Rolshoven, 2003b] Jirásek, M. and Rolshoven, S. (2003b). Regularized formulations of strain-softening plasticity. In Kolymbas, D., editor, *Advanced Mathematical and Computational Geomechanics*, Lecture Notes in Applied and Computational Mechanics, pages 269–299. Springer, Berlin, Heidelberg.

[Jirásek and Rolshoven, 2009] Jirásek, M. and Rolshoven, S. (2009). Localization properties of strain-softening gradient plasticity models. Part I: Strain-gradient theories. *International Journal of Solids and Structures*, 46(11):2225–2238.

[Jirásek and Zimmermann, 2001] Jirásek, M. and Zimmermann, T. (2001). Embedded crack model. Part II: combination with smeared cracks. *International Journal for Numerical Methods in Engineering*, 50(6):1291–1305.

[Johnson, 1965] Johnson, H. (1965). Calibrating the Electric Potential Method for Studying Slow Crack Growth. *Materials Research and Standards*, 5(1):442–445.

[Kachanov, 1958] Kachanov, L. (1958). Time of the Rupture Process under Creep Conditions. *Izvestia Akademii Nauk. S.S.R. Otd. Tekh. Nauk.*, 8:26–31.

[Kachanov, 1986] Kachanov, L. M. (1986). *Introduction to continuum damage mechanics*. Springer, Dordrecht, illustrée edition.

[Kaminski, 2007] Kaminski, M. (2007). *Modélisation de l'endommagement en fatigue des superalliages monocristallins pour aubes de turbine en zone de concentration de contrainte*. Ph.D. thesis, Ecole Nationale Supérieure des Mines de Paris, Paris, France.

[Karolak, 2016] Karolak, C. (2016). *Analysis and modelling of the failure behavior of carbonitrided parts*. Ph.D. thesis, PSL Research University, Paris.

[Khoei et al., 2013a] Khoei, A. R., Eghbalian, M., Azadi, H., and Saffar, H. (2013a). Numerical simulation of ductile crack growth under cyclic and dynamic loading with a damage–viscoplasticity model. *Engineering Fracture Mechanics*, 99:169–190.

[Khoei et al., 2013b] Khoei, A. R., Eghbalian, M., Moslemi, H., and Azadi, H. (2013b). Crack growth modeling via 3D automatic adaptive mesh refinement based on modified-SPR technique. *Applied Mathematical Modelling*, 37(1):357–383.

[Kirkesaether Brun et al., 2020] Kirkesaether Brun, M., Wick, T., Berre, I., Nordbotten, J. M., and Radu, F. A. (2020). An iterative staggered scheme for phase field brittle fracture propagation with stabilizing parameters. *Computer Methods in Applied Mechanics and Engineering*, 361:112752.

[Kitagawa and Takahashi, 1976] Kitagawa, H. and Takahashi, S. (1976). Applicability of fracture mechanics to very small cracks or the cracks in the early stage. In *Proc. of 2nd ICM*, pages 627–631, Cleveland.

[Kowalsky et al., 2012] Kowalsky, U., Meyer, J., Heinrich, S., and Dinkler, D. (2012). A nonlocal damage model for mild steel under inelastic cyclic straining. *Computational Materials Science*, 63:28–34.

[Kruch et al., 1991] Kruch, S., Chaboche, J. L., and Lesne, P. M. (1991). A New Damage Approach for Creep Crack Growth Prediction. In *Creep in Structures*, International Union of Theoretical and Applied Mechanics, pages 355–362. Springer, Berlin, Heidelberg.

[Kruch et al., 2015] Kruch, S., Kanouté, P., and Bonnand, V. (2015). ONERA's Multiaxial and Anisothermal Lifetime Assessment for Engine Components. *Aerospace Lab*, 9(8):1–12.

[Kröner, 1967] Kröner, E. (1967). Elasticity theory of materials with long range cohesive forces. *International Journal of Solids and Structures*, 3(5):731–742.

[Kuczynska et al., 2021] Kuczynska, M., Maniar, Y., Becker, U., and Weihe, S. (2021). Effect of shear and tensile-dominant cyclic loading on failure in SnAgCu solder. *Microelectronics Reliability*, 120:114101.

[Kumar et al., 2015] Kumar, S., Fourment, L., and Guerdoux, S. (2015). Parallel, second-order and consistent remeshing transfer operators for evolving meshes with superconvergence property on surface and volume. *Finite Elements in Analysis and Design*, 93:70–84.

[Kuna and Wippler, 2010] Kuna, M. and Wippler, S. (2010). A cyclic viscoplastic and creep damage model for lead free solder alloys. *Engineering Fracture Mechanics*, 77(18):3635–3647.

[Könke, 1995] Könke, C. (1995). Damage evolution in ductile materials: from micro- to macro-damage. *Computational Mechanics*, 15(6):497–510.

[Labergere et al., 2014] Labergere, C., Rassineux, A., and Saanouni, K. (2014). Numerical simulation of continuous damage and fracture in metal-forming processes with 2D mesh adaptive methodology. *Finite Elements in Analysis and Design*, 82(Supplement C):46–61.

[Ladevèze, 1983] Ladevèze, P. (1983). Sur une theorie de l'endommagement anisotrope. Rapport interne LMT Cachan 34, ENS, LMT, Cachan, France.

[Ladevèze, 1992] Ladevèze, P. (1992). A damage computational method for composite structures. *Computers & Structures*, 44(1):79–87.

[Ladevèze and Pelle, 2005] Ladevèze, P. and Pelle, J. P. (2005). *Mastering Calculations in Linear and Nonlinear Mechanics*. Mechanical Engineering Series. Springer Science & Business Media, Inc., New York.

[Ladevèze and Rougeot, 1997] Ladevèze, P. and Rougeot, P. (1997). New advances on a posteriori error on constitutive relation in f.e. analysis. *Computer Methods in Applied Mechanics and Engineering*, 150(1):239–249.

[Lan et al., 2006] Lan, W., Deng, X., Sutton, M. A., and Cheng, C.-S. (2006). Study of slant fracture in ductile materials. *International Journal of Fracture*, 141(3):469–496.

[Landgraf et al., 1969] Landgraf, R. W., Morrow, J., and Endo, T. (1969). Determination of the Cyclic Stress-Strain Curve. *Journal of Materials*, 4(1):176–188.

[Langenfeld et al., 2021] Langenfeld, K., Möhring, K., Walther, F., and Mosler, J. (2021). Modeling gradient-enhanced anisotropic ductile damage: Application to low cycle fatigue. *PAMM*, 20(1):e202000157.

[Lasry and Belytschko, 1988] Lasry, D. and Belytschko, T. (1988). Localization limiters in transient problems. *International Journal of Solids and Structures*, 24(6):581–597.

[Leblond et al., 1994] Leblond, J. B., Perrin, G., and Devaux, J. (1994). Bifurcation Effects in Ductile Metals With Nonlocal Damage. *Journal of Applied Mechanics*, 61(2):236–242.

[Leckie and Hayhurst, 1974] Leckie, F. A. and Hayhurst, D. R. (1974). Creep rupture of structures. *Proc. R. Soc. Lond. A*, 340(1622):323–347.

[Leclerc, 2020] Leclerc, J. (2020). *A damage to crack transition framework for ductile materials*. Ph.D. thesis, Université de Liège, Liège, Belgium.

[Lee and Basaran, 2021] Lee, H. W. and Basaran, C. (2021). A Review of Damage, Void Evolution, and Fatigue Life Prediction Models. *Metals*, 11(4):609. Number: 4 Publisher: Multidisciplinary Digital Publishing Institute.

[Lee et al., 2008] Lee, S., Liaw, P.K., K., Lu, Y., Fielden, D., Pike, L., and Klarstrom, D. (2008). Elevated-temperature creep-fatigue crack-growth behaviour of nickel-based Haynes® R-41, Haynes® 230® and Hastelloy® X. In *Superalloys 2008*, pages 509–514. The Minerals, Metals and Materials Society.

[Lemaitre, 1971] Lemaitre, J. (1971). Evaluation of dissipation and damage in metals submitted to dynamic loading. In *Proceedings of ICM1*, volume 1, Kyoto, Japan.

[Lemaitre, 1974] Lemaitre, J. (1974). Prévision de la progression des fissures de fatigue dans les structures minces renforcées. *Revue de Physique Appliquée*, 9(4):667–672. Publisher: Société Française de Physique.

[Lemaitre, 1985a] Lemaitre, J. (1985a). A Continuous Damage Mechanics Model for Ductile Fracture. *Journal of Engineering Materials and Technology*, 107(1):83–89.

[Lemaitre, 1985b] Lemaitre, J. (1985b). Coupled elasto-plasticity and damage constitutive equations. *Computer Methods in Applied Mechanics and Engineering*, 51(1):31–49.

[Lemaitre, 1996] Lemaitre, J. (1996). *A Course on Damage Mechanics*. Springer-Verlag, Berlin, Heidelberg, 2nd edition.

[Lemaitre, 2001] Lemaitre, J., editor (2001). *Handbook of Materials Behavior Models*. Academic Press, San Diego, CA, USA.

[Lemaitre and Chaboche, 1974] Lemaitre, J. and Chaboche, J.-L. (1974). A nonlinear model of creep-fatigue damage cumulation and interaction. In Hult, J., editor, *Proceedings of the IUTAM Symposium of Viscoelastic Media and Bodies*, pages 291–301. Springer-Verlag.

[Lemaitre and Chaboche, 1978] Lemaitre, J. and Chaboche, J.-L. (1978). Aspect phénoménologique de la rupture par endommagement. *Journal de Mécanique Appliquée*, 2(3):317–365.

[Lemaitre and Chaboche, 1990] Lemaitre, J. and Chaboche, J.-L. (1990). *Mechanics of Solid Materials*. Cambridge University Press, 1st edition.

[Lemaitre et al., 2009] Lemaitre, J., Chaboche, J.-L., Benallal, A., and Desmorat, R. (2009). *Mécanique des Matériaux Solides*. Sciences Sup. Dunod, 3ème edition.

[Lemaitre et al., 1974] Lemaitre, J., Chaboche, J.-L., and Munakata, Y. (1974). Method of Metal Characterization for Creep and Low Cycle Fatigue Prediction in Structures, Example of UDIMET 700. *Journal of the Society of Materials Science,Japan*, 23(246):217. Publisher: The Society of Materials Science, Japan.

[Lemaitre and Desmorat, 2005] Lemaitre, J. and Desmorat, R. (2005). *Engineering Damage Mechanics: Ductile, Creep, Fatigue and Brittle Failures*. Springer-Verlag, Berlin, Heidelberg, 1st edition.

[Lemaitre and Marquis, 1988] Lemaitre, J. and Marquis, D. (1988). Modelling Elasto-Plasticity, Damage and Ageing as Coupled Behaviours in Engineering Materials. In Tooth, A. and Spence, J., editors, *Proceedings of the Applied Solid Mechanics Conference 2*, volume 2, Glasgow, UK. Elsevier Applied Science.

[Lemaitre and Plumtree, 1979] Lemaitre, J. and Plumtree, A. (1979). Application of Damage Concepts to Predict Creep-Fatigue Failures. *Journal of Engineering Materials and Technology*, 101(3):284–292.

[Lemaitre et al., 1999] Lemaitre, J., Sermage, J.-P., and Desmorat, R. (1999). A two scale damage concept applied to fatigue. *International Journal of Fracture*, 97(1-4):67.

[Leo Prakash et al., 2009] Leo Prakash, D. G., Walsh, M. J., Maclachlan, D., and Korsunsky, A. M. (2009). Crack growth micro-mechanisms in the IN718 alloy under the combined influence of fatigue, creep and oxidation. *International Journal of Fatigue*, 31(11):1966–1977.

[Li et al., 2019] Li, H., Jing, H., Xu, L., Han, Y., Zhao, L., Tang, Z., and Song, K. (2019). Microstructure mechanism, cyclic deformation behavior of an Fe-Ni-Cr alloy considering non-Masing behavior. *International Journal of Fatigue*, 127:537–550.

[Li et al., 2011] Li, L., Liu, S., and Wang, H. (2011). A meshless method for ductile fracture. *International Journal for Numerical Methods in Biomedical Engineering*, 27(2):251–261.

[Li and Bettes, 1995] Li, L.-Y. and Bettes, P. (1995). Notes on mesh optimal criteria in adaptive finite element computations. *Communications in Numerical Methods in Engineering*, 11(11):911–915.

[Lian et al., 2013] Lian, J., Sharaf, M., Archie, F., and Münstermann, S. (2013). A hybrid approach for modelling of plasticity and failure behaviour of advanced high-strength steel sheets. *International Journal of Damage Mechanics*, 22(2):188–218.

[Liebe and Steinmann, 2001] Liebe, T. and Steinmann, P. (2001). Theory and numerics of a thermodynamically consistent framework for geometrically linear gradient plasticity. *International Journal for Numerical Methods in Engineering*, 51(12):1437–1467.

[Liebe et al., 2001] Liebe, T., Steinmann, P., and Benallal, A. (2001). Theoretical and computational aspects of a thermodynamically consistent framework for geometrically linear gradient damage. *Computer Methods in Applied Mechanics and Engineering*, 190(49):6555–6576.

[Ling, 2017] Ling, C. (2017). *Modeling the intragranular ductile fracture of irradiated steels. Effects of crystal anisotropy and strain gradient*. Ph.D. thesis, PSL Research University, Paris, France.

[Linse et al., 2012] Linse, T., Hütter, G., and Kuna, M. (2012). Simulation of crack propagation using a gradient-enriched ductile damage model based on dilatational strain. *Engineering Fracture Mechanics*, 95:13–28.

[Linse et al., 2014] Linse, T., Kuna, M., and Viehrig, H. W. (2014). Quantification of brittle-ductile failure behavior of ferritic reactor pressure vessel steels using the Small-Punch-Test and micromechanical damage models. *Materials Science and Engineering: A*, 614:136–147.

[Littlewood, 2011] Littlewood, D. J. (2011). A Nonlocal Approach to Modeling Crack Nucleation in AA 7075-T651. In *Proceedings of the ASME 2011 International Mechanical Engineering Congress & Exposition*, pages 567–576, Denver, CO, USA. ASME Digital Collection.

[Liu et al., 2021] Liu, B., Bao, R., and Sui, F. (2021). A fatigue damage-cumulative model in peridynamics. *Chinese Journal of Aeronautics*, 34(2):329–342.

[Liu et al., 1995] Liu, W., Jun, S., and Zhang, Y. (1995). Reproducing kernel particle methods. *International Journal for Numerical Methods in Fluids*, 20(8-9):1081–1106.

[Loo-Morrey and Reed, 2000] Loo-Morrey, M. and Reed, P. A. S. (2000). Anomalous crack shape development (tear drop cracking) in turbine disc material Udimet 720. *Materials Science and Technology*, 16(2):133–146.

[Lorentz and Andrieux, 1999] Lorentz, E. and Andrieux, S. (1999). A variational formulation for nonlocal damage models. *International Journal of Plasticity*, 15(2):119–138.

[Lorentz et al., 2008] Lorentz, E., Besson, J., and Cano, V. (2008). Numerical simulation of ductile fracture with the Rousselier constitutive law. *Computer Methods in Applied Mechanics and Engineering*, 197(21):1965–1982.

[Lorentz and Cano, 2005] Lorentz, E. and Cano, V. (2005). A nonlocal formulation applied to ductile damage. *Latin American Journal of Solids and Structures*, 2(1):17–28.

[Lorentz and Godard, 2011] Lorentz, E. and Godard, V. (2011). Gradient damage models: Toward full-scale computations. *Computer Methods in Applied Mechanics and Engineering*, 200(21-22):1927–1944.

[Lu et al., 2019] Lu, X., Li, C., Tie, Y., Hou, Y., and Zhang, C. (2019). Crack propagation simulation in brittle elastic materials by a phase field method. *Theoretical and Applied Mechanics Letters*, 9(6):339–352.

[Lu and Liu, 2010] Lu, Z. and Liu, Y. (2010). Small Time Scale Fatigue Crack Growth Analysis Under Variable Amplitude Loading. Orlando, Florida.

[Lu and Liu, 2012] Lu, Z. and Liu, Y. (2012). A comparative study between a small time scale model and the two driving force model for fatigue analysis. *International Journal of Fatigue*, 42:57–70.

[Lu et al., 2012] Lu, Z., Xu, J., and Liu, Y. (2012). A Small Time Scale Model for Creep Fatigue Crack Growth Analysis. pages 610–620. ISBN: 9780784412190 Publisher: American Society of Civil Engineers.

[Lukáš and Kunz, 1989] Lukáš, P. and Kunz, L. (1989). Effect of mean stress on cyclic stress-strain response and high cycle fatigue life. *International Journal of Fatigue*, 11(1):55–58.

[Lundström, 2014] Lundström, E. (2014). *Modelling of fatigue crack propagation in Inconel 718 under hold time conditions*. Ph.D. thesis, Linköping University, Division of Engineering Materials, Linköping, Sweden.

[Ma and Yuan, 2017] Ma, S. and Yuan, H. (2017). A continuum damage model for multi-axial low cycle fatigue of porous sintered metals based on the critical plane concept. *Mechanics of Materials*, 104:13–25.

[Maciejewski, 2013] Maciejewski, K. (2013). *The Role of Microstructure on Deformation and Damage Mechanisms in a Ni-based Superalloy at Elevated Temperatures*. Ph.D. thesis, University of Rhode Island, Kingstone, RI, USA.

[Mahmoudi et al., 2011] Mahmoudi, A. H., Pezeshki-Najafabadi, S. M., and Badnava, H. (2011). Parameter determination of Chaboche kinematic hardening model using a multi objective Genetic Algorithm. *Computational Materials Science*, 50(3):1114–1122.

[Malcher and Mamiya, 2014] Malcher, L. and Mamiya, E. N. (2014). An improved damage evolution law based on continuum damage mechanics and its dependence on both stress triaxiality and the third invariant. *International Journal of Plasticity*, 56(Supplement C):232–261.

[Maniar et al., 2017] Maniar, Y., Métais, B., Kuczynska, M., Kabakchiev, A., Binkele, P., and Schmauder, S. (2017). Nonlocal continuum damage mechanics approach in the Finite Element simulation of lead-free solder joints. In *2017 18th International Conference on Thermal, Mechanical and Multi-Physics Simulation and Experiments in Microelectronics and Microsystems (EuroSimE)*, pages 1–8.

[Mannan, 1993] Mannan, S. (1993). Role of dynamic strain ageing in low cycle fatigue. *Bulletin of Materials Science*, 16(6):561–582.

[Marchal, 2006] Marchal, N. (2006). *Propagation de fissure en fatigue-fluage à haute température de superalliages monocristallins à base de nickel*. Ph.D. thesis, Ecole Nationale Supérieure des Mines de Paris, Paris, France.

[Marchal et al., 2006] Marchal, N., Flouriot, S., Forest, S., and Remy, L. (2006). Crack-tip stress–strain fields in single crystal nickel-base superalloys at high temperature under cyclic loading. *Computational Materials Science*, 37(1):42–50.

[Marnier et al., 2016] Marnier, G., Keller, C., and Taleb, L. (2016). Tensile prestrain memory effect on subsequent cyclic behavior of FCC metallic materials presenting different dislocations slip modes. *International Journal of Plasticity*, 78:64–83.

[Marquis, 1979] Marquis, D. (1979). *Modélisation et identification de l'écrouissage anisotrope des métaux*. Thèse de 3ème cycle, Université Paris 6, Cachan, France.

[Martin and Leckie, 1972] Martin, J. B. and Leckie, F. A. (1972). On the creep rupture of structures. *Journal of the Mechanics and Physics of Solids*, 20(4):223–238.

[Masing, 1923] Masing, G. (1923). Zur Heyn'schen Theorie der Verfestigung der Metalle durch verborgen elastische Spannungen. pages 231–239. Springer, Berlin, Heidelberg.

[Masing, 1926] Masing, G. (1926). Eigenspannungen und verfestigung beim messing (Self stretching and hardening for brass). In *Proceedings of the Second International Congress for Applied Mechanics*, pages 332–335, Zurich, Switzerland.

[Mathews and Fink, 2002] Mathews, J. H. and Fink, K. D. (2002). Numerical Methods using MATLAB. Technical report, Pearson Prentice Hall, Upper Saddle River, NJ, USA.

[Maurel et al., 2020] Maurel, V., Chiaruttini, V., Abecassis, M., Koster, A., and Dezecot, S. (2020). Influence of a 3D realistic crack path in the driving forces for fatigue crack growth under mode I+II loading. *Theoretical and Applied Fracture Mechanics*, 108:102570.

[Maurel et al., 2017] Maurel, V., Köster, A., Rémy, L., Rambaudon, M., Missoum-Benziane, D., Fontanet, V., Salgado-Goncalves, F., Heudt, A., Wang, H., and Trabelsi, M. (2017). Fatigue crack growth under large scale yielding condition: The need of a characteristic length scale. *International Journal of Fatigue*, 102(Supplement C):184–201.

[Mazars, 1986] Mazars, J. (1986). A model of a unilateral elastic damageable material and its application to concrete. *Fracture Toughness and Fracture Energy of Concrete*, pages 61–71. Publisher: Elsevier Science Publishers.

[Mazars and Pijaudier-Cabot, 1996] Mazars, J. and Pijaudier-Cabot, G. (1996). From damage to fracture mechanics and conversely: A combined approach. *International Journal of Solids and Structures*, 33(20):3327–3342.

[McClung, 1991] McClung, R. C. (1991). Crack Closure and Plastic Zone Sizes in Fatigue. *Fatigue & Fracture of Engineering Materials & Structures*, 14(4):455–468.

[McClung and Sehitoglu, 1989] McClung, R. C. and Sehitoglu, H. (1989). On the finite element analysis of fatigue crack closure - 1. Basic modeling issues. *Engineering Fracture Mechanics*, 33(2):237–252.

[McClung et al., 1991] McClung, R. C., Thacker, B. H., and Roy, S. (1991). Finite element visualization of fatigue crack closure in plane stress and plane strain. *International Journal of Fracture*, 50(1):27–49.

[Mediavilla et al., 2006a] Mediavilla, J., Peerlings, R., and Geers, M. (2006a). A nonlocal triaxiality-dependent ductile damage model for finite strain plasticity. *Computer Methods in Applied Mechanics and Engineering*, 195(33-36):4617–4634.

[Mediavilla et al., 2006b] Mediavilla, J., Peerlings, R. H. J., and Geers, M. G. D. (2006b). Discrete crack modelling of ductile fracture driven by non-local softening plasticity. *International Journal for Numerical Methods in Engineering*, 66(4):661–688.

[Mediavilla et al., 2006c] Mediavilla, J., Peerlings, R. H. J., and Geers, M. G. D. (2006c). An integrated continuous–discontinuous approach towards damage engineering in sheet metal forming processes. *Engineering Fracture Mechanics*, 73(7):895–916.

[Mediavilla et al., 2006d] Mediavilla, J., Peerlings, R. H. J., and Geers, M. G. D. (2006d). A robust and consistent remeshing-transfer operator for ductile fracture simulations. *Computers & Structures*, 84(8):604–623.

[Mediavilla Varas, 2005] Mediavilla Varas, J. (2005). *Continuous and discontinuous modelling of ductile fracture*. Ph.D. thesis, Technische Universiteit Eindhoven, Eindhoven, The Netherlands.

[Michel-Ponnelle, 2011] Michel-Ponnelle, S. (2011). Éléments finis traitant la quasi-incompressibilité. Code_Aster R3.06.08, EDF, Saclay, France.

[Miehe et al., 2010a] Miehe, C., Hofacker, M., and Welschinger, F. (2010a). A phase field model for rate-independent crack propagation: Robust algorithmic implementation based on operator splits. *Computer Methods in Applied Mechanics and Engineering*, 199(45):2765–2778.

[Miehe et al., 2010b] Miehe, C., Welschinger, F., and Hofacker, M. (2010b). Thermodynamically consistent phase-field models of fracture: Variational principles and multi-field FE implementations. *International Journal for Numerical Methods in Engineering*, 83(10):1273–1311.

[Mindlin, 1965] Mindlin, R. D. (1965). Second gradient of strain and surface-tension in linear elasticity. *International Journal of Solids and Structures*, 1(4):417–438.

[Mishra and Parida, 1985] Mishra, S. C. and Parida, B. K. (1985). A study of crack-tip plastic zone by elastoplastic finite element analysis. *Engineering Fracture Mechanics*, 22(6):951–956.

[Mobasher, 2017] Mobasher, M. E. (2017). *Enhanced Continuum Damage Modeling of Mechanical Failure in Ice and Rocks*. Ph.D. thesis, Columbia University, New York, NY, USA.

[Morgeneyer et al., 2010] Morgeneyer, T. F., Proudhon, H., and Besson, J. (2010). Study of the flat to slant crack transition in ductile thin sheet material : simulations and experiments. page 8 p. DVM.

[Moslemi and Khoei, 2009] Moslemi, H. and Khoei, A. R. (2009). 3D adaptive finite element modeling of non-planar curved crack growth using the weighted superconvergent patch recovery method. *Engineering Fracture Mechanics*, 76(11):1703–1728.

[Moslemi and Khoei, 2010] Moslemi, H. and Khoei, A. R. (2010). 3D Modeling of Damage Growth and Crack Initiation Using Adaptive Finite Element Technique. *Scientia Iranica*, 17(5). Publisher: Sharif University of Technology.

[Moës et al., 1999] Moës, N., Dolbow, J., and Belytschko, T. (1999). A finite element method for crack growth without remeshing. *International Journal for Numerical Methods in Engineering*, 46(1):131–150.

[Moës et al., 2011] Moës, N., Stolz, C., Bernard, P.-E., and Chevaugeon, N. (2011). A level set based model for damage growth: The thick level set approach. *International Journal for Numerical Methods in Engineering*, 86(3):358–380.

[Moës et al., 2014] Moës, N., Stolz, C., and Chevaugeon, N. (2014). Coupling local and non-local damage evolutions with the Thick Level Set model. *Advanced Modeling and Simulation in Engineering Sciences*, 1(1):16.

[Mrozowski, 2020] Mrozowski, N. (2020). *Mécanismes de propagation de fissure dans un superalliage base nickel polycristallin en régime d'interaction fatigue-fluage-oxydation-vieillissement métallurgique*. Ph.D. thesis, ISAE-ENSMA Ecole Nationale Supérieure de Mécanique et d'Aérotechique, Poitiers, France.

[Mughrabi, 1985] Mughrabi, H. (1985). *Dislocations and properties of real materials*. Number Book no. 323 in London: The Institute of Metals. London.

[Murakami, 2012] Murakami, S. (2012). *Continuum Damage Mechanics: A Continuum Mechanics Approach to the Analysis of Damage and Fracture*, volume 185 of *Solid Mechanics and Its Applications*. Springer Science & Business Media, Dordrecht, 1st edition.

[Murakami and Liu, 1995] Murakami, S. and Liu, Y. (1995). Mesh-Dependence in Local Approach to Creep Fracture. *International Journal of Damage Mechanics*, 4(3):230–250.

[Murakami and Aoki, 1987] Murakami, Y. and Aoki, S. (1987). *Stress Intensity Factors Handbook*. Pergamon.

[Médeau, 2019] Médeau, V. (2019). *Rupture des composites tissés 3D : de la caractérisation expérimentale à la simulation robuste des effets d'échelle*. Ph.D. thesis, ISAE, ONERA - Châtillon, France.

[Nesnas and Saanouni, 2000] Nesnas, K. and Saanouni, K. (2000). A cycle jumping scheme for numerical integration of coupled damage and viscoplastic models for cyclic loading paths. *Revue Européenne des Éléments Finis*, 9(8):865–891.

[Nguyen, 2011] Nguyen, G. D. (2011). A damage model with evolving nonlocal interactions. *International Journal of Solids and Structures*, 48(10):1544–1559.

[Nguyen, 2000] Nguyen, Q. S. (2000). *Stabilité et Mécanique Non linéaire*. Hermès Science Publications.

[Nguyen et al., 2018] Nguyen, T. H. A., Bui, T. Q., and Hirose, S. (2018). Smoothing gradient damage model with evolving anisotropic nonlocal interactions tailored to low-order finite elements. *Computer Methods in Applied Mechanics and Engineering*, 328:498–541.

[Nijin and Banerjee, 2021] Nijin, I. S. and Banerjee, A. (2021). An incremental elastic–plastic triaxiality dependent fatigue model. *International Journal of Fracture*, 227(1):39–55.

[Nikbin and Webster, 1984] Nikbin, K. and Webster, G.A., C. (1984). Creep-fatigue crack growth in a nickel base superalloy. In *Proceeding of the 2nd International Conference on Creep and Fracture of Engineering Materials and Structures*, pages 1091–1104, Swansea, UK. Pineridge Press Ltd.

[Nikolakopoulos et al., 2021] Nikolakopoulos, K., Crété, J.-P., and Longère, P. (2021). Progressive failure of ductile metals: Description via a three-dimensional coupled CZM-XFEM based approach. *Engineering Fracture Mechanics*, 243:107498.

[Norton, 1929] Norton, F. (1929). *The creep of steel at high temperatures*. New York, mcgraw-hill edition.

[Nouailhas, 1988] Nouailhas, D. (1988). Modélisation de l'écrouissage et de la restauration en viscoplasticité cyclique. *Revue de Physique Appliquée*, 23(4):339–349. Publisher: Société Française de Physique.

[Nouailhas, 1989] Nouailhas, D. (1989). Unified modelling of cyclic viscoplasticity: Application to austenitic stainless steels. *International Journal of Plasticity*, 5(5):501–520.

[Nouailhas et al., 1985] Nouailhas, D., Cailletaud, G., Policella, H., Marquis, D., Dufailly, J., Lieurade, H. P., Ribes, A., and Bollinger, E. (1985). On the description of cyclic hardening and initial cold working. *Engineering Fracture Mechanics*, 21(4):887–895.

[Nouailhas et al., 1983] Nouailhas, D., Policella, H., and Kaczmarek, H. (1983). On the description of cyclic hardening under complex loading histories. Tiré à Part, ONERA, Châtillon, France.

[Ohata et al., 2014] Ohata, M., Masai, S., Shoji, H., Imai, Y., Motohashi, H., and Minami, F. (2014). Numerical Simulation of Flat-to-slant Ductile Fracture Transition in Notched Plate. *Procedia Materials Science*, 3:793–798.

[Oliver, 1996] Oliver, J. (1996). Modelling Strong Discontinuities in Solid Mechanics Via Strain Softening Constitutive Equations. Part 1: Fundamentals. *International Journal for Numerical Methods in Engineering*, 39(21):3575–3600.

[Oliver et al., 2006] Oliver, J., Huespe, A. E., and Sánchez, P. J. (2006). A comparative study on finite elements for capturing strong discontinuities: E-FEM vs X-FEM. *Computer Methods in Applied Mechanics and Engineering*, 195(37):4732–4752.

[Ortiz and Popov, 1985] Ortiz, M. and Popov, E. P. (1985). Accuracy and stability of integration algorithms for elastoplastic constitutive relations. *International Journal for Numerical Methods in Engineering*, 21(9):1561–1576.

[Oskay and Fish, 2004] Oskay, C. and Fish, J. (2004). Fatigue life prediction using 2-scale temporal asymptotic homogenization. *International Journal for Numerical Methods in Engineering*, 61(3):329–359.

[Ostwald et al., 2019] Ostwald, R., Kuhl, E., and Menzel, A. (2019). On the implementation of finite deformation gradient-enhanced damage models. *Computational Mechanics*, 64(3):847–877.

[Otin, 2007] Otin, S. (2007). *Lois d'endommagement incrémentales isotrope/anisotropes pour applications thermomécaniques complexes*. Ph.D. thesis, ENS, Cachan, France.

[Otin et al., 2007] Otin, S., Desmorat, R., Dambrine, B., and Rousel, O. (2007). Lois d'endommagement incrémentales pour le dimensionnement des chambres de combustions de turbomachines. In *S11 - Endommagement & Rupture*, Grenoble.

[Ottosen and Ristinmaa, 2005] Ottosen, N. S. and Ristinmaa, M. (2005). *The Mechanics of Constitutive Modeling*. Elsevier Science Ltd, Oxford.

[Oñate and Castro, 1991] Oñate, E. and Castro, J. (1991). Adaptive Mesh Refinement Techniques for Structural Problems. In Oñate, E., Periaux, J., and Samuelsson, A., editors, *The finite element method in the 1990's: A Book Dedicated to O.C. Zienkiewicz*, pages 133–145. Springer, Berlin, Heidelberg.

[Pandey et al., 2019a] Pandey, V., Singh, I. V., Mishra, B., Ahmad, S., Rao, A., and Kumar, V. (2019a). Creep crack simulations using continuum damage mechanics and extended finite element method. *International Journal of Damage Mechanics*, 28(1):3–34. Publisher: SAGE Publications Ltd STM.

[Pandey et al., 2021] Pandey, V. B., Singh, I. V., and Mishra, B. K. (2021). A Strain-based continuum damage model for low cycle fatigue under different strain ratios. *Engineering Fracture Mechanics*, 242:107479.

[Pandey et al., 2019b] Pandey, V. B., Singh, I. V., Mishra, B. K., Ahmad, S., Venugopal Rao, A., and Kumar, V. (2019b). A new framework based on continuum damage mechanics and XFEM for high cycle fatigue crack growth simulations. *Engineering Fracture Mechanics*, 206:172–200.

[Pardoen and Besson, 2004] Pardoen, T. and Besson, J. (2004). Micromechanics-based constitutive models of ductile fracture. In *Local Approach to Fracture*, pages 221–264. Les Presses de l'Ecole des Mines, Paris, France, 1st edition.

[Paris and Erdogan, 1963] Paris, P. and Erdogan, F. (1963). A Critical Analysis of Crack Propagation Laws. *Journal of Basic Engineering*, 85(4):528–533.

[Paris et al., 1961] Paris, P., Gomez, M., and Anderson, W. (1961). A rational analytic theory of fatigue. *The Trend in Engineering*, 13:9–14.

[Paris, 2008] Paris, T. (2008). *Modélisation du comportement mécanique des liaisons soudées hétérogènes Ta/TV6V : comportement et critère de rupture*. Ph.D. thesis, UTT, Troyes, France.

[Park et al., 1996] Park, H.-B., Kim, K.-M., and Lee, B.-W. (1996). Plastic zone size in fatigue cracking. *International Journal of Pressure Vessels and Piping*, 68(3):279–285.

[Paul, 2016] Paul, S. K. (2016). Numerical models of plastic zones and associated deformations for elliptical inclusions in remote elastic loading–unloading with different R-ratios. *Engineering Fracture Mechanics*, 152:72–80.

[Paul et al., 2011] Paul, S. K., Sivaprasad, S., Dhar, S., and Tarafder, S. (2011). Key issues in cyclic plastic deformation: Experimentation. *Mechanics of Materials*, 43(11):705–720.

[Peerlings et al., 1996a] Peerlings, R., Borst, R., Brekelmans, W., Vree, J., and Spee, I. (1996a). Some observations on localization in non-local and gradient damage models. *European Journal of Mechanics. A, Solids*, 15(6):937–953.

[Peerlings et al., 1996b] Peerlings, R., de Borst, R., Brekelmans, W., and de Vree, J. (1996b). Gradient enhanced damage for quasi-brittle materials. *International Journal for Numerical Methods in Engineering*, 39(19):3391–3403.

[Peerlings et al., 1998] Peerlings, R. H. J., Borst, R. d., Brekelmans, W. a. M., and Geers, M. G. D. (1998). Gradient-enhanced damage modelling of concrete fracture. *Mechanics of Cohesive-frictional Materials*, 3(4):323–342.

[Peerlings et al., 2000] Peerlings, R. H. J., Brekelmans, W. a. M., Borst, R. d., and Geers, M. G. D. (2000). Gradient-enhanced damage modelling of high-cycle fatigue. *International Journal for Numerical Methods in Engineering*, 49(12):1547–1569.

[Peerlings et al., 2002] Peerlings, R. H. J., de Borst, R., Brekelmans, W. A. M., and Geers, M. G. D. (2002). Localisation issues in local and nonlocal continuum approaches to fracture. *European Journal of Mechanics - A/Solids*, 21(2):175–189.

[Peerlings et al., 2001] Peerlings, R. H. J., Geers, M. G. D., de Borst, R., and Brekelmans, W. A. M. (2001). A critical comparison of nonlocal and gradient-enhanced softening continua. *International Journal of Solids and Structures*, 38(44):7723–7746.

[Peerlings et al., 2008] Peerlings, R. H. J., Javani, H. R., Mediavilla, J., and Geers, M. G. D. (2008). Modelling of damage initiation and propagation in metal forming. *International Journal of Material Forming*, 1(1):1123–1126.

[Peerlings, 1999] Peerlings, R. R. (1999). *Enhanced damage modelling for fracture and fatigue*. Ph.D. thesis, Technische Universiteit Eindhoven, Eindhoven, The Netherlands.

[Pelloux, 1970] Pelloux, R. M. N. (1970). Crack extension by alternating shear. *Engineering Fracture Mechanics*, 1(4):697–704.

[Perić et al., 1996] Perić, D., Hochard, C., Dutko, M., and Owen, D. R. J. (1996). Transfer operators for evolving meshes in small strain elasto-placticity. *Computer Methods in Applied Mechanics and Engineering*, 137(3):331–344.

[Perić et al., 1994] Perić, D., Yu, J., and Owen, D. (1994). On error estimates and adaptivity in elasto-plastic solids: Applications to the numerical simulation of strain localization in classical and Cosserat continua. *International Journal for Numerical Methods in Engineering*, 37(8):1351–1379.

[Pijaudier-Cabot and Bažant, 1987] Pijaudier-Cabot, G. and Bažant, Z. P. (1987). Nonlocal Damage Theory. *Journal of Engineering Mechanics*, 113(10):1512–1533.

[Pijaudier-Cabot et al., 2004] Pijaudier-Cabot, G., Haidar, K., and Dubé, J.-F. (2004). Non-local damage model with evolving internal length. *International Journal for Numerical and Analytical Methods in Geomechanics*, 28(7-8):633–652.

[Pineau, 1981] Pineau, A. (1981). High Temperature Fatigue: Creep-Fatigue-Oxidation Interactions in Relation to Microstructure. In Larsson, L., editor, *Subcritical Crack Growth Due to Fatigue, Stress Corrosion and Creep*, volume 4 of *Ispra Courses on Mechanical Science and Materials*, pages 483–530. Elsevier Applied Science, London & New-York.

[Pineau, 2006] Pineau, A. (2006). Development of the Local Approach to Fracture over the Past 25 years: Theory and Applications. *International Journal of Fracture*, 138(1-4):139–166.

[Plumtree and Abdel-Raouf, 2001] Plumtree, A. and Abdel-Raouf, H. A. (2001). Cyclic stress–strain response and substructure. *International Journal of Fatigue*, 23(9):799–805.

[Plumtree and Lemaitre, 1984] Plumtree, A. and Lemaitre, J. (1984). Damage Mechanics Applied to High Temperature Fatigue. In Carlsson, J. and Ohlson, N. G., editors, *Mechanical Behaviour of Materials*, pages 323–329. Pergamon.

[Poh and Sun, 2017] Poh, L. H. and Sun, G. (2017). Localizing gradient damage model with decreasing interactions. *International Journal for Numerical Methods in Engineering*, 110(6):503–522.

[Pollock and Tin, 2006] Pollock, T. M. and Tin, S. (2006). Nickel-Based Superalloys for Advanced Turbine Engines: Chemistry, Microstructure and Properties. *Journal of Propulsion and Power*, 22(2):361–374.

[Polák et al., 2001] Polák, J., Fardoun, F., and Degallaix, S. (2001). Analysis of the hysteresis loop in stainless steels I. Austenitic and ferritic steels. *Materials Science and Engineering: A*, 297(1):144–153.

[Pommier, 2003] Pommier, S. (2003). Cyclic plasticity and variable amplitude fatigue. *International Journal of Fatigue*, 25(9):983–997.

[Pommier, 2007] Pommier, S. (2007). Cyclic Plasticity of a Cracked Structure Subjected to Mixed Mode Loading. *Key Engineering Materials*, 348-349:105–108. Conference Name: Advances in Fracture and Damage Mechanics VI ISBN: 9780878494484 Publisher: Trans Tech Publications Ltd.

[Pommier, 2015] Pommier, S. (2015). Development of an Incremental Model for Fatigue Crack Growth Predictions. *Aerospace Lab*, 9(11):1–12.

[Pommier and Bompard, 2000] Pommier, S. and Bompard, P. (2000). Bauschinger effect of alloys and plasticity-induced crack closure: a finite element analysis. *Bauschinger effect of alloys and plasticity-induced crack closure: a finite element analysis*, 23(2):129–139. Place: Oxford Publisher: Blackwell Science.

[Pommier et al., 2011] Pommier, S., Gravouil, A., Combescure, A., and Moës, N. (2011). *Extended Finite Element Method for Crack Propagation*. ISTE Ltd and John Wiley & Sons, Inc., 1st edition.

[Pommier and Hamam, 2007] Pommier, S. and Hamam, R. (2007). Incremental model for fatigue crack growth based on a displacement partitioning hypothesis of mode I elastic–plastic displacement fields. *Fatigue & Fracture of Engineering Materials & Structures*, 30(7):582–598.

[Pommier and Risbet, 2005] Pommier, S. and Risbet, M. (2005). Time-derivative equations for fatigue crack growth in metals. *International Journal of Fracture*, 131(1):79–106.

[Prisacari, 2018] Prisacari, V.-I. (2018). *Modeling of partial mean stress relaxation and biaxial mechanical testing of Inco718DA*. Ph.D. thesis, Université Paris-Saclay, Cachan, France.

[Pétry, 2006] Pétry, C. (2006). *Caractérisation et modélisation du comportement et de l'endommagement d'alliages métalliques sur une grande plage de température*. Ph.D. thesis, École normale supérieure de Cachan - ENS Cachan, Cachan, France.

[Qian et al., 1996] Qian, Z., Takezono, S., and Tao, K. (1996). A nonlocal damage mechanics approach to high temperature fatigue crack growth. *Engineering Fracture Mechanics*, 53(4):535–543.

[Rabczuk, 2013] Rabczuk, T. (2013). Computational Methods for Fracture in Brittle and Quasi-Brittle Solids: State-of-the-Art Review and Future Perspectives. *ISRN Applied Mathematics*, 2013:1–38.

[Rabczuk and Belytschko, 2007] Rabczuk, T. and Belytschko, T. (2007). A three-dimensional large deformation meshfree method for arbitrary evolving cracks. *Computer Methods in Applied Mechanics and Engineering*, 196(29):2777–2799.

[Rabotnov, 1969] Rabotnov, J. N. (1969). *Creep Problems in Structural Members*, volume 7 of *North-Holland Series in Applied Mathematics and Mechanics*. North-Holland Publishing Company. Google-Books-ID: HtRMQwAACAAJ.

[Rahimi et al., 2017] Rahimi, S., King, M., and Dumont, C. (2017). Stress relaxation behaviour in IN718 nickel based superalloy during ageing heat treatments. *Materials Science and Engineering: A*, 708:563–573.

[Rahman and Bahrami, 2010] Rahman, S. and Bahrami, R. (2010). Numerical modeling the effects of overloading and underloading in fatigue crack growth. *Engineering Failure Analysis*, 17(6):1475–1482.

[Ramesh and Maniatty, 2005] Ramesh, B. and Maniatty, A. M. (2005). Stabilized finite element formulation for elastic–plastic finite deformations. *Computer Methods in Applied Mechanics and Engineering*, 194(6):775–800.

[Rastiello et al., 2018] Rastiello, G., Giry, C., Gatuingt, F., and Desmorat, R. (2018). From diffuse damage to strain localization from an Eikonal Non-Local (ENL) Continuum Damage model with evolving internal length. *Computer Methods in Applied Mechanics and Engineering*, 331:650–674.

[Reckwerth and Tsakmakis, 2003] Reckwerth, D. and Tsakmakis, C. (2003). The Principle of Generalized Energy Equivalence in Continuum Damage Mechanics. In Hutter, K. and Baaser, H., editors, *Deformation and Failure in Metallic Materials*, Lecture Notes in Applied and Computational Mechanics, pages 381–406. Springer Berlin Heidelberg, Berlin, Heidelberg.

[Reed et al., 1993] Reed, P. A. S., Gale, W. F., and King, J. E. (1993). Intrinsic thresholds in polycrystalline Udimet 720. *Materials Science and Technology*, 9(4):281–287.

[Reed, 2006] Reed, R. (2006). *The Superalloys: Fundamentals and Applications*. Cambridge University Press.

[Ren et al., 2016] Ren, S. C., Rousselier, G., Morgeneyer, T. F., Mazière, M., and Forest, S. (2016). Numerical investigation of dynamic strain ageing and slant ductile fracture in a notched specimen and comparison with synchrotron tomography 3D-DVC. *Procedia Structural Integrity*, 2:3385–3392.

[Reusch et al., 2003] Reusch, F., Svendsen, B., and Klingbeil, D. (2003). A non-local extension of Gurson-based ductile damage modeling. *Computational Materials Science*, 26:219–229.

[Rice, 1967] Rice, J. (1967). Mechanics of Crack Tip Deformation and Extension by Fatigue. *Fatigue Crack Propagation*, ASTM STP 415:247–309. Publisher: ASTM International.

[Rice, 1968] Rice, J. R. (1968). A Path Independent Integral and the Approximate Analysis of Strain Concentration by Notches and Cracks. *Journal of Applied Mechanics*, 35(2):379–386. Publisher: American Society of Mechanical Engineers Digital Collection.

[Risbet et al., 2001] Risbet, M., Feaugas, X., and Clavel, M. (2001). Study of the cyclic softening of an under-aged gamma'-precipitated nickel-base superalloy (Waspaloy). *Le Journal de Physique IV*, 11(PR4):Pr4–301. Publisher: EDP Sciences.

[Rodriguez and Bhanu Sankara Rao, 1993] Rodriguez, P. and Bhanu Sankara Rao, K. (1993). Nucleation and growth of cracks and cavities under creep-fatigue interaction. *Progress in Materials Science*, 37(5):403–480.

[Rodríguez-Ferran et al., 2005] Rodríguez-Ferran, A., Morata, I., and Huerta, A. (2005). A new damage model based on non-local displacements. *International Journal for Numerical and Analytical Methods in Geomechanics*, 29(5):473–493.

[Rouse et al., 2020] Rouse, J. P., Engel, B., Hyde, C. J., Pattison, S. J., Whittaker, M. T., Jones, J. P., Cockings, B., and Barnard, N. C. (2020). A viscoelastic-viscoplastic material model for superalloy applications. *International Journal of Fatigue*, 136:105579.

[Rousselier, 1986] Rousselier, G. (1986). Les modèles de rupture ductile et leurs possibilités acuelles dans le cadre de l'approche locale de la rupture. Moret-sur-Loing, France.

[Rousselier, 1987] Rousselier, G. (1987). Ductile fracture models and their potential in local approach of fracture. *Nuclear Engineering and Design*, 105(1):97–111.

[Rousselier, 2001] Rousselier, G. (2001). Dissipation in porous metal plasticity and ductile fracture. *Journal of the Mechanics and Physics of Solids*, 49(8):1727–1746.

[Réthoré et al., 2004] Réthoré, J., Gravouil, A., and Combescure, A. (2004). A stable numerical scheme for the finite element simulation of dynamic crack propagation with remeshing. *Computer Methods in Applied Mechanics and Engineering*, 193(42):4493–4510.

[Saanouni, 2008] Saanouni, K. (2008). On the numerical prediction of the ductile fracture in metal forming. *Engineering Fracture Mechanics*, 75(11):3545–3559.

[Saanouni, 2012] Saanouni, K. (2012). *Damage Mechanics in Metal Forming - Advanced Modeling and Numerical Simulation*. John Wiley & Sons, Ltd, London, 1st edition.

[Saanouni and Chaboche, 2003] Saanouni, K. and Chaboche, J.-L. (2003). Computational Damage Mechanics: Application to Metal Forming Simulation. In Milne, I., Ritchie, R. O., and Karihaloo, B., editors, *Comprehensive Structural Integrity*, pages 321–376. Pergamon, Oxford.

[Saanouni et al., 1989] Saanouni, K., Chaboche, J.-L., and Lesne, P.-M. (1989). On the creep crack-growth prediction by a non local damage formulation. *European Journal of Mechanics - A/Solids*, 8(6):437–459.

[Saanouni et al., 1994] Saanouni, K., Forster, C., and Hatira, F. B. (1994). On the Anelastic Flow with Damage. *International Journal of Damage Mechanics*, 3(2):140–169.

[Sabnis, 2012] Sabnis, P. A. (2012). *Modélisation numérique de la propagation et de la bifurcation des fissures dans les superalliages monocristallins à base de nickel*. Ph.D. thesis, Ecole Nationale Supérieure des Mines de Paris, Paris, France.

[Sabnis et al., 2016] Sabnis, P. A., Forest, S., and Cormier, J. (2016). Microdamage modelling of crack initiation and propagation in FCC single crystals under complex loading conditions. *Computer Methods in Applied Mechanics and Engineering*, 312:468–491.

[Saloustros et al., 2019] Saloustros, S., Cervera, M., and Pelà, L. (2019). Challenges, Tools and Applications of Tracking Algorithms in the Numerical Modelling of Cracks in Concrete and Masonry Structures. *Archives of Computational Methods in Engineering*, 26(4):961–1005.

[Samal, 2007] Samal, M. K. (2007). *Nonlocal damage models for structural integrity analysis*. Ph.D. thesis, Universität Stuttgart, Stuttgart, Germany.

[Samal et al., 2009a] Samal, M. K., Seidenfuss, M., and Roos, E. (2009a). A new mesh-independent Rousselier's damage model: Finite element implementation and experimental verification. *International Journal of Mechanical Sciences*, 51(8):619–630.

[Samal et al., 2009b] Samal, M. K., Seidenfuss, M., Roos, E., Dutta, B. K., and Kushwaha, H. S. (2009b). A mesh-independent Gurson-Tvergaard-Needleman damage model and its application in simulating ductile fracture behaviour. *Proceedings of the Institution of Mechanical Engineers, Part C: Journal of Mechanical Engineering Science*, 223(2):283–292.

[Saouma and Zatz, 1984] Saouma, V. E. and Zatz, I. J. (1984). An automated finite element procedure for fatigue crack propagation analyses. *Engineering Fracture Mechanics*, 20(2):321–333.

[Schijve, 1981] Schijve, J. (1981). Shear lips on fatigue fractures in aluminium alloy sheet material. *Engineering Fracture Mechanics*, 14(4):789–800.

[Schoettle, 2013] Schoettle, C. (2013). *Sustained macroscopic deflected cracking in Nickel based superalloys: mechanism and design criteria*. Ph.D. thesis, University of Southampton, Southampton, UK.

[Schoettle et al., 2012] Schoettle, C., Sinclair, I., Starink, M. J., and Reed, P. A. S. (2012). Deflected 'teardrop cracking' in nickel based superalloys: Sustained macroscopic deflected fatigue crack growth. *International Journal of Fatigue*, 44:188–201.

[Schreiber et al., 2020] Schreiber, C., Kuhn, C., Müller, R., and Zohdi, T. (2020). A phase field modeling approach of cyclic fatigue crack growth. *International Journal of Fracture*, 225(1):89–100.

[Schwarz et al., 2011] Schwarz, W., Schwub, S., Quering, K., Wiedmann, D., Höppel, H. W., and Göken, M. (2011). Life prediction of thermally highly loaded components: modelling the damage process of a rocket combustion chamber hot wall. *CEAS Space Journal*, 1(1):83.

[Seabra et al., 2013] Seabra, M., Šuštarič, P., César de Sá, J., and Rodič, T. (2013). Damage driven crack initiation and propagation in ductile metals using XFEM. *Computational Mechanics*, 52(1):161–179.

[Seabra, 2012] Seabra, M. R. R. (2012). *Continuous-Discontinuous Approach for the Modelling of Ductile Fracture*. Ph.D. thesis, Universidade Do Porto - Faculdade de Engenharia - Departamento de Engenharia Mecânica, Porto, Portugal.

[Seidenfuss and Linse, 2016] Seidenfuss, M. and Linse, T. (2016). Micromechanical-Based Models for Describing Damage of Ferritic Steels. In Hütter, G. and Zybell, L., editors, *Recent Trends in Fracture and Damage Mechanics*, pages 353–416. Springer Science & Business Media, Cham, Switzerland, springer international publishing switzerland 2016 edition.

[Seidenfuss et al., 2011] Seidenfuss, M., Samal, M. K., and Roos, E. (2011). On critical assessment of the use of local and nonlocal damage models for prediction of ductile crack growth and crack path in various loading and boundary conditions. *International Journal of Solids and Structures*, 48(24):3365–3381.

[Seleš et al., 2021] Seleš, K., Aldakheel, F., Tonković, Z., Sorić, J., and Wriggers, P. (2021). A general phase-field model for fatigue failure in brittle and ductile solids. *Computational Mechanics*, 67(5):1431–1452.

[Sellars and McTegart, 1966] Sellars, C. M. and McTegart, W. J. (1966). On the mechanism of hot deformation. *Acta Metallurgica*, 14(9):1136–1138.

[Seupel et al., 2018] Seupel, A., Hütter, G., and Kuna, M. (2018). An efficient FE-implementation of implicit gradient-enhanced damage models to simulate ductile failure. *Engineering Fracture Mechanics*, 199:41–60.

[Seupel et al., 2020] Seupel, A., Hütter, G., and Kuna, M. (2020). On the identification and uniqueness of constitutive parameters for a non-local GTN-model. *Engineering Fracture Mechanics*, 229:106817.

[Seupel and Kuna, 2019] Seupel, A. and Kuna, M. (2019). A gradient-enhanced damage model motivated by engineering approaches to ductile failure of steels. *International Journal of Damage Mechanics*, 28(8):1261–1296.

[Shakoor et al., 2019] Shakoor, M., Trejo Navas, V. M., Pino Munõz, D., Bernacki, M., and Bouchard, P.-O. (2019). Computational Methods for Ductile Fracture Modeling at the Microscale. *Archives of Computational Methods in Engineering*, 26(4):1153–1192.

[Si et al., 2020] Si, Y., Rouse, J. P., and Hyde, C. J. (2020). Potential difference methods for measuring crack growth: A review. *International Journal of Fatigue*, 136:105624.

[Sidoroff, 1981] Sidoroff, F. (1981). Description of Anisotropic Damage: Application to Elasticity. In Hult, J. and Lemaitre, J., editors, *Physical Non-Linearities in Structural Analysis*, International Union of Theoretical and Applied Mechanics, pages 237–244, Berlin, Heidelberg. Springer.

[Silling and Askari, 2014] Silling, S. and Askari, A. (2014). Peridynamic model for fatigue cracks. SNL Report SAND2014-18529C, Sandia National Laboratories, Albuquerque, NM, USA.

[Silling, 2000] Silling, S. A. (2000). Reformulation of elasticity theory for discontinuities and long-range forces. *Journal of the Mechanics and Physics of Solids*, 48(1):175–209.

[Simatos, 2010] Simatos, A. (2010). *Méthode XFEM pour la Modélisation de grandes propagations de fissure en déchirure ductile : Transition d'un Milieu Continu vers une Fissure via un modèle de zone cohésive pour le modèle de Rousselier*. These de doctorat, Lyon, INSA.

[Simkins and Li, 2006] Simkins, D. C. and Li, S. (2006). Meshfree simulations of thermo-mechanical ductile fracture. *Computational Mechanics*, 38(3):235–249.

[Simo and Hughes, 1998] Simo, J. and Hughes, T. (1998). *Computational Inelasticity*, volume 7 of *Interdisciplinary Applied Mathematics*. Springer, New-York, NY, springer-verlag new york, inc. 1998 edition.

[Simo and Ju, 1987] Simo, J. C. and Ju, J. W. (1987). Strain- and stress-based continuum damage models—I. Formulation. *International Journal of Solids and Structures*, 23(7):821–840.

[Simo and Ju, 1989] Simo, J. C. and Ju, J. W. (1989). Strain- and stress-based continuum damage models—I. Formulation. *Mathematical and Computer Modelling*, 12(3):378.

[Simo et al., 1993] Simo, J. C., Oliver, J., and Armero, F. (1993). An analysis of strong discontinuities induced by strain-softening in rate-independent inelastic solids. *Computational Mechanics*, 12(5):277–296.

[Simo and Taylor, 1985] Simo, J. C. and Taylor, R. L. (1985). Consistent tangent operators for rate-independent elastoplasticity. *Computer Methods in Applied Mechanics and Engineering*, 48(1):101–118.

[Simone et al., 2004] Simone, A., Askes, H., and Sluys, L. J. (2004). Incorrect initiation and propagation of failure in non-local and gradient-enhanced media. *International Journal of Solids and Structures*, 41(2):351–363.

[Simone et al., 2003] Simone, A., Wells, G. N., and Sluys, L. J. (2003). From continuous to discontinuous failure in a gradient-enhanced continuum damage model. *Computer Methods in Applied Mechanics and Engineering*, 192(41):4581–4607.

[Simonsen and Li, 2004] Simonsen, B. and Li, S. (2004). Mesh-free simulation of ductile fracture. *International Journal for Numerical Methods in Engineering*, 60(8):1425–1450.

[Skallerud and Zhang, 1997] Skallerud, B. and Zhang, Z. L. (1997). A 3D numerical study of ductile tearing and fatigue crack growth under nominal cyclic plasticity. *International Journal of Solids and Structures*, 34(24):3141–3161.

[Skelton and Gandy, 2008] Skelton, R. P. and Gandy, D. (2008). Creep-fatigue damage accumulation and interaction diagram based on metallographic interpretation of mechanisms. *Materials at High Temperatures*, 25(1):27–54.

[Skrzypek and Ganczarski, 1999] Skrzypek, J. J. and Ganczarski, A. (1999). *Modeling of Material Damage and Failure of Structures*. Foundations of Engineering Mechanics. Springer-Verlag, Berlin, Heidelberg, 1st edition.

[Sládek et al., 2003] Sládek, J., Sládek, V., and Bažant, Z. P. (2003). Non-local boundary integral formulation for softening damage. *International Journal for Numerical Methods in Engineering*, 57(1):103–116.

[Solanki et al., 2004] Solanki, K., Daniewicz, S. R., and Newman, J. C. (2004). Finite element analysis of plasticity-induced fatigue crack closure: an overview. *Engineering Fracture Mechanics*, 71(2):149–171.

[Song et al., 2008] Song, J.-H., Wang, H., and Belytschko, T. (2008). A comparative study on finite element methods for dynamic fracture. *Computational Mechanics*, 42(2):239–250.

[Soniak and Rémy, 1987] Soniak, F. and Rémy, L. (1987). Behaviour of long and short fatigue cracks in a powder metallurgy superalloy at room and at high temperature. In *Proceeding of the 3rd International Conference on Fatigue and Fatigue Thresholds*, pages 351–360, Charlotesville, Virginia, USA.

[Sornin, 2007] Sornin, D. (2007). *Sur les formulations élastoplastiques non locales en gradient d'endommagement*. Ph.D. thesis, UTT, Troyes, France.

[Spanier and Oldham, 1987] Spanier, J. and Oldham, K. B. (1987). *An Atlas of Functions*. Hemisphere Pub. Corp., New York, NY, USA, 1st edition.

[Staroselsky et al., 2014] Staroselsky, A., Martin, T. J., and Cassenti, B. (2014). Transient Thermal Analysis and Viscoplastic Damage Model for Life Prediction of Turbine Components. *Journal of Engineering for Gas Turbines and Power*, 137(042501).

[Storgärds, 2015] Storgärds, E. (2015). *High Temperature Fatigue Crack Growth in a Ni-based Superalloy*. Ph.D. thesis, Linköping University, Division of Engineering Materials, Linköping, Sweden.

[Sun et al., 2013] Sun, Y., Maciejewski, K., and Ghonem, H. (2013). A damage-based cohesive zone model of intergranular crack growth in a nickel-based superalloy. *International Journal of Damage Mechanics*, 22(6):905–923. Publisher: SAGE Publications Ltd STM.

[Suresh, 1998] Suresh, S. (1998). *Fatigue of Materials*. Cambridge University Press, 2nd edition.

[Suresh and Ritchie, 1984] Suresh, S. and Ritchie, R. O. (1984). Propagation of short fatigue cracks. *International Metals Reviews*, 29(1):445–475.

[Szmytka et al., 2010] Szmytka, F., Rémy, L., Maitournam, H., Köster, A., and Bourgeois, M. (2010). New flow rules in elasto-viscoplastic constitutive models for spheroidal graphite cast-iron. *International Journal of Plasticity*, 26(6):905–924.

[Tamayo-Mas, 2013] Tamayo-Mas, E. (2013). *Continuous-discontinuous modelling for quasi-brittle failure: propagating cracks in a regularised bulk*. Ph.D. thesis, Universitat Politècnica de Catalunya, Barcelona, Spain.

[Tamayo-Mas and Rodríguez-Ferran, 2014] Tamayo-Mas, E. and Rodríguez-Ferran, A. (2014). A new continuous-discontinuous damage model: Cohesive cracks via an accurate energy-transfer process. *Theoretical and Applied Fracture Mechanics*, 69:90–101.

[Tamayo-Mas and Rodríguez-Ferran, 2015] Tamayo-Mas, E. and Rodríguez-Ferran, A. (2015). A medial-axis-based model for propagating cracks in a regularised bulk. *International Journal for Numerical Methods in Engineering*, 101(7):489–520.

[Tang et al., 2020] Tang, Z., Jing, H., Xu, L., Chi, D., Zhao, L., Han, Y., Li, H., and Ma, N. (2020). Investigation of creep-fatigue crack growth of G115 steel using a novel damage model. *International Journal of Mechanical Sciences*, 183:105827.

[Tarnowski et al., 2018a] Tarnowski, K., Nikbin, K., Dean, D., and Davies, C. (2018a). A Unified Potential Drop Calibration Function for Common Crack Growth Specimens. *Experimental Mechanics*, 58(6):1003–1013.

[Tarnowski et al., 2018b] Tarnowski, K. M., Nikbin, K. M., Dean, D. W., and Davies, C. M. (2018b). Improvements in the measurement of creep crack initiation and growth using potential drop. *International Journal of Solids and Structures*, 134:229–248.

[Thierry et al., 2019] Thierry, F., Rastiello, G., Giry, C., and Gatuingt, F. (2019). Analyse unidimensionnelle de la transition " endommagement non local eikonal-fissure cohésive ". In *14ème Colloque National en Calcul des Structures, CSMA 2019*, Presqu'île de Giens, France.

[Thébaud, 2017] Thébaud, L. (2017). *Etude des relations entre microstructure et propriétés mécaniques du nouveau superalliage base nickel AD730™*. Ph.D. thesis, ISAE-ENSMA, Poitiers, France.

[Thébaud et al., 2016] Thébaud, L., Thébaud, L., Villechaise, P., Cormier, J., Hamon, F., Crozet, C., Devaux, A., Franchet, J.-M., Rouffié, A.-L., and Organista, A. (2016). Relationships Between Mi-

crostructural Parameters and Time-Dependent Mechanical Properties of a New Nickel Based Superalloy AD730™. In *Superalloys 2016*, pages 877–886. Wiley-Blackwell.

[Tong et al., 1997] Tong, J., Byrne, J., Hall, R., and Aliabadi, M. (1997). A comparison of corner notched and compact tension specimens for high temperature fatigue testing. In *Proceedings of the Conference Engineering Against Fatigue*, University of Sheffield, U.K. Taylor & Francis Group.

[Tourjansky, 2013] Tourjansky, I. (2013). Développement d'un banc d'essai de propagation de fissure en fatigue à haute température : application à un superalliage pour disque de turbine. Master's thesis, Ecoles des Mines d'Albi-Carmaux, Châtillon, France.

[Trabelsi, 2019] Trabelsi, M. (2019). *Propagation de fissures en fatigue oligocyclique multiaxiale à haute température pour le superalliage HAYNES® 188*. Ph.D. thesis, PSL Research University, Paris, France.

[Truesdell, 1969] Truesdell, C. (1969). *Rational Thermodynamics*. McGraw-Hill.

[Truesdell and Toupin, 1960] Truesdell, C. and Toupin, R. (1960). The Classical Field Theories of Mechanics. In Flügge, S., editor, *Principles of Classical Mechanics and Field Theory / Prinzipien der Klassischen Mechanik und Feldtheorie*, Encyclopedia of Physics / Handbuch der Physik, pages 226–858. Springer, Berlin, Heidelberg.

[Tuhkuri, 1997] Tuhkuri, J. (1997). Dual boundary element analysis of closed cracks. *International Journal for Numerical Methods in Engineering*, 40(16):2995–3014.

[Tvergaard and Needleman, 1984] Tvergaard, V. and Needleman, A. (1984). Analysis of the cup-cone fracture in a round tensile bar. *Acta Metallurgica*, 32(1):157–169.

[Tvergaard and Needleman, 1995] Tvergaard, V. and Needleman, A. (1995). Effects of nonlocal damage in porous plastic solids. *International Journal of Solids and Structures*, 32(8):1063–1077.

[Tvergaard and Needleman, 1997] Tvergaard, V. and Needleman, A. (1997). Nonlocal effects on localization in a void-sheet. *International Journal of Solids and Structures*, 34(18):2221–2238.

[Ulloa et al., 2021] Ulloa, J., Wambacq, J., Alessi, R., Degrande, G., and François, S. (2021). Phase-field modeling of fatigue coupled to cyclic plasticity in an energetic formulation. *Computer Methods in Applied Mechanics and Engineering*, 373:113473.

[Vaz and Owen, 2001] Vaz, M. and Owen, D. R. J. (2001). Aspects of ductile fracture and adaptive mesh refinement in damaged elasto-plastic materials. *International Journal for Numerical Methods in Engineering*, 50(1):29–54.

[Velde, 2010] Velde, J. (2010). *3D Nonlocal Damage Modeling for Steel Structures under Earthquake Loading*. Ph.D. thesis, Technische Universität Braunschweig, Braunschweig, Germany.

[Venables and King, 1984] Venables, R. A. and King, J. E. (1984). Effects of dynamic strain ageing on fatigue crack propagation and threshold behaviour in a Ni-base superalloy. In *Fatigue 84: proceedings of the 2nd International conference on fatigue and fatigue thresholds; Birmingham, 3-7 September 1984*, pages 1371–1378.

[Vincent, 2010] Vincent, S. (2010). *Caractérisation et modélisation du comportement et de l'endommagement de deux alliages de cuivre sous chargements thermo-mécaniques sévères*. Ph.D. thesis, Université Paris 6, Paris, France.

[Voce, 1955] Voce, E. (1955). A practical strain hardening function. *Metallurgia*, 51:219–226.

[Vor, 2009] Vor, K. (2009). *Etude expérimentale et modélisation numérique de la fermeture de fissures longues et courtes dans un acier inoxydable 304L*. Thèse, ISAE-ENSMA, Poitiers, France.

[Voyiadjis and Al-Rub, 2005] Voyiadjis, G. Z. and Al-Rub, R. K. A. (2005). Gradient plasticity theory with a variable length scale parameter. *International Journal of Solids and Structures*, 42(14):3998–4029.

[Voyiadjis et al., 2012] Voyiadjis, G. Z., Hoseini, S. H., and Farrahi, G. H. (2012). Effects of stress invariants and reverse loading on ductile fracture initiation. *International Journal of Solids and Structures*, 49(13):1541–1556.

[Vultos, 2019] Vultos, W. (2019). *Influence de la microstructure sur les micromécanismes de déformation en fluage dans le superalliage AD730TM*. Ph.D. thesis, Université de Toulouse, Toulouse, France.

[Wang and Zhang, 2015] Wang, Y. Q. and Zhang, H. B. (2015). Low Cycle Fatigue Study for GH901 Material Based on Damage Mechanics Theory. *Applied Mechanics and Materials*, 711:40–43. Conference Name: Mechanical Engineering, Materials Science and Civil Engineering III ISBN: 9783038353720 Publisher: Trans Tech Publications Ltd.

[Warren and Wei, 2006] Warren, J. and Wei, D. Y. (2006). The cyclic fatigue behavior of direct age 718 at 149, 315, 454 and 538°C. *Materials Science and Engineering: A*, 428(1):106–115.

[Washizu, 1955] Washizu, K. (1955). On the variational principles of elasticity and plasticity. Technical report, MIT Cambridge Aeroelastic and Structures Research Lab. Section: Technical Reports.

[Wheeler, 1972] Wheeler, O. E. (1972). Spectrum Loading and Crack Growth. *Journal of Basic Engineering*, 94(1):181–186.

[Wierzbicki et al., 2005] Wierzbicki, T., Bao, Y., Lee, Y.-W., and Bai, Y. (2005). Calibration and evaluation of seven fracture models. *International Journal of Mechanical Sciences*, 47(4):719–743.

[Wilkins, 1964] Wilkins, M. L. (1964). Calculation of elastic-plastic flow. *Methods of Computational Physics*, 3.

[Willenborg et al., 1971] Willenborg, J., Engle, R., and Wood, H. (1971). A Crack Growth Retardation Model Using an Effective Stress Concept. *Defense Technical Information Center*, (Technical Memorandum 71-1-FBR):22. Google-Books-ID: s1VanQAACAAJ.

[Wolf, 2016] Wolf, J. (2016). *Traitement numérique de la fissuration dans les matériaux structuraux ductiles sous l'effet de sollicitations sévères*. Ph.D. thesis, Université de Toulouse, Toulouse, France.

[Wolf et al., 2018] Wolf, J., Longère, P., Cadou, J. M., and Crété, J. P. (2018). Numerical modeling of strain localization in engineering ductile materials combining cohesive models and X-FEM. *International Journal of Mechanics and Materials in Design*, 14(2):177–193.

[Wu et al., 2016] Wu, C. T., Ma, N., Takada, K., and Okada, H. (2016). A meshfree continuous–discontinuous approach for the ductile fracture modeling in explicit dynamics analysis. *Computational Mechanics*, 58(3):391–409.

[Wu and Yeh, 1991] Wu, H. C. and Yeh, W. C. (1991). On the experimental determination of yield surfaces and some results of annealed 304 stainless steel. *International Journal of Plasticity*, 7(8):803–826.

[Wu et al., 2012] Wu, L., Noels, L., Adam, L., and Doghri, I. (2012). A multiscale mean-field homogenization method for fiber-reinforced composites with gradient-enhanced damage models. *Computer Methods in Applied Mechanics and Engineering*, 233-236:164–179.

[Wöhler, 1860] Wöhler, A. (1860). Versuche über die festigkeit der eisenbahnwagenachsen. *Zeitschrift für Bauwesen*, 10.

[Xenos, 2015] Xenos, D. (2015). *Nonlocal modelling of fracture in heterogeneous quasi-brittle materials*. Ph.D. thesis, University of Glasgow, Glasgow, UK.

[Xia et al., 1993] Xia, S., Takezono, S., and Tao, K. (1993). Nonlocal elastic damage near crack tip. *International Journal of Fracture*, 62(1):87–95.

[Xiao et al., 2005] Xiao, L., Chen, D. L., and Chaturvedi, M. C. (2005). Shearing of γ" precipitates and formation of planar slip bands in Inconel 718 during cyclic deformation. *Scripta Materialia*, 52(7):603–607.

[Xu et al., 2017] Xu, L., Zhao, L., Gao, Z., and Han, Y. (2017). A novel creep-fatigue interaction damage model with the stress effect to simulate the creep–fatigue crack growth behavior. *International Journal of Mechanical Sciences*, 130:143–153.

[Xue and Wierzbicki, 2008] Xue, L. and Wierzbicki, T. (2008). Ductile fracture initiation and propagation modeling using damage plasticity theory. *Engineering Fracture Mechanics*, 75(11):3276–3293.

[Xue and Wierzbicki, 2009] Xue, L. and Wierzbicki, T. (2009). Ductile fracture characterization of aluminum alloy 2024-t351 using damage plasticity theory. *International Journal of Applied Mechanics*, 01(02):267–304.

[Yan and Nguyen-Dang, 1995] Yan, A. M. and Nguyen-Dang, H. (1995). Multiple-cracked fatigue crack growth by BEM. *Computational Mechanics*, 16(5):273–280.

[Yang, 2017] Yang, F. (2017). *Simulation of continuous damage and fracture in metal-forming processes with 3D mesh adaptive methodology*. Ph.D. thesis, Université de Technologie de Compiègne, UTC, Compiègne, France.

[Yang et al., 2018] Yang, F. T., Rassineux, A., Labergere, C., and Saanouni, K. (2018). A 3D h-adaptive local remeshing technique for simulating the initiation and propagation of cracks in ductile materials. *Computer Methods in Applied Mechanics and Engineering*, 330:102–122.

[Yin et al., 2022] Yin, B., Zreid, I., Zhao, D., Ahmed, R., Lin, G., and Kaliske, M. (2022). Thermo-mechanical fatigue life prediction of metallic materials by a gradient-enhanced viscoplastic damage approach. *International Journal for Numerical Methods in Engineering*, (preprint).

[Yu et al., 2011] Yu, Q., Zhang, J., Jiang, Y., and Li, Q. (2011). Multiaxial fatigue of extruded AZ61A magnesium alloy. *International Journal of Fatigue*, 33(3):437–447.

[Yun et al., 2019] Yun, K., Wang, Z., Chang, M., Liu, J., Kim, T.-J., Son, N., Ji, K., and Ronald, S. (2019). A computational methodology for simulating quasi-brittle fracture problems. *Computers & Structures*, 215:65–79.

[Zeramdini, 2018] Zeramdini, B. (2018). *Apport des méthodes de remaillage pour la simulation de champs localisés. Validation en usinage par corrélation d'images.* Ph.D. thesis, ENSAM, Paris, France.

[Zhang et al., 2016] Zhang, G., Le, Q., Loghin, A., Subramaniyan, A., and Bobaru, F. (2016). Validation of a peridynamic model for fatigue cracking. *Engineering Fracture Mechanics*, 162:76–94.

[Zhang et al., 2012] Zhang, J., Cherouat, A., and Borouchaki, H. (2012). FE Simulation of Metal Orthogonal Cutting Processes Based on 3D Adaptive Remeshing Procedure. *Advanced Materials Research*, 409:461–466. Conference Name: THERMEC 2011 Supplement ISBN: 9783037853047 Publisher: Trans Tech Publications Ltd.

[Zhang et al., 2021] Zhang, K., Badreddine, H., Yue, Z., Hfaiedh, N., Saanouni, K., and Liu, J. (2021). Failure prediction of magnesium alloys based on improved CDM model. *International Journal of Solids and Structures*.

[Zhang, 2016] Zhang, Y. (2016). *Modélisation et simulation numérique robuste de l'endommagement ductile*. Ph.D. thesis, PSL Research University, Paris, France.

[Zhang et al., 2018] Zhang, Y., Lorentz, E., and Besson, J. (2018). Ductile damage modelling with locking-free regularised GTN model. *International Journal for Numerical Methods in Engineering*, 113(13):1871–1903.

[Zhao et al., 2012] Zhao, L., Jing, H., Han, Y., Xiu, J., and Xu, L. (2012). Prediction of creep crack growth behavior in ASME P92 steel welded joint. *Computational Materials Science*, 61:185–193.

[Zhao et al., 2021] Zhao, Q., Abdel Wahab, M., Ling, Y., and Liu, Z. (2021). Fatigue crack propagation within Al-Cu-Mg single crystals based on crystal plasticity and XFEM combined with cohesive zone model. *Materials & Design*, 210:110015.

[Zhao et al., 2020] Zhao, Y., Hu, D., Zhang, M., Dai, W., and Zhang, W. (2020). In Situ Measurements for Plastic Zone Ahead of Crack Tip and Continuous Strain Variation under Cyclic Loading Using Digital Image Correlation Method. *Metals*, 10(2):273. Number: 2 Publisher: Multidisciplinary Digital Publishing Institute.

[Zhou et al., 2018] Zhou, J., Sun, Z., Kanouté, P., and Retraint, D. (2018). Experimental analysis and constitutive modelling of cyclic behaviour of 316L steels including hardening/softening and strain range memory effect in LCF regime. *International Journal of Plasticity*, 107:54–78.

[Zhu, 2017] Zhu, Y. (2017). *Studies on strain localization, ductile fracture and damage in structural metals*. Ph.D. thesis, University of Texas, Austin, TX, USA.

[Zienkiewicz et al., 1999] Zienkiewicz, O. C., Boroomand, B., and Zhu, J. Z. (1999). Recovery procedures in error estimation and adaptivity Part I: Adaptivity in linear problems. *Computer Methods in Applied Mechanics and Engineering*, 176(1):111–125.

[Zienkiewicz and Taylor, 2000] Zienkiewicz, O. C. and Taylor, R. L. (2000). *The Finite Element Method: Solid mechanics*, volume 1. Butterworth-Heinemann, 1st edition.

[Zienkiewicz et al., 1971] Zienkiewicz, O. C., Taylor, R. L., and Too, J. M. (1971). Reduced integration technique in general analysis of plates and shells. *International Journal for Numerical Methods in Engineering*, 3(2):275–290.

[Zienkiewicz et al., 2013] Zienkiewicz, O. C., Taylor, R. L., and Zhu, J. Z. (2013). *The Finite Element Method: Its Basis and Fundamentals*. Butterworth-Heinemann, 7th edition.

[Zienkiewicz and Zhu, 1987] Zienkiewicz, O. C. and Zhu, J. Z. (1987). A simple error estimator and adaptive procedure for practical engineerng analysis. *International Journal for Numerical Methods in Engineering*, 24(2):337–357.

[Zienkiewicz and Zhu, 1992] Zienkiewicz, O. C. and Zhu, J. Z. (1992). The superconvergent patch recovery (SPR) and adaptive finite element refinement. *Computer Methods in Applied Mechanics and Engineering*, 101(1):207–224.

[Zuidema and Blaauw, 1988] Zuidema, J. and Blaauw, H. S. (1988). Slant fatigue crack growth in A1 2024 sheet material. *Engineering Fracture Mechanics*, 29(4):401–413.

[Zuo et al., 2004] Zuo, J., Deng, X., Sutton, M., and Cheng, C.-S. (2004). Crack tunneling: effect of stress constraint. In *Proceedings of IMECE04*, pages 1–8, Anaheim, California, USA. ASME.

université PARIS-SACLAY

ÉCOLE DOCTORALE
Sciences mécaniques et énergétiques, matériaux et géosciences (SMEMAG)

Titre: Modélisation de la propagation de fissure en fatigue à haute température dans les superalliages base Nickel par une approche locale de la rupture

Mots clés: Fatigue, Modèle incrémental en temps, Comportement, Endommagement, Modèle non-local, Transition endommagement-rupture, Superalliage base Nickel

Résumé: Cette thèse vise à évaluer les capacités d'une approche locale de la rupture à simuler la propagation d'une fissure longue de fatigue dans des composants structurels. Une démarche en trois étapes est envisagée. Tout d'abord, le comportement cyclique non linéaire du superalliage base Nickel AD730™ est étudié à l'aide d'essais de caractérisation cyclique à trois températures cibles (20, 550 et 700°C). Des essais de propagation de fissures sur éprouvettes sont ensuite réalisés afin de mettre en évidence les principaux mécanismes pilotant la fissuration. Un modèle décrivant le comportement cyclique non-linéaire de l'AD730™ est proposé. Un couplage fort comportement-endommagement est ensuite établi conduisant à un modèle d'endommagement incrémental pour la fatigue. Ce modèle est implémenté dans un code éléments finis à l'aide d'un schéma de résolution purement implicite. Pour résoudre le problème de dépendance au maillage, une extension non-locale du modèle d'endommagement est proposée en utilisant une formulation à gradient implicite. Puis, une étape d'adaptation de maillage basée sur un estimateur d'erreurs est utilisée pour raffiner la discrétisation dans la zone d'élaboration de la fissure. Une fois l'amorçage atteint, un algorithme de suivi du chemin de fissure est utilisé pour définir la géométrie et la direction de l'incrément de fissure. Enfin, une transition endommagement-rupture incluant des étapes de remaillage, de transfert de champs et de rééquilibrage de la structure est effectuée. La cinétique associée à l'avancée de la fissure est alors retranscrite. La boucle numérique est évaluée lors de calculs sur une éprouvette SEN-T soumise à des chargements complexes de fatigue et fatigue-fluage. Les capacités de l'approche proposée et ses limites sont finalement discutées.

Title: High temperature fatigue crack growth modeling in Nickel-based superalloys using a local approach to fracture

Keywords: Fatigue, Time-incremental model, Constitutive equations, Damage, Non-local model, Damage-to-fracture transition, Nickel-based superalloy

Abstract: This PhD project aims at assessing the capabilities associated with the local approach to fracture to simulate the propagation of a long fatigue crack in structural components. To this end, a three-step approach is considered. First, the cyclic non-linear behavior of the Nickel-based superalloy AD730™ is studied using dedicated cyclic characterization tests at three target temperatures (20, 550 and 700°C). Crack propagation tests on laboratory specimens are then performed in order to evidence the main crack driving mechanisms. Next, a set of constitutive equations for the cyclic non-linear behavior of AD730™ is proposed and calibrated. A strong behavior-damage coupling is settled leading to a time-incremental damage model for fatigue. The model is implemented in a finite element code using a fully implicit resolution scheme. In order to solve for the mesh-dependency issue, a non-local extension of the damage model is proposed using an implicit gradient formulation. Finally, an error-based mesh adaption procedure is considered in order to refine the mesh in the fracture process zone, close to the crack-tip where the non-linear phenomena occur. Once crack onset is achieved, a crack path tracking algorithm is used to evaluate the geometry and the direction of the crack increment. Then, a damage-to-crack transition consisting in remeshing steps, fields transfer and equilibrium recovery is performed. This way, crack growth kinetics can be captured. The whole numerical loop is assessed on calculations conducted on a SEN-T specimen subjected to complex fatigue and creep-fatigue loading conditions. The capabilities of the proposed approach and its limitations are finally discussed.